COMPUMAG 2003

Conference on the Computation of Magnetic Fields

Saratoga Springs, New York
July 13–17, 2003

Volume I

COMPUMAG

14th Conference on the Computation of Magnetic Fields

July 13-17, 2003
Saratoga Springs, New York USA

Record of the 14th COMPUMAG Conference
on the Computation of Magnetic Fields

Volume I: Monday, July 14

COMPUMAG 2003

14th Conference on the Computation of Magnetic Fields
Saratoga Springs, New York, USA
July 13-17, 2003

Compumag 2003 Committee:

Prof. Sheppard J. Salon, Chairman
Rensselaer Polytechnic Institute, Troy, NY USA
Philippe Wendling, Vice Chairman
Magsoft Corporation, Troy, NY USA
David Burow, Secretariat
Genfo, Inc., Troy, NY USA

Local Organizing Committee:

M. DeBortoli K. Sivasubramaniam
M. Lean M. Shah
I. Mayergoyz S. Babic
U. Deshpande

Editorial Board Chairmen:

J. Webb, McGill University, Montreal, Quebec Canada
D. Giannacopoulos, McGill University, Montreal, Quebec Canada
Email: edboard.compumag2003@mcgill.ca

Correspondence:

Compumag 2003
1223 Peoples Ave
Troy, NY 12180 USA
Email : secretariat@compumag2003.com

Lodging Arrangements Made By:

Sherie Klein, Carlson Wagonlit/Albany Travel
30 Corporate Drive, Clifton Park, NY 12065 USA
Phone: +1 (518) 292-9000
Email: corporate@albanytravel.com

COMPUMAG 2003 Chairman's Welcome

Welcome to COMPUMAG 2003, the 14th Conference on the Computation of Electric and Magnetic Fields!

In the 27 years since the first COMPUMAG Conference in 1976 at Oxford, we have seen the society and the conference continue to grow in numbers, in significance and in international renown and respect. We are honored, therefore, to carry on what has become a well-established tradition of presenting the leading research and thought in the area of computational electromagnetics.

Because of its high standards and rigorous review process, the Conference has become the place to present in our field. This year 429 papers were approved for presentation in 8 oral sessions and 32 poster sessions. The contributors represent 30 different countries. Our deep thanks go to the editorial board and to the co-chairs Jon Webb and Dennis Giannacopoulos, who did an outstanding job.

And welcome to Saratoga Springs, New York! Those of us fortunate to live and work in New York's Capital District can take advantage of some of the best opportunities in the United States for research and education; cultural, historical and recreational resources; and small cities and towns where neighbors still don't lock their doors. Nearby research institutions and universities include Rensselaer, GE Global Research Laboratories, Knolls Atomic Power Laboratory, IBM Research Laboratory and others. New York City, Boston, and Montreal, with their rich historical and cultural resources, are all within a few hours' drive. Finally, there is the peace and friendliness of smaller towns and villages, like Saratoga Springs, where you are sure to enjoy the activities we have planned; we hope you will also take time to explore on your own.

COMPUMAG 2003 offers lively scientific exchange to charm the intellect and convivial activities to warm the heart. Welcome!

Prof. Sheppard J. Salon
COMPUMAG 2003 Chairman

City of Saratoga Springs

Kenneth Klotz, Mayor
Hank Kuczynski, Deputy Mayor

July, 2003

Welcome!

On behalf of the entire City of Saratoga Springs, I would like to welcome the ***14th Conference on the Computation of Electromagnetic Fields*** to Saratoga Springs!

As you know, Saratoga Springs is a world-class resort destination, which offers cosmopolitan amenities without the drawbacks of a typical metropolitan area. Our city takes great pride in its hospitality to visitors. We offer world-class attractions, wonderful restaurants, unique shops and a host of related activities that your attendees are sure to enjoy!

Saratoga Springs looks forward to hosting the ***14th Conference on the Computation of Electromagnetic Fields and its attendees.***

Once again, Welcome to our City, where we invite you to.....***Experience Saratoga!***

Sincerely,

Kenneth Klotz
Mayor

City Hall, Saratoga Springs, New York 12866-2296
518/587-3550 • 518/587-1688 fax

COMPUMAG 2003 Editorial Board

Chairmen: J. Webb, D. Giannacopoulos

COMPUMAG 2003 Program at a Glance

	July 13 Sunday	July 14 Monday	July 15 Tuesday	July 16 Wednesday	July 17 Thursday	
7:00		Continental Breakfast Buffet	Continental Breakfast Buffet	Continental Breakfast Buffet	Continental Breakfast Buffet	7:00
8:00		Formulations Saratoga Ballroom	Devices Saratoga Ballroom	Quasistatic Saratoga Ballroom	Inverse Problems Saratoga Ballroom	8:00
10:15		Coffee Break	Coffee Break	Coffee Break	Coffee Break	10:15
10:45		Numerical Techniques I Coupled Problems I Devices I Statics I	Numerical Techniques II Coupled Problems II Machines II Statics II	Numerical Techniques III Coupled Problems III Devices III Software	Numerical Techniques IV Coupled Problems IV Machines IV Devices IV	10:45
12:00		Lunch: Grand Ballroom – High Rock	Lunch: Grand Ballroom – High Rock	Lunch: Grand Ballroom – High Rock	Lunch: Grand Ballroom – High Rock	12:00
1:30		Optimization I Waves I Machines I Quasistatic I	Optimization II Waves II Devices II Quasistatic II	Optimization III EMC Machines IIII Materials I	Optimization IV Materials II Education – TEAM Quasistatic III	1:30
2:45		Afternoon Break	Afternoon Break	Afternoon Break	Afternoon Break	2:45
3:15	Registration* 2:00 – 6:00 p.m.	Methodologies Saratoga Ballroom	Materials Saratoga Ballroom	Waves Saratoga Ballroom	Optimization Saratoga Ballroom	3:15
5:30		Enjoy Saratoga!	5:00 Short Break (no refreshments)		Have a safe and pleasant journey home!	5:30
			5:15 Panel Session: Topic To Be Announced Saratoga Ballroom			
6:30	Evening Reception Saratoga Ballroom		6:15 Enjoy Saratoga!	Banquet at the Canfield Casino		6:30

* Registration will also be available each day from 7:00 AM to 12:00 noon and from 1:30 to 2:45 PM.

COMPUMAG 2003 Technical Program

Monday, July 14, 2003

	8:00 – 10:15
Oral Session	
	Formulations Saratoga Ballroom
	10:45 – 12:00
Poster Session	
	Numerical Techniques I: Mesh generation and parallel computations
	Coupled Problems I: Global coupling; Rigid body kinematics
	Devices I: Biomedical and Biological Applications
	Statics I: Electrostatics
	1:30 – 2:45
Poster Session	
	Optimization I
	Waves I: FDTD and TLM
	Machines I: Linear, SR, SynRel
	Quasistatic I
	3:15 – 5:30
Oral Session	
	Methodologies Saratoga Ballroom

Formulations
Monday, July 14, 8:00am - 10:15am
Chairmen
Dr. Bill Trowbridge
Prof. Arnulf Kost

Numerical Techniques I: Mesh generation and parallel computations
Monday, July 14, 10:45am - 12:00pm
Chairman
Dr. Ilaria Perugia

Coupled Problems I: Global Coupling, Rigid Body Kinematics Chairman
Monday, July 14, 10:45am - 12:00pm Saku Suuriniemi

Devices I: Biomedical and Biological Applications Chairman
Monday, July 14, 10:45am - 12:00pm Dr. Frederic Bouillault

Statics I: Electrostatics

Monday, July 14, 10:45am - 12:00pm

Chairmen
Dr. Dave Rodger
Dr. Zoran Andjelic

Optimization I

Monday, July 14, 1:30pm - 2:45pm

Chairmen
Dr. Xiang Cui
Dr. Kay Hameyer

Waves I: FDTD and TLM Chairman
Monday, July 14, 1:30pm - 2:45pm Dr. Milica Popovic

Machines I: Linear, SR, SynRel Chairman
Monday, July 14, 1:30pm - 2:45pm Dr. Tan H. Pham

Quasistatic I Chairman
Monday, July 14, 1:30pm - 2:45pm Dr. Virgiliu Fireteanu

Methodologies Chairman
Monday, July 14, 3:15pm - 5:30pm Prof. Norio Takahashi

COMPUMAG Saratoga Springs, New York USA
July 13 - 17, 2003

The question of forces: Long-standing controversies, modern geometrical tools

Alain Bossavit†
†LGEP, 11 Rue Joliot-Curie, 91192 Gif-sur-Yvette CEDEX, France

Abstract—**An introduction to the *Lie derivative,* a standard concept in differential geometry, here seen as a tool for force computation in electro-magneto-mechanical problems.**

Attending all Compumag conferences so far was a pleasurable experience, but doesn't qualify one to reminisce on this series of events with anything even remotely like thoroughness, balance, and accuracy. Asked to give a historical twist to the present contribution, I will evoke only one of the trends that can be discerned in our multi-faceted activity: the *geometrization* of its underlying theory, which now-predictible advances on the question of *forces* should confirm in the future.

The saga of edge elements is a case in point: first seen as a rather exotic brand of finite elements ("mixed" ones, we said at the time, with telltaling obscurity), they came to be recognized as the *natural* finite elements for the kind of fields they were meant to approximate, namely, differential forms. Just as classical scalar elements are barycentric coordinates of *points*, with respect to mesh-nodes of a mesh, edge elements can be seen as barycentric coordinates for *segments*, with respect to mesh-edges. In both cases, one approximates a differential form (DF) of degree p, with $p = 0$ and $p = 1$ respectively, thanks to degrees of freedom (DoF) assigned to mesh-elements of dimension p.

More recently, efforts to bridge the gap between "variational", finite-element based, methods, and modern avatars of FDTD—quite efficient, and apparently free of any references to approximants—such as FIT and the "cell method", led some of us to investigate how the *Hodge operators,* ν and ε, relate with the constitutive coefficients thus usually denoted. Whether the gap *is* now bridged is an open question, but that a debate on such *computational* issues took place within a *differential geometric* arena is something that was hardly predictable 25 years ago. Yet, it's in tune with the evolution of contemporary physics, including computational physics, in the direction of increasing geometrization.

This being considered, one can justifiably wonder whether differential geometry cannot be mined further for other useful tools. The *Lie derivative,* as we shall see here, is one, relevant to the vast application field of force computations. The Lie derivative of a tensor (and more generally, of a vaster class of geometric objects), with respect to a given vector field v, is the rate of variation of this object as convected by v. The "object", there, can be the density of magnetic (co-)energy, hence the connexion with the virtual work principle. This will be explained below, along with suggestions on how a specific *calculus* can be developed on this basis. It's not taking a big risk to predict that we shall see more and more of such calculations in the future [4, 5]: expanding fields of applied research such as micro-motors, magnetostriction, etc., whose modelling involves coupled problems, will require them.

Flows, Lie dragging, Lie derivative

The right approach to forces, in numerical work inclusively [3], is via the virtual power principle: Force is the dual object f in a duality bracket $\langle f ; v \rangle$, where the primal object v is virtual displacement, the real value of the bracket being virtual power. Here, we are after the force density field inside a massive body, so v must be a vector field (independent of time). By solving the differential equation $d_t y = u(y)$ with initial condition $y(0) = x$, one finds a curve $t \to u_t(x)$ which can be interpreted as the *trajectory* of a particle sitting at x at time 0, and dragged along by the flow the velocity field of which is v. This word, *flow* (of v), is used to refer to the t-indexed family of mappings u_t, from Euclidean space E_3 into itself, thus obtained. Now, if R is the region occupied by some body B at time 0, the set $u_t(R) = \{u_t(x) : x \in R\}$ of images of points of R via u_t can be considered as the result of *dragging* (and hence, deforming) B by the flow of v *from time* 0 *to* t. The concept of dragging applies to many kinds of such "bodies", not only 3D regions, but lines, surfaces, etc. In particular, a pair of nearby points $\{x, y\}$ is dragged onto another pair $\{u_t(x), u_t(y)\}$, and by letting y tend to x, we find what it means to drag a *vector* ξ anchored at x: the flow "convects" it to another vector, anchored at $u_t(x)$, traditionally denoted by $(u_t)_*\xi$, and computable from the derivative of u_t (the so-called "tangent map") in an obvious way.

Now (as an example, but the generalization to all kinds of DFs should be obvious), let's consider a 2-form such as b, magnetic induction, that is to say, the map that assigns to any oriented surface S the magnetic flux $\int_S b$ embraced by this surface. (We rather denote this flux $\langle S ; b \rangle$, here, for merely typographical reasons.) To avoid confusion between the above parameter t and actual time, let's assume, provisionally, that b is stationary. Now imagine surface S as made of material particles that are dragged along, and measure the flux embraced by this moving "material surface", that is to say, $\langle u_t(S) ; b \rangle$, as time goes on. The *Lie derivative* of b, a 2-form like b itself, denoted $L_v b$, is by definition the map

$S \to \lim_{t=0} t^{-1} [\langle u_t(S) ; b\rangle - \langle S ; b\rangle]$, that is to say, the assignment to S of the *rate of change* of the measured flux. An alternative definition, once defined the *pull-back* $u_t^* b$ of b, that is to say, the 2-form $S \to \langle u_t(S) ; b\rangle$, is this: $L_v b = \lim_{t=0} [u_t^* b - b]/t$. Both definitions are more precise, but somewhat less illuminating, than the following graphical description: The *Lie derivative* of a field is its *rate of variation as perceived by an observer who moves with the flow*. (Now, if b depends on time, this variation is $\partial_t b + L_v b$.) Beyond differential forms, the Lie derivative acts on all kinds of tensorial objects, and in particular, on the Hodge operator: Setting ν_u such that $\nu_u u^* = u^* \nu$ (same thing with μ and σ), the Lie derivative of ν_u is

$$(1) \qquad \lim_{t=0} [\nu_{u(t)} - \nu]/t = L_v \nu - \nu L_v$$

(read this as applied, from the left, to a 2-form b), one of a handful of useful formulas, among which Cartan's "magic formula", $L_v = i_v d + d i_v$ (here a consequence of the definition), and integration-by-parts tricks like $\int L_v b \wedge h = -\int b \wedge L_v h$. Such formulas require some familiarization, but one can at all times revert to vector formalism, thanks to a small lexicon of correspondences (where ~ stands for "is the proxy of"): If $B \sim b$, then $B \times v \sim i_v b$, $\operatorname{div} B \sim db$; If $H \sim h$, then $\operatorname{rot} H \sim dh$, $v \cdot H = i_v h$; Hence the respective proxies of $L_v h$ and $L_v b$: $\operatorname{rot} H \times v + \operatorname{grad}(v \cdot H)$ and $v \operatorname{div} B + \operatorname{rot}(B \times v)$.

To this "continuous" calculus corresponds a "discrete" one, based (in addition to the usual ingredients, primal and dual mesh, incidence matrices, discrete Hodge operators) on a specific discretization of the so-called "inner product" $i_v b$. Details will be given in the full-length paper (but see [2]).

Computing Forces

To give the flavor of computations using this toolbox, let's consider the case of moving conductors, with $\mu = \mu_0$ all over. From the equations, which in Lagrangian form (i.e., in a comoving frame) are $\partial_t b + de = 0$, $h = \nu_\mu b$, $dh = \sigma_u e + j^s$, one first derives, denoting by $\Psi(u, b) = {}^1\!/_2 \int \nu_u b \wedge b$ the magnetic energy,

$$d_t[\Psi(u(t), b(t))] + \int \sigma_u e \wedge e + \int j^s \wedge e = - \langle \partial_u \Psi(u, b) ; v \rangle,$$

or in words, <rate of increase of magnetic energy> + <Joule losses> + <fed-in power> = <work exerted on outside world> (i.e., virtual power), which shows that the force field is the mapping $v \to - \partial_u \Psi(u, b)$ at $u = u_0$ (the reference configuration). By (1), $- \partial_u \Psi(u, b) = {}^1\!/_2 \int (\nu L_v - L_v \nu) b \wedge b \equiv \int L_v b \wedge h = \int i_v b \wedge dh = \int i_v b \wedge j$, that is, in terms of proxies, $\int J \times B \cdot v$, the expected formula. (On how to derive the term $- {}^1\!/_2 |H|^2 \operatorname{grad} \mu$, which appears when $\mu \neq \mu_0$, see [1].)

Next, we shall investigate the question of forces inside a permanent magnet, long considered a controversial puzzle, and solve it in a perhaps unexpected manner: It all depends on what "permanent" means, for this word can be understood in two different ways, both natural, depending on whether magnetization is handled as a 1-form or a 2-form in formulas. One may write (still, in the Lagrangian setup), either

$$(2) \qquad \text{(i)} \quad b = \mu_u h + b_r \quad \text{or} \quad \text{(ii)} \quad b = \mu_u (h + h_c),$$

where the 2- and 1-form b_r and h_c are *constant*, whatever the deformation. Both laws are realistic: By immersing a lot of microscopic hard magnets in a flexible material (some kind of putty, say), one gets a composite with "constant" b_r (at mesoscopic scale), because the flux due to b_r embraced by a fixed material surface is constant in time. On the other hand, a sprinkling of small coils bearing permanent currents (superconductive coils, say), will give a constant h_c (unchanged Amperian intensity through a material surface). The magnetic energy in cases (2-i) and (2-ii) is, respectively,

$$(3\text{-i}) \qquad \Psi(u, b) = {}^1\!/_2 \int \nu_u b \wedge (b - 2b_r),$$

$$(3\text{-ii}) \qquad \Psi(u, b) = {}^1\!/_2 \int \nu_u b \wedge b - \int b \wedge h_c,$$

and obviously, differentiation with respect to u will give different results. All computations wrapped up, and introducing the proxies $H_c \sim h_c$ and $B_r \sim b_r$, one finds as force field

$$(4\text{-i}) \qquad f = J \times B - (J + J_c) \times B_r - (H + H_c) \operatorname{div} B_r,$$

$$(4\text{-ii}) \qquad f = (J + J_c) \times B$$

respectively, where H_c in (4-i) is *defined* as $H_r = \nu_0 B_r$, with $J_c = \operatorname{rot} H_c$ in both cases.

That results diverge this way should not be felt as a paradox, in spite of the fact that (2-i) and (2-ii), expressed in terms of proxies, *do coincide* when $u = u_0$: $B = \mu_0 H + B_r \equiv \mu_0 (H + H_c)$. These constitutive laws differ, since b_r constant and $h_c = \nu_u b_r$ imply h_c *not* constant, and the other way round. In coupled magnetomechanical problems, more generally, it's the dependence of the *pair* h–σ (σ for stress, there) on the *pair* b–ε (ε for strain) that makes the overall constitutive law, so even if one does not address the problem of computing the deformation, knowing how h depends on b *and* on ε (hence, on u) is a prerequisiste to applying the virtual power principle. Distinct laws, as in (2), yield distinct force fields. A review of the history of force computations in the Compumag record will show that contradictions and controversies in this matter stemmed from imprecise specification of behavior laws. The role geometry can play, and will play more and more, is to provide this needed definiteness.

References

[1] A. Bossavit: "Edge-element Computation of the Force Field in Deformable Bodies", *IEEE Trans., MAG-28,* 2 (1992), pp. 1263-66.

[2] A. Bossavit: "Extrusion, contraction: their discretization via Whitney forms", *COMPEL, 22,* 3 (2003), pp. 470-80.

[3] J.L. Coulomb: "A methodology for the determination of global electromechanical quantities from a finite element analysis and its application to the evaluation of magnetic forces, torques and stiffness", *IEEE Trans., MAG-19,* 6 (1983), pp. 2514-19.

[4] F. Henrotte, K. Hameyer: "Differential Geometry in Computational Electromechanics", to appear.

[5] I. Nishiguchi, A. Kameari, K. Haseyema: "On the Local Force Computation of Deformable Bodies in Magnetic Field", *IEEE Trans., MAG-35,* 3 (1999), pp. 1650-3.

Working Field Theory Problems with Random Walks

Kent R. Davey
American Maglev, Inc, 2275 Turnbull Bay Rd., New Smyrna Beach, FL 32168-5941, USA

Abstract - The point solution of any Laplacian field problem can be viewed as the solid angle average of the derichlet potentials from that point. Alternatively it can be viewed as the average of the termination potential of a number of random walks. Poisson and Helmholtz equations add the complexity of collecting a number of packets along this walk. This paper generalizes the Monte Carlo theory to all classes of field theory problems, including velocity based eddy current problems, which have never been examined in this manner. The exercise is not merely pedagogical since this non standard approach lends itself quickly to parallel process coding.

Index terms - Parallel processing, Random numbers, Finite Difference

I. INTRODUCTION

Finite element and boundary element methods now dominate the industry as the methods of choice for solving field theory problems. Monte Carlo methods were introduced over 58 years ago [1], but still await the strong advent of parallel processing computers before they will be competitive with the more classical direct methods. This paper discusses a different way of approaching field theory problems, the bulk of which depends on random numbers. The work has three motivations.

1. To discuss an analysis approach which lends itself to what will undoubtedly be the trend in computers - parallel processing. There are some fundamental barriers to increasing the processor speed, but seemingly less so to the number of parallel processors.
2. To offer a method that gives the field theoretician yet another way of thinking about a field problem, hopefully one that will add to additional intuitive insight into their expected solutions.
3. To generalize the theory to a broad class of field theory problems. In researching the subject in the IEEE database, it seems that only one paper discussed application of the technique to eddy current problems [2], and none have attempted to generalize the theory to eddy problems with motion.

The number of papers discussing the use of the Monte Carlo method in the actual calculation of electric and magnetic fields are few. Micu [3]discusses a simple application of the method to electrostatic problems, and Mandayam, et.al, [4] discuss its application to a magnetostatic problem. Sadiku [5] paper that discuss it under the variant of the fixed aleatory route.

Manuscript received Nov. 1, 2002. K. Davey (386) 426-1215, kdavey@American-Maglev.com. Work supported by American Maglev, Inc.

The three classes of problems to be discussed are Laplacian, Poisson, and Helmholtz. These universal formulations have not been worked out before especially for generalized eddy problems involving velocity. A universal formulation to any 3D problem will be presented for the Laplacian problem. Then the formulation of Poisson and Helmholtz problems will be presented. These formulations remain the same regardless of the dimensionality of the problem. Given that working hypothesis, specific examples will focus on one dimensional problems for the second two classes of problems.

II. LAPLACIAN PROBLEMS

The problem

$$\nabla^2 \Phi = 0 \tag{1}$$

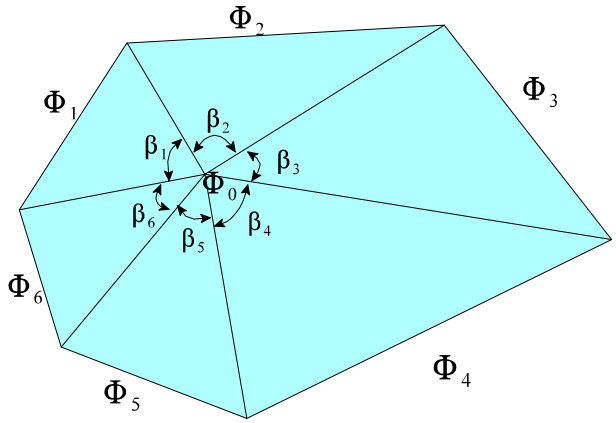

Fig. 1 The field point potential is related to the perimeter potentials through the angle subtended.

has been considered in [3] and [4] through electrostatic and magnetostatic examples. Consider first that the solution of any three dimensional Laplacian problem can be thought of as the weighted sum of the potentials as seen through the solid angle subtended from the border surfaces to the desired field point. Consider the two dimensional problem shown in Fig. 1. The potential Φ_0 is related to the perimeter potentials as

$$\Phi_0 = \frac{1}{2\pi} \sum_{k=1}^{6} \beta_k \Phi_k . \tag{2}$$

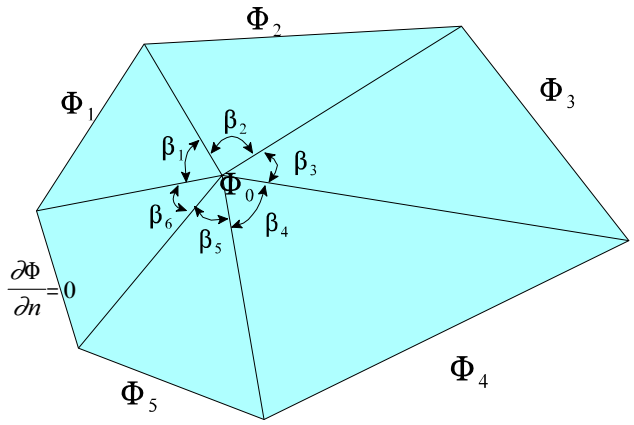

Fig. 2 A Neumann boundary condition will always act like a mirror.

If one of the borders has a Neumann boundary condition as shown in Fig. 2, the potential changes to

$$\Phi_0 = \frac{1}{(2\pi - \beta_6)} \sum_{k=1}^{5} \beta_k \Phi_k . \qquad (3)$$

It will be shown that problems such as this can be approached through a random walk process in which packets are collected along the trip. These packets are in general both added and multiplied amongst one another to build a representative solution. The details of this process will be discussed in the full paper.

Consider a magnetic field problem in two dimensions with a conducting body moving with a velocity v. The governing equation for the vector potential n a time harmonic problem can be written as

$$\nabla^2 \vec{A} - k^2 \vec{A} + \mu\sigma \vec{v} \times \nabla \times \vec{A} = -\mu \vec{J}, \qquad (4)$$

where $k^2 = j\omega\mu\sigma$. In a one dimensional embodiment, this equation can be written as

$$\frac{d^2 A}{dx^2} - k^2 A - \mu\sigma v \frac{dA}{dx} = -\mu J. \qquad (5)$$

The discretized form of this equation yields the result

$$A_0 = \frac{\left\{ A_1 \left(1 - \frac{\mu\sigma v}{2} \delta x \right) + A_{-1} \left(1 + \frac{\mu\sigma v}{2} \delta x \right) + \mu J \delta x^2 \right\}}{2 \left(1 + \frac{k^2 \delta x^2}{2} \right)} \qquad (6)$$

The random walk involves summing the packets involving μJ, again with the multiplier $(1+k^2 \delta x^2/2)$. The random walk would be that in (7), and the solution the average of a number of such walks. The multiplier has a ± sign. If the random is to the right, a minus sign is employed, while if to the left, a plus sign. Let μJ=100, μσv=24, and k^2=3. The results of three random walks are shown in Fig. 3, Fig. 7. The direction dependent sign, and the results argue for a larger number of walks for the same accuracy.

$$R_{walk\ m} = A_n \prod_{step\ i=1}^{n} \frac{\left(1 \pm \frac{\mu\sigma v}{2} \delta x \right)}{\left(1 + \frac{k^2 \delta x^2}{2} \right)} + \sum_{i=1}^{n} \left\{ \frac{\mu J \delta x^2}{2} \prod_{step\ j=1}^{i} \frac{\left(1 \pm \frac{\mu\sigma v}{2} \delta x \right)}{\left(1 + \frac{k^2 \delta x^2}{2} \right)} \right\}. \qquad (7)$$

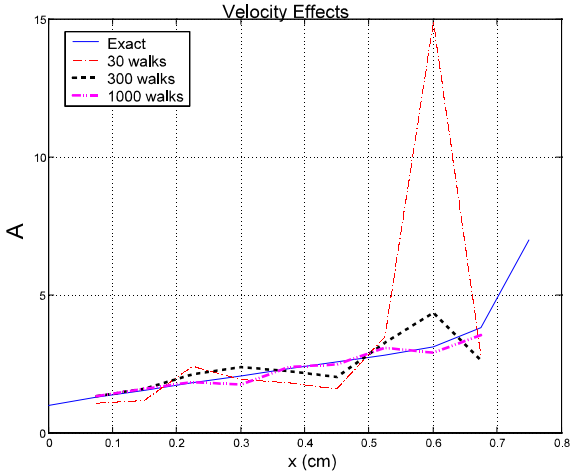

Fig. 3 Random walk predictions with velocity.

VI. CONCLUSIONS

Monte Carlo methods are useful in providing a new ways of looking at field theory problems. The collection of packets with appropriate multipliers has proven to be one approach applicable to a range of problems.

IV. REFERENCES

[1]. S. Katatuni, "Two dimensional Brownian Motion and Harmonic Functions", *Proceedings of the Imperial Academy of Japan*, vol. XX, no. 9, pp. 706-714, November 1944.

[2]. K. R. Davey and M. B. Nair, "A Monte Carlo Technique for Solving Eddy Current Problems", *IEEE Transactions on Magnetics*, vol. 29, no. 2, pp. 1376-1379, March 1993.

[3]. Dan Micu, Numerical Synthesis of Electrostatic Fields by the Monte Carlo Method", *IEEE Transactions on Magnetics*, vol. 29, no. 2, pp. 1966-1969, March 1996.

[4]. S. Mandayam, L. Upta, S.S. Upda, and W. Lord, "Monte Carlo Methods for Modeling Magnetostatic NDE Phenomena: A Feasibility Study", *IEEE Transactions on Magnetics*, vol. 32, no. 3, pp. 1425-1427, May 1996.

[5]. M.N.O. Sadiku, "Monte Carlo Methods in an introductory electromagnetic course", *IEEE Trans. Educ.*, vol. 33, no. 1, pp. 73-79, 1990.

[6]. P. Girdinio, P. Molfino, G. Molinari, L. Puglisi, and A. Viviani, "Finite Difference Discretization Procedures with Improved Continuity of Interpolation

From thermostatistic to Maxwell equations: A variational approach of electromagnetism

Vincent Mazauric
Schneider Electric Corporate Research / A2
38050 – Grenoble Cedex 9 – France

Abstract – **In this paper, Maxwell equations are derived from thermodynamic principles. While divergence-free flux density is obtained everywhere from the stationarity of the Gibbs free energy, the Maxwell-Faraday equation and the Ohm's law with motion are obtained, in conductors, by assuming an adiabatic and reversible evolution of the field. Hence, Maxwell-Faraday equation may be extended in the dielectric region for any time-varying excitation. Besides, magnetic- and dielectric-behavior laws result from the convexity of the magnetic and electrostatic Gibbs potentials. Furthermore, the Laplace and Lorentz forces are obtained from virtual work principle. Extension to high frequencies is also proposed beyond the plasma pulsation of metal. At last, the consistency of the approach with Finite Element Method is emphasized in order to present further integration of design tools dedicated to industrial and economic growth and ecological challenges.**

I. Introduction

Usually, the Finite Element Method (FEM) is presented as a numerical tool to solve Maxwell equations. Then, electrodynamical forces are derived from virtual works or other suitable methods. The following presentation consists in starting from variational principles obtained from thermodynamics and showing that they yield functionals containing the Maxwell equations (figure 1) [1].

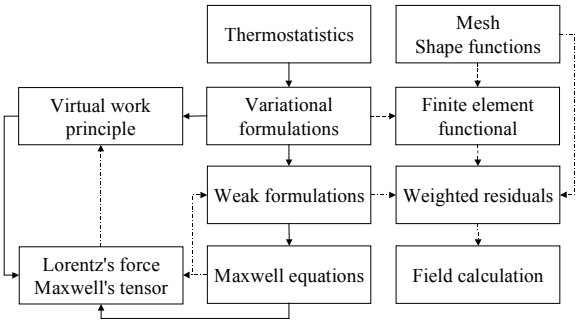

Fig. 1: Flowchart of the thermostatistic approach of electromagnetism. While the full lines give the main steps of the approach, the dashed lines indicate its numerical description. The mixed lines give the usual introduction of FEM.

To circumvent the impossibility to provide any deterministic evolution, a statistical description is adopted. The lack of information is given by the Shannon's entropy S [2]. Thermostatistics assumes that the steady-state of the system is obtained for the maximum of the entropy keeping the macroscopic information on the system (internal energy, magnetic fluxes ϕ, electric charges Q, prescribed forces $\mathbf{F}$ on the bodies…) constrained [3,4]. Such equilibrium corresponds to the so-called Boltzmann-Gibbs' statistic law. An equivalent description introduces the Gibbs potential as a functional of the state variables (respectively temperature T, net currents I or surface voltage V prescribed by generators, positions of the bodies $\mathbf{X}$…), the minimum of which gives the Gibbs free energy of the system $G(T,...,\mathbf{X})$ [5]. In a magnetic context, its differential reads

$$\mathrm{d}\,G = -S\,\mathrm{d}\,T - \phi\,\mathrm{d}\,I + \mathbf{F}\cdot\mathrm{d}\,\mathbf{X} \tag{1}$$

For dielectrics, replace the term $-\phi\,\mathrm{d}\,I$ by $-Q\,\mathrm{d}\,V$.

II. Variational principles in electromagnetism

After some spatial average on microscopic charge distribution to discard short time- and space-variations with respect of excitation provided by generators, the conservation of the electric charge reads [6]

$$\mathrm{div}\,\mathbf{j} + \frac{\partial \rho}{\partial t} = 0 \tag{2}$$

where ρ is the averaged charge density and $\mathbf{j}$ denotes the free current density, *i.e.* involving charges able to move on large scale with respect to atomic structure. Conductors may provide such non-vanishing sources. Hence, it is convenient to define the so-called electric displacement field $\mathbf{D}$ and magnetic field $\mathbf{H}$ to replace, in an unbound way, the span of the electromagnetic interaction. They check respectively:

- the Maxwell-Gauss equation
$$\mathrm{div}\,\mathbf{D} = \rho \tag{3}$$
- the Maxwell-Ampere equation
$$\mathbf{curl}\,\mathbf{H} = \mathbf{j} + \frac{\partial \mathbf{D}}{\partial t} \tag{4}$$

Among the admissible field couples ($\mathbf{D}$,$\mathbf{H}$), the thermodynamic principles will enforce those matching the complementary Maxwell equations.

A. Magnetostatics

For magnetostatics, the field $\mathbf{H}$ is just created by a static current density $\mathbf{j}$, given by the minimization of Joule losses. The equilibrium of the field is obtained by considering variations of field $\mathbf{H}$ which do not change neither the Gibbs free-energy, nor the current density. Introducing ($-\mathbf{B}$) as a conjugate field of $\mathbf{H}$ related to the energy density with respect of $\mathbf{H}$, the stationarity of

$$G(T,I) = \iiint \mathrm{d}^3 r \int^{\mathbf{H}} (-\mathbf{B})\cdot\delta\mathbf{h} \tag{5}$$

under admissible variations $\delta\mathbf{H} = -\mathbf{grad}\,\delta\Phi$ keeping $\mathbf{j}$ constant in the conductors, yields

$$\mathrm{div}\,\mathbf{B} = 0 \tag{6}$$

Thus, $\mathbf{B}$ appears as the magnetic flux density. Notice that the numerical resolution of (5) requires a magnetic behavior relation $\mathbf{B}(\mathbf{H})$. For permanent, local, non-dispersive and homogeneous media [7], this behavior law has to check

$$\delta\mathbf{B}\cdot\delta\mathbf{H}>0 \tag{7}$$

to obey the convexity of the Gibbs potential.

B. Quasi-static approximation

The so-called quasi-static approximation assumes no coexistence between free current density and displacement terms in Maxwell-Ampere equation (4). Thus, current density **j** remains divergence-free and only a steady-state averaged charge density ρ may exist in conductors. Furthermore, considering invariance of Joule losses under Galilean transformations, such charge density does vanish in the bulk of conductors. Hence, power delivered by generators reads

$$\iiint_C \sigma^{-1}\left(\mathbf{curl}\,\mathbf{H}\right)^2\,\mathrm{d}^3r+\frac{\mathrm{d}}{\mathrm{d}t}\iiint\left(\mathbf{B}\cdot\mathbf{H}\right)\mathrm{d}^3r \tag{8}$$

where:

- the first term corresponds to Joule losses observed in the conductors C (with $\sigma>0$). The order of this term is even to respect invariance of losses with inversion of time. Vanishing this term enforces an adiabatic evolution;
- the second one is related to time variation of the energy coupling the current generators and the magnetic field. Vanishing this term provides a reversible conversion between generators.

Therefore, a weak condition for an adiabatic and reversible evolution of the field is given by the minimization of (8). After a transformation on the convective derivative of the coupling energy [8], some tedious variational calculations and invariance of any magnetic flux under Galilean transformation, it follows that the electric field **E** *in conductors* [9]:

- is given through the so-called Ohm's law with motion
$$\mathbf{j}=\sigma\left(\mathbf{E}+\mathbf{v}\times\mathbf{B}\right) \tag{9}$$
where **v** is the local velocity of the conductor and σ its conductivity; and
- checks the Maxwell-Faraday equation
$$\mathbf{curl}\,\mathbf{E}=-\frac{\partial\mathbf{B}}{\partial t} \tag{10}$$

To summarize, stationarity of (5) is related to the determination of the magnetic field according to the current flow density whereas Eq. (8) yields eddy current distribution according to magnetic flux variations.

C. Surface-charges excitation

A Gibbs potential, the minimum of which provides the electrostatic Gibbs free energy, describes the electrostatic interaction between charges spread out on the surface of conductors connected to voltage generators, along with the behavior law **D**(**E**) of the dielectric media in between.

In order to enforce a reversible exchange between magnetic and electrostatic Helmoltz free-energies, the minimization of the power supplied by generators to polarize the dielectric yields the Maxwell-Faraday equation (10) in the *dielectric region* too.

Although quasi-static approximation is no more valid, metals are known to mimic a dielectric behavior beyond their plasma pulsation [7] because free-charge displacements are inhibited. Checked at high and low frequencies in conductors, Maxwell-Faraday equation is assumed to remain valid in between, where eddy-currents are known to eject any field from the bulk of conductors. Hence, divergence-free flux density becomes also valid for any regime.

D. Energy conservation: From virtual works to Lorentz force

According to Eq. 1, the force (–**F**) acting on the body is given by the virtual work principle

$$(-\mathbf{F})=-\mathbf{grad}\,G \tag{11}$$

where the derivation is performed with respect to the position **X**. Hence, Coulomb's force is obtained by considering virtual works of the electrostatic Gibbs free energy of a point charge in its rest frame. Furthermore, Galilean invariance of this force under transformation of the electric field with velocity (9) yields the Lorentz expression of the force.

Besides, the conservation of the energy supplied by generators allows to derive the Laplace force density from virtual works of the magnetic Gibbs free-energy.

III. Conclusion

The previous approach may be included in an optimization paradigm, from scratch to design scale through some relevant "coarse graining" procedures. It addresses also a deeper justification of the FEM, which consists in building an approximation of the variational formulations given at Eqs. (5) and (8) but with a finite number of degrees of freedom. Hence, the FEM is suitable to bridge design process and energy considerations involved in further ecological challenges. In this scope, current formulations are clearly relevant [10,11].

[1] V. Mazauric, "Des principes thermodynamiques aux équations de Maxwell: Une approche variationnelle de l'électromagnétisme," in *Electromagnétisme et éléments finis*, vol. 1, G. Meunier, Ed. Paris, France: Hermès, 2003, pp. 151-266.

[2] C. E. Shannon, "A mathematical theory of communication," *The Bell System Technical Journal*, vol. 27, pp. 379-423, 1948.

[3] E. T. Jaynes, "Information theory and statistical mechanics," *Physical Review*, vol. 106, pp. 620-630, 1957.

[4] A. J. M. Garrett, "Macroirreversibility and Microreversibility reconciled: The second law," in *Maximum entropy in action*, V. A. Macaulay, Ed. Oxford, UK: Oxford University Press, 1991, pp. 139-170.

[5] T. Morita, "Formal structure of the cluster variation method," *Progress in theoretical physics*, vol. 115, pp. 27-39, 1994.

[6] G. Russakoff, "A derivation of the macroscopic Maxwell equations," *American Journal of Physics*, vol. 38, pp. 1188-1195, 1970.

[7] N. W. Ashcroft and N. D. Mermin, *Solid state physics*. Tokyo, Japon: Holt-Saunders International Edition, 1981.

[8] I. S. Gradshteyn and I. M. Ryzhik, "Integral rate of change theorems," in *Table of integrals, series and products*, A. Jeffrey, Ed., 5th ed. San Diego, USA: Academic Press, 1994, pp. 1123-1124.

[9] J. D. Jackson, "Time-varying fields, Maxwell equations, Conservation laws," in *Classical electrodynamics*. New York, USA: John Wiley and sons, 1975, pp. 209-268.

[10] A. Bossavit and J. C. Vérité, "The "Trifou" code: Solving the 3-D eddy-currents problem by using H as state variable," *IEEE Transaction on Magnetics*, vol. 19, pp. 2465-2470, 1983.

[11] O. Biro, K. Preis, W. Renhart, G. Vrisk, and F. R. Richter, "Computation of 3D current driven skin effect problems using a current vector potential," *IEEE Transaction on Magnetics*, vol. 29, pp. 1325-1332, 1993.

Total/Reduced Magnetic Vector Potential and Electrical Scalar Potential for Eddy Current Calculation

E. X. Xu, J. Simkin
Vector Fields Ltd., 24 Bankside, Kidlington, Oxford, OX5 1JE, UK.
ex@vectorfields.co.uk; js@vecotrfields.co.uk

Abstract **–A low frequency electromagnetic field formulation is described using total and reduced magnetic vector potentials interpolated by edge elements and electrical scalar potentials interpolated by nodal elements. The formulation has been implemented in the frequency domain and is shown to be versatile, robust and efficient.**

INTRODUCTION

Static and quasi-static electromagnetic field formulations using total and reduced potentials are effective and have many advantages. For example, complicated coil structures do not have to be meshed and the field from coils can be calculated exactly by integration. Formulations based on reduced and total scalar potentials for non-conducting materials, coupled to vector potentials in conducting materials, minimise the number of variables [1], but give badly conditioned matrices in extreme cases, such as high aspect ratio elements combined with big changes in material properties.

In this paper a total and reduced magnetic vector potential formulation is developed and its implementation using edge elements is described. Results for a simple analytic model are used to show the accuracy of the solutions. A practical example is then used as an extreme test of the method. The model consists of thin conducting, permeable plates, solved at very low frequencies. It shows that the formulation is more robust than methods based on coupled scalar and vector potentials.

POTENTIALS AND FORMULATION

The total magnetic vector potential $\vec{A}_t$ is defined by

$$\vec{B} = \nabla \times \vec{A}_t \tag{1}$$

and the reduced magnetic vector $\vec{A}_r$ by

$$\vec{B} - \vec{B}_s = \nabla \times \vec{A}_r \tag{2}$$

where $\vec{B}_s$ is the source field magnetic flux

$$\vec{B}_s = \mu_0 \vec{H}_s \tag{3}$$

and the source field distribution, $\vec{H}_s$, is assumed to be calculated by a direct method such as Biot-Savart's law, such that

$$\nabla \times \vec{H}_s = \vec{J}_s \tag{4}$$

In conductive regions, an electric scalar potential is introduced to make the system of equations easier to solve [2] and so that voltage driven boundary conditions can be applied.

$$\vec{E} = -j\omega\vec{A}_t - \nabla V \tag{5}$$

From Ampere's law, assuming that the total current density includes eddy current density and specified current density.

$$\nabla \times \vec{H} = \vec{J} = \sigma\vec{E} + \vec{J}_s \tag{6}$$

Substituting (1), (4) and (5) into (6), in the total vector potential regions Ampere's law can be presented as

$$\nabla \times \nu\nabla \times \vec{A}_t + j\omega\sigma\vec{A}_t + \sigma\nabla V = \nabla \times \vec{H}_s \tag{7}$$

Applying Galerkin's method gives

$$\int_\Omega \nabla \times \vec{W}\nu\nabla \times \vec{A}_t d\Omega + j\omega \int_\Omega \vec{W} \bullet \sigma\vec{A}_t d\Omega + \int_\Omega \vec{W} \bullet \sigma\nabla V d\Omega + S_1 = \int_\Omega \nabla \times \vec{W} \bullet \vec{H}_s d\Omega + S_2 \tag{8}$$

where the surface integrals S_1 and S_2 are

$$S_1 = -\int_s (\vec{W} \times \nu\nabla \times \vec{A}_t) \bullet \hat{n} dS \tag{9}$$

$$S_2 = -\int_s (\vec{W} \times \vec{H}_s) \bullet \hat{n} dS \tag{10}$$

The first surface integral corresponds to the natural tangential magnetic field continuity condition, the second one to source field continuity.

In conductive regions, the divergence of the current density is used to deduce the extra equation required for the electrical scalar potential. After scaling for symmetry, the equation is

$$\frac{1}{j\omega}\int_\Omega \nabla w \bullet \sigma\nabla V d\Omega + \int_\Omega \nabla w \bullet \sigma\vec{A}_t d\Omega = \int_\Omega w\sigma(\vec{A} + \frac{\nabla V}{j\omega}) \bullet \hat{n} dS \tag{11}$$

In free space, the equation for the reduced potential is

$$\int_\Omega \nabla \times \vec{W}\nu_0\nabla \times \vec{A}_r d\Omega = \int_s (\vec{W} \times \nu_0\nabla \times \vec{A}_r) \bullet \hat{n} dS \tag{12}$$

The total and reduced potential regions are naturally coupled by the tangential field continuity condition

$$\nu\nabla \times \vec{A}_t \times \hat{n} = (\nu_0\nabla \times \vec{A}_t + \vec{H}_s) \times \hat{n} \tag{13}$$

DISCUSSION

In equation (7) the source current density was replaced by the curl of its field strength, this leads to a representation of

the source fields on the consistent function space [3], at the expense of evaluating the source fields in the total potential region.

The advantage of using reduced potentials depends on the application, for example in NMR magnet simulations the fields can be evaluated to very high accuracy because the source fields dominate and they are calculated with no discretisation error.

EXAMPLES

The first testing example is a conductive sphere of radius of 10 cm and conductivity of 10^7 S/m in uniform AC field of 100 Hz. FE result (solid green) is compared with analytical solution (dashed red) in Fig. 1. Numerical error appearing on the surface of the sphere can be overcome by fine mesh around the surface.

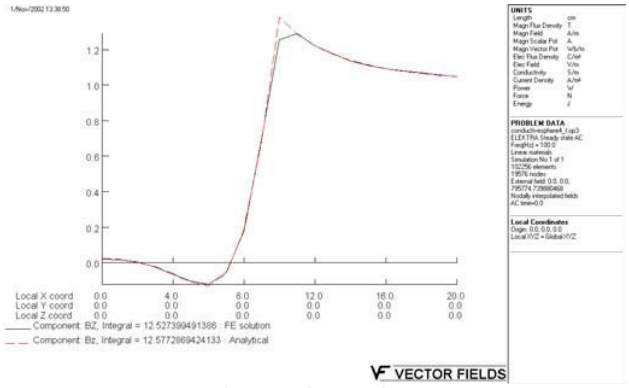

Fig. 1. Bz along x axis

Eddy currents occur in ships induced by the "rocking" motion caused by waves in the earth's magnetic field. A typical ship largely consists of thin steel and aluminium plates. Modelling these may produce a badly conditioned system of equations, because the large aspect ratio of thin shell structures and high permeability and conductivity of the plates [4]. Figure 2 shows the model of a ship, with 155-metre long steel hull of 5cm thickness, additional superstructures, bulkheads and decks, placed near a rectangular coil with AC current of 0.167 Hz. This represents the variation of the vertical component of earth magnetic field due to the rocking. Only a half of space is modelled because of symmetry. The steel has a conductivity of 3×10^6 S/m and relative permeability of 110. The conductivity of the aluminium is 2.5×10^7 S/m. A box of 1750x500x500 cubic metres around the ship is meshed by 136,448 hexahedral elements. Element aspect ratios up to 2,000:1 for free space and 100:1 for steel and aluminium plates are used. This model was solved using the total/reduced vector potentials with electrical scalar potential formulation. It required 7,554 QMR iterations to converge to a relative residual of 10^{-8} for an equation system of 412,033 freedoms. The in-phase eddy current distribution is shown in Fig. 3.

After removing scalar potential V from equation system, the number of freedoms reduces to 394,603, but the number of QMR iterations increases to 14,661.

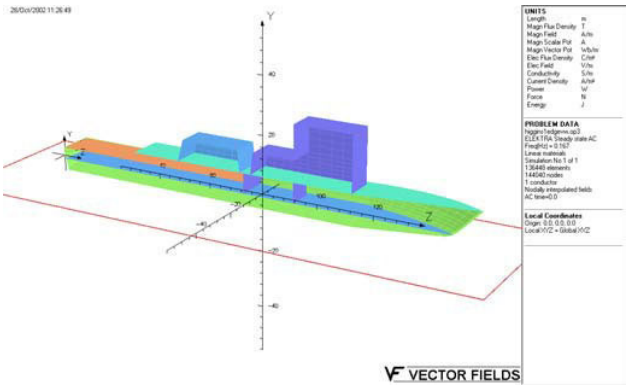

Fig. 2. A model ship with coil modelling earth's field

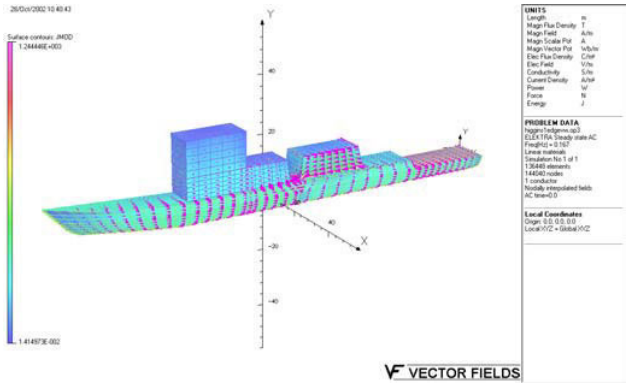

Fig. 3. Current density

More examples, such as voltage driven problems, and discussion on numerical accuracy, arrangement of vector potentials and convergence of linear equation solvers will be presented in the full paper.

CONCLUSIONS

The Total/Reduced magnetic vector potential formulation has been found to give accurate results by comparison with analytical calculations. It has been demonstrated that the QMR solution method gives reliable convergence even for models with extreme aspect ratio elements.

REFERENCES

[1] J. Simkin, "Eddy current modelling in three dimensions", *IEEE Transactions on Magnetics*, vol. 22, No. 5, pp. 609-613, Sept 1986

[2] K. Fujiwara, T. Nakata and H. Ohashi, "Improvement of convergence characteristic of ICCG method for the $A-\phi$ method using edge elements", *IEEE Transactions on Magnetics*, vol. 32, No. 3, pp. 804-807, May 1996.

[3] Z. Ren, "Influence of the R.H.S. on the convergence behaviour of the curl-curl equation", *IEEE Transactions on Magnetics*, vol. 32, No. 3, pp. 655-658, May 1996.

[4] P. Zivi, A. LeDoux and R. Pillsbury, "Electromagnetic signature of a ship rolling in earth's magnetic field", COMPUMAG 2001

COMPUMAG Saratoga Springs, New York USA
July 13 - 17, 2003

Subspace Projection Extrapolation Scheme for Transient Field Simulations

Markus Clemens, Markus Wilke, Rolf Schuhmann and Thomas Weiland

Technische Universität Darmstadt, Dept. Electrical Engineering and Information Technology,

Computational Electromagnetics Laboratory (TEMF), Schloßgartenstr. 8, D-64289 Darmstadt, Germany

email: clemens/wilke/schuhmann/weiland@temf.tu-darmstadt.de.

Abstract—**A new subspace projection extrapolation (SPE) scheme is introduced for the implicit time integration of electromagnetic discrete field formulations to construct suitable start vectors required for the iterative solution of the (non-)linear algebraic systems of equations. Numerical results show a significant improvement in numerical efficiency with this new extrapolation scheme when compared to previously proposed methods.**

I. Introduction

Spatial discretizations of transient quasistatic electromagnetic field formulations with e.g. the Finite Element Method (FEM) or the Finite Integration Technique (FIT), commonly result either in large stiff ordinary differential or differential-algebraic systems of equations of the form

$$\mathbf{D}\frac{d}{dt}\mathbf{x}(t) + \mathbf{K}[\mathbf{x}(t)]\ \mathbf{x}(t) = \mathbf{b}(t), \tag{1}$$

whose evolution of the $N-$component vector $\mathbf{x}(t) \in \mathbb{R}^N$ in time has to be considered over a given time interval. (For magneto-quasistatic formulations see e.g. [1], for electro-quasistatic systems [2].)

This task requires to use suitable implicit time integration schemes, e.g. one-step schemes such as the simple $\theta-$methods, the multi-stage embedded (singly diagonal) implicit Runge-Kutta ((SD)IRK) methods [3], [4] and linear-implicit time integration schemes of Rosenbrock-Wanner-type [3], [5], which were just recently introduced to quasistatic electro-magnetic field simulations [1], or the multi-step backward differentiation schemes [3]. In these methods in each time step one or several large (non-)linear algebraic systems of equations have to be solved. For the iterative solution methods of these systems *extrapolation schemes* can provide suitable initial start values. Such first approximations of the solutions at the respective new time steps should be computationally cheap to attain and allow to effectively reduce the number of subsequent iteration steps of the preconditioned conjugate gradient solvers. This was shown e.g. in [6], where several extrapolation techniques are compared to produce an initial vector $\mathbf{x}_0^{(n+1)}$ for the iterative solution $\mathbf{x}^{(n+1)} \approx \mathbf{x}(t^{n+1})$ of the algebraic system at time $t^{(n+1)}$

$$\mathbf{M}\mathbf{x}^{(n+1)} = \mathbf{b}^{(n+1)}, \tag{2}$$

with $\mathbf{M} = [\alpha\mathbf{D} + \mathbf{K}]$, where α is a scalar parameter depending on the chosen time step length Δt. The extrapolation schemes process available information at times $t < t^{(n+1)}$ to predict the solution at time $t^{(n+1)}$, commonly using the Taylor expansion theorem or variants thereof in case of the structurally more complicated multi-stage IRK methods. Since all the extrapolated start vectors $\mathbf{x}_{0,i}, i = 1, ..., m$, for the iterative solution of (2) are computationally cheap to attain with the different variants of Taylor expansions described in [6], a minimal residual norm selection criterion was proposed in [6] and shown to yield a robust improvement to the solution processes.

M. Wilke is supported by the Deutsche Forschungsgemeinschaft (DFG) under grants WE1239/13-1 and WE1239/17.

II. Subspace Projection Extrapolation Scheme

For the situation of multiple extrapolated start values we introduce a computationally more efficient scheme. In the new *Subspace Projection Extrapolation Scheme* we adapt an idea used in frequency domain simulations [7] to the regime of implicit time stepping methods.

To attain a suitable start solution vector $\mathbf{x}_{0,\text{S.P.E.}}$ out of m different extrapolation vectors $\mathbf{x}_{0,i}$ derived with methods from [6] for the time step solution $\mathbf{x}^{(n+1)}$ the following steps are performed:

1. Apply an orthonormalization process to the extrapolation vectors $\mathbf{x}_{0,i}, i = 1, ..., m$, (e.g. by applying a Modified Gram-Schmidt (MGS) algorithm) to yield a set of $\widetilde{m}$ vectors

$$\{\mathbf{x}_{0,i}\}_{i=1,...,m} \xrightarrow{\text{M.G.-S.}} \{\mathbf{v}_j\}_{j=1,...,\widetilde{m}}. \tag{3}$$

2. Define the orthonormal operator

$$\mathbf{V} := \{\mathbf{v}_1|...|\mathbf{v}_{\widetilde{m}}\} \in \mathbb{R}^{N\times\widetilde{m}}. \tag{4}$$

3. Solve the projected algebraic $\widetilde{m}\times\widetilde{m}$ system for $\mathbf{z} \in \mathbb{R}^{\widetilde{m}}$ with

$$\mathbf{V}^T\mathbf{M}\mathbf{V}\mathbf{z} = \mathbf{V}^T\mathbf{b}^{(n+1)}. \tag{5}$$

4. Define extrapolation vector $\mathbf{x}_{0,\text{S.P.E.}} := \mathbf{V}\mathbf{z} \ \in V_{\widetilde{m}} \subseteq \mathbb{R}^N$.

The orthonomalization process in step 1) will detect linear dependencies among the extrapolation vectors $\mathbf{x}_{0,i}$, thus $\widetilde{m} \leq m$ holds. The vectors $\mathbf{v}_j$ will also span a vector subspace $V_{\widetilde{m}} = \text{span}\{\mathbf{v}_j\} = \text{span}\{\mathbf{x}_{0,i}\} \subseteq \mathbb{R}^N$ as basis vectors. Since typically $\widetilde{m} \ll 100 \ll N$ holds, the projected system (5) in step 3) can be solved very efficiently using direct Gauss elimination. The computational effort to prepare the system (5) only involves $\widetilde{m}$ matrix-vector-multiplications and $2\widetilde{m}$ dot-products of $N-$component vectors and can be performed in parallel. For the result vector $\mathbf{x}_{0,\text{S.P.E.}}$ the Galerkin condition $\mathbf{V}^T[\mathbf{b}^{(n+1)} - \mathbf{M}\mathbf{x}_{0,\text{S.P.E.}}] = 0$ holds w.r.t. $V_{\widetilde{m}}$.

A. Nonlinear Subspace Projection Extrapolation

If the matrix $\mathbf{M} = \mathbf{M}(\mathbf{x})$ depends on the solution vector due to a nonlinear stiffness operator $\mathbf{K}(\mathbf{x})$ in (1) (ferromagnetic

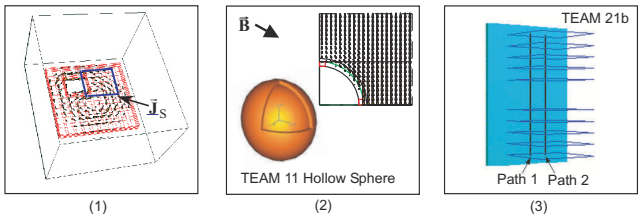

Fig. 1. Three eddy current test problems: 1) A copper plate with a hole. 2) The TEAM 11 problem. 3) Nonlinear TEAM 21b problem.

TABLE I

EXTRAPOLATION STRATEGIES FOR A FIXED TIME STEPPING BDF1-SCHEME (TOTAL NUMBER OF MXV-OPERATIONS).

Problem	No. 1	No. 2	No. 3
(a) Taylor 1st order $\mathbf{x}_0^{(n+1)} := \mathbf{x}^{(n)}$	3424	6663	-
(b) Taylor 2nd order $\mathbf{x}_0^{(n+1)} := \mathbf{x}^{(n)} + \Delta t\dot{\mathbf{x}}^{(n)}$	2554	16730	-
(c) Minimal norm hybrid method for (a), (b)	2714	6703	74392
(d) SPE scheme using (a), (b) ($m = 2$)	923	2889	41182

TABLE II

EXTRAPOLATION STRATEGIES FOR THE ADAPTIVE SDIRK3(2)-SCHEME [4] (TOTAL NUMBER OF MXV-OPERATIONS).

Problem	No. 1	No. 2	No. 3
(a) Taylor 1st order $\mathbf{x}_0^{(n+1)} := \mathbf{x}^{(n)}$	4636	12310	70647
(b) Taylor 2nd order $\mathbf{x}_0^{(n+1)} := \mathbf{x}^{(n)} + \Delta t\dot{\mathbf{x}}^{(n)}$	4473	10925	69946
(c) Stage-extension extrapolation	3877	7466	58799
(d) Continuous extension extrapolation	4145	10778	66660
(e) Minimal norm hybrid method for (a),(c),(d)	3777	6688	55198
(f) SPE-scheme using (a),(c),(d) ($m = 3$)	2743	6572	35743

TABLE III

EXTRAPOLATION STRATEGIES FOR THE ADAPTIVE LINEAR–IMPLICIT SCHEME RODAS3(2) [1] (TOTAL NUMBER OF MXV-OPERATIONS).

Problem	No. 1	No. 2	No. 3
Zero start vector $\hat{\mathbf{v}}_0^{(n+1)} := 0$	8397	8135	87277
SPE scheme using 3 last stage solutions ($m = 3$)	4766	5537	45590

materials in magneto-quasistatic problems or field-dependent conductivities in transient electro-quasistatic simulations), linearization schemes such as the Successive-Approximation method or the Newton-Raphson method have to be applied. To achieve suitable start values for these methods, steps 3. and 4. in the SPE scheme are replaced by few Successive-Approximation steps $k = 0, 1, ...,$ restricted to the subspace $V_{\widetilde{m}}$

$$\mathbf{V}^T\mathbf{M}(\mathbf{x}_{0,k})\mathbf{V}\mathbf{z}_{k+1} = \mathbf{V}^T\mathbf{b}^{(n+1)}, \quad \mathbf{x}_{0,k+1} := \mathbf{V}\mathbf{z}_{k+1}, \qquad (6)$$

where this iteration is started for $k = 0$ with $\mathbf{x}_{0,0} := \mathbf{x}^{(n)}$.

III. NUMERICAL RESULTS

Different extrapolation strategies are compared to the new SPE scheme for a FIT-based modified vector potential formulation for typical transient magnetic test configurations shown in Fig. 1. Problem 1 is related to the TEAM 7 problem, a copper plate with a hole featuring a ramped 50 Hz sinusoidal current excitation simulated for 80 time steps. Problem 2 is a hollow conductive, non-ferromagnetic sphere in an abrupt B-field (TEAM 11) integrated with 40 time steps. Problem 3 consists of the TEAM 21b problem, a nonlinear 50 Hz time harmonic eddy current problem, simulated over 50 time steps (see also [6]).

In Table I the effect of the new SPE method is displayed for the commonly used implicit BDF1 method and in Table II for a time step adaptive 4-stage SDIRK3(2)-method [4]. The solution of the linear algebraic systems is performed with a SSOR-preconditioned CG method which terminates its iterations after having reached a relative accuracy $\varepsilon_{\text{PCG}} = 10^{-5}$. The comparison of the different start strategies is given in terms of the required total number of matrix vector multiplications (MxV-operations) for the time integration process. This number corresponds well to the required computational time.

The results for both the standard fixed-time step BDF1-scheme as well as the adaptive SDIRK3(2)-scheme show that the application of the SPE speeds up the solution process by a factor ≥ 2 for linear problems when compared to just using the 1st order Taylor expansion, i.e., starting the PCG-iterations with the old solution $\mathbf{x}_0^{(n+1)} := \mathbf{x}^{(n)}$. The new SPE approach also outperforms all the extrapolation methods presented in [6]. The convergence of the nonlinear problem, in which 4 nonlinear SPE-cycles are performed before entering the nonlinear iteration scheme, is also considerably improved.

In Table III results for the linear–implicit time integration method RODAS3(2) [5], [1] are depicted. Its intermediate stage solutions, for which only linear systems have to be solved, no longer have interpolating character. Thus the extrapolation schemes available for SDIRK-methods [6] are not directly applicable and zero start vectors are commonly used. The application of the new SPE scheme to its respective three last stage solutions ($m = 3$), however, allows to achieve a considerable speed-up of the PCG solver convergence.

IV. CONCLUSION

For transient implicit time integration processes the new Subspace Projection Extrapolation (SPE) scheme was presented, which could be shown to significantly improve the numerical efficiency of quasistatic electromagnetic field simulations. The upcoming full paper will contain more details on the method, its mathematical background and additional numerical tests.

REFERENCES

[1] M. Clemens, M. Wilke, and T. Weiland, "Linear-implicit time integration schemes for error-controlled transient nonlinear magnetic field simulations," in *Proc. CEFC 2002, Perugia*, 2002, p. 332, Submitted to IEEE Trans. Magn.

[2] M. Clemens, H. De Gersem, W. Koch, M. Wilke, and T. Weiland, "Transient simulation of nonlinear electro-quasistatic problems using the finite integration technique," in *Proc. IGTE 2002, Graz*, 2002.

[3] E. Hairer and G. Wanner, *Solving Ordinary Differential Equations II, Stiff and Differential-Algebraic Problems*, Springer, Wien, New York, 1996.

[4] F. Cameron, *Low-Order Runge-Kutta Methods for Differential Algebraic Equations*, Ph.D. thesis, Tampere Univ. of Technology, 1999.

[5] J. Lang, *Adaptive Multilevel Solution of Nonlinear Parabolic PDE Systems: Theory, Algorithm and Application*, Springer-Verlag, Berlin, Heidelberg, New York, 2001.

[6] M. Clemens, M. Wilke, and T. Weiland, "Extrapolation strategies in transient magnetic field simulations," in *Proc. CEFC 2002, Perugia*, 2002, p. 331, Submitted to IEEE Trans. Magn.

[7] A. G. Tijhuis, K. Belkebir, A. P. M. Zwamborn, and A. Rubio Bretones, "Marching on in anything: solving electromagnetic field equations with a varying physical parameter," in *Proc. Int. Conf. Electromagnetics in Adv. Appl., Torino, Italy*, 1997, pp. 175–178.

Finite Element Difference Schemes for Electro- and Magnetostatics

Igor Tsukerman
Department of Electrical and Computer Engineering, The University of Akron, OH 44325-3904, USA
igor@uakron.edu

***Abstract*— Two versions of variational-difference method for solving inhomogeneous problems with curved material boundaries on regular hexahedral grids are developed. The solution is at least as accurate as in the finite element method on irregular geometrically conforming meshes but the data structures are as simple as in finite difference schemes. The proposed approach combines the ideas of the Generalized Finite Element – Partition of Unity methods, Discontinuous Galerkin Methods and Finite Difference / Finite Volume / Finite Integration Techniques.**

I. Introduction

The Finite Element Method (FEM) is well known for its flexibility of handling complex geometrical and material properties. However, this flexibility comes with a price. Mesh generation and the associated data structures can be complex, especially in 3D. Consequently, FEM is not competitive with finite difference (FD) methods for simple geometries.

The "Finite Element Difference" (FED) method proposed in this paper is expected to remedy this disadvantage at least in part. The name of the method is motivated by the fact that finite element / variational-type principles are used for its construction, whereas the resultant system is finite difference-like. We shall consider two related versions of the method, with applications to a model static equation

$$\nabla\cdot\sigma\nabla u = f \qquad (1)$$

Here σ is a material parameter (conductivity, permittivity, permeability, etc.) that can be discontinuous across material boundaries and can depend on coordinates but not, in the linear case under consideration, on the potential u. The computational domain Ω is either two- or three-dimensional, with the usual mathematical assumption of a Lipschitz-continuous boundary. Extensions of FED to other types of electromagnetic problems will certainly be explored in the future.

FED builds up on several computational techniques that over recent years have been converging, from different perspectives, to an FD-style method with FE-type capabilities: (a) "Finite Integration Techniques" and their enhancements [1], [2]; (b) heuristic homogenization by geometric averaging [3], [4]; (c) homogenization based on variational principles [5]; (d) Generalized FEM by Partition of Unity [6] and its applications to multiparticle problems [7]; (e) "discontinuous Galerkin" methods [8]; (f) the "discrete Hodge" operator in electromagnetic analysis [12], [13].

II. An Outline of the Method

Due to space limitations, only the main ingredients of the method are outlined here; a more detailed mathematical description and analysis will be given in the extended paper.

The work was supported in part by the National Science Foundation.

The first ingredient is special approximating functions satisfying the interface condition $\sigma_1\partial u_1/\partial n = \sigma_2\partial u_2/\partial n$. Such functions can be constructed by spatial mappings $(x, y, z) \rightarrow (\tilde{x}, \tilde{y}, \tilde{z})$ – see [9] for plane boundaries, [10] for spherical ones. A trilinear or higher order FE basis in terms of the transformed coordinates $\tilde{x}$, $\tilde{y}$, $\tilde{z}$ can then be used. Notably, this construction is valid even for spherical surfaces contained entirely within one hexahedral grid cell – quite a desirable feature for problems with small particles [7] .

The second ingredient is the variational scheme itself. We consider two options. The first one is based on the Generalized FEM by Partition of Unity [6] and ensures seamless integration of different local approximations.

An alternative variational scheme is formulated in the so-called "broken Sobolev space" [11] well known in Discontinuous Galerkin methods [8]. The FE method in this case is nonconforming: the continuity is imposed only at the grid nodes. The theoretical analysis is substantially more complicated than for GFEM but implementation is simpler and the initial numerical results are promising (Section III).

Both versions of FED have the following attractive features that will be explained fully in the extended paper:

- Curved interface boundaries can be handled on regular rectangular or hexahedral grids with at least the same level of accuracy as for geometrically conforming FE meshes.
- In many cases, much coarser grids can be used in FED than in FEM because small geometric details do not have to be resolved in FED.
- There is a great deal of flexibility and independence in the choice of approximating functions over each grid cell.
- The resultant discrete system is symmetric positive definite, with no additional unknowns other than the nodal values of the potential.
- Regular rectangular and hexahedral grids typically lead to 9-point and 27-point stencils, respectively, as in the standard FEM with bilinear / trilinear brick elements.
- High order approximation is possible.

III. Numerical Results

First, the following very simple 1D example highlights the role of special approximating functions. Consider the differential equation $(\sigma u')' = 0$ on segment $[0, 10]$, with $\sigma = 10$ on $[0, a]$, $\sigma = 1$ on $[a, 10]$ and with Dirichlet conditions $u(0) = 0$, $u(10) = 1$.

Within the finite element (segment) containing the discontinuity a, FED basis functions are piecewise-linear and satisfy the derivative jump condition at a, as opposed to just a linear approximation in the standard first order element.

For 20 elements and $a = 6.7$, the 1D mesh is nonconforming (i.e. point a is not a node) – hence the discrepancy between the FEM solution and the exact one (Fig. 1). In contrast, the FED solution is exact up to round-off errors.

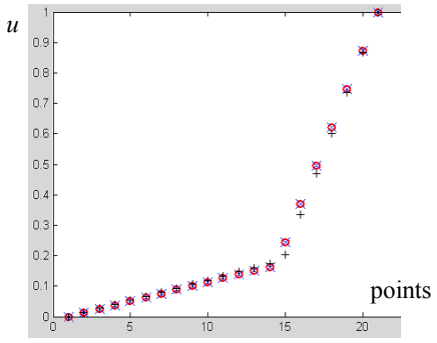

Fig. 1. FED vs. standard FEM for a simple 1D problem. + - FEM, × - FED, o – exact solution.

As a 2D example, we consider a dielectric cylinder in an external field. The domain is the unit square [0,1]×[0,1], with an inhomogeneous Dirichlet boundary condition chosen to make the analytical solution easily available. Convergence of the numerical potential as a function of mesh size h is shown in Fig. 2: the slope corresponds to order $O(h)$ or slightly better. The same is true for convergence in the energy norm and for an analogous 3D case.

Remarkably, analysis of the potential distribution shows that even for a very crude 4×4 grid, in no way capable of capturing the cylindrical boundary, the computed values of nodal potentials are quite accurate. This is again due to the special approximating functions employed.

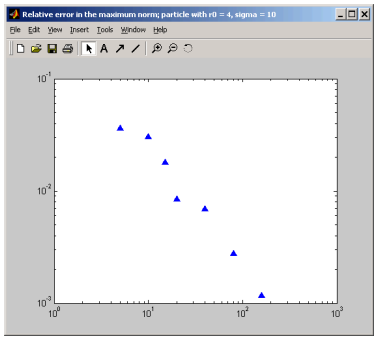

Fig. 2. Relative error in the maximum norm for the potential values computed by FED; domain [0,25]×[0,25], $r_{cylinder} = 4$, $\sigma_{cylinder} = 10$, $\sigma_{outside} = 1$; meshes from 5×5 to 160×160. relative error = $\| u_{FED} - u_{exact} \|_\infty \; / \; \| u_{exact} \|_\infty$.

Finally, both versions of FED give accurate results for a 3D test problem related to multiparticle assembly processes in nanotechnology; the setup was given in [7]. A FEMLAB™ simulation was also performed for additional comparison.

™ FEMLAB is a registered trademark of Comsol, Inc.

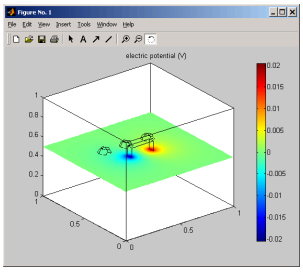

Fig. 3. Scalar potential for three magnetic particles near a magnetized substrate (FEMLAB).

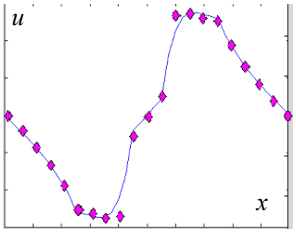

Fig. 4. Solid line: mesh 40×40×40, GFEM, trilinear elements – coincides with FEMLAB simulation, 2nd order tetrahedral elements. Diamonds: FED, mesh 20×20×20, 6,859 d.o.f.

The results obtained by GFEM, FED and FEMLAB are in good agreement (Fig. 4). Notably, the grid size in FED is equal to the radius of the particles, i.e. not at all sufficient to resolve the geometry of the spherical boundary. This is possible because the behavior of the solution at particle boundaries is analytically incorporated into the FED approximation.

IV. Conclusion

The proposed methodology allows one to solve complex inhomogeneous problems with curved boundaries on regular meshes. In contrast with finite volume – finite integration techniques, the construction of the difference scheme is based on variational principles. The approach can be viewed as a combination of finite element and finite difference methods.

V. Acknowledgment

This work was inspired by my communication with Rolf Schuhmann, Thomas Weiland and especially Markus Clemens of TU-Darmstadt. I am really grateful to them.

References

[1] B. Krietenstein, R. Schuhmann, P. Thoma, T. Weiland, *Proceedings of the XIX International Linear Accelerator Conference (LINAC 98)*, Chicago, USA, pp. 860-862, 1998.

[2] M. Clemens, T. Weiland, *IEEE Trans. Magn.*, vol. 38, No. 2, pp.389-392, 2002

[3] S. Dey, R. Mittra, *IEEE Transactions on Microwave Theory and Techniques*, vol. 47, No. 9, pp. 1737-1739, 1999.

[4] W. Yu and R. Mittra, *IEEE Microwave Wireless Comp. Lett.*, vol. 11, pp. 25–27, Jan. 2001.

[5] S. Moskow *et al.*, *SIAM Journal on Numerical Analysis*, vol. 36, No. 2, pp. 442-464, 1999.

[6] I. Babuška, J.M. Melenk, *International Journal For Numerical Methods In Engineering*, v. 40, No. 4, pp. 727-758, 1997.

[7] A. Plaks, I. Tsukerman, G. Friedman, B. Yellen, *Proceedings of IEEE CEFC Conference*, Perugia, June 2002; submitted to *IEEE Trans. Magn.*.

[8] Douglas N. Arnold *et al*, *SIAM J. Numer.Analysis*, vol. 39, No.5, pp.1749–1779, 2002.

[9] I. Babuška, G. Caloz, J.E. Osborn, *SIAM Journal on Numerical Analysis*, vol. 31, No. 4, pp. 945-981, 1994.

[10] A. Plaks, I. Tsukerman, S. Painchaud, and L. Tabarovsky, *IEEE Trans. Magn.*, vol. 36, No. 4, p.633-636, 2000.

[11] J. Tinsley Oden, Ivo Babuška, Carlos Erik Baumann, *Journal of Computational Physics*, vol. 146, pp. 491–519, 1998.

[12] R. Hiptmair, *Numer. Math.*, vol. 90, pp.265–289, 2001.

[13] T. Tarhasaari, L. Kettunen, A. Bossavit., *IEEE Trans. Magn.*, vol. 35, No. 3, pp. 1494-1497, 1999.

COMPUMAG Saratoga Springs, New York USA
July 13 - 17, 2003

Finite Element Basis Functions for Nested Meshes of Non-Uniform Refinement Level

Volker Hill, Ortwin Farle, and Romanus Dyczij-Edlinger
Lehrstuhl fuer Theoretische Elektrotechnik, Saarland University
P.0. Box 15 11 50, D-66041 Saarbrucken, Germany
E-Mail: edlinger@lte.uni-saarland.de

***Abstract*— We propose a systematic methodology for the construction of generalized hanging variables which can be used to connect finite elements of unequal refinement levels within a nested tetrahedral mesh. While conventional refinement schemes introduce irregular elements at such interfaces, which must be removed when the mesh is further refined, the suggested approach keeps the discretization perfectly nested. Thanks to enhanced regularity, mesh-based methods such as refinement algorithms or intergrid transfer operators for use in multigrid solvers can be implemented in a much simpler fashion. The present paper covers higher order H^1 and $H(curl)$ conforming elements of hierarchical type.**

I. Introduction

Nested meshes exhibit a number of special properties that make them very well-suited for adaptive finite element solvers. First, they guarantee that mesh quality does not deteriorate as portions of the mesh are repeatedly refined. Second, they are perfectly suited for multigrid methods and hence allow for highly efficient linear equation solvers. Third, they exhibit a high degree of regularity which can be exploited in error estimators or for data extrapolation. However, one difficulty with nested meshes is that, in the case of non-uniform refinement, finite elements of unequal refinement levels must be connected without destroying the proper continuity of the basis functions across element interfaces. In conventional schemes, regions of unequal refinement levels are stitched together by means of so-called "red" or "green" elements [1] [2] [3], which are irregular in the sense that they are of inferior quality than their parents and hence must be removed when the mesh is further refined. In the three-dimensional case, the number of possible element configurations to be taken into account is getting large. As a result, computer implementations of such methods tend to be rather involved.

Alternatively, one may allow finite elements of unequal refinement levels to touch (see Fig. 1) but impose constraints on the basis functions in order to maintain the proper continuity requirements along common edges or faces. Since the construction of such constraints is intimately related to that of intergrid transfer operators, this approach is particularly attractive in the context of multigrid solvers. Moreover, its computer implementation is rather straightforward.

In this paper, we develop two variants of the latter approach and compare their respective properties with regard to flexibility, memory consumption, and numerical convergence.

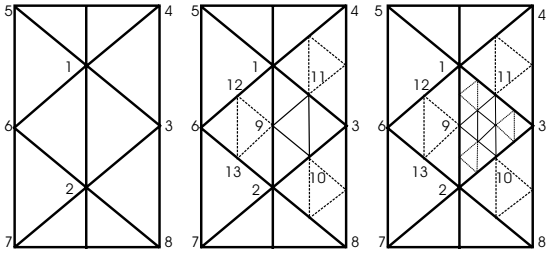

Fig. 1. a: Initial mesh. b: Nonuniform refinement. c: Recursive refinement.

II. Basic Refinement

Here, we demonstrate the idea of our basic refinement strategy just for the two dimensional case. Given the consistent mesh of Fig. 1a, assume that triangle T_{123} is to be refined. As shown in Fig. 1b, we first subdivide all elements that have an edge in common with T_{123}. In a second step, we restore the proper continuity conditions by restricting the finite element basis along the outer edges $E_{41}, E_{16}, E_{62}, E_{28}, E_{83}, E_{34}$ to that of the coarse mesh. As detailed in [5], this is accomplished by pre- and post-multiplying certain projection matrices to the element matrices of triangles $T_{134}, T_{162}, T_{283}$.

The basic refinement strategy is simple and easy to implement. When applied recursively as in Fig. 1c, it automatically creates some gradation in element size, which is often desirable in practise. On the other hand, Fig. 1b shows that the numbers of extra triangles and edges introduced by subdividing a single element may be significant. In three dimensions, this effect is even more pronounced. For higher order elements, each newly generated edge or triangle may add some extra variables to the global equation system. In auto-adaptive methods, where we want to place degrees of freedom most selectively, the basic refinement method may hence not be the best.

III. Reduced Elements

For optimum computational efficiency, we want to add to the triangles $T_{134}, T_{162}, T_{283}$ only degrees of freedom that are absolutely necessary to maintain the required interface conditions across the edges E_{12}, E_{23}, E_{31}. Let us consider the triangle T_{134} as subdivided into four fine mesh triangles. We denote the sets of fine and coarse mesh basis functions over the domain of T_{134} by $\{N^h\}$ and $\{N^{2h}\}$, respectively, and

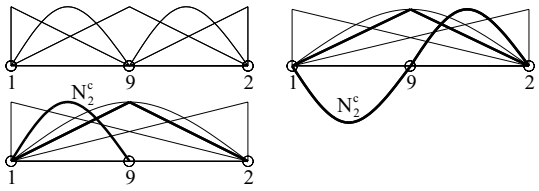

Fig. 2. a: Fine mesh functions. b, c: Coarse mesh functions plus corrections.

write $F = \#\{N^h\}$ and $C = \#\{N^{2h}\}$ for the corresponding numbers of basis functions. Since we have

$$span\{N^{2h}\} \quad \subset \quad span\{N^h\} \tag{1}$$

for both H^1- and $H(curl)$-conforming elements, we may express any basis function N^{2h} as superposition of fine mesh functions

$$\begin{bmatrix} N_1^{2h} \\ \vdots \\ N_C^{2h} \end{bmatrix} \quad = \quad [R]_{C\times F} \begin{bmatrix} N_1^{h} \\ \vdots \\ N_F^{h} \end{bmatrix}, \tag{2}$$

where $[R]$ is a well-defined restriction matrix. We state without proof that $[R]$ is unique and purely topological in nature, i.e., it does not depend on the actual geometry. To maintain the proper continuity conditions across E_{12}, we must provide corrections $N^c \in span\{N^f\}$. Of course, N^c must be chosen such that it does not destroy continuity on the other edges, E_{16} and E_{62}. Denoting by $C(N)$ the continuous components of N across interfaces, we obtain

$$\begin{bmatrix} C(N^{2h}) \end{bmatrix} \quad = \quad [A] \begin{bmatrix} [C(N^h)] \\ [C(N^c)] \end{bmatrix}. \tag{3}$$

Note that the matrix $[A]$ is not unique. Fig. 2 illustrates for the H^1 case that, even at the interface E_{12}, the second order correction N_2^c may be chosen in different ways. Also, one may always construct a valid correction $\tilde{N}^c$ from a given N^c by adding a superposition of fine mesh basis functions associated with the interior edges $E_{9,12}$, $E_{12,13}$, $E_{13,9}$. The choice of $[A]$ or $\{N^c\}$, respectively, has great impact on important properties of the global system matrix such as the number of non-zero entries or the eigenvalue distribution. Equations (2) (3) allow us to investigate these issues in a mathematical setting.

Once the matrix $[A]$ has been fixed, we are able to construct the reduced set of basis functions for the triangle T_{162}. We first generate element matrices $[M]_{klm}$ for the fine mesh triangles $T_{1,12,9}$, $T_{12,6,13}$, $T_{13,2,9}$, $T_{12,13,9}$. Then, we utilize (2) (3) to derive transformation matrices $[P]_{klm}$ to perform all necessary changes of basis and subspace restrictions. In the end, the contributions $[\tilde{M}]_{klm}$ of each of the fine grid triangles to the reduced element matrix of T_{162} are given by

$$[\tilde{M}]_{klm} \quad = \quad [P]_{klm}^T [M]_{klm} [P]_{klm}. \tag{4}$$

IV. Numerical Results

As a test example, we consider a dielectric block inside a rectangular waveguide [4] as shown in Fig. 3. By refining twice, the mesh size in the obstacle is set to be $1/4$ the size in the air region. Our finite element implementation is based on a combined vector and scalar potential formulation and employs a combination of second order H^1- and $H(curl)$-conforming basis functions. The multigrid method of [5] is used for the solver. Table I gives a comparison of the basic refinement strategy and two versions of the reduced element approach which differ in the choice of correction functions N^c. Even though the latter two methods markedly decrease the number of variables as compared to the basic approach, Version A fails to significantly improve the number of non-zero matrix entries and suffers from poor numerical convergence. On the other hand, Version B is memory-efficient and fast. We mention that the numerical results of all three methods are almost identical.

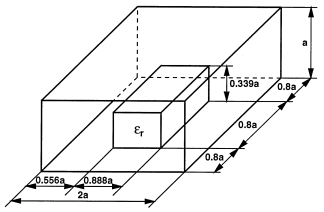

Fig. 3. Dielectric obstacle inside rectangular waveguide [4].

TABLE I
Comparison of Refinement Methods

Method	Variables	Non-Zeros	MG-Iterations
Basic Refinement	77350	2 147 185	12
Reduced, Version A	58030	1 923 775	147
Reduced, Version B	58030	1 563 746	10

V. Conclusion and Outlook

Generalized hanging variables provide an attractive alternative to the red/green refinement schemes typically used for non-uniform, nested finite element meshes. We have proposed a new reduced element approach which is more efficient than a straightforward refinement strategy, and we have outlined the underlying theory. In the full paper, a complete analysis of higher order H^1- and $H(curl)$-conforming tetrahedral elements of hierarchical type will be given. In particular, we will describe how to construct the required fine mesh corrections in an optimal way.

References

[1] F. Bornemann, B. Erdmann, R. Kornhuber, "Adaptive Multilevel Methods in Three Space Dimensions," *Report SC-92-14*, Konrad-Zuse-Zentrum für Informationstechnik, Berlin, Germany, 1992.

[2] U. Rüde, *Mathematical and Computational Techniques for Multilevel Adaptive Methods*, pp. 100-108, Philadelphia, PA: SIAM, 1993.

[3] P. Knabner and L. Angermann, *Numerik partieller Differentialgleichungen*, p. 175, Berlin, Germany: Springer-Verlag, 2000 (in German).

[4] K. Ise, K. Inoue, M. Koshiba, "Three-dimensional finite-element solution of dielectric scattering obstacles in a rectangular waveguide," *IEEE Trans. Microwave Theory Tech.*, vol. 38, pp. 1352-1359, Sept. 1990.

[5] V. Hill, O. Farle, and R. Dyczij-Edlinger, "A Stabilized Multi-Level Vector Finite Element Solver for Time-Harmonic EM Waves," *Computation of Electromagnetic Fields Conference*, Paper Nr. 409, Perugia, Italy, 2002. Manuscript available from www.lte.uni-saarland.de/publications/CEFC2002_Paper409.pdf.

Numerical Performance of the Distributed Vector Finite Element Time Domain Algorithm

Boguslaw Butrylo[(1)], Christian Vollaire[(2)], Laurent Nicolas[(2)] , Alain Nicolas[(2)]
[(1)] Bialystok Technical University
ul. Wiejska 45D
15-903 Bialystok, Poland
bogb@cksr.ac.bialystok.pl

[(2)] CEGELY, Ecole Centrale de Lyon
36, Avenue Guy de Collongue
69134 Ecully Cedex, France
{Christian.Vollaire, Laurent.Nicolas}@ ec-lyon.fr

Abstract – **This paper deals with a distributed time domain modeling of electromagnetic phenomena with the finite element method. The model is approximated by edge elements. The constitutive equations and method of parallelization of the algorithm are presented. The specific assembling by degrees of freedom technique is implemented in the algorithm. The properties of the distributed FETD algorithm are discussed. The algorithm is tested on a PC heterogeneous cluster.**

INTRODUCTION

Flexibility of the finite element technique and right physical sense of the edge elements make this formulation useful in modeling of electromagnetic phenomena. High performance simulation of the time domain problem enables to reduce either memory cost or time of computation, but as usual some weaknesses of the distributed version are revealed [1]. In this paper the properties of the vector finite element time domain algorithm are evaluated in the known distributed multi-computer environments (MPI and PVM).

PROBLEM FORMULATION

The distribution of electric field is stated by time dependent vector wave equation

$$\nabla\times\frac{1}{\mu}\nabla\times\mathbf{E}+\sigma\frac{\partial\mathbf{E}}{\partial t}+\varepsilon\frac{\partial^2\mathbf{E}}{\partial t^2}+\frac{\partial\mathbf{J}_{imp}}{\partial t}=0, \tag{1}$$

where μ, σ, ε are the parameters of the media and J_{imp} is the source current. The domain of analysis is truncated with first order Engquist-Majda absorbing boundary condition (ABC). In the case of excitation by a plane wave, according to general Galerkin scheme, the weak form of eq. (1) is given by expression

$$\int_V\frac{1}{\mu}(\nabla\times\mathbf{E})(\nabla\times\mathbf{W})dV+\int_V\mathbf{W}\sigma\frac{\partial\mathbf{E}}{\partial t}dV+\int_V\mathbf{W}\varepsilon\frac{\partial^2\mathbf{E}}{\partial t^2}+$$
$$\int_{S_{ABC}}\mathbf{W}\frac{1}{\mu c}\left(\frac{\partial\mathbf{E}}{\partial t}\times\vec{\mathbf{n}}\right)dS=\int_{S_{ABC}}\mathbf{W}\left[\frac{1}{\mu c}\left(\frac{\partial\mathbf{E}^i}{\partial t}\times\vec{\mathbf{n}}\right)-\vec{\mathbf{n}}\times\nabla\times\mathbf{E}^i\right] \tag{2}$$

where $\mathbf{W}$ is the test vector function, S_{ABC} is the external surface of the model and E^i is the incident field. This equation is discretized in time domain and in space domain to yield a system of linear equations which must be solved. Space discretization is achieved using incomplete first order H(curl) tetrahedral edge elements. Considering the central Euler difference approximations of the first and the second order derivatives, the final form of the equation is

$$\left(\mathbf{T}+\frac{\Delta t}{2}\mathbf{R}\right)\cdot\mathbf{E}_{n+1}=$$
$$\left(2\mathbf{T}-\Delta t^2\mathbf{S}\right)\cdot\mathbf{E}_n+\left(\frac{\Delta t}{2}\mathbf{R}-\mathbf{T}\right)\cdot\mathbf{E}_{n-1}-\Delta t^2\mathbf{f}_n, \tag{3}$$

where $\mathbf{R}$, $\mathbf{T}$, $\mathbf{S}$ are mass, damping and stiffness matrices. The $\mathbf{f}_n$ vector represents the dynamic load in the analyzed model.

DISTRIBUTED IMPLEMENTATION

The FETD algorithm involves many types of computing tasks, ranging from two- and three-dimensional assembling, to extensive matrix operations. These computationally intensive operations are performed in two main stages: assembling of the matrix equation, and time integration loop.

First, each processor reads the entire data file coming from the mesh generator providing a nodal description of the geometry. The entire edge description of the geometry is then performed in parallel. Finally, only the data required on each processor are stored in memory.

The distributed version of the assembling stage is based on the classical domain decomposition paradigm. Because the unknowns are connected with the edges, the set of edges is decomposed. There are no geometrical restrictions of the decomposition, because the matrices are assembled by degrees of freedom [2, 3]. Each computing unit assembles the matrices only for its local subset of edges.

As the result of the distributed assembling, the matrix equation (3) is distributed by lines among processing units of a cluster. Therefore the basic matrix and vector operations are parallelized in the time integration loop. First each processor assembles his part of the right hand side (incident wave or source antenna). These partial source terms are concatenated in SPMD mode. Then the Preconditioned Conjugate Gradient (PCG) is used to solve the matrix system. Since the matrix system is well preconditioned, diagonal preconditioning is used to avoid messages passing during this stage. Partial matrix vector multiplications [2] are performed in parallel. Only non zero terms of partial vectors are sent for the concatenation (SPMD mode).

Efficiency of the algorithm is evaluated on a heterogeneous cluster of PC workstations (COW) connected by a Giga switch. The efficient data transfer between

processing units is a critical issue in the distributed implementation. The interdependent threads communicate through either MPI or PVM message passing environment. In the MPI version, the network traffic is minimized by using broadcast communication rather than point-to-point data transfer. In the PVM version the processing units communicate only in the individual mode because of the low performances of the implemented broadcast function.

RESULTS AND DISCUSSION

The elaborated algorithm is scalable, because the number of computing units can be flexible matched in SPMD mode. The real enlargement of the FE model is limited by minimum size of memory of a single computing node, because the set of data is not totally decomposed. Table I gives the memory repartition for a 342342 degrees of freedom (DOF) problem. Global variables are the set of data duplicated on each processor (global vectors, …). Local variables concern data specific to each processor (mesh, lines of the matrix, …).

TABLE I. SCALABILITY OF THE ALGORITHM.

	Processing units in the cluster of workstations			
	1	2	3	4
Local variables	100%	100%	100%	100%
Global variables	270%	140%	98%	75%

The interdependence of the processes is different in the assembling stage and in the time integration loop. The assembling thread in the processing unit is loosely connected with the others threads. The subtasks in the distributed implementation of the PCG algorithm are tightly coupled. In this case, the workstations are loaded uniformly (table II).

TABLE II. LOAD BALANCING OF THE ALGORITHM FOR 4 PROCESSORS.

	Processing units in the cluster of workstations			
	1	2	3	4
Assembling stage	100%	106%	110%	117%
Time integration loop	100%	100%	100%	100%

The speedup of MPI implementation evolves when the size of the assembled FE model is changed (fig. 1). For the largest FE models, the speedups of MPI and PVM implementations are approximately equal.

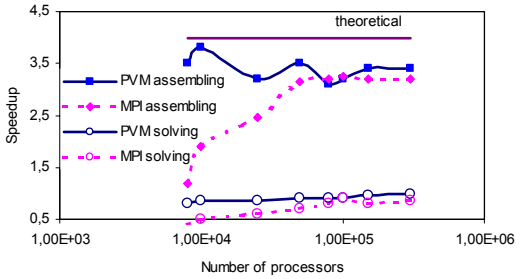

Fig. 1. Speedup of the assembling stage as a function of DOF (4 processing units in the COW).

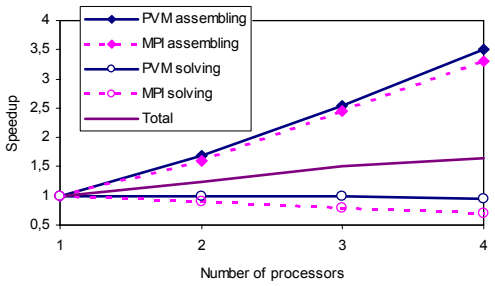

Fig. 2. Speedup of the assembling stage, one time step of the solving stage and for the total computation (342342 DOF problem).

The speedup of MPI implementation evolves with the size of the assembled FE model (fig. 1). For the largest FE models, the speedups of MPI and PVM implementations are approximately equal. They increase linearly with respect to number of processing units, however it is less than the ideal one (fig. 2). This stage is highly parallelized, but inherently sequential nature of input operations and mutual data transfers of BC data slow the overall speedup down. On the other hand the speedup of the solver stage (one time step: source term assembling and PCG) is below 1 for any FE model (fig. 2). This effect arises from non-overlapped, intensive communication and inter-dependencies between distributed threads of the PCG subroutine. Therefore, for a 342342 DOF problem, the total speedup (assembling and 300 time steps) is greater than 1 (fig. 2).

The communication pattern of the parallel FETD algorithm is fully structured and predictable. The computational load is proportional to the local size of sub-model. The communicational load is proportional to the total number of edges in the FEM model, and it depends on the number of processing units in the cluster. The heart and bottleneck of the concurrent FETD algorithm is the distributed solver for large sparse matrix equation. Furthermore, the scalability of the parallel algorithm is very good. In this way, realistic problems can be solve (fig 3).

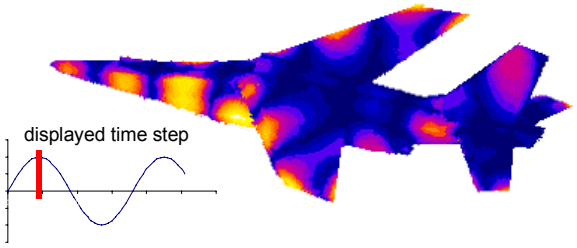

Fig. 3. Scattering by a PEC airplane in time domain (574151 DOF).

REFERENCES

[1] U. Navsariwala, S. Gedney, "An Unconditionally Stable Parallel Finite Element Time Domain Algorithm," *IEEE APS/URSI Symposium,* 1996.

[2] C. Vollaire, L. Nicolas, A. Nicolas, "Parallel Computing for the Finite Element Method," *The European Physical Journal Applied Physics*, vol.1, pp. 305-314, 1998.

[3] C. Vollaire, L. Nicolas, "Preconditioning Techniques for the Conjugate Gradient Solver on a Parallel Distributed Memory Computer," *IEEE Trans. on Magnetics*, IEEE, vol. 34, No. 5, pp. 3347-3350, 1998.

3-D Finite Element Analysis of Skewed Squirrel-Cage Induction Motor

Tadashi Yamaguchi, Yoshihiro Kawase and Shinya Sano
Department of Information Science, Gifu University
1-1, Yanagido, Gifu, 501-1193, Japan
e-mail: yamachu@info.gifu-u.ac.jp

***Abstract*— We have developed a new 3-D finite element mesh modification method for skewed motors. In this paper, the method is presented and is applied to the 3-D magnetic field analysis of a skewed squirrel-cage induction motor.**

INTRODUCTION

The magnetic field analysis for skewed motors is conventionally carried out using the 2-D finite element method with considering several cross-sections at the different axial position [1]. Using the 3-D finite element method, it is carried out with the regular coupling mesh [2] or with the mesh adapted by the auto-mesh generator at each rotation angle [3]. However, if the 2-D FEM with several cross-sections, it is difficult to obtain the three dimensional flux and eddy current distributions. On the other hand, if the 3-D FEM with the regular coupling mesh or with adapting the mesh is used, it is necessary to solve the equation for the regular coupling mesh or to modify the mesh at each rotation angle so that they require a long computing time. Then, we have developed a new 3-D finite element mesh modification method for skewed motors. In our method, the auto-mesh generator is necessary, however, the conventional method is available for the mesh modification at each rotation angle [4]. The auto-mesh generator is used for only making the initial mesh and the computational cost is very small. In this paper, the method is presented and it is applied to the 3-D magnetic field analysis of a skewed squirrel-cage induction motor.

ANALYSIS METHOD

A. Magnetic Field Analysis

The fundamental equations of the magnetic field using the 3-D finite element method can be written using the magnetic vector potential $\boldsymbol{A}$ and the electric scalar potential ϕ as follows [4]:

$$\mathrm{rot}(\nu\ \mathrm{rot}\ \boldsymbol{A}) = \boldsymbol{J}_0 + \boldsymbol{J}_e \tag{1}$$

$$\boldsymbol{J}_e = -\sigma\left(\frac{\partial \boldsymbol{A}}{\partial t} + \mathrm{grad}\ \phi\right) \tag{2}$$

$$\mathrm{div}\ \boldsymbol{J}_e = 0 \tag{3}$$

where, ν is the reluctivity, $\boldsymbol{J}_0$ is the exciting current density, $\boldsymbol{J}_e$ is the eddy current density and σ is the conductivity.

B. 3-D finite element mesh modification method for skewed motor analysis

Our newly developed method for the skewed motor analysis is carried out as follows:

First of all, the conventional 3-D mesh for the motor analysis is prepared, which is not skewed and is made by building up the 2-D mesh as shown in Fig. 1 (a). The air gap between the stator and the rotor is divided into two areas. One is in the stator region and another is in the rotor region. Next, the elements in the air gap of the rotor region are deleted as shown in Fig. 1 (b). Then, the rotor is skewed as shown in Fig. 1 (c). At last, the skewed rotor and the stator region are connected to each other by the auto-mesh generator as shown in Fig. 1 (d).

In this process, new elements, nodes and edges are generated in the air gap of the rotor region. The number and the coordinates of nodes on the surface of the new rotor region are corresponded to those on the surface of the rotor region. If the tetrahedral elements are used, it is necessary to consider the relationships of edges between the rotor and stator regions as well as those of nodes.

Using the initial mesh created by the above method, the mesh modification at each rotation angle is performed as usual [4]. In our method, the auto-mesh generator is used for making only the initial mesh and it is limited in the air gap of the rotor region. Therefore, it is not necessary to use the auto-mesh generator at each rotation angle.

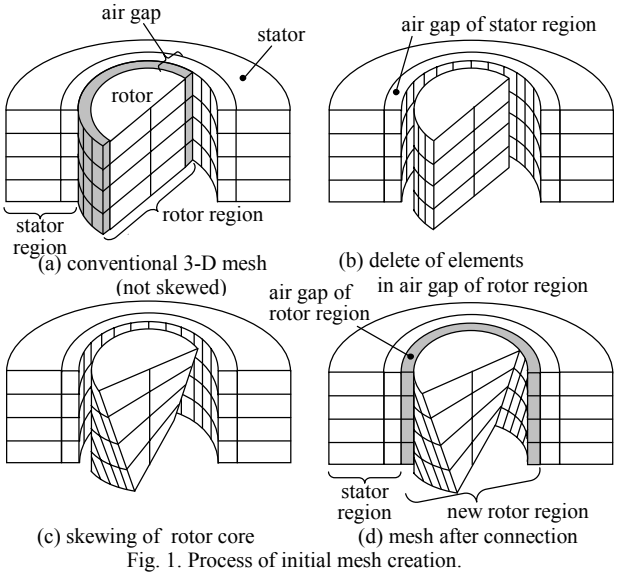

Fig. 1. Process of initial mesh creation.

ANALYZED MODEL AND CONDITION

Fig. 2 shows the analyzed model of a squirrel-cage induction motor, which rotor is skewed with one rotor slot pitch. It is 1/2 of the whole region because of the symmetry and periodicity. The three-phase coils are connected in the Y-connected circuit [5]. The rated voltage is 100V and the frequency is 50Hz. Fig. 3 shows the 3-D finite element mesh. The number of element is 494,244.

RESULTS AND DISCUSSION

Fig. 4 shows the contours of the flux density in the stator and rotor core. It is found that the flux density distributes three dimensionally due to the skew. Especially, the upper part differs from the under part on the stator teeth or the rotor surface. Fig. 5 shows the distribution of the eddy current density vectors in the secondary conductor. It is found that the eddy currents flow complexly in the bars through the end-ring. The results of measured and calculated torque and current will be shown in the full paper.

CONCLUSIONS

We have developed the new mesh modification method for the skewed motor analysis using the 3-D finite element method.

It is applied to the analysis of the skewed squirrel-cage induction motor. The validity of our mesh modification method is clarified through the computation of flux and eddy current distributions.

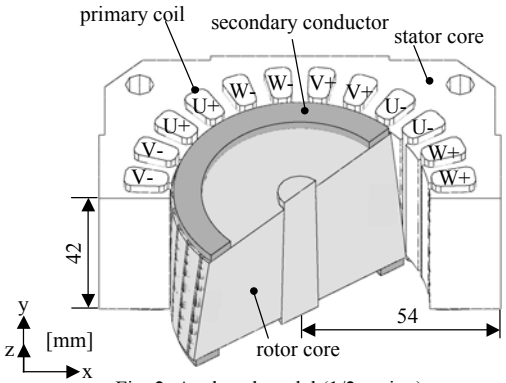

Fig. 2. Analyzed model (1/2 region).

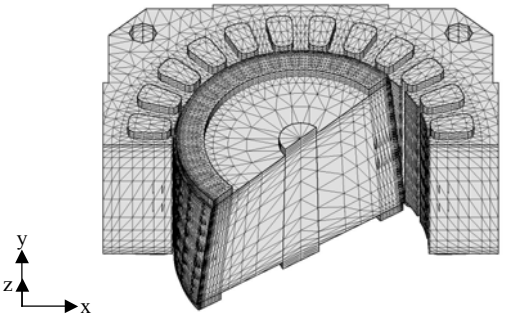

Fig. 3. 3-D finite element mesh.

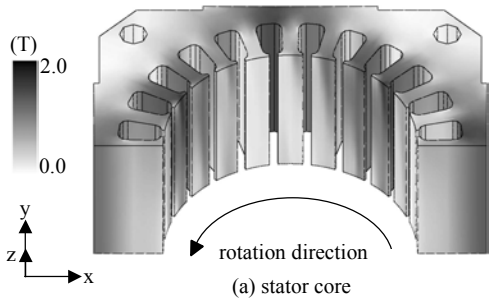

(a) stator core

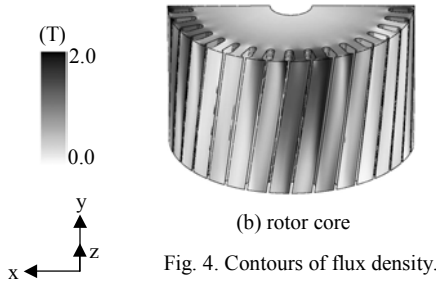

(b) rotor core

Fig. 4. Contours of flux density.

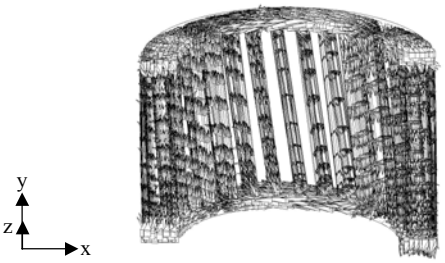

Fig. 5. Distribution of eddy current density vectors in secondary conductor.

REFERENCES

[1] T. Matsubara, Y. Ishihara, S. Kitamura, Y. Inoue and N. Takahashi, "Magnetic field analysis in condenser motor considering skewed slot effects", *IEEE Transactions on Magnetics*, vol. 33, no.2, pp.1698-1701, March, 1997.

[2] H. Kometani, S. Sakabe and A. Kameari, "3-D analysis of induction motor with skewed slots using regular coupling mesh", *IEEE Transactions on Magnetics*, vol. 36, no. 4, pp.1769-1773, July, 2000.

[3] K. Tani, T. Yamada and Y. Kawase, "A new technique for 3-D dynamic finite element anaysis of electromagnetic problems with relative movement", *IEEE Transactions on Magnetics*, vol. 34, no.5, pp.3371-3374, September, 1998.

[4] Y. Kawase, T. Yamaguchi and Y. Hayashi, "Analysis of cogging torque of permanent magnet motor by 3-D finite element method", *IEEE Transactions on Magnetics*, vol. 31, no. 3, pp.2044-2047, May, 1995.

[5] T. Yamaguchi, Y. Kawase, M. Torizawa and S. Ito, "Finite element analysis of motors taking into account Y-connected circuit", Proceedings of the First Japanese-Australian Joint Seminar on Applications of Electromagnetic Phenomena in Electrical and Mechanical Systems, pp.85-90, 2001.

Adaptive Finite Element Meshing for Eddy Current Analysis of Moving Conductor

Katsumi Yamazaki, Shinjiro Watari and Akira Egawa

Dept. of Electrical Engineering, Chiba Institute of Technology
2-17-1, Tsudanuma, Narashino, Chiba 275-0016, Japan (yamazaki@pf.it-chiba.ac.jp)

Abstract — **In this paper, we propose a novel method for the transient eddy current analysis of moving conductor using the moving coordinate system and the adaptive finite element meshing. The error estimation and the auto meshing are applied at each time-step to obtain the appropriate finite element mesh at each position of the conductor automatically. The interpolate calculation is carried out to obtain the potential of the conductor at previous time-step for the calculation of eddy currents. The proposed method is applied to the solid and cage induction motors, which include homogeneous and heterogeneous moving parts, to clarify the validity and the advantages. It is clarified that the proposed method gives accurate results with small number of finite elements.**

I. Introduction

The formulation using moving coordinate system for eddy current analyses of moving conductor [1]-[3] is widely applied to the finite element analysis of electric machines. The advantages of the formulation can be considered as follows:

(a) The oscillation of the solution caused by the high Peclet number [1], [3], [4] can be avoided.
(b) The finite set of the matrix is symmetric [1].
(c) Eddy currents in heterogeneous moving material, for example, cage rotors of induction motors, can be calculated [3].

When the position of the moving parts is changed, re-meshing of the finite elements is required. In the conventional method using moving coordinate system, the mesh in the conductive region should be fixed and the re-meshing must be carried out at the other region. However, it can be considered that the appropriate finite element mesh in the conductor may vary due to the position.

In this paper, we propose a novel method for eddy current analysis of moving conductor using the moving coordinate system and the adaptive finite element meshing at each position of the conductor. In the method, not only the finite element mesh in the nonconductive region but also the conductive region is changed automatically and properly at each time-step. Consequently, accurate results can be obtained with small number of finite elements. The proposed method is applied to solid and cage induction motors, which include homogeneous and heterogeneous moving parts respectively, to clarify the validity and the advantages.

II. Formulation

The governing equations of the moving conductor introduced in the moving coordinate system are:

$$\nabla\times(\frac{1}{\mu}\nabla\times\boldsymbol{A})=\sigma(-\frac{\partial\boldsymbol{A}}{\partial t}-\nabla\phi) \tag{1}$$

$$\nabla\cdot\{\sigma(-\frac{\partial\boldsymbol{A}}{\partial t}-\nabla\phi)\}=0 \tag{2}$$

where $\boldsymbol{A}$ an ϕ are the magnetic vector and the electric scalar potential, μ is the permeability and σ is the conductivity of the conductor. The time derivation term in (1), (2) can be discretized using the backward differential method [1]-[3] as

$$\frac{\boldsymbol{A}^{t+\Delta t}(x)-\boldsymbol{A}^{t}(x-\boldsymbol{V}\Delta t)}{\Delta t} \tag{3}$$

where Δt is the time interval, $\boldsymbol{x}$ indicates a point on the fixed coordinate system, $\boldsymbol{V}$ is the velocity of the conductor, $\boldsymbol{A}^{t+\Delta t}$ and $\boldsymbol{A}^{t}$ are the unknown and the primary values, respectively.

Fig.1 shows the re-meshing method at each time step in case of the conventional and the proposed methods. The time derivation defined by (3) at the conductive region is obtained by the potential at the point P and P', whose distance is $\boldsymbol{V}\Delta t$. In the conventional method, the mesh in the conductive region is fixed and the re-mesh is carried out at the other region. In this case, the potential $\boldsymbol{A}^{t}$ in the conductive region can be obtained directly at the same node. On the other hand, in the proposed method, not only the mesh in the nonconductive region but also the conductive region is changed properly due to the error estimation at each time step. In this case, the potential $\boldsymbol{A}^{t}$ is obtained by the interpolate calculation using the interpolate function N_{ie} of the element e as follows:

$$\boldsymbol{A}^{t}=\sum_{i=1}^{n}N_{ie}\boldsymbol{A}^{t'} \tag{4}$$

where $\boldsymbol{A}^{t'}$ is the potential of the element e at the previous time step.

When the conductor is surrounded by the region whose permeability is different, for example, cage rotors of induction motors, the element e should be selected properly. In this case, the space derivation of the magnetic vector potential is discontinuous at the boundary [3]. When the new node is generated at the boundary

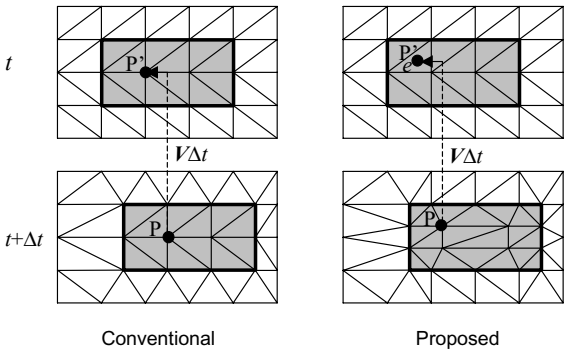

Fig.1. Re-mesh due to movement.

with arch shape as shown in Fig.2, the interpolate function in (4) should be obtained from the element e_1, not element e_2 in case of the first order element.

III. Adaptive Meshing Method

For the error estimation of the finite elements, the Zienkiewicz and Zhu error estimator [5] is applied. In order to decrease the number of the adaptive meshing iteration, the primary mesh of each time-step is obtained from the final mesh at the previous time-step [6] with minor modification. The error estimation and the re-meshing are also carried out at each nonlinear iterative step for decreasing the total number of the iterative calculations [7].

IV. Results and Discussion

Fig.3 shows the adaptive finite element mesh due to the movement of the conductor in case of a solid rotor induction motor. It indicates that the finite element mesh in the conductor is modified due to the variation of the field distribution. Fig.4 shows the calculated result of the instantaneous torque of the motor. The result obtained by the conventional method with the fixed mesh is also shown. The proposed method gives almost identical results with the short calculation time and the small number of finite elements. It can be said that the proposed method can reduce the calculation time by using proper mesh with small number of finite elements at each time-step.

Fig.5 shows the eddy current distribution at the bar of a cage induction motor. It indicates the error of the distribution around the newly generated node P on the boundary between the rotor bar and the core when A^t is calculated form the potentials of the element in the core region. It is clarified that the proper element should be selected for the interpolate calculation as shown in Fig.2 when the conductor is surrounded by the different permeability material.

References

[1] K. Muramatsu, T. Nakata, N. Takahashi and K. Fujiwara, "Comparison of Coordinate Systems for Eddy Current Anaysis in Moving Conductors," *IEEE Trans. Magn.*, vol.28, no.2, 1186, 1992.

[2] K. Yamazaki, "Generalization of 3D Eddy Current Analysis for Moving Conductors Due to Coordinate Systems and Gauge Conditions, " *IEEE Trans. Magn.*, vol. 33, no.2, 1259, 1997.

[3] K. Yamazaki, " 3D Eddy Current Formulation for Moving Conductors with Variable Velocity of Coordinate System Using Edge Finite Elements, " *IEEE Trans. Magn.*, vol. 35, 1594, 1999.

[4] AT. J. R. Hughes, "A Simple Scheme for Developing 'Upwind' Finite Elements", *Int. J. Num. Meth. Engng.* , vol.12, 1359, 1978.

[5] O.C.Zienkiewicz and J.Z.Zhu, "A simple error estimator and adaptive procedure for practical engineering analysis", *International Journal for Numerical Methods in Engineerings*, Vol.24, 337, 1987.

[6] S. Dufour, G. Vinsard and B. Laport, "2-D adaptive mesh with movement", *IEEE-Trans. Magn.,* vol.37, 3482, 2001.

[7] K. Yamazaki and T. Iwasaki, "Adaptive mesh generation within nonlinear iterative calculations for analyses of electric machines.," Presented at *CEFC 2000*, MC2-7, 2000.

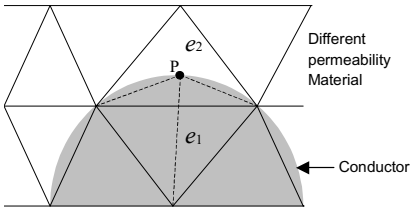

Fig.2. Selection of proper element for the interpolation.

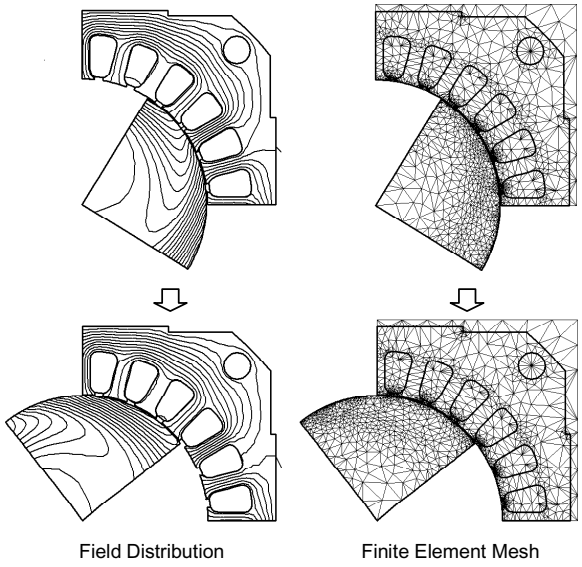

Fig.3. Adaptive meshing due to movement of conductor (Solid induction motor).

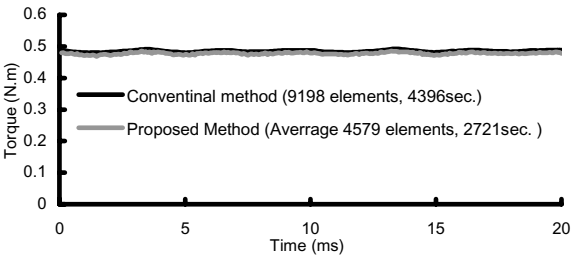

Fig.4. Instantaneous torque calculated by conventional and proposed method.

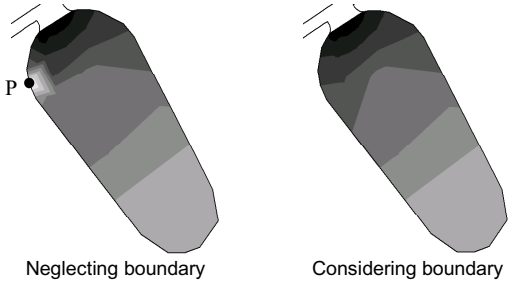

Fig.5. Eddy current distribution in bar of cage induction motor.

COMPUMAG Saratoga Springs, New York USA
July 13 - 17, 2003

Optimal Discretization-based Load Balancing for Parallel Adaptive Finite Element Electromagnetic Analysis

Dennis Giannacopoulos
Department of Electrical & Computer Engineering, McGill University
3480 University Street, Montreal, H3A 2A7, Canada
email: dennis.giannacopoulos@mcgill.ca

***Abstract*—The potential benefits of employing optimal discretization-based refinement criteria to achieve load balancing in parallel adaptive finite element electromagnetic analysis are considered. Specifically, the ability of this class of adaption refinement criteria to resolve an effective domain decomposition based on initial discretizations with only relatively few degrees of freedom are examined. The new load balancing method is evaluated with adaptively refined finite element solutions for a range of electromagnetic benchmark systems and practical adaption models.**

Introduction

Adaptive finite element analysis (AFEA) for the electromagnetic simulation of various applications has become increasingly important over the years, and is now a well-established research area [1,2]. In particular, AFEA has gained considerable attention for solving computationally large problems more efficiently than non-adaptive methods permit. In general, finite element solutions are approximate: their accuracy depends on the number of degrees of freedom (DOF) used and how effectively they are distributed throughout the problem space. In addition, the cost of solving a finite element problem grows with the number of DOF used in the discretization. Consequently, the most efficient distributions of DOF are those that yield sufficiently accurate solutions using the fewest free parameters [1]. Thus, one practical way to achieve this objective is by using adaptive solution strategies that are capable of intelligently evolving and improving efficient distributions of DOF over the problem domain, by establishing solution error distributions and selectively adding DOF to the discretization to correct them. Hence, the primary benefit of AFEA is the efficient and accurate computational analysis of large continuum problems, for only a relatively small fraction of the cost associated with non-adaptive finite element methods [1].

Despite the advantages of AFEA, the computational effort required for the electromagnetic simulation of very complex structures can still be prohibitive [3]. The main difficulty is that a very large number of DOF are necessary for computing accurate solutions of realistic systems: sufficient DOF are required to both resolve the geometric and material features of practical devices, and to represent the highly non-uniform fields. As a result, electromagnetic simulation of such systems can be intractable within conventional sequential programming models, even when using AFEA. Currently, one promising approach to overcome this type of computational barrier is to combine AFEA with high-performance computing (HPC) methods, such as parallel and distributed simulations [4,5].

Combining AFEA with HPC methods to achieve higher gains in efficiency makes it possible to solve previously intractable problems; however, major computational challenges exist for effective implementations. Parallel and distributed AFEA simulations introduce issues that do not arise with simpler solution strategies [5]. In particular, adaptive algorithms evolve non-uniform discretizations that can make the task of balancing processor computational work load more difficult than with uniform structures. For example, this type of load balancing problem can be especially problematic for distributed programming models when finite element discretizations are partitioned into subdomains, which are then assigned to specific processors. (This type of partitioning is also referred to as domain decomposition in the context of parallel finite element analysis.) Essentially, some subdomains require more refinement than others as a discretization is adapted. Thus, an initial discretization that is evenly distributed among processors in terms of workload, can lead to a severe workload imbalance as the adaption progresses towards more highly enriched discretizations [5].

Various types of load balancing approaches for AFEA have been proposed [5]. However, one common drawback is the high communication costs associated with assessing the severity of the load imbalance, computing a more balanced work load distribution, and redistributing the improved work load among the available processors at a given iteration of the adaptive process. The purpose of this contribution is to investigate the practical value of an alternative approach of addressing the load balancing problem for AFEA, which requires substantially less communication overall. Specifically, the ability of a class of adaption refinement criteria [2] to resolve an effective domain decomposition based on initial discretizations with only relatively few degrees of freedom are examined.

Optimal Discretization-based Load Balancing

Typically, remapping or redistribution of DOF to available processors is performed by load balancing algorithms for AFEA, at various stages of the adaption process, in order distribute the work load as evenly as possible. In the case of remapping, a domain decomposition is recomputed in order to repartition the entire discretization into subdomains that, ideally, represent equal amounts of computation. Alternatively, DOF can be redistributed among existing subregions in order to balance the processor workload. Sophisticated algorithms have been developed based on both approaches over the past several years [5]. However, the total communication-to-computation cost ratios involved can still be quite high and reduce the overall efficiency of the AFEA process.

An alternative load balancing approach for AFEA, which requires considerably less communication among processors, is to predict an efficient domain decomposition for the entire adaption process based on a single initial discretization containing relatively few DOF. The main advantages of this approach are two-fold: it avoids having to solve the load balancing problem repeatedly on large discretizations; and inter-processor communication, for the purpose of load balancing, is required only once. Clearly, the effectiveness of this type of approach is strongly dependent on its ability to predict how a coarse initial discretization will evolve throughout the adaptive process.

In this work, optimal discretization-based refinement criteria [2] are used to asses the relative solution error over an initial finite element discretization, during the early stages of the adaptive process. Subsequently, subregions are defined based on equally distributing the total estimated solution error over each subregion, as predicted by the refinement criteria. Thus, if the number of subregions created is an integer multiple of the number of available processors, each processor can be assigned a partition of the initial discretization with approximately equal estimated solution error. Hence, each processor may then independently apply AFEA to its corresponding partition until solution convergence is achieved. (Complete theoretical and algorithmic details will be provided in the long version of the paper). The hypothesis that must hold in order for this approach to yield a balanced work load among processors, is that having approximately equal error in each partition of the initial discretization will result in equal work for the processors in the ensuing computations. The validity of this hypothesis is examined with a fundamental benchmark system in the following section.

Results

A simple 1-D free-space example is presented first in order to examine the effectiveness of new load balancing approach for AFEA. This static benchmark system is based on resolving the classical point singularity model in free-space [2]. The objective for this benchmark system is to compute the functional value based on the resolution of a radial neighborhood close to the point charge and spanning a 100-fold decay in electric scalar potential (full analysis details will be given in the long version paper).

TABLE I
Percent of Total workload vs. Processor Number

Method	Processor			
	1	2	3	4
Uniform/non-adaptive	77.3%	9.09%	9.09%	4.54%
Uniform/adaptive	36.4%	27.3%	22.7%	13.6%
New approach	22.7%	27.3%	27.3%	22.7%

The results for the 1-D example are given in Table I. To focus ideas, three mesh partitioning strategies for achieving load balancing are considered. The first approach, labeled "uniform/non-adaptive", is based on a uniform partitioning of the initial mesh into subregions containing equal numbers of DOF. The second strategy (uniform/adaptive), is based on uniformly partitioning the discretization into subregions containing equal numbers of DOF after several adaptive refinements of the initial mesh have taken place. Finally, the new approach is based on using optimal discretization-based refinement criteria to partition the same mesh as for the second method above into subregions of equal estimated solution error, as explained in the previous section. Evidently, the new approach is able to achieve a better workload balance among the processors than the other two approaches. Full results based on additional test systems and a range of practical adaption strategies will be presented at the conference and in the long version of the paper, along with a complete discussions of the findings, in order to better understand the potential impact and merit of the concepts.

References

[1] T. Strouboulis and K. A. Haque, "Recent experiences with error estimation and adaptivity. Part 1: Review of error estimators for scalar elliptic problems", *Computer Methods in Applied Mechanics and Engineering*, vol. 97, pp. 399–436, 1992.

[2] D. Giannacopoulos, *Optimal Discretization-based Adaptive Finite Element Analysis for Electromagnetics,* Ph.D. Thesis, McGill University, 1998.

[3] D. Giannacopoulos, "Towards optimal error distributions in adaptive finite element electromagnetic analysis for microelectronic interconnection structures," *IEEE Trans. Magn.*, vol. 38(2), pp. 401–402, 2002.

[4] S. McFee and D. Giannacopoulos, "The implications of parallel processing on *h-p* adaptive finite element analysis for electromagnetics," *IEEE Trans. Magn.*, vol. 34(5), pp. 3284–3287, 1998.

[5] C-J. Liao and Y-C. Chung, "Tree-based parallel load-balancing methods for solution-adaptive finite element graphs on distributed memory multicomputers," *IEEE Trans. Parallel and Distributed Systems*, vol. 10(4), pp. 360–370, 1999.

Towards Optimal Mesh Quality Improvements for Adaptive Finite Element Electromagnetics with Tetrahedra

Mark Dorica and Dennis Giannacopoulos
Department of Electrical & Computer Engineering, McGill University,
3480 University Street, Montreal, H3A 2A7 Canada
email: dennis.giannacopoulos@mcgill.ca

***Abstract* – Finite element solution efficiency and accuracy can be directly affected by mesh quality. When employing *h*-adaptive solution strategies, a mesh improvement stage is required in order to ensure high quality tetrahedra. The potential benefits and related costs of a family of new mesh smoothing techniques are investigated with benchmark systems.**

INTRODUCTION

While finite element methods (FEMs) are presently employed extensively for electromagnetic analysis and design, the use of adaptive finite element methods (AFEMs) has increased considerably in recent years. Today, the focus is on the research and development of efficient and reliable 3-D methods for the analysis of realistic systems [1]. The primary advantage of AFEMs is the accurate computational analysis of large continuum problems for only a relatively small fraction of the cost of non-adaptive FEMs [1].

Currently, many AFEMs employ *h*-type adaption models, which add elements to the mesh to improve a discretization. AFEMs incorporating *h*-type adaption models have been used successfully for various types of engineering applications. In particular, for problems where singularities in the mathematical field solutions exist (such as those at sharp material edges and corners), *h*-type adaption models have proven to be quite effective, where a large number of smaller elements are needed close to the singularities, but fewer, larger elements suffice further away [1].

Conceptually, *h*-type adaptive refinement is straightforward; however, an effective implementation can be subject to practical limitations. For example, the manner in which new elements are defined, can affect the quality of the resulting mesh. Specifically, the formation of long, thin elements can lead to poorly conditioned finite element matrices, which, in turn, can compromise the accuracy of the solution or the efficiency with which it is computed. Therefore, considerable attention has been given to these issues over the past several years. Accordingly, various mesh quality improvement strategies have been proposed recently in order to avoid the formation of poor quality elements, and their associated problems, which can occur as a result of *h*-adaption [2-7]. Among the most promising mesh quality improvement methods for 3-D meshes are smoothing-based techniques [2-5]. In this work, a family of new smoothing-based techniques are proposed for tetrahedral meshes, in order to examine their potential benefits and related costs for *h*-type adaptive finite element electromagnetic analysis.

OPTIMAL MESH QUALITY IMPROVEMENTS

Mesh smoothing techniques have been shown to be effective in improving tetrahedral meshes [2-5]. These techniques reposition individual vertices within the mesh to improve local mesh quality without changing the mesh topology. Typically, several iterations of smoothing are performed to improve the overall quality of the mesh. Smart-Laplacian smoothing and optimization-based smoothing are two fundamental techniques that have received much attention [2-5]. Smart-Laplacian smoothing repositions a vertex to the average location of the vertices connected to it by edges only if the quality of the local submesh is improved according to a specific quality measure [2]. This yields an improved, yet non-optimal local submesh. Optimization-based approaches formulate the smoothing operation as a nonsmooth optimization problem, and use an analogue of the steepest descent method for smooth functions to maximize or minimize a given mesh quality measure [2,3,5]. This yields an optimal local submesh; however, computational experiments have shown that optimization-based approaches can be up to 10 times more expensive than smart-Laplacian smoothing [2].

In practice, the smoothing component of a mesh improvement system may be implemented as either a single technique or a combination of various smoothing approaches. Combinations of smart-Laplacian smoothing and optimization-based smoothing have been shown to perform favorably for many types of meshes [2,4]. The resulting improvement in mesh quality can be comparable to optimization-based smoothing performed alone, but at only a fraction of the cost [2,4]. In fact, it has been suggested that combined approaches can produce higher quality meshes than pure optimization-based smoothing [2].

Several combined mesh smoothing approaches have been presented in the literature [2,4,5]. Freitag's combined approaches C1, C2, C3 and C4 have been shown to be effective and efficient for improving mesh quality [2,4]. For each smoothing pass, the vertices in the mesh are examined and the type and order of operations performed on the individual vertices depends on characteristics of the local submesh. For example, in the C1 approach, if the poorest quality measure value in the submesh satisfies a user-defined threshold, smart-Laplacian smoothing is used; otherwise optimization-based smoothing is performed. In addition, if a floating threshold is employed, the threshold value is updated

after each smoothing pass. For instance, in the case of a strategy that maximizes the minimum dihedral angle, the threshold may be updated to the global minimum dihedral angle in the mesh plus a constant. (The impact of very small and very large dihedral angles is negative [4].) A major advantage of the floating threshold strategy is that the threshold value is automatically adjusted for targeting the extremal angles in the mesh.

Upon examination of C1, C2, C3 and C4, the fundamental operations can be summarized as: (1) smart-Laplacian smoothing; (2) optimization-based smoothing; (3) smart-Laplacian smoothing if the worst value does not satisfy the threshold; (4) optimization-based smoothing if the worst value does not satisfy the threshold; and, (5) optimization-based smoothing if the worst value does not satisfy the threshold, otherwise smart-Laplacian smoothing. (Note: the worst value corresponds to the poorest mesh quality measure value within the local submesh, e.g., smallest dihedral angle). Thus, it is worthwhile to investigate the potential benefits and related costs of varying the smoothing technique from one smoothing pass to the next. In fact, many combinations of the five fundamental operations may be examined (a complete discussion is presented in the full paper). One such approach (D1), would proceed as follows: (3)-(5)-(4)-(3)-(5)-(4) (six passes with a floating threshold). The effectiveness of this sample new approach is examined in the following section.

RESULTS

A basic benchmark example is considered, in order to evaluate the potential benefits of the new smoothing approach D1. The problem consists of a unit cube with an initial mesh of 25,688 tetrahedra: a standard problem for mesh quality analysis [2,4,5]. (Full analysis details will be given in the long version paper.) In practice, maximizing the minimum sine of dihedral angles of the incident tetrahedra has been shown to effectively eliminate extremal angles [2,4], and is used as an objective function in this example. The initial threshold value is set to 10° and is updated to the global minimal dihedral angle in the mesh plus 5° after each smoothing pass. Smoothing is performed over six passes.

The results for the benchmark problem are summarized in Table I. Global minimum and maximum dihedral angles, a dihedral angle distribution and average time required to smooth each local submesh are presented. It is evident that D1 yields a significantly improved quality mesh. The quality is superior to C1, C2, and C3 for similar computational time. D1 and C4 yield comparable quality meshes, yet D1 is more than twice as fast. Fig. 1 shows the percentage of angles in each six degree bin (30 bins total). D1 seems to produce more equilateral tetrahdra than C4, while removing extremal angles equally well. Overall, the new approach is seen to provide significant benefits in terms of improving mesh quality at low computational cost. Additional techniques and related findings will be examined in the long version paper.

TABLE I. NUMERICAL RESULTS FOR BENCHMARK

Case	Min. dihed.	Max. dihed.	% Dihedral angles <			% Dihedral angles >			Time (ms)
			6°	12°	18°	162°	168°	174°	
Init.	0.369°	179°	0.091	0.51	1.35	0.28	0.11	0.019	N/A
D1	16.2°	158°	0	0	0.1	0	0	0	0.398
C1	10.1°	164°	0	0.024	0.55	0.014	0	0	0.384
C2	10°	164°	0	0.034	0.61	0.018	0	0	0.378
C3	10°	165°	0	0.13	1.07	0.071	0	0	0.213
C4	16.7°	158°	0	0	0.0071	0	0	0	0.888

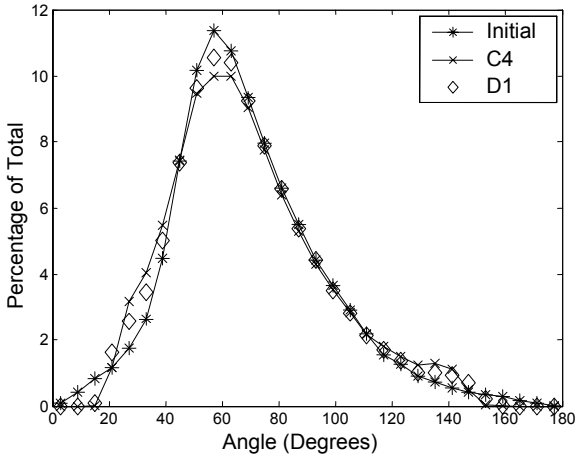

Fig.1. Distribution of dihedral angles.

REFERENCES

[1] D. Giannacopoulos and S. McFee. "Adaptive finite element methods for analyzing the electromagnetic performance of microelectronic system interconnections", *Recent Research Developments in Magnetics*, 1:83-114, 2000.

[2] L.A. Freitag. "On Combining Laplacian and Optimization-Based Mesh Smoothing Techniques", *AMD-Vol. 220 Trends in Unstructured Mesh Generation*, ASME, 37-43, July 1997.

[3] S. Canann, M. Stephenson and T. Blacker. "Optismoothing: An optimization-driven approach to mesh smoothing", *Finite Elements in Analysis and Design*, 13:185-190, 1993.

[4] L.A. Freitag and C. Ollivier-Gooch. "Tetrahedral Mesh Improvement Using Swapping and Smoothing", *International Journal for Numerical Methods in Engineering*, 40:3979-4002, 1997.

[5] L.A. Freitag, M.T. Jones and P.E. Plassmann. "A Parallel Algorithm for Mesh Smoothing", *SIAM Journal on Scientific Computing*, 20:2023-2040, 1999.

[6] B. Joe. "Construction of Three-Dimensional Improved-Quality Triangulations Using Local Transformations", *SIAM Journal on Scientific Computing*, 16:1292-1307, 1995.

[7] N.A. Golias and R.W. Dutton. "Delaunay triangulation and 3D adaptive mesh generation", *Finite Elements in Analysis and Design*, 25:331-341, 1997.

High Accuracy Torque Calculation for a Rotating Machine Using Adaptive Meshing

Masahiko Miwa, David Dibben, and Takashi Yamada
The Japan Research Institute, Ltd., Minami-Senba 3-10-19, Chuo-ku, Osaka 542-0081 Japan
e-mail : miwa@osa.sci.jri.co.jp

Abstract—A new two dimensional adaptive meshing method for the analysis of rotating machines is presented. The method takes model symmetries and the force distribution into account when refining the mesh. This allows for a more accurate determination of the cogging torque than using a standard adaptive scheme. A flat-type permanent magnet motor has been modeled to show the effectiveness of the method.

INTRODUCTION

Computer simulation using the finite element method (FEM) is an important tool for the design of small highly efficient rotating machines. To optimize the calculation time for such models, it is usual to combine the FEM calculation with an adaptive meshing method.

However, it is difficult to obtain accurate values for the torque when using the standard adaptive meshing procedures. This is because the mesh generated does not reflect any of the geometric periodicity or symmetry in the model. The resulting irregularity of the mesh makes it difficult to obtain a smooth waveform for the torque. Furthermore, the criteria used for mesh refinement usually does not consider the force distribution.

This paper proposes a new adaptive meshing algorithm specifically designed for the analysis of rotating machines, which takes into account both the geometric features of the model and the force distribution.

ANALYSIS PROCEDURE

The proposed two dimensional adaptive scheme uses an augmented error estimator, which uses the nodal force[1] distribution in addition to standard error estimation[2] to control the mesh refinement. This is combined with a method to ensure that the resultant mesh adheres to any symmetries or periodicities in the model.

The proposed method is constructed by the repetition of a two-dimension mesh coupling method, magnetic field analysis, and the proposed adaptive scheme.

Two Dimension Mesh Coupling Method

The meshes for the rotor and stator are coupled using a Delaunay triangulation procedure[3]. The air gap is re-meshed at each rotor position during the calculation. Since the air gap mesh is a normal FEM mesh, it can be refined using the adaptive scheme. This technique also requires less memory than some alternative schemes such as the boundary element method (BEM)[4].

Error Estimation for Adaptive Meshing Method

During adaptive refinement, an error estimate is found for each element in the mesh from the FEM solution. Elements with a large error are refined and the FEM calculation repeated. The error estimator used in this work is based on that described in [2], however, it is supplemented by a measure based on the nodal force distribution, as described below.

Estimation of Analysis Error Using Nodal Force

The torque is calculated from the sum of the forces on the mesh nodes as found using the nodal force method[1]. To improve the accuracy of the nodal force calculation we try to limit the change in force distribution across a single element. If the force on two of the nodes of an element differs by more than a present value, then the element is marked for refinement, as shown in Fig. 1.

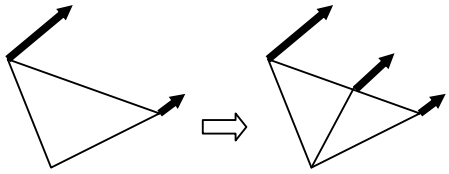

Fig. 1. Nodal forces that are smoothed by divided element

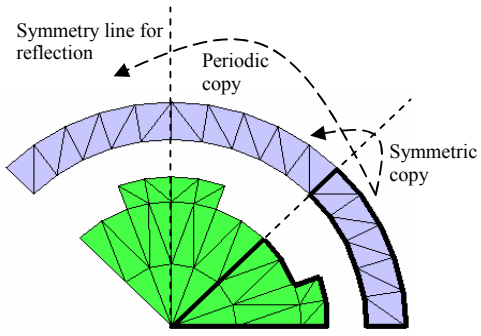

Fig. 2. Periodic and Symmetric mesh

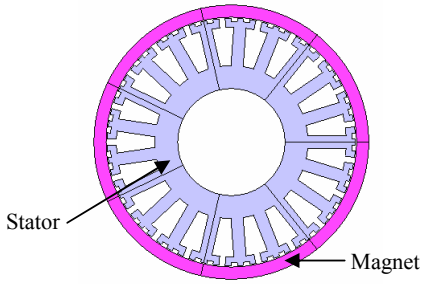

Fig. 3. Flat-type permanent magnet motor

Generating a Periodic and Symmetric Mesh

To generate periodic and symmetric meshes, regions of the model are identified and the mesher ensures that the resulting mesh is periodic and symmetric in these regions as shown in Fig. 2. While this restricts the division that can take place, it is an effective technique for reducing the numerical error.

RESULTS

The proposed method has been applied to a flat-type permanent magnet motor, shown in Fig. 3. The magnet is designed to reduce the cogging torque and the teeth are slotted to further reduce the cogging torque.

Fig. 4 shows the cogging torque calculated using the proposed method, and compares it with results found using standard adaptive refinement that uses only the error criteria for refinement. These results are for the second adaptive step. The waveform of the cogging torque calculated using the proposed method is both cyclic and symmetric.

Fig. 5 shows the convergence of the different adaptive schemes. The result for the proposed method after 6 steps (606,072 elements) was taken as the reference value, τ_T, of the cogging torque and the "error" for the schemes found using

$$Error = \sqrt{\frac{\int_0^T (\tau - \tau_T)^2 d\theta}{\int_0^T \tau_T^{\,2} d\theta}}\ , \qquad (1)$$

where τ is the cogging torque, and T is one period of the cogging torque waveform.

The use of the nodal force error estimator can be seen to improve the performance of the adaptive method, especially in the latter stages of refinement. The standard scheme only produces a small amount of refinement at each step after the third. This is clearly inefficient since many adaptive steps are required. Fig. 5 also shows that using a symmetric mesh also improves the accuracy of the calculation.

CONCLUSION

This paper has proposed a new meshing method for the analysis of rotating machines.

By taking into account model symmetries and the nodal force distribution, the method is able to produce meshes which allow the accurate determination of the cogging torque.

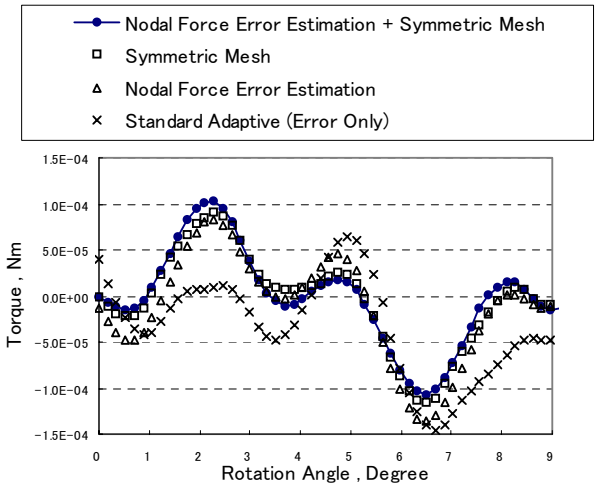

Fig.4. Cogging torque calculated using different adaptive schemes after 2 adaptive steps.

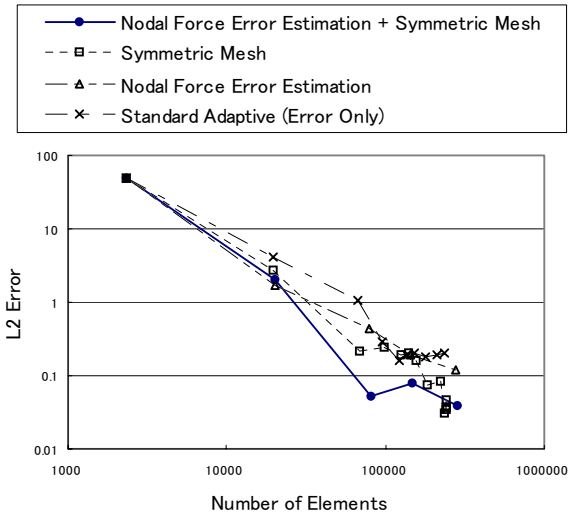

Fig.5. The accuracy of the cogging torque for the different adaptive schemes

REFERENCES

[1] I. Nishiguchi, A. Kameari and K. Haseyama, "On the local force computation of deformable bodies in magnetic field", *IEEE Transactions on Magnetics*, Vol. 35, pp. 1650-1653, May 1999

[2] T. Yokokawa, V. Cingoski, K. Kaneda and H. Yamashita, "Adaptive Finite Element Analysis Using Dynamic Bubble System Taking into Account Magnitude of Magnetic Flux Density", *Transactions IEE Japan*, Vol. 119-D, No. 11, pp. 1416-1421, 1999 (in Japanese)

[3] K. Tani, T. Yamada and Y. Kawase "A New Technique for 3-D Dynamic Finite Element Analysis of Electromagnetic Problems with Relative Movement", *IEEE Transactions on Magnetics*, Vol. 34, pp. 3371-3374, Sep 1998

[4] S. Kurz, J. Fetzer and G. Lehner, "Three dimensional transient BEM-FEM coupled analysis of electrodynamic levitation problems", *IEEE Transactions on Magnetics*, Vol. 32, pp. 1062-1065, May 1996

COMPUMAG Saratoga Springs, New York USA
July 13 - 17, 2003

Mesh Generation Based on Machine Learning

H. Igarashi, A. Yamamoto and T. Honma
Graduate School of Engineering, Hokkaido University
Kita 13, Nishi 8, Kita-ku, Sapporo, 060-8628, Japan, iga@em-si.eng.hokudai.ac.jp

***Abstract*— This paper describes a mesh generation technique for finite element analysis based on machine learning. This method does not require repeated field analysis unlike the conventional adaptive method. The level of each element is evaluated from the sum of the weighted characteristics such as the distance from salient corners of material and element area. The element at the highest level is divided into two elements, and this procedure is repeated until the number of elements reaches a given number. The weighting coefficient is optimized through learning with a number of examples such that the resultant mesh has the lowest numerical error. This method realizes fast and robust meshing for a large class of problems.**

I. Introduction

Mesh generation plays a crucial role in the finite element analysis of electromagnetic fields. One of the most popular methods for the mesh generation is the adaptive method in which the mesh refinement is performed on the basis of error estimation. This method, however, requires long computational time because fields must repeatedly be analyzed for different meshes in the error estimation. We have severer situations in the optimization problems, because a number of different meshes must be generated for different shapes and configurations in the optimization process. It would be difficult to apply the adaptive method to such cases.

In the new method proposed here, finite element meshes are generated on the basis of the machine learning without the repeated field computations. The purpose of the machine learning is, simply speaking, not to find an optimal solution but to find robust and universal rules which lead to a quasi-optimal solution. Such rules are determined by learning many different examples. In the genetic based machine learning (GBML) [1], [2], which will be here applied to mesh generation, the rules are optimized with the genetic algorithm. The present method would work like an experienced mesh designer provided that sufficient learning is executed with proper characteristics and examples.

II. Mesh Generation Procedure

We consider a two-dimensional magnetostatic problem for simplicity. The following mesh generation procedure can be extended to other electromagnetic problems as well as other field problems in fluid dynamics, structural mechanics and so on.

The two-dimensional domain Ω, which is composed of magnetic material, source and air regions, is subdivided into coarse finite elements, which are assumed here to be the first-order triangular elements. The magnetic field is once analyzed on this mesh. The following characteristics $0 \le p_i \le 1$ for each element are evaluated:

$$\begin{aligned} p_1 &= S/S_{\max}, \\ p_2 &= |\boldsymbol{B}|/|\boldsymbol{B}_{\max}|, \\ p_3 &= 1 - d_{\min}/D, \\ p_4 &= 1 - \theta_{\min}/\pi \end{aligned}$$

where S denotes element area, $\boldsymbol{B}$ the magnetic induction computed on the coarse mesh, d the distance from salient corners of the magnetic materials, D the radius of Ω and θ the angle between two edges. The index min and max represent the mimimum and maximum values. The distances are evaluated at the barycenter of the element. Other characteristics such as distance from material surface, field sources and user-specified points can be added to improve mesh quality.

The elements with large values of p_i are thought to have priority for the refinement. To measure the priority reasonably, we introduce the level P defined by

$$P = \sum_i w_i p_i, \tag{1}$$

for each element, where w_i is the weighting coefficient. The element with the largest P is divided into two elements. The method of the subdivision of the element as well as the surrounding elements is the same as the one used in the conventional adaptive meshing. The swapping is followed, if necessary, to retain the mesh regularity. The above procedure is repeated until the number of elements reaches the prescribed number.

The weighting vector $\boldsymbol{w} = \{w_1, w_2, w_3, w_4\}$, normalized as $|\boldsymbol{w}| = 1$, is determined using the genetic algorithm such that the numerical error on the resultant fine mesh becomes smallest. The numerical error ϵ is evaluated with the Zienkiewicz-Zhu method [3], which is widespread in the conventional adaptive method, that is

$$\epsilon = \sqrt{\frac{\sum_e \int_e \nu |\boldsymbol{B} - \boldsymbol{B}_{\mathrm{mean}}|^2 dS}{\sum_e \int_e \nu |\boldsymbol{B}|^2 dS}}, \tag{2}$$

where $\boldsymbol{B}_{\mathrm{mean}}$ denotes the mean magnetic induction over the adjoining elements, ν magnetic reluctivity and e elements.

The weighting vector $\boldsymbol{w}$ is optimized for selected numerical examples. It is expected that the resultant mesh quality becomes better if the number of such learning examples is increased. When the distance between $\boldsymbol{w}$ for different objects is so far that they should not be included in

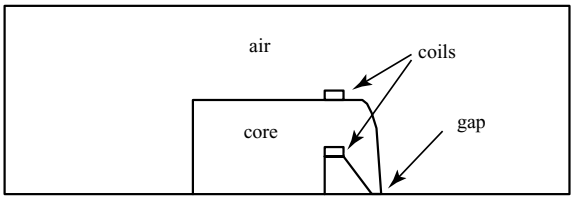

Fig.1 Magnetic head (1/2)

the same class, clustering of the learning objects into some classes would be needed to preserve the mesh quality.

Once $\boldsymbol{w}$ has been determined through the above optimization, the meshes can be generated without the time-consuming evaluation of fields necessary for the conventional adaptive method.

The present method has the following features.
(a) Since the computation required for the present mesh generator which has already been trained is only $\mathcal{O}(N)$, where N denotes the number of elements, this works much faster in comparison with the conventional adaptive method.
(b) If the adequate characteristics and numerical examples for learning are given, the resultant mesh generator is expected to work like an experienced mesh designer.
(c) When $\boldsymbol{w}$ is optimized for enough examples, the present scheme becomes so robust that satisfactory meshes would be generated for unknown objects not included in the learning examples.
(d) The characteristics and weighting vector can be adjusted for special objects such as motors and semiconductor devices. Particularly good quality in the finite element mesh is expected for this kind of ad hoc objects.

III. Numerical Results

The present method is applied to a simple model of a magnetic head, shown in Fig.1, which has uniform relative permeability 1000 without non-linearity in the core. Figure 2 shows the initial coarse mesh for which the magnetic field is analyzed where the error $\tilde{\epsilon}$ is the normalized to this case.

The resultant meshes obtained by the present method are shown in Figs.3-5. The change in $\boldsymbol{w}$ results in the different meshes as shown (a) and (b), where (a) has smaller error. The increase in N leads to the adequate concentration of the elements especially in the core where the magnetic field is expected to be strong, as shown in (a) and (c). The numerical error ϵ is found to be reduced as the increase in N. Note that the error evaluated from (2) is not the "exact error" which would reduce in proportion to $N^{-1/2}$ provided that there are no singular points, i.e., salient corners.

In the long version, $\boldsymbol{w}$ is optimized using several numerical examples, and the resultant mesh is compared with the one obtained by the conventional adaptive method. Moreover, the adequate selection of p_i, distance between $\boldsymbol{w}$ for different models and convergence of the learning process are discussed in detail.

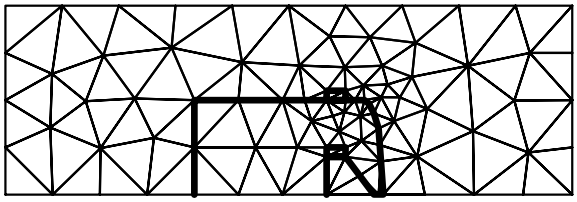

Fig.2 Initial mesh, $N = 148$, $\tilde{\epsilon} = 1.0$

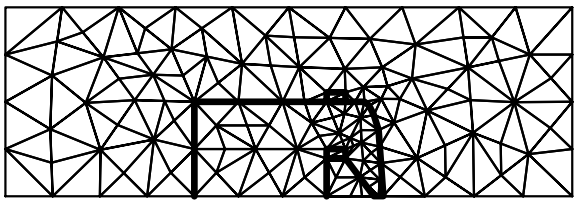

(a) $N = 250$, $\tilde{\epsilon} = 0.437$, $\boldsymbol{w} = \{0.33, 0.11, 0.55, 0.76\}$

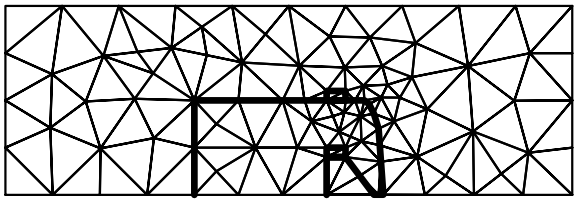

(b) $N = 250$, $\tilde{\epsilon} = 0.550$, $\boldsymbol{w} = \{0.44, 0.29, 0.73, 0.44\}$

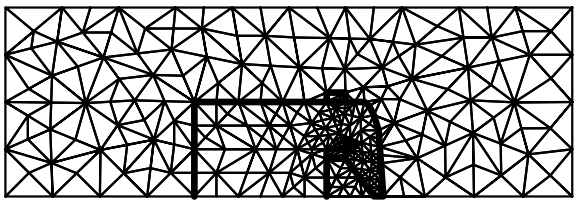

(c) $N = 500$, $\tilde{\epsilon} = 0.150$, $\boldsymbol{w}$ is the same as that in (a).

Fig. 3 Resultant meshes

IV. Conclusions

This paper has described a mesh generation technique based on the machine learning. The present method does not require repeated field analysis unlike the conventional adaptive method. The priority in the mesh refinement is determined from the level defined as the sum of the weighted element characteristics. The weights are determined with the genetic algorithm for examples so that the resultant numerical accuracy becomes smaller. Once the learning processes are completed, the learning machine is expected to generate adequate meshes without time-consuming error estimation.

References

[1] S.F. Smith, A learning system based on genetic algorithm, Univ. of Pittsburgh (1980).
[2] D.E. Goldberg, Genetic algorithm in search, optimization and machine learning, Addison-Wesley (1989).
[3] O.C. Zienkiewicz and J.Z. Zhu, "A simple error estimator and adaptive procedure for practical engineering analysis", *Int. J. Numer. Methods Eng.*, **24**, (1987), 337-357.

A Novel Mesh Regeneration Using Structural Deformation Analysis for 3D Shape Optimization of Electromagnetic Devices

Yingying Yao, Chang Seop Koh*, and Dexin Xie

School of Electrical Engineering, Shenyang University of Technology, Shenyang, Liaoning 110023, P. R. China. yaoying62@hotmail.com
*School of Electrical and Computer Engineering, Chungbuk National University, Chungbuk 361-763, KOREA. kohcs@chungbuk.ac.kr.

***Abstract*— A novel finite element mesh regeneration method is presented for 3D shape optimization of electromagnetic devices. The method has its theoretical basis on the structural deformation of an elastic body. When the shape of the electromagnetic devices changes during the optimization process, a proper 3D finite element mesh can be easily obtained using the method from the initial mesh. For the real engineering problems, the method guarantees a smooth shape with proper mesh quality, and to keep a same mesh topology with the initial mesh. Application to the optimum design of an electromagnetic shielding plate shows the effectiveness of the presented method.**

INTRODUCTION

Optimal shape design is very important for improving the performance of electromagnetic devices. During the last decade, both the deterministic and non-deterministic methods are developed and successfully applied to engineering design problems [1]. The optimal shape design of electromagnetic devices repeats the processes of performance analysis, shape modification and mesh regeneration according to the optimization algorithm till a desired performance is obtained. In this reason, it is necessary to integrate a finite element mesh generator and optimization algorithm with a finite element performance analysis system for achieving a variety of designs automatically and problem independently.

The forgoing researches on the mesh modification method in the optimal shape design might be classified into two types [2]. For the former, the directions of movement of each nodal point are specified according to the shape change, while the topology of the finite element connectivity was fixed as the initial one. This approach failed to yield the optimum design in many problems by crashing elements or destroying convexity of finite elements if an appropriate direction of the mesh movement is not specified by predicting the final shape in advance [2]. In the later case, the interior nodes are generated automatically by certain kinds of interpolation, e.g., line interpolation. This method may lead to severe mesh distortion. Another mesh modification method, introduced by Choi in the structural optimization, has its theoretical basis on the deformation theory of the elastic bosy under the stress [3]. The structural consistency of the material guarantees smooth shape contours as the elastic body deformed. If the structural deformation of the shape is obtained by a finite element solution using a certain discretization, the deformation of the surface results in an evenly distorted mesh of the body. Therefore this mesh modification method can be used for the mesh regeneration of constant topology. Weeber used such idea in 2D shape optimization of electromagnetic devices [1].

In this paper, after the simple review of 3D stress analysis, a novel 3D finite element mesh relocation method for optimal shape design of electromagnetic device is described.

3D MESH RELATION USING STRUCTURAL DEFORMATION THEORY

The strain vector of an elastic body in 3 dimensional structural analysis is defined as follows [4]:

$$\varepsilon = \left[\frac{\partial u_x}{\partial x}, \frac{\partial u_y}{\partial y}, \frac{\partial u_z}{\partial z}, \frac{\partial u_x}{\partial y} + \frac{\partial u_y}{\partial x}, \frac{\partial u_y}{\partial z} + \frac{\partial u_z}{\partial y}, \frac{\partial u_z}{\partial x} + \frac{\partial u_x}{\partial z} \right]^T \tag{1}$$

where the displacement vector is defined as follows:

$$\mathbf{u} = \begin{Bmatrix} u_x(x,y,z) \\ u_y(x,y,z) \\ u_z(x,y,z) \end{Bmatrix} = \sum_{i=1}^{4} \mathbf{N}_i \mathbf{a}_i^e = \left[\mathbf{I}N_i, \mathbf{I}N_j, \mathbf{I}N_m, \mathbf{I}N_p \right] \mathbf{a}^e \tag{2}$$

where $\mathbf{a}^e = \left[\mathbf{a}_i^{\,e}, \mathbf{a}_j^{\,e}, \mathbf{a}_m^{\,e}, \mathbf{a}_p^{\,e} \right]^T$, $\mathbf{a}_i^{\,e} = \left[u_{ix}, u_{iy}, u_{iz} \right]^T$, and N_i is the nodal shape function.

The relationship between the strain and stress for the linear elastic material is given as [4]:

$$\sigma = \mathbf{D}(\varepsilon - \varepsilon_0) + \sigma_0 \tag{3}$$

where σ_0 and ε_0 are the initial residual stress and initial strain, respectively, and the stress σ is

$$\sigma = [\sigma_x \ \sigma_y \ \sigma_z \ \tau_{xy} \ \tau_{yz} \ \tau_{zx}]^T \tag{4}$$

and the corresponding strain is $\varepsilon = \left[\varepsilon_x \ \varepsilon_y \ \varepsilon_z \ \gamma_{xy} \ \gamma_{yz} \ \gamma_{zx} \right]^T$, and $\mathbf{D}$ is the elasticity matrix contains modulus and poisson's ratio.

Applying finite element method with tetrahedral elements to (1) and (3), the matrix equation is obtained as follows:

$$[\mathbf{K}]\{\mathbf{a}\} = [\mathbf{f}] \tag{5}$$

where $\{\mathbf{a}\} = \{\mathbf{a_1}, \cdots, \mathbf{a_N}\}^T$ is the displacement of each node, $[\mathbf{f}]$ is the forcing load vector, and $[\mathbf{K}]$ is the stiffness matrix determined by the geometry and material constants of the elastic body.

Equation (5) is very similar to that of 3D static anisotropic magnetic analysis by using nodal element. The consistent and interrelated property of the deformations in an elastic body can be regarded as a design increment field. In this paper it is used for the mesh relocation during the optimal shape design of electromagnetic device by writing (5) as

$$[\mathbf{K}]\{\Delta x\} = \{\mathbf{f}_x\} \tag{6}$$

where $[\mathbf{K}]$ is the global stffiness matrix for stress analysis, $\{\Delta x\}$ is the nodal displacement, that is the amount of relocation of the nodal coordinates $\{\mathbf{x}\}$, and $\{\mathbf{f}_x\}$ is fictious load force to control the mesh density appropriately. The perturbation of the boundary can be simply considered as a displacement at the boundary. With no additional external forces and a given displacements at the boundary, (6) can be used to find the displacements of the whole nodes. Equation (6) can be rewritten as follows in segmented form:

$$\begin{bmatrix} K_{bb} & K_{bd} \\ K_{db} & K_{dd} \end{bmatrix} \begin{Bmatrix} \Delta x_b \\ \Delta x_d \end{Bmatrix} = \begin{bmatrix} f_b \\ 0 \end{bmatrix} \tag{7}$$

where $\{\Delta x_b\}$ is the known perturbation of nodes on the boundary, $\{\Delta x_d\}$ is the unkown nodal displacement vector for the interior nodes, and $\{f_b\}$ is the fictitious boundary force acting on the boundary. The unknown interior nodal displacement vector can be obtained from the following equation:

$$[K_{dd}]\{\Delta x_d\} = -[K_{db}]\{\Delta x_b\} \tag{8}$$

NUMERICAL EXAMPLE

In order to investigate the applicability of the proposed method to the 3D shape optimization, a simple block model is taken. During the application, the fictious load force is set to zero, and E and ν are set to 0.5, and 0.3, respectively. When the nodal points in a line on the upper surface move, the regenerated meshes are compared, in Fig.1, for the different boundary conditions in the structural analysis. From the figure, where the nodal displacement of the moving node is 30% of the dimension of the model block, it can be seen that proper meshes with reasonable mesh quality are obtained with various boundary conditions. It can also be seen that when the finite element mesh is regenerated using the relocation method, the boundary surface remains smooth. However when the nodal displacement is quite big(the displacement is 60% of the dimension of the block), as shown in Fig. 2, the regenerated meshes are distorted, and the mesh quality is not to be acceptible.

In the version of full paper, an application to the shape optimization of electromagnetic device will be included.

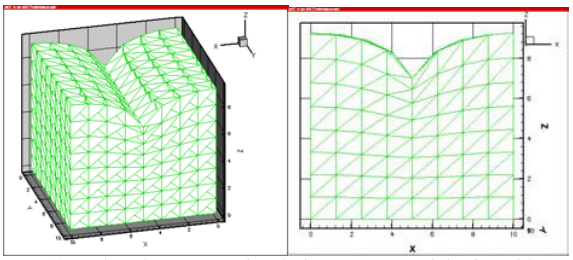

(a) when the upper surface is free to move and the four sides are fixed.

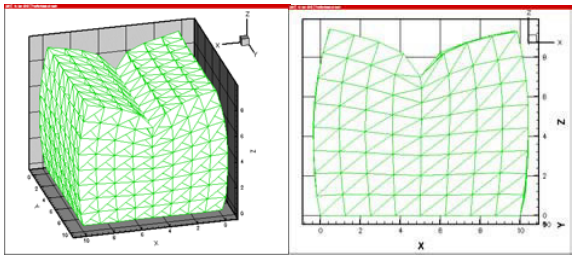

(b) when the upper, four sides are free to move.

Fig.3 The regenerated finite element meshes for different boundary conditions in structural analysis when the nodal displacement is small.

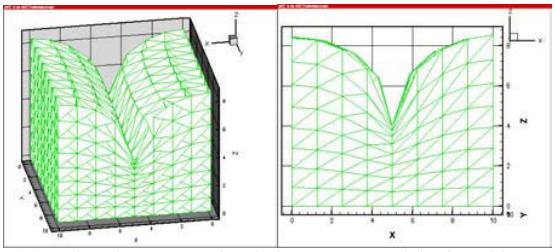

(a) when the upper surface is free to move and the four sides are fixed.

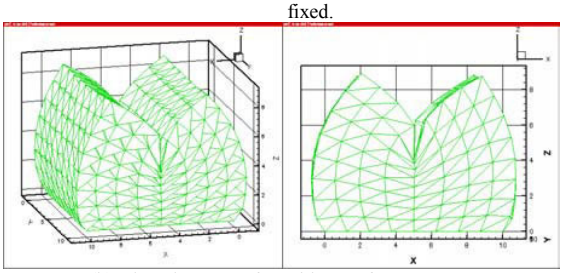

(b) when the upper, four sides are free to move.

Fig.4 The regenerated finite element mesh when the nodal displacement is quite big.

REFERENCES

[1] Konrad Weeber and S.R.H. Hoole, "A Structural Mapping Technique for Geometric Parameterization in the Optimization of Magnetic Devices," International Journal for Numerical Methods in Engineering, vol.33, pp.2145-2179, 1992

[2] P.H. Adeli, *Advances in design optimization*, Chapman & Hall, 1994. pp. 411

[3] Tse-Min Yao and Kyung K. Choi, "3-D Shape Optimal Design and Automatic Finite Element Regridding," International Journal for Numerical Methods in Engineering, pp.1-32, May 1988

[4] O.C.Zienkiewicz, *The Finite Element Method* (third edition), 1977 McGraw-Hill Book Company (UK)

Automatic Hexahedral Mesh Generation for Rotating Machine

Toshihiro Maeda, So Noguchi, Hideo Yamashita
Graduate School of Engineering, Hiroshima University, 1-4-1 Kagamiyama, Higashihiroshima 739-8527, JAPAN
E-mail: yama@eml.hiroshima-u.ac.jp

Abstract — **We have proposed the automatic mesh generator for hexahedral elements previously. This technique can be applied to almost all models. However, if it is applied to a cylindrical model, the mesh, which contains many flat elements, is generated. Using such mesh, it is time-consuming to perform finite element analysis with such mesh and its result may not be good accurate. Therefore, an automatic mesh generator for cylindrical model is required. In this paper, a hexahedral mesh generation method for cylindrical model is proposed. In this method, by using cylindrical coordinate, the mesh with well-shaped hexahedral elements is generated even for complicated analysis domain.**

I. Introduction

In order to perform finite element analysis (FEA), the analysis domain has to be divided into finite elements. For 3-D domain, the mesh generation is, in general, very laborious and time consuming, compared with 2-D domain. Therefore, 3-D FEA is prevented from practicability in many fields. Hence, it is desirable to develop an automatic 3-D mesh generator. An automatic mesh generator commonly generates tetrahedral (Tet) mesh. Tet mesh can be easily generated for a complicated analysis domain because of existing a mathematical approach. However, the number of Tet elements is about 5 times as many as that of hexahedral (Hex) elements with the same number of nodes. Consequently, the FEA with Tet mesh consumes the computation time. On the other hand, if the number of Tet elements is decreased in order to reduce the computation time, we cannot obtain the result with enough accuracy. Accordingly, there is a large interest in the automatic generation of Hex mesh for finite element electromagnetic field analysis mainly due to getting enough accuracy and good convergence. We have previously proposed an automatic mesh generator [1] based on Cartesian coordinate for hexahedral elements, whose technique can be applied to almost all models, such as transformer, actuator, and so on.

Currently, the rotating machines are often analysed by using FEA. When the model of the rotating machine, i.e. motor and generator, is subdivided into a mesh, it is required to be partly fine, such as air-gap, and the elements of any other parts may not be such fine. Of course, the previously proposed method can be applied to the rotating machines. However, the mesh, which is obtained by using the previous method, contains many flat elements. The mesh with a large number of flat elements leads to deterioration of the solution accuracy and to slow convergence. Then, we should modify the previous method to reduce the number of the flat elements for cylindrical model. Hence, we propose an automatic hexahedral mesh generator for cylindrical models, which is based on the previous method.

II. Flow of Proposed System

The main flow of the proposed system is shown in Fig. 1. It consists of:

Step 1. The input data of the proposed method are the geometrical data ("*Shape Model*") and the mesh density data, which is used to control the mesh density in the analysis domain. The mesh density data are easily given at vertices by using the GUI system [2].

Step 2. The model is split into two parts. One is "*Axis Part Model*", which is the neighbourhood around the rotation axis and includes the rotation axis. The other is the rest of the whole model ("*Cylinder Part Model*"). These parts are individually divided into Hex mesh in the following step.

Step 3. The *Cylinder Part Model*, which exists in *xyz*-coordinate (Cartesian coordinate), is changed to "*Rectangular Part Model*", which exists in $\rho\theta'z$-coordinate (Cylindrical coordinate). For generating well-shaped elements, θ-component is transformed to θ'-component and this transformation is explained later.

Step 4. By using the previously proposed method [1], the *Rectangular Part Model* is divided to Hex mesh. This divided model is called "*Divided Rectangular Part Model*".

Step 5. By transformation from $\rho\theta'z$-coordinate to *xyz*-coordinate, the *Divided Part Rectangular Model* is transformed back to "*Divided Cylinder Part Model*".

Step 6. Two parts, which are split in Step 2, are joined. Before joining, the *Axis Part Model*, which includes the rotation axis, has to be divided into Hex mesh.

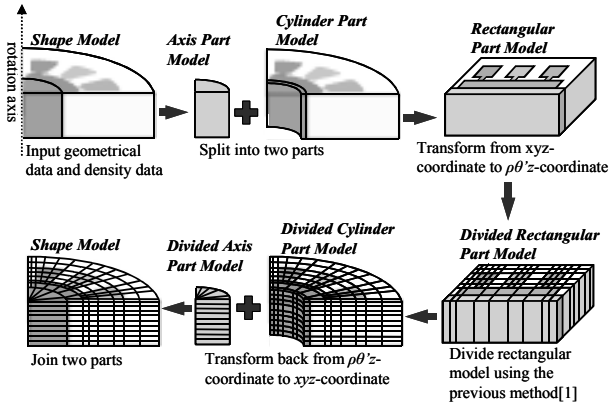

Fig. 1. Simplified algorithm for the proposed method.

In this method, a well-shaped mesh for cylindrical model is obtained due to transformation from *xyz*-coordinate to *ρθ'z*-coordinate.

III. Transformation of Coordinate

Before the transformation of the coordinate, the model is split into two parts; a small part including the rotation axis (*Axis Part Model*) and the rest of the analysis domain (*Cylinder Part Model*). Because the rotation axis cannot transform from *xyz*-coordinate to *ρθz*-coordinate with one-to-one correspondence. Then, the coordinate of the *Cylinder Part Model* is transformed from *xyz*-coordinate to *ρθz*-coordinate. Here, the unit of *θ*-component is radian in this model, however the unit of *r*- and *z*-component is meter. Consequently, for generating well-shaped elements, *θ*-component is transformed to *θ'*-component like below:

$$\theta' = \frac{r_{\max} \cdot \theta}{2\pi}, \qquad (1)$$

where $r_{\max}$ is the maximum value of *r*-component in the model. Since the maximum value of *θ* and *r* are the almost same, the shape of the whole model in *ρθ'z*-coordinate becomes good (see Fig. 2). And after this process, the *Rectangular Part Model* is divided into Hex mesh by using the previously proposed method.

IV. Adjustment Process

In order to join two parts; *Axis Part Model* and *Cylinder Part Model*, the position of nodes on the joint surface have to be in agreement (see Fig. 3). Therefore, the odd numbers of nodes are generated on arc of the joint surface, like Fig. 4. Figure 4 represents an example of 2D quadrilateral elements on the joint surface of the *Axis Part Model*. And the nodes on arc alternatively connect the rotation axis. Consequently, the quadrilateral mesh is generated. On the other hand, on the joint surface of the *Cylinder Part Model*, the same numbers of nodes are generated, so that it is easily able to join the *Axis Part Model* and the *Cylinder Part Model*. After joining, the final subdivision map is obtained (see Fig. 5).

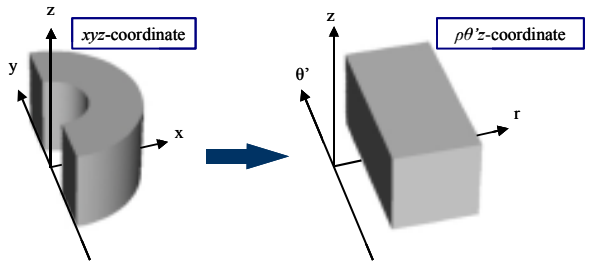

Fig. 2. The Cylinder Part Model, which exists in *xyz*-coordinate, is transformed to the Rectangular Part Model, which exists in *ρθ'z*-coordinate.

V. Applications

To verify the usefulness, the proposed method was applied to the rotating machine shown in Fig. 5, which was divided into 38,069 elements with 42,356 nodes. And, the CPU Time of mesh generation was 160 seconds (CPU:Pentium4 2.0GHz MEMORY:2048MB). As shown in Fig. 5, we confirmed that a suitable Hex mesh with the desired mesh density was generated.

VI. Conclusions

In this paper, we propose development of the previous method for cylindrical models. The key feature of this method is to transform from *xyz*-coordinate to *ρθz*-coordinate. To verify the usefulness, the proposed method was applied to the rotating machine. In the final subdivision map, the well-shaped mesh is obtained for cylindrical models. In this method, the number of the division doesn't depend on the rotating degrees on the air-gap. Therefore, we would like to decide the number of the division partly.

References

[1] S.Nagakura, et al., "Automatic Hexahedral Mesh Generation for FEM Using Shape Recognition Technique and Tree Method", *IEEE Trans. Magn.*, vol.38 no. 2, pp.417-420, March 2002.

[2] S.Nagakura, et al., "Data Input Support System for Automatic Tetrahedral Mesh Generation Using Dynamic Bubble System" *RECORD OF THE 13TH COMPUMAG CONFERENCE*, vol.1, pp.194-195, July 2001.

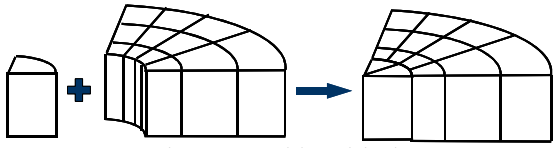

Fig. 3. Two models are joined.

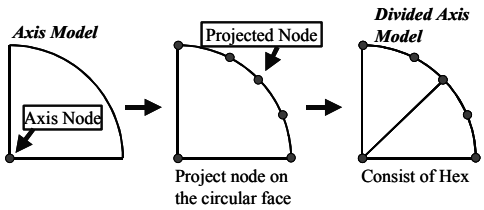

Fig. 4. Quadrilateral Mesh is consisted of the sets of two vertices on the circular surface and one vertex on the rotation axis.

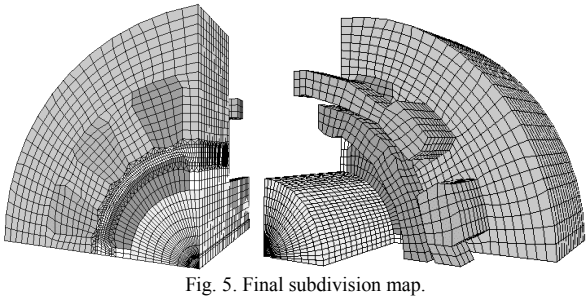

Fig. 5. Final subdivision map.

COMPUMAG Saratoga Springs, New York USA
July 13 - 17, 2003

Application of Parallelized Multigrid Method to Solution of MHD Equilibrium with MPI

[1]Toshihiro Hanawa, [1]Soichiro Ikuno and [2]Atsushi Kamitani

[1] Faculty of Engineering, Tokyo University of Technology
1404-1, Katakura-cho, Hachioji, Tokyo 192-0982 Japan
[2] Faculty of Engineering, Yamagata University
4-3-16, Johnan, Yonezawa, Yamagata 992-8510 Japan
e-mail: hanawa@cc.teu.ac.jp

Abstract—**A nonlinear eigenvalue problem appears in Magnetohydrodynamics(MHD) equilibria determined by solving the Grad-Shafranov equation numerically. After linearization of the nonlinear equation, iterative procedure for the solution of linearized equation spends most part of calculation time. We introduced multigrid method(MGM) instead of the conventional method for solving the linear equation. In this paper, the parallel processing by using Message Passing Interface(MPI) on PC cluster is adopted for the MGM to achieve higher performance.**

Introduction

The nonlinear eigenvalue problem often appears when the magnetohydrodynamics (MHD) equilibrium configurations of toroidal plasma are determined by solving the Grad-Shafranov equation numerically. Because of the nonlinearity, the iterative procedure has been so far employed to the solution of the problem and the procedure includes solving linearized equation in each steps. Therefore, the iterative procedure occupied most of execution time to solve the problem.

The fast Fourier transform and cyclic reduction methods require only $O(N^2 \log N)$ operations when applied to the boundary value problem of two-dimensional partial differential equation (PED). Therefore, these methods are nearly optimal one as the solver of PDE.

The multigrid method (MGM) is comparable to the above rapid methods in execution speed. The purpose of the present study is to make the numerical character of the multigrid method elucidate and to apply the MGM to application of nonlinear eigenvalue problem procedure for determine the MHD equilibrium configuration of low-aspect-ratio toroidal plasma numerically. Furthermore, the parallelize MGM by means of the Message Passing Interface (MPI) in a simple case is investigated.

MHD Equilibrium Configuration

The low-aspect-ratio toroidal plasma is sustained in the metallic vessel, which is called a flux conserver. In order to supply the plasma with the toroidal flux, a center conductor is inserted along the geometric axis and the electric current is applied along it. Since the equilibrium configuration of the plasma is axially symmetrical, we can determine it by solving Grad-Shafranov equation in the $z-r$plane, where $z-$axis is the symmetry axis in the cylindrical coordinate system (z, r, ϕ).

In this study, we use an analytic region Ω as drum-type of domain which size is $[0,1] \times [r_i, r_i + 1]$ and the region Ω is bounded by boundary Γ. Here, r_i denotes the radius of the center conductor.

We assume that the plasma exists only in the region Ω and also assume that the magnetic fields produced by the plasma do not extend outside of Γ[3].

Under these assumptions, the Grad-Shafranov equation can be written in the form,

$$-\hat{L}\psi = f(\lambda, r, \psi)\,, \tag{1}$$

where ψ is the magnetic flux function and $\hat{L}$ is the Grad-Shafranov operator. Further, $f(\lambda, r, \psi)$, is given function satisfies $f(C\lambda, r, \psi) = Cf(\lambda, r, \psi)$ (C, λ = const.). From the above assumptions, the boundary condition is written as $\psi = 0$ on Γ.

The Grad-Shafranov equation and its associated boundary conditions constitute a nonlinear eigenvalue problem with an eigenvalue λ.

After linearlized, the iterative procedure with two steps provides the solution of the problem. In the first step, the linearlized equation is solved by use of ordinary relaxation methods. Next, the approximate eigenvalue is corrected in the second step. Until both the eigenvalue and the flux function converge, above two steps are repeated. The procedure is iterative method, it take much CPU time to solve the problem and the procedure of solving linearized equation in each step takes most of the time. Consequently, we adopt the MGM to the first step of the iterative procedure to obtain better performance[5].

Parallelization of MGM with MPI

In this section, let us parallelize the MGM by use of Message Passing Interface(MPI) [4] to get more performance.

MPI is the standard and portable application interface for message communications among the nodes of which a distributed memory multiprocessor consists.

In practice, MGM is implemented on PC cluster by using MPI. Table I shows the environment of evaluation in this study.

Here, let us solve a 2D nonlinear eigenvalue problem by use of parallelized MGM.

Fig. 1 shows the schematic view of the assignment for 16 processing units (PUs) when the number of grid point per dimension is $N = 2^3$. On the occasion of the calculation on the finest grid, i.e. $N = 2^3$, the PU interchange the values between the adjoin grid point along the boundary of PU. At

TABLE I

EVALUATION ENVIRONMENT(NOT EXCLUSIVE USE FOR COMPUTING)

CPU	Pentium2 350MHz
Memory	128MB
OS	FreeBSD 4.3-release
# of PCs	2 – 128
Network	100Mbps Ethernet

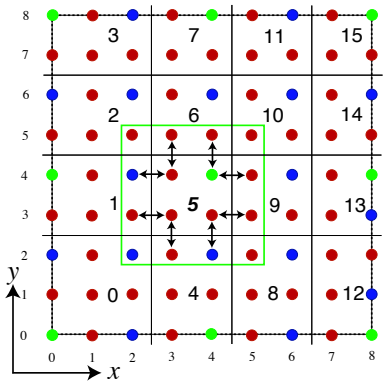

Fig. 1. The schematic view of the assignment for PU

the next step, the values are mapped to the coarser grid, i.e. $N = 2^2$, and calculated on the even number of grid point. Consequently, calculation must go over the odd number grid points and PU must interchange the values on the even number grid points. Finally, on the coarsest grid, i.e. $N = 2$, the number of grid point is smaller than the number of PUs, therefore, the PUs including the grid point need to communicate each other over the other PUs. Since the communications occur frequently and degrade the performance, in this study, data is gathered and calculated in a PU on the coarsest grid.

On each level in MGM, Red-Black Gauss-Seidel method is adopted for the sweeper to obtain higher parallelism, and the communications between processes are overlapped with the calculations possibly.

Fig. 2 shows that 128−PU demonstrates the best performance in case of $N = 2^{12}$. As the number of PUs increase, the larger problem can be solved by means of this environment.

Fig. 3 shows that the speedup ratio is plotted as functions of the number of PU in case of $N = 2^{10}$. The result by use of 32PU shows 7.6 times faster than that by use of 2PU, however, in case of 64–128PU, speedup ratio is degraded. The reason is that the communication time occupies most of total execution time as the number of PUs increases. In fact, in case of $N = 2^{10}$, though the communication ratio is about 25% by use of 8PU, that occupies about 75%, 90% by use of 64PU, 128PU respectively. In large division number, since the relative cost of communication is reduced, speedup ratio can be improved shown as Fig. 2.

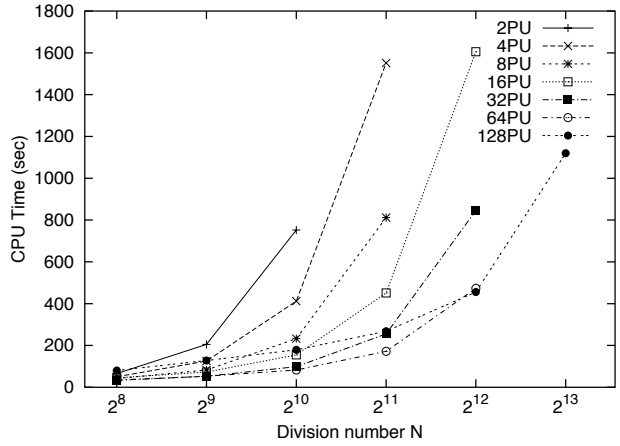

Fig. 2. The execution time vs. division number on each number of processor

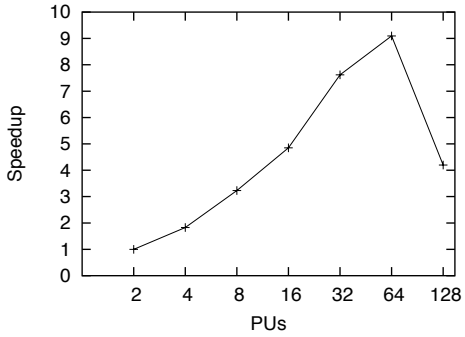

Fig. 3. The speedup ratio as functions of number of PU in case of $N = 2^{10}$

CONCLUSIONS

In this paper, we investigated the application of MGM to solution of MHD equilibrium. Furthermore, we parallelized the MGM by use of MPI on PC cluster.

We applied the MGM for the procedure of nonlinear eigenvalue problem, and solved the 2D nonlinear eigenvalue problem by use of parallelized MGM on PC cluster up to 128PU. As a result, 128PU demonstrated the best performance in case of $N = 2^{12}$, and the problem in case of $N = 2^{13}$ can be solved by use of 128PU. Also, the calculation in case of 32PU showed 7.6 times faster than that of 2PU.

REFERENCES

[1] A. Kamitani, S. Ikuno, T. Kanki, M. Nagata and T. Uyama, *MHD Stability of Tight-Aspect-Ratio Toroidal Plasma -Transition of Spheromak to Tokamak-* in *Advanced Computational Electromagnetics*, A. J. Moses and A. Basak, Eds. Amsterdam,1996,pp. 194-197.

[2] B. L. William, *A Multigrid Tutorial*, Philadelphia, SAIM, 1987.

[3] S. Ikuno, M. Natori and A. Kamitani, *Influence of External Toroidal Flux on Low-Aspect-Ratio Toroidal Plasma* Plasma Physics and Controlled Nuclear Fusion Research, Vienna, IAEA, 1999, pp. 1497-1500.

[4] P. S. Pacheco, Parallel Programming with MPI, Morgan Kaufmann, 1997.

[5] S. Ikuno, T. Hanawa and A. Kamitani, Application of Multigrid Method to Solution of MHD Equilibrium with Parallel Processing, Proc. of the Conference on Electromagnetic Field Computation, Peerugia, Jun. 2002, pp. 187

COMPUMAG Saratoga Springs, New York USA
July 13 - 17, 2003

Improving the bubble meshing technique for remeshing purposes

Vincent Leconte,
Guillaume Lemercier
and Vincent Mazauric
Schneider Electric - Research Center A2
38050 Grenoble Cedex 9, France
Email: vincent_leconte@mail.schneider.fr

Yves Maréchal
Laboratoire d'Électrotechnique de Grenoble
BP46, 38402 Saint-Martin-d'Hères Cedex, France
Email: yves.marechal@leg.ensieg.inpg.fr

***Abstract*— To take into account movement in time-stepping finite element simulations, a possible method is to remesh the changing parts of the geometry. A remeshing technique using bubbles is presented. Attention is paid to the computational cost of the algorithm. Some methods are proposed to reduce it.**

I. Introduction

The idea of the bubble meshing technique is to use a physical model that defines a satisfying node distribution, and to couple it to an algorithm that creates the triangulation, usually based on the Delaunay criterion. This method is generally used for mesh generation or optimization, and it has proven its ability to generate high quality meshes [1][2].

Taking into account the movement of parts of the geometry is essential, when simulating the behavior of electromechanical actuators. Because mesh modifications may introduce numerical noise in the solution, it is important to guarantee a good mesh quality as the geometry changes. Some previous work showed the interest of using bubbles in a remeshing procedure [3]. However, such physically-based meshing algorithm may be time consuming. This article presents a bubble remeshing technique, and proposes several methods that lower the time devoted to the movement of bubbles.

II. A physical model for the mesh

A. Bubble definition

The N nodes of the mesh are considered as particles that interact with each others. The node i of coordinates $\vec{x}_i$ is submitted to the force $\vec{F}_i$ defined as follows:

$$\vec{F}_i = \sum_{i \neq j}^{N} f_{ij} \vec{u}_{ij} \qquad with \qquad \vec{u}_{ij} = \frac{\vec{x}_i - \vec{x}_j}{\| \vec{x}_i - \vec{x}_j \|}. \tag{1}$$

where f_{ij} is the force between particles j and i. The influence of the node i is local and isotrope. That is why it is represented by a bubble centered on the node and of radius r_i. The force f_{ij} is chosen to be purely repulsive. It is set to zero when $\| \vec{x}_i - \vec{x}_j \| > 2(r_i + r_j)$. With this kind of force, the set of bubbles tends to occupy the free space as a perfect gas would do.

Only bubbles that are interior of the domain can move. Bubbles on the domain frontiers should then act as walls that constraint the bubbles to stay inside. For this reason the action of a frontier bubble is twice as much as for an interior bubble.

B. Node ditribution adaptation

The motion equation of bubble i is written as:

$$m_i \frac{d^2 \vec{x}_i}{dt^2} + c_i \frac{d\vec{x}_i}{dt} = \vec{F}_i(x) \tag{2}$$

where m_i is the bubble mass and c_i a damping coefficient. To simulate the movement of the bubbles, a set of N second-order differential equations has to be considered. It is solved using a classical Runge Kutta method.

Since the bubble radii are directly linked to the mesh element size, it is important to control their distribution. Two schemes based on bubble neighborhoods have been tested, producing different behaviors of the bubble set. For example, it can be interesting to let the bubble grow as they move away from the boundaries [3].

C. The remeshing procedure

The proposed procedure is shown in Fig. 1. For small displacements of the mobile part, it leads to an "elastic" mesh in which the nodes are repositioned. For larger movements, moving the nodes is not sufficient and topological changes occur in the mesh. As shown in Fig. 2, the procedure tends to localize these changes close to the moving part.

III. Strategies for cost reduction

Moving the bubbles is the most time consuming part of the remeshing procedure. What follows focuses on this part of the algorithm and discusses some techniques that helps to reduce its cost.

A. Bubble neighborhood

Because bubble forces are only local, the summation in equation (1) should be restricted to the neighbors of bubble i. This is possible only if this neighborhood information is available. Evaluating it is in fact the most time consuming part. Therefore, a criterion has been set up, indicating when it is necessary to update it during the bubble movement, thus reducing the number of evaluations.

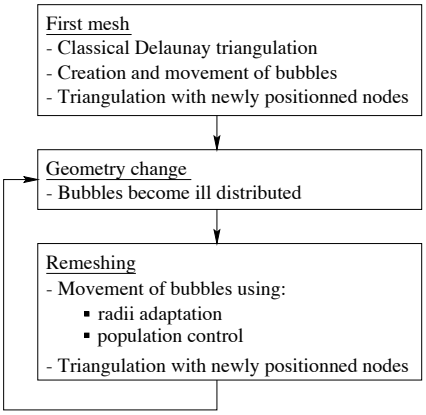

Fig. 1. Remeshing procedure based on bubbles

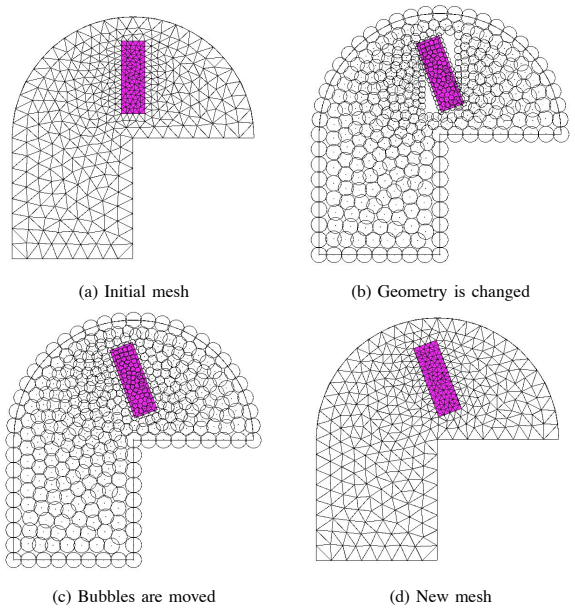

(a) Initial mesh (b) Geometry is changed

(c) Bubbles are moved (d) New mesh

Fig. 2. A 2D remeshing example using bubbles

B. Freezing the bubbles

Especially in large geometries, all the bubbles do not reach a force-balancing configuration at the same time. Hence, it is usefull to freeze bubbles that have reached an equilibrium. As shown in Fig. 3, the number of bubbles drops during the integration and nearly 50% of time can be saved using this scheme.

C. Creating subsets of bubbles

An idea inspired by the "coarse graining" technique used in physics [4], is to divide the bubble set into subsets in which a localized equilibrium is searched for. The obtained overall configuration is then close to the global equilibrium. When compared to a global resolution, this method leads to lower computational times. It is possible to find an optimal number of subsets. The number of interior bubbles of a subset

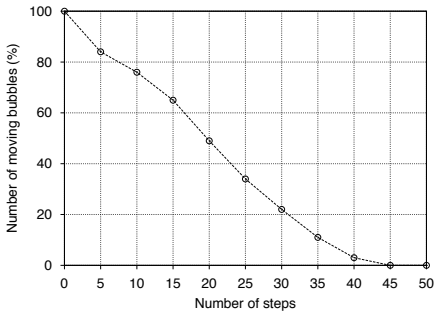

Fig. 3. Number of active bubbles during their movement

should be greater than a bubble neighborhood, and smaller than the number of frontier bubbles of the subset. Moreover, each subset being treated separately, parallel computing can be used.

D. Results

The preceding techniques have been implemented to improve the existing algorithm. The Fig. 4 displays the obtained time reduction. The main gain have been achieved by reducing the cost of the bubble neighborhood calculation and updating.

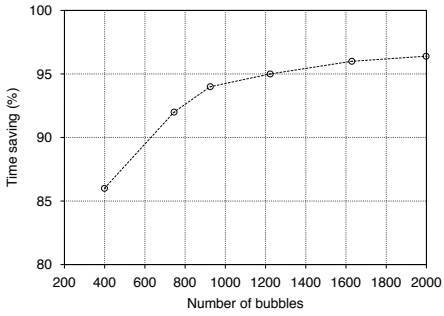

Fig. 4. Time cost comparison between

IV. Conclusion

Using bubbles allows to adapt the mesh to the geometry changes during time-stepping simulations. The proposed procedure, applicable in both 2D and 3D situations, allows to have a good control on the node distribution and generates smooth changes of the mesh. Computational time of the algorithm has been reduced. More improvements are still needed to treat large and complex geometries.

References

[1] K. Shimada and D. Gossard, "Automatic triangular mesh generation of trimmed parametric surfaces for finite element analysis," *Computer Aided Geometric Design*, vol. 15, pp. 199–222, 1998.

[2] S. Nagakura, S. Noguchi, K. Kaneda, H. Yamashita, and V. Cingoski, "Automatic quadrilateral mesh generation for fem using dynamic bubble system," *IEEE Trans. Magn.*, vol. 37, no. 5, pp. 3522–3525, 2001.

[3] V. Leconte, C. Hérault, Y. Maréchal, G. Meunier, and V. Mazauric, "Optimization of a finite element mesh for large air-gap deformations." *European Physical Journal AP*, vol. 13, pp. 137–142, 2001.

[4] S.-K. Ma, "Introduction to the renormalization group," *Reviews of Modern Physics*, vol. 45, no. 4, pp. 589–614, 1973.

Generalized *h-p* Triangles and Tetrahedra for Adaptive Finite Element Analysis in Parallel Processing Environments

Donglin Ma and Steve McFee

Computational Analysis and Design Laboratory
Electrical & Computer Engineering, McGill University
3480 University Street, Montreal, H3A 2A7, Canada
email: steve.mcfee@mcgill.ca

Abstract – **A new family of triangles and tetrahedra are proposed for *h-p* adaptive finite element analysis (AFEA), in parallel and distributed processing computational environments. The elements are constructed based on very-high-order, arbitrarily-piecewise-continuous, polynomial bases, which span the full range of local mesh refinements, and a broad variety of the primary local distributions of degrees of freedom (DOF), attainable through conventional and irregular *h-p* adaptive refinements. Irregular cut continuity constraints are used to maintain the conformity and modeling integrity of the new *h-p* elements across the external edges (faces) of the triangles (tetrahedra) to facilitate the seamless introduction and use of these elements in classical AFEA formulations. The potential benefits and related costs are explored for electromagnetics applications.**

INTRODUCTION

The use of AFEA techniques for computationally modeling and simulating the performance characteristics of engineering devices and continuum systems has grown increasingly wide-spread over the last ten years, and the study and development of AFEA methods for practical engineering applications now represents a rather mature and well-established research area [1],[2],[3]. Early advances in the design and development of finite element basis functions have facilitated the efficient use of classical Lagrangian elements for stable, well-conditioned *h*-adaption, and supported the formulation of hierarchal finite elements, for effective and reliable *p*-adaption [3],[4]. More recent research has resulted in the development of "irregular" (or irregular-cut) elements [5],[6],[7]. Taken together, these advances both promote the concept of, and provide the main foundations for, a generalized *h-p* finite element.

Finite elements are most commonly categorized in terms of the type(s) of DOF that they are able to represent, within the specific geometric region spanned by the individual element (strong definition), or over a connected multi-element region which is spanned by a partial mesh that includes the element (weak definition). For these definitions, it is key to associate points, edges and surfaces of derivative discontinuity in the model, over the region under consideration, with *h*-type DOF; while, the *p*-type DOF should be understood to represent the polynomial order(s) of the differentiable modeling functions, that span the element(s) associated with the model, within the considered region. By this classification, it is noteworthy that classical high-order Lagrangian triangles and tetrahedra meet the requirements of both "weak" *h*-type elements and "weak" *p*-type elements, and by extension, also "weak" *h-p* elements. In addition, high-order hierarchal elements can be categorized as "weak" *h*-type, "strong" *p*-type and "weak" *h-p* type. But, neither Lagrangian nor hierarchal elements satisfy the criteria established for "strong" *h*-type elements, or "strong" *h-p* type elements. A very good example of a "strong" *h*-type element is the "nested tetrahedron", however this element is limited to first-order modeling, and therefore falls short of the standards stipulated for a "weak" *p*-type element, or a "weak" *h-p* type element [8]. The purpose of this contribution is to introduce a new family simplex elements for AFEA, which meet all the requirements of the "strong" *h-p* type definition. It should be noted that by the hierarchy of the element type classification, these new elements will also satisfy all the criteria required of "strong" *h*-type and "strong" *p*-type elements. Further, these new *h-p* elements will be shown to possess a number of key attributes which render them highly amenable to parallel and distributed processing environments.

MATHEMATICAL FORMULATION

The mathematical development and derivation of "strong" *h-p* type triangles and tetrahedra is highly detailed, somewhat abstract and much too involved for a condensed presentation. Therefore, only a simple introduction to the most salient point is presented; the complete description of the formulation will be reported at the conference, and included in the long paper.

The most important aspect of the "strong" *h-p* type element formulation is the choice, structuring and management of the basis functions. One straightforward approach is to associate a separate hierarchal basis with each "sub-element" produced by an *h*-type discretization enhancement of the *h-p* element, e.g., for m "sub-elements" the *h-p* element basis becomes [3]:

$$\mathbf{N^e} = \left[(\mathbf{N^{e1}})^T \quad \cdots \quad (\mathbf{N^{ei}})^T \quad \cdots \quad (\mathbf{N^{em}})^T \right]^T \qquad (1)$$

Then, the essence of the formulation reduces to choosing and implementing how these sub-bases will interrelate. There are many options available, which make "strong" *h-p* elements a very flexible and powerful modeling tool for practical AFEA.

The concurrent processing ramifications of the formulation arise when AFEA initial meshes are constructed of "strong" *h-p* elements, and all adaptive refinements are only applied as local discretization enhancements within them. In this case, a natural domain decomposition is implied by the initial mesh, and a broad range of powerful parallel strategies applies [9].

ILLUSTRATIVE RESULTS

The correctness and effectiveness of the new family of *h-p* type finite elements have been verified numerically, through investigative tests involving a representative range of AFEA applications. One simple yet instructive example is described in Figs. 1 and 2, which illustrate the 3-D electrostatic analysis of a spherical capacitor using a "strong" *h-p* type tetrahedron. The ideal device model consists of two concentric, spherical conductors, separated by a full-thickness, homogenous, linear dielectric shell ($\gamma_r = 6$). The inner conductor is a solid sphere of radius $r_\bullet$; the outer is a hollow spherical shell with an inner radius $r_\circ = 100\, r_\bullet$. Fig. 2 describes the initial and *h-p* refined meshes for 1/24 of the full spherical geometry. The objective of this study was to resolve the capacitance of the structure. The results are summarized, in an abridged form, in Table I.

It is noteworthy that a "strong" *h-p* element automatically facilitates the purely local discretization enhancements of the inner tetrahedron, without any affect on the conformity of the mesh across the shared (internal) element face. If traditional elements were used, the refinement of the inner tetrahedron would propagate the subdivision of neighboring tetrahedra to preserve the geometrical conformity of the model; and even if "irregular" tetrahedra were employed throughout the model, the prescribed refinement of the inner element would require the use of supplementary "continuity constraints" to preserve the integrity of the model [6]. Finally, it is important to note that the full modeling advantages of irregular-cut *h-p* AFEA are preserved with the new *h-p* elements: the accuracy of the new method (6% error level) is only matched by that attained using a uniform 8-th order mesh (5.7% error level), which is only available at a far greater computational cost. A range of *h*-, *p*-, and *h-p* results for "strong" *h-p* triangles and tetrahedra will be reported at the conference and in the long paper.

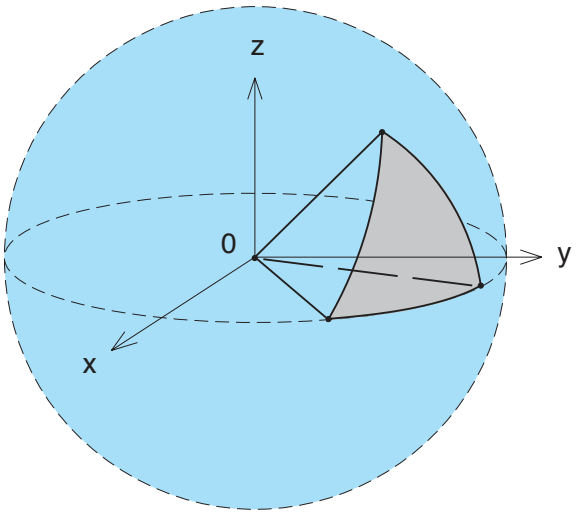

Fig. 1. Analysis model domain (1/24 full region) for the spherical capacitor. Note: All circularly-curved edges and surfaces will be modeled exactly [10].)

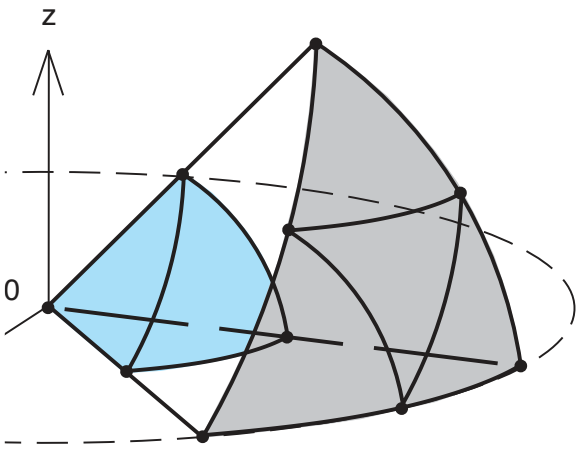

Fig. 2. Initial mesh for analysis model domain (eight conforming curvilinear tetrahedra): the annular prism region represents seven tetrahedra, as indicated by the bounding faces. The inner tetrahedron (connected to the origin) is the "strong" *h-p* type element in this study; it is defined to provide the equivalent discretization of eight mixed-order tetrahedra, which are situated interior to the *h-p* element, according to the same distribution given for the initial mesh.

Table I. *h-p* Element Modeling Performance for Spherical Capacitor

Initial Mesh Element Order	Error in Electrostatic Capacitance [1]		
	Initial Mesh [2]	*h*-Refined [3]	*h-p* Refined [4]
2	500%	220%	6%
4	200%	62%	N/A
8	28%	5.7%	N/A

[1] Error measured relative to analytical value of *dc* capacitance for the device.
[2] Mesh of 8 scalar tetrahedra for the analysis domain, as described by Fig. 2.
[3] Mesh of 7 initial mesh elements plus uniform-order version of *h-p* element.
[4] Mesh of 7 initial mesh elements plus mixed-order (i.e. 2, 4, 8) *h-p* element.

REFERENCES

[1] P.P. Silvester and R.L. Ferrari, *Finite elements for electrical engineers*, Third Edition, Cambridge University Press, New York, 1996.

[2] J. Jin, *The finite element method in electromagnetics*, John Wiley and Sons, Inc., New York, 1993.

[3] O.C. Zienkiewicz and R.L. Taylor, *Finite element method: Volume 1 – The basis*, Fifth Edition, Butterworth-Hienemann, London, 2000.

[4] M. Salazar-Palma, T.K. Sarkar, L.E. Garcia-Costillo and T. Roy, *Iterative and self-adaptive finite-elements in electromagnetic modeling*, Artech House Publishers, Boston, 1998.

[5] D. Ma and S. McFee, "Irregular triangles for finite element analysis in electromagnetics", *IEEE Trans. Magn.*, V. 35, pp. 1422-1425, 1999.

[6] S. McFee and D. Ma, "Irregular tetrahedra for finite element analysis in electromagnetics", *IEEE Trans. Magn.*, V. 37, pp. 3550-3553, 2001.

[7] S. McFee and D. Ma, "Irregular vector triangles and tetrahedra for finite element analysis in electromagnetics", *IEEE Trans. Magn.*, V. 38, pp. 353-356, March 2002.

[8] J.P. Webb and S. McFee, "Nested tetrahedral finite elements for *h*-adaption", *IEEE Trans. Magn.*, V. 35, pp. 1338-1341, 1999.

[9] R. E. Bank and P.K. Jimack, "A new parallel domain decomposition method for the adaptive finite element solution of elliptic partial differential equations", *Concur. Comp.: Prac. Exp.*, V.13, pp.327-350, 2001.

[10] D. Villeneuve and J.P. Webb, "Exact treatment of curved boundaries in large finite elements by re-parameterization", *IEEE Trans. Magn.*, 36, pp. 1527-1530, 2000.

Overlapping Elements and Layered Meshes for *h-p* Adaptive Finite Element Analysis

Steve McFee and Donglin Ma

Computational Analysis and Design Laboratory
Electrical & Computer Engineering, McGill University
3480 University Street, Montreal, H3A 2A7, Canada
email: steve.mcfee@mcgill.ca

Abstract **– The irregular finite element formulations, in combination with the concept of irregular-cut continuity constraints, are extended to develop structurally overlapping finite elements, which may be used to construct quilted and layered mesh geometries. These constructs reveal a revised interpretation of generalized *h-p* refinements, and new insight on adaptive meshing. The extended formulations, with implementation practicalities and test results, are reported for triangles and tetrahedra.**

INTRODUCTION

The formulation and practical techniques of C_0 conforming irregular finite elements for continuum analysis, together with the concept of irregular-cut continuity constraints, is extended to develop a basis for the introduction and use of overlapping elements and layered meshes in *h*-, *p*- and *h-p* adaptive finite element analysis (AFEA) scenarios [1,2,3]. The generality of the overlapping element technique should not be equated with the method of "nested tetrahedra", which only incorporates a specialized and restricted partition of the overlapping element formulation and its inherent attributes [4]. The basic concepts and potential significance of overlapping finite elements were recently envisioned on a theoretical level, without connection to the feasibility of irregular-cut method implementations [5]. The primary objective of this contribution is to formulate and introduce the use of overlapping elements and layered meshes for practical AFEA; then investigate the implications of these constructs. It should be noted that overlapping elements offer the potential for a far broader range of *h*-, *p*- and *h-p* adaptive refinement trajectories, compared to that given by "standard" (non-overlapping) irregular elements – *however* – this added range comes at the cost of added computational complexity.

The underlying concept of overlapping finite elements, and their basic application in AFEA, are illustrated in two stages, using triangles for clarity. First, the two simplest refinement constructs are defined to be purely local to a single element; they are described in Fig. 1. Under these two interpretations, overlapping element methods offer an operational framework within which to model and explore the potential implications of generalized *h-p* finite elements. Second, and perhaps more interesting, the refinement constructs involving multi-element spanning overlaps, and the associated layering of sub-meshes, are illustrated in Fig. 2. Under this generalized construction, a range of significant and potentially powerful interpretations are available, depending on how the overlapping elements, or sub-meshes, and their associated degrees of freedom (DOF), are incorporated into the refined discretization. For example,

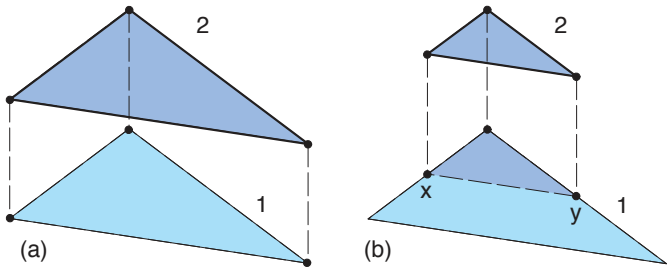

Fig. 1. Key implications of overlapping element construct: (a) two identical triangles with different orders; (b) two different triangles of the same order. For triangle 2 of higher (hierarchal) order than 1 in (a), the addition of 2 to 1 results in a standard *p*-refinement of 1. For (b), the addition of triangle 2 to 1 yields a basic *h*-refinement of 1, i.e. introduces a C_0 edge (xy) into triangle 1.

two immediate possibilities are apparent: the DOF associated with the overlapping element(s) can be added to those of the underlying mesh, to enrich the discretization on the overlap region; alternatively, the DOF of the overlapping element(s) can be substituted for those of the underlying mesh, in order to replace the preexisting discretization on the overlap region. These two approaches yield quite different AFEA refinement implications. The first permits the direct augmentation of the

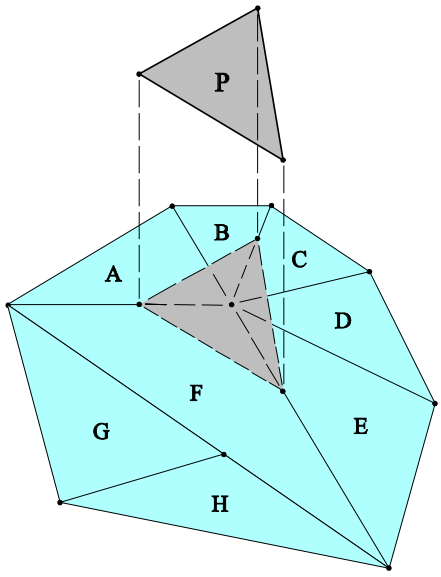

Fig. 2. General, multi-element spanning, overlap example: a single-element sub-mesh patch (labeled P) is applied to update and refine a preexisting mesh discretization, defined locally by the union of triangles A, B, C, D, E and F.

preexisting discretization, through the introduction of added C_4 (interior) DOF and C_0 (edge) DOF, without removing or compromising any preexisting DOF. The second refinement approach facilitates the localized removal and replacement of unnecessary or inefficient preexisting DOF (both C_4 interior, and C_0 edge, types). Further, it should be noted that a variety of intermediate refinement scenarios are also available, based on combinations of these two limit approaches. In addition, it is also important to note that combined simultaneous *h*- and *p*-refinements are supported by the generalized formulations, for both 2-D and 3-D applications. Finally, repeated, multi-layered and recursive overlap refinements are facilitated; and mesh layer superposition models, and discretization pruning procedures for redundant (e.g. fully overlapped) elements, are available for managing AFEA discretization evolution.

MATHEMATICAL FORMULATION

The mathematical development, derivation and formulation of overlapping elements for FEA depends on a generalization and reinterpretation of the irregular-cut continuity constraints ([1], [2] and [3]), to realize the concept of "irregular overlap" connectivity relations. For the general case, the mathematics behind the derivation and definition of the constraint relations which connect two adjoining elements, that share an arbitrary face-on-face overlap (2-D case), or a common sub-volume of intersection overlap (3-D case), is both rather subtly detailed, and somewhat heavily involved. In particular, certain aspects of the primary development, efficiency reformulation, and the implementation of the DOF connectivity equations, including the computational algorithms that are needed to impose them, are intrinsically abstract and quite challenging in a condensed presentation. In the following, only a simplified introductory overview of the salient points is presented; an expanded and complete description of the formulation will be developed in the long version of the paper, and reported at the conference.

Presented in its conceptually simplest form, the derivation of the method of overlapping elements may be developed as the conjunction of two sequential phases: the assembly of the unconstrained and disconnected global matrices; followed by the assembly and application of the "connectivity" constraints which are responsible for both specifying the connected DOF for the non-overlapping elements, as well as (most important) for prescribing the intended interpretation of the DOF related to the overlapping and layered elements. Only the first phase is addressed in this abridged presentation; the second is subtle and rather detailed – it will only be covered in the long paper.

The assembly of the unconstrained and disconnected forms of the global matrices is straightforward, and highly similar to that of non-overlapping FEA formulations [8]. The important difference is that while non-overlapping elements yield block diagonal "K" matrices (one block per element), overlapping elements introduce off-diagonal blocks into K, corresponding to each pair of overlapping elements. While the supplemental entries add to the complexity of matrix assembly, it is key to note they are easy to define and cheap to compute, based on irregular-cut element-to-element transformations [1,2]. For example, for the overlap parts of triangles P and A in Fig. 2, the off-diagonal local matrices are: $K^{PA} = T_{PA} K^{A} = (K^{AP})^{T}$.

ILLUSTRATIVE RESULTS

The validity and effectiveness of overlapping refinements have been tested and investigated over a wide range of AFEA applications. One simple yet instructive example is described by Fig. 3, which details some initial *h*-adaptive analyses of an ideal coaxial line. The system consists of two long, straight, loss-less conductors, separated in air. The inner conductor is a rod of radius $r_{\bullet}$; the outer is a hollow cylinder with an inner radius $r_{\circ} = 100\, r_{\bullet}$. Fig. 3 defines the initial and once-refined meshes for 1/12 of the sectional geometry. The objective of this study was to resolve the inductance (per unit length) for the structure. The results are provided in Table I. A range of converged *h*-, *p*-, and *h*-*p* results, for triangles and tetrahedra, will be reported at the conference and in the long paper.

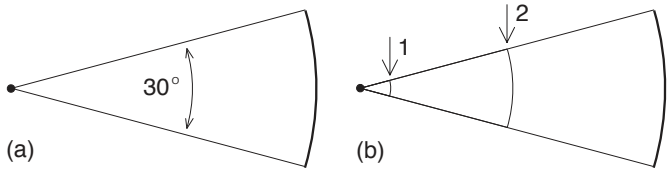

Fig. 3. Initial and overlap refined meshes for circular coaxial line inductance analyses: (a) single full-domain curvilinear triangle; (b) full-domain triangle with one overlapping sub-domain triangle ("1" shows position of curved base of optimal overlap triangle; "2" locates base of half-radius overlap triangle). (Curved edges modeled exactly [6]; optimal overlap located analytically [7].)

Table I. Overlapping Element Modeling Performance for Coaxial Line

Uniform Element Order	Error in Direct Current Inductance per Unit Length [1]		
	Single Element	Half Overlap [2]	Optimal Overlap [2]
1	150%	76%	39%
2	60%	32%	9%

[1] Error measured relative to analytical value of *dc* inductance per unit length.
[2] Mesh of 2 elements: original full-domain △; plus 1 sub-domain overlap △.

REFERENCES

[1] D. Ma and S. McFee, "Irregular triangles for finite element analysis in electromagnetics", *IEEE Trans. Magn.*, 35, pp. 1422-1425, 1999.

[2] S. McFee and D. Ma, "Irregular tetrahedra for finite element analysis in electromagnetics", *IEEE Trans. Magn.*, 37, pp. 3550-3553, 2001.

[3] S. McFee and D. Ma, "Irregular vector triangles and tetrahedra for finite element analysis in electromagnetics", *IEEE Trans. Magn.*, 38, pp. 353-356, March 2002.

[4] J.P. Webb and S. McFee, "Nested tetrahedral finite elements for *h*-adaption", *IEEE Trans. Magn.*, 35, pp. 1338-1341, 1999.

[5] T. Strouboulis, K. Copps and I. Babuska, "The generalized finite element method", *Comp. Meth. Appl. Mech. Eng.*, 190, pp. 4081-4193, 2001.

[6] D. Villeneuve and J.P. Webb, "Exact treatment of curved boundaries in large finite elements by re-parameterization", *IEEE Trans. Magn.*, 36, pp. 1527-1530, 2000.

[7] D. Giannacopoulos and S. McFee, "Towards optimal *h*-*p* adaptation near singularities in finite element electromagnetics", *IEEE Trans. Magn.*, 30, pp. 3523-3526, 1994.

Practical *h-p* Adaptive Finite Element Analysis Strategies for Irregular Triangles and Tetrahedra

Steve McFee and Donglin Ma

Computational Analysis and Design Laboratory
Electrical & Computer Engineering, McGill University
3480 University Street, Montreal, H3A 2A7, Canada
email: steve.mcfee@mcgill.ca

***Abstract* – Practical *h-p* adaptive finite element methods and strategies designed to exploit the *h*-refinement modeling attributes and efficiencies of irregular triangles and tetrahedra are developed and investigated. A range of fundamental *h*- and *h-p* adaptive approaches for both scalar and vector elements are proposed and explored. The main advantages and drawbacks of these techniques are illustrated, and evaluated in terms of the traditional *h*- and *h-p* adaption models.**

INTRODUCTION

Adaptive finite element analysis (FEA) for electromagnetic systems has become increasingly important over the years, and is now a mature and well-established research area. Irregular triangles and tetrahedra, for scalar- and vector-element-based electromagnetics, were first introduced in 1999-2002 [1],[2],[3]. This work concluded that these elements should be well-suited for adaption. The purpose of this contribution is to investigate the efficient and effective application of irregular triangles and tetrahedra in a practical, very-high-order, *h-p* adaptive setting.

The main advantage of irregular finite elements for adaption is that they facilitate the unrestricted insertion and refinement of *h*-type degrees of freedom (DOF) ! via purely localized element subdivisions ! without compromising the geometric quality of the mesh or the continuity of the model [1]. In effect, irregular triangles and tetrahedra support a genuine *h*-refinement analog to mixed-order *p*-adaption, by allowing for the truly unrestricted subdivision of individual elements within a mesh.

The potential value of new and improved adaption strategies specialized for irregular elements is directly connected with the vastly increased range of *h*- and *h-p* trajectories available with the Airregular cut@ refinement model [1]. Standard approaches were never intended to exploit this expanded space effectively, and revised schemes designed to capitalize on the flexibility of the model are strongly indicated.

ADAPTIVE STRATEGIES FOR IRREGULAR ELEMENTS

Practical adaptive FEA system implementations are based on four primary modules, which interact according to the classical FEA adaptive feedback model, described below [4]. They are: initial mesh generation (A); matrix assembly and solution (B); error estimation (C, D, E); and discretization refinement (E, F). In most adaptive FEA systems, these modules are designed, and often tuned or optimized, to exploit the specific advantages and avoid the inherent limitations of the refinement models and type of finite element used. Therefore, it is important to consider all components of the integrated adaptive process when developing new strategies for irregular elements ! not only the implications for the refinement model. In the end, these parts will be closely interrelated, and must function effectively as a whole to achieve efficient and reliable adaption performance. Taking this view, this investigation will focus on the four primary components of the adaptive process, both individually, and finally in synergistic combination. First, the primary implications and corresponding strategies associated with the three primary refinement models will be studied. (The *r*-refinement model will not be evaluated.) Second, the potential advantages of using irregular cut elements for initial mesh generation, together with some straightforward irregular element meshing approaches, will be explored. It may be noted that this component study is equally relevant to purely *p*-adaptive FEA, in addition to general *h*- and *h-p* formulations. Third, the key benefits and related strategies associated with the adaptive refinement and maintenance of evolving irregular cut discretizations will be investigated. Finally, the implications of irregular triangles and tetrahedra on error estimation, and simple strategies to reinterpret the significance of the error indicators, and then successfully exploit them, will be reported.

A. Generate initial finite element discretization.
Repeat:
  B. Assemble and solve finite element problem.
  C. Evaluate solution accuracy; if adequate then **STOP**.
  D. Identify regions of inadequate discretization.
  E. Determine required discretization refinements.
  F. Update finite element discretization.

One fairly simple, and immediate improvement facilitated by irregular elements, over traditional (geometrically conforming) *h*-adaptive practices is to consider the expected modeling value and efficiency of the secondary DOF normally associated with subdividing a triangle or tetrahedron. These DOF occur when adjacent triangles or tetrahedra are bisected to maintain solution continuity in traditional FEA formulations, but they are optional when irregular elements are used. Such bisection DOF tend to have strong orientation bias, with high symmetry dependence. Therefore, it is straightforward and inexpensive to assess their potential modeling value, based on approximate field solutions. Then, for irregular element FEA formulations, such secondary DOF can be added into the discretization when they are useful,

and excluded when they are superfluous or even detrimental to the future refinement of the mesh. This simple strategy, together with a range of other, less obvious, and more in-depth strategies and techniques, will be presented at the conference, and in the long version of the paper. In each case, supporting illustrative results, which demonstrate the potential impact and efficacy of these methods, will also be provided. One example numerical investigation, which explores the potential benefits and related costs of employing an irregular triangle FEA formulation to aid in the generation of more efficient and productive initial meshes for *p*-adaptive analyses of high-frequency Helmholtz systems is presented (in summary form) in the following section.

ILLUSTRATIVE RESULTS

A variety of practical 2-D and 3-D electromagnetic systems have been analyzed. Both regular and irregular cut triangle and tetrahedra formulations were applied to compute *h*-, *p*- and *hp*-adaptive FEA solutions, to illustrate and comparatively evaluate the potential implications, benefits and strategies associated with irregular element methods. One test system is a dielectric slab waveguide which terminates in free space. The geometry, open-boundary model [5], and comparable initial *p*-meshes (regular and irregular) are described in Figs. 1 and 2. The slab dielectric constant is 5 and the waveguide is driven in its dominant mode, at a frequency of $k_0 d = 0.15$ (d is the thickness of the slab). The analysis goal was to compute the phase angle of the reflection coefficient (S_{11}) at the input port of the device. Four *p*-adaptive analyses, based on both regular and irregular initial *p*-meshes, were computed; the comparative performance results are plotted in Fig. 3. In addition, two examples of the adaptively converged *p*-refinements are provided in Figs. 1 and 2. These results show that irregular elements can facilitate significant performance gains in mixed-order *p*-adaptive applications when they are used to define and construct irregular *p*-meshes. The *p*-adaption cost comparison is striking ! exceeding 10:1 for errors below 0.25°. Similar gains are evident for the uniform *p*-refinement model. A selection of additional examples, based on tetrahedral analyses, and vector (edge) element formulations, will be presented at the conference and in the long version of the paper.

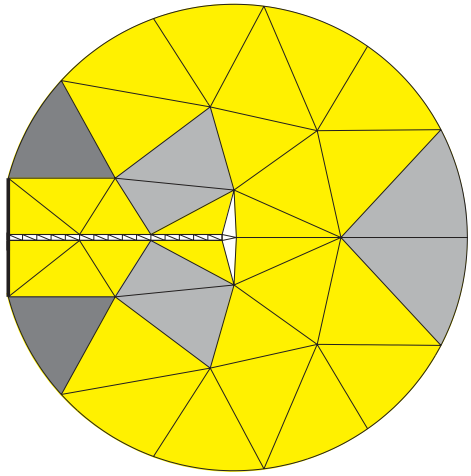

Fig. 1. System geometry, initial irregular *p*-mesh (69 2nd-order triangles), and *p*-adaptively converged discretization for dielectric waveguide analysis. Thick line denotes input port excitation plane; circular arcs mark absorbing boundary condition. Orders: white = 2; light grey = 4; medium grey = 6; dark grey = 8.

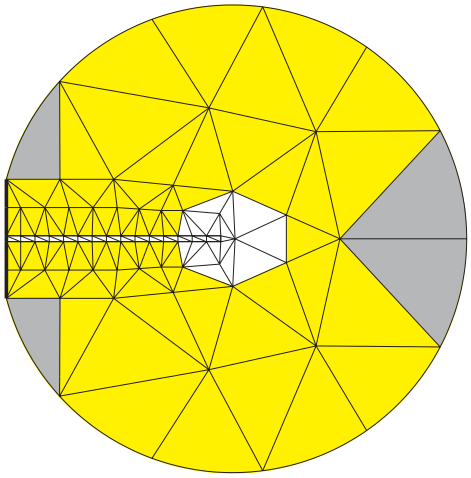

Fig. 2. Initial regular *p*-mesh (134 2nd-order triangles) and *p*-adaptively converged discretization for dielectric waveguide analysis. Orders as per Fig. 1.

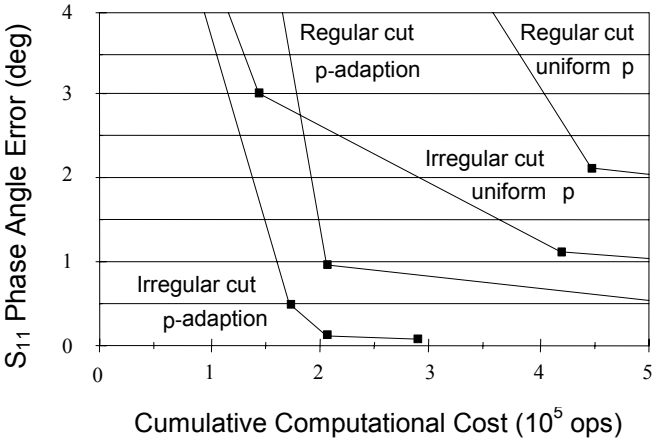

Fig. 3. Cumulative cost of *p*-adaptive solution versus phase error in reflection coefficient (S_{11} measured at input port) for dielectric slab waveguide analyses.

REFERENCES

[1] D. Ma and S. McFee, "Irregular triangles for finite element analysis in electromagnetics@, *IEEE Trans. Magn.*, 35, pp. 1422-1425, May 1999.

[2] S. McFee and Donglin Ma, "Irregular tetrahedra for finite element analysis in electromagnetics", *IEEE Trans. Magn.*, 37, pp. 3550-3553, September 2001.

[3] S. McFee and Donglin Ma, "Irregular vector triangles and tetrahedra for finite-element analysis in electromagnetics", *IEEE Trans. Magn.*, 38, pp. 353-356, March 2002.

[4] D. Giannacopoulos and S. McFee, ATowards optimal *h-p* adaption near singularities in finite element electromagnetics@, *IEEE Trans. Magn.*, 30, pp. 3523-3526, September 1994.

[5] J.P. Webb, AAbsorbing boundary conditions for finite element analysis of planar devices@, *IEEE Trans. Micr. Theory Tech.*., 38, pp. 1328-1332, September 1990.

Different Finite Element Approaches for Electromechanical Dynamics

O. Bottauscio, A. Manzin
Istituto Elettrotecnico Nazionale *Galileo Ferraris*
Strada delle Cacce 91, I-10135 Torino, Italy
e-mail: botta@ien.it, manzin@ien.it
M. Chiampi
Politecnico di Torino, Dipartimento di Ingegneria Elettrica Industriale
Corso Duca Abruzzi 24, I-10129 Torino, Italy
e-mail: chiampi@polel1.polito.it)

***Abstract*—Two 2D Finite Element techniques for the analysis of the transient evolution of electromechanical devices are proposed and compared. The two techniques are based on a FEM/BEM formulation and on a FEM approach based on overlapping meshes. The merits and drawbacks of the two approaches are discussed when applied to the analysis of actual devices.**

INTRODUCTION

The Finite Element Method (FEM) is well known as a very efficient tool for the analysis of electromagnetic devices. However, difficulties arise in the application of this technique to electromechanical actuators, mainly if the motion of components is not limited to a relative rotation, as in rotating machines. The approaches usually proposed in literature can be classified in two categories depending on the use of:

- a unique mesh on the whole domain which is regenerated or modified at each instant;
- separate FEM meshes for each component which are coupled by analytical relations or by mesh-less techniques.

This paper proposes and discusses two 2D FEM techniques for the electromechanical transient analysis of voltage driven devices. Both the methods use fist order shape functions and employ the Fixed Point (FP) scheme for the handling of magnetic non-linearity. For the time evolution of electromagnetic and mechanic quantities, a step-by-step procedure is developed, approximating the time derivative in the interval ($t \div t+h$) by the derivative at $t+kh$, with $0 < k \leq 1$.

2D FEM TECHIQUES

The first approach makes use of overlapping finite elements. Two meshes are independently developed. The first one (moving mesh) involves only the armature with a narrow air border; the second one (stationary mesh) include winding, fixed core and the whole region surrounding the actuator. The moving mesh can slide on the domain covering totally or partially some elements of the stationary mesh. A suitable algorithm at each instant updates the stationary mesh near the armature, eliminating the covered triangles and creating new elements around the border. An example of remeshing is presented in Fig. 1. Non-conforming stationary nodes are allowed on the moving boundary; in order to guarantee continuity, their potentials are interpolated in term of those of the moving nodes on the same interface. At the end of this operation a standard FEM problem is to be solved.

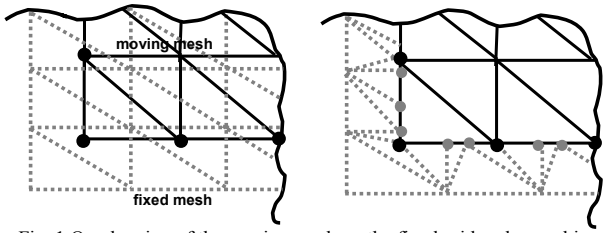

Fig. 1 Overlapping of the moving mesh on the fixed grid and remeshing

In the second approach, the moving core (with a narrow air border) and the fixed components (including the core, the windings and a portion of air around it) are discretised using two separate FEM grids, which are never modified during the time evolution. The coupling between the two regions is obtained by the Boundary Element Method (BEM), formulated in terms of the magnetic vector potential.

Both the numerical techniques lead to the following differential system, which describes the electromagnetic behavior:

$$\begin{cases} B_{NN}\dot{x} = -A_{NN}x - A_{NM}y + c_N \\ 0 = -A_{MN}x - A_{MM}y + c_M \end{cases} \quad (1)$$

In this equation, the problem unknowns (nodal values of magnetic vector potential and their normal derivatives, circuit currents) are divided into N state variables x and M algebraic variables y. Matrix B, which takes into account the phenomena of electromagnetic induction, is defined only for conductive parts of the device and it is invariable in time. Matrix A, divided into four sub-matrices, is modified during the motion and, in the overlapping method, also its dimension M can change at each instant. Finally, vector c includes all the external sources and the contribution of FP residuals.

By applying the step-by-step procedure, at the instant i the system becomes

$$\begin{cases} B_{NN}x^i + kh\left(A^i_{NN}x^i + A^i_{NM}y^i\right) = khc^i_N + p^{i-1}_N \\ A^i_{MN}x^i + A^i_{MM}y^i = c^i_M \end{cases} \quad (2)$$

where h is the time interval, k is the coefficient of the time stepping scheme and vector p^{i-1}, involving the behaviour at the previous instant, can be computed by the recursive form:

$$p_N^{i-1} = \frac{1}{k} B_{NN} x^i - \frac{1-k}{k} p_N^{i-2} \quad (3)$$

After the solution of the electromagnetic problem, the force (torque) acting on the moving core can be computed by the Maxwell Stress method. It can be noted that the Maxwell tensor is integrated on closed paths laying on the moving border, which is never modified during the time evolution, ensuring a satisfactory accuracy in the calculation.

The computed electromagnetic force (torque) F_{em} is inserted into the mechanic equation:

$$m\frac{d^2 s}{dt^2} + k_0 + k_1 s + k_2 \frac{ds}{dt} = F_{em} \quad (4)$$

where m is the mass (inertial moment) of the core, k_0 is a constant opposing force (torque), k_1 is the constant of possible spring elements, and k_2 is the constant of possible viscosity effects. This equation is integrated by the step-by-step procedure taking into account the geometrical constraints, in order to compute the displacement of the core during the considered time interval h. The motion is finally applied to the armature, in order to update system (2) for the next instant.

APPLICATION

The models are applied to the analysis of a C-shape electromagnet. A step voltage is imposed to the exciting coil through a resistance, in order to analyze the closing action of the device, including the presence of spring element and a threshold initial force. The simulation results are compared in the following figures, that present the waveforms of the supply current (Fig. 2a), the attractive magnetic force (Fig. 2b) and the core stroke (Fig. 2c). In each figure, one curve is obtained with the FEM/BEM technique and the other two refer to overlapping method considering two different domain size. In fact, while the hybrid FEM/BEM approach is developed in an open boundary space, the other technique requires the preliminary definition of a finite domain, within the electromagnetic phenomena are enclosed. The computations have shown that the results are sensibly influenced by the FE domain choice: greater dimensions produce results closer to the ones provided by the FEM/BEM approach.

The results, obtained by the application of the two methods, are found to be in a very good agreement. From the computational point of view, the FEM/BEM approach, giving rise to a densely populated system matrix, increases the processing burden.

A more detailed comparison between the two techniques will be developed in the full paper considering different kinds of electromagnetic actuators.

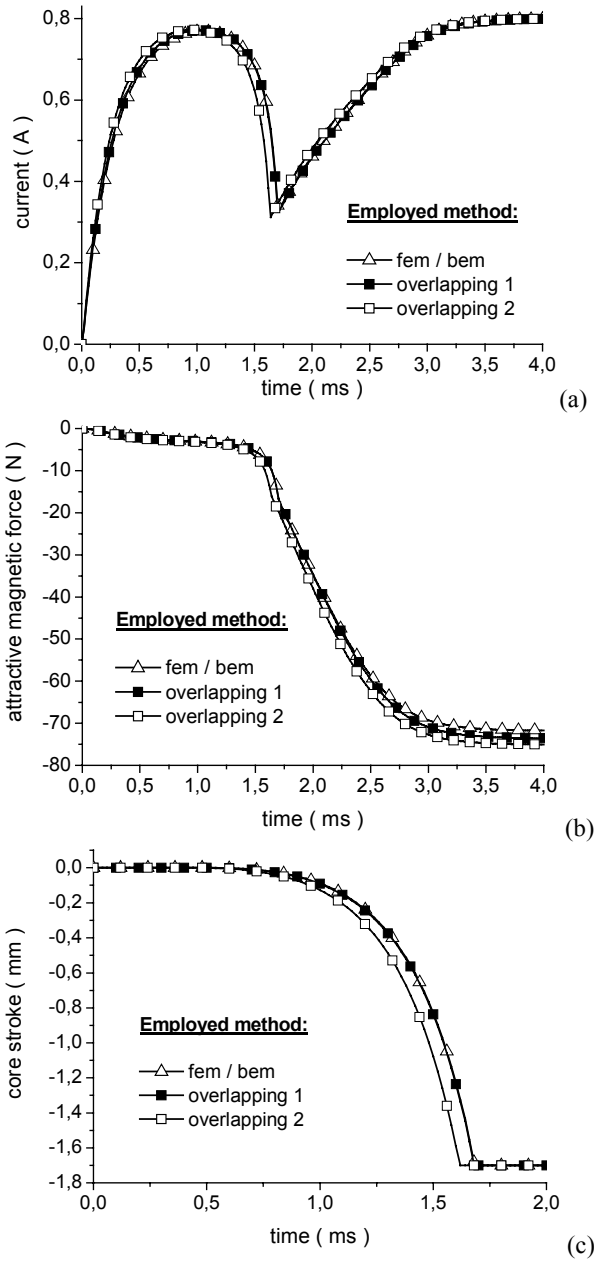

Fig. 2 Time evolution of the exciting winding current (a), electromagnetic force acting on the armature (b) and core stroke (c).

REFERENCES

[1] H. C. Lai, P. C. Coles, D. Rodger, P. J. Leonard, "Transient Analysis of an Electromagnetic Actuator Using an Overlapping Finite Element Scheme", *IEEE Transaction on Magnetics*, Volume: 36, n. 4, 2000, pp. 1238 –1241.

[2] H. Mohellebi, M. E. Latrèche, M. Féliachi, "Coupled Axisymmetric Analytical and Finite Element Analysis for Induction Devices having Moving Parts", *IEEE Transaction on Magnetics*, Volume: 34, n. 5, 1998, pp. 3308 –3310.

COMPUMAG Saratoga Springs, New York USA
July 13 - 17, 2003

Finite Element Computation of Nonlinear Magnetic Diffusion and its Effects when Coupled to Electrical, Mechanical, and Hydraulic Systems

J. R. Brauer and I. D. Mayergoyz
Ansoft Corporation University of Maryland
Four Station Square, Pittsburgh, PA 15219 USA ECE Dept., College Park, MD 20742 USA

Abstract—**Finite elements are used to compute eddy currents and magnetic diffusion time constants in steel cylinders with nonlinear B-H curves. Computations are made of diffusion times versus current in a typical axisymmetric magnetic actuator, showing good agreement with recently published approximate analytical formulas. The computed nonlinear diffusion time constants are then used to compute an equivalent resistor that is used in a systems model coupling the magnetic actuator in a coupled electrical, mechanical, and hydraulic system.**

I. INTRODUCTION

Magnetic diffusion time [1] is the time required for B in the center of a material to rise from 0 to approximately 63% of its final value after a step current excitation. A useful concept in predicting eddy current effects on transient magnetic fields, the magnetic diffusion time constant τ_m has been derived analytically for several simple geometries of *linear* steel [1]. Magnetic diffusion time has been used recently to help predict transient force and motion of magnetic actuators [2].

Saturation is common in magnetic actuators and other magnetic apparatus, but no derivations and computations have been found for *nonlinear* diffusion time. This paper examines the effects of nonlinear steel B-H curves on magnetic diffusion time. It begins by deriving a new formula for diffusion time in cylinders made of steel with a simple "step" B-H curve. It then uses nonlinear transient finite element analysis to compute nonlinear diffusion times for comparison with the analytic formula and for typical actual steel B-H curves. Finally, the finite element computations of nonlinear diffusion time are used in a systems model of a typical magnetic actuator in a coupled electrical, mechanical, and hydraulic system.

II. NONLINEAR DIFFUSION TIME FOR "STEP" B-H CURVE

A recent book [3] derives formulas for transient eddy currents and magnetic fields in steel cylinders with a very simple B-H curve. The curve is assumed to be a step with infinite permeability (slope) from B=0 to B=±B_m, where B_m is the saturation flux density. The magnitude of B cannot exceed B_m, because the permeability (slope) is assumed zero for nonzero H.

Assuming the above step B-H curve for a steel cylinder of radius R and conductivity σ, [3] found that the magnetic field diffuses into the cylinder following a step wavefront at moving position $r_0(t)$. A formula [3] for the wavefront $r_0(t)$ derived for a field switched between $-B_m$ and $+B_m$ is here altered to account for a field switched from 0 to $+B_m$ by an applied $H_o(t)$:

$$2\int H_o dt / [\tfrac{1}{2}\sigma R^2 B_m] = \lambda(\ln\lambda - 1) + 1 \quad (1)$$

where $$\lambda = r_0^2(t)/R^2 \quad (2)$$

The above two formulas are here applied to determine magnetic diffusion time. Because the current is a step applied at time zero, H_o is also a step, and thus the left hand side of (1) has its integral over time replaced by $H_o\tau_m$. The value of λ is zero, since $r_0(t) = 0$ when $t = \tau_m$. Thus (1) becomes

$$4H_o \tau_m / [\sigma R^2 B_m] = 1 \quad (3)$$

giving $$\tau_m = [\sigma R^2 B_m] / [4H_o] \quad (4)$$

III. NONLINEAR DIFFUSION TIME IN BESSHO MAGNETIC ACTUATOR

The magnetic actuator analyzed here was originally analyzed by Bessho et al [4]. It is pictured elsewhere [2],[4] and is axisymmetric of axial length 270 mm. The radius of its cylindrical plunger and of its cylindrical stopper is 20 mm.

The diffusion time of (4) can be evaluated for the nominal applied current I = 0.5 amp in the 3300 turn coil [2] as follows. The applied H_o needed in (4) is found from

$$H_o = NI/\,l \quad (5)$$

where N = 3300. The path length l is assumed to be the 250 mm axial length of the coil window, meaning that the cylindrical core of radius 20 mm drops all amp-turns (the outer yoke has negligible mmf drop). The assumed B_m in steel is 2 teslas. Thus I=0.5 amp gives H_o=6600 amp/m. Substituting in (4) with the steel σ = 1.7E6 S/m [2],[4] gives τ_m = 51.5 ms, which is listed in Table 1. The other analytical value listed in Table 1 is for the current quadrupled to 2 amps, for which (5) and (4) obtain one fourth the diffusion time, τ_m = 12.9 ms. *Both of these nonlinear diffusion times are much less than the 93 ms diffusion time obtained using an existing linear formula* [1],[2].

Nonlinear transient finite element analysis is next used to verify (4) and to allow computation of nonlinear diffusion time with a variety of B-H curves. Rather than model the entire Bessho actuator, the 10 mm slice shown in Fig. 1 is modeled.

|-- 20 mm core ---| w i n d i n g yoke

Fig. 1. Slice (height 10 mm) of Bessho magnetic actuator, showing computed magnetic flux lines at t= 20 ms with actual B-H and I = 0.5 amp.

The finite element model of Fig. 1 is first used to verify (4) for a step B-H curve. Because a piecewise linear B-H curve must be entered that has finite slopes suitable for Newton's iterative method, the numerical B-H curve cannot have either infinite nor zero permeability. Instead, the step B-H was approximated with a constant relative permeability of 10,000 for B below 1.93 T. Above 1.93 T the slope was gradually reduced to the permeability of free space above 2.07 T.

For the step B-H curve, finite element analyses of Fig. 1 were made with input currents of 0.5 and 2 amps. Fig. 2a shows the FEA computed magnetic flux density waveshape in the core at a typical instant; note that it is a steep step to 2 T as expected. The time when the wavefront reaches zero radius is the magnetic diffusion time entered in Table 1. The computed diffusion times agree well with the times predicted using (4).

Other transient finite element computations were then made using the actual Bessho core and yoke B-H curves [2],[4]. Fig. 2b shows the computed flux density waveshape at a typical instant; note that it now has a more gradual rise. The computed diffusion time constants with the actual B-H curves are also listed in Table 1. Note that B-H curve shape has a significant effect on the computed nonlinear diffusion time.

TABLE 1.
BESSHO ACTUATOR NONLINEAR MAGNETIC DIFFUSION TIME CONSTANTS (ms)

Current (amps)	Analytical (4)	FEA (step B-H)	FEA (real B-H)
0.5	51.5	53.0	42.0
2.0	12.9	13.4	11.5

a)

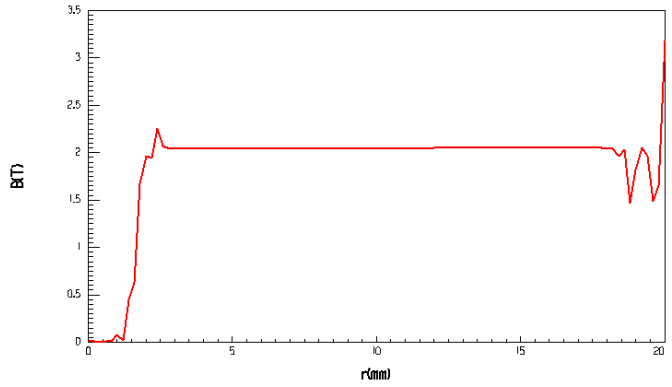

b)

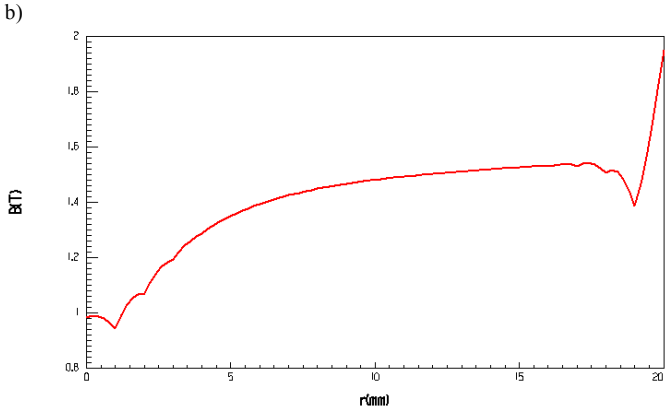

Fig. 2. B (teslas) versus radius (mm) in core computed by nolinear transient FEA; a) with step B-H at t = 51 ms, b) with actual B-H at t = 40 ms.

IV. Diffusion Resistor in Coupled System Model

Eddy current diffusion effects can be included in circuit models by adding a parallel resistor, which for an axisymmetric actuator with linear B-H and height h is given by [2]:

$$R_{EL} = 4\pi\,(N/½)^2\,/[2\sigma\,h] \qquad (6)$$

This resistor is in parallel with the magnetizing inductance [2], and the resulting L-R circuit simulates the linear diffusion time.

To include nonlinear B-H effects, the L/R time constant must be adjusted by the ratio of linear to nonlinear diffusion times, giving a nonlinear eddy resistor:

$$R_{EN} = (\tau_{ml} / \tau_{mn})\; 16\pi\, N^2 /[2\sigma\, h] \qquad (7)$$

From above computations at 0.5 amps, $(\tau_{ml}/\tau_{mn})=(93/42)$. Also N=3300 and h=0.27 m. Thus R_{EN} = 1320 Ω, which the full paper will show is a reasonable value.

The above resistor can now be added to circuit models of a wide variety of coupled systems, including electrical, mechanical, and hydraulic systems. Adding the resistor to a recent model of the Bessho actuator controlling a hydraulic cylinder and load mass [5], the resulting armature position versus time without and with R_{EN} are plotted in Fig. 3. The nonlinear diffusion causes a noticeable delay in the response of this coupled system. The system model will be shown in the full paper, along with various electrohydraulic results.

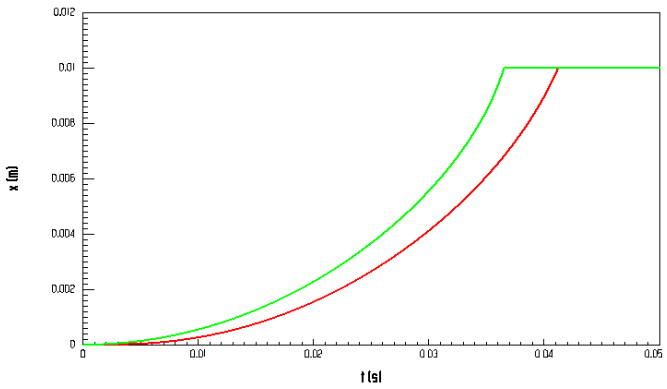

Fig. 3. Computed armature position x (in meters) versus time (in seconds) for step input of 0.5 amps to Bessho actuator in electrohydraulic system [5] with load mass = 1000 kg. The left curve is without a nonlinear diffusion resistor, while the right curve is with R_{EN} = 1320 ohms included.

References

[1] Herbert H. Woodson and James R. Melcher, *Electromechanical Dynamics*, New York: John Wiley & Sons, 1968, volume 2.

[2] John R. Brauer and Q. M. Chen, "Alternative dynamic electromechanical models of magnetic actuators containing eddy currents," *IEEE Trans. Magnetics,* v. 36, July 2000, pp. 1333-1336.

[3] Isaak Mayergoyz, *Nonlinear Diffusion of Electromagnetic Fields,* San Diego, CA: Academic Press, 1998, p. 61.

[4] K. Bessho, S. Yamada, and Y. Kanamura, "Analysis of transient characteristics of plunger type electromagnets," *Electrical Engineering in Japan*, v. 98, July 1978, pp. 56-62.

COMPUMAG Saratoga Springs, New York USA
July 13 - 17, 2003

Harmonic Weighting Functions at the Sliding Interface of a Finite Element Machine Model Incorporating Angular Displacement

Herbert De Gersem, Thomas Weiland

Technische Universität Darmstadt, Computational Electromagnetics Laboratory (TEMF),
Schloßgartenstraße 8, D-64289 Darmstadt, Germany
Email: degersem/weiland@temf.tu-darmstadt.de

Abstract— **The formulation presented in this paper couples the magnetic vector potential and the tangential component of the magnetic field strength at a sliding interface in the air gap of a 2D finite element machine model using Fast Fourier Transforms. The angular displacement between stator and rotor is represented by a simple, diagonal operator. The approach substantially reduces the cost of system assembly during a transient simulation and offers a convenient way for torque computation.**

Introduction

Transient, finite element (FE) simulation of rotating electrical machines commonly relies upon a Lagrangian technique to consider the relative motion of stator and rotor: between two successive time steps, the rotor mesh and field are rotated over an angle determined by the solution of the motion equation. Common techniques for connecting stator and rotor meshes are the moving band technique [1] and the sliding-interface technique [2], possibly in combination with mortar element projection [3]. Alternatively, the air-gap region can be modeled by boundary elements [4], analytical solutions [5] or discontinuous Galerkin techniques [6], which are more convenient for the introduction of relative motion. These techniques, however, require the calculation of parts of the system matrix or the projection operator at the sliding interface, at each time step. In this paper, harmonic functions are applied to enforce the continuity of the fields at the sliding surface. The particular choice of test space simplifies the application of rotation and the computation of the torque.

FE Model with Spectral Interface Conditions

Consider a stator and rotor model $\Omega_{\rm st}$ and $\Omega_{\rm rt}$ with a common interface $\Gamma = \Gamma_{\rm st} = \Gamma_{\rm rt}$ with radius R in the middle of the air gap (Fig. 1). If the rotor is rotated over an angle α, a point (r_0, θ) at $\Gamma_{\rm st}$ corresponds to the point $(r_0, \theta' - \alpha)$ at $\Gamma_{\rm rt}$. Both model parts are meshed such that the meshes match at Γ if $\alpha = 0$. The discretization of

$$-\frac{\partial}{\partial x}\left(\nu\frac{\partial A_z}{\partial x}\right) - \frac{\partial}{\partial y}\left(\nu\frac{\partial A_z}{\partial y}\right) + \sigma\frac{\partial A_z}{\partial t} = -\sigma\nabla V \qquad (1)$$

H. De Gersem is working in the cooperation project "DA-WE1 (TEMF/GSI)" with the "Gesellschaft für Schwerionenforschung (GSI)", Darmstadt.

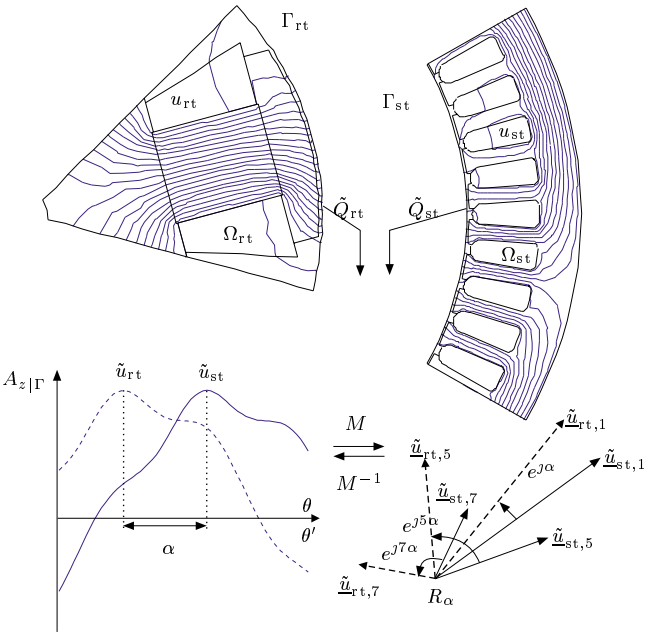

Fig. 1. Spectral interface conditions at the sliding interface in the air gap of an electrical machine model.

with A_z the z-component of the magnetic vector potential, ν the reluctivity, σ the conductivity and V the voltage, for both model parts separately, yields

$$K_{\rm st}u_{\rm st} + g_{\rm st} = f_{\rm st} \qquad (2)$$
$$K_{\rm rt}u_{\rm rt} + g_{\rm rt} = f_{\rm rt} \qquad (3)$$

where K and f denote the FE stiffness matrices and load vectors and the underscripts $_{\rm st}$ and $_{\rm rt}$ distinct between the stator and rotor model parts. The boundary integrals

$$g_{{\rm st},i} = -\int_\Gamma H_\theta(\theta) N_i(\theta)\,{\rm d}\Gamma\ ; \qquad (4)$$
$$g_{{\rm rt},i} = \int_\Gamma H_\theta(\theta') N_i(\theta')\,{\rm d}\Gamma\ , \qquad (5)$$

represent the magnetic field strength H_θ weighted at the sliding interface. The approach proposed in this paper, is based on the discretization of $H_\theta(\theta)$ in terms of N harmonic

functions:

$$H_\theta(\theta) = \sum_{-N/2+1}^{N/2} \underline{h}_{\mathrm{st},\lambda} e^{\jmath\lambda\theta} \; ; \tag{6}$$

$$H_\theta(\theta') = \sum_{-N/2+1}^{N/2} \underline{h}_{\mathrm{rt},\lambda} e^{\jmath\lambda\theta'} \; . \tag{7}$$

The continuity of A_z across Γ, i.e., $A_{z,\mathrm{st}}(\theta) = A_{z,\mathrm{rt}}(\theta' - \alpha)$, is introduced in a weak form, weighted by the harmonic functions $e^{-\jmath\lambda\theta}$, resulting in

$$-R\alpha M \tilde{u}_{\mathrm{st}} + M \tilde{u}_{\mathrm{rt}} = 0 \tag{8}$$

where $\tilde{u}_{\mathrm{st}} = \tilde{Q}_{\mathrm{st}} u_{\mathrm{st}}$ and $\tilde{u}_{\mathrm{rt}} = \tilde{Q}_{\mathrm{rt}} u_{\mathrm{rt}}$ are the FE degrees of freedom at Γ_{st} and Γ_{rt} selected from u_{st} and u_{rt} at Γ by the matrix operator $\tilde{Q}_{\mathrm{st}}$ and $\tilde{Q}_{\mathrm{rt}}$ respectively. The hybrid mass matrix M is defined by

$$M_{i\lambda} = \int_\Gamma N_i(\theta) e^{-\jmath\lambda\theta} \, \mathrm{d}\Gamma \; . \tag{9}$$

The diagonal operator $R_{\alpha,\lambda\lambda} = e^{\jmath\lambda\alpha}$ models the angular displacement between stator and rotor. The continuity of H_θ, i.e., $H_{\theta,\mathrm{st}}(\theta) = H_{\theta,\mathrm{rt}}(\theta' - \alpha)$, is incorporated in the formulation by

$$g_{\mathrm{st}} = \tilde{Q}_{\mathrm{st}}^T M^{-1} R_\alpha^{-1} \underline{\tilde{h}}_{\mathrm{rt}} \; ; \tag{10}$$

$$g_{\mathrm{rt}} = \tilde{Q}_{\mathrm{rt}}^T M^{-1} \underline{\tilde{h}}_{\mathrm{rt}} \; , \tag{11}$$

in terms of the Fourier coefficients $\underline{\tilde{h}}_{\mathrm{rt}}$ of H_t at Γ_{rt}. The coupled system of equations is

$$\begin{bmatrix} K_{\mathrm{st}} & 0 & -\tilde{Q}_{\mathrm{st}}^H M^H R_\alpha^H \\ 0 & K_{\mathrm{rt}} & \tilde{Q}_{\mathrm{rt}}^H M^H \\ -R_\alpha M \tilde{Q}_{\mathrm{st}} & M \tilde{Q}_{\mathrm{rt}} & 0 \end{bmatrix} \begin{bmatrix} u_{\mathrm{st}} \\ u_{\mathrm{rt}} \\ \underline{\tilde{h}}_{\mathrm{rt}} \end{bmatrix} = \begin{bmatrix} f_{\mathrm{st}} \\ f_{\mathrm{rt}} \\ 0 \end{bmatrix} \tag{12}$$

where $\underline{\tilde{h}}_{\mathrm{rt},\lambda}$ play the role of Lagrange multipliers. The formulation is equivalent to a mortar-element formulation [3] in which harmonic test functions are used instead of standard piecewise linear test functions. To enhance the numerical efficiency of the approach, (9) is not computed exactly but replaced by Fast Fourier Transforms (FFTs). The angular displacement is characterized by R_α. All other system parts are independent from α and do not have to be rebuilt between successive transient step except for nonlinearities.

Iterative Solution Technique

The coupled system is indefinite and combines the real-valued unknowns u with complex-valued unknowns $\underline{\tilde{h}}_{\mathrm{st}}$ which requires specialized solution techniques. The system, however, can also be solved in the positive-definite, real-valued form $P^H K P u = P^H f$ where the projectors P and P^H are defined by the operations

$$P \; : \; \tilde{u}_{\mathrm{rt}} \leftarrow M^H R_\alpha M \tilde{u}_{\mathrm{st}} \tag{13}$$

$$P^H \; : \; \begin{cases} \tilde{f}_{\mathrm{st}} \leftarrow \tilde{f}_{\mathrm{st}} + M^H R_\alpha R \tilde{f}_{\mathrm{rt}} \\ \tilde{f}_{\mathrm{rt}} \leftarrow 0 \end{cases} \; . \tag{14}$$

For numerical efficiency, only the FE stiffness matrices K_{st} and K_{rt} are assembled into matrices. The coupled system is solved by the Conjugate Gradient method using the Fast Fourier Transform algorithm for M and M^H, vector-vector multiplications for R_α and selections for $\tilde{Q}_{\mathrm{st}}$ and $\tilde{Q}_{\mathrm{rt}}$.

Torque Computation

The magnetic vector potential at Γ_{rt} transformed into Fourier coefficients $\underline{\tilde{u}}_{\mathrm{rt}} = M \tilde{u}_{\mathrm{rt}}$ combined with $\underline{\tilde{h}}_{\mathrm{rt}}$ leads to a cheap and accurate formula for the torque,

$$T = 2\pi \ell_z r_0 \underline{\tilde{h}}_{\mathrm{st}}^H \underline{\tilde{u}}_{\mathrm{st}} \; , \tag{15}$$

which offers better convergence properties of the discretization error than the Maxwell tensor method.

Application

The spectral sliding-interface technique is used to simulate the transient phenomenon occurring when a synchronous generator is connected to the grid. The 2D FE model is augmented by an external electric circuit dealing with the line impedances. The position of the rotor, determined by the solution of the motion equation, only affects the operator R_α. The FE stiffness matrices only have to be rebuilt due to the non-linearity of the ferromagnetic material. This fact substantially simplifies transient simulation for rotating devices. The spectral sliding-mesh coupling technique can be extended with factors accounting for the skewing of the rotor or stator part [7].

Conclusions

Representing the angular displacement between stator and rotor substantially simplifies the transient, Lagrangian simulation of finite element machine models. A convenient and accurate torque calculation relies upon the combination of the magnetic vector potential with the tangential magnetic field strength at the sliding interface.

References

[1] N. Sadowski, Y. Lefèvre, M. Lajoie-Mazenc, and J. Cros, "Finite element torque calculation in electrical machines while considering the movement," *IEEE Transactions on Magnetics*, vol. 28, no. 2, pp. 1410–1413, Mar. 1992.

[2] Y. Marechal, G. Meunier, J.L. Coulomb, and H. Magnin, "A general purpose tool for restoring inter-element continuity," *IEEE Transactions on Magnetics*, vol. 28, no. 2, pp. 1728–1731, Mar. 1992.

[3] A. Buffa, Y. Maday, and F. Rapetti, "Calculation of eddy currents in moving structures by a sliding mesh-finite element method," *IEEE Transactions on Magnetics*, vol. 36, no. 4, pp. 1356–1359, July 2000.

[4] S. Kurz, J. Fetzer, G. Lehner, and W.M. Rucker, "A novel formulation for 3D eddy current problems with moving bodies using a Lagragian description and FEM-BEM coupling," *IEEE Transactions on Magnetics*, vol. 34, no. 5, pp. 3068–3073, Sept. 1998.

[5] K.S. Lee, M.J. DeBortoli, M.J. Lee, and S.J. Salon, "Coupling finite elements and analytical solution in the airgap of electrical machines," *IEEE Transactions on Magnetics*, vol. 27, no. 5, pp. 3955–3957, Sept. 1991.

[6] P. Alotto, A. Bertoni, I. Perugia, and D. Schötzau, "Discontinuous finite element methods for the simulation of rotating electrical machines," *COMPEL*, vol. 20, no. 2, pp. 448–462, 2001.

[7] H. De Gersem, K. Hameyer, and T. Weiland, "Skew interface conditions in 2D finite element machine models," in *Tenth Biennial IEEE Conference on Electromagnetic Field Computation (CEFC2002)*, Perugia, Italy, June 2002, p. 95.

Numerical Analysis of the Eddy Current on Moving Conductor Problems Based on Finite Element Method

Zhang Huijuan, Yan Weili, Wang Yanting
Number 8 Guang rongdao Dept.of Electrical Engineering
Hebei University of Technology, Tianjin, 300130, China
wangzhanghj@eyou.com.cn

***Abstract*--In this paper, numerical techniques to solve moving problems are presented. The induced eddy current and its coupled field in moving media are computed with 3D FEM. A proper gauge condition for this problem is also indicated. Upwinding adaptive iteration scheme is used to suppress the oscillation and accelerate the convergence. The calculated results are compared with the measurements.**

***Index Terms*-- numerical technique, moving problems, eddy current, upwind method.**

I. INTRODUCTION

It is imperative to analyze the coupled field between electromagnetic field and force field in studying of the 3D non-linear eddy current field of moving electromagnetic medium. Eddy current may be generated by motion of the conductor in the electromagnetic system. We encounter the problems of moving conductors at calculations of eddy currents and forces in magnetic levitation devices. The difficulty in this problem lies in the treatment of the velocity terms in the governing equations. To solve the problem, 3D finite element method is used for achieving a set of simultaneous partial differentiation equations, which contain a first derivative term. The numerical oscillation will be encountered in the Galerkin finite element solution because of the influence of the mesh's size, the material properties of the conductor and the boundary conditions imposed [1].

The existence of moving term causes the lack of diagonal dominance in the coefficient matrix of finite elements equation while destroying its symmetry. That leads to coefficient matrix of finite element equation become worse to solve, sets off that the numerical solution oscillates distortedly. To solve the issue, upwinding adaptive iteration scheme is used in the solution of coefficient matrix to remedy the weakening from the moving term, improve the efficiency and accelerate the convergence of the Bi-conjugate Gradient (BICG) method, drop down the equivalent Peclet number and clear up the distortion oscillation efficiently.

In region of high permeability, which moves, enforcing the Coulomb gauge[2] can additionally optimize the stability of the solution. The calculation of the force taken into account of the eddy current in the conductor is presented.

II. MATHEMATICAL MODEL

The problem volume is partitioned into conducting and non-conducting regions when the $\vec{A}, \varphi - \vec{A}$ method is used for solving 3D eddy current problems. So the fundamental equation of the magnetic field can be written as follows

$$\nabla \times \nu \nabla \times \vec{A} + \sigma\left(\nabla\varphi + \frac{\partial \vec{A}}{\partial t} - \vec{\upsilon} \times \nabla \times \vec{A}\right) = \vec{J}_s \tag{1}$$

$$\nabla \cdot \sigma\left(\nabla\varphi + \frac{\partial \vec{A}}{\partial t} - \vec{\upsilon} \times \nabla \times \vec{A}\right) = 0 \tag{2}$$

In order to impose Coulomb gauge $\nabla \cdot \vec{A} = 0$, we provide the term

$$\int \nu_0 \nabla \cdot \vec{N} \nabla \cdot \vec{A} d\Omega$$

in (1) and (2). Using the Galerkin weighted residual technique, we have

$$\int_\Omega \left[\nu \nabla \times \vec{A} \cdot \nabla \times \vec{N} + \nu_0 \nabla \cdot \vec{N} \cdot \nabla \cdot \vec{A} + \sigma \vec{N} \cdot (\nabla\varphi + \frac{\partial \vec{A}}{\partial t} - \vec{\upsilon} \times \nabla \times \vec{A})\right] d\Omega = \int_\Omega \vec{N} \cdot \vec{J}_s d\Omega \tag{3}$$

$$\int_\Omega \nabla N \cdot \sigma(\nabla\varphi + \frac{\partial \vec{A}}{\partial t} - \vec{\upsilon} \times \nabla \times \vec{A}) d\Omega = 0 \tag{4}$$

Where N is the shape function, ν_0 is the reluctivity of the vacuum. The matrix equation can be shown as

$$[S][U] = [F] \tag{5}$$

A. Modeling of the velocity terms

Numerical oscillation will occur when the Peclet number, $P = \upsilon h \sigma / \nu / 2$, is greater than 1 (h is the average element length in the direction of the velocity). An Adaptive-Upwind FEM is used in this method.

B. Modification of the artificial diffusion terms

As it was mentioned above, the velocity term drops the diagonal elements of the stiffness matrix down resulted from the standard Galerkin method. That leads to the numerical

oscillations. In order to guarantee BICG's convergence, the artificial diffusion elements are modified .

C. *Solution of the unsymmetrical equation*

The coefficient matrix S in (5) is unsymmetrical because of the velocity terms modeled. Three components of magnetic potential and one electric scalar potential are required inside the eddy current region, only three components of magnetic potential are required inside the non-eddy current region. Two 1D variables are used to store the coefficient matrix S, one is for the non-zero entries of the upper triangular, the other is for the non-zero entries of the lower triangular. The finite element equations are solved by BI-CGSTAB method[3].

III. Results

The method has been tested through analyzing the TEAM Problem 9-1[4]. Fig.1 shows the calculated data of the flux for several coil velocities.

In the operating magnet of an AC electromagnetic contactor, the displacement, z, the velocity, υ, of the armature are obtained by solving the following motion equations

$$m\frac{d\upsilon}{dt} + F_g + F_s = F_a \tag{6}$$

$$\frac{dz}{dt} = \upsilon \tag{7}$$

where m is the mess of the moving conductor (armature), F_g is the force of the gravity, F_s is the spring force and F_a is the attractive force to be calculated.

The electric circuit equation is given as

$$u = ir + L\frac{di}{dt} + i\frac{dL}{dt} \tag{8}$$

$$\frac{di}{dt} = \frac{u - ir}{L} - \frac{i}{L}\frac{dL}{dt} \tag{9}$$

$$L = \frac{2}{i^2}\int_{\Omega}\frac{1}{2}HBd\Omega \tag{10}$$

In (9), u is the source voltage, r is the resistance of the exciting coil and L is the inductance.

Since the applied voltage changes over time, the electrical and mechanical equations are solved step by step using the Runge-Kuta method coupled with the field equation (5).

The comparison of the exciting current of an AC ontactor is shown in Fig.2.

IV. Conclusions

In solving the motional induction problems, the existence of moving term causes the lack of diagonal dominance in the coefficient matrix of finite element equation while destroying its symmetry. That leads to coefficient matrix of finite element equation become worse to solve, and sets off that the numerical solution oscillates distortedly. Adaptive upwinding scheme is used in the solution of coefficient matrix to remedy the weakening from the moving term, improve the efficiency and accelerate the convergence of BI-CGSTAB, drop down the equivalent Peclet number and clear up the distortion oscillation efficiently.

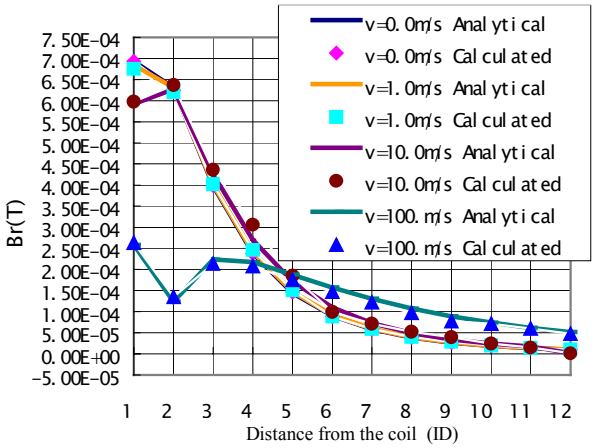

Fig.1. Comparison between different results: the analytical results and the calculated results by presented method

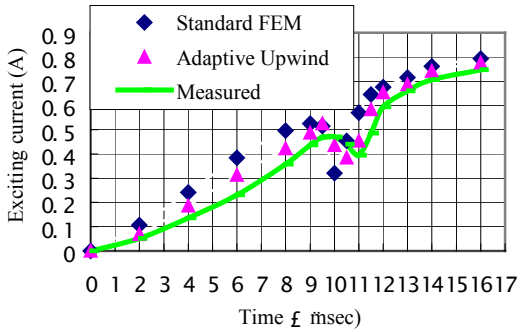

Fig.2. Comparison of the exciting current of an AC contactor.

References

[1] E. K. C Chan and S. Willimson, " Factors Influencing the Need for Upwinding in Two-dimensional Field Calculation," *IEEE Trans. on Magn.,* vol. 28, pp1161-1614, March 1992.

[2] A. Kameari, K. Koganezawa, "Convergence of ICCG method in FEM using edgy elements without gauge condition," *IEEE Trans. on Magn.* vol. 33, pp1223-1226, March, 1997.

[3] H. A. van der Vorst, "BI-CGSTAB: A fast and smoothly converging variant of BI-CG for the solution of nonsymmetric linear systems", *SIAM J. SCI. STAT. COMPUT.* Vol.13, No.2, pp631-644, March 1992.

[4] "Problem 9: Velocity effects and low level fields in axisymmetric geometries", *Proceedings of the European TEAM workshop and International Seminar on Electromagnetic field analysis*. Oxford, England, 23-25 April 1990.

3D Multiply Connected Magnetic Circuits, Solid Conductors and Electric Circuits Coupling Formulations

Yann Le Floch [1,2], Gérard Meunier[2], Christophe Guérin[1], Patrice Labie[2], Xavier Brunotte[1].

Abstract— **This paper presents theory and validation of new Finite Element formulations to realize the coupling between electric circuits and multiply connected magnetic circuits surrounded by stranded coils or by multiply connected solid conductors, using a magnetic scalar potential and an electric vector potential as state variable. For this purpose, we used formulations in reduced magnetic scalar potential versus $\mathbf{T}_0$ taking into account electric circuits and a total magnetic scalar potential taking into account cuts.**

I. Introduction.

Formulations in magnetic scalar potential $\mathbf{T}_0\phi$ allowing to treat ferromagnetic devices coupled with electric circuits have already been developed by Bouissou [1] and the authors [2]. We have also developed and implemented in FLUX3D software a formulation to take into account multiply connected magnetic circuits surrounded by stranded coils coupled to external circuit [3]. Treating solid conductors with n terminals supplied by an electric circuit is also possible with a $\mathbf{TT}_0\phi$ formulation [4]. Our aim is to treat both situations at the same time. In this paper, we have studied an example (Fig.1), with a multiply connected magnetic circuit surrounded by stranded coil and by a multiply connected solid conductor supplied by an electric circuit. This paper presents the formulations and some results on this example.

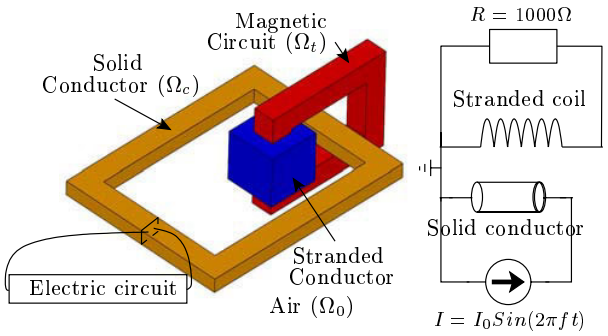

Fig. 1. Studied example.

II. Formulations and current-voltage relation for stranded coil.

When a $\mathbf{T}_0\phi$ formulation in the air (Ω_0) and total magnetic scalar potential in the magnetic material (Ω_t) is used, problems appear to verify the Ampere's theorem if Ω_t is a multiply connected domain. For example, on the closed path C_1 (Fig.2), $\mathbf{H}$ circulation is not zero in theory, whereas it is zero in this example ($\mathbf{H} = -\mathbf{grad}(\phi)$). The solution which was found to solve this problem is the introduction

[1] Cedrat , 10 chemin du pré Carré, Zirst 38246 Meylan, France.
[2] Laboratoire d'Electrotechnique de Grenoble, ENSIEG, BP 46, 38402 Saint Martin d'Hères Cedex, France.

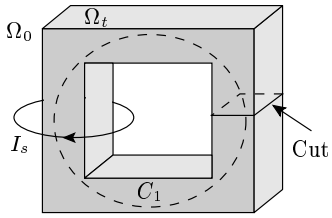

Fig. 2. Multiply connected magnetic circuit surrounded with a stranded coil.

of a magnetic circuit cut (with potential jump). The jump value of the total scalar potential is equal to the total current which surrounds it [3]. For this purpose, a ($\mathbf{T}_0\phi$) formulation is used with an original $\mathbf{t}_{0s}$ for the stranded coil [2].

$$\mathbf{t}_{0s} = I_s(\mathbf{h}_{0s} - \mathbf{grad}(\delta\phi_s))$$

Where :

- $\mathbf{h}_{0s}$ is the field due to a unit current in the stranded coil, calculated with Biot and Savart's formula.
- $\delta\phi_s$ is the reduced-total increment [5] [6] calculated with a unit current in the stranded coil such as:

$$\mathbf{grad}(\delta\phi_s) \times \mathbf{n} = \mathbf{h}_{0s} \times \mathbf{n} \; on \; \Gamma = (\Omega_t \cap \Omega_0) \cup Cut$$

As the reduced-total increment is calculated on the interface Γ, we have the choice to integrate it into Ω_t or into Ω_0. We choose the integration in Ω_t because it allows the immediate consideration of cuts. Finaly, the formulations are :

- In the magnetic circuit (Ω_t): $\mathbf{H} = -\mathbf{grad}(\phi - I_s\delta\phi_s)$
- In the air (Ω_0) : $\mathbf{H} = I_s\mathbf{h}_{0s} - \mathbf{grad}(\phi)$

The relation between the current and voltage can be written [3] :

$$U_s = R_s I_s + \int_{\Omega_0} \mathbf{h}_{0s} \cdot \frac{\partial \mathbf{B}}{\partial t} d\Omega + \int_{\Omega_t} \mathbf{grad}(\delta\phi_s) \cdot \frac{\partial \mathbf{B}}{\partial t} d\mathbf{\Omega}$$

Where ϕ and I_s are state variables.

III. Formulation and current-voltage relation for solid conductors.

On Fig.1, we have, in addition to the stranded coil, a solid conductor which surrounds the magnetic circuit in which a nonnull current flows. This nonnull current also creates a connexity problem. The aim of this part is to show how to treat this type of problem. The proposed solution to take into account non simply connected solid conductors with n (n≥2) terminals coupled with circuit equations is developed in [4]. The solution used a reduced field versus $\mathbf{T}_0$ in the air and in the solid conductor. In the case of a solid conductor with two terminals (Fig.3), we define a path of currents I_c that joins the two terminals. We computed on this path an electrokinetic current density

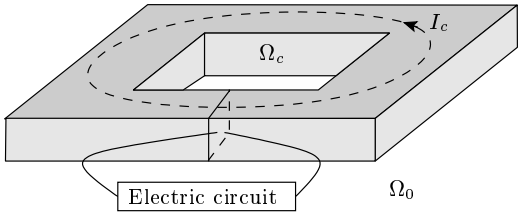

Fig. 3. Solid conductor

$\mathbf{j}_{0c}$ producing an elementary current of 1A and a $\mathbf{t}_{0c}$ such as $\mathbf{j}_{0c} = \mathbf{curl}(\mathbf{t}_{0c})$ in a box including the solid conductor with $\mathbf{t}_{0c} \times \mathbf{n} = 0$ on its boundary. The current voltage relation on this path is :

$$U_c = \int_{\Omega_c} \mathbf{j}_{0c} \cdot \mathbf{E} d\Omega + \frac{\partial}{\partial t} \int_{\Omega_0 \cup \Omega_c} \mathbf{t}_{0c} \cdot \mathbf{B} d\Omega$$

The following problem (Fig. 4) presents a connexity problem due to the solid conductor. So we need to compute a potential jump equal to the total current I_c, in the solid conductor.

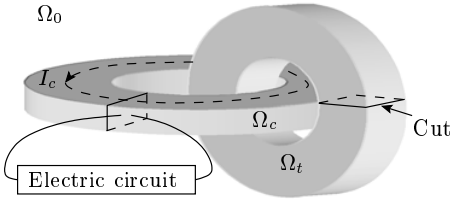

Fig. 4. Solid conductor

To compute the value of the jump, we compute the $\mathbf{t}_{0c}$ of the solid conductor as in part II :

$$\mathbf{t}_{0c} = I_c(\mathbf{h}_{0c} - \mathbf{grad}(\delta\phi_c))$$

Where :

- $\mathbf{h}_{0c}$ is the field due to a unit current in the solid conductor in the air. $\mathbf{h}_{0c}$ is calculated with the FEM in the whole domain $(\Omega_0 \cup \Omega_t \cup \Omega_c)$ such as $\mathbf{j}_{0c} = \mathbf{curl}(\mathbf{h}_{0c})$.
- $\delta\phi_c$ is the reduced-total increment calculated with a unit current in the solid conductor such as:

$$\mathbf{grad}(\delta\phi_c) \times \mathbf{n} = \mathbf{h}_{0c} \times \mathbf{n} \; on \; \Gamma = (\Omega_t \cap \Omega_0) \cup Cut$$

Finally, the formulation for stranded coils and solid conductors, is written:

- In the solid conductor (Ω_c):

$$\mathbf{H} = \mathbf{T} + \sum_{k=s,c} I_k \mathbf{h}_{0k} - \mathbf{grad}\phi$$
$$\mathbf{J} = \mathbf{curl}(\mathbf{T}) + I_c \mathbf{curl}(\mathbf{h}_{0c})$$

- In the magnetic circuit (Ω_t):

$$\mathbf{H} = -\mathbf{grad}(\phi - \sum_{k=s,c} I_k \delta\phi_k)$$

- In the air (Ω_0) :

$$\mathbf{H} = \sum_{k=s,c} I_k \mathbf{h}_{0k} - \mathbf{grad}(\phi)$$

- Current-voltage relation for solid conductor :

$$U_c = \int_{\Omega_c} \mathbf{j}_{0c} \cdot \mathbf{E} d\Omega + \frac{\partial}{\partial t} \int_{\Omega_0 \cup \Omega_c} \mathbf{h}_{0c} \cdot \mathbf{B} d\Omega + \int_{\Omega_t} \mathbf{grad}(\delta\phi_\mathbf{c}) \cdot \frac{\partial \mathbf{B}}{\partial \mathbf{t}} \mathrm{d}\mathbf{\Omega}$$

- Current-voltage relation for stranded coil :

$$U_s = R_s I_s + \int_{\Omega_0 \cup \Omega_c} \mathbf{h}_{0s} \cdot \frac{\partial \mathbf{B}}{\partial t} \mathrm{d}\Omega + \int_{\Omega_t} \mathbf{grad}(\delta\phi_\mathbf{s}) \cdot \frac{\partial \mathbf{B}}{\partial \mathbf{t}} \mathrm{d}\mathbf{\Omega}$$

Where $\mathbf{T}$, ϕ, I_s and I_c are state variables.

IV. Simulation and results.

The test problem is described by figure 1. A sinusoidal current ($I_0 = 20kA$ and $f = 50Hz$) in the solid conductor is imposed and the induced current of the stranded coil (5000 turns) is obtained. Tests were carried out with a transient model, non linear materials in Ω_t and copper in Ω_c. To confirm the results given by this new formulations, we computed an equivalent problem where the magnetic circuit is cutted by a small airgap (the airgap reluctance is very small compared to the magnetic circuit reluctance).

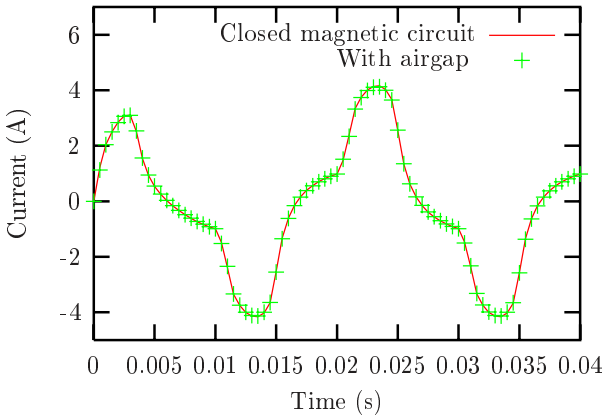

Fig. 5. Induced current of the stranded coil.(A)

The results are the same in both cases.

V. Conclusion and persectives.

This new formulation which takes into account multiply connected magnetic circuits surrounded by stranded coils and by multiply connected solid conductors supplied by an electric circuit allows us to have a coarser mesh (because no numerical air-gap has to be meshed). Furthermore, the use of the magnetic scalar potential is an economical and powerful alternative to the magnetic vector potential. Moreover the given linear system to solve is symmetric. All this developement have been implemented in FLUX3D software.

References

[1] S. Bouissou, F. Piriou, C. Kieny, G. Tanneau, *A Numerical Simulation of a Power Transformer using 3D Finite Element Method Coupled to Circuit Equation*, IEEE Trans. Magn., vol. 30 n° 5, pp. 3224-3227, September 1994.

[2] Y. Le Floch, C. Guérin, D. Boudaud, G. Meunier, X. Brunotte, *A Current Transformer Modeling*, COMPEL, vol. 21 n° 4, pp. 505-511, 2002.

[3] Y. Le Floch, G. Meunier, C. Guérin, P. Labie, X. Brunotte, D. Boudaud, *Coupled Problem Computation of 3D Multiply Connected Magnetic Circuits and Electric Circuits*, In proceedings of CEFC 2002, page 277.

[4] G. Meunier, Y. Le Floch, C. Guérin, *A non linear circuit coupled* $\mathbf{T} - \mathbf{T}_0 - \phi$ *formulation for solid conductors*, In proceedings of CEFC 2002, page 278.

[5] H.T. Luong, Y. Maréchal, P. Labie, C. Guerin, G. Meunier, *Formulation of magnetostatic problems in terms of source, reduced and total scalar potentials*, Proccedings of 3rd International Worshop on Electric And Magnetic Field, Liege (Belgium), 6-9 May 1996, pp 321-326.

[6] I. D. Mayergoyz, M. V. K. Chari, J. D'Angelo, *A new scalar potentiel formulation for three-dimensional magnetostatic problems*, IEEE Trans. Magn., vol.23, n° 6, pp. 3889-3894, 1987.

Using High Order Finite Elements in Problems with Movement

O. J. Antunes, J.P.A. Bastos, N. Sadowski
GRUCAD/EEL/CTC/UFSC
Florianópolis – 88040-900 – P.O. Box 476 – Brazil
e-mail: {orlando, jpab, nelson}@grucad.ufsc.br

Abstract — **This work analyses the use of different finite elements (lagrange, hierarchic and hermite) to improve the calculation accuracy when they are submitted to distortion due to the movement. The moving band technique is used with complete elements in thin airgaps machines. Results are shown to compare the performance of lagrange, hierarchic and hermite elements.**

INTRODUCTION

When coupling field and circuit and/or a dynamic case is considered, the time step is variable. With electronic circuits, having diodes for example, the time step can to be strongly reduced to ensure correct switch transitions. In these cases just some methods taking into account the movement can be used.

The Lagrange multipliers technique [3] produces a resultant matrix weakly conditioned and new formulations are necessary for each problem. Nodal interpolation method [4] does not ensure the continuity of the vector potential *A* and its efficiency has not been yet tested on the electromotive force calculation. The boundary element and the macro-element method leads to a fully populated matrix in the region associated with the movement. The Moving Band (MB) technique, described in [1], does not have any of these drawbacks; the resultant matrix is well conditioned and the dynamic storage of the (anti-)periodicity conditions does not change the size of the system. However, the distortion of the elements and the reconstruction of their connections create discontinuities on the electromotive force (e.m.f.). The contribution of this paper consisting in using high order finite elements to reduce the sensibility of the solution to the distortion of the elements.

MOVING BAND WITH HIGH ORDER ELEMENTS

The use of complete or modified elements inside the moving band, with the remaining mesh with first order ones, improve significantly the f.e.m results. For modified elements in the moving band, the lower and upper boundaries have linear interpolation [2]. However, in cases with thin airgaps, complete elements have to be used. For this, transition modified elements (with linear interpolation on two sides and high order one on the remaining one, as shown in Fig. 1.) are placed between the moving band and the remaining mesh.

Lagrange Elements

The interpolation functions may be obtained in this case using the expression:

$$N_{(u,v)}=P_{(u,v)}\mathbf{C}^{-1}, \quad (1)$$

where $P_{(u,v)}$ is the polynomial base and **C** is a matrix in which each row is the node coordinates of the element substituted in the polynomial base. Here, it is tedious to obtain the interpolation functions for modified transition elements. The matrix **C** is usually singular in this case and its necessary to try different combinations of polynomial base and node coordinates. A software is proposed in [6] to overcome this problem. Moreover to obtain a balanced solution, the polynomial base must have the geometry isotropy property, meaning that for each term of the form $u^r v^s$ there is also a term $u^s v^r$. Another approach is to impose a linear constraint equation handling the mid side DOF (degree of freedom). The interpolation functions of a modified element can be obtained by:

$$N_m=N_c\mathbf{T}, \quad (2)$$

where N_c is the vector of interpolation functions of a complete element and **T** the transformation for the rows having a constraint equation.

Hermite Elements

The hermite elements consider not only the function value at the nodes but also its derivatives with respect to *x* and *y*. The interpolation function may be obtained also by expression (1) by including in the rows of **C** the derivatives of the polynomial base at each node. This type of element enforces the continuity of the function derivative at the nodes. Then, the lagrange-hermite transition elements (Fig. 1(b)) have to be placed in the air to allow the refraction of magnetic field. The same difficult, as for lagrange elements, appears to generate the interpolation functions of the modified transition lagrange-hermite elements.

Hierarchic Elements

The hierarchical concept is to obtain the high order interpolation functions from the low order ones. By using the Legendre polynomials [7], the second order hierarchic function for the edge *ij* are:

$$N_{ij}=KN_iN_j, \quad (3)$$

where N_i is the standard first order shape function and K is a constant. For cubic interpolation:

$$N_{ij}=KN_iN_j(N_j-N_i). \quad (4)$$

In this case, for a complete polynomial base, it is necessary to include an internal hierarchic function, which are identically zero on the boundaries. The function $N_1N_2N_3$ could be used. To generate transition elements is necessary only to eliminate the DOF of high order functions. Moreover the hierarchic functions due to the orthogonality of the Legendre polynomials produce a better conditioned system than lagrange elements, and, in the case of moving band, the (anti-)periodicity boundary conditions are imposed as for lagrange or hermite elements, without the need of transformations.

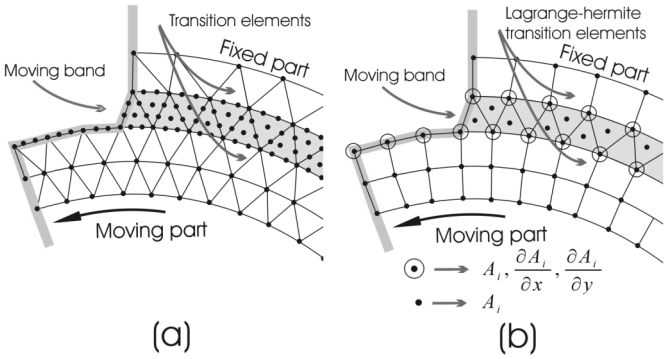

Fig.1 Moving band with lagrange (a) and hermite (b) cubic elements

RESULTS

The results presented in Fig. 2, for a permanent magnet machine with thin airgap, show that for this case the hierarchic cubic complete elements produce excellent results. With lagrange cubic complete elements, as shown in Fig. 3, we obtain the same result as for hierarchic ones. The simplicity to obtained the shape functions and the better conditioned resultant system indicate the hierarchic elements as the more interesting ones. The hermite elements, however, are very sensitive to the deformation produced by de movement (Fig. 4). When there is no deformation, the three types of interpolation yield the same result.

CONCLUSION

The moving band technique may produce excellent results even in thin airgap machines, if high order complete lagrange or hierarchic elements are used inside it. Complete elements in the MB avoid a very dense mesh in the remaining part of the domain. At this point of our investigation, the hermite elements, from our tests concerning e.m.f., are very sensitive to deformation, especially in complex geometry machines with thin airgaps. So, it seems that there is no advantage on enforcing continuity higher than what C^o lagrange or hierarchic elements have.

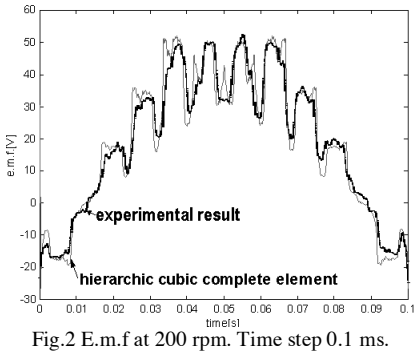

Fig.2 E.m.f at 200 rpm. Time step 0.1 ms.

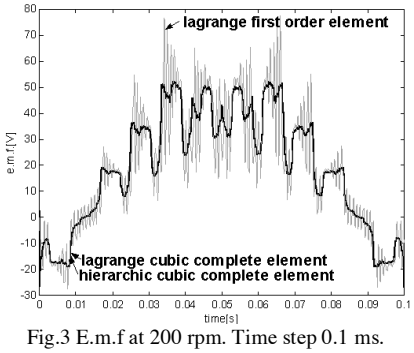

Fig.3 E.m.f at 200 rpm. Time step 0.1 ms.

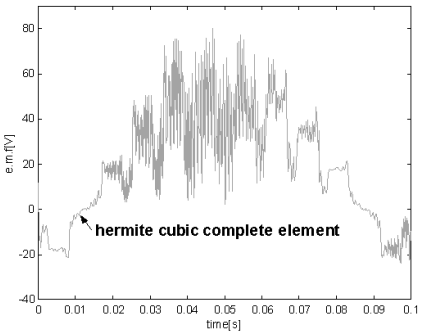

Fig.4 E.m.f at 200 rpm. Time step 0.1 ms.

REFERENCES

[1] B. Davat, Z. Ren, M. Lajoie-Mazenc, "The movement in field modeling', *IEEE Trans. Magn.*, vol. 21, no.6, pp. 2296-2298, November 1985.

[2] O. J. Antunes, J. P. A. Bastos, and N. Sadowski, "Using diferent types of finite elements in electrical machines thin airgaps", *The Fourth International Conference on Computation in Eletromagnetics CEM2002, Bournemouth UK,* IEE, Savoy Place, April 2002.

[3] D. Rodger, H. C. Lai , and P. J. Leonard, "Coupled elements for problems involving movement", *IEEE Trans. Magn.,* vol. 26, no. 2, pp. 548-550, March 1990.

[4] R. Perrin-Bit and J. L. Coulomb,"A three dimensional finite element mesh connection for problems involving movement", *IEEE Trans. Magn.*,vol. 31, no. 3, pp. 1920-1923, May 1995.

[5] N. Ida, and J. P .A. Bastos, "Electromagnetics and calculations of fields*", Second Edition, Springer-Verlag, New York*, 1997.

[6] C. Chee, L. Tong and G. Steven, "Shape functions generation using Macsyma", *Communications in Applied Numerical Methods*, no. 16, pp.705-719, 2000.

[7] O. C. Zienkiewicz and R. L. Taylor, "The finite element method", vol. 1, fourth edition, McGraw-Hill, 1994.

COMPUMAG Saratoga Springs, New York USA
July 13 - 17, 2003

Weighted-residual finite element mesh coupling

Enrique Melgoza
Instituto Tecnológico de Morelia
Av. Tecnológico 1500
Morelia, Mich., 58120 México
Email: emelgoza@itmorelia.edu.mx

Rafael Escarela
Universidad Autónoma Metropolitana
Av. San Pablo 180, Col. Reynosa
Azcapotzalco, 02200 Mxico, D.F.
Email: r.escarela@ieee.org

Marco Arjona
Instituto Tecnológico de La Laguna
Boulevard Revolución
Torreón, Coah., 27000 México
Email: marjona@ieee.org

***Abstract*— A weighted-residual method is presented to address the problem of coupling two separate meshes sharing a common boundary. It is shown that the imposition of a potential continuity condition together with a suitable penalty constant can be used to achieve the coupling. The further requirement of continuity of the normal derivative results in a quicker convergence. A magnetostatics test problem in two dimensions is used to verify the scheme. The method can be used in movement simulation of magnetic devices.**

I. Introduction

The problem of taking into account the movement of certain parts of magnetic devices has received considerable attention. Several approaches have been proposed, among them the remeshing of the geometry, the use of a slip band, analytic solutions in the airgap and coupling with integral formulations. The method of Lagrange multipliers has been successful in providing a general method, with applications in two- and three-dimensional problems [1], [2]. It has been argued, however, that the use of these Lagrange multipliers results in an increased number of degrees of freedom in the problem and makes the global matrix non-positive definite, which may be undesirable features in certain applications [3].

This paper addresses the problem of mesh coupling from the point of view of the finite element weighted-residuals formulation, with the aim of circumventing these shortcomings. In this scheme, no additional degrees of freedom are required to achieve the coupling. Only the two-dimensional magnetostatic case in terms of the z component of the magnetic vector potential is considered. However, the same ideas may be applied to the three-dimensional case in terms of the magnetic scalar potential [2].

II. The conventional Lagrange multipliers method

For the magnetostatic field problem in terms of the magnetic vector potential component A_z (for two-dimensional problems), the coupling condition

$$A_a - A_b = 0 \tag{1}$$

is imposed on Γ_c, the common boundary between meshes a and b. An augmented functional is constructed, given by

$$\Pi' = \Pi + \int_{\Gamma_c} \lambda (A_a - A_b) d\Gamma_c, \tag{2}$$

where Π is the functional for the uncoupled problem and λ is the Lagrange multiplier. The value of λ at each node in the boundary Γ_c is treated as an additional degree of freedom, and additional rows are added to the global stiffness matrix in the form

$$K_i^{\lambda} = \int_{\Gamma_c} N_i^a \left(\mathbf{N}^a - \mathbf{N}^b \right) d\Gamma_c, \tag{3}$$

where N_i^a is the shape function for node i in mesh a, and $\mathbf{N}^a$, $\mathbf{N}^b$ are the vectors of shape functions in meshes a and b. The nodes in mesh a along the boundary Γ_c have an extra degree of freedom corresponding to λ. The integration (3) is calculated on the corresponding boundary of only one of the meshes.

III. Galerkin formulation of the coupling condition

The equation for the two-dimensional magnetostatic field problem is

$$\nabla \cdot (\nu \nabla A_z) + J_z = 0, \tag{4}$$

in the domain Ω with boundary Γ. The corresponding weak formulation is

$$\int_{\Omega} \nu \nabla w \cdot \nabla A_z d\Omega - \int_{\Omega} w J_z d\Omega - \oint_{\Gamma} w \nu \frac{\partial A_z}{\partial n} d\Gamma = 0, \tag{5}$$

where w is the weighting function. The directional derivative in the normal direction n appears in the boundary integral. In the Galerkin formulation the weighting function is the node shape function N_i, and (5) leads to the element equation row

$$\sum_{j=1}^{m} A_j \int_{\Omega} \nu \nabla N_i \cdot \nabla N_j d\Omega - \int_{\Omega} N_i J_z d\Omega - \oint_{\Gamma} \nu N_i \frac{\partial A_z}{\partial n} d\Gamma, \tag{6}$$

in which m is the number of nodes in the element.

The coupling condition (1) stating the continuity of the potential can be imposed by adding the following integral to the left hand side of (5):

$$\int_{\Gamma_c} w (A_a - A_b) d\Gamma_c. \tag{7}$$

Taking N_i as weight again, this results in the following expressions being added to (6):

$$\alpha \int_{\Gamma_c} N_i^a \left[\sum_{j=1}^{m_a} N_i^a A_{a_j} - \sum_{j=1}^{m_b} N_i^b A_{b_j} \right] d\Gamma_c, \tag{8}$$

$$\alpha \int_{\Gamma_c} N_i^b \left[-\sum_{j=1}^{m_a} N_i^a A_{a_j} + \sum_{j=1}^{m_b} N_i^b A_{b_j} \right] d\Gamma_c. \tag{9}$$

The α constant is a penalty number which has to be added since the integrals in (8) and (9) are several orders of magnitude smaller than the entries in (6). Two terms are necessary to preserve the symmetry of the global matrix and each boundary integral is carried out on the corresponding mesh, contrasting to the Lagrange multipliers method where only one integration is required. The inverted signs reflect the fact that the directions of integration in the two meshes are opposite.

The scheme described above has been implemented in a computer program. Results for a test problem are presented in

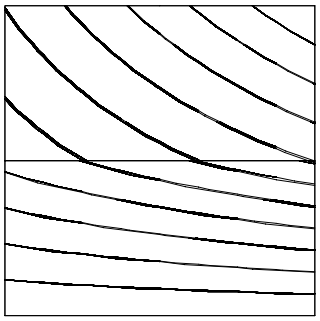

Fig. 1. Superposed contours of A_z for single mesh and coupled mesh, with potential continuity condition. Penalty constant $\alpha = 10^8$. The coupling boundary is clearly visible.

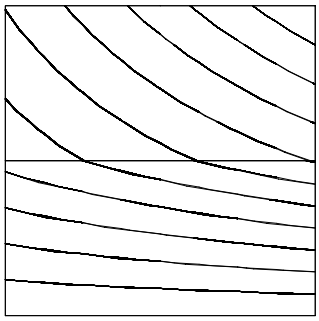

Fig. 2. Superposed contours of A_z for single mesh and coupled mesh, with potential and normal derivative continuity conditions. Penalty constant $\alpha = 10^2$

Fig. 1 in which the superposed contours of A_z are displayed for both a single-mesh model and a coupled-mesh model, with a penalty constant α set to 10^8. This is two to three orders of magnitude larger than the uncoupled-mesh terms in the stiffness matrix. Only the absolute value of the penalty number is relevant, the sign can be either positive or negative.

Correct results are obtained even for very large penalty constants: values up to 10^{20} were verified before the penalty terms dominate the solution. Values outside the range $10^8 - 10^{20}$ give incorrect results. For a penalty number slightly smaller than the lower value of this range, the values of potential are still reasonably accurate, but the contour plots are jagged at the interface. For the contours transition at the boundary to be smooth, a sufficiently large α has to be set, and the process for its selection is one of achieving convergence: subsequently larger values are tried until a predefined tolerance is met. Once determined for a given type of problem, the penalty number may be confidently used in subsequent cases.

IV. Weighted-residual formulation for normal derivative continuity

The normal derivative term in (5) suggests a further coupling condition requiring it to be continuous along the common boundary. The additional integral would be

$$\int_{\Gamma_c} w\nu \left(\frac{\partial A_a}{\partial n} - \frac{\partial A_b}{\partial n} \right) d\Gamma_c. \tag{10}$$

In this case, the use of N_i as weighting function leads to an asymmetric matrix. We avoid it by using the normal derivative as weight, with the additional stiffness entries given by:

$$\beta \int_{\Gamma_c} \nu \frac{\partial N_i^a}{\partial n} \left[\sum_{j=1}^{m_a} \frac{\partial N_i^a}{\partial n} A_{a_j} - \sum_{j=1}^{m_b} \frac{\partial N_i^b}{\partial n} A_{b_j} \right] d\Gamma_c, \tag{11}$$

$$\beta \int_{\Gamma_c} \nu \frac{\partial N_i^b}{\partial n} \left[-\sum_{j=1}^{m_a} \frac{\partial N_i^a}{\partial n} A_{a_j} + \sum_{j=1}^{m_b} \frac{\partial N_i^b}{\partial n} A_{b_j} \right] d\Gamma_c. \tag{12}$$

The β constant is another penalty number. We have used $\alpha = \beta$ and obtained satisfactory results, as can be appreciated in Fig. 2, which shows the contours for both a single-mesh model and the coupled-mesh model, for a penalty constant of 10^2.

As in the case of the potential continuity condition alone, the values of potential are relatively immune to variations in the penalty constant in a wide range. In this case, where both the potential and its normal derivative are used as coupling conditions, the range of acceptable values for the penalty constant is $10^2 - 10^{12}$.

Despite the increased computational cost of imposing both of the potential continuity condition (7), and the normal derivative condition (10), the scheme has the advantage of requiring a much lower value of the penalty constant α, which translates in a better conditioned global stiffness matrix.

V. Conclusions

The conventional Lagrange multipliers method for mesh coupling was briefly reviewed, and the implementation of the corresponding coupling condition presented in form of an equivalent Galerkin formulation. In the latter, a penalty number is necessary to correctly couple the meshes, and guides for its selection were discussed. A more complete mesh coupling scheme which relies in the continuity both of the potential and of its normal derivative was outlined. This new scheme was found to be quicker to converge in the sense that a smaller penalty constant is required; this has the advantage of resulting in a better conditioned global matrix. For both methods, the range of allowable values of penalization was found to span around ten orders of magnitude. Also, the solution is remarkably immune to the magnitude of the penalty number inside the allowable range.

Acknowledgment

EMV thanks the support of CONACYT for the development of this work, under grant I39326A.

References

[1] D. Rodger, H.C. Lai and P.J. Leonard, "Coupled elements for problems involving movement," *IEEE Transactions on Magnetics*., **vol.26, No.2, pp.548–550, March 1990.**

[2] H.C. Lai, D. Rodger and P.J. Leonard, "Coupling meshes in '3D' problems involving movements," *IEEE Transactions on Magnetics*., **vol.28, No.2, pp.548–550, March 1992.**

[3] F. Rapetti, L. Santandrea, F. Bouillault, A. Razek, "Calculation of eddy currents in moving structures using a finite element method on non-matching grids", *COMPEL*, **vol.19. No.1, pp.10-29**

COMPUMAG Saratoga Springs, New York USA
July 13 - 17, 2003

A 3D Overlapping Finite Element scheme for modelling movement

H.C. Lai and D. Rodger
University of Bath,
Claverton Down,
BATH BA2 7AY, UK

***Abstract*—This paper describes a 3D overlapping finite elements scheme for modelling moving eddy currents problems in which motion of the moving part causes the air gap between it and the non-moving part to change continuously with time.**

I. Introduction

The finite element method, in its standard form, is not suited to model electromagnetic problems which contain air gaps that change constantly in size due to the present of parts that move in a linear fashion. Examples of these include the modelling of electromagnetic actuators that produce linear stroke motion and jumping eddy current disc type experiment. To tackle this type of problem, the coupled Boundary Element-Finite Element method[1] or even some form of remeshing technique[2] can be used.

In this paper, we describe an alternative 3D finite element scheme which can be used to solve this type of problem. The scheme allows one 3D finite element mesh to move freely within the space occupied by a second independent 3D finite element mesh. The two meshes are not 'joined' together and remain as two separate meshes at all times. The immediate benefit of this flexibility is that modelling devices at many different air gaps can now be carried out without the need to produce a new finite element mesh for each air gap. Moreover, simulations of devices in which the size of air gaps change dynamically with the motion of the moving parts can now be readily carried out.

In a previously published paper[3], we have presented an overlapping elements scheme which works in 2D only. The verification of the method using experimental results was also demonstrated. This paper shows how the previous 2D scheme is extended to deal with 3D cases.

II. Overlapping Elements

In 3D Finite Element problems, we use the magnetic scalar potential ψ and the reduced scalar potential ϕ to model non-conducting regions while conducting regions are modelled using the magnetic vector potential. The following equations are solved for:

$$-\nabla\cdot\mu_1\nabla\psi = 0 \quad \text{scalar regions} \tag{1}$$

$$-\nabla\cdot\mu_2\nabla\phi = 0 \quad \text{reduced scalar regions} \tag{2}$$

$$\nabla\times\left(\frac{1}{\mu}\nabla\times\mathbf{A}\right) = -\sigma\left[\frac{\partial\mathbf{A}}{\partial t}\right] \quad \text{conducting regions} \tag{3}$$

The scheme used in this paper allows one finite element mesh to be 'embedded' inside another finite element mesh. This is illustrated with a simple diagram shown in Fig. 1. For clarity, the figure depicts the meshes and elements as 2D objects. In our case, however, both are 3D objects.

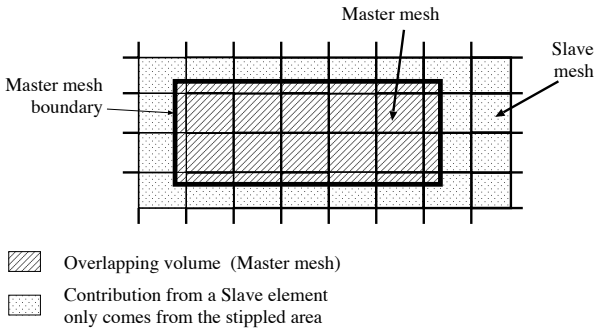

Fig. 1. Overlapping meshes.

Electromagnetically, the two meshes in Fig. 1 represent two independent domains and there is no interaction between them. To couple the two meshes together, the Lagrange Multipliers method is used [4]. The method weakly enforces the following constraint at the boundary surface between the two meshes.

$$\psi_{\text{master}} - \psi_{\text{slave}} = 0 \tag{4}$$

In the case of Fig. 1, the boundary surface coincides with the outer faces of the elements of the inner master mesh. The 'embedding' of one mesh inside another mesh results in finite elements from both meshes overlapping one another. These overlapping finite elements are dealt with using the master-slave elements approach. In this approach, one mesh is assigned the master mesh and the other one the slave mesh. Slave elements that overlap with the elements in the master mesh have to be dealt with in such a way that the contributions from one of these elements to the system matrix only come from that portion of the element outside the boundaries of the master mesh.

III. Simulations

The 3D overlapping scheme was used to model a jumping disc problem. The model contains a conducting cylindrical disc placed concentrically above a set of cylindrical coils in which a 50Hz AC current flows. The finite element model of the set up contains two meshes, the master and the slave mesh. The master mesh discretised the disc and the air in its immediate vicinity. The slave mesh is the mesh that discretised the coil and all the surrounding air. Fig. 2 shows a 3D view of the finite element model used. The 3D model has about 120,000 nodes, 120,000 elements and 130,000 unknowns.

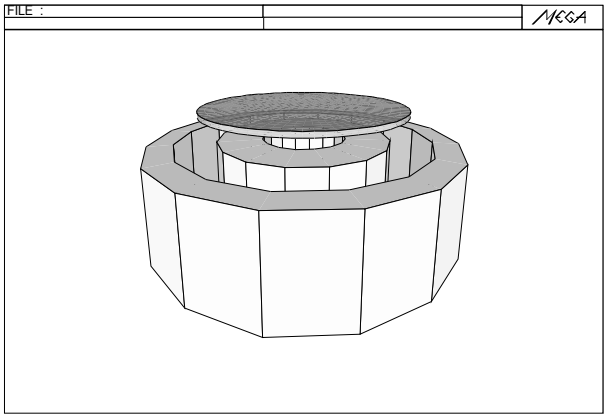

Fig. 2. Computer model.

The upward force acting on the conducting disc at different fixed height from the coils when a 50Hz AC current is flowing in the latter was calculated with the new scheme. The results are shown in Fig. 3. This series of calculations were also repeated using standard finite element meshes, one mesh for each case. The results are also shown in Fig. 3 for comparison.

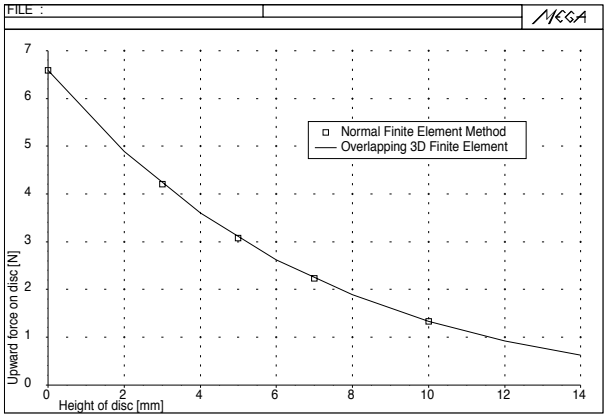

Fig. 3. Graph of upward force on disc against height of disc.

IV. Conclusions

A time-transient simulation of the vertical movement of the disc under the influence of the field generated by the coils was carried out. In the simulation, the disc was constrained to move only along in the axial direction. In another words, there is no sideways and twisting movement. Fig. 4 shows the graph of the disc height against time. The same graph also shows the results of a 2D axi-symmetric simulation of the movement of the disc using a previously verified 2D overlapping finite element scheme[3]. The discrepancies observed in Fig. 4 are most likely due to the fact that the 3D mesh used is coarser that the 2D mesh.

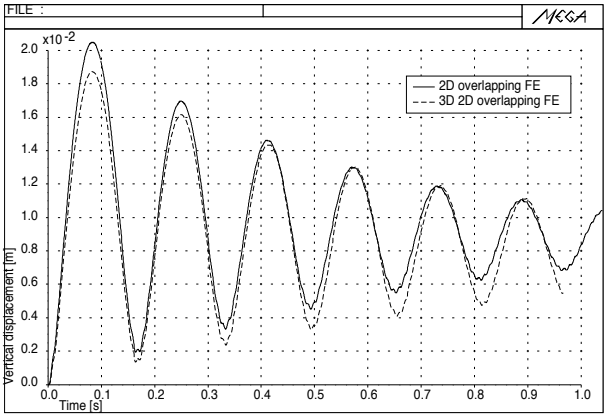

Fig. 4. Graphs of vertical displacement against time.

V. Conclusions

This paper described a new 3D overlapping finite element scheme which allows electromagnetic problems with constantly changing air gap sizes to be modelled conveniently. The new scheme was used to modelled a jumping disc problem and the results compare well with the previously verified 2D finite element method.

References

[1] F.Henrotte, A.Nicolet, H.Hedia, A.Genon, and W.Legros. Modelling of electromechanical relays taking into account movement and electric circuits. *IEEE Trans-Mag*, 30(5):3236–3239., September 1994.

[2] Yokoyama T, Cingoski V, Kaneda K, and Yamashita H. 3-d automatic mesh generation for FEA using dynamic bubble system. *IEEE Trans-Mag*, 35(5):1318–1321, May 1999.

[3] H.C.Lai, P.C.Coles, D.Rodger, and P.J.Leonard. Transient analysis of an electromagnetic actuator using an overlapping finite element scheme. *IEEE Trans. Magn.*, 36(4):1462–1467, July 2000.

[4] H.C.Lai, D.Rodger, and P.J.Leonard. "Coupling meshes in 3D problems involving movement". *IEEE Trans. Magn.*, 28(2):1732–1734, March 1992.

Computation of the induced Current Density into the Human Body due to LF Magnetic Field generated by Realistic Devices

R. Scorretti, N. Burais, O. Fabregue, A. Nicolas, L. Nicolas
CEGELY - Ecole Centrale de Lyon
BP 163 – 69134 Ecully cedex - France
e-mail: riccardo.scorretti@eea.ec-lyon.fr

***Abstract*— A Finite element formulation to compute induced currents into the human body due to low frequency magnetic field is described. Magnetic source field and induced currents are computed separately, allowing to handle sources due to realistic devices. This method is validated using analytical solutions over a sphere. The limit of validity of the formulation is established. Computations using an accurate model of the human body are presented.**

INTRODUCTION

The daily exposure to an electromagnetic environment raises the question of the effects of low frequency (LF) magnetic fields on human health. The accurate assessment of the currents induced in the human body by a time varying magnetic field is a major issue, not only for its relevance in medical research, but also for its implications on the definition of industrial standards [1]. Generally, either the magnetic source or the geometric model of the human body are considered to be very simple. As example in [2], the magnetic field is assumed to be uniform, or at most generated by a wire system. Our purpose is to compute accurately the currents induced into the human body by realistic devices, such as transformers, motors or electronic article surveillance devices. In this paper, a method based on a finite element (FE) discretization of the A-ϕ formulation is presented, allowing to compute separately the magnetic source field and the induced currents into the human body. The formulation is first presented. It is then validated and frequency limits of validity are established. Computations using an accurate model of the human body are finally presented.

FINITE ELEMENT FORMULATION

Let **A** be the vector magnetic potential generated by the device in the free space, and Ω the region occupied by the human body. At low frequency, displacement currents are negligible. Moreover, due to the low values of conductivity of the human tissues, the magnetic field is not modified in an appreciable way by induced currents into the human body [3], so that the electric field **E** is given by:

$$\nabla\times\mathbf{E}=-\frac{\partial}{\partial t}\nabla\times\mathbf{A}\Rightarrow\mathbf{E}=-\frac{\partial\mathbf{A}}{\partial t}-\nabla\phi \qquad (1)$$

Assuming that the vector potential **A** is known, the scalar potential ϕ needs solely to be found over Ω in order to compute the current density $\mathbf{J}=\sigma\mathbf{E}$. The Galerkin form is obtained by using the charge conservation law:

$$\iiint_{\Omega}\left[\sigma\left(\nabla\phi+j\omega\mathbf{A}\right)\cdot\nabla W\right]d\Omega=0 \qquad (2)$$

where W is the weighting function. It is solved by the FE method with classical nodal elements. There are two main advantages to such a formulation, compared to a general one. First, the induced currents are computed separately from the magnetic source field, which obviously represents a great simplification. It is then possible to use accurate geometric models for both the magnetic source device and the human body. Second, conductivities of the human tissues [4] (Table I) are not of the same order than those of the electrical devices, leading to ill-conditioned matrices. By decoupling both problems – the magnetic vector potential due to the source, and the induced currents into the human body – better solving may be obtained.

TABLE I
CONDUCTIVITIES OF USUAL HUMAN TISSUES

	10 Hz	1 kHz	10 kHz	100 kHz	1 MHz
Fat	0.0122	0.0224	0.0238	0.0244	0.0251
Muscle	0.2020	0.3211	0.3408	0.3618	0.5027
Bone	0.0756	0.0815	0.0204	0.0839	0.0244
Kidney	0.0544	0.1127	0.1377	0.1713	0.2782
Liver	0.0277	0.0414	0.0535	0.0846	0.1866
Blood	0.7	0.7	0.7	0.7029	0.8221
Intestine	0.5111	0.5324	0.5597	0.5942	0.8649
Bladder	0.2028	0.2076	0.2130	0.2189	0.2361

VALIDATION OF THE FORMULATION

In order to validate the method, numerical results have been compared with exact solutions over a sphere [5] on the basis of the criterion error :

$$\varepsilon_1(\mathbf{E})=\frac{1}{\max(|\mathbf{E}_{an}|)V}\int_V|\mathbf{E}_{EF}-\mathbf{E}_{an}|dv \qquad (4)$$

where $\mathbf{E}_{EF}$ is the FE solution and $\mathbf{E}_{an}$ is the analytical electric field. As shown in Table II, good agreement is found. The numerical solution converges toward the exact one when the mesh size is reduced.

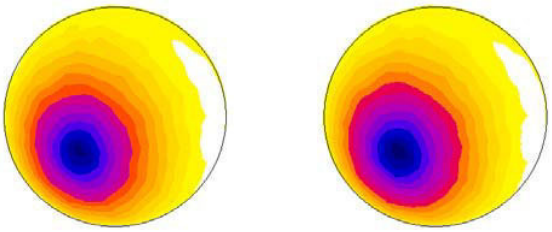

Fig. 1. Magnitude of the electric field on the sphere due to a space dependent magnetic field (f=100 kHz,σ=1, μ_r=1, a=0.1m). Left: analytical solution [5], right: numerical solution (2982 nodes)

TABLE II
ERROR CRITERION DEPENDING ON THE MESH SIZE

Number of surface points	Number of nodes	Number of elements	Error on potential	Error on magnitude of the field
100	132	427	2.31%	3.81%
200	229	651	2.86%	3.99%
400	510	1676	1.64%	2.28%
500	1775	9075	0.45%	2.20%
850	2982	15309	0.38%	1.75%

The effectiveness of the formulation has been checked by comparing the results with those obtained using a general vector potential formulation, computed with the FLUX3D package [6]. The electric field induced in a sphere by a circular coil is computed for different values of the product σf, where σ is the conductivity of the sphere and f is the frequency of the source currents. Fig. 3 shows that the threshold of validity of the formulation is found in the range $10 < \sigma f < 10^7\ \Omega^{-1}s^{-1}m^{-1}$. From the values of conductivity of the human tissues (table I), it is seen that the formulation can be used for a wide range of LF magnetic source fields.

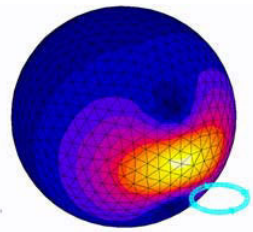

Fig. 2. Magnitude of the electric field on the sphere (f=100 kHz, σ=1, μ_r=1, a=0.1m) induced by a circular coil.

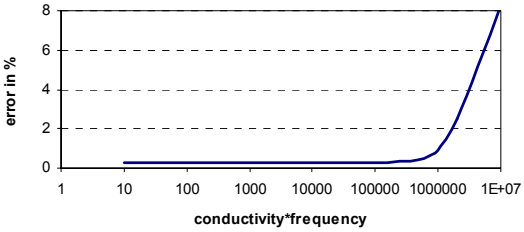

Fig. 3. Comparison with a general formulation: error criterion depending on the product σf.

CURRENTS INDUCED BY A SERIES AC MOTOR

As example, the currents induced in a human body by an AC motor are computed. The mesh of the human body is created from 60 Computerized Tomography scans. It is made of 182650 elements and 33181 nodes. The vector magnetic potential due to the motor is computed separately using the FLUX3D package, with 16163 nodes. Two orientations of the motor are compared (fig. 4). The axis of the motor is first located vertically. Second, the rotor is rotated toward the human body in such a way that the distances are unchanged. It is observed that in the first case the induced currents are larger due to the flux leakage.

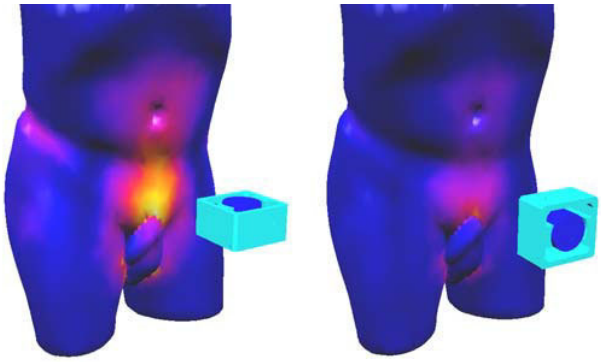

Fig. 4. Electric field for 2 orientations of the AC motor.

CONCLUSIONS

A method to compute the currents induced by realistic devices in the human body is presented. It can be used for a wide range of LF magnetic sources. It allows to describe accurately both radiating device and human body.

REFERENCES

[1] ICNIRP, "Guidelines for limiting exposure to time-varying electric, magnetic and electromagnetic fields (up to 300 GHz), " Health Phys., vol. 74, no 4, pp. 494–522, 1998.
[2] T.W. Dawson, K. Caputa and M.A. Stuchly, "Organ dosimetry for human exposure to non-uniform 60-Hz magnetic fields", IEEE Trans. Pow. Del., vol. 14, no4 , October 1999.
[3] W. Wang and S.R. Eisenberg, "A three-dimensional finite element method for computing magnetically induced currents in tissues, " IEEE Trans. Mag., vol. 30, no 6, November 1994.
[4] S. Gabriel, R.W. Lau and C. Gabriel, "The Dielectric Properties of Biological Tissues: III. Parametric Models for the Dielectric Spectrum of Tissues," Phys. Med. Biol. pp. 2271-2293, no. 41, 1996.
[5] M. Bencsik, R. Botwell and R.M. Bowley, "Electric fields induced in a spherical volume conductor by temporally varying magnetic field gradients,". Phys. Med. Biol., vol. 47, pp. 557-576, 2002.
[6] *2D/3D FEM software products developed by INPG/LEG and CEDRAT.*

Classify the Multiplicity of the EEG Sources Using Support Vector Machines

Qing Wu, Xueqin Shen, and Weili Yan
Hebei University of Technology
No. 1 road, Ding Zi Gu, Tianjin, 300130, China
E-mail: qingwu@hebut.edu.cn

Abstract — **Classifier based on support vector machines (SVMs) has had successful applications in many fields for it's simple structure and excellent learning performance. In this paper we apply such classifiers to estimate the multiplicity of the sources of the electroencephalogram (EEG), and use them to determine the number of active current sources according to the potentials recorded on the scalp. Experimental results indicate that SVM classifier is an effective and promising approach for this task.**

INTRODUCTION

Support vector machine is an effective machine learning method proposed by Vapnik et al. for general purpose pattern recognition [1-2]. Based on the idea of VC dimension and the principal of structural risk minimization, a SVM is intuitively a two-class classifier in the form of a hyperplane which leaves the largest possible fraction of points of the same class on the same side, while maximizing the distance of either classes from the hyperplane. The points of either classes which have closest distance to the hyperplane are called support vectors and the distance is called margin. The hyperplane, called optimal separating hyperplane (OSH), minimizes not only the empirical risk, but also the expectant risk, and thus has better generalization ability compared with traditional classifiers. Because of their excellent performances, SVMs have been successfully applied to many fields.

Electroencephalogram is the integrated representation of the electric biological activities of the neuron groups within the brain on the scalp after being conducted by the volume conductor (including the cortex, cerebrospinal fluid, skull, scalp, etc.) [3]. Interpretation of the clinical EEG almost always involves speculation as to the possible locations of the sources inside the brain that are responsible for the observed potential distribution on the surface of the head. Generally, bioelectromagnetic field is viewed as a quasistatic current system and the EEG sources are modeled as current dipoles. Localization of focal electrical activity in the brain using equivalent dipoles, is usually performed by iteratively modifying the parameters of the model source, until optimal correspondence is reached between the observed and the predicted potential vectors on the head. So it is necessary to choose the source configuration that can satisfy all of the known constraints in advance. However, in most applications the exact forms of the source are difficult to know. For example, in single time-slice source localization, there is no quantitative way of estimating the multiplicity of the sources. But if the number of dipole sources is not correctly estimated beforehand, it is likely that none of the predicted source locations will be correct.

In this paper, the practice of using SVM to determine the source multiplicity is carried out. In our experiments, training samples are formed by solving EEG forward problem on the source model assumed. During the training process, the SVM based classifier builds up its own memory reflecting the relationship between the scalp potentials and source models. Then, it can give out the dipole source multiplicity when new EEG data are given.

METHOD

Usually, support vector machines perform pattern recognition for two class problems by determining the optimal separating hyperplane. Given a training set S: $\{(\mathbf{x}_1, y_1), \cdots, (\mathbf{x}_l, y_l)\}$, where $\mathbf{x}_i \in R^n$ is the data point and $y_i \in \{+1, -1\}^l$ is the class label, constructing OSH can be expressed as:

$$\begin{aligned} &\textit{Minimize} \qquad \Phi(\mathbf{w}, b) = \frac{1}{2}\|\mathbf{w}\|^2 \\ &s.t. \qquad y_i(\mathbf{x}_i \cdot \mathbf{w} + b) - 1 \geq 0 \quad i = 1,2,\cdots,l \end{aligned} \tag{1}$$

If the data is not linearly separable in the input space, a non-linear transformation $\Phi(\cdot)$ can be applied which maps the data points $\mathbf{x}_i \in R^n$ into a Hilbert space H and an OSH is found there. The mapping $\Phi(\cdot)$ is represented by a kernel function $K(\cdot,\cdot)$, which defines an inner product in H, i.e. $K(x_i, x_j) = \Phi(x_i) \cdot \Phi(x_j)$. Eventually, through introducing Lagrange multipliers and using Karush-Kuhn-Tucker (KKT) conditions, we can transform the problem of constructing an OSH into solving a linearly constrained quadratic programming problem in a number of variables equal to the number of data points [1-2]:

$$\begin{aligned} &\textit{Maximize} \quad W(\boldsymbol{\alpha}) = \sum_{i=1}^{l}\alpha_i - \frac{1}{2}\sum_{i,j}^{l}\alpha_i\alpha_j y_i y_j K(\mathbf{x}_i, \mathbf{x}_j) \\ &s.t. \qquad \sum_{i=1}^{l}\alpha_i y_i = 0 \\ &\qquad\quad 0 \leq \alpha_i \leq C \qquad i = 1,\cdots,l \end{aligned} \tag{2}$$

where α_i is Lagrange multiplier, l is the number of training points, and $C > 0$ is an penalty factor allowing for non-separable cases (or imperfect separation). In the solution of (1), only a fraction of the α_i's (suppose m) will be nonzero and data points connected to them are the so-called support vectors. Then the decision function of SVM gets the following form:

$$f(\mathbf{x}) = \mathrm{sgn}(\sum_{i=1}^{m} \alpha_i^* y_i K(\mathbf{x_i}, \mathbf{x_j}) + b) \qquad (3)$$

where α_i^* represents support vector, and the classification threshold b can be computed by using any support vector which satisfies the equation constraint in (1) or by using any two of the support vectors carrying out the same computation and then take the median.

While SVMs were initially proposed for two-class problems, there has been ways for combining many binary classifiers into a multiclass classifier [1]. One of the widely used is the voting scheme. In a q class problem, training $q \times (q-1)/2$ so-called one-vs-one binary classifiers with each separates a pair of classes; then in the test stage, a point is inputted into all the classifiers, each classifier gives a vote, and the class which gets the most votes will be the final output.

SIMULATION RESULTS

A four-concentric-shell structure with different conductivity values (0.33, 1, 0.0042, 0.33) $s.m^{-1}$ respectively representing the brain, cerebrospinal fluid, skull and scalp is used as a head model, and their relative radii are (0.8, 0.85, 0.92, 1) cm. Using this four-shell spherical head model and considering the case in which the number of simultaneously active dipoles is one, two, or three. In order to obtain the training and testing samples, we assume random dipole location vectors whose three components obey the uniform distribution are independently generated, and then the dipole moments are generated randomly using the zero-mean, unit-variance Gaussian distribution. Once the source models were formed, we solve the forward solution for each model to form the respective sample set [4], over 138 measurement points corresponding to 138 channel measured EEGs. In this way, we have obtained four sample sets, one for training, and the other three for testing as shown in table I.

TABLE I. THE NUMBER OF PATTERNS IN EACH SAMPLE SETS

Training set	Test set No.1	Test set No.2	Test set No.3
4500	7876	12292	12422

Each pattern was composed of two parts, 138-dimension scalp potentials and 1-dimension target value (the number of active EEG sources). We trained three one-vs-one binary classifiers using Gaussian kernel:

$$K(\mathbf{x}_i, \mathbf{x}_j) = \exp(-\| \mathbf{x}_i - \mathbf{x}_j \|^2 / 2\sigma^2$$

with σ^2 the variance of the Gaussian. The best result was obtained using the classifiers trained with C=300, σ^2=0.5 (on our computer, a 1.5GHz Pentium PC, it needs 29 seconds to train). Table II gives the classification results on the test sets, using voting schemes to combine the binary classifiers.

TABLE II. TEST RESULTS FOR THREE TEST SETS

	Test set No.1	Test set No.2	Test set No.3
Accuracy $(\frac{\text{correct}}{\text{total}} \times 100\%)$	99.39%	99.51%	99.05%
Time (seconds)	35.8	53.5	53.7

As we can see, the classification results are excellent and the time needed almost linearly scales with the sample size which assures the dynamic analyses of EEG. To further check the validity of the classifiers when the input is corrupted by noise, we add a 10dB normally distributed noise to the test data and test again. The results are also optimistic as shown in table III (the time is nearly the same as in table II).

TABLE III. TEST RESULTS FOR NOISY DATA

	Test set No.1	Test set No.2	Test set No.3
Accuracy $(\frac{\text{correct}}{\text{total}} \times 100\%)$	97.18%	97.70%	94.71%

CONCLUSION

SVM classifiers with Gaussian kernels are used to classify the number of EEG current sources, and experimental results showed great efficiency. Further study will be focus on determining the distribution of dipoles of different shapes according to the scalp potentials.

REFERENCES

[1] V. Vapnik, *The nature of statistical learning theory*. New York: Springer-Verlag, 1995.

[2] K. R. Muller, S. Mika, G. Ratsch, K. Tsuda, and B. Scholkopf, "An introdutction to kernel-based learning algorithms," *IEEE Trans. Neural Networks*, vol. 12, no. 2, pp. 181-201, March, 2001.

[3] Z. J. Koles, "Trends in EEG source localization" *Electroenceph. and clinical neurophysiol.*, vol. 106, pp. 127-137, 1995.

[4] Mingui Sun, "An efficient algorithm for computing multishell spherical volume conductor models in EEG dipole source localization," *IEEE Trans. biom. eng.*, vol. 44, no. 12, pp. 1243-1252, Dec. 1997.

Real Field Simulating and Passive Shimming of a Permanent magnet for MRI

Xie Dexin, Sun Xianjing, *Xia Pingchou,Yao Yingying

School of Electrical Engineering, Shenyang University of Technology
Shenyang, Liaoning 110023, P.R.CHINA E-mail: xiebaiy@mail.sy.ln.cn
*Electrical Engineering Institute of Chinese Academy Science, Beijing 100080

Abstract **– A method of shape optimization combined with finite element analysis is applied to simulate the real magnetic field with deviation in a permanent magnet for magnetic resonance imaging (MRI) device. Based on the real field the passive shimming is carried out to elevate the homogeneity of the field in a large imaging space. With the improved genetic algorithm and Hook-Jeeves method as the searching tools, the size and locations of the ferromagnetic shimming pieces could be readily determined, and the high uniformity of the magnetic field is approached using the method proposed in this paper.**

INTRODUCTION

The main magnet is the primary part in magnetic resonance imaging devices. It is required that the homogeneity of the magnetic field created by the magnet should be high up to the order of 10^{-5}-10^{-6} in a large imaging space. Although an ideal design of the magnet can reach such a high target, the homogeneity is reduced by the manufacturing deviation. Therefore the active and passive shimming are needed to increase the uniformity of the field [1,2]. Most of the papers published used analytical methods to implement the shimming, in which the magnetic field in the imaging space is decomposed into spacial harmonics of spherical coordinate at first, then the shimming pieces are placed in proper locations to cancel the deviation of the field. This is a repetitive process of testing and attempting.

This paper presents a new method which is based on numerical analysis of the magnetic field and optimization strategy, that is, applying the technique of shape optimization developed in computational electromagnetics during recent years to the passive shimming of the permanent main magnet of MRI. With this method, the locations, size and numbers of the shimming pieces could be determined rapidly and the shimming time be reduced significantly.

DESCRIPTION OF THE METHOD

Figure 1 is a model of a permanent MRI magnet. The distribution of the ideal magnetic field created by the magnet is shown in figure 2.

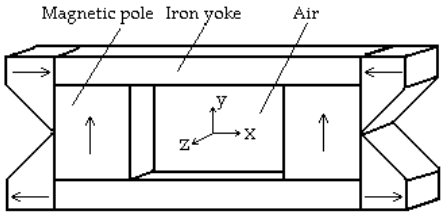

Fig.1 Configuration of the permanent MRI magnet

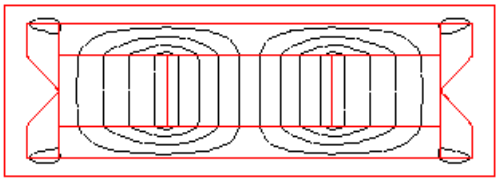

Fig. 2 Ideal magnetic field distribution of the magnet

A. Simulation of the real field

Different from the analytical method aiming at the deviated field obtained by measurement, the method of numerical optimization for shimming has to start with the real whole field with the deviation. Therefore, we should simulate the real magnetic field produced by the magnet corresponding to the measured values at first.

The simulation could be done as follows. Based on the configuration of the main magnet shown in Fig. 1, place small cavities and pieces of iron at the proper locations around the imaging region to simulate the defects of the configuration sizes or material characteristics resulting from manufacturing. With the finite element analysis as the tool of optimal target evaluation and the optimization method described in the next section as the searching tool, the simulation of the real field is implemented. When the criterion given as

$$\left|B_n' - B_n\right| \le \varepsilon_1 \qquad (n = 1, 2, \cdots, m) \qquad (1)$$

is satisfied, it is considered the distribution of the simulated magnetic field in the imaging region is close to the real

field (see Fig.3). In (1) B_n stands for the flux density at the measured point n in the real field, B_n' for the flux density at the corresponding point in the simulated field, ε_1 for the controlling tolerance, m for the number of sampling points.

It is worth noting that in general the solution of a inversion problem may not be unique. That means the simulated field with cavities and pieces of iron may not be (or almost always not be) the solution of the whole real-field, but it could be very close to the real field within the given region of interest, so that this un-uniqueness does not affect the correct determination of the size and locations of shimming pieces.

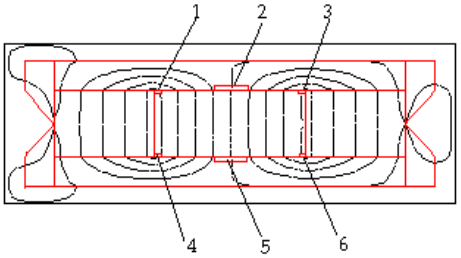

Fig. 3 Distribution of the simulated magnetic field
(1, 3, 4, 6 — Small piece of iron; 2, 5, — Small cavity)

B. *Implementation of the passive shimming*

To compensate the field distortion the small shimming pieces of iron are placed in proper locations. The feasible region of the locations could be determined by experts' experience. In general, the bigger pieces put in the middle of working region at the surface of the wall will "converge the flux lines"; while the little ones put around the working region at the wall surface could "make the flux lines flat".

The shimming process to accomplish the compensation is similar with the method mentioned in section A, whereas the starting point is the simulated field shown in Fig. 2 instead of the field produced by the ideal configuration of the magnet.

The criterion for the satisfied result of the passive shimming is given by

$$\frac{|B_n'' - B_0|}{B_0} \le \varepsilon_2 \qquad (2)$$

where B_n'' is the flux density in the optimized field at the position corresponding to the measured point n in the real field; B_0 is the flux density at the center of the optimized field and ε_2 is the controlling tolerance for homogeneity. Fig. 4 shows the flux lines of the magnetic field after shimming.

C. *Selection of the optimization method*

An improved genetic algorithms combined with the

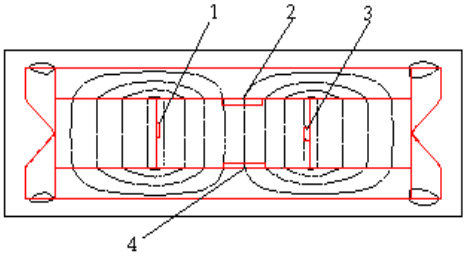

Fig. 4 Distribution of the magnetic field after shimming
(1, 2, 3, 4 — Shimming region)

determined searching of Hook-Jeeves method is developed as the optimization strategy. Different from the ordinary operations, i.e. reproduction, crossover and mutation, of conventional genetic algorithms, the alternating between the fixed probabilities of crossover and mutation and the self-adapting probabilities[3] integrated with the individual protection tactics are adopted, which speeds up the convergence considerably.

NUMERICAL RESULTS

In the example described in this paper, the inhomogeneity of the magnetic field in the region of interest is up to 66.7 ppm. It is reduced to 39.0 ppm after the numerical optimization and shimming.

CONCLUSIONS

A numerical shape optimization method with finite element analysis is applied to the compensation of the magnetic field distortion of a permanent MRI magnet caused by manufacture tolerance. Based on the simulation of the real field and the improved genetic algorithms combined with Hooke-Jeeves search the proper size, positions and numbers of the shimming pieces can be indicated, which is helpful for the implementation of the compensation.

REFERENCE

[1] Mark D.Bird et al, "Progress Towards 1 ppm at 25 T," IEEE Trans.Magn.,vol.10,no.1,pp.443-446,2000.

[2] Pavel Konzbul et al, "Design of Matrix Shim Coils System for Nuclear Magnetic Resonance," IEEE Trans.Magn,vol.36,no.4, 2000, pp.1732-1735,2000.

[3] J.A.Vasconcelos et al, "Improvements in Genetic Algorithms for Global Optimization of Electromagnetic Problems," IEEE Trans.Magn.,vol.37,no.5,pp.3579-3583, 2001.

Novel Multi-dipole Searching Technique for MEG Source Localization

Kwang-Ok An*, Chang-Hwan Im*, Hyun-Kyo Jung*, Hyuk-Chan Kwon**, and Yong-Ho Lee**
*School of Electrical Engineering, Seoul National University, San 56-1, Shillim-dong, Kwanak-gu, Seoul, 151-742, KOREA
** Korea Research Institute of Standards and Science, P.O. Box 102, Yuseong, Daejeon, 305-600, KOREA
e-mail : anko97@elecmech.snu.ac.kr

***Abstract*— A novel multi-dipole searching technique using moving dipole concept is proposed for magnetoencephalography (MEG) source localization. Since the number of dipoles needs not to be given *a priori*, the proposed method can be a promising method to resolve the critical disadvantage of the conventional equivalent current dipole methods. From some simulation results, the accuracy and effectiveness of the method are verified.**

INTRODUCTION

Functional localization of the human brain have attracted much interest recently for many researchers. Nowadays, to reconstruct the brain electric sources, measurements of magnetic fields outside the head is frequently used instead of the conventional electrical potential measurements. Usually, such a process is called magnetoencephalography (MEG) source localization. Among the various localization methods, the equivalent current dipole (ECD) method is widely used because it is not only very easy to apply but also very accurate for most of problems. The ECD method assumes dipolar current sources to approximate the electrical current in a small brain area. The spatial parameters of dipoles are then determined by using some optimization algorithms [1].

However, the ECD has a critical limitation that the number of current dipoles should be given *a priori*. Generally, the number of dipoles is assumed according to the number of stimuli. However, when no stimulus is given or when multiple stimuli are delivered simultaneously as a higher-order cognitive process, it is impossible to estimate the number of dipoles in advance.

In this paper, a novel technique is proposed to solve this problem. To begin with, numerous dipoles are randomly dispersed in a source space. Then, during the optimization process, some dipoles are eliminated or merged into other dipoles. Design sensitivity analysis with steepest decent update scheme is used for the optimization. Through the processes, exact dipole parameters can be obtained without any prior information on the number of dipoles. From some simulation results, the usefulness and effectiveness of the method will be verified.

MEG SOURCE LOCALIZATION

A. An MEG System

The human head was modelled as a homogeneous conducting sphere. This assumption is usually acceptable except for some special cases. The magnetic field due to the brain electric activity was measured by superconducting quantum interference device (SQUID) systems. The SQUID system used for the simulation is shown in Fig. 1. The 87 hemispherical sensors can measure the radial component of magnetic fields outside the brain. The distance between the sensors and the head surface was assumed to be 25 mm.

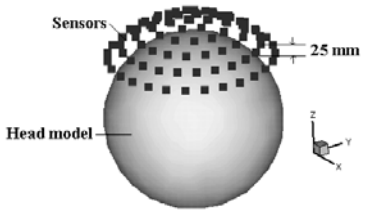

Fig. 1. Structure of sensors and head model.

B. Forward Solutions

For the given head model, volume conductor effects can be expressed as an analytic formula. The magnetic field measured at sensor positions can be calculated by using Sarvas's formula [2].

C. Proposed Algorithm

To realize the proposed method, a lot of dipoles should be handled simultaneously. Therefore, the sensitivity analysis, which is a kind of deterministic algorithm, was adopted for this study [3]. The proposed optimization procedure is as follows:

Step1: *m* dipoles are generated randomly in a source space. To prevent dipoles from converging to a local optimum at the initial stage, dipoles were generated at a constant distance.

Step2: The objective function for sensitivity analysis is defined as

$$\boldsymbol{OF} = \sum_{i=1}^{n} (\boldsymbol{B}_{fi} - \boldsymbol{B}_{ci})^2 \qquad (1)$$

where, B_{ci} represents the calculated magnetic flux density and B_{fi} the forward one with 20-dB Gaussian noise. Design variables of a dipole consist of position vectors (x_Q, y_Q, z_Q) and dipole vectors (Q_x, Q_y, Q_z). For each iteration, design

sensitivities of the the design variables were calculated. The sensivity can be expressed as

$$\boldsymbol{sen} = \sum_{i=1}^{n} 2(\boldsymbol{B}_{ci} - \boldsymbol{B}_{fi})(\boldsymbol{B}_{ci})' \,. \qquad (2)$$

Step3: The number and parameters of dipoles were determined on the basis of calculated sensitivities, using steepest decent updating scheme [4]. If a distance between adjacent dipoles is shorter than a criterion value (20 mm), they were considered as a single dipole. Meanwhile, if the amplitude of a dipole is smaller than a predetermined value (70 % of maximum value), the dipole was eliminated.

Step 4: From the results of *Step3*, the objective function for the sensitivity analysis is recalculated with a reduced number of dipoles. The process of (*Step2 – Step3)* was repeated until a terminating condition was met.

SIMULATION RESULTS

To verify its effectiveness, the proposed method was applied to single- and multi-dipole cases. The head model was assumed to be spherically symmetric conductor with an outer radius of 90 mm. 20-dB Gaussian noise was added to the magnetic field data in the forward calculation.

Table I and II show minimum, maximum, exact, and localized values of design variables, for the single- and multi-dipole cases, respectively. Fig. 2 and Fig. 3 show the convergence process of the current dipoles. From these results, it can be seen that the proposed method can yield very accurate results effectively without any prior information on the number of dipoles.

CONCLUSION

In this paper, a novel multi-dipole searching technique using the moving dipole concept was proposed for MEG source localization. Since the number of dipoles needs not to be given *a priori*, the proposed method can be a very powerful method, compared to conventional equivalent current dipole methods. By applying it to single- and multi-dipole cases, it was shown that the method could yield an accurate solution effectively. Further details of the results will be shown in the extended version of this paper.

ACKNOWLEDGEMENT

This work was supported in part by the NRL Project of the Ministry of Science and Technology, Korea.

REFERENCE

[1] C. Wolters, "Comparing regularized and nonregularized nonlinear dipole fit methods : A study in a simulated sulcus structure," *Brain Topography*, vol. 12, no. 1, pp.3-18, 1999.

[2] J. Sarvas, "Basic mathematical and electromagnetic concepts of the biomagnetic inverse problem," *Phys. Med. Biol.,* 32(1), pp. 11-22, 1987.

[3] E. J. Haug, et al., *Design sensitivity analysis of structural systems*, NewYork: Academic Press, 1986.

[4] P. Neittaanmaki, et al., *Inverse Problems and optimal design in electricity and magnetism*, Oxford: Clarendon Press, 1996.

TABLE I. DISIGN VARIABLES FOR SINGLE DIPOLE CASE
Units : *x,y,z*- [mm], *r* – [10^{-9} Am], θ, φ - [rad]

Variables	*x*	*y*	*z*	*r*	θ	φ
Minimum	-50.0	-50.0	-50.0	0.0	0.0	0.0
Maximum	50.0	50.0	50.0	2.0	3.14	3.14
Exact	12.3	49.0	39.2	1.0	1.57	1.57
Localized	12.8	49.1	39.1	1.0	1.57	1.56

TABLE II. DISIGN VARIABLES FOR MULTI-DIPOLE CASE
Units : *x,y,z*- [mm], *r* – [10^{-9} Am], θ, φ - [rad]

	x	*y*	*z*	*r*	θ	φ
Minimum	-50.0	-50.0	40.0	0.0	0.0	0.0
Maximum	50.0	50.0	90.0	2.0	3.14	3.14
Exact 1	-20.0	4.0	72.5	1.0	1.57	1.57
Exact 2	20.0	4.0	72.5	1.0	1.57	1.57
Localized 1	-19.2	3.8	73.3	1.0	1.77	1.52
Localized 2	20.9	4.2	72.5	0.9	1.52	1.55

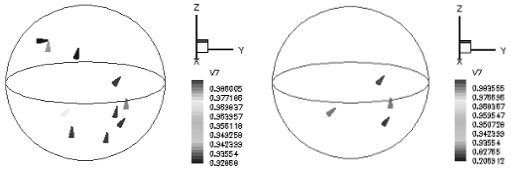

(a) Iteration 1: 10 dipoles (b) Iteration 10: 4 dipoles

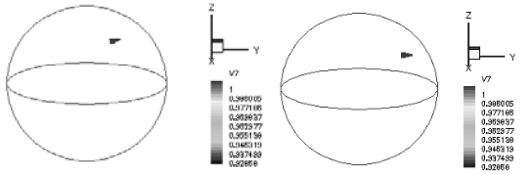

(c) Iteration 30: 1 dipole (d) Iteration 70: 1 dipole

Fig. 2. Convergence process of localized dipole sources : single-dipole case.

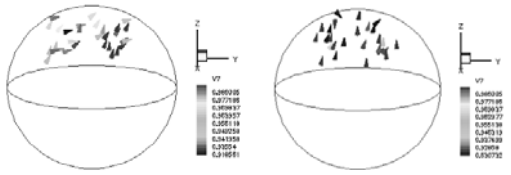

(a) Iteration 1: 30 dipoles (b) Iteration 25: 26 dipoles

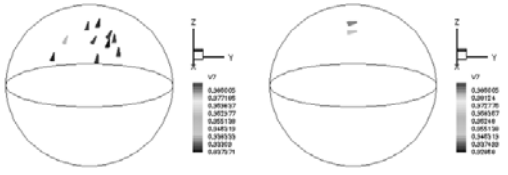

(c) Iteration 50: 10 dipoles (d) Iteration 188: 2 dipoles

Fig. 3. Convergence process of localized dipole sources : multi-dipole case.

Information content in single component versus three component cardiomagnetic fields

C. M. Arturi[1], L. Di Rienzo[1], J. Haueisen[2]

[1] Dipartimento di Elettrotecnica, Politecnico di Milano, Piazza L. da Vinci, 32, 20133 Milano, Italy
e-mail: luca.dirienzo@etec.polimi.it

[2] Biomagnetic Center, Department of Neurology, Friedrich-Schiller-University, Philosophenweg 3, 07743 Jena, Germany

***Abstract* — Magnetoencephalography (MEG) and Magnetocardiography (MCG) provide non-invasively information about the normal and pathological electrical activity in the human body. The goal of our research is the determination of the information content of different measurement setups for MEG and MCG. Here, we compare the information content in magnetic vector measurements with single component measurements. Our results indicate that both the resolution of multiple dipole solutions and the estimation of extended sources will improve with magnetic vector measurements.**

Introduction

Magnetoencephalography (MEG) and Magnetocardiography (MCG) provide non-invasively information about the normal and pathological electrical activity in the human brain and heart, a kind of information that is difficult to obtain by other methods. Especially the detection of fast transient phenomena such as cortical oscillations and spread of excitation in the human heart require these techniques.

Because of the extremely low magnitude of biomagnetic signals, their feasible detection is possible only by means of very sensitive superconducting quantum interference devices (SQUIDs). Commonly, multi-channel SQUID-systems detect only one single component of the magnetic field at the locations of the sensors. Recently, multi-channel SQUID systems capable of measuring the three components of biomagnetic fields have been proposed [1-3]. But only a few preliminary studies about the information gain passing from mono-dimensional to three-dimensional measurement systems have been carried out.

The main goal of our research is the determination of the information content of different measurement setups for MEG and MCG. In this paper, we compare numerical simulations of three-component and one-component cardiomagnetic fields based on realistic patient geometries.

Methods

The magnetic fields due to a set of current dipoles in a realistic piecewise homogeneous and isotropic volume conductor was computed using the boundary element method with linear potential approximation. The model was constructed out of a T1 weighted MRI data set of the torso of a healthy volunteer. The model consisted of five compartments (torso boundary, two lung boundaries, heart and ventricular blood mass boundaries). A homogeneous conductivity of 0.2 S/m, 0.04 S/m and 0.6 S/m (torso boundary, two lung boundaries and two ventricular mass boundaries) was assumed.

We modeled the QRS interval of the human heart cycle with the help of 13 dipoles placed around the left ventricle (normal to its surface) representing the basal, medial and apical slice with each containing the four anatomical directions anterior, lateral, inferior and septal. The apex was represented by a separate dipole. Each dipole was fixed in direction and strength. All computations were carried out with the software ASA (ANT Software, Enschede, The Netherlands).

Fig. 1 shows the simulation setup. A sensor configuration with 64 positions was employed for the simulation of the magnetic fields [4]. At these positions the three magnetic field components were computed. For a configuration of 8x8 sensors of mono-axial sensitivity, given the 13 components of the dipoles in the heart, one can write:

$$\begin{bmatrix} B_1 \\ B_2 \\ \vdots \\ B_{64} \end{bmatrix}_{64x1} = \begin{bmatrix} L(1,1) & \cdots & L(1,39) \\ L(2,1) & & L(2,39) \\ \vdots & & \vdots \\ L(64,1) & \cdots & L(64,39) \end{bmatrix}_{64x39} \begin{bmatrix} p_{1x} \\ p_{1y} \\ p_{1z} \\ \vdots \\ p_{13z} \end{bmatrix}_{39x1} \qquad (1)$$

where $L(i,j)$ is the lead-field (kernel) matrix.

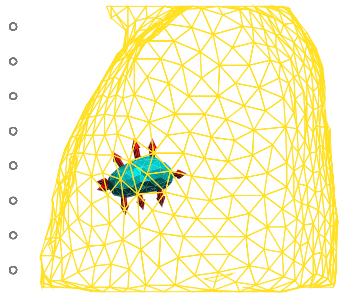

Fig. 1. Setup of the simulations with the boundary element model, the dipolar sources in the heart, the left ventricular blood mass, and the position of the magnetic field sensors (left side view).

Composing the 3 lead field matrices of the single component measurement systems the lead field matrix for the configuration of three component sensors can be obtained.

Results and Discussion

Figures 2-4 show the respective maps of the computed x, y and z components of the magnetic field when only one dipole is active (dipole strength 1 μAm). Please note the different scaling of the magnetic fields in Fig. 2-4. Since the dipole in this example is oriented mainly into z-direction, the sensors in this direction (Fig. 4) exhibit the smallest magnetic field strength.

Information content of a sensor configuration can be related to the singular values of the lead field matrix, by means of the singular value decomposition (SVD, [5]). The more zero or nearly zero singular values characterize the matrix, the less information is contained in the corresponding sensor array. As it can be noted from Fig. 5, the singular values of the lead field matrix of the 3-D measurement system are higher than those of any of the three 1-D systems. The condition numbers for the lead field matrices are $1.4*10^5$, $9.3*10^4$, $1.9*10^5$, and $5.3*10^3$ (x-, y-, z-direction, and all three directions).

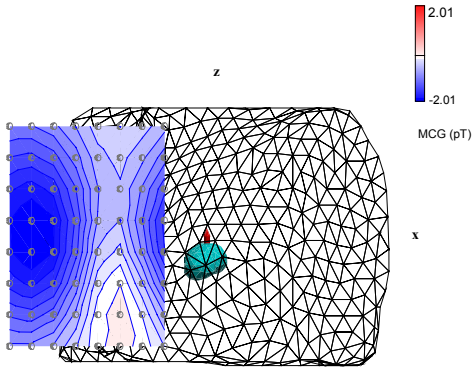

Fig. 2. Computed magnetic field map (x-direction sensors, left anterior view).

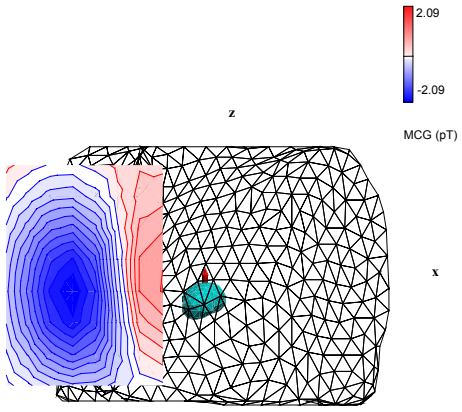

Fig. 3. Computed magnetic field map (y-direction sensors).

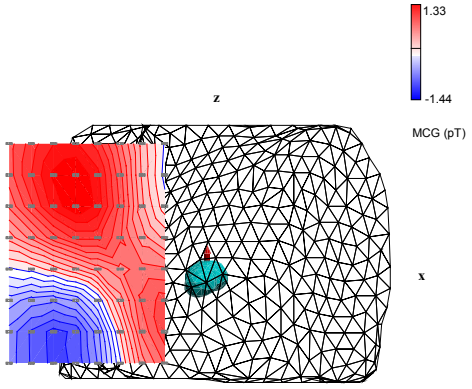

Fig. 4. Computed magnetic field map (z-direction sensors).

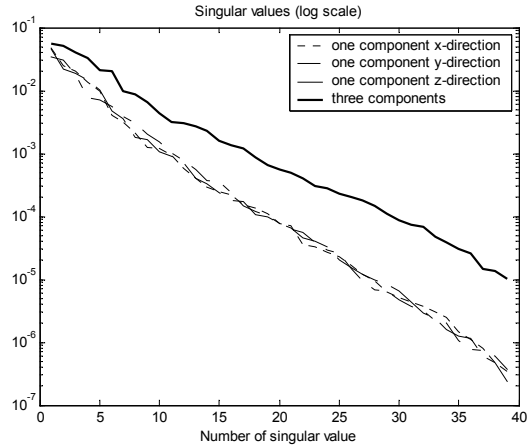

Fig. 5. Singular values of the lead field matrix for the case of one component and three components measurements.

In this paper we presented numerical forward simulations only. In conclusion, based on these simulations we believe that the measurement of all three components of the magnetic field will provide superior performance in the localization of multiple and extended cardiomagnetic sources. Current research focuses on the quantification of the expected gain with the help of inverse computations.

References

[1] K. Kobayashi and Y. Uchikawa, "Estimation of multiple sources using a three-dimensional vector measurement of a magnetoencephalogram", J. Appl. Phys., vol. 83, pp. 6462-6464, 1998.

[2] K. Kobayashi and Y. Uchikawa, "Development of a three-dimensional biomagnetic measurement system with 39-channel SQUIDs", in Recent Advances in Biomagnetism, Eds, Japan: Tokou University Press, 1999.

[3] K. Kobayashi and Y. Uchikawa, "Estimation of multiple sources using spatio-temporal data on a three-dimensional measurement of MEG", IEEE Trans. Magnetics, vol. 37, No. 4, pp. 2915-2917, 2001.

[4] J. Haueisen, J. Schreiber, H. Brauer, T.R. Knösche, "The Dependence of the Inverse Solution Accuracy in Magnetocardiography on the Boundary Element Discretization," *IEEE Transactions on Magnetics*, vol. 38, pp. 1045 – 1048, 2002.

[5] W. H. Press, S. A. Teukolsky, W. T. Vetterling, B. P. Flannery, in *Numerical Recipies in C: The Art of Scientific Computing,* 2nd ed. New York: Cambridge Univ. Press, 1992.

The Electrical Properties of Real Head Model Based on Electrical Impedance Tomography (EIT)

Guizhi Xu, Qingxin Yang, Ying Li, Qing Wu and Weili Yan
Hebei University of Technology, Tianjin, 300130, China,
E-mail: gzxu@hebut.edu.cn

***Abstract*--The real head models have been reconstructed from the MRI head pictures, their electrical properties have been analyzed based on EIT using FEM. The results show that surface potential distributions change with the increases and reduce of conductivity within head, and it is the biggest when the bone conductivity are changed.**

INTRODUCTION

The electrical characteristic of brain tissue is a basis for analyzing brain electrical and magnetic actives and clinical diagnosis. Information about the internal electrical properties of the head could have many medical uses, such as noninvasive monitoring of brain and blood flow, screening for brain cancer and epilepsy. Electrical impedance tomograghy (EIT) is relatively new imaging modality that produces images by computing electrical conductivity within the object [1], [2]. During the research and development, a number of clinical investigations have been undertaken and several possible applications have been identified in which useful physiological information may be obtained. But, there are many problems for head EIT at present. In order to map the electric properties inside the brain, our group constructed real head numerical models from MRI pictures [3], gave the complete mathematical EIT model, analyzed their electrical properties, and built an 16 electrode EIT system[1].

THE MATHEMATICAL MODEL FOR EIT

The underlying relationships that govern the interaction of electricity and magnetism are summarized by Maxwell's equations. For the case of EIT, several simplifying assumptions can be applied to reduce the complexity of the problem. Mathematically, the known quantities are the voltages and currents at certain points on the body, the unknown is the impedivity or resistivity within the body. At low frequencies, these quantities are related by the equation

$$\nabla \cdot \gamma(x,\omega)\nabla u = 0 \qquad (1)$$

Here is appoint in Ω, u is the electric potential or voltage, and the admittivity γ is given by $\gamma(x,\omega) = \sigma(x,\omega) + i\omega\varepsilon(x,\omega)$, where σ is the electric conductivity, ε is the admittivity, and ω is the angular frequency of the applied current.

In practice, we apply currents to electrodes on the surface $\partial\Omega$ of the body. There currents produce a current density on the surface whose inward pointing normal component is denoted by j. Thus

$$\gamma \frac{\partial u}{\partial v} = j \quad \text{on } \partial\Omega \qquad (2)$$

The model for EIT is (1) and (2), together with the conservation of charge condition

$$\int_{\partial\Omega} j = 0 \text{ and the condition } \int_{\partial\Omega} u = 0 \square$$

which amounts to choosing a "ground" or reference voltage. Unfortunately, the model is a poor model for experiments because we do not know the current density j. In practice, we known only the currents that are sent down wires attached to discrete electrodes, which in turn are attached to the body. We need to account for two main effects: the discreteness of the electrodes, and the extra conductive material (the electrodes themselves) we have added. The integral of the current density over the electrode is equal to current that flows to that electrode. Thus we have

$$\int_{el} \gamma \frac{\partial u}{\partial v} ds = I_l, \quad l = 1,2,...,L \qquad (3)$$

Where I_l is the current sent to the lth electrode and e_l denotes the part of $\partial\Omega$ that corresponds to the lth electrode. This is combined with

$$\gamma \frac{\partial u}{\partial v} = 0 \quad \text{in the gaps between electrodes.} \qquad (4)$$

$$u + z_l \gamma \frac{\partial u}{\partial v} = V_l \qquad \text{on } e_l,\ l=1,2,L \qquad (5)$$

Here, a number z_l denotes the impedance of the layer between electrode and body, which we call surface impedance. V_l denotes the imposed constraints.

The complete model consists of (1), (2), (3), (4), and (5), together with the conditions

[1]This work is supported by the National Nature Science Foundation of China (59937160) and the Natural Science Foundation of Hebei Province (501037)

$$\sum_{l=1}^{L} I_l = 0 \quad \text{, and} \quad \sum_{l=1}^{L} V_l = 0 \,.$$

The numerical methods such as the finite element method (FEM), the boundary element method (BEM), and some others can solve the equations above.

THE REAL HEAD MODEL RECONSTRUCTION AND ELECTRICAL PROPERTY ANALYSIS

2D axial and sagittal real head models from MRI pictures have been reconstructed using image process and reconstruction technique, and the FEM mesh and equi-potential line distributions in opposite drive pattern are shown in Fig.1. Here, each layer conductivity from inside to outside are 0.33 s/m (brain)□1.0 s/m (CSF: Cerebra-spinal fluid)□0.0042 s/m (bone) and 0.33 s/m (scalp).

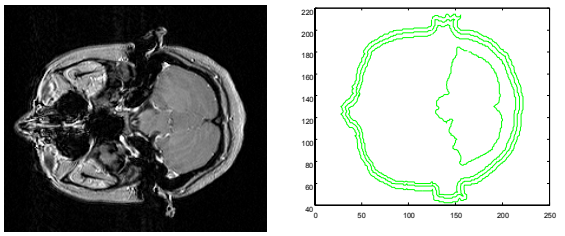

(a) (b)

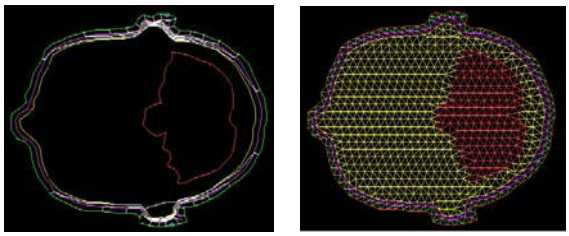

(c) (d)

Fig.1. (a) 2D axis MRI head picture. (b) The head model construction. (c) FEM mesh . (d) Equi-potential line in opposite drive pattern

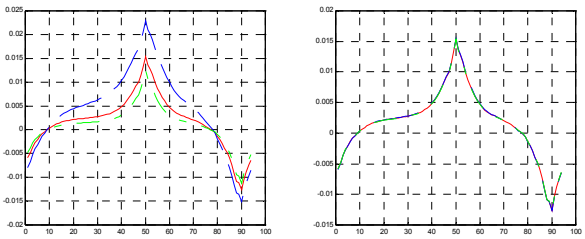

(a) (b)

Fig.2. Surface potential distribution. (a) Bone conductivity is changed. (b) Brain conductivity is changed. (Real line--normal, dot-and-dash line--reduce 50%, dotted line--increase 50%).

Different tissues have different conductivities, and the electrical properties vary with a physiological and pathological change. From Fig.2, we can see that the surface potential distributions vary with bone and brain conductivity changes, and it is the biggest that bone conductivity changes.

THE 16 ELECTRODES EIT SYSTEM

This system for EIT is designed, which can reconstruct and display approximate pictures of the electric conductivity inside body using the back-projection method by measuring the surface voltages of body, as shown in Fig.3. The data collection, process and imaging reconstructions are done by a computer. It is stable, real time, convenient and extended.

(a) (b)

Fig.3. (a) 16electrodes EIT system (b) impedance imaging is reconstructed by computer.

CONCLUSIONS

In this paper, many works, such as real head model reconstruction, their electrical property analysis, and the hardware build, have been done for studying the head EIT. The results are satisfied, which are good basis for our next work to study head impedance image reconstruction.

REFERENCES

[1] K.Boone, D.Barber, et al., "Review Imaging with Electricity: Report of the European Concerted Action on Impedance Tomography", Journal of Medical Engineering & Technology, Vol.21, No.6, pp.201-232, Nov./Dec., 1997

[2] H.R.Gamba, D.T.Delpy. "Measurement of Electrical Current Density Distribution within the Tissues of the Head by Magnetic Resonance Imaging", Medical & Biological Engineering & Computing, pp.164-170, March, 1998

[3] Shijuan He, Xueqin Shen, et al., "Research on MRI Brain Segmentation Algorithm with the Application in Model-Based EEG/MEG.IEEE", Trans. Magn., vol.37, no.5, pp.3741-3744, 2001.

Numerical Simulation of Electric and Magnetic Brain Stimulation

Jacek Starzyński, Bartosz Sawicki, Robert Szmurło, Stanisław Wincenciak,
Chair of the Theory of Electrical Engineering, Warsaw University of Technology,
ul. Koszykowa 75, 00-661 Warsaw, Poland,
e-mail: *jstar@iem.pw.edu.pl*

Andrzej Krawczyk,
Institute of Electrical Engineering,
ul. Pożaryskiego 28, 04-703 Warszawa, Poland,
e-mail: *krawczyk@iel.waw.pl*

Tomasz Zyss
Collegium Medicum, Jagiellonian University,
ul. Kopernika 21a, 31-501 Kraków, Poland,
e-mail: *mzzyss@cyf-kr.edu.pl*

***Abstract*— The paper presents comparison of the electric (ECT) and magnetic (TMS) stimulation of the brain with low-frequency magnetic field.**

Numerical models used in both cases are briefly shown. ECT and TMS finite element models use the same, realistic grid created on the basis of NMR scans of the head. Model of the electric field is simple (brain tissue is assumed to be a passive medium) yet exact—it was compared with results of measurements. The model of magnetic field is based on the $\vec{T}$-Ω formulation, that, by the low electric conductivity and constant magnetic permeability of the human tissue, allows us to build finite element model of the head only.

INTRODUCTION

The transcranial magnetic stimulation (TMS) has been thought as a tool in psychiatric treatment, especially in treating endogenous deep depression. TMS is expected to replace (at least to some extent) the electro-convulsive treatment (ECT). The key-point in the stimulation process is to ensure that the effect of the eddy currents evoked in the brain will meet therapeutical expectations. Thus, it is necessary to design such a TMS system, which will be able to evoke eddy currents similar to those during ECT.

To avoid human experiments, which are troublesome from various points of view, the attempts have been made to employ the numerical modelling in order to evaluate the current that flows throughout the brain tissues and to predict the system parameters. The effective calculation of the field in the region of interest (cerebral cortex of the human head) is the crucial point of simulation.

MODEL OF THE HEAD USED FOR SIMULATIONS

The previous works the authors have shown that the reliable computer simulation should use a very exact model of human head [1, 2]. Use of $\vec{T}$-Ω formulation presented at Compumag in Evian [3] allows us to restrict the model of the magnetic field to the head only and thus both ECT and TMS can be simulated with the same accuracy.

FIELD CALCULATION

Nature of therapeutic effect of the electromagnetic brain stimulation is quite complicated. Current flowing through the tissue stimulates neurons up to the artificially generated self-sustaining after-discharge (SSAD) – convulsive attack which is believed to be necessary for therapy of depression.

Fig. 1. The ideas of ECT (left) versus TMS (right): in ECT two metallic electrodes are placed on the skin and head is subjected to voltage pulses up to several hundreds volts; in TMS a coil operating in pulse mode is placed close to the head.

In present simulations we do not model the SSAD, but we would like to calculate the current distribution in the head (especially in the brain tissue) just before the convulsive attack. Therefore we consider brain as a "passive" medium, characterized only by its electrical parameters: magnetic permeability μ_0, electric permeability $\varepsilon \approx 1000\varepsilon_0$ and electric conductivity γ that does not exceed 1 S/m [4].

The signals used in stimulation of human brain in both cases, ECT and TMS are not sinusoidal. Harmonic analysis shows that the pulse signal has spectrum in extremely low frequency field (ELF)–up to 20 kHz. Because the material coefficients of the tissue are linear (for low frequencies) and because the skin effect is very weak, we can use Fourier expansion of the stimulus and solve several time-harmonic field problems. This saves a lot of computation time. Further we write all equations for complex fields.

Electric field

Mathematical model of flowing current electric field is well known, simple Laplace equation:

$$\nabla \cdot (\gamma + j\omega\varepsilon)\nabla V = 0 \tag{1}$$

Dirichlet boundary conditions are set on electrodes and natural Neumann condition on the rest of external surface. Numerical stability of Laplace equation is high, so results can be obtained fast even for such complicated model.

Due to extremely low frequency and low electric permeability ε, displacement current can be ignored and current density distribution can be expressed as

$$-\gamma \nabla V = \vec{J} \tag{2}$$

Magnetic field

To avoid adding extra FE grid in the space surrounding head and coil and due to difficulties with establishing boundary condition we prefer $\vec{T}$-Ω formulation over description with magnetic vector potential $\vec{A}$. Creation of $\vec{T}$-Ω based model allow us to cover with FE mesh only the head.

We assume that magnetic permeability of the tissue is constant, so considering magnetic field in the head placed in an external magnetic field $\vec{H}_s$ we can write:

$$\vec{H} = \vec{H}_s + \vec{T} - \nabla\Omega, \tag{3}$$

where $\vec{T}$ and $\nabla\Omega$ represent field induced in the tissue.

Using Maxwell equations for harmonic fields in homogenous, diamagnetic material and definition $\vec{J} = \nabla \times \vec{T}$, we can form partial differential equation for $\vec{T}$. To get unambiguous result and improved conditioning of global algebraic equations system (FEM) we use Coulomb gauging [6, 5]. The final equation is:

$$\nabla \times \frac{1}{\gamma} \nabla \times \vec{T} - \nabla(\frac{1}{\gamma} \nabla \cdot \vec{T}) + j\omega\mu_0 \vec{T} = -j\omega\mu_0 \vec{H}_s. \tag{4}$$

Coulomb gauging assure that divergence of vector $\vec{T}$ is equal zero.

On external surface of conducting area (skin) there are only tangential components of eddy currents. This means that vector $\vec{T}$ has only normal component, $\vec{T} \times \vec{n} = 0$. On boundary between the low conducting area and air we need to assure:

$$J_n = 0, \text{ and } \nabla \cdot \vec{T} = 0, \tag{5}$$

where J_n is normal component of the current density.

Algorithm of calculations for $\vec{T}$-Ω and boundary conditions used on the head surface have been discussed in authors' previous works [3].

Comparison of ECT and TMS

Experiments presented here were aimed on design of the coil which can excite eddy currents of similar density to those during ECT.

The results of calculation of the eddy currents evoked in the human head by coil placed near to the right temple (TMS) and current distribution from electrodes (ECT), as shown on Fig. 1, are shown on Fig. 2. In both cases the head horizontal cross-sections are presented.

Currents induced in brain by magnetic field are much stronger than one forced by voltage connected to the electrodes. Additionally TMS allows one to focus stimulation to desired region of the brain, so therapy can be more precise and side effects reduced.

Detailed analysis of results will be included in full, four page paper.

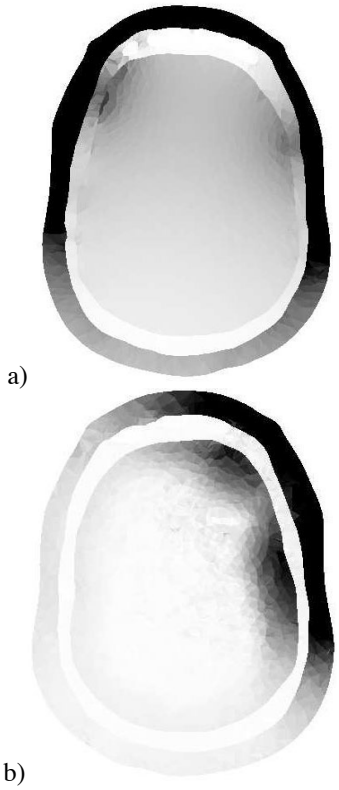

Fig. 2. Eddy currents density evoked by a) ECT and b) TMS

Conclusion

The numerical simulations allow us to calculate eddy currents induced in human brain during ECT and TMS. To the authors' knowledge it is not possible to verify local values of current density, but ECT model was verified by comparison of global quantities (as total electrode current). The TMS model was validated by calculations of eddy currents evoked in object of simple shape placed in homogeneous field [3].

Basing on results of simulations we believe that TMS can replace ECT for treating deep depression. The TMS should allow even better, more precise stimulation.

References

[1] J. Starzyński, A. Krawczyk, R. Sikora, T. Zyss. Optimal Design of the Transcranial Magnetic Stimulation System, *International Symposium on Nonlinear Electromagnetics, ISEM '99*, Pavia, May, 1999.

[2] J. Starzyński, B. Sawicki, A. Krawczyk, T. Zyss. CSG model of the human head for ECT simulation. *COMPEL, The International Journal for Computation and Mathematics in Electrical and Electronic Engineering*, vol. 19, no. 2, 2000.

[3] J. Starzyński, B. Sawicki, S. Wincenciak, A. Krawczyk, T. Zyss: *Simulation of Magnetic Stimulation of the Brain*, *IEEE Transactions on Magnetics*, vol. 38, No. 2, March 2002

[4] S. Rush and D.A. Driscoll. Current distribution in the brain from surface electrodes. *Anesth. Analog*, 47(6):717–723, Nov-Dec 1968.

[5] K. Preis, O. Bíró and I. Ticar. Gauged Current Vector Potential and Reentrant Cornes in the FEM Analysis of 3D Eddy Currents. *IEEE Transactions on Magnetics*, 36(4):840–843, July 2000.

[6] O. Bíró and K. Preis. On the use of the magnetic vector potential in the finite element analysis of three-dimensional eddy currents. *IEEE Transactions on Magnetics*, 25(4):3145–3159, July 1989.

Spatiotemporal Source Imaging of Brain Magnetic Fields Associated with Short-term Memory by Linear and Nonlinear Optimization Methods

Seiji Nakagawa[1*], Toshiaki Imada[2], Shoogo Ueno[3] and Mitsuo Tonoike[1]

[1]Life Electronics Lab, National Institute of Advanced Industrial Science and Technology (AIST), 1-8-31 Midorigaoka, Ikeda, Osaka 563-8577, Japan; [2]Ctr. for Mind, Brain & Learning, Univ. of Washington, 368 Old Fisheries, Seattle, WA 98195-7988, USA; [3]Dept. of Biomedical Eng., Univ. of Tokyo, 7-3-1 Hongo, Bunkyo-ku, Tokyo 113-0033, Japan. *s-nakagawa@aist.go.jp

***Abstract* - In biomagnetic inverse problem, it is important to select optimal method, especially in the case of estimating internal electrical sources for higher functions with poor information about their source profile. In this study, internal sources of brain magnetic fields associated with short-term memory processes were estimated by (1) nonlinear parameter optimization method using multi dipole model, and (2) linear optimization method using L1 minimum norm estimation (L1-MNE) technique. Both methods showed internal sources in the inferior part of the occipital lobe, the supramarginal gyrus and the angular gyrus, and the inferior frontal gyrus. This result indicate the reliability and availability of these methods for brain magnetic data associated with higher brain function.**

INTRODUCTION

The measurement of brain magnetic fields outside of the head (MEG: magnetoencephalography) is effective for imaging of the brain functions in human subjects since it is a completely non-invasive technique, which detects direct neural activity in the brain with temporal resolutions better than 1 ms. The ill-posedness of MEG inverse problem, estimation of the internal electrical source distribution in the human brain from surface measurements of MEG, requires some simple modelings of the neural current profile, e.g., a small number of equivalent current dipoles (ECDs), which assume few localized current sources [1]. Single ECD model has been used to estimate the source locations of magnetic fields with relatively simple patterns, such as evoked fields generated from the primary auditory or somatosensory cortex [1]. However, source estimation using a small number of ECD model is problematic when the source current distribution is not localized, when many brain regions are activated simultaneously, or when a priori knowledge about generator profile is poor.

Many methods have been proposed to overcome this difficulty. Imada et al. [2, 3] and Nakagawa et al.[4] proposed a nonlinear parameter optimization method using multi-dipole model. Matsuura et al. [5] and Uutela et al. [6] proposed one of linear optimization methods, L1-minimum norm estimation (L1-MNE) technique. In this study, internal electrical sources associated with short-term memory processes were estimated by these entirely different two methods, (1) nonlinear parameter optimization method using multi dipole model and (2) linear optimization method using L1-MNE technique, in order to evaluate their reliability and availability with measured magnetic data associated with higher brain function with poor a priori information.

METHODS

Source Analysis

(1) *Nonlinear parameter optimization method using multi dipole model* [2-4]: The localization of ECDs was based on the spherical conductor model, which takes into account the volume current within the sphere. The radius and the center of the sphere were determined by fitting a sphere onto the surface points of the cortex. We determined the active brain areas by first localizing single ECDs in various local regions of a spherical head model using simplex-method [1]. Among the calculated ECDs, those having a goodness-of-fit > 80% and with a 95%-confidence volume < 268 mm^3 [4] (corresponding to the volume of a 4 mm radius sphere), were selected.

(2) *Linear optimization method using L1-MNE technique* [5, 6]: The calculation was based on real-head-shape model obtained from magnetic resonance images (MRIs) of each subject. About 10,000 dipoles were set at each grid position in the head model. Sources were explained with the smallest sum of absolute dipole amplitudes (minimum L1-norm).

For both methods, the source location was registered in each subject's MRIs.

MEG Recordings

Recordings of event-related magnetic fields were carried out in a magnetically shielded room using a 122-channel whole-head neuromagnetometer (Neuromag-122™; Neuromag Ltd., Finland). The visual stimuli were delivered from a LCD projector, located outside the shielded room, through an optical fiber bundle. The vertical electrooculogram (EOG) was recorded with subjects' infra- and supraorbital electrodes to monitor artifacts from eye blinks and eye movements. The magnetic data were sampled at 0.5 kHz after band-pass-filtered between 0.03 Hz and 100 Hz. Any epoch coinciding with magnetic signals exceeding 3,000 fT/cm and/or a vertical EOG deflections beyond 150 μV were rejected from further analysis. The average of more than 100 correct trials were digitally low-pass-filtered at 40 Hz. The average of 0.2 s pre-Sample period served as the baseline.

Tasks, Stimuli, and Subjects

Fig. 1 shows a schematic illustration of a stimulus sequence, in a delayed paired comparison task. Each trial

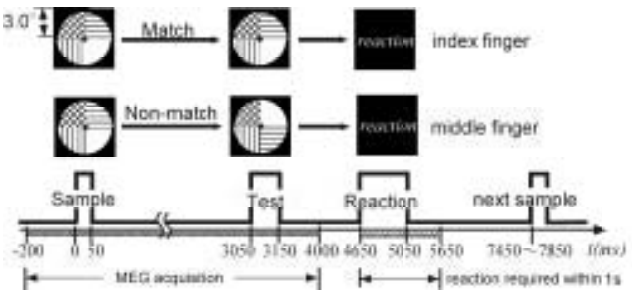

Fig. 1. Schematic illustration of a stimulus sequence.

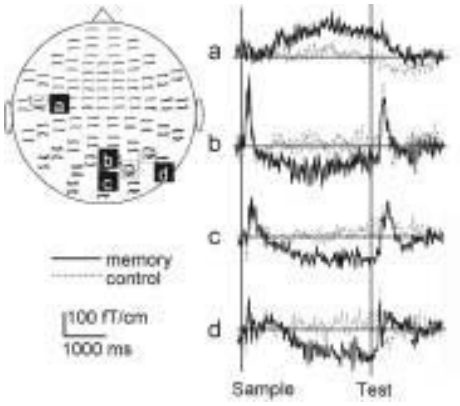

Fig. 2 Magnetic wave forms, in the channels which show the extremely low frequency components during the memory condition (subject S1). Vertical lines denote the Sample and the Test onset.

	Left Hemisphere							Right Hemisphere				
	S1	S2	S3	S4	S5	S6	S7	S1	S2	S3	S4	S5
triangular area	○ ●		○			○	○ ●					
operculum	○ ●		○ ●			○	○ ●					
precentral gyrus				○		○ ●						
postcentral gyrus	○		○ ●		○	●						
insula												
cingulate gyrus (BA 24/33)							○ ●					
cingulate gyrus (BA 23/30)					○ ●	○ ●		○ ●	○ ●		●	○
superior temporal sulcus		○ ●					○ ●					
lateral sulcus		◎ ◉	○ ●	○ ●			○ ●			○ ●	○	○
supramarginal gyrus	○ ●	◎ ◉	◎ ◉	○ ●	○ ●	◎ ◉		○ ●	○ ●	○ ●	○ ◉	◎ ◉
angular gyrus	○ ●	○ ●	○ ●	○ ●		○ ●		○ ●	○ ●			○
fusiform gyrus	○ ●		○ ●	○ ●	◎ ◉	◎ ◉	◉	◎ ◉	○	◎ ◉		○
lingual gyrus	◎ ◉	◉	◎ ◉		◎ ◉	○ ●	○ ●	◎ ◉	◎ ◉	○ ●		○
inferior temporal gyrus				○ ●				○ ●			○ ●	
arround hippocampus						○ ●						
intraparietal sulcus								●	●			
parietooccipital sulcus								○ ●				○

TABLE I. Source locations for the extremely low frequency components, estimated by multi-dipole method (white circle) and L1-MNE technique (black circle). Double-circles denote sustained sources more than 300 ms.

consisted of a pair of circles with different colors (blue, red, green, and orange) in each quadrant. The first stimulus (Sample) was presented for 50 ms. After a constant period of 3.0 s, the second stimulus (Test) was presented for 100 ms. The subject was instructed to react immediately after the third stimulus (Mark), which was presented 1.5 s after the Test. Two experiments were performed with separate conditions; a memory condition and a control condition. In the memory condition, subjects were requested to move the index finger when the Test was identical to the Sample, and the middle finger when it was different. In the control condition, the subjects were instructed to ignore the Sample, and to alternately move the index or middle finger immediately after the Mark. Seven healthy Japanese volunteers (5 males and 2 females, 23-33 years old, all right-handed) took part in this experiment.

RESULTS

Extremely low frequency components of brain magnetic fields were observed in the temporal and/or occipital areas of all subjects for a period beginning 500 ms after the Sample onset in the memory condition. They sustained during retention period (between Sample and Test). In contrast, these components were not seen in the control condition. Sources for the low frequency components were localized in the latency between 500 and 2500 ms. Table I shows source locations of all subjects for the both multi-dipole and L1-MNE methods. In the both methods, sources were primarily localized in the vicinity of the fusiform gyrus (seven out of seven subjects in the left and/or right hemispheres), the lingual gyrus (six subjects), near the supramarginal gyrus/the angular gyrus (seven subjects), the inferior frontal gyrus (five subjects), and the posterior part of the cingulate gyrus (four subjects).

DISCUSSION

Sustained signals during retention period of short-term memory tasks were also observed in electroencephalographic recordings [7, 8]. Sources for the low frequency components were localized in the inferior part of the occipital lobe, in the vicinity of the supramarginal gyrus and the angular gyrus, and the inferior frontal gyrus. The occipital lobe widely participates in visual information processing. The activities of the angular gyrus were reported in visual pattern recognition and short-term memory [9]. It is reasonable brain regions which employ visual processing play a roll as visual-memory storage. Therefore, we considered these extremely low frequency components reflected the storage processes of the visual short-term memory.

The both nonlinear parameter optimization method using multi dipole model and linear optimization method using L1-MNE technique showed almost same source locations. This results indicate reliability and availability of these method when they are applied to magnetic data associated with higher brain function with poor information about their source profile.

REFERENCES

[1] M. S. Hämäläinen, R. Hari, R. J. Ilmoniemi, J. Knuutila, and O. V. Lounasmma, "Magnetoencephalography -theory, instrumentation, and applications to non-invasive studies of the working human brain," *Rev. Mod. Physics*, vol. 65, pp. 413-497, 1993.

[2] T. Imada, M. Kawakatsu, and M. Kotani, "Analysis of magnetic signals related to reading Japanese characters (hiragana)," *Electroenceph. Clin. Neurophysiol. Suppl.*, vol. 47, pp.199-208, 1996.

[3] T. Imada, T. Mashiko, and M. Sekine, "Estimation Errors of single dipole model applied to twin dipole activity: computer simulation study", *Biomag2000*, pp. 733-737, 2000.

[4] S. Nakagawa, S. Ueno, and T. Imada, "Measurements and Source Estimation of extremely low frequency brain magnetic fields in a short-term memory task by a whole-head neurogradiometer," *IEEE Transactions on Magnetics*, 35(5), 4130-4132, 1999.

[5] K. Matsuura, and Y. Okabe, "Selective minimum-norm solution of the biomagnetic inverse problem," IEEE Trans. Biomed. Eng., vol. 42(6), pp. 608-615, 1995.

[6] K. Uutela, M. S. Hämäläinen, E. Somersalo, "Visualization of magnetoencephalographic data using minimum current estimates, NeuroImage, vol. 10, pp. 173-180, 1999.

[7] D. S. Ruckin, R. Johnson Jr., H. Canoune, and W. Ritter, "Working memory and preparation elicit different patterns of slow wave event-related brain potentials," *Psychobiology*, vol. 32, pp. 399-410, 1990.

[8] P. Rämä, S. Carlson, J. Kekoni, and H. Hämäläinen, "A spatial oculomotor memory-task performance produces a task-related slow-shift in human electroencephalography," *Electroenceph. Clin. Neurophysiol.*, vol. 94, pp. 371-380, 1995.

[9] C. S. Carter, W. Perlstein, R. Ganguli, J. Brar, M. Mintun, and J. D. Cohen, "Functional hypofrontality and working memory dysfunction in schizophrenia," *American J. of Psychiatry*, vol. 155, pp. 285-287, 1998.

Shape Optimization of Cochlear Implant Electrode Array using Genetic Algorithms and Computational Neuroscience models

C. T. M. Choi
Department of Electrical Engineering, I-Shou University, Kaohsiung, Taiwan, ROC
California Ear Institute at Stanford, Palo Alto, CA, USA
email: c.t.choi@ieee.org

Abstract- **Finite element analysis is used to compute the current distribution of the human cochlea during cochlear implant electrical stimulation. Genetic algorithms are then applied in conjunction with computational neuroscience model and the finite element analysis to optimize the shape and dimensions of cochlear implant electrode array. The goal is to improve the focus of electrical energy delivered to the auditory nerves in the human cochlea, thus, reducing energy wasted and improve the efficiency and effectiveness of the cochlear implant system.**

Keywords: **Electrical stimulation, activating function, cochlear implant electrode, genetic algorithm, cochlear neuron, volume conduction analysis.**

I. Introduction

While cochlear implant (CI) has been widely used clinically to restore some hearing to hearing impaired patients, the functioning of cochlear implant is not well understood, i.e. variation in performance for different person. Typically, the functioning of the cochlear implant can be divided into: (1) the electrode array delivers electric current through the cochlea and (2) the generation of the auditory neural response. Due to the miniature size of the human cochlea, accurate experimental result is very difficult to obtain. An alternative approach is to study this using the computational approach. Computational modeling allows studies of electrical stimulations for the human cochlea without the measurement error so frequent in experimental sciences-the measurement interfering with the experiments. Until recently all the computation studies focus more on the potential distribution in the cochlea model [1] and did not cover the electrode design and its performance. Most studies assume point electrodes or ball electrodes as the source of stimulations, while the available electrode designs include the ball electrodes, banded electrodes, half banded electrodes, and planar electrodes [3].

In this paper, planar electrodes will be studied in terms of their potential distribution and neural response [1, 3] for a half turn human cochlea model using coupling genetic algorithm [2], finite element analysis, and activating function.

II. Method

A finite element model of the first half turn of a spiraling human cochlea used in this paper is shown in Fig. 1. This 3D cochlea model was created by extruding the 2D cochlea cross section (Figure 2) into 3D around the axis of the modiolus. The model consists of perilymph, spiral ganglion, endolymph, Reissner's membrane, basilar membrane, stria vascularis, and organ of corti. The material resistivities are taken from [1]. Volume conduction analysis using finite element method is applied to determine the potential distribution of electrical stimulated cochlea. The response of the cochlea neurons is determined by the activating function. Activating function [1, 3] is used to obtained an impression of the excitation pattern of the electrical stimulation. Activating function can be computed from the nerve fiber nodes given in Fig. 2.

The complete model (Fig. 1) is embedded into a cylinder of bone. In order to maintain an optimal shape and size for the 3D finite elements, it is determined that the thickness of the basilar membrane, Reissner's membrane, and the stria vascularis and their resistivities will be adjusted.

Planar electrodes, will be tested to compute their neural excitation profile for monopolar and bipolar stimulating modes. Results will show comparison of the potential distribution and activating function contour along the nerve fiber and the basilar membrane for the planar electrode configurations with monopolar and bipolar stimulating modes.

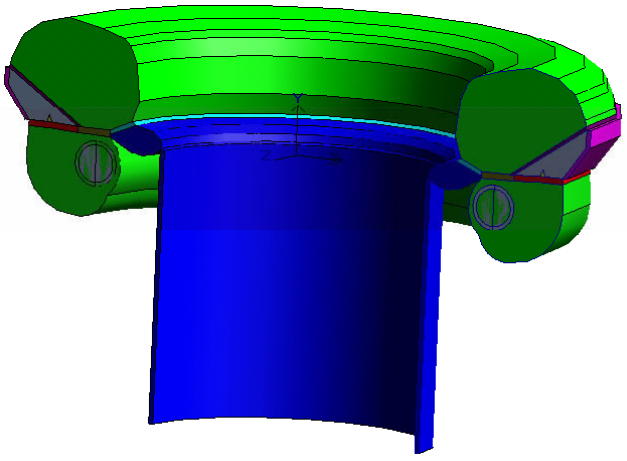

Fig. 1. A model of the first half turn of a spiraling human cochlea

Manuscript received by November 15, 2002. This work was supported by the National Science Council under contract: NSC 91-2213-E-214-022-

A typical CI planar electrode array is shown embedded in the cochlea model in Figure 2. Notice the spiral ganglion cells (n5 to n12) is located near the electrode pair. Electric conduction analysis is performed using finite element analysis. The activating function computed using values from n3 to n12 are defined as the objective function in the genetic algorithm. Fig. 3 shows the activating function contour of an planar electrode electrically excited cochlea model.

The CI electrodes are shaped by its boundary nodes. The coordinates of the boundary nodes are represented by binary codes. GA can then be used to search the binary codes which represent the coordinates of the boundary nodes (and shape of the electrodes) for optimum values in terms of the objective function.

The electrode shape and dimensions will be given certain constrained to reduce the search space. Figure 4 shows the flowchart of how the electromagnetic analysis and neuroscience model are coupled with the genetic algorithm. Preliminary results show that GA-FEM-AF model can be applied to optimize electrode shape and dimensions.

ACKNOWLEDGMENT

The author wishes to acknowledge the assistance of T. Hanekom.

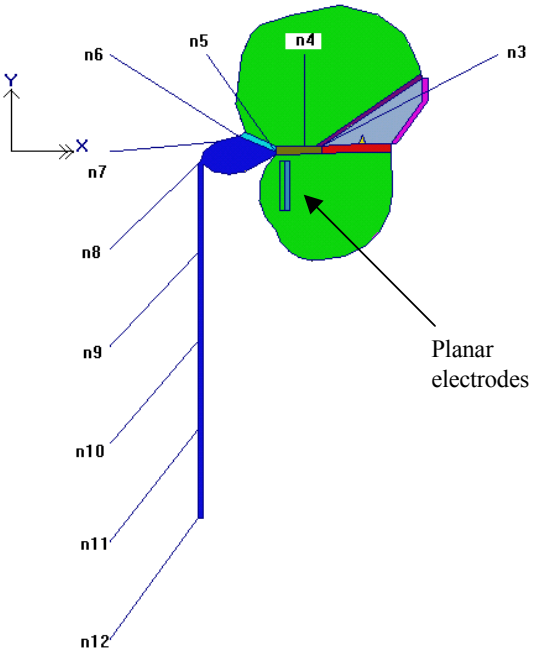

Fig. 2. A 2D cross section of a cochlea model. n3 to n12 are nerve fiber nodes used for computation of the activating function contour in Fig. 3.

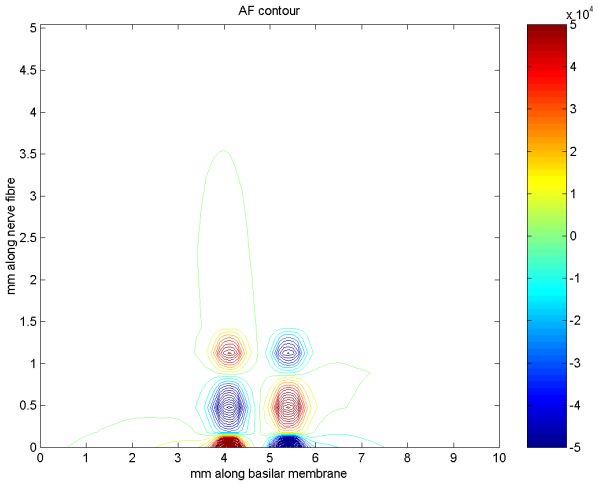

Figure 3 The activating function contour of a electrically stimulated cochlea with a planar electrode array.

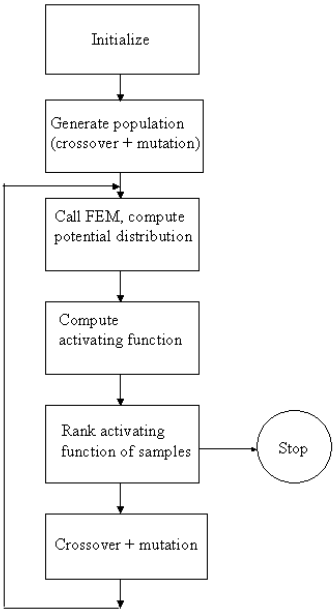

Figure 4 Flowchart of genetic algorithm coupled with electromagnetic analysis based on finite element method and neuroscience model.

REFERENCES

[1] Hanekom, T., "Three-dimensional spiraling finite element model of the electrically stimulated cochlea," *Ear and Hearing,* vol. 22, pp. 300-315, 2001.

[2] Choi, C.T.M. and Y.P. Chen, "Shape optimization and current focus of cochlear implant electrode array," Proceedings of the IEEE EMBS annual conference, Istanbul, Turkey, October. 2001.

[3] Choi, C.T.M. and Y.P. Chen, "Neural excitation patterns of four cochlear implant electrode array configurations," Proceedings of the IEEE EMBS annual conference, Houston, Texas, October, 2002.

Large-Domain Approach to Electrical Impedance Tomography: 1-D Analysis

Milica Popović
McGill University, Department of Electrical and Computer Engineering
3480 University Street, Montréal, Québec, CANADA H3A 2A7
poppy@ece.mcgill.ca

Branko Popović
University of Belgrade, Faculty of Electrical Engineering, Belgrade, Yugoslavia

Abstract – **This paper investigates the possibility of using large-domain approach to electrical impedance tomography (EIT). EIT has attracted considerable attention as a possible low-cost imaging method. However, most approaches used in the EIT image reconstruction are based on the subdomain method. For two- and three-dimensional problems, the number of unknowns involved in the subdomain methods can be prohibitively large. Large-domain approach to EIT may decrease the number of unknowns and thus improve computational efficiency.**

I. BACKGROUND

In electrical impedance tomography (EIT), imaging of an object is based on the estimation of its interior electrical properties by using the measurement data obtained at its surface [1]. The currents are injected through surface electrodes, the impedance distribution within the object determines their distribution, and the resulting surface electrode voltages are measured. The backbone of the EIT methodology is the reconstruction algorithm which uses the knowledge of the applied currents and the measured voltages to compute the electrical properties (conductivity and permittivity) in the object [4]. The challenge of the EIT is to employ optimal current patterns and reconstruction algorithm to overcome the difficulty of relatively large impedance profile changes being reflected in small changes in the measured surface voltages [5].

In geological applications [2], this technique is often referred to as electrical resistance tomography (ERT), since only the resistive component of the impedance is determined. In medicine and biology, EIT has been used as a non-ionizing modality for imaging of the human body, providing the possibility of continuous low-cost patient monitoring [1,3].

II. MOTIVATION AND METHODS

Reconstructions algorithms (comprised of a forward solver and an error-minimization procedure) developed for the EIT to date are based on the subdomain methods. The object of interested is meshed into small voxels. In the reconstruction process, the electrical parameters within each voxel are considered constant. This approach often results in a large number of unknowns.

This work explores the possibility of using the large-domain approach [6] to EIT, with the aim of reducing the number of unknowns. The initial analysis is performed in several steps:

- Step 1: Development of basic theorems which confirm that the process can, in principle, lead to useful results;
- Step 2: Introduction of basic concepts and procedures for large-domain EIT;
- Step 3: Development of a one-dimensional (1-D) large-domain EIT algorithm for numerical analysis of possibilities and limitations.

If steps 1-3 imply method's feasibility, further extension to two-dimensional structures will follow.

III. BASIC THEOREMS

In essence, EIT is based on three basic theorems, the proof of which is omitted in this paper for conciseness. Their key implications on the validity of the EIT method are as follows:

T1. Theorem on the influence of material dielectric properties in dc and low-frequency (l.f.) current fields on current distribution: for dc or l.f. currents, the influence of the dielectric properties of materials under investigation on the EIT procedure can be neglected.

T2. Theorem on uniqueness of dc currents in an inhomogeneous conducting body excited by sources over its surface: if the potential at all points of a closed surface bounding a dc or l.f. current field is known, then the potential is uniquely determined at all points inside the surface.

T3. Theorem on uniqueness of conductivity in an inhomogeneous conducting body determined from values of potential on the body surface: the relative value of conductivity (resistivity) in an inhomogeneous conducting body determined from the values of potential on the body surface is unique.

Large-domain approach will be adopted for the subsequent 2-D and 3-D studies and we briefly outline its basic concepts. In the large-domain approach, the key step is to represent the geometrical domain of interest by means of the least possible number of smaller domains. Trilinear hexahedrons have shown to be an advantageous choice for the domain shape, with hexahedron facets being in the form of bilinear quadrilaterals defined uniquely by their four vertices [6]. The three generalized coordinates running along

three hexahedron edges meeting at the same node are used to define any quantity inside the hexahedron.

IV. 1-D Case Study – Theory

In the 1-D study, the current density vector remains the same at all points along the *x*-axis. For the resistivity $\rho(x)$ and electric field and $E_x(x)$ along the axis,

$$\rho(x)J_x = E_x(x), \tag{1}$$

J_x can have any value. For simplicity $J_x = 1$ A/m^2 is adopted. In this case, Eq. (1) becomes

$$\rho(x) = E_x(x) = -\frac{dV(x)}{dx}, \text{ (for } J_x = 1 \text{ A/m}^2\text{)} \tag{2}$$

which completes the solution in the 1-D case. Since $V(x)$ is usually given in table form, its derivative needs to be determined numerically.

The described simple solution has the following specific value in this study. It enables the inverse procedure, i.e. with adopted values of $\rho(x)$, the exact solution given by Eq. (2) yields values $V(x)$. These values can be used to validate the results of numerical experiments.

Note that the measured (or simulated measured) potential at a point x can be expressed in terms of the electric field strength along the wire as

$$-\int_0^x E_x(x)dx = V(x) \ . \tag{3}$$

If the (unknown) $E_x(x)$ is represented in the form of a series, for example, as a polynomial with unknown coefficients $e_k, k = 0,1,...,m$:

$$E_x(x) = \sum_{k=0}^{m} e_k x^k, \tag{4}$$

then, substituting Eq.(4) in Eq.(3) results in

$$\sum_{k=0}^{m} e_k \frac{x^{k+1}}{k+1} = V(x) \ . \tag{5}$$

There are several methods for solving Eq. (5) approximately. All of these methods must transform Eq.(5) into a system of m linear equations. The two methods considered in this study were the point-matching method and the method of moments. In addition, results are obtained with the subdomain method for comparison.

V. 1-D Case Study – Results and Conclusions

As a numerical example, let us consider a 1-m wire with the origin $x = 0$ at one wire end and the *x*-axis directed towards the other end. For comparison with numerical results, the following exact wire resistivity is assumed:

$$\rho(x) = 1 + \cos(10x) \ . \tag{6}$$

The potential distribution along the wire, with the reference point adopted at $x = 0$, is

$$V(x) = -x - \frac{\sin(10x)}{10}, \text{ (for } J_x = 1 \text{ A/m}^2\text{)} . \tag{7}$$

For the simulated measured data, the potential is calculated at adopted number n_m of "measuring points". Random noise (1%) is added to these values to simulate measurements errors. Three solution methods are used for comparison: point-matching, method of moments and subdomain.

Numerical results can be summarized in several points:

1. The most accurate method was the point-matching method.
2. Method of moments is extremely sensitive to accuracy of integration and is unstable.
3. For comparable accuracies, In 1-D case, subdomain method requires a number of unknowns that is an order of magnitude larger than that needed by the point-matching method. This contrast is expected to increase with progress to 2-D and 3-D examples.

Figure 1 plots $\rho(x)$ computed at 20 equidistant points by point-matching (with $n = 10$ degrees of approximation) and the subdomain medhod (with $n_S = 500$ subsegments). The exact solution is also plotted for comparison.

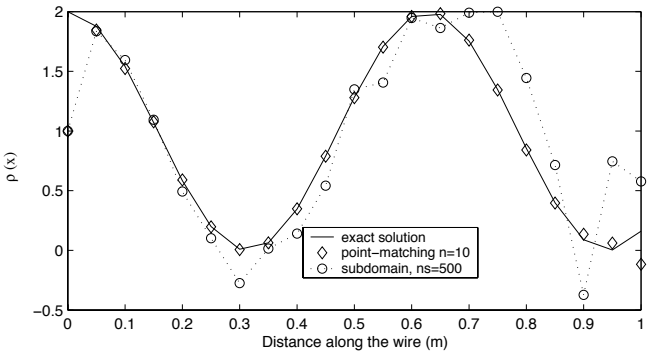

Figure 1. $\rho(x)$: Exact solution and the numerical result computed at 20 equidistant points by point-matching ($n = 10$ degrees of approximation) and the subdomain medhod (with $n_S = 500$ subsegments).

References

[1] G. J. Saulnier, R. S. Blue, J. C. Newell, D. Isaacson, and P. M. Edic, "Electrical Impedance Tomography", *IEEE Signal Processing Magazine*, pp. 31-43, November 2001.

[2] K. A. Dines and R. J. Lytle, "Analysis of electrical conductivity imaging", *Geophysics*, vol. 46, pp. 1025-1036, 1981.

[3] D. Holder, *Clinical and Physiological Applications of Electrical Impedance Tomography*, London, U.K.: UCL Press, 1993.

[4] M. Cheney and D. Isaacson, "Distinguishability in impedance imaging", *IEEE Transactions on Biomedical Engineering*, vol. 39, pp. 852-860, August 1992.

[5] E. J. Woo, P. Hua, J.G. Webster, and W. J. Tompkins, "A robust image reconstruction algorithm and its parallel implementation in electrical impedance tomography", *IEEE Transactions on Medical Imaging*, vol. 12, pp. 137-146, June 1993.

[6] B. M. Notaroš and B. D. Popović, "Large-domain integral-equation method for analysis of general 3-D electromagnetic structures", *IEE Proc. Microwave Antennas and Propagation*. Vol. 145, No. 6, December 1998.

Simulation of Eddy Currents in Biomedical Applications

[1]K. Hollaus, [1]Ch. Magele, [2]R. Merwa, [2]H. Scharfetter
Institute for Fundamentals and Theory in Electrical Engineering, IGTE
Institute for Biomedical Engineering, BMT
Graz University of Technology
Kopernikusgasse 24, A-8010 Graz, Austria
e-mail: hollaus@igte.tu-graz.ac.at

***Abstract* — Magnetic induction tomography of biological tissue is used for reconstructing the complex conductivity distribution $\kappa = \sigma + j\omega\varepsilon$ in a human body by measuring the perturbation $\Delta\mathbf{B}$ of an alternating magnetic field $\mathbf{B_0}$. The aim is to simulate the occurring eddy currents in biomedical applications by the finite element method.**

INTRODUCTION

Since magnetic induction tomography (MIT) is a non-invasive and contact-less imaging method it is especially attractive for biomedical applications, for instance, brain edema monitoring. MIT tries to reconstruct the conductivity distribution $\kappa = \sigma + j\omega\varepsilon$ in a target object. A sinusoidal time varying magnetic field $\mathbf{B_0}$ generated by excitation coils penetrates the conducting object. Eddy currents are induced perturbing the primary field $\mathbf{B_0}$. The corresponding voltages V_0 and ΔV induced in receiver coils are exploited for the image reconstruction. To solve the eddy current problem, a finite element (FE) program has been implemented capable of considering arbitrary complex geometries such as anatomical structures in the human body. Simulated and measured data are compared of a simple but representative experiment with weakly conducting materials and low contrast.

POTENTIAL FORMULATION AND FINITE ELEMENTS

A time harmonic eddy current problem excited by coils have to be simulated, see Fig. 1. This means that in the non-conducting region Ω_n a stationary magnetic field is assumed, whereas in the conducting region Ω_c eddy currents are considered. The complex formalism can be exploited advantageously. The formulation $\mathbf{A_r}, V - \mathbf{A_r}$ has been implement which employs a reduced magnetic vector potential $\mathbf{A_r}$ valid in the entire problem region $\Omega = \Omega_c \cup \Omega_n$ and a modified electric scalar potential V applied in the conducting region Ω_c only [1]. The magnetic flux density $\mathbf{B}$ is split into a field $\mathbf{B_s}$ caused by the sources, i.e., the excitation coils, and $\mathbf{B_m}$ due to the presence of the material to introduce the reduced magnetic vector potential $\mathbf{A}_{rn}$ in Ω_n:

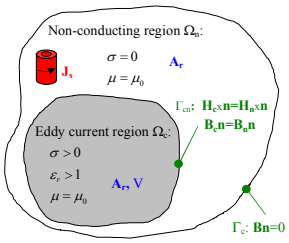

Fig. 1. Eddy current problem excited by coils.

$$\mathbf{B} = \mathbf{B_s} + \mathbf{B_m} = \mu_0\mathbf{H_s} + curl\mathbf{A}_{rn}\,. \tag{1}$$

The magnetic field intensity $\mathbf{H_s}$ in (1) is the Biot-Savart field of the coils satisfying

$$\mathbf{J_0} = curl\mathbf{H_s}\,, \tag{2}$$

where $\mathbf{J_0}$ is the current density in the coils. Exploiting (2) avoids modeling the coil volume by FEs. Inserting of (1) and (2) in Ampère's law yields

$$curl\left(\nu curl\mathbf{A}_{rn}\right) = curl\mathbf{H_s} - curl\nu\mu_0\mathbf{H_s}\,. \tag{3}$$

Similarly to Ω_n, the magnetic flux density $\mathbf{B}$ in Ω_c is split into two parts

$$\mathbf{B} = curl\mathbf{A_s} + curl\mathbf{A}_{rc}\,. \tag{5}$$

The vector potential $\mathbf{A_s}$ describes $\mu_0\mathbf{H_s}$. This assumption allows to represent the electric field intensity $\mathbf{E}$

$$\mathbf{E} = -j\omega\left(\mathbf{A_s} + \mathbf{A}_{rc} + gradV\right) \tag{6}$$

taking into account Faraday's law and introducing a modified electric scalar potential V. Next, the electric field intensity $\mathbf{E}$ in (6) together with Ampère's law results in

$$curl\left(\nu curl\mathbf{A}_{rc}\right) + j\omega\kappa\left(\mathbf{A}_{rc} + gradV\right) =$$

$$= -j\omega\kappa\mathbf{A}_s - curl\left(\nu\mu_0\mathbf{H}_s\right) \tag{7}$$

wherein the complex conductivity

$$\kappa = \sigma + j\omega\varepsilon \tag{8}$$

has been introduced.
The missing equation for V is obtained by the aid of the fact that the current density $\mathbf{J}$ is divergence free that yields

$$div\left(j\omega\kappa\left(\mathbf{A}_{rc} + gradV\right)\right) = -div\left(j\omega\kappa\mathbf{A}_s\right). \tag{9}$$

The corresponding boundary value problem is solved by the FE Galerkin technique using the tetrahedral FEs of second order [2]. The arrangement of the nodes and edges as well as the associated shape functions of the tetrahedral FEs are geometrically symmetric and the shape functions are invariant for permutations of the barycentric coordinates. The use of tetrahedral elements facilitates also modeling of complex geometries, for instance, a human head with brain. The vector potential $\mathbf{A}_r$ is approximated by edge basis functions $\mathbf{N}_i$ and the scalar potential V is represented by nodal basis functions N_i. The nodal FE of second order is shown in Fig. 2 on the left side. It consists of 14 nodes with midpoints of the nodes at the edges and facets. The shape functions N_i satisfy the orthogonal condition $N_i = \delta_{ij}$ at node j. The edge FE consists of 24 degrees of freedom. For the sake of clarity only the edges of one facet are shown in Fig. 2 on the right side. The edge shape functions $\mathbf{N}_i$ satisfy the integral orthogonal condition $\int \mathbf{N}_i \cdot \mathbf{ds}_j = \delta_{ij}$ along edge j.

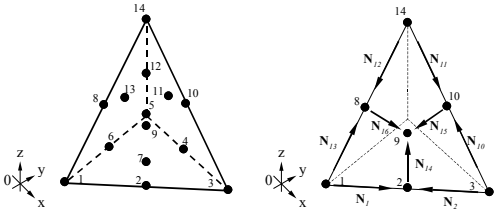

Fig. 2. Symmetric tetrahedral nodal (left side) and edge (right side) finite element of second order (only edges and nodes of one facet are represented).

NUMERICAL SIMULATIONS

The simple but representative setup depicted in Fig. 3. consists of a cylindrical saline tank (the diameter and height are $160mm$) supplemented by an extension tunnel [3]. An agar sphere (with a diameter of $56mm$) is moved from the center of the tank along the x-axis as drafted. The specific electric conductivity of agar is $\sigma = 8S/m$ and that of saline is $\sigma = 4S/m$ which means that the conductivities as well as the contrast are very small. The relative permittivity of agar as well as of saline is $\varepsilon_r = 80$. The excitation frequency has been chosen to be $f = 700kHz$.

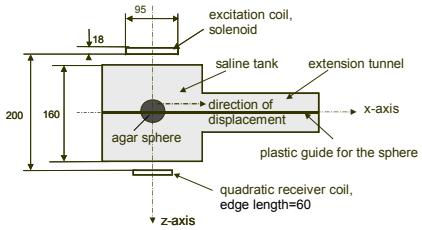

Fig. 3. Setup of the experiment with dimensions in mm.

The measured imaginary part of the sensitivity

$$S = \frac{U - U_0}{U_0} \tag{16}$$

has been compared with the simulated one. The voltages U and U_0 induced in the receiver coil refer to the perturbed and unperturbed case, respectively. The results compared in Fig. 4 are within the measurement accuracy and, thus, very satisfactory. The good agreement of the simulated data with the measured ones demonstrates the applicability of the implemented FE program for objects with low conductivities.

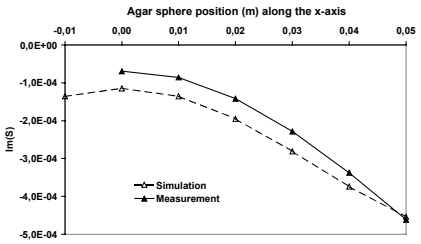

Fig. 4: Sensitivity of the agar sphere in the sodium tank.

ACKNOWLEDGEMENT

This work was supported by the Austrian "Fond zur Förderung der wissenschaftlichen Forschung" under the Grant No. F003.

REFERENCES

[1] O. Bíró, "Edge element formulations of eddy current problems", *Computer methods in applied mechanics and engineering*, vol. 160, pp. 391-405, 1999.

[2] A. Kameari "Symmetric Second Order Edge Elements for Triangles and Tetrahedra", *IEEE Transactions on Magnetics*, vol. 35, pp. 1394-1397, May 1999.

[3] H. Scharfetter, P. Riu, M. Populo and J. Rosell, "Sensitivity maps for low-contrast perturbations within conducting background in magnetic induction tomography (MIT)", *Physiol. Meas.*, vol. 23, pp. 195-202, 2002.

Trim Simulations of Thin Film Resistors by the Boundary Element Method

Klaus Schimmanz[+] , Arnulf Kost[++]
[+] Chair of Numerical and Applied Mathematics, TU Cottbus, Universitätsplatz 3-4, 03044 Cottbus, Germany
[++] Chair of Fundamentals in Electrical Engineering and Computational Electromagnetics, TU Cottbus, Universitätsplatz 3-4, 03044 Cottbus, Germany

Abstract--**The reliability of resistors in the modern hybrid Integrated Circuit (IC) production becomes more and more important. This paper discusses a method to evaluate post-trim drift behavior of laser trimmed thin film resistors. Based on numerical flux field computations a dynamic post-trim drift model is deduced and it will be shown how the Boundary Element Method (BEM) is used to simulate such processes (see also [1]).**

INTRODUCTION

High precision resistors are responsible for functionality, capability and reliability of modern hybrid ICs. In practice high precision resistors are difficult to manufacture. In difference to monolithic diffusion resistors planar thin film resistors on silicon wafers are trimable and that's why they are frequently applied to meet precise resistance specifications. Furthermore, film resistors on silicon wafers are mainly used to compensate various manufacture process variations of other circuit components. Today, such singular resistance adjustments are performed by laser trimmings on wafer level. This has become the most popular method of individually tailoring each die on a silicon wafer to meet precise resistor specifications. The used lasers operate in pulsed mode due to energy reasons. When the laser beam travels rapidly across the resistor being trimmed each pulse vaporizes a small spot of film material and the individual pulses overlap creating a close, and clean cut line into the resistor. These shape changes always increase their resistance, pulse by pulse - dependent on the concrete trim path figure.

The laser process itself has an impact on the long term stability of each trimmed resistor. This disadvantage is caused by thermal and mechanical shock each laser pulse induces into material next to any trim kerf edge. The region is called *Heat Affected Zone* (*HAZ*) and it shows altered, unstable properties. This effect cannot be avoided completely. Relaxation processes in that zone are responsible for the additional resistance drift of trimmed resistors. Thus, it is essential to know for resistor layout processes how trimmed resistors behave, if there is a premium on high accuracy and stability. Because of the high costs involved in the trim process, there is the desire to evaluate trim and post-trim drift resistance changes, rather by carrying out of simulations than by real world experiments. Thus, the following sections introduce an approach to model such effects numerically, whereby the main focus here is on drift issues. For trim simulation usage in resistor shape and for trim path layout processes see [2].

RESISTANCE COMPUTATION AND METHOD SELECTION (BEM)

The resistance of a film resistor is determined by its geometry and by the electrical property of the used film material. The effect of laser trimmings stems from changing the geometry by vaporizing the film partially, as mentioned above, which increases its resistance. For the pure ohmic resistance a stationary current flux field through the domain Ω is to consider. The resulting stationary potential field φ has to satisfy the Laplacian partial differential equation under the assumption that the used material within the domain is a homogeneous, linear, and isotropic one. To excite a stationary flux field within the resistor a constant potential difference between the two terminals is necessary. In the examples of Fig.1 the terminals are at the vertical sides of the resistor. Because the objective for film resistors is to produce a constant sheet thickness z and having all over the same conductivity κ, the whole problem is treatable as a 2-dimensional one. Thus, the domain has exact two different Dirichlet boundaries, Γ_1 and Γ_3 - distinct from each other - and all other edges are homogeneous Neumann ones.

Ohm's law says that the resistance is the quotient of voltage by total current through the structure. The voltage is given by the used potential difference of the Dirichlet edges and the structur's total current can be obtained by integration of the normal current density $\mathbf{n}\nabla\varphi$ along one Dirichlet boundary multiplied by κ and z. All together it gives for the film resistance R:

$$R = \left| \frac{\varphi(\Gamma_3) - \varphi(\Gamma_1)}{\kappa z \int_{\Gamma_3} \frac{\partial \varphi(x,y)}{\partial n} d\Gamma} \right| , \text{ where } \Delta\varphi(x,y) = 0 \text{ on } \Omega \qquad (1)$$

where $\mathbf{n}$ is the outward unit normal.

For almost all outlines used here, Laplacian equation is not solvable analytically. But several numerical methods are applicable for this, like Finite Element Method (FEM) or Boundary Element Method (BEM). The BEM, however, proves to be beneficial for this application. First of all, the problem here is a homogeneous and linear one, where no volume discretization is necessary and so it is dedicated for the BEM. Hence, the mesh generation is a one-dimensional problem only. Refinement issues can remain in user's responsibility because insufficient results become pretty soon obvious during the simulation process. Therefore adaptional refinement cycles can be avoided and thus, preset and equidistant elements are useable. Second of all, values of the directed derivatives needed by the integration in (1) are already present in the collocation points and no further effort is necessary for that. This simplifies and speeds up the integration procedure. Third of all, the BEM minimizes the residuum on the boundary by design. This is not the case by the FEM. Hence, the BEM provides more consistent results than the FEM. Furthermore, the BEM shows a better treatment of boundary singularities than the FEM. All this leads to significant time savings for computation (together up to a factor of 5). In addition,

BEM's memory usage is smaller than for FEM in the same case and for similar results (relation often about 2:3). The same is to say about the program code complexity (relation is greater than 1:6 for number of source code lines). [1], [2]

Power Density Distribution

Sheet power density distribution is one of the driving factors for layout sizing during resistor design. Minimizing of resistor real estate usage is a prime priority there. On the other hand, the power distribution within the domain rules most of the aging and drift effects, as well as those in the HAZ. An interpretation of the global, average power conversion is not qualified to describe them. The local power density can be calculated by $\varrho(x,y) = z\kappa(\nabla\varphi(x,y))^2$ on $\Omega\backslash\Gamma$.

By using first derivatives of the fundamental solutions in the formula for interior points of the BEM the gradient can be calculated with a high resolution. This results in smooth and reliable power distribution maps (Fig. 1). Again, an important benefit of the BEM for the following modeling where the power density distribution in the HAZ will be explored.

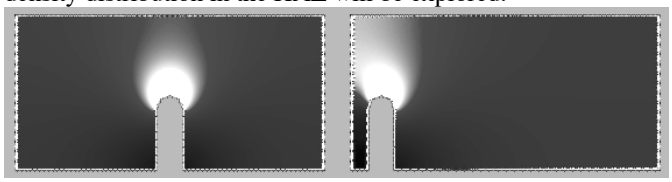

Fig. 1 Power density distribution of a centric P-cut (left) and an excentric P-cut (right)

Post-Trim Drift Model

The laser trim process is changing the resistor geometry by a trim strategy which always leaves an unstable zone next to each cut path. The material being vaporized very quickly provokes a short, intense pressure blast what compresses the remaining rim zone material along the cut pathway mechanically. Since the intensity within the beam is approximately Gaussian distributed the laser energy at rim zone locations is not high enough for vaporizing of film material. It will be thermally stressed anyhow. The material within that zone gets cracked and anneals amorphous and chaotic. It will have other electrical characteristics than the film material somewhere else within the domain. But it is still a part of the electrical current path. The HAZ conductivity is usually unknown, as well as its geometrical size. The amorphous, chaotic zone character destabilizes the resistor in use because of a lot of microscopic sharp reenty corners. At these locations the power density can be extreme, if a current flow is present. That means there will be an intense electrical energy conversion into heat what will release the "frozen" mechanical strains in that region and round down reentry corners. The electrical zone property will alter again and a post-trim drift of resistance occurs. The whole HAZ becomes more and more relaxed and the drift process continues to slow down with time.

In practice it can be observed that the temperature accelerates the drift, but it has no influence on final post-trim drift amount. The drift height is to gain by one exemplary experiment. Furthermore, it can be shown that other conductivities at border lines can be modelled by local domain scaling. Using the geometrical equivalence in dependence on local zone temperature delivers a method to model this dynamical behavior by BEM. Therefore each node i of trim kerfs boundary gets a close, interior sample point assignment where the local power density ϱ_i will be taken from. Discrete integration over time under respect of an energy loss gives the energy density Q_i at this position, which is an equivalent expression of local temperature. The higher the temperature Q_i the faster the node i will move accordingly. Hence, a node moving function m_i is to define as model hypothesis:

$$m_i(t_j) = \begin{cases} \tilde{m} := m_\infty\left(1 - e^{-\alpha\, t_j\,(Q_i(t_j) + Q_T)}\right), & \tilde{m} > m_i(t_{j-1}) \\ m_i(t_{j-1}) & \text{, otherwise} \end{cases} \qquad (2)$$

where m_∞ is the maximum move range; t_j the discrete time; α a HAZ material constant; and Q_T an external energy density. Iteration of (2) changes domain geometry $\Omega(t_j)$ for each time step and it produces a view graph of post-trim drift over time by resistance computation for each t_j, see Fig. 2.

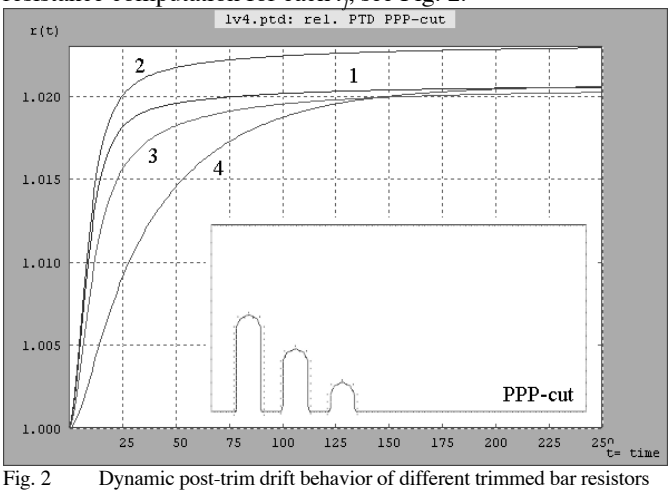

Fig. 2 Dynamic post-trim drift behavior of different trimmed bar resistors
1: excentric P-cut; 2: centric P-cut; 3: PPP-cut; 4: L-cut; [t]= h

Conclusions

The usefullness of the BEM as a fast, precise and robust method is shown for the computation of film resistor's post-trim drift behavior. It is also shown that other well known methods, like FEM, are less suitable to model the phenomenon of post-trim drift. Resistor precision requirements in IC production increase permanently, and so also the necessity to choose proper trim pathways. These computations deliver additional, fundamental selection criterions for designers and hereby are of future importance.

References

[1] A. Kost, *Numerische Methoden in der Berechnung elektromagnetischer Felder,* Springer Verlag, Berlin, 1994.

[2] K. Schimmanz, *Konzipieren und Bewerten von Hochpräzisions-Hybridwiderständen durch Laser-Trimm-Simulation,* Dr.-Ing. thesis, TU Berlin, 2002.

An Efficient Algorithm for Cutting Multiply Connected Regions

J. Simkin, S. C. Taylor, E. X. Xu
Vector Fields Ltd., 24 Bankside, Kidlington, Oxford, OX5 1JE, UK.
js@vectorfields.co.uk sct@vectorfields.co.uk ex@vectorfields.co.uk

***Abstract* –This paper presents a method for checking the connectivity of a set of finite elements and for dividing the set into simply connected sub-sets. The algorithm is based on expansion from a simply connected sub-set. The algorithm could be used to determine cut surfaces, but it is shown that simply connected sub-sets are more suitable in practice.**

INTRODUCTION

Discrete methods for electromagnetic field simulation depend on knowledge of the topology of the domain of analysis. With total and reduced scalar potential formulations it is convenient to have single valued potentials and this can be achieved by introducing appropriate cuts [1]. Coupling to external circuits or the use of total and reduced vector potential formulations introduces the requirement for cuts and knowledge of topology for vector potential formulations [2].

Analysis of topology based on the geometry of the model, or its boundary representation, is being developed [3]. However it has been shown that the finite element discretisation of a model can be used to develop cuts for multiply connected domains [1].

This paper presents an improved algorithm for determining cuts and shows that dividing the discretisation into simply connected sub-sets provides an optimal approach that will work even for domains with knots.

CUTTING ALGORITHM

It has been shown [1] that a 'Volume integration' technique can be used to determine minor cuts (the cutting surface through a volume). This approach follows naturally from the definition of a simply connected volume as one where any closed curve can be contracted to a point without cutting the surface. The algorithm was restricted to enlargement of an initially simply connected volume by an addition of simplexes that shared faces with the volume, and it cannot therefore analyse volumes with edge or vertex only connections.

A less restrictive form of the addition operator is now proposed.

Given a contiguous simplex finite element discretisation D in R^3, where each element (E) is simply connected, a simply connected sub-set (S) of elements can be found by growing from any seed element with the expansion operator

$$S = S + E \tag{1}$$

if and only if, all vertices of E that exist in S are continuously linked by edges that also exist in S.

The sub-set is closed when no further elements can be added. D can be divided into a set of simply connected sub-sets by repeated application of this procedure, choosing the initial seed element external to any existing simply connected sub-sets. Applying this algorithm to completely divide D into simply connected subsets requires **O** (number of elements) operations.

CUT SURFACES OR SIMPLY CONNECTED SUB-DOMAINS

The gradient of a scalar potential can be used to represent magnetostatic fields external to any region where currents are flowing. The external space will be multiply connected, and a multivalued scalar potential will be required. If the external space is cut by surfaces so that it becomes simply connected, a jump in scalar potential across the cut surfaces can be related to the current flowing through the major cut that links to the cut surface (minor cut). This makes it possible to have a single valued scalar potential at all points, to which the jump values must be added for a selected orientation of the cut surface.

A complicated assembly of coils will create many cut surfaces and with automatically created cut surfaces, several may come together at some points. In order to incorporate the correct jump in scalar potential for each cut it would be necessary to know the orientation of the cut surfaces for each element that referenced such a point. However, if the external space is modelled using the simply connected sub-sets of elements each sub-set can use its own gauge condition and all the jumps in scalar potential for each sub-set can be stored with respect to a unique global reference value [4]. This greatly reduces the computational complexity of the procedures required.

Furthermore, the exterior fields from knotted coils can be represented on the independently gauged set of simply connected sub-domains.

MODEL SYMMETRY

The cutting algorithm must be related to the symmetry of the model and hence the boundary conditions applied on the surface of the model. Periodic boundary conditions and assigned potential boundary conditions imply symmetrical geometry, which may cause global multiple connectivity through the boundary surfaces.

For models with periodic boundary conditions, the boundary surfaces are processed first. It is sufficient to first cut any potential global multiple connectivity by covering all the periodic boundary surfaces with added simply connected cuts. All cuts on a pair of periodic boundary surfaces must be synchronised, because the surfaces are paired to each other.

Then the assigned scalar potential boundary surfaces can be processed, by covering all surfaces of the boundary condition except the first one.

EXAMPLES

A finite element mesh around a knot coil is used to test the algorithm. A knot is a special multiply connected geometry that provides a thorough test of the algorithm. The knot coil is constructed by 12 sections of straight conductors as shown in Fig. 1. Reduced potential is defined in the region around the coil, which is then surrounded by a rectangular total potential box. A mesh of about 145,000 nodes and 852,000 tetrahedra elements is built by automatic meshing.

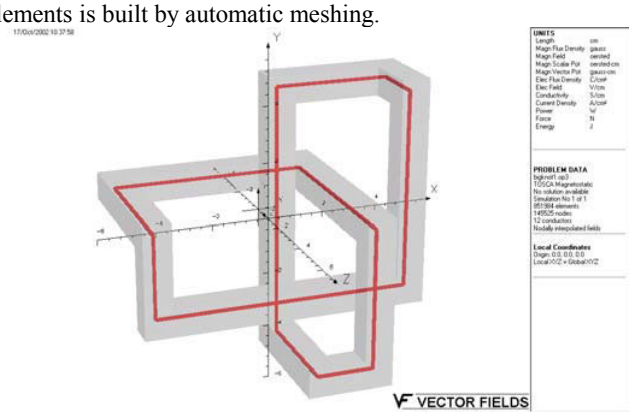

Fig. 1. A knot coil with reduced potential region around

The geometry of the multiply connected total potential region is detected and cuts are found, as shown in Fig. 2, by the algorithm with insignificant CPU time. In Fig. 3 a slice of the cuts with the coil around Y-Z plane reveals the complexity of the cuts in three dimensions.

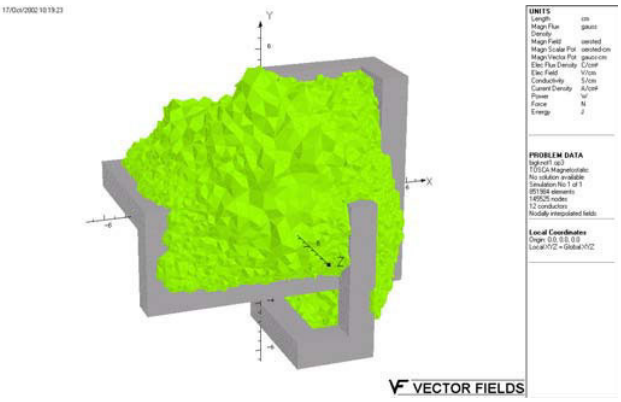

Fig. 2. Cuts around a knot

The knot causes the space of the cuts to be multiply connected, this has to be cut by two secondary cuts, as shown in Fig. 4, a big one in middle and a small one on right. The figure is rotated forwards to get clear separation of the cuts.

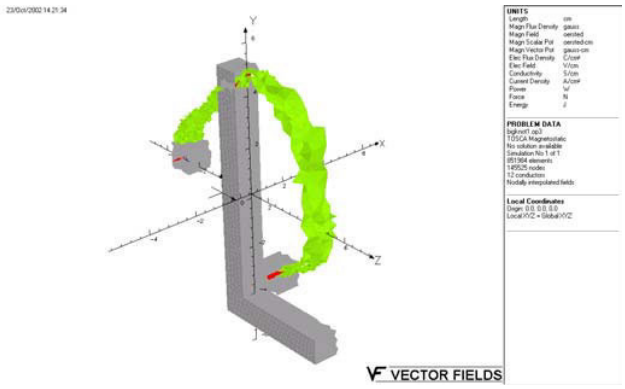

Fig. 3. A slice of cuts around Y-Z plane

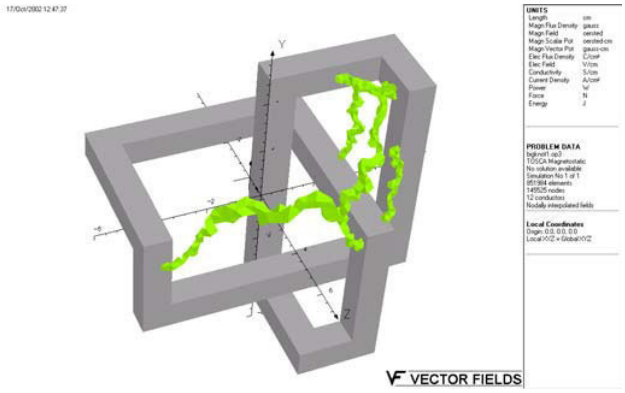

Fig. 4. Two secondary Cuts

More examples with boundary conditions will be presented in the full paper.

CONCLUSIONS

A cutting algorithm for creating simply connected sub-domains of elements has been developed and shown to be effective even for complex geometry around knotted coil structures. The automatically generated cuts may have complex geometry. The cutting algorithm assures that every cut is simply connected.

REFERENCES

[1] C. S. Harrold and J. Simkin, "Cutting multiply connected domains", *IEEE Transactions on Magnetics*, vol. 21, No. 6, pp. 2495-2498, November 1985.

[2] Z. Ren "T-Ω formulation for eddy current problems in multiply connected regions" *IEEE Transactions on Magnetics*, vol. 38, No. 2, pp. 557-560, March 2002.

[3] S. Suuriniemi and L. Kettunen, "Trade-off between information and computability: a technique for automated topological computations", submitted to IGTE-2002/Compel.

[4] L. Kettunen, private communication.

Analysis of Grounding Systems in Multi-layer Soil with Finite Volumes of Different Resistivities by Using the Electromagnetic Method

Zhibin Zhao, Xiang Cui, *Senior Member*, Lin Li and Bo Zhang
Department of Electrical Engineering, North China Electric Power University
No. 204, Qingnian Road
Baoding, Hebei, 071003 China
E-mail: hjbdcuix@heinfo.net

***Abstract* —Based on the method of moments and the Boundary Element Methods, the analysis of grounding systems buried in multi-layer soils with finite volumes of different resistivities is presented. The unknowns are smaller than other method, and the multi-layer soil can be in at least ten layers. Validation of the method is presented by comparing it with the result gotten by experiments.**

INTRODUCTION

The grounding grid is one of the important components in substation to insure the safety of the operators and the equipments when fault occurs. Until now, there are still many papers concerning the performance of the grounding grid. Several researchers have recently analyzed the study of grounding systems in uniform and multi-layer soils [1, 2].Analysis of grounding systems buried in soils with finite volumes of different resistivities has also been carried out [3]. However, the analysis considers the sources of electric are total (both free and bound) electric charges in the system, especially on the boundary surface between the soil layers of different resistivities, so the unknowns is large. Moreover, if soil structure is multi-layer, this method is unavailable.

According to the MOM and BEM, in this paper, a method to analyze the performance of the grounding grid buried in multi-layer soils with finite volumes of different resistivities is presented. This type of soil structure is ordinary, such as the substation in the city where many buildings are around the substation, or the substation near the reservoir. The unknowns are only the leakage current densities from conductor segments and the surface charge densities on the boundary surface between the finite element and the multi-layer soil. This method considers not only the soil with the number of layers up to ten, but also the frequency of the inject current that can be up to 1MHz. The calculated results obtained with the method presented in this paper are in agreement with the results gotten by experiments. From the comparison of the potential distribution, it can be seen that the results with the method that consider the influence of the finite volumes are better than that does not consider them.

THEOY OF THE METHOD

Formula of the method

Let us consider a soil model consisting of a finite volume in a multi-layer soil as shown in Fig.1. Because of unbalanced distribution of the currents in the grid, the MOM is used to analyze the grid [1]. At the boundary of the finite volume and the soil layer of resistivity, the sources of the electric field are surface electric charges of unknown densities. This enables formulation of a system of integral equations expressing the boundary conditions: on the surface of the conductor, on the boundary surface between the finite volume and the multi layer soils and on the boundary surfaces between the each multi layer soils. For the third condition, if we select suitable Green's function, it will be satisfied.

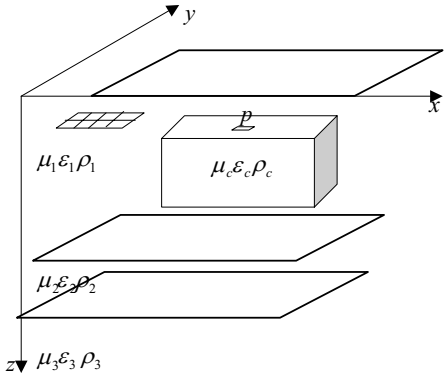

Fig. 1. Soil model with a finite volume

Let J_k is the leakage current density from conductor segment k, and η_p is the surface charge density on surface element p.

Based on the boundary condition on the surface between the finite volume and the multi-layer soil, the surface charge density η_p can be gotten by:

$$\eta_p = 2\varepsilon_1 \frac{\varepsilon_1\sigma_c - \varepsilon_c\sigma_1}{\varepsilon_1\sigma_c + \varepsilon_c\sigma_1}\mathbf{n}_p \cdot \left(\mathbf{E}^{(s)} + \mathbf{E}^{(o)}\right) \tag{1}$$

where $\mathbf{E}^{(s)}$ is due to all the charges on the surface between the finite volume and the multi-layer soils except surface element p, $\mathbf{E}^{(o)}$ is due to all the leakage currents on the conductor segments. Then $\mathbf{E}^{(s)}$ and $\mathbf{E}^{(o)}$ on element p can be expressed as:

$$\mathbf{E}^{(s)}{}_p = \frac{1}{4\pi\varepsilon}\sum_{\substack{l=1\\ l\neq p}}^{m}\eta_l \int_{s'}\frac{\mathbf{r}-\mathbf{r}'}{|\mathbf{r}-\mathbf{r}'|^3}\mathrm{d}s' \tag{2}$$

$$\mathbf{E}^{(o)}{}_p = \frac{1}{4\pi\sigma}\sum_{j=1}^{n}J_j \int_{l'}\frac{\mathbf{r}-\mathbf{r}'}{|\mathbf{r}-\mathbf{r}'|^3}\mathrm{d}l' \tag{3}$$

Let ϕ_k is the scalar electric potential at the central point of conductor k, we have

$$\phi_k = \frac{1}{4\pi\varepsilon}\sum_{l=1}^{m}\eta_l\int_{s'}\frac{1}{|\mathbf{r}-\mathbf{r}'|}\mathrm{d}s' + \frac{1}{4\pi\sigma}\sum_{j=1}^{n}J_j\int_{l'}\frac{1}{|\mathbf{r}-\mathbf{r}'|}\mathrm{d}l' \quad (4)$$

If there are m surface elements and n conductor segments, based on (1) and (4), we have $m+n$ unknowns and the same number equations.

Calculation of electric field

In order to get η_p, $\mathbf{E}^{(s)}$ and $\mathbf{E}^{(o)}$ must be calculated first. Because Green's function has infinite terms in multi-layer soil if the traditional image method is used, the computation will become very complex. Here we use the complex image method by which Green's function has only a few terms.

VALIDATION

In order to verify this method, experiments are done on a real small grid system for test. Around the grid, there are three buildings, the grid and the buildings are shown in Fig. 2. The grid to be test is shown in Fig. 3. The builds' grounding system is embedded in concrete. The soil has four layers, and the resistivities are shown in Table 1. When 30A current with the frequency 30Hz is injected into the grid at point A, comparison of the ground potential rise distribution along the line 1, 2, 3 on the ground surface between measurement and the calculation is shown in Fig. 4, Fig. 5, and Fig. 6.

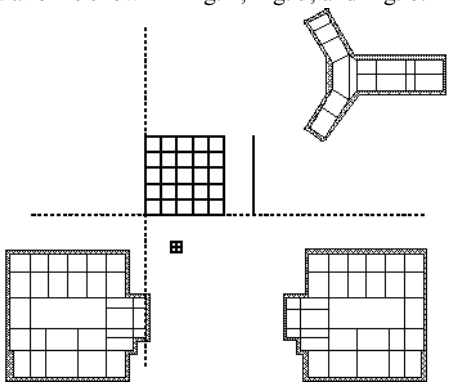

Fig. 2. The buildings around the grid

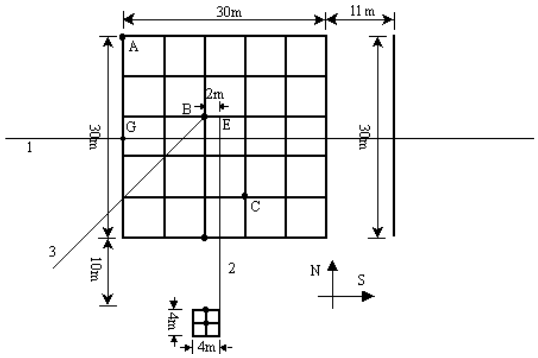

Fig. 3. The grid for testing

TABLE I SOIL RESISTIVITIES

Layer	Resistivity (Ωm)	thickness (m)
1	54.66	3.867
2	12.31	3.432
3	213.7	19.12
4	12.72	∞

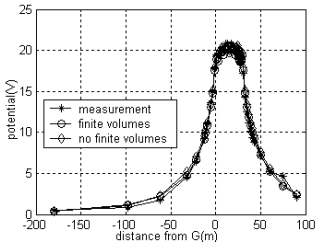

Fig. 4. Comparison of the potential distribution along the line 1

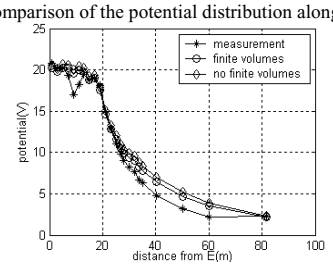

Fig. 5. Comparison of the potential distribution along the line 2

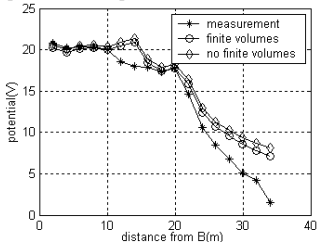

Fig. 6. Comparison of the potential distribution along the line 3

CONCLUSION

In this paper, based on the method of moment and boundary element method, a method to analyze the grounding grids in frequency domain is present. This method can analyze the grounding grid in multi-layer soil structure with finite volume of different resistivities. Comparison show that the method presented in this paper is effective and better than the method does not consider the influence of the finite volume of different resistivities.

REFERENCES

[1] Bo Zhang, Zhibin Zhao, Xiang Cui and Lin Li, "Diagnosis of Breaks in Substation's Grounding Grid by Using the Electromagnetic Method," *IEEE Trans. On Magnetics*, Vol. 38, pp473-476, October 1993.

[2] J. Ma, F. P. Dawalibi, and R. D. Southey, "On the Equivalence of Uniform and Two-layer Soils to MultiLayer Soils in the Analysis of Grounding Systems," *IEE Procedings-Generation, Transmission and Distribution*, Vol 143, pp49-55, January 1996

[3] M. B. Kostic, "Parametic Analysis of Foundation Grounding Systems Surrounded by Two-Layer Soil," *IEEE Trans. On Power Delivery*, Vol. 9, pp1406-1411,July 1994

Numerical Simulation of Charge Relaxation in Low Conductivity Fluids Stored in Cylindrical Tanks

Kazimierz Adamiak
Dept. of Electrical and Computer Engineering
University of Western Ontario
London, Ontario
Canada N6A 5B9
kadamiak@eng.uwo.ca

Abstract – **A numerical algorithm for simulation of the electric field, generated by charged fluid in a partially filled cylindrical tank is presented. The fluid is originally uniformly charged to some level. Then, the charge is dissipated due to volume and surface conductions. The rate of charge dissipation is calculated by solving the current continuity equation. The electric field distribution is also evaluated at each instant of time. Both problems are solved using the Finite Element Method in the time domain. The results of simulation show the effect of both the volume and surface conduction on the process dynamics.**

INTRODUCTION

Electric charging of low conductivity liquids is a commonly known phenomenon in chemical engineering; this happens, for example, during handling of gasoline in the petroleum industry. Shortly after filling a storage tank with such a fluid there is a substantial space charge, which quickly disappears, if the fluid conductivity is sufficiently large. However, for poorly conductive liquids the charge relaxation can be very slow.

The space charge accumulated in the stored liquid is a source of the electric field; when its value exceeds the breakdown limit of the gas above the liquid it can cause a discharge and ignite an explosion. In order to reduce the probability of the accident, the charge relaxation time should be evaluated, so some operations are not performed until most of the charge relaxes to the walls of a metal tank.

The estimation of the charge relaxation time and calculation of the electric field distribution was a subject of some publications, for example [1,2]. However, in all of them different analytical approaches were used. While this was sufficient for regularly shaped tanks, most often cylindrical ones, many important factors couldn't be analyzed: for example diffusion and electroconvection of charges and electrohydrodynamic flow. The analytical approach is also ineffective for more complicated charge transport models, especially when the initial space charge density is not uniform.

The presented paper describes a numerical model for the problem of the electric charge relaxation in a partially filled cylindrical tank, and it is based on the Finite Element Method (FEM). For a given space charge density, the electric field is calculated. Then, the dynamics of the charge relaxation is analyzed by solving the charge conservation equation: the FEM is used again, but in time domain. The model includes the charge diffusion, motion of the fluid and the effect of the surface charge and surface conduction.

MATHEMATICAL MODEL

It is assumed that a cylindrical tank of radius R and height h is partially filled with a charged fluid, so that the fluid layer has a thickness a. The fluid is conducting, with conductivity σ and permittivity ε, charged with the space charge density ρ. The gas above the fluid is air (permittivity ε_0).

The charge density produces the electric field, which can be easily calculated by solving the Poisson equation

$$-\varepsilon\nabla^2 V = \rho \tag{1}$$

where V is the electric scalar potential.

As the medium is conducting, the electric charge will dissipate to the tank walls. At any point of space the charge conservation equation has to be satisfied:

$$\frac{\partial\rho}{\partial t} + \nabla\cdot\vec{J} = 0 \tag{2}$$

where $\vec{J}$ is the electric current density. In general case $\vec{J}$ depends on the charge density, velocity of the charge motion and the charge diffusion

$$\vec{J} = \rho\vec{v} - D\nabla\rho \tag{3}$$

where $\vec{v}$ is the charge velocity and D – diffusion coefficient.

Two factors affect the charge velocity: fluid motion $\vec{u}$ and electric force, which depends on the assumed charge transport model. For a relatively well conducting fluids the ohmic conduction model can be assumed and

$$\vec{J} = \sigma\vec{E} - D\nabla\rho \tag{4}$$

Substitution (4) into the charge conservation law (2) yields the equation for the space charge relaxation [3]

$$\frac{\partial\rho}{\partial t} + \nabla\cdot(\rho\vec{u}) + \frac{\sigma}{\varepsilon}\rho - D\nabla^2\rho = 0 \tag{5}$$

The analytical solution for this equation exists only if $\vec{u} = 0$ (stationary fluid) and $D=0$ (no charge diffusion). In this case

$$\rho(t) = \rho_0 \exp(-\frac{\sigma}{\varepsilon}t) \tag{6}$$

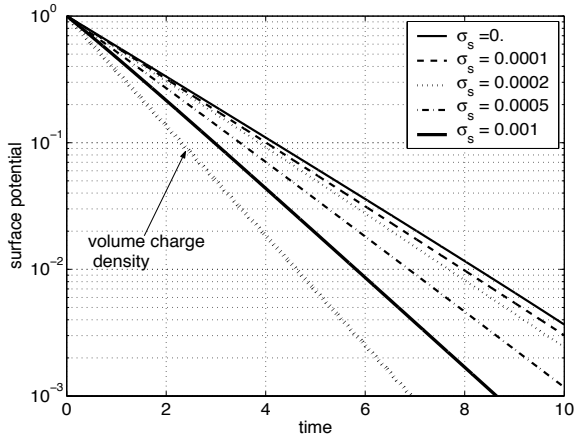

Fig. 1 Electric potential decay on the surface of charged fluid for different values of the relative surface conductivity

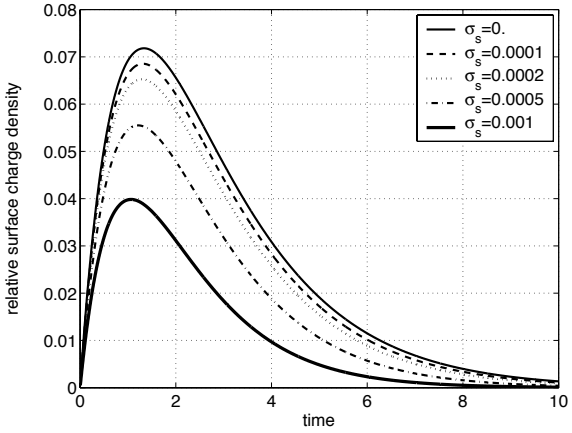

Fig.2 Relative charge density on the surface of the charged liquid

There is evidence that during the charge relaxation in a tank, some charge accumulates on the fluid-air interface, what significantly alters the relaxation dynamics. Dissipation of this charge is strongly affected by the surface conduction. The following equation can be derived from the charge conservation equation for the surface charge density [4]

$$\frac{\partial \rho_s}{\partial t} = \sigma E_n - \sigma_s \nabla_s \cdot E_t \qquad (7)$$

where: ρ_s is the surface charge density, σ_s - surface conductivity, E_n and E_t – normal and tangential components of the electric field on the fluid surface, respectively.

NUMERICAL ALGORITHM

The numerical algorithm for simultaneous solution of (1), (5) and (7) is based on the Finite Element Method. The Poisson equation (1) is handled in a conventional way with the possibility of taking into account both space and surface charges. Equation (5) needs to be solved in the time domain; the FEM is used again with the time derivative expressed by the explicit differential scheme. A simple integration technique is sufficient to compute the surface charge density (7).

The charge diffusion term in (5) is usually small and the resulting algebraic system is not diagonally dominant. A special upwinding scheme has to be used in order to avoid numerical instabilities.

RESULTS

The problem has been simulated for a tank partially filled to different levels, assuming that the fluid relative permittivity was equal to 2.0. The whole domain was discretized into about 10000 triangular elements and the linear interpolation of solution has been used. The time step has been selected by trial-and-error method, to compromise the accuracy of calculations and as short as possible time of computations.

The decay of the electric potential on the surface of fluid at the point on the axis of symmetry, for different surface conductivity values and stationary fluid, is shown in Fig. 1. In the logarithmic scale all curves are practically linear and their slope can be compared with the charge relaxation curve, which in this case follow the theoretical curve given by (6). The potential decay is much slower than the charge decay, due to accumulation of the surface charge. The surface conduction accelerates the process and for very high surface conductivity both charge and potential decay should follow the same line.

The surface charge density first increases due to repulsion of the volume charge density, then it starts to decrease as a result of the surface conduction (Fig. 2).

CONCLUSIONS

The presented numerical algorithm can be effectively used to predict the electric charge relaxation and electric field distribution in a conducting tank partially filled with a slightly conducting and electrically charged fluid. The results of simulation can be used to predict the relaxation time and magnitude of the electric field, which is responsible for the eventual electric discharge.

REFERENCES

[1] R.J. Pazda, T.B. Jones and Y. Matsubara, "General theory for transient charge relaxation in a partially filled vessel", *J. of Electrostat.*, vol. 32, pp. 215-231, 1994.

[2] K. Asano, "Electrostatic potential and field in a cylindrical tank containing charged liquid", *Proc. IEE*, vol.124, pp. 1277-1281, 1977.

[3] K. Adamiak, "Analysis of charge transport in high resistivity conductors under different conduction models", *J. of Electrostat.*, in print.

[4] R.J. Pazda and T.B. Jones, "Effect of surface conduction on charge relaxation in partially filled vessels", *J. of Electrostat.*, vol. 28, pp. 175-185, 1992.

A different approach to BEM by means of a harmonic function basis

Mircea Cehan-Racovita
Advanced Research Institute for Electrical Engineering
MCRacovita@k.ro

***Abstract*— Within the framework of BEM, one switches from the integral eq. technique to that one of integral relations. Therefore a finite basis of harmonic functions is involved. In this way the polar kernel used in the classical BEM is now avoided. Consequently a higher accuracy and a significant reduction of required redundant data are achieved. Moreover a wide range of kernels ensures versatility of the approach.**

INTRODUCTION

The deriving of *Kirchhoff*'s formula, the nucleus of BEM, starts from the 2.nd *Green* identity:

$$\oint_{(A)}(U\,\partial V/\partial n - V\,\partial U/\partial n)dA = \int_{(V)}(U\Delta V - V\Delta U)dv \qquad (1)$$

where $R = R(P,P') = |\mathbf{r}_P - \mathbf{r}_{P'}|$ [1], [2]. This function induces analytical troubles, but more seriously, originates additional computation errors. Moreover BEM requires redundant field data during the computation of φ in the domain. This feature is implied by the particular structure of the used Kirchhoff's formula. These two features of BEM may be relaxed by a different approach to BEM. The aim of the paper is to avoid the above specified negative aspects, and thereby to improve method accuracy and reduce computing time. At the same time, to obtain a higher generality of BEM, by different kernel types and more space for computation experiments.

IMPACT OF SOME BEM CHARACTERISTICS

The *Kirchhoff's formula*. This one results from (1) by taking $U = \varphi$, $V = R^{-1}$; one assumes that within (V) the permittivity ε =const, and the *Poisson* eq. $\Delta\varphi = \rho_v / \varepsilon$, is verified, where ρ_v denotes the volume density of electric charge. As (1) holds provided all integrands are continuous functions, by isolating the singularity point one comes to the result

$$\Omega(P)\cdot\varphi(P) = \frac{1}{\varepsilon}\int_V R^{-1}\rho_v(P')dv' + \oint_A \left[R^{-1}\,\partial\varphi/\partial n(P') - \partial R^{-1}/\partial n\cdot\varphi(P')\right]dA'. \qquad (2a)$$

with

$$\Omega(P) = 4\pi;\ P\in(V);\ 2\pi, P\in(A);\ 0, P\notin(V)\cup(A) \qquad (2b)$$

If $\rho_v = 0$ we get the *Kirchhoff*'s formula. The polar kernel R is the mathematic tool necessaary to extract φ from the first integral in the right- side of (1). Eq.(2a) is used by BEM in order to determine φ on (A) and within (V). The new approach should produce non-polar kernels. This possibility is due to the fact, that the *extraction off is not mandatory*.

The Fredholm integral eq. In order to determine φ or $\partial\varphi/\partial n$ on boundary (A), point P will be placed on (A). Just now there occur significant troubles induced by $1/R\to\infty$. There results a *Fredholm* eq. As one knows, its form is

$$a(P)\,\varphi(P) + \int_A K(P,P')\,\varphi(P')\,dA = F(P). \qquad (3)$$

Above, $a(P)$, $F(P)$ and $K(P,P')$ are given functions. With respect to (2a)

$$K(P,P') = R(P,P') \qquad (4)$$

where R was defined above. If a *Dirichlet* problem is considered, with respect to φ eq. (3) is a *Fredholm* eq. of 2.nd kind If a *Neumann* problem has to be solved, (3) turns into a *Fredholm* eq. of 1.st kind, as $a(P)\equiv 0$.

Depending on the kernel, the *Fredholm* eq. may *not possess unique solution.* Fortunately for $K = R^{-1}$ a unique solution is ensured. Therefore, the use of another kernel has to be carefully considered. The new approach *will produce a new type of problem.*

THE PROPOSED METHOD

Integral relations obtained by means of a K_i finite basis. Integral eq. technique will not be more applied here. Instead of $K(P,P')$, a set of $K_i(P')$ should be used. Taking $U = \varphi$ with f verifying *Poisson* eq. and $V = K(P')$, with harmonic K, eq. (1) turns into

$$\oint_{(A)}\partial K/\partial n\cdot\varphi dA = \oint_{(A)} K\cdot\partial\varphi/\partial n\,dA + 1/\varepsilon\int_{(V)} K\rho_v dv. \qquad (5)$$

With $i = \overline{1,N}$ eq. (5) generates a system of integral relations. By the discretization $P' = P_j$, $j = \overline{1,N}$ one gets an algebraic system with the unknowns $\varphi(P_j)$ or $\partial\varphi/\partial n(P_j)$ depending on the given boundary values. One has to take care that $\{K(P')\}$ is not reductible to $\{K(P_i,P')\}$. This requirement will be satisfied by using a set of *linearly independent harmonic functions* $K_i(P')$. As such a function basis, one may take a certain subset of *harmonic polynomials* of *completely different degrees*.

Homogeneous harmonic polynomials. Any harmonic polynomial $P_n(x,y)$ of degree n is a linear combination of homogeneous harmonic polynomials $Q_m(x,y), m=\overline{0,n}$:

$$P_n(x,y)=\sum_{m=0}^{n} Q_m(x,y). \tag{6}$$

But any *harmonic* $Q_m(x,y)$ includes *only two* independent coefficients (except the constant polynomial). Indeed, we write Q_m in the form

$$Q_m(x,y)=y^m q_{m,0}(x)+y^{m-1}q_{m,1}(x)+\ldots+q_{m,m}(x). \tag{7}$$

where $q_{m,l}(x)=a_{m,l}x^l$. By a recurrent procedure one derives the expressions $a_{m,2k}=\lambda_{m,2k}a_{m,0}$ with

$$\lambda_{m,2k}=(-1)^k\binom{m}{2k},\quad k=\overline{0,[m/2]} \tag{8}$$

and $a_{m,2k+1}=\lambda_{m,2k+1}a_{m,1}$, with

$$\lambda_{m,2k+1}=(-1)^k m^{-1}\binom{m}{2k+1},\quad k=\overline{0,[(m-1)/2]}. \tag{9}$$

If a 3D problem will be solved, homogeneous harmonic polynomials $Q_m(x,y,z)$ are to be considered. By quite similar but more complicated developments a suitable algorithm is built up.

Field computation within the domain. Let us consider the question of potential determination. Let be a surface (*S*) intersecting the domain (*V*). This surface (*S*) will intercept on the boundary (*A*) the portion (A_1) respectively (*A*) on (*S*) the portion (A_0). If

$$K_i(P')=0,\quad P'\in(A_0) \tag{10}$$

then (5) becomes

$$\int_{(A_0)}\partial K_i/\partial n\cdot\varphi dA=-\int_{(A_1)}(\partial K_i/\partial n\cdot\varphi-K_i\,\partial\varphi/\partial n)dA +1/\varepsilon\int_{(V_1)}K\rho_v dv. \tag{11}$$

System (11), $i=\overline{1,N}$ is discretized for $P'=P'_k, k=\overline{1,N}$; finally one gets the node values $\varphi_k=\varphi(P'_k)$.

Eq. (11) allows to assess φ on (A_0) by means of $\varphi-$ and $\partial\varphi/\partial n-$ values *upon the portion* $(A_1)\in(A)$ *only*, and of charge density within the respective *subdomain* $(V_1)\subset(V)$. This result may be explained by the fact that $\partial\varphi/\partial n$ on (A_1) also includes the effect of φ given upon the portion $(A)-(A_1)$. Similar considerations are valid with respect to the influence of ρ_v included in $(V)-(V_1)$. Thereby (at this computation step) a significant *reduction of(redundant) data* is achieved.

Obviously, there are many P_n that meet the above requirement for *K*. Note that eq.s (2a),(11) refer to a subdomain with constant ε. Accordingly, we have to determine φ and $\partial\varphi/\partial n$ on all media separating surfaces. Each surface involves many additional K_i.

Fig. 1a shows a 2D domain in connection with a saving time procedure. First, a coarse domain dividing by the segments *AB* and *CD* is done,wherein (A_0) = (*OB*) ∪ (*OC*). Afterwards a fine mesh will be practised. The last one provides with eq.s including much less unknowns . A better accuracy is achieved if one starts from the four subdomain boundaries.

Secondly, one may also determine the field strength components For instance by taking K_i verifying the requirement

$$K_i(P')=0,\quad P'\in(A_0) \tag{12}$$

one gets $\partial\varphi/\partial n$. Using suitable K_i the other two field strength components will also be obtained.

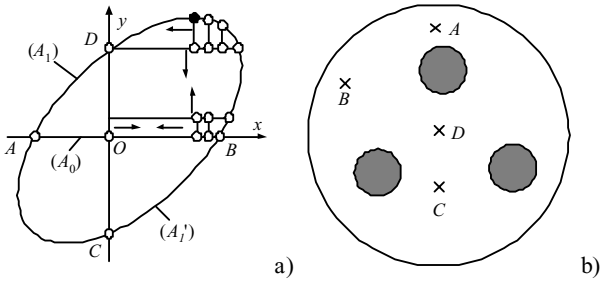

Fig. 1 a) A time saving algorithm to compute the potential in domain. b) Configuration used for performance comparison

NUMERICAL RESULTS

A multiconductor configuration was considered [3]. The field computation results obtained by both BEM and the proposed approach (PA) were compared. The relative values are presented in TABLE I.

TABLE I. φ - VALUE RATIO

Point	A	B	C	D
BEM/PA-values	1.01	0.98	0.99	1.02

The processing time referring to some variants was 2.6-8.0 lower at the proposed approach.

REFERENCES

[1] C. Brebbia, J. Telles, and L. Telles, *Boundary element techniques.* Berlin, New York, Tokio: Springer, 1984.

[2] J.Fetzer, *The Solving of Static and Quasistationary Electromagnetic Fieldproblems by Coupling Finite and Boundary Methods.* Duesseldorf, VDI Verlag: 1996.

[3] V. Amarusso, M. Helali, F. Latlarulo, 1984, "Multiconductor cable parameters calculated by diakoptic technique", *P1-8*, *IEEE* '02, Perugia, Italy, June 2002.

Analysis of Three Dimensional Electrical Field of High Voltage Interrupter by Virtual Boundary Element Method

Tao Rui Min Wang Er Zhi Li Pei Pei
School of Electric Engineering, Shenyang University of Technology
58 Xinghua Street, Tiexi District, Shenyang, 110023, China
spuwang@pub.sy.ln.cn

***Abstract*-In order to avoid the singularity of Boundary Element Method (BEM), the Virtual Boundary Element Method (VBEM) is investigated for calculating the three dimensional electrical field distribution of SF_6 high voltage interrupter. the mathematic model and its discretized form of VBEM have been set up. As an example, the three dimensional electrical field distribution of a 500kV SF_6 high voltage interrupter has been well calculated.**

Key words: virtual boundary element method, interrupter, electrical field

INTRODUCTION

As it is known that the thorny problem of BEM is the singular integral problem. To avoid the singularity, an attempt is made on calculating the three dimensional electrical field distribution. In view of the electrical field problem, the virtual boundary element method has been investigated. The mathematic model and its discretized form of VBEM have been set up. As the virtual boundary has a properly distance from the real boundary, the singular integral problem will not ever emerge. As an example, the three dimensional electrical field distribution of a 500kV SF_6 high voltage interrupter is well calculated. The method developed in this paper has opened a way in calculating three dimensional electrical field problem as well as in investigation of insulation and open properties.

BASIC EQUATION

The electric field distribution in high voltage interrupter can be described by Laplace equation with Dirichet and Neuman boundary conditions, i.e.

$$\begin{cases} \Delta\varphi = 0 \quad X \in \Omega \\ \varphi = \varphi_0 \quad X \in \Gamma_1 \\ \dfrac{\partial\varphi}{\partial n} = q_0 \quad X \in \Gamma_2 \end{cases} \tag{1}$$

Suppose that a limited virtual boundary is made in the unlimited region, and that the unknown distributed virtual sources are acted on that virtual boundary and write it as $F(\xi)(\xi \in \Gamma')$ which makes the virtual boundary Γ' to satisfy the boundary condition. Thus the problem for solving original equation (1) is transformed into the problem of solving unknown distributed virtual sources F acted on the virtual boundary.

According to the basic solution and superposition principle, the integral expressions of φ and $\dfrac{\partial\varphi}{\partial n}$ of arbitrary point to be solved among the region Ω or on the boundary Γ' can be set up as

$$\varphi(X) = \int_{\Gamma'} \varphi^*(X,\xi) F(\xi) d\Gamma'(\xi) \tag{2}$$

$$\frac{\partial}{\partial n}\varphi(X) = \int_{\Gamma'} \frac{\partial}{\partial n}\varphi^*(X,\xi) F(\xi) d\Gamma'(\xi) \tag{3}$$

where $\varphi^* = 1/4\pi R$ is the basic solution. In equations (2) and (3), F is unknown function to be solved. For solving F, the variance functional equation is set up as

$$\begin{aligned} J_R[F(\xi)] = &\sum_{j=1}^{N_1} \int_{\Gamma_{1j}} \beta_1 [\varphi(x) - \varphi_0(x)]^2 d\Gamma \\ &+ \sum_{j=1}^{N_2} \int_{\Gamma_{2j}} \beta_2 [(\frac{\partial\varphi}{\partial n} - q_0(x)]^2 d\Gamma \end{aligned} \tag{4}$$

Where N_1, N_2 are the number of node point divided on Γ_1 and Γ_2 ; β_1, β_2 are relative weighted coefficent. Take the extreme of equation (4), i.e. $\delta J_R = 0$, from which the virtual boundary element equation is obtained

$$\sum_{j=1}^{N_1} \int_{\Gamma_{1j}} \beta_1 [\varphi(x) - \varphi_0(x)] \delta u(x) d\Gamma + \sum_{j=1}^{N_2} \int_{\Gamma_{2j}} \beta_2 [(\frac{\partial\varphi}{\partial n} - q_0(x)] \delta \frac{\partial\varphi}{\partial n} \Gamma = 0 \tag{5}$$

DISCRETIZATION

Discretize the virtual boundary surface by 8 node quadrilateral element, then

$$F(\xi) = \sum_{l=1}^{n} N_i(\xi,\varsigma) F_l$$

Substitute equation (6) into equation (2) and (3), we get

$$\begin{aligned} \varphi(X) &= \int_{\Gamma'} \varphi^*(X,\xi) F(\xi) d\Gamma'(\xi) \\ &= \sum_{l=1}^{M} \{ \int_{\Gamma'} \varphi^*(X,\xi) N^l d\Gamma'(\xi) \} \{F_l\}^T \end{aligned} \tag{6}$$

$$\begin{aligned} \frac{\partial}{\partial n}\varphi(X) &= \int_{\Gamma'} \frac{\partial}{\partial n}\varphi^*(X,\xi) F(\xi) d\Gamma'(\xi) \\ &= \sum_{l=1}^{M} \{ \int_{\Gamma'} \frac{\partial}{\partial n}\varphi^*(X,\xi) N^l d\Gamma'(\xi) \} \{F_l\}^T \end{aligned} \tag{7}$$

Where M is the element division number on the virtual boundary. Accumulate the integral term of virtual sources of the same node point between two adjoint elements, and

according to the order number of node point to arrange the virtual sources, then we have

$$\varphi(x) = \mathbf{H} \cdot \mathbf{X}$$

$$\frac{\partial \varphi}{\partial n} = \mathbf{T} \cdot \mathbf{X}$$

Where

$\mathbf{H} = \{h_1, h_2, \cdots, h_N\}; \mathbf{T} = \{t_1, t_2, \cdots t_N\}; \mathbf{X} = \{F_1, F_2, \cdots, F_N\}^T$

in this way, the integral equation (5) is transformed into the following form

$$(\sum_{j=1}^{N_1} \int_{\Gamma_{1j}} \int \beta_1 [H] h_K d\Gamma' d\Gamma) \cdot \mathbf{X} + (\sum_{j=1}^{N_2} \int_{\Gamma_{2j}} \int \beta_2 [(T] t_K d\Gamma' d\Gamma) \cdot \mathbf{X}$$

$$= \sum_{j=1}^{N_1} \int_{\Gamma_{1j}} \beta_1 [\varphi_0(x)] \cdot h_{K,j} d\Gamma + \sum_{j=1}^{N_2} \int_{\Gamma_{2j}} \beta_2 [q_0(x)] \cdot t_{K,j} d\Gamma \qquad (8)$$

It can be seen from equation (8) that the unknown variables are not contained in the integrand. Thus the equation (8) is a algebraic equation set with N unknown variables. The matrix form is

$$\mathbf{G} \cdot \mathbf{X} = \mathbf{B} \qquad \square 9 \square$$

EXAMPLE

As an example, the field of a 500 kV high voltage interrupter is calculated by VBEM provided in this paper. The structure to be calculated is shown in Fig.1. As it has a parallel capacitor, the electric field distribution is a three dimensional problem.

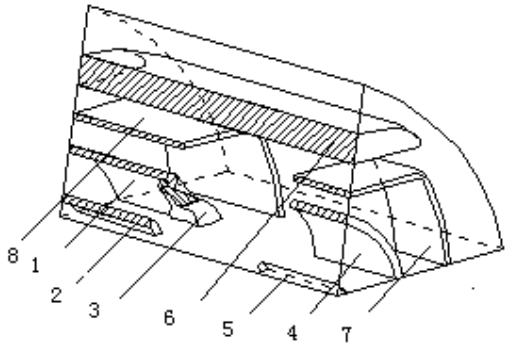

1. moveable main contact 2. moveable arc contact 3. arc nozzle
4. stational main contact 5. stational arc contact 6.parallel capacitor
7,8. shield

Fig.1. Structure diagram

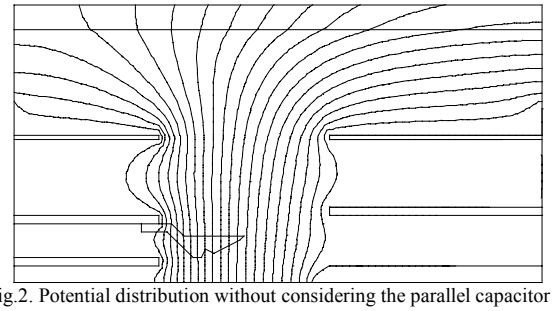

Fig.2. Potential distribution without considering the parallel capacitor

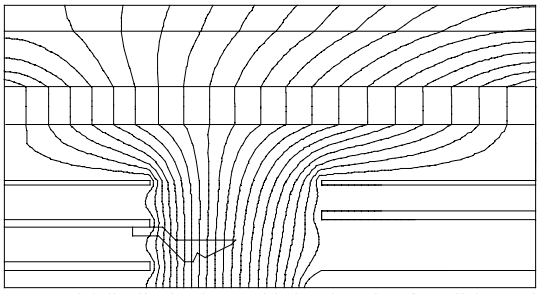

Fig.3. Potential distribution by considering the exist of parallel capacitor

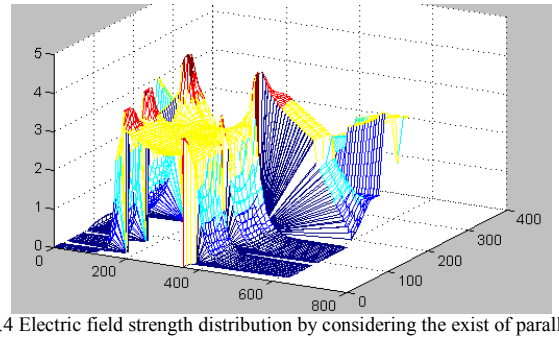

Fig.4 Electric field strength distribution by considering the exist of parallel capacitor

The virtual boundary surface is discretized into 1094 elements with 3240 nodes. The way of constructing virtual boundary is that, select a proper point from inside field area as the central point, from which to real boundary point make a radial line and the virtual boundary point is required to be on this line, and then take double distance from central point to real boundary point as this virtual boundary point. The calculation result is shown in Fig.3. Fig.2 is the equal potential distribution without parallel capacitor calculated by axisymmetric boundary element method. Fig.4 is electric field strength distribution by considering the exist of parallel capacitor.

CONCLUSION

In this paper, the virtual boundary element method is introduced to calculate three dimensional electrid field distribution of high voltage apparatus. The mathematic model and its discretizing form are set up for electric field analysis problem.

The singularity problem of BEM is naturally avoided. The calculation result shows that the method provided in this paper is feasible for calculating the electric field problem and can be used in analyzing the insulation problem and open property of high voltage equipment.

REFERENCES

[1]G.Beer,J.Q.Watson, Introduction to Finite and Boundary Element Methods for Engineers, WILEY Publisher, 1992

[2]B.H.Mcdonaid,A.Wexler "Boundary element solution of unbounded field problems" IEEE Prans. MTT Vo1.mtt 20 pp.841-847, 1992

[3]Xu Qiang, Three Dimensional analysis of thick shell by Least Square Method of Boundary Element. Journal of Da Lian University of Science and Engineering, 1996

Application of Multiple Grid Method in Electric Field Calculation of High Voltage Interrupter

LI LI Wang Erzhi
College of Electrical Engineering
Shenyang University of Tecuonlogy, shenyang,110023,China

Abstract–In view of the disadvantage of Finite Difference Method (FDM) in handling the electric field with complicated boundary , in this paper, the differential equation is employed to generate an regular calculation grid from original calculated region, so the approximation of boundary condition in calculation is avoided. The Multiple Grid Method (MGM) is adopted in electric field calculation on the transformed region for speeding up the convergency and increase the calculation precision.

INTRODUCTION

The electric field calculation possesses a significant position in researching dielectric property which is tightly connected with open property investigation and rational structure design of interrupter. In numerical calculation, the FDM is a very simple, and earliest developed method, but its disadvantage is complicated boundary manipulation. In view of this problem, the differential equation has been employed to produce a simple calculation region with rectangular grid and boundary which corresponds to the original region with complicated boundary. So the approximation of boundary condition in FDM is avoided and the electric field calculation can be proceeded in transformed simple region. In order to speed up the convergency and increase the precision, the multiple grid method has been adopted to calculate the electric field. of sF_6 high voltage interrupter.

REGULAR GRID GENERATION

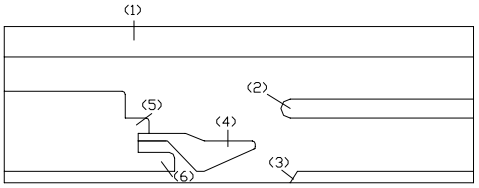

(1) porcelain insulator (2) stationary main contact
(3) stationary arc contact (4) arc nozzle
(5) movable main contact (6) movable arc contact

Fig. 1 schematic structure of sF_6 high voltage interrupter

Fig 1 is the schematic structure diagram of sF_6 high voltage interrupter. In this paper, the Laplace equation is employed to generate the regular grid. The method is based on the coordinate transformation. Let x, y to express the physical plan(original region) and ξ, η is the calculated plan(transformed plan).

Take the equation set

$$\begin{cases} \xi_{xx} + \xi_{yy} = 0 \\ \eta_{xx} + \eta_{yy} = 0 \end{cases} \tag{1}$$

as the Direchet boundary problem then the physic plan with complicated boundary can be transformed to the calculated plan with rectangular grid and boundary by solving the difference form of equation (1) using relaxed iteration method. Fig.2 shows the mesh diagram of sF_6 high voltage interrupter generated by this method, the meshes in this region corresponds one by one to $[0,1]\times[0,1]$ square mesh on regular region as shown in Fig.3.

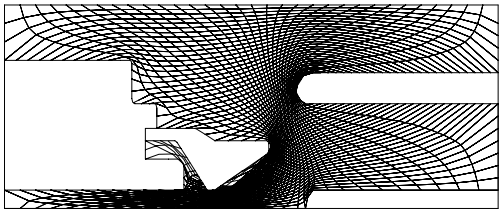

Fig.2 mesh diagram of sF_6 high voltage interrupter

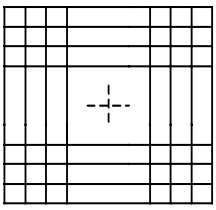

Fig.3 calculation region with regular mesh and boundary

APPLICATION OF MULTIPLE GRID METHOD

The electric field distribution of sF_6 high voltage interrupter can be described by equation

$$\begin{cases} \dfrac{\partial^2 \phi}{\partial x^2} + \dfrac{\partial^2 \phi}{\partial y^2} = 0 \\ \phi = \phi_0 \qquad \phi \in s_1 \\ \dfrac{\partial \phi}{\partial n} = 0 \qquad \phi \in s_2 \end{cases} \tag{2}$$

through coordinate transformation

$$x = x(\xi, \eta), \qquad y = y(\xi, \eta)$$

we obtain the electric field equation on the calculation plan (regular region)as

$$\begin{cases} A\dfrac{\partial^2\phi}{\partial^2\xi}+2B\dfrac{\partial^2\phi}{\partial\xi\partial\eta}+C\dfrac{\partial^2\phi}{\partial\eta^2}=0 \\ (\dfrac{\partial\phi}{\partial\xi}\dfrac{\partial\xi}{\partial x}+\dfrac{\partial\phi}{\partial\eta}\dfrac{\partial\eta}{\partial x})\cos\alpha+(\dfrac{\partial\phi}{\partial\xi}\dfrac{\partial\xi}{\partial y}+\dfrac{\partial\phi}{\partial\eta}\dfrac{\partial\eta}{\partial y})\cos\beta=0 \end{cases} \quad (3)$$

where $A=\xi_x^2+\xi_y^2 \qquad B=\xi_x\eta_x+\xi_y\eta_y \qquad C=\eta_x^2+\eta_y^2$

using the traditional central difference to discretize above equation, we obtain

$$A\frac{\phi_{i+1,j}-2\phi_{i,j}+\phi_{i-1,j}}{\Delta\xi^2}+C\frac{\phi_{i,j+1}-2\phi_{i,j}+\phi_{i,j-1}}{\Delta\eta^2}+$$

$$2B\frac{\phi_{i+1,j+1}+\phi_{i-1,j-1}-\phi_{i+1,j-1}-\phi_{i-1,j+1}}{4\Delta\xi\Delta\eta}=0 \quad (4)$$

take $\phi_{i,j}^n$ and $\phi_{i,j}^{n+1}$ as the n^{th} and $n+1^{th}$ iteration value respectively, the Jacobi iteration can be written as

$$A\frac{\phi_{i+1,j}^n-2\phi_{i,j}^{n+1}+\phi_{i-1,j}^n}{\Delta\xi^2}+C\frac{\phi_{i,j+!}^n-2\phi_{i,j}^{n+1}+\phi_{i,j-1}^n}{\Delta\eta^2}$$

$$+2B\frac{\phi_{i+1,j+1}^n+\phi_{i-1,j-1}^n-\phi_{i+1,j-1}^n-\phi_{i-1,j+1}^n}{4\Delta\xi\Delta\eta}=0 \quad (5)$$

the large storage for Jacobi-iteration is required for both old iteration value storage as well as new iteration value storage, and also the convergency of Jacobi-iteration is poor . In this paper, the Gauss-iteration form

$$A\frac{\phi_{i+1,j}^n-2\phi_{i,j}^{n+1}+\phi_{i-1,j}^{n+1}}{\Delta\xi^2}+C\frac{\phi_{i,j+!}^n-2\phi_{i,j}^{n+1}+\phi_{i,j-1}^{n+1}}{\Delta\eta^2}$$

$$+2B\frac{\phi_{i+1,j+1}^n+\phi_{i-1,j-1}^{n+1}-\phi_{i+1,j-1}^n-\phi_{i-1,j+1}^{n+1}}{4\Delta\xi\Delta\eta}=0 \quad (6)$$

is adopted. Comparing with Jacobi-iteration, the Gauss-iteration has the advantages of fast convergency; less storage requirement and effectiveness for eliminating the high frequency error components. Well ,the low frequency error components can be considered as the high frequency error components on coarse grid and also can be eliminated through Gauss-iteration. The multiple grid method is just a method that the iteration is proceeded again and again supersede at the different scale. The electric field distribution of sF_6 high voltage interrupter with 200mm strock is calculated on the [0,1]×[0,1] calculation plan by multiple grid method. The discretized equation can be written in matrix form

$$\mathbf{L_M\varphi_M=f_M} \quad (7)$$

the calculation steps are as follow:

step1: take $\boldsymbol{\varphi}_{\mathbf{M}}^{(0)}=\mathbf{0}$ at refined grid of M^{th} layer(the grid scale $\Delta x=\Delta y=1/32$), solve equation (7) by Gauss iteration method, after μ_1 times iterations, the approximation $\boldsymbol{\varphi}_{\mathbf{M1}}$ is obtained and satisfacted by

$$\mathbf{L_M\varphi_{M1}=f_{M1}}$$

step2: transform $\boldsymbol{\varphi}_{\mathbf{M1}}$ to the coarse grid of $M-1$ layer(the grid scale $\Delta x=\Delta y=1/16$), the transformation from refined grid to coarse grid is controlled by restrict operator $\mathbf{I}_{\mathbf{h}}^{\mathbf{2h}}$ which is satisfacted by

$$\boldsymbol{\varphi}_{\mathbf{M-1}}^{\mathbf{0}}=\mathbf{I}_{\mathbf{h}}^{\mathbf{2h}}\boldsymbol{\varphi}_{\mathbf{M1}}$$

let $\mathbf{f_{M-1}=L_{M-1}\varphi_{M-1}^0+I_h^{2h}(f_M-f_{M_1})}$

and take $\boldsymbol{\varphi}_{\mathbf{M-1}}^{\mathbf{0}}$ as initial value, solve equation

$$\mathbf{L_{M-1}\varphi_{M-1}=f_{M-1}}$$

through μ_2 times iterations, then again transform $\boldsymbol{\varphi}_{\mathbf{M-1}}$ to even more coarse grid. The rest procedure may by deduced be analogy until we have $\boldsymbol{\varphi}_1$ at most coarse grid layer ($\Delta x=\Delta y=1/2$).

Step3: interpolate $\boldsymbol{\varphi}_1$ to refiner grid layer ($\Delta x=\Delta y=1/4$). In this procedure, the nodes should be added and the process should be controlled by interpolation operator $\mathbf{I}_{\mathbf{2h}}^{\mathbf{h}}$ which satisfacted by

$$\boldsymbol{\varphi}_{\mathbf{2}}=\mathbf{I}_{\mathbf{2h}}^{\mathbf{h}}\boldsymbol{\varphi}_{\mathbf{1}}$$

take new $\boldsymbol{\varphi}_2$ as initial value $\boldsymbol{\varphi}_{\mathbf{2}}^{\mathbf{0}}$, solve equation

$$\mathbf{L_2\varphi_2=f_2}$$

a more accurate value $\boldsymbol{\varphi}_2$ is obtained after q times iterations. Then again back substitution and solve $\boldsymbol{\varphi}_3$, and so on utile $\boldsymbol{\varphi}_{\mathbf{M}}$ is obtained. Through iteration on refined grid and modifying on coarse grid, the potential distribution of sF_6 high voltage interrupter is obtained as shown in Fig.4

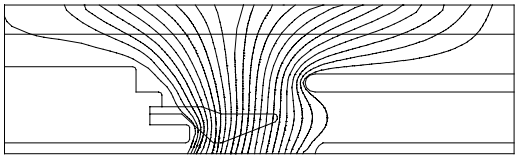

Fig.4 potential distribution

The peculiarity of MGM is of high speed convergency, even when the discretizing becomes much more fine, the convergency speed is no ever slow down. But it doesn't for traditional FDM.

CONCLUSION

The differential equation has employed in this paper for transforming the physic plan to regular plan which makes the finite difference method well suitable for handling the complicated boundary problem, and MGM and Gauss-iteration method have been used for calculating the electric field of sF_6 high voltage interrupter. The calculation shows that it needs only 2~3 times iteration to get a certain calculation precision. So the DFM is well improved by virson presented by this paper.

REFERENCE

1.Xu Tao, Sui Hong Shou, "construct method of two dimensional numerical grid" Numerical calculation and computer application.

2.W.Hanckbuen Multiple grid method Science publish company, 1988

3.Zhou ke Ding "Numerical calculation method for Engineering Electric Magnetic Field" High Education publish company,1991

Benchmark for Computation of Electric Field with Charge Simulation Method

K.Palaniswamy and K.Udayakumar
High Voltage Division, Anna University,
Chennai - 600025, India.
E-mail: palsy48@hotmail.com

Abstract- **In this paper, evaluation of the accuracy of computation of electric field with Charge Simulation Method and exploration of the possibility of increased accuracy are discussed. The problem identified for this test could be solved by analytical method and hence the reference results are free from errors. This test problem can also be applied to other numerical codes to a limited extent. Simulation of this problem is done with a Hybrid Charge Method, which is a combination of Charge Simulation Method and Surface Charge Simulation Method.**

I. Introduction

Charge Simulation Method (CSM), [1] though powerful to solve many electric field problems, has some limitations in its application, as in the case of multi-dielectric field problems, asymmetric problems and problems with thin regions. Moreover, effective application of this method depends on proper placing of discrete charges. The ratio of the depth of simulation of a charge from its contour point to the distance between this contour point and the neighboring contour point influences the accuracy. Different values are assigned to this ratio, known as assignment factor, ranging from 0.5 to 2 [1,2].

Studies are being made on benchmarking a new code, by comparison with other codes. But other numerical codes could not be relied upon too much for this purpose, as they too introduce errors. This study is on CSM, a popular code, with a test problem whose analytical results are free from errors. This test problem could be applied to other numerical codes also, along with some other problems for simulation of asymmetry and thin regions. A Hybrid Charge Method [3] (a combination of CSM and Surface Charge Simulation Method) has been made use of in this study. The study could not be treated as exhaustive but aims at improving computation with CSM.

II. Errors in Computation with CSM

In conventional estimation of the accuracy of results with CSM, some test points are chosen at the electrode surfaces and dielectric interfaces. The deviation of the computed potential at a test point on an electrode from the applied potential gives potential error. The discrepancy in the normal components of computed flux density (or in the tangential components of computed field) on either side of a dielectric interface gives field discrepancy. In a similar way potential discrepancies at the dielectric interfaces are found.

Unlike potential error at the electrode surface, field discrepancy is only a relative error, as the field values are unknown beforehand. Moreover, field discrepancy could project even a normal level of errors in computation as abnormally high, by comparing computed values on both sides of a location where the actual level of the field itself is very weak. Also, it does not indicate the actual magnitude of errors in computation, however large, if such errors occur in the same scale on both sides of the dielectric interfaces.

A Study on the Insulator Shown in Fig. 1a)

Fig. 1a) shows an insulator with ε_r=6 and a disc electrode at a potential of 100 kV. Computations were done with CSM for maximum values of field at the dielectric interface of this problem (near the electrode) for different values of assignment factor and they are given in Table I.

Table I. Results with CSM for the Insulator in Fig. 1.a)

Assmt. Factor	0.5	0.6	0.8	1.	1.2	1.6	2.	2.4	2.8
$E_{max.}$ V/cm	212	204	198	197	196	196	196	196	197

The results show different values of computed field with variation in assignment factor. The maximum potential discrepancy and field discrepancies at the dielectric interface in all the above computations were less than 1%. But these estimated errors do not indicate which results are closer to the correct value. In complicated problems this deviation is very high. Hence, special tests are required to quantify the errors in multi-dielectric problems.

III. Test Problem For Benchmarking

If a conducting sphere is introduced in a uniform external electric field, the field is distorted. The resultant field pattern could be computed analytically using Legendre polynomials. If the polar axis of the sphere is assumed parallel to the external field, the magnitude of the maximum resultant field is at the poles of the sphere, being three times the external field. The field is normal at the surface of the sphere, with sinusoidal variation. This problem was applied to find out the influence of assignment factor on the results with CSM. The floating electrode (conducting sphere) in this example is simulated as a dielectric with a very high value of dielectric constant ε_r (10^6), a method adopted by some authors [4].

Benchmarking requires a very accurate simulation of uniform field free from any deviation, both in magnitude and

direction. CSM is not suitable for this purpose, since discrete charges introduce distortions. Only distributed charges are suitable for simulation of uniform field for the test problem.

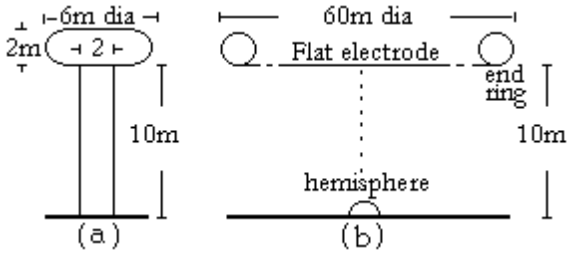

Fig 1. (a) A cylindrical insulator with HV electrode
(b) Axi-symmetric test problem for benchmarking

Fig. 1b) shows the arrangement for simulation. The main electrode is flat and wide enough to produce uniform field. A hemisphere, axi-symmetric with the main electrode, is simulated with its flat surface on the ground plane. Its diameter can be varied for study, but it must be very small (1.5 meter or less in this study) compared to the height of the main electrode. This hemisphere together with its image forms a sphere, at the center of the space covered by the main electrode and its image. First, the main electrode alone (at a potential of 10 volts) was simulated with distributed charges to ascertain the uniformity and the accuracy of the field (1 volt/meter) in and around the region where the hemisphere was to be simulated later. This simulation produced uniform field with errors less than 0.00005% in this region.

IV. Results

Applying Hybrid Charge Method, the hemisphere was simulated with discrete charges and the main electrode with distributed charges. Assignment factors adopted to simulate the hemisphere (1 meter diameter) and the corresponding computed field E_{max} at the hemispheric pole are given in Table II. When the assignment factor was above 1.3, condition- number of the matrix and field discrepancy were increasingly large, sometimes leading to near singularity; even otherwise, the results were almost constant for this factor above 1.3. Hence those results are not shown.

As seen from Table II, errors in computation are large if assignment factor is below 0.8, but if it is in the range of 0.8 to 1, results are moderately accurate. If its value is in the range of 1 to 1.2, fairly good results are achieved. The results are highly accurate when this factor is in the range of 1.2 to 1.3. (The exact value of E_{max} on top of the hemisphere is 3000 milli-volt/m). Only a little increase in accuracy is achieved when it is in the range of 1.3 to 1.5, but it sometimes leads to near singularity.

Graphs for the computed field at the surface of the hemisphere were found very close to sinusoidal. The percentage errors in the computed field along the surface of the hemisphere are as shown in Fig. 2.

Results on increasing the diameter of the hemisphere to 1.5 meter, or reducing ε_r to 10^4, were in close conformity with those given in Table II, with a slight increase in error, by 0.02% or less. Stable results were obtained without the problem of near-singularity when the value of ε_r was reduced to 10^4.

TABLE II. RESULTS FOR THE TEST PROBLEM IN FIG. 1.b)

Assmt. Factor	0.7	0.8	0.9	1.	1.1	1.2	1.3
$E_{max.}$ mV/m	2963	2980	2989	2994	2997	2999	2999.6

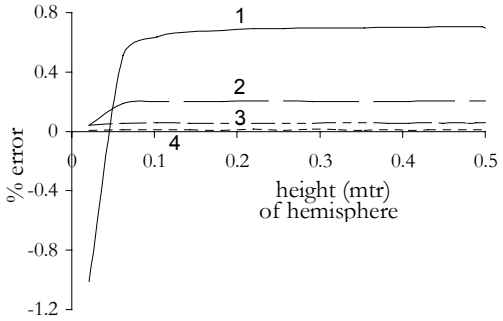

Fig 2. % Errors in field on the surface of the hemisphere (curves 1 to 4 are due to the assignment factors at 0.8, 1.0, 1.2 and 1.4 respectively)

The value of ε_r can be reduced to any value to simulate the hemisphere as a practical dielectric material but the maximum field at the pole would be less than three times the external field. The computed results are compared with the actual values obtained analytically using Legendre polynomials, and the errors are quantified in absolute terms, the details of which will be published later.

Simulation of the main electrode with discrete charges in the absence of the hemisphere resulted in lesser potential error when the assignment factor was in the range of 1.2 to 1.5, very similar to the above study for dielectric simulation.

V. Conclusion

In this paper, details of the study with a test problem for benchmarking and quantitative assessment of CSM are given. Assignment factor in the range of 1.2 to 1.5 gives highly accurate results, but if it is above 1.3, near-singularity may sometimes occur.

References

[1] H.Singer, H.Steinbigler and P.Weiss, 'A charge simulation method for the calculation of high voltage fields', IEEE Trans. PAS, Vol. 93, pp.1660-1668, 1974.

[2] Nazar H..Malik, 'A review of the Charge simulation method and its applications', IEEE Trans. Elec. Ins. Vol. 24, No. 1, pp. 3-20, 1989.

[3] Paper submitted by the same authors to 'COMPUMAG 2003 '.

[4] N.O.Morales, E.S.Asenjo and J.L.Inostroza, 'Calculation of 3- dimensional Fields in a Medium with Several Dielectrics', IEEE Trans. Dielec & Elec. Ins., Vol. 4, No. 2, pp. 172-176, Apr. 1997.

Analysis of Large Grounding Grid with Two-end Grounded Cables by the Method of Coupling Electromagnetic Field with Circuit Equations

Bo Zhang, Xiang Cui, *Senior Member, IEEE*, Lin Li, and Zhibin Zhao
Department of Electrical Engineering, North China Electric Power University
No. 204, Qingnian Road
Baoding, Hebei, 071003 China
E-mail: hjbdcuix@heinfo.net

***Abstract*—Based on the method of moment, a numerical method coupling electromagnetic field with circuit equations is presented to analyze the grounding grid with cables connected to it in frequency domain. The grounding grids can be buried in multi-layer soil. The number of the unknown variables is equal to the number of the segments needed by the method of moment. The effect on the performance of a large grounding grid made of steel by a coaxial shielded cable which is grounded at its two ends is analyzed. Both the method and the results are useful for designing the large grounding grids.**

INTRODUCTION

The grounding grid is an important component for safety in substation. To transmit the signal for control, there are many coaxial shielded cables in substation. In order to reduce the disturbance produced by inductive coupling, the cables' sheaths are connected to the grounding grid at their two ends. This is based on the supposition that there is little voltage difference on the grounding grid between the cable's two ends. In fact, because of the existence of resistance in the material of grounding grid, the voltage difference always exists. Thus, current will flow through the sheath of the cable, which may not only change the current distribution on the grounding grid but also change the step voltage and the touch voltage distribution. In china, steel is often used to build the grounding grid. Steel has larger resistivity and much larger permeability than copper. If the area is very large, the voltage difference on grounding grid may become apparent.

Many papers have analyzed the performance of the grid [1-3], but they don't take account of the situation that other kind of conductors is connected to the grid. In this paper, by using the method of coupling electromagnetic field with circuit equations, a method that can be used to analyze the grounding grid with cables connected to it is presented. With the method, the effect on the performance of a large grounding grid made of steel by a coaxial shielded cable which is grounded at its two ends is analyzed.

PRINCIPLES

Method of moment is used to analyze the grid. On the conductor's surface, the potential difference on the inner surface of the conductor must be equal to that on the outer surface. The potential difference on the inner surface is determined by:

$$\phi_i = Z_s \boldsymbol{I}_l \tag{1}$$

where

$$Z_s = l(j\omega L + Z_c) \tag{2}$$

Z_s is the self inductance of the conductor, L and Z_c are the external inductance and the internal impedance of the conductor of a unit length [3]. The potential difference on the outer surface is determined by:

$$\phi_e = \sum_{j=1}^{N} R_j \boldsymbol{I}_{n,j} \tag{3}$$

where R_j is equal to the scalar electric potential caused by conductor j when a unit current leaks from the conductor [3], $\boldsymbol{N}$ is the number of the segments, and $\boldsymbol{I}_{n,j}$ is the current leaked from the segment j.

Let's suppose that the longitudinal current in the conductor is centralized on the axis, and the leakage current in the conductor is discharged from the central point of the conductor. If the segment is connected to a cable, it can be treated as following :

Suppose a grounding grid be divided into N segments. For segment k as shown in Fig. 1, the leakage current of the k-th segment $\boldsymbol{I}_{n,k}$ can be expressed by the longitudinal currents as:

$$\boldsymbol{I}_{n,k} = \boldsymbol{I}_{l,k^-} - \boldsymbol{I}_{l,k^+} \tag{4}$$

where $\boldsymbol{I}_{l,k^-}$ and $\boldsymbol{I}_{l,k^+}$ are the longitudinal currents of conductor k at the end points k^- and k^+ respectively. From the equivalent circuit of Fig. 1 shown in Fig. 2, we use the node analysis and select node k^- and p^+ to write equations:

$$\begin{cases} \left(\dfrac{1}{Z_{cable}} + \sum\limits_{i=0}^{m} \dfrac{1}{Z^l_{k-i,k^-}}\right)\phi_{k^-} - \dfrac{1}{Z_{cable}}\phi_{p^+} = \sum\limits_{i=0}^{m} \dfrac{\phi_{k-i}}{Z^l_{k-i,k^-}} \\ \left(\dfrac{1}{Z_{cable}} + \sum\limits_{i=0}^{q} \dfrac{1}{Z^l_{p+i,p^+}}\right)\phi_{p^+} - \dfrac{1}{Z_{cable}}\phi_{k^-} = \sum\limits_{i=0}^{q} \dfrac{\phi_{p+i}}{Z^l_{p+i,p^+}} \end{cases} \tag{5}$$

where ϕ_{k-i} and ϕ_{p+i} are the potentials at point k-i and p+i and can be determined from (3), Z^l_{k-i,k^-} and Z^l_{p+i,p^+} are the self inductances between the corresponding points of the conductors and can be determined from (2). Z_{cable} is the inductance of the cable's sheath. By solving (5), the voltages at node k^- and p^+ are obtained. Then, $\boldsymbol{I}_{l,k^-}$ can be gotten by:

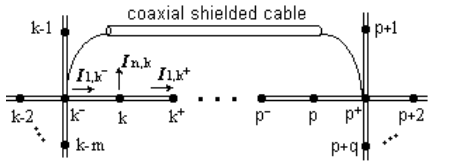

Fig. 1. A part of a grid connected to a cable.

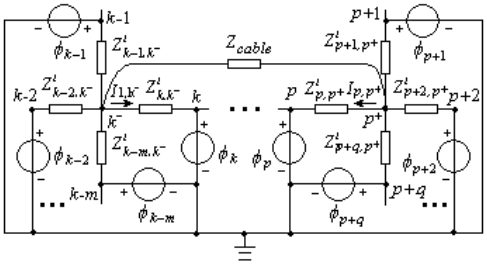

Fig. 2. The equivalent circuit of Fig. 1.

$$\boldsymbol{I}_{l,k^-} = (\phi_{k^-} - \phi_k) \Big/ Z^l_{k,k^-} \tag{6}$$

By substituting (3) into (5), $\boldsymbol{I}_{l,k^-}$ in (6) can be expressed by all the leakage currents. If there is another cable connected to point k^+, $\boldsymbol{I}_{l,k^+}$ can also be determined just like $\boldsymbol{I}_{l,k^-}$. If no cable is connected to segment k, Z_{cable} in (5) is equal to infinite. Then, (4) will have only the leakage currents:

$$\boldsymbol{I}_{n,k} = \sum_{j=1}^{N} c_{j,k} \boldsymbol{I}_{n,j} \tag{7}$$

where $c_{j,k}$ is a coefficient. The injected currents to the grid can substitute $\boldsymbol{I}_{l,k^-}$ directly. Then, by putting $\boldsymbol{I}_{n,k}$ to the left side of (7) and putting the injected currents to the right side of (7), an equation with N unknown leakage currents is obtained. For each segment, there is a corresponding equation and for the whole grounding grid, we will obtain N equations. By solving the group of equations, the leakage currents on each segment are obtained. From the leakage currents, the grounding resistance, the touch voltage and the step voltage can be determined.

APPLICATION

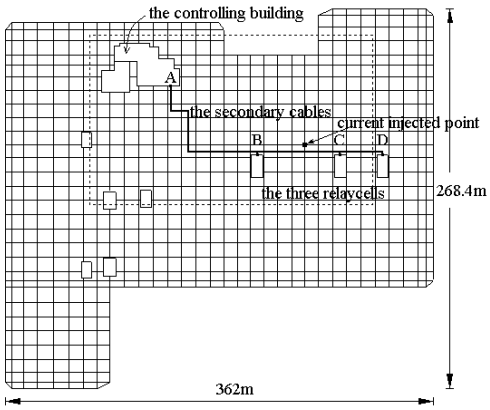

Fig. 3. The grounding grid of the 500kV substation.

By using the method, the effect on the performance of a real 500kV grounding grid made of steel by a coaxial shielded cable which is grounded at its two end is analyzed. The grid is shown in Fig. 3. There are three corresponding coaxial shielded cables to transmit the signal between the controlling building and the three relay cells. The paper mainly focuses on the cable between the controlling building *A* and the relay cell *C*, neglects the cables from *A* to *B* and from *A* to *D*. All the results are obtained at 50Hz.

If the cable does not exist, the grounding resistance is 0.2688Ω, and if the cable exists, the resistance is 0.2672Ω. The current flowing through the cable's sheath is 1242A.

TABLE I. VOLTAGE DIFFERENCE NEAR THE CONTROLLING BUILDING *A*.

	Surface Potential (V)	Touch Voltage (V)	Step Voltage (V)
Without Cable	6013	370.3	4.355
With Cable	6024	311.7	4.726

TABLE II. VOLTAGE DIFFERENCE NEAR THE RELAY CELL *C*.

	Surface Potential (V)	Touch Voltage (V)	Step Voltage (V)
Without Cable	6108	213.0	8.438
With Cable	6102	170.0	8.929

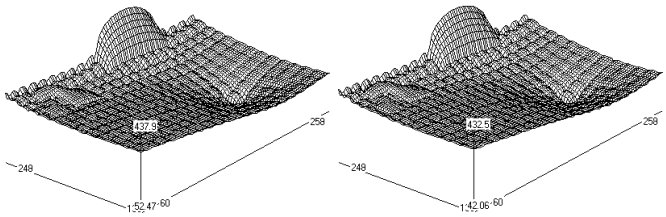

(a) Without cable (b) With cable

Fig. 4. The distribution of touch voltage in the frame of broken line in Fig.3.

Thus, except the touch voltage is changed apparently near the region where the cable is connected to the grid, there is almost no difference between with cable and without cable.

CONCLUSION

In this paper, a method coupling electromagnetic field with circuit equations is presented to analyze the grounding grid with cables connected to it in frequency domain. The effect on a 500kV grounding grid by a coaxial shielded cable which is grounded at its two ends is analyzed.

REFERENCES

[1] Jiansheng Yuan, Huina Yang, Liping. Zhang, Xiang Cui, Xishan Ma, "Simulation of Substation Grounding Grids with Unequal-Potential," *IEEE Trans. on Magn*., Vol. 36, No. 4, pp. 1468-1471, July 2000.

[2] Leonid D. Grcev, "Computer Analysis of Transient Voltages in Large Grounding Systems," *IEEE Transaction on Power Delivery*, Vol.11, No.2, pp. 815-823, April 1996.

[3] Bo Zhang, ZhiBin Zhao, Xiang Cui, and Lin Li, "Diagnosis of Breaks in Substation's Grounding Grid by Using Electromagnetic Method," *IEEE Trans. on Magn.,* Vol. 38, No. 2, pp. 473-476, March 2002.

Multigrid Algorithms for the Fast Calculation of Space-Charge Effects in Accelerator Design

Gisela Pöplau, Ursula van Rienen
Rostock University, Albert–Einstein–Straße 2, D-18051 Rostock, Germany
gisela.poeplau|ursula.van-rienen@etechnik.uni-rostock.de
Bas van der Geer
Eindhoven University of Technology, NL-5600 MB Eindhoven, The Netherlands
s.b.van.der.geer@tue.nl
Marieke de Loos
Pulsar Physics, NL-3762 XA Soest, The Netherlands
gpt@pulsar.nl

Abstract— **Numerical prediction of charged particle dynamics in accelerators is essential for the design and understanding of these machines. Methods to calculate the self-fields of the bunch, the so-called space-charge forces, become increasingly important as the demand for high-quality bunches increases.**

We report on our development of a new 3D space-charge routine in the General Particle Tracer (GPT) code. It scales linearly with the number of particles in terms of CPU time, allowing over a million particles to be tracked on a normal PC. The model is based on a non-equidistant multigrid Poisson solver that has been constructed to solve the electrostatic fields in the rest frame of the bunch.

Numerical investigations have been performed with a wide range of cylindrically shaped bunches (from very long to very short) occuring in recent applications. The results show small errors for the computed electric field and a stable multigrid performance for an appropriate choice of the multigrid components.

Introduction

Nowadays, particle accelerators play an important role for scientific research as well as for medical and industrial applications. Demanding applications such as high-energy linear colliders and self-amplified spontaneous emission free electron lasers (SASE-FELs) require very high quality electron bunches, where any anomaly severely degrades the final performance.

The calculation of space-charge forces is an important part of the simulation of the behaviour of charged particles. Depending on charge density and energy, a direct point-to-point model can not be used to calculate space-charge forces because of granularity problems and the inherent $O(N^2)$ scaling between the number of sample particles and CPU time [1]. Widely used methods to avoid these problems are the restriction to 2D models which are valid with certain symmetry assumptions, the application of the FFT method or the parallelization of large problems derived from 3D models.

In this paper we present a 3D space-charge model based on a multigrid algorithm adapted for non-equidistant meshes. This method is appropriate for a variety of applications and allows a million particles to be tracked on a normal PC. It has been implemented in the widely used tracking code GPT (General Particle Tracer) [2] which calculates the trajectories of a large number of sample particles through the combined external and self-induced fields generated by the charged particles.

Gisela Pöplau was supported by DESY, Hamburg.

The numerical investigations present tests with cylindrically shaped electron bunches with different aspect ratios varying from 'cigar' to 'pancake' shape.

3D Space-Charge Calculation based on a Multigrid Poisson Solver

The space-charge calculations are performed within the tracking procedure. The trajectories of the particles are described by the relativistic equations of motion which are solved with a 5^{th} order Runge–Kutta scheme in the tracking code GPT [1]. In each time step of the numerical integration the space-charge fields have to be taken into account. The space-charge calculation is performed in the rest frame of the bunch as follows:

1. Transformation of the particles from the laboratory frame to the rest frame by Lorentz transformation.
2. Determination of a non-equidistant 3D Cartesian grid in correspondence to the charge density of the bunch (see Figure 1).
3. Approximation of the charge at the grid points.
4. Calculation of the electrostatic potential at the grid points via Poisson's equation applying a geometric multigrid algorithm adapted to non-equidistant meshes. The finite difference scheme is used for the discretization of Poisson's equation.
5. Derivation of the electric field in the rest frame and trilinear interpolation of the field values to the particle positions.
6. Transformation of the field to the laboratory frame by Lorentz transformation.

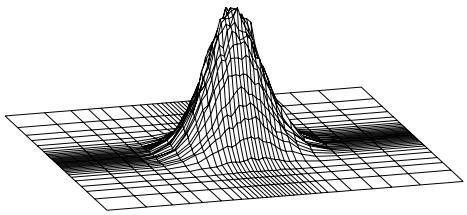

Fig. 1. Mesh line positions ((x, y)–plane) for a Gaussian charge density. The vertical axis shows the total charge in each mesh box, where the height of the top has been normalized in both plots.

The efficiency and accuracy of the space-charge calculation mainly depends on the determination of the 3D mesh and the applied multigrid scheme to solve Poisson's equation[5].

Numerical Investigations

Charged particle bunches ranging from very short to very long play an important role in accelerator design. The aspect ratio A for cylindrically shaped bunches is defined as $A = R/\gamma L$ where R denotes the radius of the cylinder, L the length and γ the Lorentz factor by which the bunch will be stretched in the transformation from the laboratory frame to the rest frame. The particles in the cylinder are assumed to have a uniform distribution. The performance of the 3D space-charge routine was tested within a range of aspect ratios $A = 10^k$ with $k = -2,-1,\ldots,2$ which covers many real life applications.

The first numerical investigation concerns the error caused by the 3D space-charge model. Here the computed electric fields of various uniformly charged hard-edged cylindrically symmetric bunches have been compared to the analytical expressions. This can be considered a worst-case scenario because the fields near the hard edges have singularities, but they are typically not present in physical bunches with relative smooth boundaries. Fig. 2 shows that except for the bunch with $A = 100$ where nearly ten times as much particles are needed, convergence reaches field errors in the range of a few percent for a rather small number of particles .

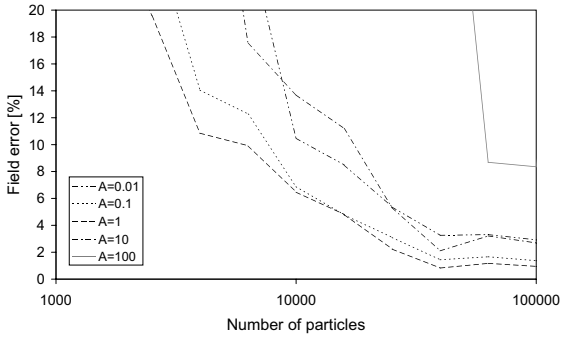

Fig. 2. Error of the electric field for electron bunches with cylindrical shape of different aspect ratios A. The space charge calculations have been performed on a $n \times n \times n$ grid for all shapes, where n^3 =number of particles.

The second numerical test concerns the performance of the geometric multigrid algorithm constructed for non-equidistant meshes shown in Fig. 1. It has been demonstrated in [4] that the crucial part of a multigrid scheme on such meshes is the coarsening strategy. In this paper we present the results of three geometric multigrid algorithms. All schemes apply two pre-smoothing and two post-smoothing steps with red-black Gauss–Seidel relaxation (MG(2,2)). Half restriction has been tested versus full restriction as grid transfer operator. Third, the multigrid preconditioned conjugate gradient method has been applied with two V-cycles in every CG-iteration step (MG-PCG(2,2)(2)). To ensure convergence the components of this multigrid scheme have to be modified so that the iteration operator is positive and symmetric (see [3]).

The performance of the multigrid algorithms has been tested with the tracking of a pancake bunch with $A = 2$ moving in free space. The particles of this bunch have been tracked over a time of 100 ps which corresponds to 37 time steps in the simulation. Fig. 3 shows that the multigrid scheme with full restriction and the multigrid preconditioned CG-method have the most stable performance while the multigrid algorithm with half restriction is very sensitive to certain meshes which yield no optimal coarsening.

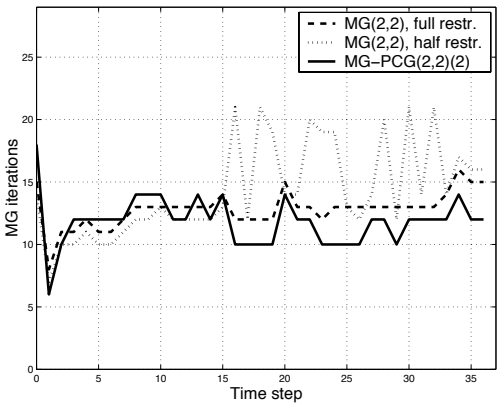

Fig. 3. Number of multigrid iterations for several multigrid schemes (MG: multigrid, MG–PCG: multigrid preconditioned CG). The calculations have been performed with a pancake bunch of 10,000 particles, where the particles have a uniform distribution. The multigrid iteration has been performed on a $33 \times 33 \times 33$ mesh to a relative residual of less than 10^{-13} in the maximum norm.

Conclusions

A new 3D space-charge routine implemented in the GPT code has been described in this paper. The new method allowing 3D simulations with a large number of particles on a common PC is based on a multigrid Poisson solver adapted to non-equidistant meshes for the calculation of the electrostatic potential in the rest frame. Numerical results of the 3D routine show good convergence and a stable multigrid performance.

Further improvement of the 3D space-charge routine is foreseen regarding adaptive meshing and adaptive choice of sample particles.

References

[1] S.B. van der Geer and M.J. de Loos: *The General Particle Tracer Code. Design, implementation and application*. PhD thesis, Einhoven, 2001.

[2] General Particle Tracer (GPT), release 2.60, Pulsar Physics, De Bongerd 23, Soest, The Netherlands, `www.pulsar.nl/gpt`.

[3] M. Jung and U. Langer: *Applications of multilevel methods to practical problems*. Surv. Math. Ind. **1**, pp. 217–257, 1991.

[4] G. Pöplau and U. van Rienen: *Multigrid Solvers for Poisson's Equation in Computational Electromagnetics*. Proceedings of the 3rd Conference on Scientific Computating in Electrical Engineering (SCEE–2000), (U. van Rienen, D. Hecht, M. Günther, eds.), LNSCE **18**, Springer, Berlin, pp. 169–176, 2001.

[5] G. Pöplau, U. van Rienen, M.J. de Loos and S.B. van der Geer: *A Fast 3D Multigrid Based Space-Charge Routine in the GPT Code* Proceedings of EPAC 2002 (Paris), pp. 1658–1668, 2002.

MV line electric field evaluation near a concrete pole

D. Desideri, M. Guarnieri, E. Poli
Department of Electrical Engineering - University of Padova
via Gradenigo 6/A
35131 Padova (Italy)
E-mail: desideri@die.unipd.it

Abstract - **The electric field component along the direction of a MV line near a concrete pole has been studied, at first with a simplified analytical model, then with a 3D finite element commercial code and finally with the charge simulation method. The results are in good agreement and have been validated experimentally. A possible application is outlined.**

INTRODUCTION

The evaluation of the electric field at power frequency generated in close proximity of a MV transmission line is of interest both for environmental consideration and for possible technical applications in detecting line fault conditions.

In this work, the region near a concrete pole of a MV line not too close to the top has been investigated. At first a simplified geometry has been used with a single conductor, and then the three-phase MV line has been considered. In both configurations, simple analytical models have been proposed for a preliminary intuitive comprehension and then numerical analyses have been performed. The results have been experimentally validated.

PRELIMINARY ANALYTICAL CONSIDERATIONS

A. Single conductor model

The analyzed simplified geometry consists of a pole with height a and a single conductor at a distance b over the concrete pole (Fig. 1).

A linear charge distribution with total negative charge $-q_1$ has been assumed along the pole (as suggested by a preliminary Lehmann's analysis) together with a concentrated charge at the top of the pole. The ground has been considered resorting to the image charge principle. The charge distribution on the conductor has not been considered in estimating the electric field component E_x in the x-z plane (Fig. 1) near the pole because, due to the symmetry, the electric field caused by the charge on the conductor and its charge image only has a vertical component on the pole. The same simplifying assumption holds for the concentrated charge at the top of the pole and its image charge, in the region near the concrete pole not too close to the top.

The assumed charge density with linear distribution along the concrete pole allows to compute, in the region near the pole, i.e. for small values of x, the voltage and therefore the electric field component E_x in the x-z plane. It results:

This work was supported by C.R.E.I. Ven - Consorzio di Ricerca in Elettronica Industriale – Veneto, Padova, Italy and S.G.E. Società Generale di Elettronica S.r.l., Padova, Italy.

$$E_x \approx -\frac{q_1}{4\pi\varepsilon_0}\frac{4}{a^2}\frac{z}{x} = -\frac{1}{\pi\varepsilon_0 a^2}\frac{z}{x}C\,e(t)\ , \qquad (1)$$

where, according to the quasi-static condition, q_1 has been expressed as product of the voltage $e(t)$ and the capacitance C between conductor and pole.

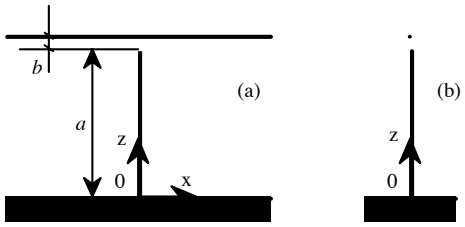

Fig. 1. Pole with height a and single conductor at a distance b: lateral (a) and frontal view (b).

B. Three-phase model

The configuration of a three-phase overhead line with a pole top design has been studied. In a simple model, an expression of the electric field component E_x in the x-z plane near the concrete pole and not too close to the top can be derived assuming that (1) holds for each of the three phases and with equal capacitance between each phase and the pole. It results:

$$E_x \approx \frac{-zC}{\pi\varepsilon_0 a^2 x}\left[e_1(t)+e_2(t)+e_3(t)\right] = \frac{-zC}{\pi\varepsilon_0 a^2 x}3e_0(t)\ , \qquad (2)$$

where $e_1(t)$, $e_2(t)$, and $e_3(t)$, are the three phase voltages and $e_0(t)$ is the voltage zero-sequence component.

NUMERICAL ANALYSIS

A. 3D finite element evaluation

Both the configurations have been studied with a Maxwell® 3D finite element commercial code.

In the first case, the pole and the conductor have been taken as equipotential conducting cylinders, with diameter equals to 0.08 m and 0.3 m respectively; a has been chosen equal to 10 m, b equal to 0.85 m and the ground has been taken 60x10 m^2. The 0.3 m value has been chosen in order to obtain a better code convergence. With a mesh of about 10^5 elements, the computed values near the concrete pole, not too close to the

top, present almost linear dependence with z and inverse with x, in agreement with (1). A C value of about 17 pF has also been derived.

The three-phase overhead line has been studied by completing the previous single conductor configuration with two cylindrical lateral conductors with the same diameter as the central one, located at a distance b at each side of the top of the pole. The capacitances between the central phase and the pole and between each lateral phase and the pole result to differ of about 30%.

B. Charge simulation method

Both configurations have also been studied with a code based on the charge simulation method (CSM), that replaces the conductors and their surface charges with sets of charges inside equipotential contours [1-3].

In this study, the phase conductors were simulated by conducting cylinders, 0.01 m diameter, extending 30 m apart from the pole in order to avoid boundary effects: also, the pole has been represented by a cylindrical conductor.

A preliminary check on the accuracy of the computed equipotential surfaces was done in two different ways: on the potentials, finding an error generally lower than $2*10^{-4}$, and on the electric field, whose angle respect to the normal to the conductors was smaller than one degree.

As the shape of the pole conductive core is not known, a parametric analysis of the diameter of its simulating cylinder was also carried out. The field along the pole at a distance x = 0.15 m was computed for three different diameters: 0.1, 0.2 and 0.3 m. Results differ no more than 15%, showing that, within these limits, no knowledge of the internal composition of the pole is required.

With a diameter of 0.2 m as reference, the distributions of charge density along the pole were computed both in the single conductor model (1 kV applied) and in the three-phase configuration (1 kV applied to one phase and 0 V applied to the other ones), reported in Fig. 2. The corresponding charge density on the phase conductors was also computed.

Results confirm the simple assumption of a linear distribution of charge density along the pole used in the analytical formulation, within 10% up to z = 6 m.

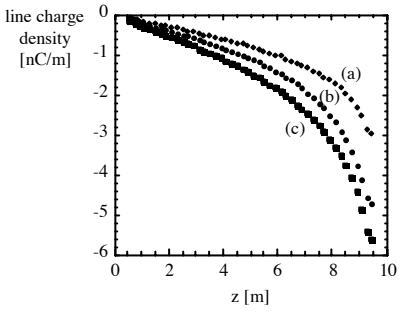

Fig. 2. Charge density distribution along the pole. Three-phase: (a) 1 kV applied to the central phase, 0 V on the others; (b) 1 kV applied to one lateral phase and 0 V on the others. Single conductor: (c) 1 kV applied.

Then the capacitances between each phase conductor and the pole have been calculated. Values of C_0 = 20 pF in the single phase model and, respectively, of C_1 = C_3 = 16 pF (lateral phase - pole) and C_2 = 11 pF (central phase - pole) in the three-phase configuration were found.

Finally, the distribution of E_x at 1 kV on the central phase and –0.5 kV on the lateral phases was computed as a function of x and z. An example of the results is shown in Fig. 3, where for comparison, the data obtained from the finite element commercial code are also reported.

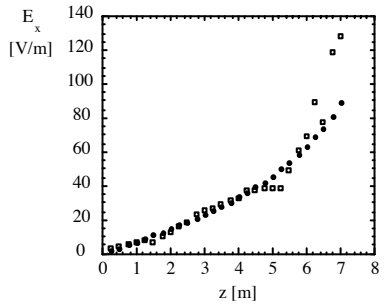

Fig. 3. Electric field component E_x at x=0.1 m versus z. Maxwell® 3D code data (squares) and charge simulation method data (circles) are reported.

CONCLUSIONS

Taking into account the difference $\Delta C = C_1 - C_2$ and using (1) for each of the three phases, it results:

$$E_x = \frac{-z}{\pi\varepsilon_0 a^2 x}\left[3C_1 e_0(t) - \Delta C e_2(t)\right], \qquad (3)$$

showing the same simple dependence on z and x as in (1) and allowing an easy evaluation of the variations of E_x at the occurring of $e_0(t)$ on the line.

The model has been experimentally validated on a MV line with a floating electric field measurement equipment developed in accordance with IEC 833 Standard [4].

The very simple calculation provided by (3) gives satisfactory agreement with the much more complex computer solutions, allowing its use in low cost detection systems of zero-sequence voltage which are under development.

REFERENCES

[1] H. Singer, H. Steinbigler, P. Weiss, "A charge simulation method for the calculation of high voltage fields", *IEEE Transactions on Power Apparatus and Systems*, vol. 93, pp. 1660-1668, September 1974.

[2] N. H. Malik, "A review of the charge simulation method and its applications", *IEEE Transactions on Electrical Insulation*, vol. 24, pp. 3-20, February 1989.

[3] E. Poli, "The use of image charges in the charge simulation method: a parallel-plane dielectric plate covering a conductor", *IEEE Transactions on Magnetics*, vol. 28, n. 2, pp. 1076-1079, March 1992.

[4] IEC 833, Measurement of Power Frequency Electric Fields, 1987.

COMPUMAG Saratoga Springs, New York USA
July 13 - 17, 2003

Electrostatic Finite Element Modelling of a Silicon Diode

Masidlover, A. R. and Gibson, A. A. P.

Electromagnetics Centre, UMIST
Manchester, M60 1QD, United Kingdom
email: a.masidlover@postgrad.umist.ac.uk, a.gibson@umist.ac.uk

***Abstract*— The purpose of this work is to produce physical finite element models of silicon semiconductor diodes. A p-n junction device is described here and the finite element calculated potential and charge solutions are used to extract the capacitance parameter in reverse bias.**

I. Introduction

The aim of this work is to use a full numerical semiconductor device simulation to extract a key parameter from a silicon diode, that of the capacitance of the device when in reverse bias. The numerical solution takes the boundary conditions (current and voltage) and internal conditions (doping) and uses them in a finite element formulation to generate the values of internal electric field and carrier concentration. The capacitance can then be calculated from the carrier concentration.

II. The Physical Model

A. Sub-domain Equations

The two domains (the anode and cathode) are described by the same set of equations, only the concentrations of donor atoms change. The equations describe how the charge carriers distribute themselves through the material and also how they flow when a steady state has been achieved. This gives the current and the charge distribution. To determine the current flow the Boltzmann transport equation is used as a starting point and results in equations (1) and (2)

$$\overrightarrow{J_n} \cong q.n.\mu_n.\overrightarrow{E} + q.D_n.\bigtriangledown.n \tag{1}$$

$$\overrightarrow{J_p} \cong q.p.\mu_p.\overrightarrow{E} - q.D_p.\bigtriangledown.p \tag{2}$$

where $\overrightarrow{J_n}$ and $\overrightarrow{J_p}$ are the final device current densities for electrons and holes respectively, q is the electron charge, n and p are the electron and hole concentrations, $\mu_{n,p}$ are their mobilities, $\overrightarrow{E}$ is the electric field and $D_{n,p}$ are the diffusion mobilities.

Equations (1) and (2) must be solved in conjunction with the quasi-static Maxwell's equations. For an actively charged region Maxwell's equations combine to produce Poisson's equation and the continuity equations for electrons and holes. These governing equations are written as follows:

$$\bigtriangledown(\bigtriangledown.\psi) = \frac{q}{\varepsilon}(n-p-Q_d) \tag{3}$$

$$\bigtriangledown\overrightarrow{J_n} = q.R \tag{4}$$

$$\bigtriangledown\overrightarrow{J_p} = q.R \tag{5}$$

where ψ represents the electrostatic potential, ε is the permittivity, Q_d is the fixed charge on the dopant atoms and R is the recombination rate. Equations (1) to (5) are coupled through $\overrightarrow{E}$, $\overrightarrow{J_{n,p}}$, n and p

Shockley, Read and Hall introduce an equation (6) which describes the recombination in terms of n, p, the intrinsic carrier concentration n_i, the carrier lifetimes $\tau_{n,p}$, trap energy level parameters $n_1$and p_1. The trap energy levels are set such that when the trap energy level is in the middle of the band gap then n_1 and p_1 equal n_i.

$$R^{SRH} = \frac{n.p - n_i^2}{\tau_p.(n+n_1) + \tau_n.(p+p_1)} \tag{6}$$

B. Boundaries and Initial Conditions

For boundaries with an insulator, it is assumed that no electrostatic field or current flows into the insulator. This assumptions give the Neumann boundary conditions in equations (7), (8) and (9).

$$\overrightarrow{n}.E = 0 \tag{7}$$

$$\overrightarrow{n}.J_n = 0 \tag{8}$$

$$\overrightarrow{n}.J_p = 0 \tag{9}$$

The contacts are the final type of boundary and are more complex. The assumptions are made that the holes and electrons recombine with infinite velocity, implying that the mass action law (10) is valid, and the contact voltages are fixed. It is also assumed that space charge vanishes at the contact boundaries and this gives equation (11).

$$n_i^2 = np \tag{10}$$

$$n - p - N = 0 \tag{11}$$

where n_i is the intrinsic carrier concentration and N is the doping concentration at the contact.

The finite element model depends on the voltage control of the diode, this means that at the contacts the boundary condition is that described by equation (12).

$$\psi(t) - \psi_b - \psi_D(t) = 0 \tag{12}$$

where $\psi(t)$ is the electrostatic potential at the contact boundary, ψ_b is the built in potential, and $\psi_D(t)$ is the applied contact voltage. The built in potential is the potential which results from the diffusion of carriers away from their donor atoms. Although ψ and ψ_D are denoted as time dependent, the finite element model solves the system for a specific contact voltage, not a time varying voltage, therefore the model will not depend on time.

Solving and rearranging equations (10), (11) and (12) and the built-in potential as defined in [1] for ψ, n and p gives equations (13), (14) and (15).

$$\psi = \psi_D + \frac{kT}{q} ln\left(\frac{\frac{N}{2} + \sqrt{\left(\frac{N}{2}\right)^2 + n_i^2}}{n_i}\right) \tag{13}$$

$$n = \frac{N}{2} + \sqrt{\left(\frac{N}{2}\right)^2 + n_i^2} \tag{14}$$

$$p = -\frac{N}{2} + \sqrt{\left(\frac{N}{2}\right)^2 + n_i^2} \tag{15}$$

The carrier concentrations for the first iteration of the solution solving process are the doping levels. The assumption is that the substrate is diffusion doped from both sides and that the doping falls off from the maximum of $10^{17} cm^{-1}$ exponentially towards the junction[2]. This should give a reasonable approximation to the actual doping.

III. The Finite Element Solution

A. Scaling

When solving a semiconductor problem the main difficulty is that of scaling, the carrier concentrations can vary by 6 or 7 orders of magnitude in a very small distance. Unfortunately this is exacerbated by trying to simulate a diode in reverse bias, where the depletion region has virtually no free carriers and the regions near the contacts have very high concentrations of carriers. To solve this problem scaling equations have to be set up. For the carrier concentrations, the geometry, the carrier mobilities and the diffusivities the maximum values are used as scaling constants, to give ranges of 0 to 1. For the potential, the scaling constant is given by Boltzmann's constant times 300 Kelvin divided by the electron charge.

B. Solving

The sub domain and boundary equations are solved using the finite element method in two dimensions. Firstly a mesh is formed across the geometry, this mesh is then refined around the junction since this is where the carrier concentrations will vary most rapidly. The equations are then converted into a weak form which is a form consisting of functionals which describe the sub domain and boundary conditions and include test functions. This weak form can then be changed directly into a matrix equation which can be solved for the solution vector, which describes the spatial distribution of the carrier concentrations and potential [2]. The software used to model and solve this system of equations was FEMLAB by COMSOL Inc. The charge concentrations after calculation are shown in figure (1).

IV. Capacitance Extraction

The obvious starting point when extracting capacitance from a model is the definition of capacitance itself (16). This differential version of the capacitance definition is used for calculating depletion region capacitance [3].

$$C = \frac{dQ}{dV} \tag{16}$$

Since the amounts of free charge on either side of the depletion region and the contact voltages are a fundamental part of the model, no further mathematical development is required.

The calculation begins by taking the integral of the free charge on either side of the depletion region at each voltage. The differences are then calculated between each voltage and resulting charge. Placing the charge and voltage differences in equation (16) gives two capacitances for each voltage, one for the anode and one for the cathode.

V. Conclusions

Starting from a knowledge of the geometry and doping levels the finite element method has been used to solve the carrier concentration distribution and electric potential in a silicon diode structure. The model was based on the solution of the Boltzmann transport equation together with the quasi-static form of Maxwell's equations. The junction was reverse biased and a varactor capacitance was extracted. The method used the charge - voltage definition of capacitance with data derived directly from the numerical solution. In the full paper two other methods of approximation will be included together with experimental results.

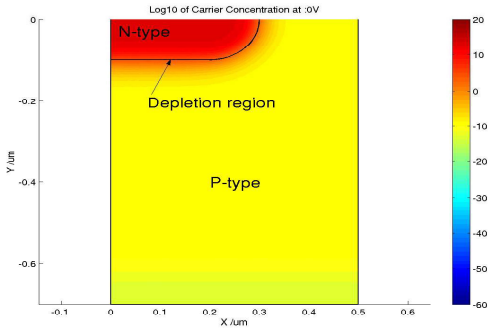

(a) 0V

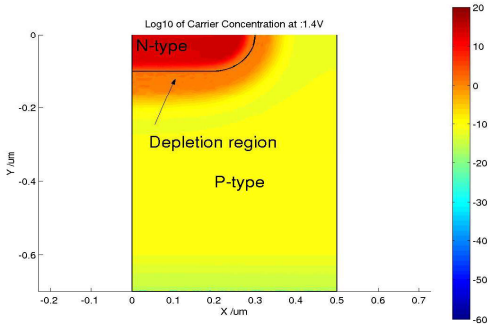

(b) -1.4V

Fig. 1. Charge concentrations at a) 0V and b) -1.4V

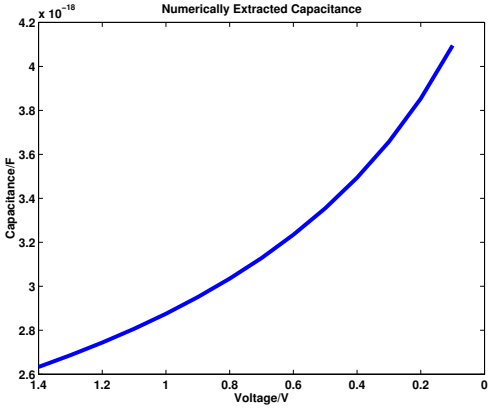

(a) Analytical Approximation and Numerical Calculation

Fig. 2. C-V Results

Acknowledgments

The authors would like to thank COMSOL and the Engineering and Physical Research Sciences Council for their support.

References

[1] S. Selbrherr, *Analysis and Simulation of Semiconductor Devices*, Springer-Verlag, Wien, 1984.

[2] Comsol, *FEMLAB - Model Library*, COMSOL, Inc, 2001.

[3] S. M. Sze, *Semiconductor Devices, Physics and Technology*, John Wiley & Sons, 2001.

COMPUMAG Saratoga Springs, New York USA
July 13 - 17, 2003

3D Capacitance Extraction of IC Interconnects Using Field Solvers and Homogenization Technique

Z. Ren and C. Lage
Cadence Design Systems, Inc.
555 River Oaks Parkway, San Jose, CA 95134
zren@candece.com, lage@cadence.com

***Abstract*—In the extraction and simulation of IC chips using electromagnetic field solvers, one of the difficulties is the modeling of the multilayered dielectric structures. The consideration of these thin layers in the field solvers increases dramatically the memory and the computation time. This paper presents a numerical homogenization strategy of multilayered dielectric media that allows removing the dielectric layers from the field solver models. A technique that transforms the homogenized anisotropic material to an isotropic material is also developed. This homogenization strategy has been applied in both the finite element method and a fast multipole expansion accelerated boundary element method. A case of 3D critical net capacitance extraction of a real digital chip is given as an example.**

***Index Terms*—VLSI circuit parameter extraction, homogenization of multilayered media.**

I. Introduction

In the modern design of IC chips, the shrink of circuit elements and the increase of operating frequency make the accurate determination of parasitic circuit parameters more and more critical in the analysis of the performance and the signal integrity of integrated circuits. Traditional extraction tools based on the pattern match techniques provide only limited accuracy in many cases, mainly because the important 3D effects cannot be accurately considered in such patterns. For that reason, electromagnetic field solvers play now a days a more and more important role in the extraction and simulation of IC chips. One of the applications consists in the accurate critical net circuit parameter extraction in the submicron IC chip design. In the IC application, due to the large scale of the problem, the computation speed is a crucial requirement. However, since the field solvers solve the partial differential equation or the integral equation with the numerical discretization, they are memory and time consuming. This limits their practical use in the IC extraction and simulation. The reduction of the memory and the acceleration of speed are very challenging in the development of field solvers, as the speed and accuracy are two (balanced) requirements in the IC area.

One of the difficulties encountered in the IC modeling is the multilayered dielectrics. Due to the field refraction and reflection on the interfaces of different materials, correct modeling using the field solvers requires meshing these layers (the finite difference method, the finite element method) or their interfaces (the boundary element method). This increases dramatically the memory and the computation time. In addition, the mesh quality of thin dielectric layers has a big impact on the accuracy of results. This increases the meshing difficulty. Since in the circuit extraction and simulation, we are mostly interested in the global phenomena rather than local filed distribution, the multilayered media can be homogenized without affecting the global behaviors of the circuit. An appropriate homogenization technique can significantly improve the performance of the field solvers.

In the case of planar layered media, there exists an analytical formula to determine the equivalent homogenized material. This formula is derived with the assumption of planar fields and cannot be directly used to our case due to the small size of interconnects which involves important corner singularity.

Another method concerns the use of dyadic Green's function in the layered media. It is widely used in the method of moment or the boundary element method to model the micro-strips (transmission lines) and the RF fields. It is also adapted to the static field case to extract parasitic circuit parameters [1]. The layered Green's function is derived in the spectral domain. The transformation of the layered Green's function from the spectral domain to the spatial domain requires the so called Sommerfeld integration which is very time consuming. In addition, the spatial layered Green's function is usually stored in a data file in a discrete form. This requires additional memory and the further interpolation that may introduce additional errors. Also, the layered Green's function cannot be applied to the field solvers which solve the local partial differential equation such as the finite difference or the finite element method.

In this paper, we present a numerical homogenization strategy to homogenize the multilayered media. The strategy is based on the homogenization for different metal layers using a numerical training technique, and the transformation of so obtained anisotropic media to the isotropic media with appropriate geometry transformation. The numerical training is performed with few 2D field calculations. The equivalent homogenized constant can be easily determined. This technique has been applied in both the finite element method and the FME (fast multipole expansion) boundary element method, and successfully used to the critical net extraction.

II. Homogenization Strategy

A typical IC chip process is composed of layered metal lines embedded in planar layered dielectric media (Fig.1). Each metal layer is surrounded by several dielectrics layers of very different dielectric constants and thicknesses.

With the assumption of planar fields, a structure of n planar layer dielectrics with the dielectric constant ε_i and the thickness d_i, can be homogenized in the horizontal (xy) and the vertical (z) directions, respectively, by the following analytical expressions:

$$\varepsilon_{xy} = \sum_{i=1}^{n} d_i \varepsilon_i \Big/ \sum_{i=1}^{n} d_i \,, \quad \varepsilon_z = \sum_{i=1}^{n} d_i \Big/ \sum_{i=1}^{n} d_i / \varepsilon_i \qquad (1)$$

As mentioned previously, above analytical expressions are not valid for the case of small size interconnects because of important corner singularity. Numerical determination of corner effect is hence necessary.

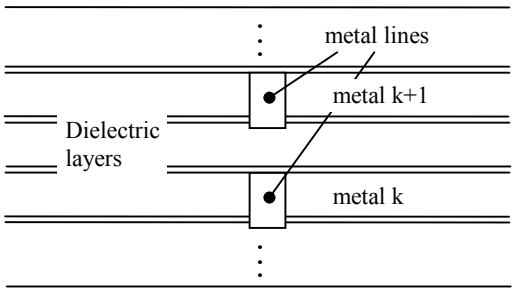

Fig.1. Typical structure of IC chip process.

On the other hand, in the IC process, the dielectric media surrounding the metal lines may be different from metal layer to metal layer, especially for the lower and upper metal layers. Homogenizations of the whole region at once averages the dielectric constants of all metal layers and ignore the local effect for different metal levels. That may introduce important errors.

Taking all these points account, the following numerical homogenization strategy is proposed.

1. Homogenization of dielectric layers for each metal layer and inter-metal layer using the expressions (1) and (2), together with a numerical correction. The numerical correction is performed using a 2D field solver training on few simple structures. This step gives an equivalent anisotropic dielectric constant for each metal layer and inter-metal layer.

2. Replacing the anisotropic constants of each metal layer and inter-metal layer by equivalent isotropic constants using the formula: $\varepsilon = \sqrt{\varepsilon_{xy}\varepsilon_z}$. The geometry of the layered structure is adequately transformed based on the energy balance before and after the transformation.

3. Homogenization of layered isotropic dielectrics resulting from the step 2 on the whole process. An equivalent anisotropic dielectric material is obtained for the whole process.

4. Replacing the anisotropic constants of the whole process by equivalent isotropic constant with corresponding geometrical transformation.

5. Modifying the thickness of metal layers and the distance of inter-metal layers by appropriate constants to take into account the local effect for different metal layers.

It can be noted that, the equivalent homogenized media obtained after each step can be applied to field solvers such as the finite element method with the decreasing meshing difficulty. Whereas for the method which solves global integral equation such as the boundary element method, only the isotropic constant can be used.

Finally, note that the homogenization is performed only one for a given IC process and can be used for the extraction and simulation the entire circuits.

III. Example of a Critical Net Extraction

Fig. 2 shows a interconnect structure around a given (critical) net of a digital IC chip. The critical net is highlighted in dark. Note that in this process, there are 6 layers of metal nets embedded in about 30 layers of dielectric media. For the reason of clarity, the layered media are not shown. The problem consists of calculating the self capacitance of the critical net and the coupling capacitances with its neighbors.

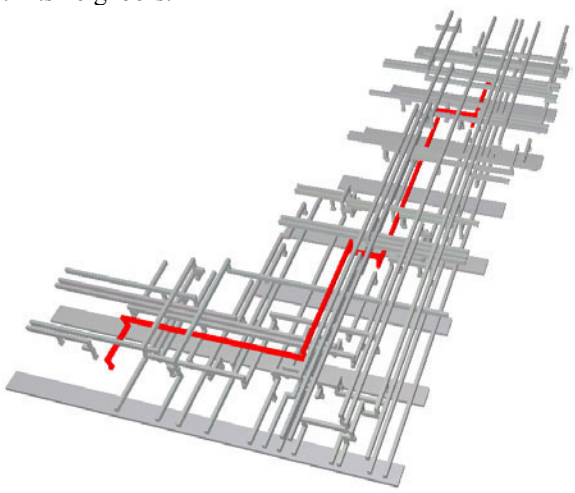

Fig.2. Interconnect structure around a critical net of an IC chip.

The problem is solved using both the finite element method using the dual formulations [2] and a fast multipole expansion accelerated boundary element method [3]. The homogenized isotropic dielectric constant is obtained by the previously described strategy. The self capacitances of the critical net given by the FEM and BEM are respectively 7.35fF, 7.29fF, which are to be compared to 7.30fF obtained on the original structure by a field solver based on the stochastic approach [4] with an uncertainty of 0.4% (standard deviation).

Details and more results will be reported in the full paper.

In order to promote the practical use of the field solver in the IC area, we intend to propose this example as a benchmarking in the COMPUMAG Society.

IV. References

[1] J. Zhao, W. W.-M. Dai, S. Kapur and D. E. Long, "Efficient three-dimensional extraction based on static and full-wave layered green's functions", Proceedings of the 35th Design Automation Conference, June, 1998

[2] Z. Ren and A. Razek "Computation of 3-D electromagnetic field using differential forms based elements and dual formulations", *Int. J. Numerical Modelling, Electronic Networks, Devices and Fields*, Vol. 9, Nos 1& 2, January-April 1996, pp.81-98

[3] M. Bachtold, M. Spasojevic, C. Lage, P. B. Ljung, "A system for full-chip and critical net parasitic extraction for ULSI interconnects using a fast 3D field solver", *IEEE Trans .Computer-Aided Design*, Vol.19, No.3, 2000, pp.325-338

[4] Y. L. Le Coz and R. B. Iverson, "Stochastic algorithm for high speed capacitance extraction in integrated circuits", *Solid State Electron.* Vol. 35, No.7, 1992, pp.1005-1012

Worst-case tolerance analysis in static field problems

L.Egiziano, G.Spagnuolo
DIIIE - Università di Salerno
Via Ponte Don Melillo, Fisciano (SA), Italy
spanish@ieee.org

M.Vitelli
DII - Seconda Università di Napoli
Real Casa dell'Annunziata, Aversa (CE), Italy
vitelli@unina.it

***Abstract* – An evolutionary approach to worst-case analysis of static field problems ruled by Poisson equation, over suitable spatial domains and with appropriate boundary conditions, is presented. It ensures a better estimation of the true worst case especially if parameters are affected by large uncertainties and whenever the performance function is non-linear or, even worse, non-monotonical with respect to parameters.**

I. Introduction

Nowadays, in systems' design the analysis of performances in presence of parameters' variations is rising to a central role. In fact, on one side it is important to evaluate the maximum tolerances of parameters ensuring that the customer specifications are still not violated. On the other side, the analysis of the effects of the variation of input design parameters in specific intervals or ranges allows to test the performance of different design solutions and to carry out safety or reliability analysis. This paper is focused on the Worst-Case Analysis (WCA) of static field problems ruled by Poisson equation over suitable spatial domains with appropriate boundary conditions. WCA assumes that the variations of parameters within their own ranges are uncorrelated and uniformly distributed. The analysis is usually performed by running a sufficiently high number of Monte Carlo (MC) trials, with a considerable amount of computation time. In this paper, an efficient Evolutionary Algorithm (EA) – based approach to WCA is presented. Its performances are tested by means of a pilot example outlined in Section II.

II. Formulation of the pilot example

As test problem, the 2-D L-shaped domain Ω, with boundary $\partial\Omega$, filled with a isotropic, homogeneous insulating material of permittivity ε depicted in fig.1 has been considered [1].

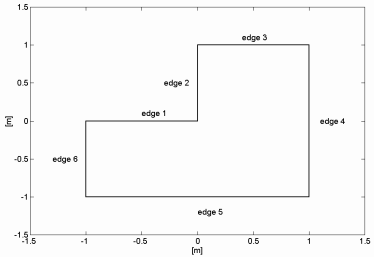

Figure 1: L-shaped domain Ω adopted for simulations

The Poisson problem (1) in Ω is:

$$\begin{aligned} &\nabla^2 V(x,y) = -\frac{\rho(x,y)}{\varepsilon} && (x,y)\in\Omega \\ &V(x,y) = f(x,y) && (x,y)\in\partial\Omega_1 \\ &\frac{\partial V(x,y)}{\partial n} = g(x,y) && (x,y)\in\partial\Omega_2 \end{aligned} \qquad (1)$$

Dirichlet boundary conditions have been assigned on $\partial\Omega_1$=edge1∪edge2∪edge3∪edge5, while Neumann boundary conditions have been assigned on $\partial\Omega_2$=edge4∪edges6. In the sequel, the following ranges for the Dirichlet boundary conditions are accounted for:

$$\begin{aligned} &f(x,y) = [9,11]\ \text{V} && (x,y)\in \text{edge1}\cup\text{edge2}\cup\text{edge3} \\ &f(x,y) = [90,110]\ \text{V} && (x,y)\in \text{edge5} \\ &g(x,y) = 0 && (x,y)\in \text{edge4}\cup\text{edge6} \end{aligned} \qquad (2)$$

The potential distribution V(x,y) is calculated by FEA: a mesh including N=150 nodes has been used.

The WCA puts in the determination of the range of values assumed by V(x,y) if the permittivity ε, the volume charge density ρ and the Dirichlet boundary conditions span variation intervals. By solving WCA problems using statistical approaches, such as MC, results into an underestimation of the TWC. The main MC limit is in the big amount of trials required to get a "good solution", namely close to the True Worst Case (TWC). If the potential distribution V(x,y) is an implicit function of parameters, its non-linearity and/or its non-monotonicity within the parameters' ranges of variation is not easily foreseen. Consequently, it becomes very difficult to catch by MC analysis the combination of parameters corresponding to maxima and minima of V. Moreover, it is not easy to foresee the minimum number of MC trials needed to obtain a quite good estimation of the TWC. Nevertheless, if the set of parameters to be tested is not chosen purely randomly, as in the MC analysis, but trying to select the combinations which likely give the solutions closest to the TWC, the analysis should be more fruitful. To this aim, an index expressing the contribution given to the worst-case by the solution obtained taking each combination of parameters can be useful to drive a global optimization method. Evolutionary Algorithms (EA) can be of great help in performing this task; in Section III the EA used to perform the WCA is outlined.

III. The evolutionary algorithm-based WCA

The EA works on a population of real-coded individuals represented by a vector of three real values $[\varepsilon,\rho(x,y),f(x,y)]$. Each set of parameters, or individual, corresponds to a potential distribution V(x,y) in the N points of the chosen mesh. Consequently, a Worst-Case Envelope (WCE) can be built up for each EA generation, collecting the potential maps of all the individuals of the population and picking the maximum and the minimum values in each node. Referring to the evaluation of the upper bound of the worst case, the fitness associated to each individual is given by the sum of

the improvements that the solution exhibits in those nodes where it overcomes the WCE obtained up to the current generation. Afterwards, the WCE is updated according to the current population and then the population is evolved and the offspring takes the place of the parents. Note that the current WCE is not given by an only set of parameters: it is a collection of the best parts of all the solutions explored during the evolution. The same operation has to be repeated for the lower bound, thus getting the whole estimation of the TWC.
The algorithm has been implemented in MATLAB®, adopting standard EA operators (selection, crossover and mutation). In the next section numerical results are presented and discussed.

IV Results and discussion

Two test cases taken from [1] have been considered to show the reliability of the proposed EA-based technique.
Firstly, the case taken from [1], exhibiting the variations (2) and (3) has been considered:

$$\begin{aligned}
&\rho_{max}(x,y) = (2\cdot10^{-8} - 8\cdot10^{-8}\cdot x^{9} - 4\cdot10^{-8}\cdot y^{12})\frac{C}{m^3} && (x,y)\in\Omega \\
&\rho_{min}(x,y) = (-8\cdot10^{-8}\cdot x^{9} - 4\cdot10^{-8}\cdot y^{12})\frac{C}{m^3} && (x,y)\in\Omega \\
&\varepsilon \in [2\varepsilon_0, 10\varepsilon_0]
\end{aligned} \tag{3}$$

It is worth noting that, even if the constitutive relation in (3) is linear, the electric potential dependence on parameters is non-linear. Nevertheless, this case has been chosen since the exact solution has been evaluated in [1], so that the reference solution is just available. Simulation results of the WCA are reported in fig.2, where the potential values are plotted versus mesh node numbers. The EA solution obtained by evolving a population of 80 individuals over 200 generations (16000 potential map evaluations for the upper bound and the same number for the lower bound) is almost coincident with the exact TWC [1] and it is sensibly larger than the corresponding MC solution obtained with 32000 trials, as evident from fig.3.
The second test case considered refers to a non-linear problem in which the dielectric permittivity depends on the electric field *E* by means of the function depicted in fig.4.
Summarizing:

$$\begin{aligned}
&\rho_{max}(x,y) = (2\cdot10^{-8} - 8\cdot10^{-8}\cdot x^{9} - 4\cdot10^{-8}\cdot y^{12})\frac{C}{m^3} && (x,y)\in\Omega \\
&\rho_{min}(x,y) = 0.1\cdot(-8\cdot10^{-8}\cdot x^{9} - 4\cdot10^{-8}\cdot y^{12})\frac{C}{m^3} && (x,y)\in\Omega \\
&\varepsilon = 2 + [0,1]\cdot nl(E)
\end{aligned} \tag{4}$$

Discrepancies between MC ($6\cdot10^4$ trials) and EA (population =100, generations=300) for the upper and lower bounds are reported in fig.5. In this involved case, neither vertex analysis nor MC gives a good estimation of the TWC, while the EA greatly improves the MC result within the same computation time.

V. Conclusions

In this paper, the worst-case tolerance analysis of static field problems ruled by Poisson equation, over suitable spatial domains and with appropriate boundary conditions, is afforded by means of an evolutionary algorithm. Results are encouraging in terms of computation time and accuracy if compared with those ones obtained by classical Monte Carlo analysis.

References

[1] M. Vitelli: "Range analysis in electroquasistatic field linear problems", in print on IEEE Trans on DEI.

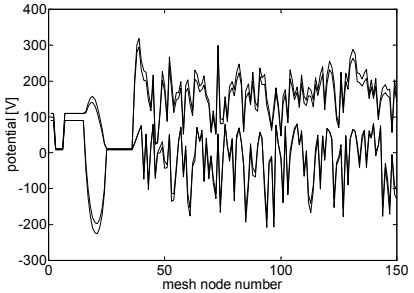

Figure 2. Potential distribution: thin line=MC, thick line=EA.

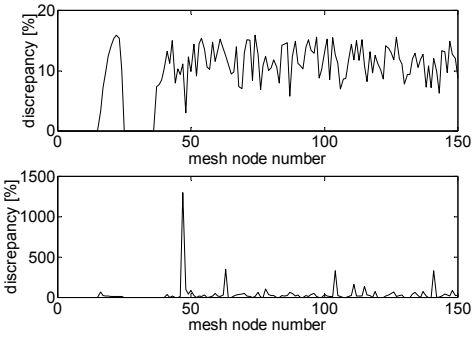

Figure 3. Potential discrepancy MC vs EA on upper bound and lower bound.

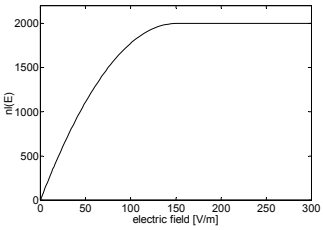

Figure 4. Non-linear contribution to permittivity

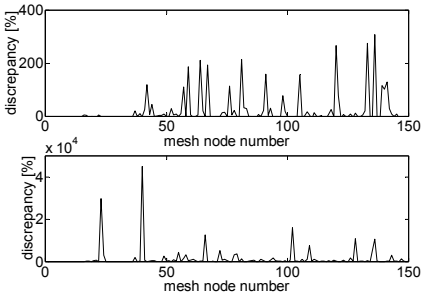

Figure 5. Potential discrepancy MC vs EA on upper bound and lower bound.

COMPUMAG Saratoga Springs, New York USA
July 13 - 17, 2003

Electrostatic Imaging Via Conformal Mapping

Ibrahim Akduman
Istanbul Technical University
Electrical and Electronics Engineering Faculty
80626 Maslak, Istanbul, Turkey

Abstract- **We present the solution of an inverse boundary value problem for harmonic functions arising in electrostatic imaging through conformal mapping techniques. The numerical method consists of two parts. In a first step, by successive approximations a nonlinear equation is solved to determine the boundary values of a holomorphic function on the outer boundary circle of an annulus. Then in a second step an ill-posed Cauchy problem is solved to determine the holomorphic function in the annulus. We establish a convergence result for the iteration procedure and through numerical examples we illustrate the feasibility of the method.**

I. Definition of problem and its solution

The modelling of electrostatic, magnetostatic, or thermal imaging methods in non-destructive testing and evaluation leads to inverse boundary value problems for the Laplace equation. In principle, in these applications an unknown inclusion or crack within a conducting medium is assessed from overdetermined measurements on the accessible part of the boundary of the medium. In this paper, as a model case we consider the inverse problem to determine the shape of a perfectly conducting inclusion or a perfectly conducting crack within a two-dimensional homogeneous conducting medium in the electrostatic case. To this aim a second perfectly conducting test cylinder with boundary curve Γ_1 is located in the same medium. Then one impose a voltage pattern f at a number of electrodes attached to the boundary Γ_1 and measure the resulting currents through electrodes. The inverse problem is then to reconstruct the boundary of the unknown body, say Γ_0, through the given voltage and current data.

In the region between the curves Γ_0 and Γ_1, say D, the potential distribution u satisfies the Laplace equation

$$\Delta u = 0 \quad \text{in } D \tag{1}$$

with boundary condition

$$u = 0 \quad \text{on } \Gamma_0, \quad u = f \quad \text{on } \Gamma_1. \tag{2}$$

The inverse problem we are concerned with is: Given the Dirichlet data f on Γ_1, i.e., an imposed voltage on the accessible outer boundary Γ_1 of the conducting medium, and the (measured) Neumann data

$$g := \frac{\partial u}{\partial \nu} \quad \text{on } \Gamma_1, \tag{3}$$

i.e., the resulting currents on Γ_1, determine the shape of the boundary Γ_0.

For a survey of some of the various methods that have been developed and used for solving inverse boundary value problems for the Laplace equation we refer to [1-3]. Our approach is based on the conformal mapping of the domain D onto an annulus $B := \{z \in \mathbb{C} : \rho < |z| < 1\}$ with radius $0 < \rho < 1$. The two components of the boundary of B are denoted by $C_0 := \{z \in \mathbb{C} : |z| = \rho\}$ and $C_1 := \{z \in \mathbb{C} : |z| = 1\}$. By the conformal mapping theorem there exists a uniquely determined radius ρ of the annulus and a holomorphic function Ψ that maps B bijectively onto D such that the boundaries C_0 and C_1 are mapped onto Γ_0 and Γ_1, respectively. The problem is then reduced to the determination of the mapping function Ψ through the given voltage and current values on the boundary Γ_1. The numerical method that we developed to obtain the mapping function consists of two parts. In a first step, by successive approximations a nonlinear equation is solved to determine the boundary values of a mapping function on the outer boundary C_1 of the annulus. During this steps one gets also the unknown radius ρ of the inner circle of the annulus. Then by solving an ill-posed Cauchy problem we determine the mapping function in the whole annulus through its Laurent expansion. The coefficients of the resulting Laurent expansion are determined by the measured data. By replacing the points of the inner circle C_0 one gets the unknown curve Γ_0 with simple calculations.

II. Numerical results

In this section we present the results of some numerical experiments in order to show the accuracy and effectiveness of the reconstruction method described above. For the sake of simplicity, the test boundary Γ_1 is chosen as the unit circle. The data which should be collected by real measurements are calculated synthetically by solving the direct problem defined by (1) and (2) through the double

layer potential approach. To this aim the field u in D is represented as the sum of appropriately modified double layer potentials due to double layer densities on the boundaries Γ_0 and Γ_1 [1] . The use of the jump relations on the boundaries Γ_0 and Γ_1 yields a system of coupled integral equations of the second kind for the related double layer density functions, which can be solved through the Nyström method [1]. In what follows, all the examples are constructed for the boundary data

$$f(t) = 3 + 2\cos^2 t, \quad t \in [0, 2\pi]. \tag{4}$$

Figure 3 shows the exact and reconstructed curves for a kite-shape boundary given by the parametrization

$$\Gamma_0 = \{(0.2+0.3\cos t+0.15\cos 2t-0.15, 0.3\sin t) : t \in [0, 2\pi]\}. \tag{5}$$

The inner radius of the annulus B for this case is $\rho = 0.32504404$.

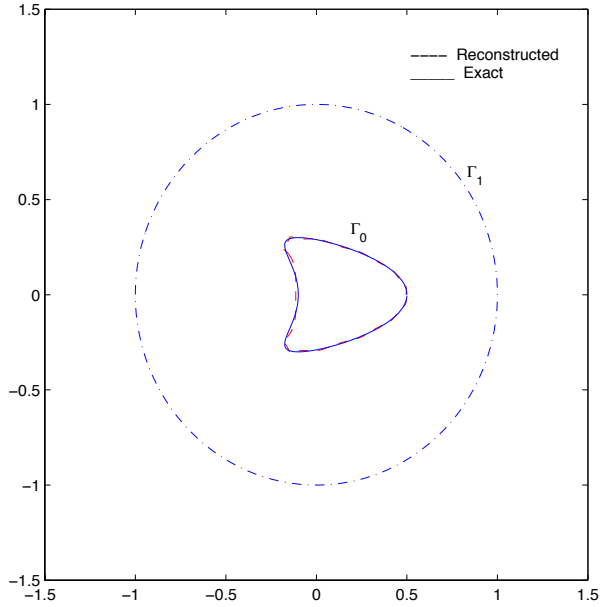

Figure 1: Exact and reconstructed curves for the boundary data (4) and Γ_0 given in (5)

Note that the reconstruction in the above example is achieved with the data which contain only computational errors in the solution of related direct problem. We also check the sensitivity of the method to noise by adding %10 random noise to the Neumann data on Γ_1. The exact and reconstructed values of Γ_0 with parametrization

$$\Gamma_0 = \{(0.2 + 0.3\cos t, 0.5\sin t) : t \in [0, 2\pi]\}. \tag{6}$$

are illustrated in Figure 2. The reconstruction is made for 15 iterations and $\rho = 0.41092673$. From these figures we observe that the method yields quite satisfactory results.

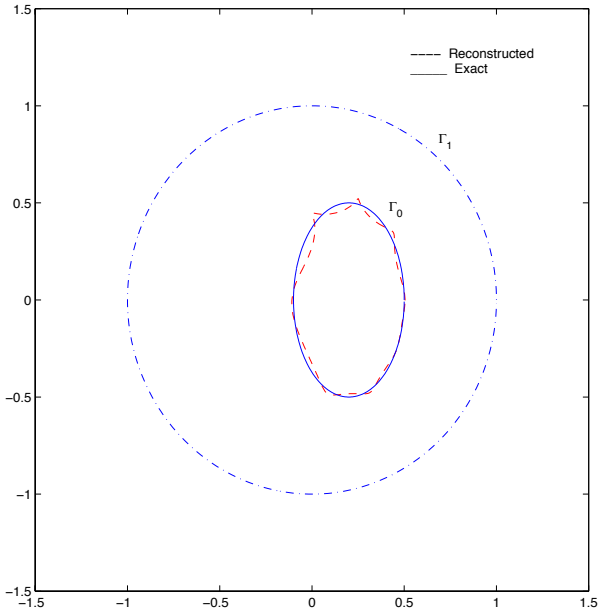

Figure 2: Exact curve of Γ_0 given in (4.5) and its reconstruction obtained by the Neumann data which contains %10 random noise.

References

[1] R. Kress: *Linear Integral Equations,* Springer-Verlag, New York 1999.

[2] R. Kress: "Inverse boundary value problems in potential theory," Cubo Mathematica Educational **3**, 393–414, 2001.

[3] M. Idemen and I. Akduman "Some geometrical inverse problems connected with two-dimensional static fields," SIAM J. Appl. Math. **48**, 703–718, 1988.

Source Region Contracting Method for EEG Source Reconstructions

J. Zou, Y. Q. Xie, J. S. Yuan, X. S. Ma
Department of Electrical Engineering, Tsinghua University, Beijing, 100084, China
zoujun@tsinghua.edu.cn
X. Cui
Department of Electrical Engineering, North China Electric Power University, Baoding, Hebei, 071003, China
hjbdcuix@heinfo.net

Abstract— **A new EEG source reconstruction method is presented. The method reduces the number of unknown quantities of the basic EEG equation by contracting the source region iteratively. The equation system turns from an underdetermined system to an overdetermined system step by step. At last the least square algorithm is used to get a unique solution. The simulation shows that a high-resolution result can be obtained by using the method proposed.**

INTRODUCTION

The electroencephalogram (EEG) inverse problem is to estimate the information about the source inside the brain from the measured electric potential distribution on the surface of the scalp. The Low resolution electromagnetic tomography algorithm (LORETA) is a representative linear method for the source locating of EEG [1]. However, it can only acquire a low-resolution tomography. In order to get a high-resolution tomography, a new method to reconstruct the source tomography by contracting the source region iteratively is presented. The simulation and the experimental result prove the effectiveness of the method proposed.

SOURCE REGION CONTRACTING METHOD

Similar with LORETA source estimation approach, the source region is divided into M grids. If the grids are dense enough, it can be assumed that the dipole source can only locate on each of the grid points. The dipole sources with different strengths and directions can be expressed as the linear combination of the unit dipoles along x, y, z directions. N observed points are placed on the scalp outside the source region. Thus the relationship between the strength of the unit dipoles along the x, y, z directions at each grid point and the potential at the observed points can be written as

$$\boldsymbol{v} = \boldsymbol{K}\boldsymbol{J} \tag{1}$$

where $\boldsymbol{J} = [\boldsymbol{j}_1^T, \boldsymbol{j}_2^T, \cdots, \boldsymbol{j}_M^T]^T$ is a vector with $3M$ ranks comprised of the current densities $\boldsymbol{j}$ (3-vector) at M points with known locations inside the brain volume; $\boldsymbol{v} = [v_1, v_1, \cdots, v_N]^T$ is the vector with N ranks comprised of measurements. $\boldsymbol{K}_{N\times 3M}$ is the transfer matrix with $N \times 3M$ ranks, that is, $\boldsymbol{K} = [\boldsymbol{k}_1, \boldsymbol{k}_2, \cdots, \boldsymbol{k}_{3M},]^T$, where $\boldsymbol{k}_i$ is the vector with N ranks. Generally speaking, the coefficients of $\boldsymbol{K}$ must be calculated by the numerical method, saying the finite element method, however, the analytical expression is available for the sphere model of brain [2]. The simultaneous equation group of (1) is an underdetermined system due to $3M > N$, so a generalized weighted minimum-norm scheme is utilized to make the solution of the source distribution concentrate inside the brain as possible, that is,

$$\boldsymbol{J} = \boldsymbol{W}(\boldsymbol{K}\boldsymbol{W})^{+}\boldsymbol{v} \tag{2}$$

where $\boldsymbol{W}$ is a $3M \times 3M$ diagonal matrix with $W_{ii} = \|\boldsymbol{k}_i\|$. The superscript '+' denotes the pseudo-inverse of matrix and the symbol $\|\cdot\|$ represents of the infinite norm of a vector. It is no doubt that only low-resolution tomography can be obtained in this way. However, such low-resolution tomography contains the useful information about the source location and strength to a certain extent. According to the result of physiological study, the source inside the brain is sparse, synchronized and highly concentrated. When one deals with a set of measured data with the consideration of above assumptions, a low-resolution tomography can be obtained by (2) at first. Based on this tomography, one can find some grid points that have less possibility to be the position of the dipoles. For example, these grid points, whose strength is less than 1% of the maximal strength of the current source distribution, are excluded from the source region. Thus, the source region concerned is contracted; as a

result, the number of elements of $\boldsymbol{J}$ is also reduced and the corresponding columns should be deleted from the matrix $\boldsymbol{K}$. By using the matrix $\boldsymbol{K}$ newly obtained, a new tomography could be acquired by (2) again. From this new tomography, some grid points will be excluded from source region again, which leads the rank of $\boldsymbol{J}$ to decrease further. By repeating the above approach, the simultaneous equation system will turn from an underdetermined system to a determined system step by step, or even to an overdetermined system, from which one can use the least square algorithm to locate the source position. In fact, in order to suppress the influence of noise in the experimental data, a truncated singular value decomposition technology (TSVD) is used as follows.

$$\boldsymbol{J} = \boldsymbol{W}\sum_{i=1}^{N}\left(\frac{1}{\lambda_i} p_i q_i^T\right)\boldsymbol{v}, \qquad |\lambda_i| \geq \frac{1}{\max_i |\lambda_i|} \tag{3}$$

where p_i and q_i are the element of right and left singular vector of $\boldsymbol{KW}$ respectively. It should be noted that TSVD improves the numerical stability dramatically.

NUMERCIAL EXAMPLES

For a sphere model of the brain with the constant conductivity σ, if two current dipoles with the unit strength are placed inside the brain, the numerical simulation results are shown in Fig.1, where Fig.1(a) is the tomography reconstructed by (2) directly, Fig.1(b) is the result by using the contracting source region method 3 times and Fig.1(c) is the final tomography after using the method 7 times. Obviously, it is a very satisfying result for EEG problem. In addition, we also verify the method proposed by using the experimental data. The brain is modeled by a lampshade filled with the NaCl liquor. The current dipole substituted by two sliver sphere with small gap is placed at the coordinate of $(2,0,0)$ cm along the positive direction of x axis and measured potential points in XOY plane is marked by $1,2,\cdots,38$ as shown in Fig.2 (a). The measured voltages are shown in Fig.2 (b) and Fig.2(c) is the final tomography. The details of experiment and the comparison between the method proposed and other existed methods are omitted in purpose because of the length restriction and will be reported in the extended paper.

CONCLUSION

A source region contracting method is presented to reconstruct the EEG tomography. The further work is to verify the method with the real head model and data obtained from the hospital.

REFERENCES

[1] R. D. Pascual-Marqui et al. "Low resolution electromagnetic tomography: a new method for localizing electrical activity in the brain", *Inter. Journal of Psychophysiology*, vol.18, pp.49-55, 1994.

[2] J. C. De Munck. "The potential distribution in a layered anisotropic spheroidal volume conductor." *Journal of applied physics*, vol.64, pp.464-470, Feb., 1988.

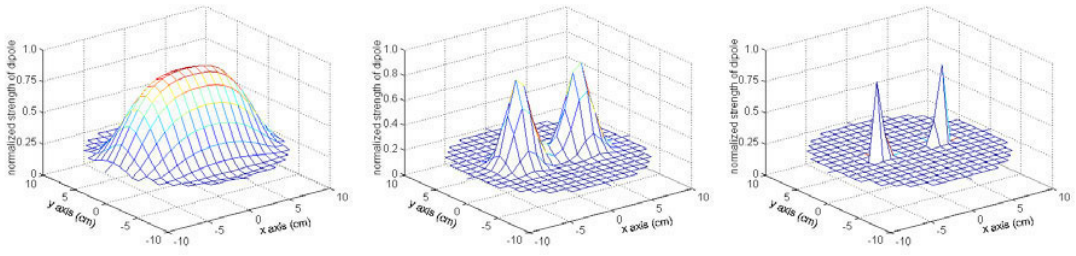

(a) (b) (c)

Fig.1 Simulation of two sources inside the brain by source region contracting method

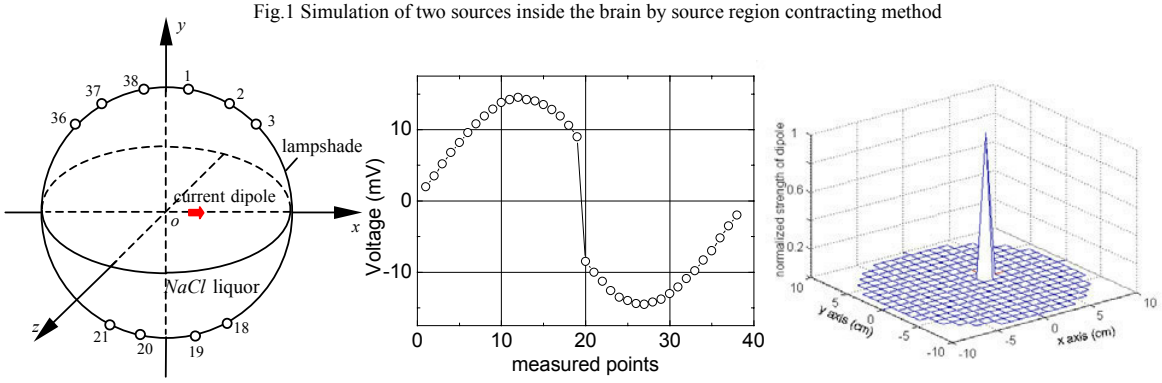

(a) (b) (c)

Fig.2 Results of the source region contracting method with experimental data

Estimation of Multi-Layer Earth Structure by Using Complex Image Method

Bo Zhang, Xiang Cui, *Senior Member, IEEE*, and Lin Li
Department of Electrical Engineering, North China Electric Power University
No. 204, Qingnian Road
Baoding, Hebei, 071003 China
E-mail: hjbdcuix@heinfo.net

***Abstract*—Based on the local searching algorithm, an efficient method for estimating earth structure with any number of layers from Wenner's four-probe test data is presented. Green's function is approximated by an analytical expression by using complex image method. Partial differentials' values of the Green's function to the earth parameters, which were formerly obtained by solving integrals with infinite limit by numerical integration, are obtained directly from the approximating expression. Thus, with the method, not only a satisfied result is obtained, but also the computation time is shortened.**

INTRODUCTION

The earth structure is one of the necessary data for the design of a safe grounding grid under the substation. Usually the earth can be approximated by a horizontally stratified multi-layer structure. Since the earth structure determines the voltage distribution on the earth surface due to the current injected into the earth, by using a set of Wenner's four-probe test data which is a set of voltage values measured on the earth surface due to the injected current, the multi-layer earth structure can be estimated by solving an electric field inverse problem.

Some methods for estimating two or three layers earth structure have been developed [1]. But two or three layers structure is not always enough to reflect the practical situation. In fact, the number of the layers can be any positive integer as long as the combination of the number of layers and the parameters of the layers is the best one to approximating the Wenner's test data. What's more, because the local searching algorithm is used, in each iterative procedure, partial differentials' values of the Green's function to the parameters of each layer should be determined once again. However, there exists an integral with infinite limit in the Green's function. To get the partial differentials' values, some authors used numerical integration that needs to find a large enough value as the upper limit for the corresponding integral to insure preciseness. Thus, the computation time was very long.

This paper presents an efficient method for estimating earth structure with any number of layers from Wenner's test data. In each iterative procedure, the corresponding Green's function is approximated by an analytical expression by using complex image method. A new method is presented to determine the partial differentials' values of the Green's function to the earth parameters directly from the approximating expression. Thus, not only a satisfied result is obtained, but also the computation time is shortened.

PRINCIPLES

Green's function on the earth surface When both the current source and the observation point are located on the surface of the earth with any number of layers, the Green's function of the electric protential can be expressed by:

$$V = \rho_1 I[r^{-1} + \int_0^\infty f(\lambda) J_0(\lambda r) d\lambda] / 2\pi \,, \qquad (1)$$

where I is the current injected into the earth, r is the distance between the current source and the observation point, $J_0(\lambda r)$ is the first kind of zero order Bessel's function, $f(\lambda) = \alpha_1(\lambda) - 1$,

$$\alpha_1(\lambda) = 1 + \frac{2K_1 e^{-2\lambda h_1}}{1 - K_1 e^{-2\lambda h_1}},\ K_1(\lambda) = \frac{\rho_2\alpha_2 - \rho_1}{\rho_2\alpha_2 + \rho_1},$$

$$\alpha_2(\lambda) = 1 + \frac{2K_2 e^{-2\lambda h_2}}{1 - K_2 e^{-2\lambda h_2}},\ K_2(\lambda) = \frac{\rho_3\alpha_3 - \rho_2}{\rho_3\alpha_3 + \rho_2},$$

$$\ldots, \qquad \ldots,$$

$$\alpha_{N-1}(\lambda) = 1 + \frac{2K_{N-1} e^{-2\lambda h_{N-1}}}{1 - K_{N-1} e^{-2\lambda h_{N-1}}},\ K_{N-1}(\lambda) = \frac{\rho_N - \rho_{N-1}}{\rho_N + \rho_{N-1}},$$

h_i (i=1, 2, . . . , N-1) and ρ_i (i=1, 2, . . . , N) are the thickness and the resitivity of the *ith* layer respectively, and N is the number of layers which can be any positive integer.

Wenner's test and apparent resitivity Wenner's four-probe test data are often used to estimate the earth srtucture as shown in Fig.1. Details of the test can be seen in [1]. From Wenner's test data and supposing the data have M values, a set of apparent resitivities varied with l is defined as:

$$\rho_r^t = 2\pi l V / I \,. \qquad (2)$$

With the same definition, another set of theoretical apparent resitivities can be obtained from (1) as following :

$$\rho_r^c = 2\rho_1 \left\{ (2l)^{-1} + \int_0^\infty f(\lambda)[J_0(\lambda l) - J_0(2\lambda l)] d\lambda \right\}. \qquad (3)$$

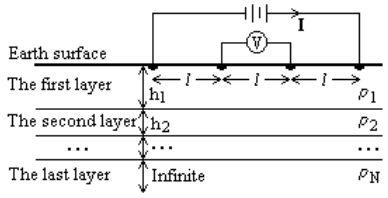

Fig. 1. Wenner's test method and the multi-layer earth structure

Then, an object function is set up by the least square method:

$$\varphi(\rho_1,\rho_2,\cdots,\rho_N,h_1,h_2,\cdots,h_{N-1})=\sum_{i=1}^{M}[(\rho_{r_i}^t-\rho_{r_i}^c)^2\Big/\rho_{r_i}^{c^2}]. \quad (4)$$

Based on the local searching algorithm, the most satisfied parameters h_i and ρ_i can be determined by minimizing φ.

Complex image method It is difficult to get the value of ρ_r^c. In this paper, complex image method [2] is used to solve this problem. That is, $f(\lambda)$ is approximated by a series of complex exponentials by Prony's method [2]:

$$f(\lambda)\approx\sum_{i=1}^{n}b_i e^{a_i\lambda}, \quad (5)$$

where a_i and b_i are complex values. Then, by using Lipschitz integration:

$$\int_0^\infty e^{-c\lambda}J_0(\lambda l)d\lambda=(c^2+l^2)^{-1/2}, \quad (6)$$

ρ_r^c is approximated as:

$$\rho_r^c=2\rho_1\left\{(2l)^{-1}+\sum_{i=1}^{n}b_i\left[(a_i^2+l^2)^{-1/2}-(a_i^2+4l^2)^{-1/2}\right]\right\}. \quad (7)$$

Partial differentials of the Green's function Because the local searching algorithm is used, in each iterative procedure, partial differentials' values of ρ_r^c to the earth parameters should be determined. In this paper, these values are obtained directly from (7) with the help of (5), not from (3) by solving corresponding integral with the help of numerical integration after the partial differentials of $f(\lambda)$ are obtained [1]. Form (7), it can be seen that the partial differentials' values of ρ_r^c can be determined easily if those of a_i and b_i are determined. From (5), the following equation can be obtained :

$$\frac{\partial f(\lambda)}{\partial p}=\sum_{i=1}^{n}(c_i e^{a_i\lambda}+\lambda b_i d_i e^{a_i\lambda}), \quad (8)$$

where $p=\rho_1,\rho_2,\cdots,\rho_N,h_1,h_2,\cdots,h_{N-1}$, $c_i=\dfrac{\partial b_i}{\partial p}$, $d_i=\dfrac{\partial a_i}{\partial p}$.

In (8), $\dfrac{\partial f(\lambda)}{\partial p}$ can be accurately deduced directly from the expression of $f(\lambda)$ in (1), $\rho_1,\rho_2,\cdots,\rho_N,h_1,h_2,\cdots,h_{N-1}$ are the known quantities in each iterative procedure, and a_i and b_i can also be obtained by Prony method, only c_i, d_i and λ are the unknown variables. Because (5) approximates $f(\lambda)$ along λ-axis very well, for each earth parameter, we let λ be equal to $2n$ different values in (8) and get $2n$ linear equations with $2n$ unknown variables: c_i and d_i (i=1, 2, . . . , n). By solving the equations, c_i and d_i can be obtained. Then, the partial differentials' values of ρ_r^c can be determined from (7).

Determination of initial values According to the computation experiences and the principles of the apparent resistivities, the suitable number of the layers must be larger than the total number of wave crests and troughs in the distribution of the apparent resistivities along with different l, ρ_i must be larger than the wave crest or smaller than the trough, and h_i must be no larger than the l of the wave crest or troughs. Based on the above analysis, a method to estimate the suitable number and the initial parameters of the layers is developed. Detials will be presented in the extended paper.

RESULTS

Table I shows the earth parameters determined from the measured apparent resistivities shown in Fig. 2 (a). Both the measured apparent resistivities and their calculated results by (7) are shown in Fig. 2 (a), the root-mean-square error between them is 3.633%. Fig. 2 (b) shows the comparison of $f(\lambda)$ between the exact values and the approximated values by (5) with the earth parameters shown in table I.

TABLE I. THE CALCULATED RESULT OF THE EARTH PARAMETERS

Layer Number	Resistivity(Ωm)	Thickness(m)
1	71.13	1.169
2	619.5	0.2809
3	7.278	1.119
4	387.4	1.938
5	7.625	1.916
6	119.4	Infinite

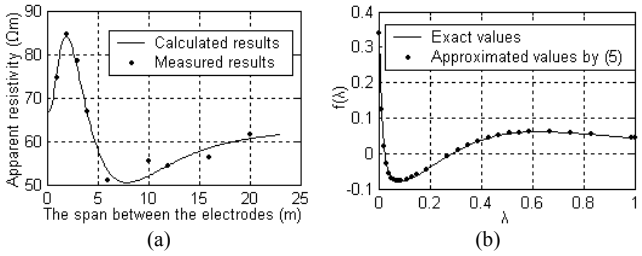

Fig. 2. Some comparison results

CONCLUSION

This paper presents a fast and efficient method for estimating earth structure with any number of layers from Wenner's four-probe test data. By using complex image method, the values of the Green's function and its partial differentials to the earth parameters can be obtained easily and quickly.

REFERENCES

[1] Huina Yang, Jiansheng Yuan, and Wei Zong, "Determination of three-layer earth model from Wenner four-probe test data," *IEEE Transactions on Magnetics*, vol. 37, pp. 3684-3687, September 2001.

[2] Y. L. Chow, J. J. Yang, and K. D. Srivastava, "Complex images of a ground electrode in layered soils," *J. Appl. Phys.*, vol. 71, pp. 569-574, January 1992.

A New Respond Surface Model for Reducing the Excessive Computations of Inverse Problems Using Improved Compactly Supported Radial Basis Function

S. L. HO[1], Shiyou YANG[2], Guangzheng NI[2], H.C. WONG[3]
[1]EE Department, [3]Industrial Centre, The Hong Kong Polytechnic University, Hong Kong
[2]EE College, Zhejiang University, China
Email: eeslho@polyu.edu.hk

***Abstract*—The compactly supported Radial Basis Function (RBF) is improved and employed to design a new response surface model. The model is incorporated into stochastic global optimal methods to develop a fast global optimal design technique for reducing the excessive computations which are generally required in solving inverse problems. To validate the proposed algorithm, typical numerical results on two different examples are reported.**

RESPONSE SURFACE MODEL USING COMPACTLY SUPPORTED RBF

Stochastic methods such as genetic, simulated annealing, and tabu search methods are among the most popular solvers in dealing with global optimal design problems of electro-magnetic devices. However, the excessive computations required by the aforementioned methods often makes them inefficient or impractical for some practical design problems which require, for example, finite-element (FE) solutions repeatedly. To circumvent this problem, the Response Surface Methodology (RSM) has been introduced to reduce the number of function calls that involve the time consuming FE simulations without sacrificing the quality of the numerical solutions. So far the RSMs used are based on globally supported RBFs which will result in a full coefficient matrix. Due to the inefficiency of RSMs in dealing with a full matrix, the sample point of the present RSMs could not exceed an upper limit of, for example, a few thousands such as 2500 as mentioned in [1]. To tackle this inefficiency, the compactly supported RBFs are improved and then extended to develop a new response surface model. To enhance the accuracy of the proposed response surface model whilst constructing the derivatives in boundary points, a new interpolation scheme as described below is introduced.

In general, the reconstruction of an objective function $f(X): D \to R$ on the basis of its values f_i at a set of sample points $X_i \in D(i = 1,2,\cdots,N)$ in terms of some compactly supported radial basis function H is

$$f(x) = \sum_{j=1}^{N} c_j H(\left\| X - X_j \right\|) \tag{1}$$

As demonstrated in [2], although the interpolation of the objective function using (1) performs very well in the inner region of the parameter space, it will give rise to significant errors in the derivatives on the boundary. To solve this problem, the information of the derivatives on the boundary of the parameter space is incorporated into (1), and the interpolation becomes

$$f(x) = \sum_{j=1}^{N} c_j H(\left\| X - X_j \right\|) + \sum_{k=1}^{N_B} d_k H'(\left\| X - X_j \right\|) \tag{2}$$

where, N is the number of the total sample points, N_b is the number of the boundary sample ones.

The coefficients c_j and d_k are determined from the following matrix equation

$$\begin{bmatrix} c_j \\ d_k \end{bmatrix} = \begin{bmatrix} H_{11} & H_{12} \\ H_{21} & H_{22} \end{bmatrix}^{-1} \begin{bmatrix} f_j \\ f_k' \end{bmatrix} \tag{3}$$

where

$$\begin{aligned} (H_{11})_{ij} &= H(\| X_i - X_j \|) \quad (i, j = 1,2,\cdots,N) \\ (H_{12})_{ij} &= H'(\| X_i - X_j \|) \quad (i = 1,2,\cdots,N; j = 1,2,\cdots,N_B) \\ (H_{21})_{ij} &= H(\| X_i - X_j \|) \quad (j = 1,2,\cdots,N; i = 1,2,\cdots,N_B) \\ (H_{22})_{ij} &= H'(\| X_i - X_j \|) \quad (i, j = 1,2,\cdots,N_B) \end{aligned} \tag{4}$$

Due to the compactly supported nature of the RBFs, the coefficient matrix H is sparse and positively definite. Moreover, the RBFs used in this paper is

$$H(r) = \begin{cases} (1-r)^4(4+16r+12r^2+3r^3) & (0 \le r \le 1) \\ 0 & (\text{otherwise}) \end{cases} \tag{5}$$

Further research shows that the performances of the RBFs as formulated in (5) is often overshadowed in many practical engineering design problems that has high dimensions in which the objective functions have significant differences in the "curvatures" of the directions of different decision variables. To address this issue in practical engineering problems, an improved RBF which is constructed using the tensor product of 1-D RBFs is proposed. Mathematically, the high dimensional RBFs being proposed is defined as

$$H_j(r) = \prod_{i=1}^{n} H(\| x_i - (x_i)_j \| / D_i) \tag{6}$$

where n is the dimension of the decision parameters, D_i is a positive number called the scale parameter which controls the 'curvature' of the reconstructed function in the i^{th} direction at sample point X_j.

AN EFFICIENT PROCEDURE TO INCREASE THE EFFICIENCY OF STOCHASTIC OPTIMAL METHODS USING THE PROPOSED RSMS

To accelerate the speed of stochastic algorithms for solving computationally heavy design problems, a procedure based on the combination of the proposed Response Surface Model of the improved RBFs and stochastic algorithms is proposed and is described as:

Initialization: Generate a number of sample points; Compute the objective function values using computationally heavy algorithms such as FE analysis at these sample points; determine the value of the derivatives of the objective

functions on the boundary sample points;

Step 1: Determine the optimal values for the scale parameter D_i using an "exclusion algorithm" [3];

Step 2: Reconstructed the optimal problem using the proposed RMFs and solve it by a stochastic method, then report all the searched local /global optimal solutions;

Step 3: Solve the original optimal problem by using a deterministic method starting from the newly searched local optimal solutions to find the final ones.

NUMERICAL APPLICATIONS

Validation: A mathematical function as formulated in (7) is deliberately designed with a significant difference in the 'curvatures' among different variable directions to elucidate the approximation power of the proposed RSM using the improved compactly supported RBFs. Moreover,

$$f(x,y) = e^{-x}\sin(4x)e^{-y}\sin(30y) \tag{7}$$

Case Study: The multi-objective shape optimization of a rectangular coreless solenoid as reported in [4] is generalized and then solved by using the proposed procedure to demonstrate its advantages over traditional approaches. The goals of the optimal design of this problem are to obtain a maximum inductance and to maintain a minimum volume of the solenoid under specific parametric conditions defined as

$$\begin{aligned} \min \quad & f = w_1 \frac{V(a,b)}{V_{\max}} - w_2 \frac{L(a,b)}{L_{\max}} \\ \text{s.t.} \quad & 0 \le a \le 0.07, 0 \le b \le 0.02 \\ & a \ge \sqrt{\frac{10^{-5}}{4\pi b}} \end{aligned} \tag{8}$$

where, L and V are, respectively, the inductance and the volume of the solenoid, w_1 and w_2 are the weighting factors, a and b are the rectangular cross-sectional parameters to be optimized.

To reconstruct the mathematical function of (7), 16 equidistance sampling points along each coordinate direction are used, and the reconstructed and the close-form functions are shown, respectively, in Fig. 1 and Fig. 2. For the specific case study, the objective functions (including derivatives of boundary points) on 21 equidistance sampling point along each coordinate direction are firstly determined using the FE analysis in order to illustrate the efficiency of the proposed procedure although they could in fact be determined using a close-form expression. The optimal problem is then reconstructed and solved by using a tabu search algorithm to find the 'nearly' optimal solution. Moreover, the searched 'nearly' optimal solutions are used as the starting point of a deterministic method which runs directly on the original computationally heavy design problem to find the final optimal solution. The final optimal solutions obtained by the proposed procedure as well as those by using the tabu search, together with their performance comparison, are given in Table 1. From these numerical results one can see that (1) the proposed RSM using the improved compactly supported RBF is robust in reproducing a high dimensional function with significantly different dimensional sizes; (2) the proposed approach is very efficient in solving optimal problems in which the objective function must be determined by means of computationally heavy approaches such as the 3-D FE analysis since the number of the FE analysis of the proposed method is less than one seventh of that needed by the popular stochastic optimal method. In short, the proposed work provides an alternative for fast and efficient optimizations of complex engineering design problems.

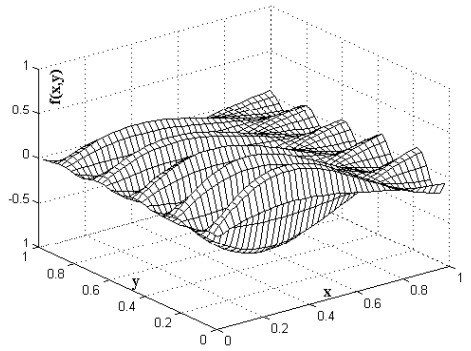

Fig. 1. The reconstructed mathematical function using the proposed RSM

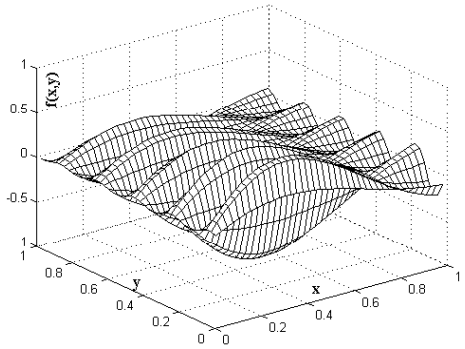

Fig. 2. Illustration of the close-form mathematical function

TABLE 1. PERFORMANCE COMPARISON OF THE PROPOSED AND TRADITIONAL APPROACHES FOR SOLVING THE SOLENOID PROBLEM

Method	a(m)	b(m)	f_{opt}	No. of FEM Computations
Tabu	0.01624	0.01057	-0.4386	6628
Proposed	0.01623	0.01059	-0.4381	441+18

REFERENCES

[1] P. Alotto, A. Bertoni, M. Nervi, "An efficient hybrid algorithm for the optimization of problems with several local minima," *Int. J. Numer. Meth. Engng.*, vol. 50, pp.847-868, 2001.

[2] X. Zhang, K.Z. Song., X. Liu, " Meshless methods based on collocation with radial basis functions, " *Computational Mechanics*, vol. 26, pp. 333-343, 2000.

[3] Th. Ebner, et al., "Approximation of the objective function: multiquadrics versus neural network, " *COMPEL*, vol. 18, pp. 250-265, 1999.

[4] P. Di. Barba, M. Farina, A. Savini, "An improved technique for enhancing diversity in Pareto evolutionary optimization of electromagnetic devices, " *COMPEL*, vol. 20, pp. 482~496, 2001.

Two-Stage Algorithm for Inverting Structure Parameters of the Horizontal Multi-layer Soil

J. Zou, J. L. He, R. Zeng, W. M. Sun, G. Yu
Department of Electrical Engineering, Tsinghua University, Beijing, 100084, China
zoujun@tsinghua.edu.cn

***Abstract*—A fast algorithm is presented to invert the structure parameter of the horizontal multi-layer soil. The procedure is divided into two independent stages. First, Fredholm equation of the first kind with respect to the apparent resistivity is solved by the technology of decay spectrum to reduce computation time greatly. Second, the structure parameter of soil is determined by the generalized Newton-Kantorovich method, which is more robust and less noise sensitive because of using the generalized inverse algorithm to solve the nonlinear equation group. The numerical results show the validities and main features of the proposed approach.**

INTRODUCTION

In a host of engineering applications, multilayer soils are modeled by N horizontal layers with distinct resistivities and depths. In nature, the inversion of soil parameter and structure is an unconstrained nonlinear minimization problem. However, there exist two basic difficulties. On one hand, the curves relating to the apparent resistivity and the electrode distance need to be calculated with different parameter to fit the measurement data, which is referred as computationally demanding. On the other hand, it is hard to obtain the derivatives of the optimized expression. The efficiency of the optimization algorithm without utilizing the derivatives information is usually rather low. In this paper, a fast algorithm is presented to invert the parameter of horizontal multi-layer earth. The key point to bypass the difficulties aforementioned is to invert the kernel function of the integral equation of apparent resistivity and soil parameter in two stages independently. The contribution of this paper lays the following aspects. First, it can save calculating time dramatically due to introducing a decay spectrum function; second, it is more robust and less noise sensitive because of using the generalized inverse algorithm to solve the nonlinear equation group.

TWO-STAGE INVERSION ALGORITHM

Inversion of the Kernel Function

The placement of electrodes in Wenner's configuration for a N-layer earth structure is shown in Fig.1, where h_i and ρ_i are the thickness and resistivity of layer i respectively. The distance between any two electrodes is a .According to the solution of the potential at earth surface produced by point current source, the apparent resistivity $\rho(a)$ satisfies the following Fredholm integral equation of the first kind,

$$\int_0^\infty [J_0(a\lambda) - J_0(2a\lambda)]B(\lambda)\mathrm{d}\lambda = \frac{1}{4a}\left(\frac{\rho(a)}{\rho_1} - 1\right) \qquad (1)$$

where J_0 is the Bessel function of the first kind of order zero. $B(\lambda)$ is the unknown kernel function of integral equation relating to the different earth model. Let $B(\lambda)$ express in terms of the decay spectrum:

$$B(\lambda) = \int_0^\infty A(k)\mathrm{e}^{-\lambda k}\mathrm{d}k \qquad (2)$$

Substituting (2)into (1), one can obtain

$$\int_0^\infty \left[\frac{1}{\sqrt{a^2+k^2}} - \frac{1}{\sqrt{4a^2+k^2}}\right] A(k)\mathrm{d}k = \frac{1}{4a}\left(\frac{\rho(a)}{\rho_1} - 1\right) \qquad (3)$$

The integral identical equation (4) is applied to (3) implicitly.

$$\int_0^\infty \mathrm{e}^{-\lambda|z|} J_0(\lambda r)\mathrm{d}\lambda = \frac{1}{\sqrt{z^2+r^2}} \qquad (4)$$

By using quadrature rule and truncating N terms as the

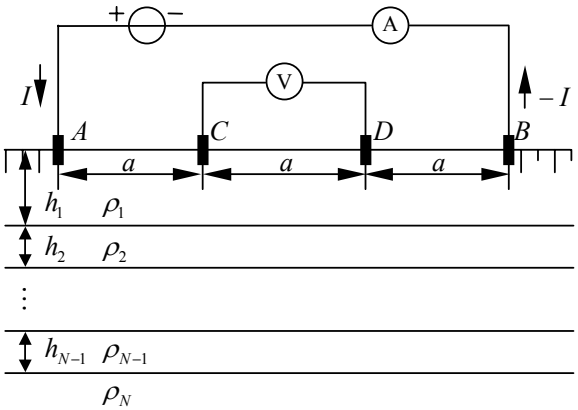

Fig. 1 Wenner configuration for N-layer earth

approximating value of integral, (3) can be discretized as

$$\sum_{n=1}^{N}\left[\frac{1}{\sqrt{a_m^2+k_n^2}}-\frac{1}{\sqrt{4a_m^2+k_n^2}}\right]\alpha_n=\frac{1}{4a_m}\left(\frac{\rho(a_m)}{\rho_1}-1\right) \quad (5)$$
$$m=1,2,\cdots,M$$

where $\alpha_n = A(k_n)\Delta k$, is the weight coefficients to be determined. k_n is the n-th decay constant corresponding to the n-th sampling of integral. Δk is the interval between two sampling points. a_m is the m-th measurement distance of Wenner's four electrodes method. α_n can be determined by solving (5) by using generalized inverse method with M greater than N, so $B(\lambda)\approx\sum_{n=1}^{N}\alpha_n e^{-\lambda k_n}$.

Inversion of the Soil Parameter

The theoretical expression of apparent resistivity for an arbitrary number of layers has been established in many papers [1] and can be given by in the following formulation.

$$\widetilde{B}(\boldsymbol{x},\lambda)=\frac{\widetilde{B}_1(\boldsymbol{x},\lambda)}{\widetilde{B}_2(\boldsymbol{x},\lambda)} \quad (6)$$

where $\boldsymbol{x}=(\rho_1,\cdots,\rho_N,h_1,\cdots,h_{N-1})$. We try to estimate the soil parameter by solving a nonlinear multivariable equation instead of using the optimized method. Let us define a nonlinear multivariable equation

$$\Delta\widetilde{B}(\boldsymbol{x},\lambda)=\widetilde{B}_1(\boldsymbol{x},\lambda)-B(\lambda)\widetilde{B}_2(\boldsymbol{x},\lambda)=0 \quad (7)$$

The inversion procedures adopted for determining the soil parameter is the generalized Newton-Kantorovich [2]. The iteration of this algorithm can be summarized as follows:

$$\begin{cases}\boldsymbol{K}_{\text{Jacob}}(\boldsymbol{x}^{(k)},\lambda_q)\Delta\boldsymbol{x}^{(k)}+\Delta\widetilde{B}(\boldsymbol{x}^{(k)},\lambda_q)=0\\ \boldsymbol{x}^{(k+1)}=\boldsymbol{x}^{(k)}+\Delta\boldsymbol{x}^{(k)}\end{cases} \quad q=1,2,\cdots,Q \quad (8)$$

where $\boldsymbol{K}_{\text{Jacob}}(\boldsymbol{x}^{(k)},\lambda_q)$ is Jacobian matrix. $\boldsymbol{x}^{(k)}$ and $\Delta\boldsymbol{x}^{(k)}$ are the solution of (7) and its modified value for the k-th iteration respectively. To improve the numerical stability, Q is greater than number of variables in (7) and (8) is solved by using generalized inverse method for every iteration.

NUMERCIAL EXAMPLES

Field measurement data of the apparent resistivity obtained by the Wenner four electrodes method is plotted in Fig.2. The inversion results of soil parameter are summarized in Tab. I by two-stage approach developed and the software package CDEGS [3] respectively. Moreover, the actual soil parameter is also listed in Tab. I by the geophysical exploration for the comparison purpose.

CONCLUSION

A two-stage approach to invert the soil parameter for an arbitrary number of layers is proposed in term of the conception of the decay spectrum. The numerical results show good agreement indicating that the soil parameter technology developed could be practically applied to grounding design problems.

REFERENCES

[1] Takahashi T, Kawase T.,"Analysis of apparent resistivity in a multi-layer earth structure", *IEEE T-PWRD*, vol. 5, pp. 604-612, Feb. 1990.

[2] Press W H, *Numerical recipes: the art of scientific computing*. New York : New York Cambridge University Press, 1986.

[3] Dawalibi F□ Donoso F., "Integrated analysis software for gounding, EMF and EMI", *IEEE computer application in power*, vol. 6, pp.19-24, Feb. 1993.

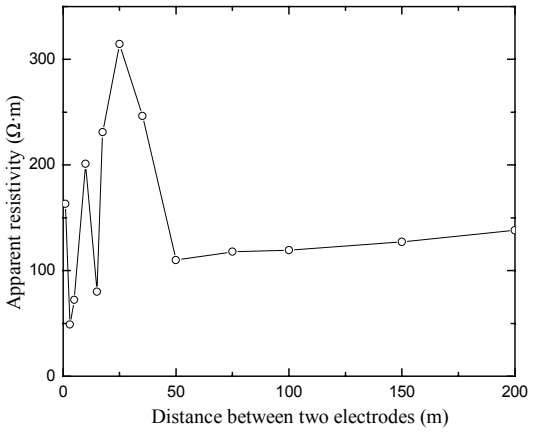

Fig. 2 Field measurement of the apparent resistivity

Tab. I results of inverting the soil structure parameters

Result	1st layer		2nd layer		3rd layer		4th layer
	h_1 (m)	ρ_1 (Ω·m)	h_2 (m)	ρ_2 (Ω·m)	h_3 (m)	ρ_3 (Ω·m)	ρ_4 (Ω·m)
This paper	0.9	350	2.3	31	5.1	340	103
CDEGS	0.7	311	1.95	26	3.9	260	125
Actual	0.8□1.1	331□387	2.0□2.6	25□40	4.3□6.1	295□387	87□110

Inverse problem for magnetic sensors based on a Preisach formalism

L. Dupré [1] and M. Slodička [2]

1 Department of Electrical Energy, Systems and Automation, Ghent University
Sint-Pietersnieuwstraat 41
Ghent B-9000, Belgium
luc.dupre@rug.ac.be

2 Department of Mathematical Analysis, Ghent University
Galglaan 2
Ghent B-9000, Belgium
ms@cage.rug.ac.be

***Abstract*—This paper deals with the inverse problem in order to identify microstructural features of a steel sheet on the basis of magnetization loops. The authors discuss the main iterative principles, based on finite element techniques and the Marquardt method.**

INTRODUCTION

Mechanical properties such as hardness, ductility are directly related to the microstructure, composition and fabrication methods. Classical magnetic hysteresis properties such as remanent induction, coercive force, permeability and saturation magnetization are sensitive to the same composition, microstructure and processing conditions. Therefore, measurement of magnetic hysteretic properties can provide a sensor for the mechanical properties of metallic materials and serve as a magnetic-based nondestructive evaluation method. It is evident that a nondestructive evaluation method improves when considering whole family of hysteresis return branches, or minor order hysteresis loops instead of the classical magnetic hysteresis properties.

PREISACH HYSTERESIS MODEL

The Preisach model [1], is an accurate method of describing the scalar hysteresis effects in magnetic materials. According to Preisach's approach, the hysteresis model gives as response the magnetization M as a function of the applied magnetic field H and its history H_{his}. It rests upon the idea of a material structure containing an infinite set of magnetic dipoles. Each dipole has a rectangular nonsymmetrical hysteresis loop defined by two characteristic parameters, which are denoted by α and β ($\beta \le \alpha$). In the Preisach model, the state $\eta(\alpha,\beta,t)$ of the dipole (α,β) at time point t only may take the value +1 or –1:

$$\eta(\alpha,\beta,t)=\begin{cases}+1: in\ case\ H(t)>\alpha\ or\ (\beta<H(t)<\alpha\ and\ H_{his}>\alpha)\\ -1: in\ case\ H(t)<\beta\ or\ (\beta<H(t)<\alpha\ and\ H_{his}<\beta)\end{cases} \quad (1)$$

Here H_{his} is the last extreme value of the magnetic field kept in memory outside the interval $[\beta,\alpha]$ and which is physically remembered in the domain structure of the material.

The density of the dipoles is represented by the Preisach distribution function $P(\alpha,\beta)$ (PDF). The resulting magnetization M is obtained from the accumulated magnetization of all the dipoles. The magnetization is then given by

$$M(H(t),H_{his}(t))=\frac{1}{2}\int_{-\infty}^{+\infty}d\alpha\int_{-\infty}^{\alpha}d\beta\ P(\alpha,\beta)\eta(\alpha,\beta,H(t),H_{his}(t)) \quad (2)$$

In order to quantify how the PDF changes due to a variation of microstructural features, a Lorentzian PDF is considered:

$$P(\alpha,\beta)=\frac{k_1 b^2}{(b^2+(\alpha-a)^2)(b^2+(\beta+a)^2)}+\delta_{\alpha\beta}\left(\frac{k_2 c^2}{c^2+\alpha^2}\right) \quad (3)$$

with $\delta_{\alpha\beta}$ denoting the Kronecker delta.

The effect of the average grain size ξ and crystallographic texture on the distribution function (PDF) in the Preisach model was identified by a large number of measurements [2]. Taking into account the results of [3], one may rewrite the parameters a, b, k_1 and k_2 in (3) as a function of grain size ξ and dislocation density ζ_d:

$$a=a_0(G_1+G_2/\xi)\sqrt{\zeta_d} \quad (4)$$

$$b=b_0(G_1+G_2/\xi)\sqrt{\zeta_d} \quad (5)$$

$$k_1=k_{10}-k_{11}\sqrt{\zeta_d} \quad (6)$$

$$k_2=k_{20}+\frac{k_{21}}{\sqrt{\zeta_d}} \quad (7)$$

The parameter c is assumed independent from ξ and ζ_d.

MAGNETODYNAMIC MODEL FOR LAMINATED STEEL

The goal is to develop a numerical scheme for the accurate recovery of the microstructural material parameters ξ and ζ_d starting from the experimentally observed magnetic behavior of laminated materials under time varying flux excitation.

The magnetic behavior of laminated steel with thickness $2d$ can be described in terms of the macroscopic fields, taking into account the interacting hysteresis and eddy current phenomena. Making a few justifiable assumptions [4], one obtains from Maxwell's laws the diffusion equation

$$\frac{1}{\sigma}\frac{\partial^2 H}{\partial x^2}=\frac{\partial B}{\partial t}=\mu_d(H,H_{his})\frac{\partial H}{\partial t},0\le x\le d,t\ge 0 \qquad (8)$$

Here $H(x,t)$ and $B(x,t)=\mu_0(H(x,t)+M(x,t))$ are the magnetic field and the induction respectively. σ and μ_d are the electrical conductivity and the differential permeability of the material, the latter calculated from the Preisach model (2)-(3). The x-axis is chosen to be perpendicular to the sheet. Throughout the lamination, the time-dependent flux ϕ flows in the z direction and the magnetic field has only one component, namely $\boldsymbol{H}=H(x,t)\mathbf{e}_z$. To obtain a well-posed boundary value problem (BVP), (8) must be completed with the suitable boundary conditions and initial conditions:

$$\frac{\partial H}{\partial x}(0,t)=0,\frac{\partial H}{\partial x}(d,t)=\frac{\sigma}{2}\frac{d\phi}{dt},H(x,0)=0 \qquad (9)$$

The average induction B_a and the magnetic field at the surface of the material H_b can be identified experimentally in a straightforward way and are defined in the model by:

$$B_a(t)=\frac{\phi(t)}{2d}=\frac{1}{d}\int_0^d B(x,t)dx,\ H_b(t)=H(d,t) \qquad (10)$$

The average magnetic induction $B_a(t)$ is enforced by the boundary condition while the time-dependent magnetic field strength $H_b(t)$ is obtained by solving the BVP (1)-(3), (9)-(10).

Starting from a measured B_aH_b-loop, the above magneto-dynamic model, in combination with (4)-(7), can be used for the identification of the parameter set $p[\xi;\zeta_d]$. The function to be fitted in this *inverse problem* is $H_b=H_b(t;p)$. The merit function to be minimized is

$$\chi^2=\sum_{i=1}^{N}\left(H_{bi}-H_b(t_i;p)\right)^2 \qquad (11)$$

where H_{bi} is the measured 'target' magnetic field at the surface of the steel at the time points t_i and $H_b(t_i;p)$ is the magnetic field, calculated by the direct problem using the parameter set p. The Marquardt scheme, which varies smoothly between the extremes of the inverse Hessian method and the deepest descent method, is used as nonlinear least square method [5].

NUMERICAL RESULTS

We tested the numerical scheme by enforcing an average magnetic induction $B_a=\phi/2d$ of the following form:

$$B_a(t)=\begin{cases}\frac{t}{5T}B_p\sin(\frac{2\pi t}{T}) & 0\le t\le 5T\\ B_p\sin(\frac{2\pi t}{T}) & 5T\le t\le 7T\\ \frac{12T-t}{5T}B_p\sin(\frac{2\pi t}{T}) & 7T\le t\le 12T\end{cases} \qquad (12)$$

The corresponding target magnetization loop is shown in Fig.1. The induction waveform $B_a(t)$ is chosen in such a way that the magnetic memory behavior of the material is included. Fig.2 depicts the variation of the magnetic field at the surface of the material during the Marquardt iteration procedure. The variation of χ^2,ξ and ζ_d are given in Table I. It was observed that after 9 iterations, $H_b(t;p)$ accurately approximated the target H_{bi}.

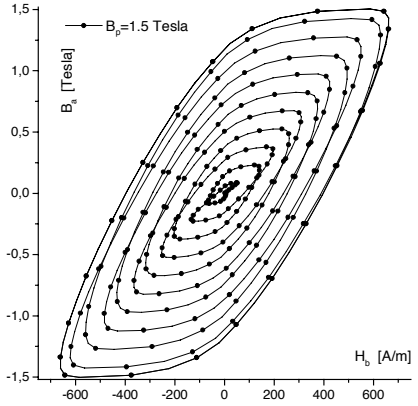

Fig.1. Measured B_aH_b-loop at f=1/T=500Hz

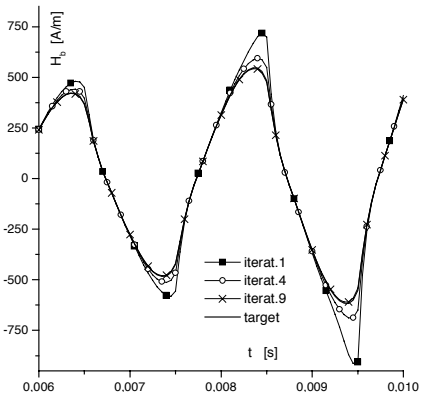

Fig.2. The calculated H_b(t) during the Marquardt iteration, N=4800

TABLE I: VALUES DURING ITERATION PROCEDURE

	START	IT.2	IT.4	IT.6	IT.9
ξ	15	19,068	18,179	19,978	19,997
ζ_d	8	3,8	4,375	4,992	5,001
χ^2	6264304	2899816	8008	14,387	5,093

REFERENCES

[1] I.D. Mayergoyz, *Mathematical models of hysteresis.* Berlin, Springer, 1991.

[2] L. Dupré, G. Bán, M. von Rauch and J. Melkebeek, "Relation between the microstructural properties of electrical steels and the Preisach modeling", *J. Magn. Magn. Mat.,* vol. 195**,** pp. 233-249, 1999.

[3] M.J. Sablik, "Modeling the effect of grain size and dislocation density on hysteretic magnetic properties in steels", *J. Appl. Phys.,* vol. 89, pp. 5610-5613, 2001.

[4] S. Ohteru, H. Kobayashi, T. Kato, K. Sudo, "Eddy current analysis in an iron sheet considering hysteresis characteristics", Intermag Conf., Denver, Colorado, 1971, pp.457-460.

[5] W.H. Press et al., *Numerical Recipes, The Art of Scientific Computing*.Cambridge, Cambridge University Press, 1990.

Optimization Design on Electrode Contour Based on Novel Hybrid Algorithm

Cao Yundong, Liu Xiaoming, Hou Chunguang, Lai Changxue, Wang Erzhi

College of Electrical Engineering, Shenyang University of Technology

58#, Xinghua South Street, Tiexi District

Shenyang 110023, China

***Abstract*-In this paper, the genetic algorithm (GA) and taboo search (TS) algorithm are well analyzed. A novel optimization method for continuous variables of global optimization, hybrid algorithm is proposed, that is, the TS is embedded into the optimization processes of GA. It combines the advantages of both GA and TS algorithm, possessing quicker convergence and obtaining global optimum in the most probability. The feasibility and validity of the proposed hybrid algorithm are verified by solving the typical mathematical function. And the practicability is proven by optimizing the electrode contour.**

INTRODUCTION

For the optimization of electric apparatus, there are two main requirements for the methods: Firstly, it must be a global optimization algorithm, and cannot entrap into a local optimum or the probability is very little. Secondly, the algorithm should be of higher efficiency, that is, the faster speed of seeking for the optimum and the availability of the optimum. For optimizing the complex electromagnetic problem, it is necessary to employ more known data, and to reduce the times of numerical evaluation. Presently, some contributions have been obtained in the optimization of the discrete problem. However, the convergency, robustness and efficiency of the optimizing tool are still the bottleneck. Aiming at these problems, for improving the convergency and efficiency as well as the robustness of the optimization method, a hybrid optimization algorithm is proposed in this paper.

HYBRID ALGORITHM OF GA AND TS

In heuristic algorithm, TS algorithm is a very efficient one [1,2]. It is the existence of the tabu list (TL) that avoids the repeats of search and combines the previous route. More exactly optimized solutions can be obtained through controlling of the searching neighborhood region. But there exist some disadvantages in conventional TS algorithm. Firstly, "mobile search" leads to that the universality of searching is not enough and the time for calculation is largely influenced by the original state. Secondly, the size of TL and the taboo region during continuously searching is hard to be defined.

GA has been widely applied in the optimization of various problems [3]. And it has a particular parallel mechanism that guarantees the diversity of solution to a certain degree. But the converging speed will become very slow when the solution approaching the optimum.

In view of the convergency and universality of TS and GA in optimization, the hybrid optimization method of improved TS and GA is proposed, in which GA is applied as the main frame because the global information can be clearly reflected by using it and it boasts the strong ability of general search. The improved TS is embedded in the "regeneration stage" of GA to overcome the disadvantages of centralizing search of GA. Main steps of the hybrid algorithm are as follow:

(1). Initialization: Initialize the variables of GA and TS. A solution information list is built.

(2). GA stage: Optimize the objective function F (x) using the GA. Judge the stop criterion, if it is satisfied, ends the program.

(3). Regeneration judgment: If the current optimum does not satisfy the convergence criteria and if $N>N_0$, then go to step (4), but if $N<N_0$, go to step (2), where N and N_0 represent the appearance times of current optimum and the permitted maximal appearance times of current optimum respectively.

(4). Regeneration stage of GA: The current optimum, as the initial state of the TS, starts centralizing search using improved TS.

(5). Judgment of the convergence criteria: If the convergence criterion is satisfied, renew the solution information list and go to step (2).

CALCULATION EXAMPLES

A Typical Testing Function

In order to test the feasibility of the proposed hybrid optimization algorithm, a typical mathematical function is introduced. The function expression is as follow:

$$f(x,y) = 0.5 - \frac{\sin^2\sqrt{x^2+y^2} - 0.5}{(1+0.001(x^2+y^2))^2}$$

$$(x, y) \in (-4, 4)$$

The global optimum is (x, y) = (0, 0), and the function value is 1.According to the characteristic of this function, the function values are recorded in the TL rather than the variables.

The testing results of GA, improved TS and hybrid algorithm are obtained. In which, Fig. 1-Fig. 3 illustrate the searching course of GA, TS and hybrid algorithm, respectively. And the calculation results are given in Table I.

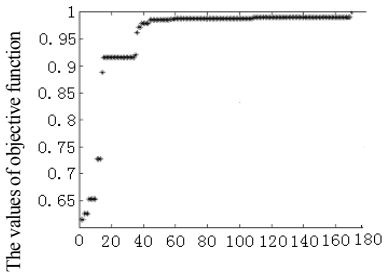

Fig.1. The searching course using GA

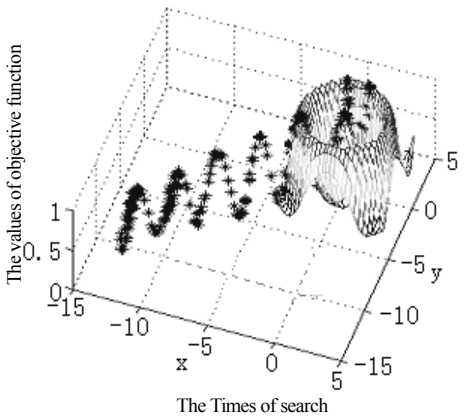

Fig.2. The searching course using TS

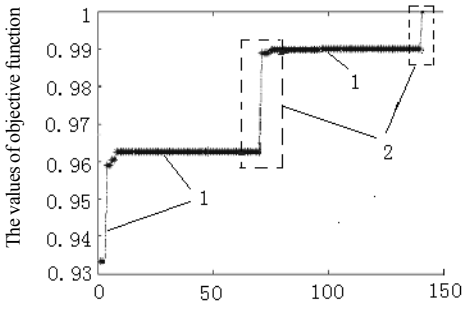

1. GA stage 2. TS stage

Fig.3. The searching course using hybrid algorithm

TABLE I. CALCULATION RESULTS

	TS	GA	Hybrid Algorithm
The times of computation	260	171	138
Value of objective function	0.995658	0.990356	0.999996

From the calculation results, it can be seen that the calculation results using hybrid algorithm possess higher precision and quicker convergency speed than those of GA and improved TS.

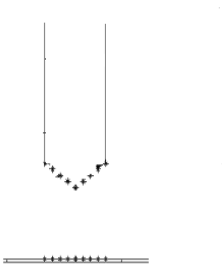

Fig.4. The sketch of electrode contour

Optimization of the Electrode Contour

The original electric contour is shown in Fig.4, where * represents the optimized point. When the applied voltage is 12kV, the maximum of the electric field strength is 1197.812 V/mm. After preprocessing of the self-adaptive grid and the electric field computation using the finite element method, optimization result is obtained by applying the proposed hybrid algorithm, as shown in Fig.5, and the maximum of the electric field strength is 857.5803 V/mm.

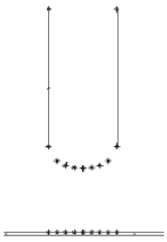

Fig.5. Optimization result of the electrode contour

CONCLUSIONS

The feasibility and validity of the proposed hybrid algorithm are verified by solving the typical mathematical function. And practicability is proved by optimizing the electrode contour. The hybrid algorithm of GA and improved TS can be used for solving the continuous variables of global optimization.

REFERENCES

[1] F. Glover, "Tabu search: Part I," ORSA J. on Computing. 1, pp.190－206, 1989.
[2] F. Glover, "Tabu search: Part II," ORSA J. on Computing. 2, pp.4－32, 1990.
[3] Liu Xiaoming, Cao Yunong, Wang Erzhi, Xu Dongyang, Jin Li, "Optimization design of the contact and shield in vacuum interrupter based on the genetic algorithm," XIXth ISDEIV, pp.463-466, Sep 2000.

COMPUMAG Saratoga Springs, New York USA
July 13 - 17, 2003

Electrical Impedance Imaging of Two-Phase Fields with an Adaptive Mesh Grouping Technique

K.Y. Kim[a], S.I. Kang[a], B.S. Kim[a], M.C. Kim[a], S. Kim[a], Y.J. Lee[a], H.J. Jeon[b], B.Y. Choi[b], and M. Vauhkonen[c]
[a] Department of Electrical and Electronic Engineering, Cheju National University, Cheju, 690-756, Korea
(Tel: +82-64-754-3664; Fax: +82-64-756-1745; E-mail: kyungyk@cheju.ac.kr)
[b] Department of Electrical Engineering, Kyungpook National University, Taegu, 702-701, Korea
(Tel: +82-53-950-6553; Fax: +82-53-959-7336; E-mail: bychoi@ee.knu.ac.kr)
[c] Department of Applied Physics, University of Kuopio, PO Box 1627, FIN-70211, Kuopio, Finland
(Tel: +358-17-162035; Fax: +358-17-162373; E-mail: Marko.Vauhkonen@uku.fi)

***Abstract*— In electrical impedance tomography (EIT), cross-sectional resistivity distribution is reconstructed using current and voltage measurements made from the boundary. In this paper, a novel adaptive mesh-grouping scheme is presented to enhance the spatial resolution in the Gauss-Newton algorithm.**

INTRODUCTION

In EIT, an array of disjoint electrodes is attached on the boundary of the object and a set (frame) of small alternating currents is injected into the object through these electrodes, and then the corresponding set of voltages is measured on the same array of the electrodes. The objective is to estimate (reconstruct) the resistivity distribution inside the object based on the set of measured voltages and injected currents [1]. Image reconstruction in EIT is obtained from the iterative solution of the forward and inverse problems. The forward solution is obtained by solving the Laplace equation based on the FEM (finite element method). The inverse problem in EIT is highly nonlinear and ill-posed problem. Lots of inverse solvers with various regularization methods have been developed [2,3].

This paper describes a novel adaptive mesh-grouping scheme to enhance the spatial resolution of the Gauss-Newton (GN) algorithm for the visualization of two-phase fields. The key idea of the scheme is to reduce successively the number of unknowns (elements) in the inverse procedure and thus diminish the ill-conditioned characteristic of the inverse problem.

IMAGING WITH MESH GROUPING SCHEME

Due to the ill-posedness of the ERT inverse problem, the cost functional to be minimized necessitates regularization such that

$$\Phi(\rho) = \frac{1}{2}\{\|V(\rho) - U\|^2 + \alpha\|R\rho\|^2\} \tag{1}$$

where the vectors V and $U \in \Re^{LP}$ are the computed and measured voltages, respectively and L and P are the number of electrodes attached on the surface and injected current patterns, respectively. α and $R \in \Re^{N\times N}$ are the regularization parameter and matrix, respectively. In this work we use a deterministic approach called generalized Tikhonov regularization and N denotes the number of elements in the FEM meshes.

The most popular inverse solver for the nonlinear minimization problem of the regularized cost functional (1) is the iterative Gauss-Newton method [1]:

$$\rho_{i+1} = \rho_i + (H_i^T H_i)^{-1} H_i^T g_i \tag{2}$$

where $H_i \in \Re^{(LP+N)\times N}$ and $g_i \in \Re^{(LP+N)\times 1}$ is defined by

$$H_i \equiv \begin{pmatrix} J_i \\ \sqrt{\alpha}R \end{pmatrix}, \quad g_i \equiv \begin{pmatrix} U - V(\rho_i) \\ -\sqrt{\alpha}R\rho_i \end{pmatrix} \tag{3}$$

where $J_i \equiv J(\rho_i) \in \Re^{LP\times N}$ denotes the Jacobian of the mapping $V(\rho)|_{\rho=\rho_i}$ with respect to ρ and i is the iteration number.

One of the major problems in the Gauss-Newton algorithm is the rapid increase of the computational burden and poor convergence characteristics as the number of unknowns (elements) is increased. Since there are just two representative resistivity values in the two-phase fields, the intermediate resistivity values obtained from the Gauss-Newton algorithm are examined and classified into three groups such as target group (TG), background group (BG) and unadjusted group (UG), of which each TG and BG is considered as one element. A simple classification criterion can be obtained as:

$$\mu_j \equiv \frac{\rho_i(j)}{\rho_o}, \quad j = 1, 2, \cdots, N \tag{4}$$

where ρ_o is the best homogeneous resistivity value defined in a least-square sense as:

$$\rho_o \equiv (\bar{V}^T\bar{V})^{-1}\bar{V}^T U \tag{5}$$

where $\bar{V} \in \Re^{LP}$ is the computed voltages when $\rho = 1\ \Omega cm$. The value of ρ_o is always between background and target resistivity value in the two-phase fields. After calculating μ_j from (4), the intermediate elements are classified into three groups: if μ_j is larger than μ_{TH} then $\rho_i(j)$ belongs to TG, else if μ_j is smaller than μ_{TL} then $\rho_i(j)$ belongs to BG, otherwise $\rho_i(j)$ belongs to UG.

We can construct the grouping matrix at each iteration after classification for all of the elements; Let W_{TG}, W_{BG} and

$W_{UG} \subset \Omega$ be subdomain for TG, BG and UG, respectively and define

$$\rho_i \equiv G_i \rho_i^g \tag{6}$$

where $\rho_i^g \equiv (\rho_1, \rho_2, \cdots, \rho_{N-(p+q)}, \rho_{TG}, \rho_{BG})^T \in \Re^{(N-(p+q)+2)\times 1}$ and $G_i \in \Re^{N\times(N-(p+q)+2)}$, where p and q are the number of elements merged in the subdomain W_{TG} and W_{BG}, respectively so that the number of elements in the subdomain W_{UG} are equal to $N-(p+q)$. Each subdomain W_{TG} and W_{BG} is considered as one element. The grouping matrix G_i is a sparse matrix that includes ones in the specific locations such that it maps the resistivity value in ρ_i^g to the correct element locations in ρ_i.

Then, at the grouping instant, one-cycle of the Gauss-Newton algorithm can be modified as follows:

$$\rho_{i+1}^g = \rho_i^g + \{(H_i^g)^T H_i^g\}^{-1}(H_i^g)^T g_i^g \tag{7}$$

where $H_i^g \in \Re^{(LP+N-(p+q)+2)\times(N-(p+q)+2)}$ and $g_i^g \in \Re^{(LP+N-(p+q)+2)\times 1}$ are defined by

$$H_i^g \equiv \begin{pmatrix} J_i^g \\ \sqrt{\alpha} R_i^g \end{pmatrix}, \quad g_i \equiv \begin{pmatrix} U - V(\rho_i^g) \\ -\sqrt{\alpha} R_i^g \rho_i^g \end{pmatrix} \tag{8}$$

where $J_i^g \in \Re^{LP\times(N-(p+q)+2)}$ and $R_i^g \in \Re^{(N-(p+q)+2)\times(N-(p+q)+2)}$ are grouped Jacobian and regularization matrix, respectively obtained by

$$J_i^g = J_i G_i \tag{9}$$

$$R_i^g = G_i^T R G_i \tag{10}$$

Experimental Results

We have developed an EIT measurement system that consists of a Pentium PC, data acquisition board and control software, current generator and switching board, and a cylindrical phantom (8 cm in diameter) with 32 electrodes which cover approximately 55% of the inner circumference. The phantom simulates a two-dimensional situation such that the electrodes are extended from the bottom of the tank to the top of the tank. The phantom was filled up with saline (NaCl) having resistivity of 330 Ωcm and a cylindrical plastic target (3 cm in diameter) was placed at the center of the phantom.

In the forward computations we used the FEM with a mesh of 3104 elements and 1681 nodes. In the inverse computations, we used the FEM with a mesh of 776 elements (N) and 453 nodes to reduce the computational burden. The regularization parameter (α) was set to 5×10^{-4}. The upper and lower threshold values (μ_{TH} and μ_{TL}) for the classification are set to 1.7 and 2.0, respectively.

Fig. 1 shows the reconstructed images from the GN method and proposed scheme. The spatial resolution of the proposed scheme is enhanced considerably than that of the conventional GN method.

The grouping scheme was applied at each iteration and the number of elements in the subdomain W_{TG}, W_{BG}, and W_{UG} were 26, 737, and 13, respectively after 2 iterations and 36, 740, and 0, respectively after 3 iterations. As the grouping scheme was applied successively, the number of the elements in W_{UG} is reduced to zero and finally we have just two elements. The elapsed CPU time (1 *GHz* Pentium PC) for the GN algorithm and proposed scheme are 967 *sec*. and 526 *sec*., respectively. Fig. 2 represents the condition number (CN) which is defined by the ratio of the maximum and minimum eigenvalues of the Hessian matrix in (7). As can be expected, the condition number of the proposed scheme is reduced considerably compared to that of the GN algorithm.

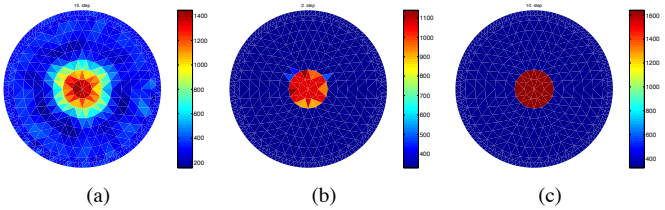

(a) (b) (c)

Fig. 1. Reconstructed images from (a) GN method with 10 iterations, (b) proposed scheme with 3 iterations, and (c) proposed scheme with 10 iterations

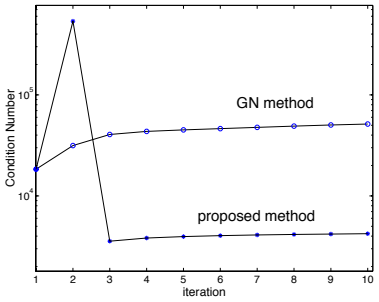

Fig. 2. The Condition number

Conclusion

A novel adaptive mesh grouping scheme is proposed to improve the spatial resolution of the Gauss-Newton algorithm in the two-phase electrical resistance tomography. The number of unknowns (elements) in the inverse procedure is reduced successively and thus the ill-conditioned characteristics of the inverse problem is diminished.

Acknowledgment

This work was supported by the Nuclear Academic Research Program of the Ministry of Science and Technology (MOST) and by grant No. R01-2002-000-0040-0(2002) from the Basic Research Program of the Korea Science and Engineering Foundation.

References

[1] T.J. Yorkey, J.G. Webster, and W.J. Tompkins, "Comparing reconstruction algorithms for electrical impedance tomography," *IEEE Trans. on Biomedical Engr.*, vol. 34, pp. 843-852, 1987.

[2] K.Y. Kim, S.I. Kang, M.C.Kim, S. Kim, Y.J. Lee, and M. Vauhkonen, "Dynamic image reconstruction in electrical impedance tomography with known internal structures," *IEEE Trans. on Magnetics*, vol. 38, no. 2, pp. 1301-1304, 2002.

[3] K.Y. Kim, B.S. Kim, M.C. Kim, Y.J. Lee, and M.Vauhkonen, "Image reconstruction in time-varying electrical impedance tomography based on the extended Kalman filter," *Measurement Science and Technology*, vol. 12, no. 8, pp. 1032-1039, 2001.

COMPUMAG Saratoga Springs, New York USA
July 13 - 17, 2003

Magnetostatic Permeability Tomography

H. Igarashi, K. Ooi and T. Honma
Graduate School of Engineering, Hokkaido University
Kita 13, Nishi 8, Kita-ku, Sapporo, 060-8628, Japan, iga@em-si.eng.hokudai.ac.jp

***Abstract*— This paper describes reconstruction of permeability distribution in material. Magnetostatic fields are imposed to the material including magnetic substance. The normal and tangential components of the resultant magnetic fields consisting of the external and perturbed fields are measured on the surface. The permeability distribution is iteratively improved so that the magnetic fields computed from the normal and tangential components become identical in the material. It is shown that this approach yields successful reconstruction of the position of the magnetic substance while the inferred maximum permeability does not always converges.**

I. Introduction

Structural materials in reinforced concrete, often made of iron, are rusted by salty wind and acid rain, to have less permeability. It would be possible, therefore, to inspect the damage of the structural materials if the permeability is evaluated from the outside of the concrete.

In the impedance tomography, the conductivity distribution has successfully been reconstructed from the electrostatic potentials and currents at the electrodes located on the surface of the domain. In one of the most standard approaches, called Wexler's method [1], the conductivity distribution is iteratively improved so that the current density computed from the surface potential becomes identical with that computed from the surface current in the domain. The mathematical aspects of this approach have been discussed [2], [3].

In this work, static magnetic fields are imposed to the concrete including iron poles, and the resultant magnetic fields, which are influenced by the distributed permeability, are measured on the surface of the concrete. The permeability is reconstructed on the basis of Wexler's method. The difficulty particular for this magnetostatic inverse problem comes from the substantial difference between the background and iron permeability. This point will be discussed in detail.

II. Inverse analysis

Let us consider a two-dimensional simply connected region Ω with permeability μ, which will be reconstructed from the magnetic-field data on the boundary $\partial\Omega$. The external magnetostatic fields are generated by a pair of coils $((p_i, q_i),\ i = 1, 2, ..., 6)$, as shown in Fig.1, along which anti-parallel currents flow. Thus six different patterns of magnetic fields can be generated for the reconstruction.

Provided that there are no currents in Ω, we express the magnetic fields in terms of the magnetic scalar potential,

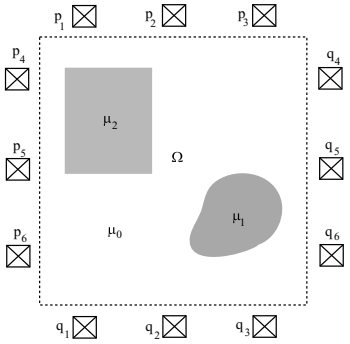

Fig.1 Coils and magnetic material

that is, $\boldsymbol{H} = -\nabla\varphi$. Substitution of this expression into $\nabla \cdot \boldsymbol{B} = 0$ yields the Laplace equation

$$\nabla \cdot (\mu \nabla \varphi) = 0, \tag{1}$$

which will be solved by the finite element method under appropriate boundary conditions.

When the normal magnetic flux Φ per length δ is measured on $\partial\Omega$, the Neumann boundary condition can be obtained from $\Phi = -\mu\delta\partial\varphi/\partial n$. Thus the potential φ can be determined by solving (1) under this boundary condition if the arbitrary constant in φ is determined.

On the other hand, the Dirichlet boundary condition is obtained from $\varphi = -\int_c \boldsymbol{H} \cdot d\boldsymbol{s}$, where c is a path on $\partial\Omega$, assuming that $\boldsymbol{H}$ is measured on $\partial\Omega$. Equation (1) is solved under this condition again. The permeability μ in Ω is reconstructed from these solutions satisfying the Neumann and Dirichlet conditions.

On the first stage of the reconstruction, μ is assumed to be constant over Ω. Then two kinds of magnetic fields $\boldsymbol{B} = -\mu\nabla\varphi$ and $\boldsymbol{B}' = -\mu\nabla\varphi'$ are computed by solving (1) under the Neumann and Dirichlet data, respectively. Note that in general $\boldsymbol{B}$ is not identical with $\boldsymbol{B}'$ because the assumed μ distribution is incorrect.

To improve the μ distribution, we consider the problem

$$R = \sum_i \sum_e \int_{\Omega_e} |\boldsymbol{B} + \mu\nabla\varphi|^2 \, dS \to \min., \tag{2}$$

where i represents the pattern of the external magnetic fields and Ω_e the finite element. Assuming that μ is constant in each Ω_e, whose value is denoted by μ_e, the condition $\partial R/\partial\mu_e = 0$ provides

$$\mu_e = -\frac{\sum_i \int_{\Omega_e} \boldsymbol{B} \cdot \nabla\varphi \, dS}{\sum_i \int_{\Omega_e} \nabla\varphi \cdot \nabla\varphi \, dS}. \tag{3}$$

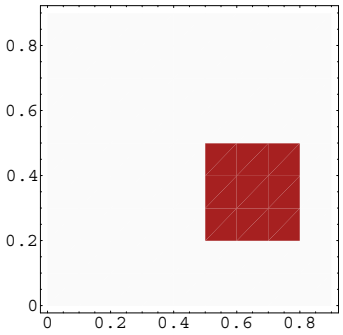

Fig.2 Original distribution

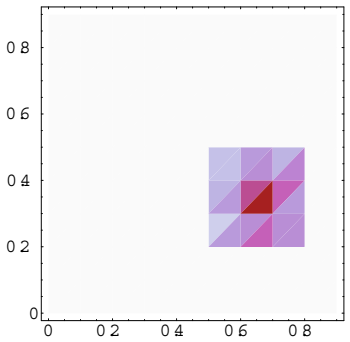

Fig.3 Reconstructed distribution ($\mu_r = 10$)

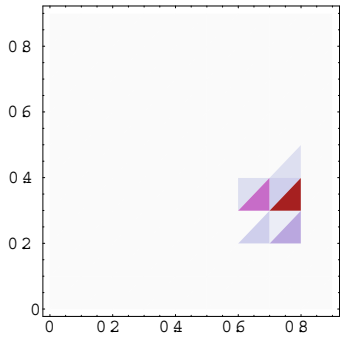

Fig.4 Reconstructed μ distribution ($\mu_r = 1000$)

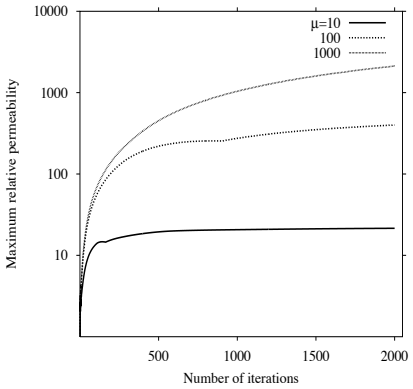

Fig.5 Convergence of reconstruction procedure

We solve again (1) with μ determined from (3), and this procedure is repeated until the error defined by

$$\epsilon = \sqrt{\frac{\sum_j |\varphi_j - \varphi'_j|^2}{\sum_j {\varphi'_j}^2}} \tag{4}$$

becomes less than some tolerance, where φ_j is the nodal potential value obtained by solving the Neumann problem while φ'_j is the boundary condition for the Dirichlet problem.

III. Numerical Results

The original distribution of permeability is shown in Fig.2, where the dark square represents the magnetic material with uniform relative permeability μ_r. Figures 3 and 4 show the reconstructed permeability distribution for the cases $\mu_r = 10$ and $\mu_r = 1000$. The overall property of the reconstructed distribution is in good agreement with that of the original distribution. The shape of the magnetic material is reconstructed better for the case $\mu_r = 10$ than for $\mu_r = 1000$.

Figure 5 shows the convergence of the maximum value μ_r^{max} in the reconstracted μ_r. When $\mu_r = 10$, μ_r^{max} converges to the value somewhat larger than the real value. In contrast, μ_r^{max} does not converge within the performed iterations when μ_r is over 100. In particular, it is observed that μ_r^{max} linearly increases when $\mu_r = 1000$, whereas ϵ approaches zero. (Note that the vertical axis of Fig. 5 is in log plot.) Such a rapid increase in μ is remarkable especially in the darkest element in Fig.4.

It is concluded that the direct application of Wexler's method to our problem does not work well when permeability of the magnetic material is rather high, and this is the case for usual magnetic materials. The divergence of μ suggests that the solution falls into one of the local minima. We will, therefore, apply the stochastic method to find the minimizer instead of the direct method (3).

IV. Conclusions

Wexler's method, which is standard in the impedance tomography, is applied to the permeability reconstruction. It is shown that the method gives satisfactory results when the original relative permeability is up to 10 while the reconstructed permeability does not converge when the original one is over 100. The stochastic method will be introduced to find the global minimum.

References

[1] A. Wexler, B. Fry and R. Neuman "Impedance-computed tomography algorithm and system", *Applied Optics*, **24**, (1985), 3985-3992.

[2] R. Kohn and M. Vogelius "Relaxation of variational method for impedance computed tomography", *Communications on Pure and Applied Mathematics*, **40**, (1987), 745-777.

[3] S. Gutman "Alternating directions method for impedance computed tomography", *Inverse Problems*, **5**, (1989), 1027-1047.

Reconstruction of Transient Currents from Magnetic Data: Inverse Problem Formulation Employing High Order Surface Impedance Boundary Conditions

Cesare Mario Arturi [1], Luca Di Rienzo [1], Nathan Ida [2] and Sergey Yuferev [3]

[1] Dipartimento di Elettrotecnica - Politecnico di Milano, Piazza L. da Vinci, 32, 20133, Milano, ITALY;
e-mail: cesaremario.arturi@polimi.it, luca.dirienzo@polimi.it

[2] The University of Akron, Akron OH, 44325-3904, USA; e-mail: ida@uakron.edu

[3] Nokia Corporation, P.O.Box 86, Salo FIN-24101, FINLAND; e-mail: sergey.yuferev@nokia.com

Abstract **– The reconstruction of transient currents flowing in parallel conductors is achieved by means of a new time-domain Boundary Integral Equation (BIE) formulation involving Mitzner's and Rytov's high order Surface Impedance Boundary Conditions (SIBCs). Input data of the inverse problem are the magnetic fields at given locations near the conductors. In order to validate the inversion algorithm, the magnetic field data are computed solving the direct problem with FEM for given current waveforms. The improvement in accuracy of the inverse solution employing high-order instead of low-order SIBCs is demonstrated numerically.**

INTRODUCTION

The theoretical problem of reconstructing transient currents flowing in parallel conductors generating magnetic field data around them arises in the design of innovative current sensors ([1, 2, 3]) and has been solved in the time domain using a BIE formulations employing low order SIBCs. As a matter of fact this type of problems features low electromagnetic penetration depth in the conductors. A natural approach in this case is to eliminate the conducting region from the numerical procedure by using SIBCs at the conductor/dielectric interface. Then only the surface of the conductors has to be discretized and the Boundary Element Method (BEM) can be used.

In order to improve the accuracy of the inverse solution and extend the range of applicability of the novel sensors low order SIBCs must be replaced by high order SIBCs.

In this paper an invariant formulation employing high order SIBCs is developed for the inverse problem of reconstructing transient currents. The goal of the work is to demonstrate the improvement in reconstruction accuracy of the new formulation compared with previously proposed methods.

BIE-SIBC FORMULATION

Consider a system of N parallel conductors in which transient currents $I_i(t)$, $i=1,2...N$, flow from an external source (2-D problem). Introducing the magnetic scalar potential one can write

$$\vec{H} = \vec{H}^{fil} - \nabla\phi \quad (1); \qquad \vec{H}^{fil} = \sum_{i=1}^{N} \left|\vec{H}_i^{fil}\right| = \frac{I_i}{2\pi R_i} \quad (2);$$

where G is the fundamental solutions of the two-dimensional Laplace equation. The BEM yields the following surface integral equation [4]

$$c\phi + \sum_{i=1}^{N} \int_{L_i} \phi \frac{\partial G}{\partial \vec{n}} dl = \sum_{i=1}^{N} \int_{L_i} G\vec{n} \cdot \left(\vec{H}^{fil} - \vec{H}\right) dl \quad (3)$$

Assume that the duration τ of the incident current pulse is so that the penetration depth $\delta = \sqrt{\tau/(\sigma\mu)}$ remains small compared to the characteristic size D of the conductor. Then ϕ and $\vec{n}\cdot\vec{H}$ on the conductor's surface are related by the well-known SIBC of Mitzner's order of approximation, that in our two-dimensional case can be represented in the form [4]

$$\vec{n}\cdot\vec{H} = H_\eta = \frac{1}{\sqrt{\pi\sigma\mu t}} * \frac{\partial H_\xi}{\partial \xi} + \frac{1}{2d}\frac{U(t)}{\sigma\mu} * \frac{\partial H_\xi}{\partial \xi} \quad (4)$$

where the asterisk denotes a time-convolution product. Here $U(t)$ is the unit step function, the coordinate ξ is directed along the contour of the conductor's cross section, η is directed normal to it inside the conductor and d is the local radius of curvature corresponding to coordinate ξ.

Let M magnetic sensors be located in the dielectric space near the conductors. A magnetic sensor gives an output voltage signal equal to

$$V_k(t) = \vec{S}_k \cdot \vec{H} = \sum_{i=1}^{N} \alpha_{ki} I_i - \vec{S}_k \cdot \nabla\phi, \quad k=1,...M \quad (5)$$

In the inverse problem (3)-(5) the quantities V_k, α_{ki} and $\vec{S}_k$ are considered to be known (measured) and the currents I_i are determined using an iteration scheme similar to that described in [3].

It was demonstrated [4] that the SIBC (5) can be represented in the form of asymptotic expansion in the small parameter $p = \delta/D << 1$. Thus it is natural to represent the functions for which the solution is sought, i.e. the scalar potential and total current, in the form of power series in the same small

parameter. Substituting the expansions into the formulation (3)-(5) and equating the coefficients of equal powers of p, the following integral equations for the coefficients ϕ_k and I_k, $k=0,1,2$, of the expansions are obtained:

k=0 (perfect electrical conductor approximation)

$$\frac{\phi_0}{2}+\sum_{i=1}^{N}\int_{L_i}\phi_0\frac{\partial G}{\partial \vec{n}}d\xi=\sum_{i=1}^{N}\int_{L_i}G\vec{n}\cdot\vec{H}_0^{fil}\,d\xi \qquad (6a)$$

$$V_k(t)=\sum_{i=1}^{N}S_k\alpha_{ki}I_{0i}-S_k\vec{s}_k\cdot\nabla\phi_0 \quad k=1,\ldots,M \qquad (6b)$$

k=1 (Leontovich's approximation)

$$\frac{\phi_1}{2}+\sum_{i=1}^{N}\int_{L_i}\phi_1\frac{\partial G}{\partial \vec{n}}d\xi=$$

$$=\sum_{i=1}^{N}\int_{L_i}G\left\{\vec{n}\cdot\vec{H}_1^{fil}-L_1\left[\left(\vec{H}_0^{fil}\right)_\xi-\frac{\partial\phi_0}{\partial\xi}\right]\right\}d\xi \qquad (7a)$$

$$0=\sum_{i=1}^{N}S_k\alpha_{ki}I_{1i}-S_k\vec{s}_k\cdot\nabla\phi_1, \quad k=1\ldots M \qquad (7b)$$

k=2 (Mitzner's approximation)

$$\frac{\phi_2}{2}+\sum_{i=1}^{N}\int_{L_i}\phi_2\frac{\partial G}{\partial \vec{n}}d\xi= \qquad (8a)$$

$$=\sum_{i=1}^{N}\int_{L_i}G\left\{\vec{n}\cdot\vec{H}_2^{fil}-L_1\left[\left(\vec{H}_1^{fil}\right)_\xi-\frac{\partial\phi_1}{\partial\xi}\right]-L_2\left[\left(\vec{H}_0^{fil}\right)_\xi-\frac{\partial\phi_0}{\partial\xi}\right]\right\}$$

$$0=\sum_{i=1}^{N}S_k\alpha_{ki}I_{2i}-S_k\vec{s}_k\cdot\nabla\phi_2 \qquad k=1\ldots M \qquad (8b)$$

where operators L_1 and L_2 have been introduced as follows

$$\nabla_\xi^2\phi=\frac{\partial^2\phi}{\partial\xi^2};\ L_1[f]=\frac{1}{\sqrt{\pi\sigma\mu t}}*\frac{\partial f}{\partial\xi};\ L_2[f]=\frac{U(t)}{2d\sigma\mu}*\frac{\partial f}{\partial\xi} \qquad (9)$$

and

$$\left|\vec{H}_k^{fil}(\vec{r},t)\right|=\sum_{i=1}^{N}I_{ki}(t)/(2\pi R_i) \quad k=0,1,2 \qquad (10)$$

As it was proved in [5], these equations admit separation of variables into space and time components if currents are correlated in time so that an invariant formulation is possible.

PRELIMINARY RESULTS

Two parallel copper conductors of circular cross-sections of equal diameters D = 50 mm are considered (Fig. 1). The direct problem of calculating the output voltages of sensors measuring the x-component of magnetic field at given locations near the conductors (points P_1, … , P_4) is solved by means of a commercial FEM software. The following current waveform of maximum value 1A is supposed to flow into the conductors in opposite directions and the error in inversion is shown in Fig. 2

$$I_2(t)=-I_1(t)=1-\exp\left[-\left(t\cdot10^3/2\right)^2\right] \qquad (11)$$

In the full version of the paper the derivation of the invariant inverse formulation employing Rytov's SIBC will be given.

The convergence of the algorithm will also be discussed and the influence of the following factors on the computational results will be investigated: duration and shape of the transient current, number and position of the sensors and distance between the conductors.

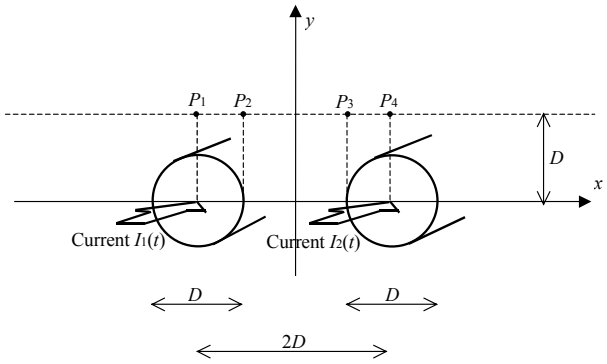

Fig. 1. Geometry of the problem

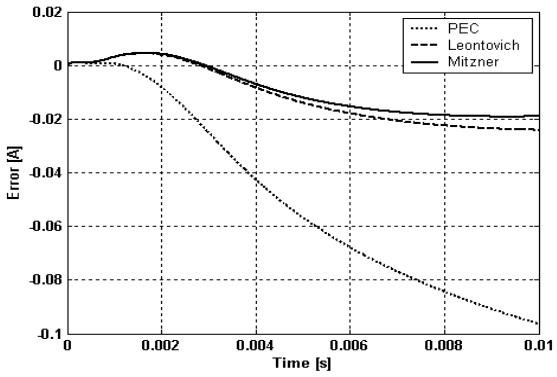

Fig. 2. Error in reconstruction: difference between current I_2 given by (11) and that calculated by inversion.

REFERENCES

[1] G. D'Antona, L. Di Rienzo, A. Manara and R. Ottoboni, "Processing Magnetic Sensor Array Data for AC Current Measurement in Multiconductor Systems", *IEEE Trans. Instrum. and Meas.*, vol.50, No..5, pp.1289-1295, 2000.

[2] G. D'Antona, L. Di Rienzo, R. Ottoboni and S. Yuferev, "Advanced Signal Processing Technique for Current Sensing Based on the Boundary Element Method", *Proc. of Sicon '01 Sensors for Industry Conference*, Rosemount, Illinois, USA, November 5-7 2001, pp. 230-234.

[3] L. Di Rienzo, N. Ida and S. Yuferev, "Application of the Surface Impedance Concept to the Inverse Problems of Reconstructing Transient Currents", *Proc. of the Tenth Biennial IEEE Conference on Electromagnetic Field Computation*, Perugia, Italy, June 16-19 2002.

[4] S. Yuferev and L. Kettunen "A Unified Surface Impedance Concept for both Linear and non-Linear Skin Effect Problems", *IEEE Trans. Magn.,* vol. 35, No. 3, pp. 1454-1457, 1999.

[5] S. Yuferev, N. Ida and L. Kettunen, "Invariant BEM-SIBC Formulations for Time- and Frequency Domain Eddy Current Problems", *IEEE Trans. Magn.,* vol. 36, No. 4, pp. 852-855, 2000.

Three-dimensional defect localization from time-of-flight/eddy current testing data

A. Tamburrino
Ass. EURATOM/ENEA/CREATE, DAEIMI, Laboratory of Computational Electromagnetics and Electromagnetic Nondestructive Evaluation, Università degli Studi di Cassino, Via G. Di Biasio 43, I-03043, Cassino, Italy

R. Fresa
DIFA, Università della Basilicata, Contrada Macchia Romana, Potenza, Italy

S. S. Udpa, Y. Tian
Department of Electrical and Computer Engineering, Michigan State University, East Lansing, MI 48824-1226

***Abstract* — This paper deals with the inverse problem of defect characterization in a conductive material using eddy current nondestructive evaluation (NDE) methods. We consider a full 3D time-domain problem in the quasi-static regime. The inversion method exploits the properties of the Q-Transform, an integral operator mapping wave propagation fields into diffusive fields. Specifically, we show that by properly choosing the waveform of the exciting current, the peak of the measured quantity can be easily related to the distance between probe and defect, as in time-of-flight measurements employed in wave propagation NDE methods.**

INTRODUCTION

In this paper eddy current NDE test data is analyzed from an unusual perspective. Specifically, we show that under proper conditions one can obtain time-of-flight information from eddy current NDE measurements as well.

As is well known, the concept of time-of-flight (TOF) is meaningful only in the case of wave propagation phenomenon. In the time domain, TOF refers to the time required for a wave to travel from the transmitter to the receiver. The time-of-flight is directly related to the distance d traveled by the wave (for homogeneous materials $d = c \cdot \mathrm{TOF}$, where c is the velocity of the wave) and can be used to reconstruct positions of material discontinuities, interfaces, flaws etc.

With reference to diffusive phenomenon, as in the case of eddy current testing, the term "time-of-flight" has no meaning. We show in this paper that by properly choosing the waveform (in the time domain) of the excitation signal, it is possible to process the data appropriately to obtain the distance d. This approach has been proposed for scalar problems in [1-3]; preliminary results for the vector case are reported in [2].

Once that the equivalent time-of-flight information is extracted, the inverse problem can be solved by using method employed for wave propagation inverse problems.

In addition, time-of-flight information obtained from eddy current tests can be fused with time-of-flight information from ultrasonic tests. Data fusion is of interest for the nondestructive evaluation (NDE) community since it is possible to improve the accuracy of the measurement by conducting more than one NDE test method and combining the information appropriately.

We extract the time-of-flight information from eddy current testing data using the Q-Transform, an integral operator mapping solutions of wave propagating fields to diffusive fields.

In the full paper we will present theoretical as well as numerical results for a 3D problem Involving the estimation of the position of a defect embedded in an infinite homogeneous conductor.

THE Q-TRANSFORM

The time-domain Maxwell equations in the magneto-quasi-static limit for linear, non-magnetic and non-dispersive materials are:

$$\begin{cases} \nabla \times \mathbf{e} = -\mu_0 \partial_t \mathbf{h} \text{ in } \Omega, \forall t \geq 0 \\ \nabla \times \mathbf{h} = \sigma \mathbf{e} + \mathbf{J}_0 \text{ in } \Omega, \forall t \geq 0 \\ \mathbf{h}(\mathbf{x},0) = \mathbf{0} \text{ in } \Omega \\ \mathbf{h}(\mathbf{x},t) \times \hat{\mathbf{n}} = \mathbf{0} \text{ on } \partial\Omega, \forall t \geq 0 \end{cases} \quad (1)$$

where $\mathbf{e}$ is the electric field, $\mathbf{h}$ is the magnetic field, $\mathbf{J}_0$ is the impressed current density (the source term), μ_0 is the free-space magnetic permeability, $\sigma(\mathbf{x})$ is the electric conductivity, and $\Omega \subset \Re^3$ is a bounded domain.

The solution of (1) is related to the solution of a fictitious wave propagation problem through the Q-Transform which is an the integral operator acting only on the time coordinate, defined as:

$$Q : \mathbf{u}(\mathbf{x},q) \rightarrow \mathbf{v}(\mathbf{x},t) = \int_0^{+\infty} \frac{q}{2\sqrt{\pi t^3}} e^{-q^2/4t} \mathbf{u}(\mathbf{x},q) dq \quad (2)$$

where $\mathbf{u}$ and $\mathbf{v}$ are vector fields, $\mathbf{x}$ is the spatial coordinate, t is the time coordinate and q is the fictitious time coordinate. Notice that $[q] = [\mathrm{T}^{1/2}]$

The main property of the Q-Transform is its ability to map solutions of hyperbolic problems to those of

This work has been supported by NASA, Italian Ministero dell'Istruzione, dell'Università e della Ricerca (MIUR), Italian Space Agency and EURATOM.

parabolic problems. This property holds for both scalar [4] and vector problems [5].

Following the approach of [5], we found for the interior problem that [2]:

$$\mathbf{h}(\mathbf{x},t)=Q\left[\tilde{\mathbf{h}}(\mathbf{x},q)\right],\ \mathbf{e}(\mathbf{x},t)=Q\left[\partial_q\tilde{\mathbf{e}}(\mathbf{x},q)\right] \tag{4}$$

where $\tilde{\mathbf{e}}(\mathbf{x},q)$, $\tilde{\mathbf{h}}(\mathbf{x},q)$ are solutions of:

$$\begin{cases}\nabla\times\tilde{\mathbf{e}}=-\mu_0\partial_q\tilde{\mathbf{h}}\ \text{in}\ \Omega,\ \forall q\ge 0\\ \nabla\times\tilde{\mathbf{h}}=\sigma\partial_q\tilde{\mathbf{e}}+\mathbf{j_0}\ \text{in}\ \Omega,\ \forall q\ge 0\\ \tilde{\mathbf{h}}(\mathbf{x},0)=\mathbf{0},\ \tilde{\mathbf{e}}(\mathbf{x},0)=\mathbf{0}\ \text{in}\ \Omega\\ \tilde{\mathbf{h}}(\mathbf{x},q)\times\hat{\mathbf{n}}=\mathbf{0}\ \text{on}\ \partial\Omega,\ \forall q\ge 0\end{cases} \tag{5}$$

under the constraint $\mathbf{J_0}=Q[\mathbf{j_0}]$.

We refer to (5) as the fictitious wave propagation problem.

TIME-OF-FLIGHT FOR DIFFUSIVE FIELDS

The Q-Transform is the key to design both the excitation waveform and the data processing steps necessary to extract information relating to the distance between the source and the inhomogeneity.

Assuming that, as is usual in eddy current testing, the measurements consist of magnetic quantities such as flux levels or field values, it follows from (4) that:

$$m(t)=Q[\tilde{m}(q)] \tag{6}$$

where m is a time-domain (scalar) eddy current measurement and $\tilde{m}$ its wave propagation counterpart (e.g. m is a component of the magnetic flux density at the probe location).

Then, by exploiting the fact that $\tilde{m}$ comes from a wave propagation phenomenon, we notice that:

$$\tilde{m}(q)=\alpha h(q-q_f) \tag{7}$$

where α is a constant, h is a known function and q_f is the time-of-flight. From (6) and (7) it follows that:

$$m(t)=Q[\alpha h(q-q_f)]. \tag{8}$$

Therefore, the time-of-flight information q_f is embedded in time-domain eddy-current measurements.

The inverse problem of retrieving q_f from m by exploiting (8) has been tackled in [1]. Specifically, it is shown that if $h(q_f^+)$ is finite and different from zero, $h(q)$ is differentiable for $q>q_f$, $|h'(q)|$ is bounded by the constant M satisfying $M<<|h(q_f^+)|/q_f$, then m has a peak at $t_{peak}=q_f^2/2$.

Similarly, when u contains a Dirac pulse, i.e. $h(q)=\alpha\delta(q-q_f)+\beta(q-q_f)$, where a vanishes for $q<0$ and $|\beta|$ is bounded by a constant M_1 satisfying $M_1<<\alpha/q_f$, then m has a peak at $t_{peak}=q_f^2/6$.

SOLUTION OF THE INVERSE PROBLEM

In this section we discuss some preliminary results for the canonical problem of estimating the position of a "small" anomaly embedded in a homogenous conductor whose conductivity is σ_0.

We assume that the exciting field is produced by an (arbitrarily oriented) elementary magnetic dipole located at the origin of the coordinate system and that the anomaly is contained in a small sphere or radius R and centered at $\mathbf{x}_0$ with $R<<|\mathbf{x}_0|$. Let $\gamma(t)$ be the magnetic moment of the dipole and let the eddy current measurement $m(t)$ be a component of the anomalous magnetic field (that is the magnetic field due to the presence of the anomaly) evaluated at the origin of the coordinate system. Let the contrast χ be defined as $\chi(\mathbf{x})=\sigma(\mathbf{x})/\sigma_0-1$, where σ is the conductivity when the anomaly is present ($\chi(\mathbf{x})=0$ outside the anomaly).

Under proper approximations [2], the fictitious measurement $\tilde{m}$ related to m by (6) is:

$$\tilde{m}(q)=K\xi(q-q_f) \tag{9}$$

$$\xi(q)=\frac{\tilde{\gamma}^{(4)}(q)}{(c|\mathbf{x}_0|)^2}+2\frac{\tilde{\gamma}^{(3)}(q)}{c|\mathbf{x}_0|^3}+\frac{\tilde{\gamma}^{(2)}(q)}{|\mathbf{x}_0|^4} \tag{10}$$

where $q_f=2|\mathbf{x}_0|/c$ is the time-of-flight, $c\doteq(\sigma_0\mu_0)^{-1/2}$ is the velocity of the fictitious wave, K depends on $\mathbf{x}_0/|\mathbf{x}_0|$ and $\tilde{\gamma}$ is related to γ through $\gamma=Q[\tilde{\gamma}]$.

For large $|\mathbf{x}_0|$ we approximate ξ by the leading term thus obtaining $\tilde{m}$ proportional to $\tilde{\gamma}^{(4)}(q-q_f)$. Therefore, the shape of $\tilde{m}$ is given by $\tilde{\gamma}^{(4)}(q-q_f)$, regardless of the unknown parameter $|\mathbf{x}_0|$. By choosing $\tilde{\gamma}$ proportional to q^4 or q^3, the waveform $m(t)$ presents a peak at $q_f^2/2$ or $q_f^2/6$ as discussed in the previous section. Once the peak position t_{peak} is estimated from the measurements, it is possible to estimate $|\mathbf{x}_0|$.

REFERENCES

[1] A. Tamburrino, S. S. Udpa, "Solution of inverse problems for scalar parabolic equations using a hyperbolic to parabolic transformation: Time Domain Analysis", submitted for publication

[2] A. Tamburrino, S. S. Udpa, Internal Report, MSU/ECE/02-11, Michigan State University, June 2002.

[3] Y. Tian, A. Tamburrino, S.S.Udpa, and L.Udpa, Proc. of 29th Annual Review of Progress in Quantitative Nondestructive Evaluation (QNDE 2002), *Washington, USA, July 2002.*

[4] L. R. Bragg, J. W. Dettman, *Bull. Amer. Math. Soc.*, vol. 74, pp. 375-78, 1968.

[5] K. H. Lee, G. Liu and H. F. Morrison, *Geophysics*, vol. 54, pp. 1180-1192, 1989.

A Novel Ray Tracing Procedure for the Localization of EM Field Sources in Urban Environment

Salvatore Coco, Antonino Laudani and Letizia Mazzurco
DIEES, University of Catania
Viale A. Doria 6
Catania, I-95125, Catania
alaudani@dees.unict.it

Abstract – **In this paper a novel procedure for the localization of EM sources in the presence of multipaths and reflections, such as those occurring in urban environment, is presented. The procedure requires a few measurements taken at accessible points to individuate accurately the sources positions. This inverse problem is solved by using an algorithm of localization based on the minimization of a cost function, which requires the computation of a field map, obtained by exploiting the ray tracing method. The presented numerical example shows the applicability of this procedure to model realistic situations.**

INTRODUCTION

The development and extensive diffusion of wireless communication systems has generated an increasing alert for the possible effects on human health due to electromagnetic pollution in urban scenarios and also inside buildings. This leads to the necessity of a continuous monitoring of electromagnetic field strength and of the individuation of the interesting EM field sources [1]. Given that the position and the intensity of all the EM source are not generally available, it is highly desirable to recover this information by using few measurements taken at accessible points. The localization of sources from few measures is a complicated inverse problem.[2][3]

In this paper a procedure is presented in order to individuate the positions of electromagnetic field sources in generic situations, such as urban scenarios or indoor environments, exploiting the knowledge of few measured values taken at arbitrarily selected points and the ray tracing algorithm for the construction of the complete EM field strength map.

The adoption of a complex method like ray tracing is due to the necessity of accurate calculations of field strength in an environment containing obstacles, for which it is not possible to use the simplified model of propagation of the EM field in free space. In fact, differently from some radio communication direct links, which work under LOS (Line Of Sight) conditions, for wireless communications in urban scenarios or indoor environments the propagation conditions are NLOS (No Line Of Sight), and thus a more sophisticated approach is necessary for field strength evaluation. The ray tracing technique, which is the most popular technique for the design and the development of mobile networks, satisfies this need.

The localization procedure is based on the minimization of a 'cost function' related to the field strength in correspondence of measurement points in the set of candidate positions for sources within the region of interst.

The presented numerical example shows the applicability of this procedure to model realistic situations.

EM SOURCES LOCALIZATION PROCEDURE AND CONSTRUCTION OF EM FIELD STRENGTH MAP BY MENAS OF RAY TRACING ALGORITHM

In the localization procedure a finite set of candidate positions for sources belonging to a regular grid, covering the region of interest is considered. Moreover a set of measurement points, chosen in such a way to be easily accessible, is also established. The positions of these measurement points belong also to a regular grid whenever possible and the distance between every two measurement points is chosen to be greater than a prefixed distance.

The localization procedure minimizes the following cost function:

$$U = ||U_{rt} - U_m||$$

where

U_m is the vector containing the known values at the established measurement points.

U_{rt} is the vector containing the values computed in correspondence of the above measurement points by using the ray tracing method for a certain configuration of sources belonging to the finite set of candidate points.

The minimization algorithm explores the universe of all the possible source configurations belonging to the finite set of candidate points.

The construction of the field map required for the evaluation of each cost function U is performed by following the ray tracing algorithm. This is a popular numerical method to compute accurately field strength maps from the knowledge of all the information about sources and propagation environment, taking into account the effects of scattering, reflection, etc.[4]

This method is based on optical geometry (GO) and on its generalization, that is geometric theory of the diffraction (GTD). The two main assumptions of GTD are that all the obstacles must have dimensions larger than wave's length and that reflections can be described by plane wave formulas.

It is worth noticing that since field propagation depends on obstacle characteristics (electrical characteristics, dimensions, etc), which determine reflection and scattering coefficients, all these information are necessary for the field strength evaluations.

The first step of (the ray tracing) algorithm is the individuation of all the possible propagation paths, between each source and each measurement point, considering even multipath propagation. In fig. 1 all the multipaths between a source and a measurement point are shown considering reflection or diffraction of rays due to obstacles under NLOS.

In order to reduce the computational effort only multi-paths of order less than a specified threshold are considered. After having individuated these multipaths and having selected those to be considered, the ray tracing method computes the contribute of each path to the total field.

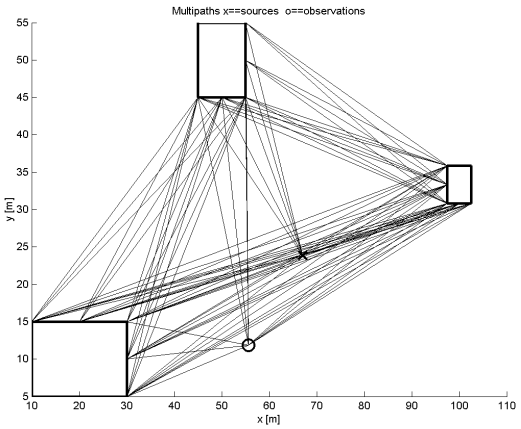

Fig. 1 – Multipath propagation between a source (o) and a point (x)

The values of EM field at point P is the sum of the contributes relative to all the admissible multipaths and the considered sources. Each contribute due to a specific path is computed considering the kind of the path: if it is a direct visibility path the field strength depends only on the distance between the source and the observation point; if reflections or diffractions are involved in the analysed paths the field strength is determined also by using reflection and diffraction coefficients of the obstacles, which depend on frequency, electromagnetic characteristic of the obstacles, angles of incidence, etc.

Once all the data for the construction of ray tracing model are determined, the localization procedure is able to determine the source positions.

More details about the ray tracing model used and the localization algorithm will be given in the full paper.

NUMERICAL EXPERIMENT

To test the developed localization procedure a simple square region of side 120 m is considered, which contains 3 buildings (EM field reflecting and diffracting obstacles) of rectangular shape and different sizes, and a certain number of sources, positioned as shown in fig. 2. The contour lines of electric field intensity coming out from the ray tracing algorithm is shown in fig. 3.

A total number of 14 measurement points for this experiment have been positioned uniformly inside the above region in such a way to guarantee that the distance between any two points is higher than 20 m. A uniform grid of 25×25 points has been used to represent the set of positions of "candidate sources".

The results of the localization procedure for this example are shown in figure 2, where real (o) and estimate (+) positions of EM field sources are indicated. This example shows that the procedure is able to individuate with good accuracy EM field sources located in a typical urban environment even in the presence of reflections and diffractions.

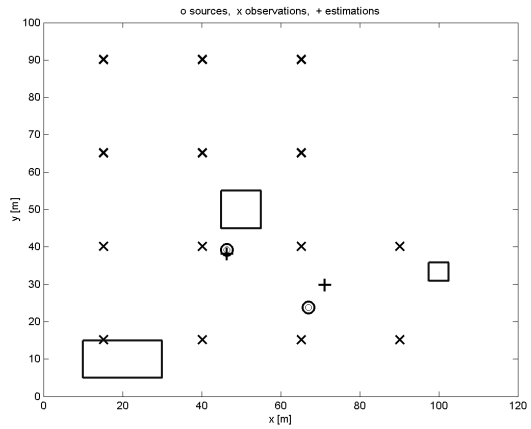

Fig. 2 – Geometry of numerical example, showing real and estimates positions of sources, obstacles and measurement points

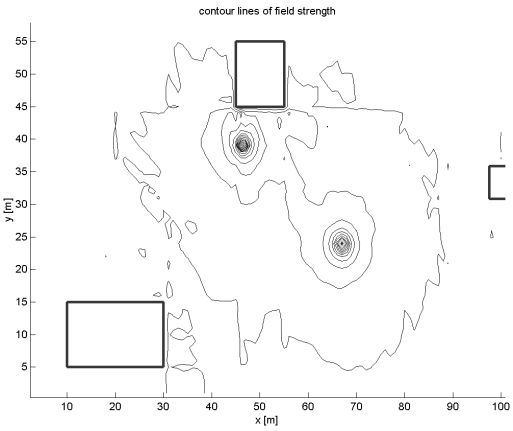

Fig. 3 – Contour lines of the field strength for the considered example.

REFERENCES

[1] F.M. Landstorfer, "Wave Propagation Models for the Planning of Mobile Comunication Network", European Microwave Week 1999, Munich (Germany), Oct. 1999.

[2] S. Fiori and P. Burrascano, "Electromagnetic Environmental Pollution Monitoring: Source Localization by the Independent Component Analysis", Third International Conference on Independent Component Analysis, and Signal Separation, pp. 575 - 580, San Diego, California, December 9-13, 2001

[3] L. Albini, P. Burrascano, E. Cardelli, A. Faba, S. Fiori, "Numerical Modeling for the Localization and the Assessment of Electromagnetic Field Sources", Proc. of the Tenth Biennial Congress on Electromagnetic Field Computation (CEFC'2002), Perugia (Italy), 16-19 June, p. 251, 2002.

[4] K. Rizk, J.F. Wagen, F. Gardiol, "Two Dimensional Ray Tracing Modeling For Propagation Prediction In Microcellular Environment", IEEE Trans, Veh. Technol., vol 46, no 2, pp. 508-517, May 1997.

Some Considerations on the Regularization of Inverse Magnetostatic Problems

A. Formisano and R. Martone
Dipartimento di Ingegneria Dell'Informazione, Seconda Università di Napoli,
Via Roma 29, Aversa, (CE) I-81031 ITALY
e-mail: a.formisano@unina.it, martone@unina.it).

Abstract – Inverse problems in electromagnetics are usually ill-conditioned, requiring as such the adoption of some regularization technique in order to obtain reliable results. Anyway, the choice of the regularization method and of the related parameters represent a quite critical issue. Such choice must be based on the knowledge of reliable additional information on the problem to get satisfactory results.

INTRODUCTION

The interest of the scientific community on both theoretical and applied aspects of problems involving reconstruction and identification from external measurements is growing steadily. An example of such problems is represented by the identification of the current density distribution in superconducting cables from external magnetostatic measurements using Hall Probes [1].

This class of *inverse problems* is mathematically formulated starting from the *direct* problem formulation which, generally, is based on a *direct operator*, able to provide the *effects* (fields, fluxes) associated to known *sources* acting trough known *systems*. The direct operator is usually a simplified representation of the physics behind the phenomenon under examination, the simplification coming either from the approximation of real world sources in terms of suitable representation basis or from system simplified modelling, in order to take into account only a subset of the actual interactions. Furthermore, also the effects, being usually associated to measurements provided by devices characterized by a certain degree of *uncertainty*, must be considered known only within a certain approximation.

On the other hand, the related inverse problems, such as the reconstruction and the identification problems, are aimed at reconstructing, in the most reliable way, the sources or the system characteristics, in spite of the uncertainties characterizing the system model and the measurements. Unfortunately, the direct operators involved in many real world problems lead to ill conditioned inverse problems, showing as such a quite relevant sensitivity to uncertainties. In particular, measurement errors and system modelling inaccuracy may lead to poor accuracy and limited smoothness in the inverse problem solution.

Many of the commonly used inversion procedures, starting from the assumption that the solutions must be smooth, pursue such regularity also trough the adoption of various *regularization techniques*. Unfortunately, improper use of regularizations may unduly constrain the approximated solution and, consequently, cause significant lack of accuracy.

This paper examines the effect of some popular regularization techniques on the resolution of the inverse problems in the class of current density reconstruction problems, briefly discussing limits and applicability conditions, and assessing their impact on the performance of reconstruction procedures. Some criteria for an effective application of regularization will also be discussed with reference to an example of current density identification, showing in particular how proper choices, founded on a careful analysis of the direct problem, may reveal quite effective in improving the solution quality.

MATHEMATICAL FORMULATION

The typical formulation of a *linear* source reconstruction problem consists in the search for a function f (source function) belonging to a search space Φ (sources space) projecting into the known function g (data function), belonging to the "data" space Γ, trough a projection operator $\wp$ to be inverted ($\wp$ being the direct operator describing the sources-effects relationship):

$$\wp f = g. \tag{1}$$

In the particular case of finite number m of measurements, and adopting a suitable base of dimension n for the space Φ, the functions f and g may be described trough a finite set of degrees of freedom (their "coordinates" in the basis spanning Φ and Γ), the operator $\wp$ can also be discretized according to the chosen representation basis for Φ, leading to a *discrete* formulation of the direct problem:

$$\underline{\underline{\mathbf{P}}}\mathbf{f} = \mathbf{g}, \tag{2}$$

where $\mathbf{f}$ and $\mathbf{g}$ are vectors of $\Re^m$ and $\Re^n$ respectively, and the matrix $\underline{\underline{\mathbf{P}}}$ is the dicretized version of $\wp$.

The operator $\underline{\underline{\mathbf{P}}}$ must then be inverted to obtain the inverse problem formulation. Usually, $\underline{\underline{\mathbf{P}}}$ is ill-conditioned, and the inverse operator will amplify the undetermination on the data vector $\boldsymbol{g}$ by a factor related to its conditioning number, leading to quite relevant errors in the reconstructed source vector $\mathbf{f}$.

The general philosophy of the regularization techniques is to restrict the search space Φ to a subset Φ', characterized by additional properties not considered in (1) (or in its discrete counterpart (2)). Note that the choice of the restriction criteria should be based on actual and robust knowledge, otherwise such criteria may hinder the search of solutions similar to the actual, noisy one, driving the solution process towards inaccurate, although more "appealing" (e.g. smoother), solutions.

REGULARIZATION TECHNIQUES

The first, fundamental contributions to the subject, known in literature as "Tichonov techniques", date back to early 60's [2]. Some of them (e.g. Constrained Least

Squares) constrain the maximum norm of the solution vector **f**; such techniques result attractive when $\|\mathbf{f}\|^2$ is related to an energy. Others (e.g. Phillips methods [2]) constrain the maximum norm of an image **g** of the solution; such formulations are in some sense dual to the previous ones, and are then suitable in cases when $\|\mathbf{g}\|^2$ is related to an energy function. Some others combines the two aspects. Following these seminal contributions, many other techniques have been proposed, both for continuous formulations (1) and for discrete formulations (2). As an example, for the discrete formulation, it has been proposed [3] an approach based on the representation of f in a basis composed of a suitably chosen number of singular functions of the inverse of $\underline{\underline{\mathbf{P}}}$. Other approaches suggest to weight differently the elements of **g** based on the level of confidence associated to each measurement [4], or to constrain the variation of the elements of **f** [5].

Note that the performance of practically all the techniques depend critically on one or more parameters characterizing the various methods, which allow to balance the relative weight of the model equations (1) or (2) and of the regularizing constraints.

Such a variety of regularization methods and the associated choice of the critical parameters impose a careful assessment before selecting the most adequate technique, and the best values of the associated parameters. The general criterion to be adopted is to relate such decisions only to the consistent and reliable additional information because lack of physical insight may lead to unrealistic, tough mathematically appealing (i.e. smooth), solutions.

In the full paper, some of the most interesting proposals for magnetostatic inverse problems will be critically compared, both in terms of physical relevance and of impact on the problem resolution.

PRELIMINARY RESULTS.

As a preliminary case study for the assessment of some of the above exposed ideas, a "mock-up cable" realised by the Institute of Electrical Engineering (IEE), Slovak Academy of Sciences, Bratislava, is considered, composed of 6 massive brass conductors, simulating the 6 "petals" of the superconducting busbar feeding the Iter Toroidal Field Model Coil at Forschungszentrum Karlsruhe (see Fig. 1 for a comparison of the mockup geometry and of the actual busbar). The unknown sources are the currents in each petal, which are fed independently, while the measurements are constituted by the magnetic fields, measured around the cable using 6 Hall Probes along assigned directions (see Fig.1 for a picture of the measuring device).

Eq. (2) can be specialised as:

$$\underline{\underline{\mathbf{G}}}\mathbf{I} = \mathbf{b}_{HP}, \qquad (3)$$

where **I** is the vector of the 6 currents in the massive brass petals, $\mathbf{b}_{HP}$ is the vector of HP readings, and **G** is the Green matrix relating currents and fields. The currents in the petals are found trough a pseudo-inversion of the Green matrix.

As an example of regularization techniques, a further equation has been added, imposing the (known) total current. In Fig. (2) results obtained using (black) or not using (grey) the information on total current are reported, in the case of

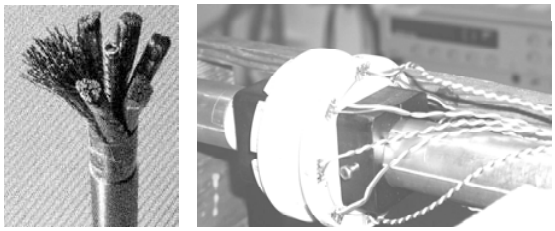

Fig. 1. Comparison of TFMC cable (left) and mockup cable (right). Courtesy of ENEA Frascati and IEE Bratislava.

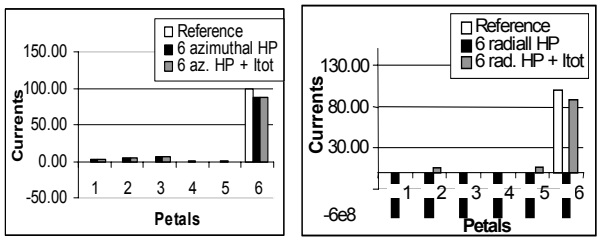

(a) (b)

Fig. 2. Comparison of current reconstruction schemes in the mockup cable for 6 tangential HP (a) and for 6 radial HP system (b). Grey bars refer to 6HP+Total Current, black to just 6 HP. Actual currents are also reported for comparison (white bars). Negative scale for (b) is cut to show the current values (in the order of -6×10^8).

reconstruction using 6 Hall Probes oriented parallel to the nominal cable field (left) or perpendicular to the field lines (right). The exact solution is also reported for comparison (white).

It appears quite evident that the information about total current effectively regularizes the problem in the case of Hall Probes perpendicular to the nominal field, while it does not in the other case, due to the Ampere law, and the regularizing equation is redundant. Note also that a regularization technique based on the smoothness constraint would have not been useful in this particular case.

In the full paper a more detailed analysis of the effect of various regularization techniques will be presented, on a number of experimental cases, in order to perform a critical comparison of regularization techniques for the source reconstruction problems in magnetostatics.

ACKNOWLEDGEMENTS

Authors wish to thank Dr. Polack and Dr. Della Corte for their precious help and suggestions.

REFERENCES

[1] A. Formisano, R. Martone, "Current Reconstruction from Magnetic Measurement in Superconducting Cables", *Proceedings of 10th IGTE Symposium*, Graz (Austria), 10-18 Sept. 2002.

[2] M. Bertero, "Linear Inverse and Ill-Posed Problems", in Advances in Electronics and Electron Physics, vol. 75, San Diego: Academic Press, 1989.

[3] J. M. Varah, "A Practical Examination of Some Numerical Methods for Linear Discrete Ill-Posed Problems", *SIAM Review*, vol. 21 n°1, pp. 100-111, January 1978.

[4] R. J. Hanson, "A numerical Method for Solving Fredholm Integral Equations of the First Kind Using Singular Values", *SIAM Journal of Numerical Analysis*, Vol. 8, No. 3, pp. 616-622, 1970.

[5] M. Yu, D. E. Dougherty, "Modified Total Variation Methods for Three-dimensional Electrical Resistance Tomography Inverse Problems", *Water Resources Research*, vol. 36, pp. 1653-1664, July 2000.

COMPUMAG Saratoga Springs, New York USA
July 13 - 17, 2003

On the Reconstruction of Inhomogeneous Surface Impedance of Cylindrical Bodies

Hülya Şahintürk
Technical University of Yıldız
Department of Mathematical Engineering
Davutpasa, Istanbul, Turkey

Abstract- **A method whose aim is to reconstruct the inhomogeneous surface impedance of a cylindrical body from the measured far field scattering data is given. The scattered field is represented in terms of a single layer potential and the field values on the surface of the scatterer are obtained through the jump relations. Then the surface impedance is reconstructed directly from the boundary condition itself.**

I. Introduction

aces. The determination of the Impedance Boundary Conditions IBC for a given scatterer constitutes an important class of problems in the electromagnetic theory and various approximate methods have been established in the literature for special kind of geometries and surfaces [1]. In all these methods one first tries to solve the direct scattering problem for a given scattering structure and then express the IBC in terms of the electric and magnetic field on the boundary. The surface impedance of a scattering object can also be obtained by using the scattered data obtained through measurements on a certain domain. In such a case the problem is considered as an inverse scattering problem which aims to get the fields on the boundary of the object in terms of the measured data. A method for the reconstruction of the surface impedances of planar boundaries has been proposed in [2].

The inverse boundary value problem we consider here is, for a known shape of the scatterer, to reconstruct the inhomogeneous surface impedance of the cylinder through far field measurements in the case of plane wave illumination. First, the scattered field is represented by a single-layer potential and the density of the single-layer potential is obtained by solving the resulting ill-posed integral equation of the first kind through Tikhonov regularization. The use of the jump relations for single-layer potentials leads to explicit expressions of the scattered field and its derivative on the impedance surface. Then by using the boundary condition itself one can achieve the reconstruction. Since the use of the boundary condition itself constitutes an ill-posed problem, a regularized solution in a least squares sense is also described.

II. Formulation of the problem

We consider the electromagnetic scattering problem related to an infinitely long cylindrical body with cross-section D. The body is located in an infinite homogeneous background medium with constitutive parameters ε, μ, and σ. On the boundary of the cylinder, say ∂D, the applicable boundary condition is the standard inhomogeneous impedance boundary condition (SIBC) with a non-constant continuous normalized impedance coefficient $\eta = \eta(x)$, that is,

$$-n \times (n \times E) = \frac{\eta(x)}{ik}\, n \times H \quad \text{on } \partial D, \tag{1}$$

where E and H are the total electric and magnetic field vectors and n is the outward unit normal vector of ∂D, where ∂D is the surface of the cylinder.

The inverse impedance problem related to this configuration consists of reconstructing the impedance function η from the far measured far field data, say u_∞. When the boundary ∂D is known a priori, the far field pattern u_∞ uniquely determines the scattered field u^s and consequently the total field $u = u^i + u^s$ in the exterior of the scatterer D. Therefore in view of (1) the surface impedance can be obtained from the values of the total field u and its normal derivative $\partial u/\partial n$ on ∂D via

$$\eta(x) = -ik\, \frac{u(x)}{\dfrac{\partial u}{\partial n}(x)}\,, \quad x \in \partial D. \tag{2}$$

Possible zeros in the denominator on the right hand side of (2) will be taken care off by a least squares regularization. In the sequel we will describe a method for reconstructing the required field values on the boundary ∂D from the far field data. To this aim we first represent the scattered field as a single-layer potential of the form

$$u^s(x) = \int_{\partial D} G(x,y)\varphi(y)\, ds(y), \tag{3}$$

with an unknown density function φ. We have that the

far field pattern of (3) is given by

$$u_\infty(\hat{x}) = \frac{e^{i\pi/4}}{\sqrt{8k\pi}} \int_{\partial D} e^{-ik\,\hat{x}\cdot y} \varphi(y)\, ds(y) \tag{4}$$

for the observation direction $\hat{x} = (\cos\theta, \sin\theta)$ with observation angle θ. Hence, given a far field pattern u_∞, we need to solve the integral equation of the first kind

$$A\varphi = u_\infty \tag{5}$$

for the density φ, where the integral operator A is given by

$$(A\varphi)(\hat{x}) := \frac{e^{i\pi/4}}{\sqrt{8k\pi}} \int_{\partial D} e^{-ik\,\hat{x}\cdot y} \varphi(y)\, ds(y). \tag{6}$$

The operator A has an analytic kernel and therefore (5) is severely ill-posed. For that reason some kind of stabilization such as Tikhonov regularization has to be applied. For a regularized solution in the sense of Tikhonov we solve the equation

$$\alpha\varphi + A^* A\varphi = A^* u_\infty \tag{7}$$

with a regularization parameter $\alpha > 0$ and the adjoint A^* of A as given by

$$(A^* g)(y) = \frac{e^{-i\pi/4}}{\sqrt{8k\pi}} \int_\Omega e^{ik\,\hat{x}\cdot y} g(\hat{x})\, ds(\hat{x}), \quad y \in \partial D.$$

Once the single-layer density φ is known, the values u and $\partial u/\partial n$ of the total field on the boundary ∂D can be recovered through the jump relations for the single-layer potential, that is, by

$$u(x) = u^i(x) + \int_{\partial D} G(x,y)\varphi(y)\, ds(y), \quad x \in \partial D, \tag{8}$$

and

$$\frac{\partial u}{\partial n}(x) = \frac{\partial u^i}{\partial n}(x) + \int_{\partial D} \frac{\partial G(x,y)}{\partial n(x)} \varphi(y)\, ds(y) - \frac{1}{2}\varphi(x). \tag{9}$$

It is obvious that the solution (2) will be sensitive to errors in the normal derivative of u in the vicinity of zeros. To obtain a more stable solution, we express the unknown impedance function in terms of some basis functions ϕ_n, $n = 1, \ldots, N$, as a linear combination

$$\eta = \sum_{n=1}^{N} a_n \phi_n \quad \text{on } \partial D. \tag{10}$$

A possible choice of basis functions consists of splines or trigonometric polynomials. Then we satisfy (2) in the least squares sense, that is, we determine the coefficients $a_1, \ldots, a_N$ in (10) such that for a set of grid points $x_1, \ldots, x_M$ on ∂D the least squares sum

$$\sum_{m=1}^{M} \left| u(x_m) + \sum_{n=1}^{N} a_n \phi_n(x_m) \frac{\partial u}{\partial n}(x_m) \right|^2 \tag{11}$$

is minimized. The number of basis functions N in (10) can be considered as some kind of regularization parameter.

IV. Numerical results

In order to see the accuracy and the applicability of the theory we consider an illustrative example. The reconstructions of the surface impedance have been obtained by using both the direct method and the least squares solution. In the application of the least squares solution the basis functions are chosen as $\phi_n(x(t)) = e^{-int}$, $n = 0, \pm 1, \ldots \pm N$. The body is illuminated from the direction $\phi_0 = 0$ and the far field data are collected at 50 equally spaced points of the semi circle. The number of basis functions in the least square solution is $N = 5$. Figure 1 illustrates the exact and reconstructed values of the real and imaginary parts of the surface impedance in the case of a drop-shaped cylinder. Obviously the least squares solution still yields satisfactory results.

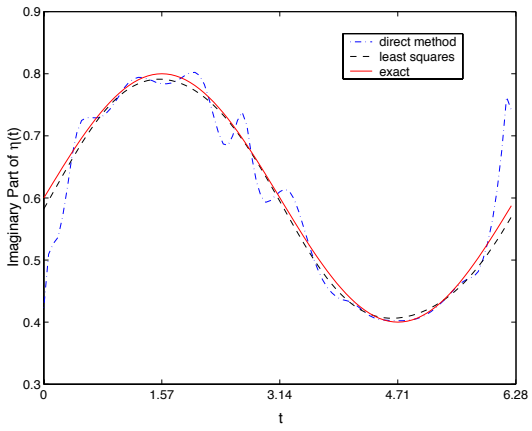

Figure 1: Imaginary parts of the exact and reconstructed values of the normalized surface impedance for the drop-shaped cylinder.

References

[1]Hoppe, D.J. and Rahmat-Samii, Y., *Impedance boundary conditions in electromagnetics*, Taylor & Francis, 1995

[2]İ. Akduman and A. Yapar, Surface impedance determination of a planar boundary by the use of scattering data IEEE Trans. on Antennas and Propagation, vol.49 no.2, pp. 304-307, February 2001.

An Improved Tabu Based Vector Optimal Algorithm for Design Optimizations of Electromagnetic Devices

YANG S.Y.[1], CARDOSO J.R.[2], NI P.H.[1], and HO S.L.[3]
[1]EE College, Zhejiang University, China
[2] Escola Politecnica da USP, São Paulo-SP, Brazil
[3]EE Department, The Hong Kong Polytechnic University, Hong Kong

Abstract— An improved tabu based vector (multi-objective) optimal algorithm is introduced in this paper. The improvements include a division of the search process, a new method for fitness assignment, a novel scheme for the generation and selection of neighborhood solutions and so forth. Numerical results validate the robustness and advantages of the proposed method for solving vector optimal design problems.

AN IMPROVED TABU BASED VECTOR OPTIMAL ALGORITHM

Thanks to the effort of scientists and engineers in the last two decades, a wealth of multi-objective optimizers have been developed, and some multi-objective optimization problems that could not be solved hitherto were successfully solved by using these optimizers. In terms of robustness and efficiency of the available vector optimizers, these optimizers are still in need of improvements and hence there are many unresolved open problems [1]. An improved tabu based vector optimizer is proposed in this paper.

Diversification and Intensification Phases

In general, an ideal solver of multi-objective designs should have the following features: (1) to efficiently find the Pareto solutions, and (2) to uniformly sample the Pareto optimal front, i.e., to maintain the diversity of the searched Pareto Solutions. To achieve the first goal, the algorithm should reinforce the moves that incorporate the merits of the Pareto solutions found in the previous search process. To obtain the second objective, the search process should also drive the search into unexplored regions to sample the Pareto front uniformly. Consequently, the search process of the proposed algorithm is divided into two phases, i.e., a diversification and an intensification phase. Once a solution is identified as a new Pareto solution, an intensifying search around the specified point using a gradient based Newton method is activated to quickly search for better or new Pareto solutions. The algorithm will continue in this phase until a transition criterion is satisfied, and the algorithm will then switch into the diversification phase for the next iterative cycle.

Assigning Fitness Value for New States

It is well known that in the selection of new current points for a tabu search, it is necessary to obtain the objective function values of their neighborhood solutions. As the objective function in a multi-objective optimization problem is a vector, some scalarization techniques must be used. The non-dominated sorting technique is improved and used in the proposed algorithm to decide the "fitness" value of a neighborhood solution [2]. The general procedure for assigning the fitness value of a neighborhood solution in the proposed algorithm is described as:

Choose a large dummy fitness value v_{fit}. Find the non-dominated individuals among the neighborhood solution using solutions in both the neighborhood and the Pareto optimal archives [3], set the fitness value of the found solutions to v_{fit};

Repeat

$v_{fit} = \alpha v_{fit}$;

Find the non-dominated individuals among the neighborhood solutions whose fitness values are not set;

Set the fitness value of the solutions just found to v_{fit};

Until fitness values of all neighborhood solutions are set.

The initial value of the fitness value, v_{fit}, and the decreasing rate, α, in the proposed algorithm are, respectively, set to *3*, and $1/3$, so as to guarantee that a Pareto optimal in the neighborhood solutions will always be selected as the new current one despite the introduction of fitness sharing functions in both parameter and objective spaces.

Fitness Sharing Function

To produce a uniform distribution of the searched Pareto solutions not only in the objective but also in the parameter spaces, the fitness sharing concept is introduced. In order to reduce the implementing complexity, a simple fitness sharing function as defined below is proposed. Mathematically, the fitness sharing function is

$$f_{share}(\bar{x}^{(i)}) = \frac{1/d_f(\bar{x}^{(i)})}{\sum_{j=1}^{N_h} 1/d_f(\bar{x}^{(j)})} + \frac{1/d_X(\bar{x}^{(i)})}{\sum_{j=1}^{N_h} 1/d_X(\bar{x}^{(j)})} \qquad (1)$$

where, $d_u(\bar{x}^{(k)})(u = f, X)$ is the point density of the Pareto optimal obtained around the specified point $\bar{x}^{(i)}$ in the *u*-space, N_h is the number of the total neighborhood solutions of $\bar{x}^{(i)}$, *f* and *X* are, respectively, the objective and parameter spaces.

To compute the density of the Pareto optimal for a

specified point, a hyper-box with the point as the centre is constructed and the number of the Pareto optimal points which lie in this box is used as a measure for its fitness sharing function. The fitness value of a neighbourhood solution, $\bar{x}^{(i)}$, is the sum of its fitness and fitness sharing function values, i.e.,

$$f_{fit}(\bar{x}^{(i)}) = v_{fit}(\bar{x}^{(i)}) + f_{share}(\bar{x}^{(i)}) \quad (2)$$

Generation and Selection of Neighborhood Solutions

Unlike the procedure that generates the total number of N_h neighborhood solutions and then choose the best one as the new current solution, the proposed algorithm will accept a new neighborhood solution if its total fitness value is not worse than that of the current one regardless of whether the number of neighborhood solutions generated so far has reached N_h or not during the neighborhood generating process. This will lead to a reduction in the number of total function evaluations. Moreover, to maintain the diversity of the searched Pareto solutions, the number of neighborhood solutions generated in the i^{th} neighbor of the current solution is proportional to the step length of the neighbor.

Transition between Intensification and Diversification Phases

The proposed algorithm will start from the diversification phase. Once a new Pareto solution is identified, the algorithm will automatically switch to the intensification phase to intensify the search around the specific point. The algorithm will continue in this phase until either there is no further possible improvement on the specific point, or there is no other Pareto solution found around the specific point.

NUMERICAL VALIDATION

The geometrical optimal design of the multi-sectional pole arcs of large hydro-generators as reported in [3] is solved by using the proposed method to demonstrate its efficiency and robustness. The problem is formulated as

$$\begin{aligned} \max \quad & B_{f1}(X) \\ \min \quad & e_v \\ \text{s.t} \quad & SCR - SCR_0 \geq 0 \\ & X'_d - X'_{d0} \leq 0 \\ & THF - THF_0 \leq 0 \end{aligned} \quad (3)$$

The corresponding geometrical parameters to be optimized are the center positions and radii of the multi-sectional arcs of pole shoes. The searched Pareto solutions for the optimal design of five-sectional pole arcs of a 300 MW, 20-pole hydro-generator by using the proposed algorithm, together with those of [3], are shown in Fig. 1. The corresponding iterative numbers used by the two methods are given in Table 1. To further validate the proposed algorithm, it is employed to study the multi-sectional pole arc design of another 300 MW, 44-pole hydro-generator. The computed Pareto solutions are shown in Fig. 2. From these two numerical examples one can see that for the geometrical optimal designs of the multi-sectional pole arcs of large hydro-generators, the Pareto fronts searched by the two algorithms, i.e., one with and another without the improvements proposed in this paper, are virtually the same and are equally uniformly distributed in the objective spaces. However the iterative number used by the proposed method is significantly less than that required by the original one.

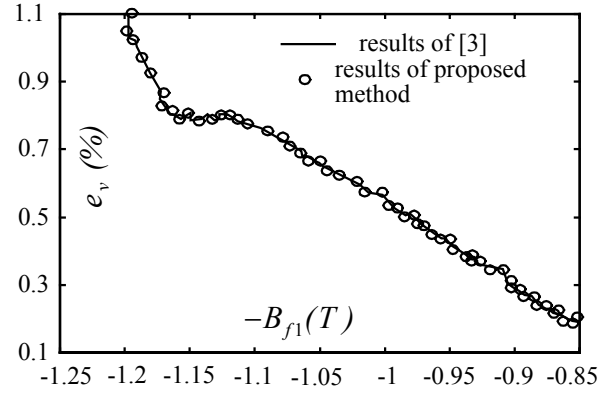

Fig. 1. The searched Pareto solutions of a 300 MW, 20-pole hydrogenerator

TABLE 1 PERFORMANCE COMPARISON OF DIFFERENT METHODS

Method	The Proposed Method	Results of [3]
Iterative Number	4864	6500

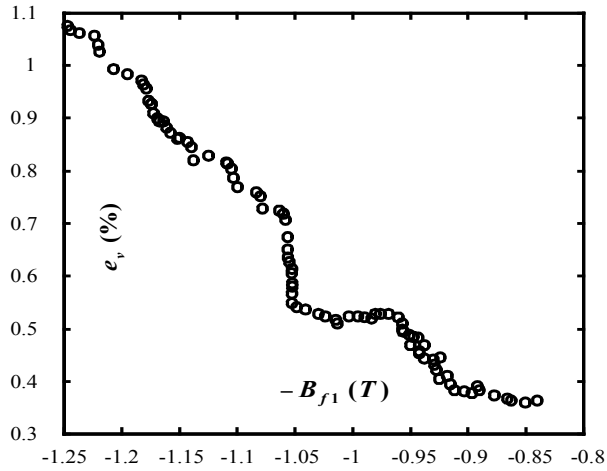

Fig.2. The searched Pareto solutions of a 300 MW, 44-pole hydrogenerator.

REFERENCES

[1] Zitzler, E., Deb, K., Thiele, L., "Comparison of multiobjective evolutionary algorithms: empirical results," *Evolutionary Computation*, vol. 8, pp. 173-195, 2000.

[2] Knowles, J.D., Corne, D.W., "Approximating the non-dominated front using the Pareto archived evolution strategy," *Evolution Computation*, vol. 8, pp. 149-172, 2000.

[3] Ho, S.L., Yang, S.Y., Ni, G.Z., Wong, H.C., "A tabu method to find the Pareto solutions for multi-objective optimal problems in electromagnetics," *IEEE Trans. Magn.*, vol. 38, pp. 1013-1016, 2002.

Reconstruction of the Complex Conductivity Distribution in 3D

K. Hollaus, Ch. Magele
Institute for Fundamentals and Theory in Electrical Engineering, IGTE
Technical University of Graz
Kopernikusgasse 24, A-8010 Graz, Austria
e-mail: hollaus@igte.tu-graz.ac.at

***Abstract* — In electrical impedance an inverse problem has to be solved to reconstruct the complex conductivity distribution $\boldsymbol{\kappa} = \boldsymbol{\sigma} + j\omega\boldsymbol{\varepsilon}$. The problem is ill-posed and, therefore, a regularization has to be used. The aim is to achieve the same resolution for the conductivity $\boldsymbol{\sigma}$ as well as for the permittivity $\boldsymbol{\varepsilon}$ in 3D applying finite elements of second order.**

INTRODUCTION

Electrical impedance tomography (EIT) is used for reconstructing the $\boldsymbol{\kappa} = \boldsymbol{\sigma} + j\omega\boldsymbol{\varepsilon}$ in a region by injecting electrical currents in electrodes and simultaneously measuring the resulting potential distribution $\mathbf{U}_0$ on the surface [1]. For instance, in biomedical applications it is extremely important to reconstruct $\boldsymbol{\kappa}$ accurately to be able to determine the parameters of the Cole-model (CM) exactly. Physiological parameters, like the hydration state, etc., can be extracted from the CM parameters [2]. The inverse problem is posed in such a way that the regularization is applied to $\boldsymbol{\sigma}$ and to $\boldsymbol{\varepsilon}$ separately. A small numerical example is analyzed and some preliminary results are shown.

THE INVERSE PROBLEM

To solve the inverse problem as mentioned above an objective function f is posed as shown in (1) to minimize the deviation between simulated voltages $\mathbf{U}(\boldsymbol{\kappa})$ and measured ones $\mathbf{U}_0$ on electrodes by varying $\boldsymbol{\kappa}$. The voltage vectors $\mathbf{U}(\boldsymbol{\kappa})$ and $\mathbf{U}_0$ are complex, where m is the number of voltage ports. The finite element method (FEM) is used to simulate the forward problem. To each finite element (FE) i of n FEs a constant value σ_i and ε_i is assigned.

$$f = \min_{\boldsymbol{\sigma},\boldsymbol{\varepsilon}} \left\{ \left\| \mathbf{U}(\boldsymbol{\kappa}) - \mathbf{U}_0 \right\|_2^2 + \alpha_\sigma \left\| \mathbf{L}\boldsymbol{\sigma} \right\|_2^2 + \alpha_\varepsilon \left\| \mathbf{L}\omega\boldsymbol{\varepsilon} \right\|_2^2 \right\} \tag{1}$$

$$\left\| \mathbf{U}(\boldsymbol{\kappa}) - \mathbf{U}_0 \right\|_2^2 = \left(\mathbf{U}^*(\boldsymbol{\kappa}) - \mathbf{U}_0^*(\boldsymbol{\kappa}) \right)^T \cdot \left(\mathbf{U}(\boldsymbol{\kappa}) - \mathbf{U}_0(\boldsymbol{\kappa}) \right) \tag{2}$$

$$\left\| \mathbf{L}\boldsymbol{\sigma} \right\|_2^2 = \boldsymbol{\sigma}^T \mathbf{L}^T \mathbf{L}\boldsymbol{\sigma} = \sum_{i=1}^{n} \sigma_i \left(\sum_{j=1}^{n} l_{ij}\sigma_j \right) \tag{3}$$

$$\mathbf{U}^T(\boldsymbol{\kappa}) = \left(U_1(\boldsymbol{\kappa}) \quad \dots \quad U_m(\boldsymbol{\kappa}) \right)^T, \quad \mathbf{U}_0^T = \left(U_{01} \quad \dots \quad U_{0m} \right)^T \tag{4}$$

$$\boldsymbol{\sigma}^T = \left(\sigma_1 \quad \dots \quad \sigma_n \right)^T, \quad \boldsymbol{\varepsilon}^T = \left(\varepsilon_1 \quad \dots \quad \varepsilon_n \right)^T \tag{5}$$

$$U = U_{re} + jU_{im}, \; U^* = U_{re} - jU_{im} \tag{6}$$

Since the problem is ill-posed, i.e., large changes in $\boldsymbol{\kappa}$ in the interior can result in small voltage changes on the surface. Therefore, a regularization, [3], is introduced by a "smoothing" operator $\mathbf{L}$ controlled by regularization factors α_σ and α_ε for $\boldsymbol{\sigma}$ and $\boldsymbol{\varepsilon}$, respectively. The entries of $\mathbf{L}$ are determined as follows: $l_{ij} = -1$, if $i \neq j$ and FE i is adjacent to FE j; $l_{ij} = 0$, if $i \neq j$ and FE i is not adjacent to FE j; $l_{ii} = -\sum_{j=1}^{n} l_{ij}$ with $i \neq j$. The Gauss-Newton method, [4], is used to reconstruct $\boldsymbol{\kappa}$ by minimizing the non-linear equation (1) iteratively as shown in (7). The update $\left(\Delta\boldsymbol{\sigma} \quad \Delta\boldsymbol{\varepsilon} \right)^T$ is determined by the Hessian matrix $\mathbf{G}$ and the gradient $\mathbf{g}$, see (8). In (7) and (8) t represents the iteration step. The Hessian matrix $\mathbf{G}$ as shown in (10) is approximated only neglecting the second order derivatives.

$$\begin{pmatrix} \boldsymbol{\sigma} \\ \boldsymbol{\varepsilon} \end{pmatrix}^{(t+1)} = \begin{pmatrix} \boldsymbol{\sigma} \\ \boldsymbol{\varepsilon} \end{pmatrix}^{(t)} + \begin{pmatrix} \Delta\boldsymbol{\sigma} \\ \Delta\boldsymbol{\varepsilon} \end{pmatrix}^{(t)} \tag{7}$$

$$\begin{pmatrix} \Delta\boldsymbol{\sigma} \\ \Delta\boldsymbol{\varepsilon} \end{pmatrix}^{(t)} = -\left(\mathbf{G}^{(t)}\left(\boldsymbol{\sigma}^{(t)}, \boldsymbol{\varepsilon}^{(t)} \right) \right)^{-1} \mathbf{g}\left(\boldsymbol{\sigma}^{(t)}, \boldsymbol{\varepsilon}^{(t)} \right) \tag{8}$$

$$\mathbf{g}(\boldsymbol{\sigma}, \boldsymbol{\varepsilon}) = 2\mathbf{J}\mathbf{r} + 2\alpha_\sigma \mathbf{L}^T\mathbf{L}\boldsymbol{\sigma} + 2\alpha_\varepsilon \omega \mathbf{L}^T\mathbf{L}\boldsymbol{\varepsilon} \tag{9}$$

$$\mathbf{G}(\boldsymbol{\sigma}, \boldsymbol{\varepsilon}) = 2\mathbf{J}\mathbf{J}^T + 2\alpha_\sigma \mathbf{L}^T\mathbf{L} + 2\alpha_\varepsilon \mathbf{L}^T\mathbf{L} \tag{10}$$

The entries of the Jacobian matrix $\mathbf{J}$ in (11) are computed with the aid of the sensitivity theorem [5] and decomposed in real and imaginary parts. The residuum $\mathbf{r}$ is also separated in real and imaginary parts, see (12). The superscripts in (13) indicate partial derivatives of the voltage U_i at port i either with respect to σ_j and or $(\omega\varepsilon_j)$ of the FE j.

$$\mathbf{J} = \begin{pmatrix} \mathbf{J}_{re}^{\sigma} & \mathbf{J}_{im}^{\sigma} \\ \mathbf{J}_{re}^{\varepsilon} & \mathbf{J}_{im}^{\varepsilon} \end{pmatrix} \tag{11}$$

$$\mathbf{r} = \left(\mathbf{r}_{re} \quad \mathbf{r}_{im}\right)^T = \left(\mathrm{Re}\left\{\mathbf{U}^T(\kappa)\text{-}\mathbf{U}_0^T\right\} \quad \mathrm{Im}\left\{\mathbf{U}^T(\kappa)\text{-}\mathbf{U}_0^T\right\}\right)^T \tag{12}$$

$$J_{ij}^{\sigma} = \frac{\partial U_i}{\partial \sigma_j}, \; J_{ij}^{\varepsilon} = \frac{\partial U_i}{\partial\left(\omega\varepsilon_j\right)} \tag{13}$$

QUASI-STATIC ELECTRIC FIELD

The Maxwell's equations to be solved describing a quasi-static electric field in the time harmonic case represented advantageously by the complex formalism are

$$\nabla \times \mathbf{E} = \mathbf{0} \tag{14}$$

$$\nabla\left(\mathbf{J} + j\omega\mathbf{D}\right) = 0\,, \tag{15}$$

where $\mathbf{E}$ is the electric field intensity, $\mathbf{J}$ is the conduction current density, $\mathbf{D}$ is the electric displacement, ω is the angular frequency and j denotes the imaginary unit. The relation (14) enables to introduce the electric scalar potential V as

$$\mathbf{E} = -\nabla V\,. \tag{16}$$

Considering the constitutive laws

$$\mathbf{J} = \sigma\mathbf{E} \tag{17}$$

$$\mathbf{D} = \varepsilon\mathbf{E}\,, \tag{18}$$

where σ and ε are assumed to be constant, yields the partial differential equation (19) for V.

$$\nabla\left(\left[\sigma + j\omega\varepsilon\right]\nabla V\right) = 0 \tag{19}$$

The corresponding boundary value problem is solved by the finite element Galerkin technique using nodal tetrahedral finite elements of second order, [6].

NUMERICAL SIMULATIONS

The small imaging problem shown in Fig. 1 has been analyzed. The gray surfaces represent one opposite pair of current electrodes. Currents are injected successively in pairs of opposite current electrodes while all voltages on opposite voltage electrodes are measured, [7]. The arrangement consists of 8 current electrodes at the bottom and 8 voltage electrodes at the top of the generated surface of the cubic problem region. The region is subdivided in 48 FEs. The conductivity σ is $1S/m$ and the relative permittivity ε_r is 1 in the entire region except in a smaller cube (one eighth of the entire volume) where σ is $5S/m$ and ε_r is 5. The initial values for the Gauß-Newton algorithm are assumed to be as follows: σ equals $10S/m$ and ε_r equals 10. In Fig. 2 is the error defined in (20) of the reconstructed σ with respect to α_σ is represented. Similar results are obtained for ε.

$$\varepsilon_\sigma = \frac{1}{n}\sqrt{\sum_i^n \frac{\left(\sigma_i - \sigma_{i,true}\right)^2}{\sigma_{i,true}^2}} \tag{20}$$

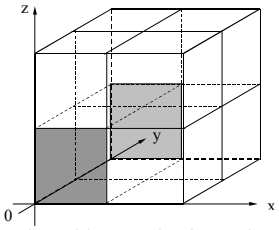

Fig. 1. Cubic problem region with one pair of opposite current electrodes at the bottom.

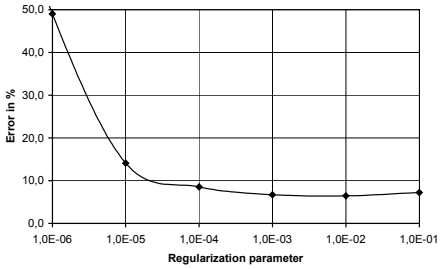

Fig. 2. Error ε_σ with respect to the regularization parameter α_σ.

ACKNOWLEDGEMENT

This work was supported by the Austrian "Fond zur Förderung der wissenschaftlichen Forschung" under the Grant No. F003.

REFERENCES

[1] Webster, J. G.: "Electrical Impedance Tomography", Bristol, England: Adam Hilger, 1990.

[2] Morucci J. P., Marsili, P. M.: "Bioelectrical impedance techniques in medicine. III. Impedance imaging. Second section: reconstruction algorithms", Crit. Rev. Biomed. Eng, vol. 24, 599-654, 1996.

[3] M. Vauhkonen, D. Vadász, P. A. Karjalainen, E. Somersalo, J. P. Kaipio, "Tikhonov Regularization and Prior Information in Electrical Impedance Tomography", IEEE Trans. Med. Eng., vol. 17, pp. 285-293., 1998.

[4] Fletcher, R.: "Practical Methods of Optimization", John Wiley & Sons New York, 1987.

[5] D. B. Geselowitz, "An Application of Electrocadiographic Lead Theory to Impedance Plethymography", IEEE Trans. Biomed. Eng., vol. 18, pp. 38-41., 1971.

[6] A. Kameari "Symmetric Second Order Edge Elements for Triangles and Tetrahedra", *IEEE Transactions on Magnetics*, vol. 35, pp. 1394-1397, May 1999.

Design and Analysis of Planar Printed Microwave Filters using FDTD Method in Conjunction with an Unsplit-Anisotropic Perfectly Matched Layer Technique

Ming-Sze Tong[1], Yilong Lu[1], Yinchao Chen[2] and Viktor Krozer[3]

[1]School of Electrical and Electronic Engineering, Nanyang Technological University, Singapore 639798
Email address: emstong@ntu.edu.sg or eylu@ntu.edu.sg

[2]Department of Electrical Engineering, University of South Carolina, Columbia, SC 29208, USA
Email address: chenyin@engr.sc.edu

[3]Ørsted·DTU, Technical University of Denmark, Electromagnetic Systems, DK-2800 Kgs. Lyngby, Denmark
Email address: vk@oersted.dtu.dk

Abstract – In this paper, the well-known Finite Difference Time Domain (FDTD) method is incorporated with an unsplit anisotropic perfectly matched layer (UA-PML) technique to design and analyze different types of microwave filters planar-printed on microstrip-line circuits. The developed FDTD solver is first validated by comparing the computed data with those published in literature, and an excellent agreement is observed between the results. Next, based on the specified criteria, various planar printed microwave filter structures are designed and analyzed, and the theoretical predictions match excellently with the computed results for the characteristics of the proposed filter systems.

INTRODUCTION

In the area of electromagnetics, it has always been a challenge to analytically solve the Maxwell's equations, particularly for the structures that consist of complex geometry, irregular boundary conditions, and hybrid materials. Thanks to the advance of computer technology, finding a full-wave solution of the Maxwell's equations becomes achievable using various numerical techniques.

One of the well-known numerical techniques is the Finite Difference Time Domain (FDTD) method [1]. It expands the Maxwell's curl equations using central finite differences. The method is popularly adopted due to its robustness, versatility and simplicity for implementation.

To this extent, an in-house computer solver has been developed based on the FDTD algorithm in conjunction with an unsplit anisotropic perfectly matched layer technique [2] for absorbing boundary condition (ABC) treatment. The solver is first validated by comparing the computed data with some microwave integrated circuits (MICs) given in other literature, and an excellent agreement has been found with those published results. The solver is then applied into the design and analysis of various planar printed microwave filter structures based on their specified design criteria, and it has been found that the computed results match very well with the theoretical predictions for the characteristics of those proposed filter structures.

THEORY

UA – PML Technique

The technique [2] assumes an artificial absorbing medium in which the Maxwell's equations are to be modified as

$$\nabla \times \vec{H} = j\omega\varepsilon_0\varepsilon_r \overline{\overline{s}}\vec{E} \tag{1a}$$

$$\nabla \times \vec{E} = -j\omega\mu_0\mu_r \overline{\overline{s}}\vec{H} \tag{1b}$$

where $\overline{\overline{s}}$ is a diagonal tensor with a matrix form

$$\overline{\overline{s}} = \begin{bmatrix} s_y s_z / s_x & 0 & 0 \\ 0 & s_z s_x / s_y & 0 \\ 0 & 0 & s_x s_y / s_z \end{bmatrix} \tag{2}$$

and each element s_u ($u = x$, y, or z) is described as

$$s_u = 1 + \frac{\sigma_u}{j\omega\varepsilon_0} \tag{3}$$

to which σ_u is the attenuation factor for absorption of the radiating electromagnetic fields.

Filter Design and FDTD Set-up

The supporting substrates used for the filter designs are assumed to be lossless dielectric materials with $\mu_r = 1$, and all conducting strips and the ground plate are assumed to be perfectly electric conductor (PEC) and infinitesimally thin.

Excitation is realized by either a Gaussian or a Blackman-Harris pulse at the input microstrip line feed. Time-stepping stability is governed by the Courant's Stability condition, and the characteristics of the designed filters are determined through Fourier analysis of the extracted time domain data.

The above-mentioned UA-PML technique as explained in [2] is adopted for the ABC treatment. In general, a 4-layer UA-PML medium is used for the side and top walls, while an 8-layer APML medium is adopted for the end walls whose normal is the direction of electromagnetic wave propagation.

NUMERICAL RESULTS AND DISCUSSIONS

The developed FDTD solver is first validated through a microstrip low pass filter whose layout is given in Fig. 1 [3].

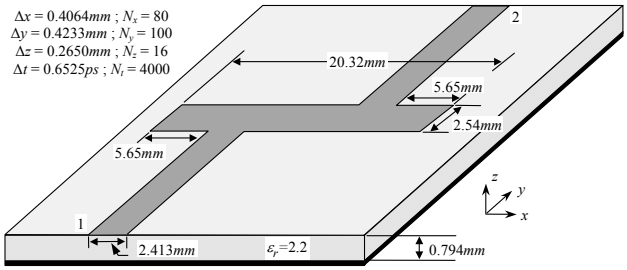

Fig. 1. Configuration of the microstrip low pass filter.

The frequency responses in terms of S-parameters are plotted in Fig. 2 and compared with those published in the literature. It is found that the computed results are excellently in agreement with those given in [3].

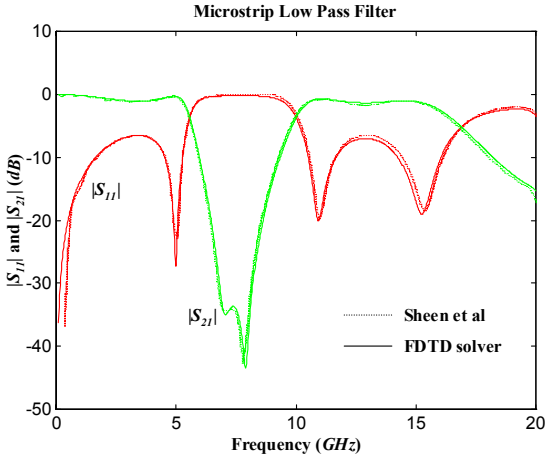

Fig. 2. Frequency characteristics for the microstrip low pass filter.

The solver is applied for design and analysis of various planar printed filter structures. One of them is a cascaded band pass filter as shown in Fig. 3. A fourth order maximally flat filter is selected as the filter type, with a central frequency at 2.8*GHz* and a 3*dB* fractional bandwidth of 0.45.

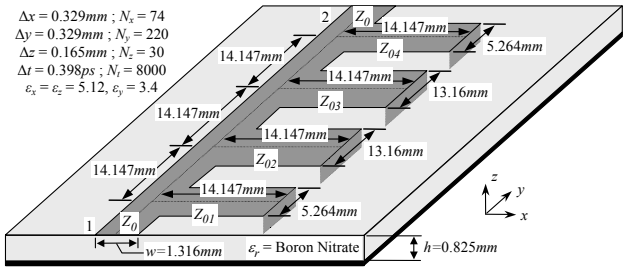

Fig. 3. Configuration of the cascaded band pass filter.

The frequency dependence of the S-parameters for the structure is depicted in Fig. 4. It is found from the graph that the computed pass band properties, *i.e.*, the central frequency and its 3*dB* bandwidth, match generally well with the predicted theoretical ones. In particular, the central pass band frequency, which is computed by the average of the 3*dB* frequencies in $S_{21}(f)$, is found at around 2.9*GHz*.

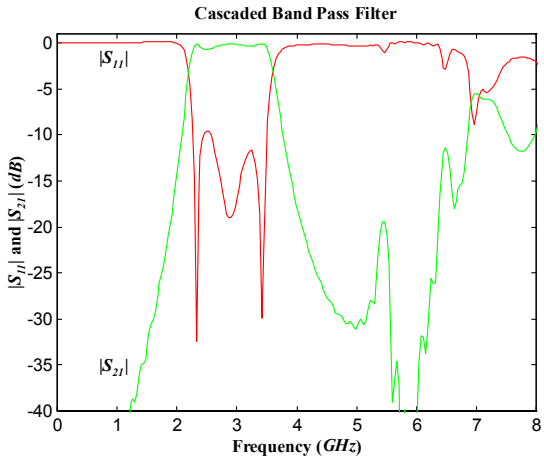

Fig. 4. Frequency characteristics for the cascaded band pass filter.

CONCLUSION

A computing solver based on conventional FDTD method incorporated with an UA-PML technique has been developed and successfully applied to design and analyze planar printed microwave filters. The validation results matched excellently with those published in literature, while the computed results in the filter design and analysis agreed very well with theoretical predictions and expectations. Results show that FDTD is a robust, versatile and powerful tool in designing and analyzing such planar printed microwave filter systems.

ACKNOWLEDGEMENT

This project was supported by the Hong Kong Polytechnic University under Grant V312. Ming-Sze Tong acknowledges the current and previous financial support given by the Singapore Millennium Foundation (SMF) and the Alexander von Humboldt (AvH) Foundation respectively.

REFERENCES

[1] K. S. Yee, "Numerical solution of initial boundary value problems involving Maxwell's Equations in isotropic media," *IEEE Transactions on Antennas and Propagation,* vol. AP-14, pp. 302- 307, May 1966.

[2] S. D. Gedney, "An anisotropic perfectly matched layer-absorbing medium for the truncation of FDTD lattices," *IEEE Transactions on Antennas and Propagation,* vol. AP-44, no. 12, pp. 1630-1639, Dec. 1996.

[3] D. M. Sheen, S. M. Ali, M. D. Abouzahra, and J. A. Kong, "Application of the three-dimensional finite-difference time-domain method to the analysis of planar microstrip circuits," *IEEE Transactions on Microwave Theory and Techniques*, vol. MTT-38, no. 7, pp. 849-857, July 1990.

The Non-Standard FDTD Method using Complex Formulation

Kenji Taguchi [1], Tadao Ohtani [2], Tatsuya Kashiwa [1], Yasushi Kanai [3]
[1] Kitami Institute of Technology, Kitami, Japan, 090-8507
[2] Mitsubishi Heavy Industries, Ltd., Nagoya, Japan, 455-8515
[3] Niigata Institute of Technology, Kashiwazaki, Japan, 945-1195
e-mail:kashiwa@klab2.elec.kitami-it.ac.jp

Abstract **— In this paper, a new formulation for the non-standard FDTD (NS-FDTD) method using a complex correction function is proposed to treat lossy media. In order to show the propagation characteristics of the NS-FDTD method for lossy media, the numerical dispersion equation and the stability condition are derived. The proposed NS-FDTD method is used to analyse a periodic electromagnetic wave absorber to demonstrate its validity. It is shown that the proposed NS-FDTD method is more accurate than the standard FDTD method and the NS-FDTD method for lossy media.**

INTRODUCTION

The NS-FDTD method has been proposed as a high accuracy FDTD method [1, 2, 3]. The method was originally developed for lossless media and has recently been modified to be able to treat lossy media. However, good numerical characteristics have not been obtained [4]. Thus the development of high accuracy NS-FDTD method for lossy media has been desired.

In this paper, a highly accurate NS-FDTD method is proposed for lossy media. The method is based on a complex formulation using the Sin-Cosine method. The phase velocity error and the stability condition are examined. The method has been applied to the analysis of a fin ferrite electromagnetic wave absorber.

COMPLEX NS-FDTD DIFFERENCE EQUATION

In this paper, the two-dimensional TE case is described. The difference equations for the complex NS-FDTD method are expressed as follows,

$$E_{x,sin}^{t+\Delta t/2}(x,y+\Delta y/2)=\frac{u_-}{u_+}E_{x,sin}^{t-\Delta t/2}(x,y+\Delta y/2) + Im\left[\frac{\alpha_{0y}}{u_+\dot{S}_y(\Delta y)}\left\{\dot{H}_z^t(x,y+\Delta y)-\dot{H}_z^t(x,y)\right\} + \frac{(1-\alpha_{0y})}{2u_+\dot{S}_y(\Delta y)}\left\{\dot{H}_z^t(x+\Delta x,y+\Delta y)-\dot{H}_z^t(x+\Delta x,y) + \dot{H}_z^t(x-\Delta x,y+\Delta y)-\dot{H}_z^t(x-\Delta x,y)\right\}\right], \quad (1)$$

$$E_{y,sin}^{t+\Delta t/2}(x+\Delta x/2,y)=\frac{u_-}{u_+}E_{y,sin}^{t-\Delta t/2}(x+\Delta x/2,y) + Im\left[\frac{\alpha_{0x}}{u_+\dot{S}_y(\Delta x)}\left\{\dot{H}_z^t(x+\Delta x,y)-\dot{H}_z^t(x,y)\right\} + \frac{(1-\alpha_{0x})}{2u_+\dot{S}_y(\Delta x)}\left\{\dot{H}_z^t(x+\Delta x,y+\Delta y)-\dot{H}_z^t(x,y+\Delta y) + \dot{H}_z^t(x+\Delta x,y-\Delta y)-\dot{H}_z^t(x,y-\Delta y)\right\}\right], \quad (2)$$

and

$$H_{z,sin}^{t+\Delta t}(x,y)=\frac{u_-^*}{u_+^*}H_{z,sin}^t(x,y) - Im\left[\frac{1}{u_+^*\dot{S}_y(\Delta x)}\left\{\dot{E}_y^{t+\Delta t/2}(x+\Delta x/2,y)-\dot{E}_y^{t+\Delta t/2}(x-\Delta x/2,y)\right\}\right] + Im\left[\frac{1}{u_+^*\dot{S}_y(\Delta y)}\left\{\dot{E}_x^{t+\Delta t/2}(x,y+\Delta y/2)-\dot{E}_x^{t+\Delta t/2}(x,y-\Delta y/2)\right\}\right]. \quad (3)$$

In (1) – (3),

$u_\pm=\varepsilon_0\varepsilon_r/S_\omega(\Delta t)\pm\sigma_e/\widetilde{S}_\omega(\Delta t)$, $u_\pm^*=\mu_0\mu_r/S_\omega(\Delta t)\pm\sigma_h/\widetilde{S}_\omega(\Delta t)$,

$S_\omega(\Delta t)=2sin(\omega\Delta t/2)/\omega$, $\widetilde{S}_\omega(\Delta t)=2cos(\omega\Delta t/2)$,

$\dot{S}_\gamma(\Delta)=2sinh(\dot{\gamma}\Delta/2)/\dot{\gamma}$,

and

$$\dot{F}^t=F_{cos}^t+jF_{sin}^t, \quad (4)$$

where $F^t=E_x^t(x,y),\ E_y^t(x,y),\ and\ H_z^t(x,y)$.

NUMERICAL PHASE VELOCITY AND THE STABILITY CONDITION

The numerical phase velocity of the method is obtained from the following equation,

$$\left[\mu_0\mu_r\frac{2jsin(\omega\Delta t/2)}{S_\omega(\Delta t)}+\sigma_h\frac{2cos(\omega\Delta t/2)}{\widetilde{S}_\omega(\Delta t)}\right]\cdot\left[\varepsilon_0\varepsilon_r\frac{2jsin(\omega\Delta t/2)}{S_\omega(\Delta t)}+\sigma_e\frac{2cos(\omega\Delta t/2)}{\widetilde{S}_\omega(\Delta t)}\right] -\left(\frac{2sinh(\dot{\gamma}_x\Delta x/2)}{\dot{S}_\gamma(\Delta x)}\right)^2\dot{\rho}_x-\left(\frac{2sinh(\dot{\gamma}_y\Delta y/2)}{\dot{S}_\gamma(\Delta y)}\right)^2\dot{\rho}_y=0. \quad (5)$$

where, $\rho_i=\alpha_{0i}+(1-\alpha_{0i})cosh(\dot{\gamma}_i\Delta i),\ (i=x,y)$.

The stability condition can be obtained using the following procedure. Using finite difference equations (1), (2), and (3) we can obtain the matrix relation

$$v^{n+1/2}=[G]v^{n-1/2}, \quad (6)$$

where, $v^n=\left[E_{x,sin}^n\quad E_{x,cos}^n\quad E_{y,sin}^n\quad E_{y,cos}^n\quad H_{z,sin}^{n+1/2}\quad H_{z,cos}^{n+1/2}\right]^T$.

The stability condition can then be obtained when the eigenvalues, g's, of equation (6) satisfy the condition $|g|\le 1$.

RESULTS

Fig. 1 shows the normalized attenuation constant α_N/α_0 in ferrite, where, α_0 is the theoretical physical attenuation constant, and α_N is the numerical attenuation constant. Fig. 2 shows the normalized phase velocity C_N/C_0 in ferrite, where C_0 is the physical speed of light in ferrite, and C_N is the numerical speed of light in ferrite. In these figures, the results from the FDTD method and the NS-FDTD method considering lossy media are shown. Only the results obtained using the complex NS-FDTD method agree well with the theoretical values. In these figures, (h:h/2) indicates that $\Delta x = h$ and $\Delta y = h/2$.

Fig. 3 shows a cross-sectional view of a fin ferrite electromagnetic wave absorber. In this analysis, Δx, Δy, and Δz are set to $\Delta\lambda$ /10. Fig. 4 shows the reflection characteristics of the fin ferrite electromagnetic wave absorber. In the figure, results obtained using the FDTD method are also shown. The complex NS-FDTD results agree well with the predicted results in Ref. [5].

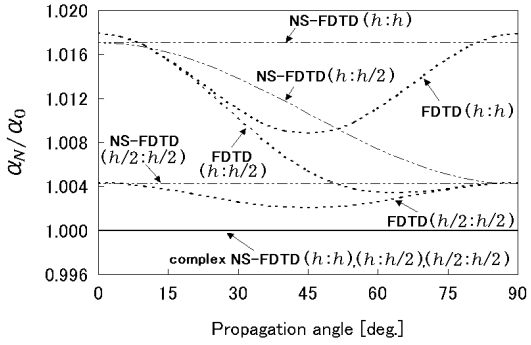

Fig. 1 Numerical attenuation constant in ferrite.

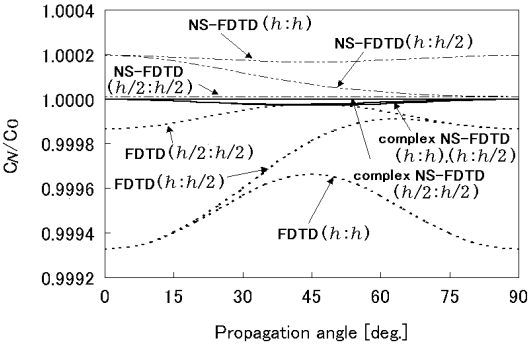

Fig. 2 Numerical phase velocity in ferrite.

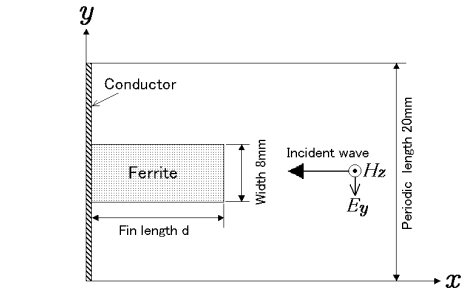

Fig. 3 Cross-sectional view of the fin ferrite electromagnetic wave absorber.

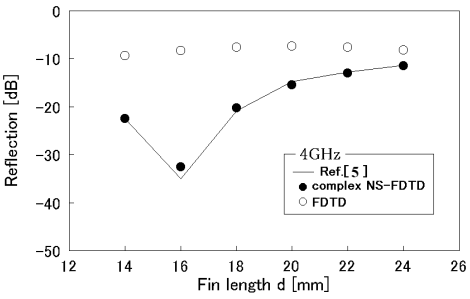

Fig. 4 Reflection characteristics of the fin ferrite electromagnetic wave absorber.

CONCLUSION

In this paper, a NS-FDTD method based on a complex formulation has been presented. The phase velocity error and the stability condition were examined. It was shown that the method has a high accuracy characteristic, not only for lossless media but also for lossy media. The method has been applied to the analysis of a fin ferrite electromagnetic wave absorber and the effectiveness of the method has been shown.

REFERENCES

[1] J. B. Cole, "A high-accuracy realization of the Yee algorithm using non-standard finite differences," *IEEE Trans. Microwave Theory and Tech.*, vol. 45, no. 6, pp. 991-996, June 1997.

[2] N. V. Kantartzis and T. D. Tsiboukis, "A higher-order FDTD technique for the implementation of enhanced dispersionless perfectly matched layers combined with efficient absorbing boundary conditions," *IEEE Trans. Magn.*, vol. 34, no. 5, pp. 2736-2739, Sep. 1998.

[3] T. Kashiwa, H. Kudo, Y. Sendo, T. Ohtani, and Y. Kanai, "Phase velocity error and the stability condition of the three dimensional non-standard FDTD method," *IEEE Trans. Magn.*, vol. 38, no. 2, pp. 661-664, Mar. 2002.

[4] T. Ohtani, Y. Sendo, and T. Kashiwa, "The non-standard FDTD method in lossy media," *IEICE Trans.* (in Japanese, to be published)

[5] Y. Naito, M. Takahashi, T. Mizumoto, and H. Nose, "Wide-band characteristics of fin ferrite electromagnetic wave absorber," *IEICE Trans.,* vol. J76-B-II, no. 7, pp. 641-646, July 1993. (in Japanese)

A Dispersion-Reduction Scheme for the Higher-Order (2,4) FDTD Method

Theodoros T. Zygiridis and Theodoros D. Tsiboukis
Dept. of Electrical and Computer Engineering, Aristotle University of Thessaloniki, GR 54124 Thessaloniki, Greece

***Abstract*—A technique for the suppression of phase inaccuracies due to numerical dispersion in the (2,4) finite-difference time-domain (FDTD) method is developed and evaluated in the present paper. Based on a systematic choice of the material parameters, the optimization procedure is combined with the fourth-order accurate spatial operators in order to substantially enhance the finite difference approach. Although the corrected values are extracted for a single frequency, improvement can be verified for a wide frequency range by theoretical and experimental results. The efficiency of the proposed practice is finally exhibited through a variety of two and three dimensional test problems.**

INTRODUCTION

The presence of numerical dispersion in simulations with the finite-difference time-domain (FDTD) method has been recognized as a considerable source of error that limits its reliability range. The inability to reproduce the exact phase velocity within the computational lattice leads to inaccuracies that are inherently accumulative and, therefore, have detrimental effect in the case of large domains or long simulation times. Due to the numerical wavenumber's dependence on the frequency and the cell shape, additional errors are observed in wideband problems and non-uniform spatial discretizations. Aiming at dispersion correction, several researchers have suggested the exploitation of higher-order difference and time integration schemes [1-3], while techniques that are based on second-order approaches have also been developed [4-7].

A means of reducing numerical dispersion in the Yee algorithm was proposed in [6], which accomplishes a significant suppression of the error in the numerical wavenumber calculation by slightly altering the properties of the modeled materials. In this paper, a similar approach is combined with the higher-order (2,4) FDTD scheme, in order to derive a methodology that yields sufficiently low levels of phase discrepancies, even when coarse meshes are used and without resorting to very small time steps. The proposed technique also decreases errors originated by the use of non-cubic cells, while it maintains its simplicity, as its implementation to existing (2,4) FDTD codes requires no significant modifications. In addition, overall improvement can be achieved at a specific frequency band by carefully choosing the optimization frequency. Several numerical results demonstrate the usefulness and the applicability of the presented method.

DISPERSION REDUCTION IN THE (2,4) FDTD METHOD

The dependence of the numerical phase velocity on the angle of propagation implies an anisotropic behavior when modeling isotropic materials. The technique developed herein can be regarded as an amendment to the aforementioned deficiency, according to which proper material parameters that result in a more accurate estimate of the physical wavenumber are determined. For the 2-D case, we consider the propagation of a TE wave ($E_x, E_y, H_z \neq 0$) in a lossless medium with diagonal electric anisotropy $\bar{\varepsilon}_r = diag[\varepsilon_{rx}, \varepsilon_{ry}]$. The dispersion relation for the (2,4) scheme is apparently calculated by admitting plane wave solutions of the form $f = f_0 e^{j\omega t} e^{-j(k_x x + k_y y)}$. Using the conventional symmetric fourth-order approximation of the spatial derivatives

$$\partial_u f\big|_i = \frac{27\left(f\big|_{i+1/2} - f\big|_{i-1/2}\right) - \left(f\big|_{i+3/2} - f\big|_{i-3/2}\right)}{24\Delta u} \tag{1}$$

and inserting the plane wave expressions in the discretized Maxwell's equations, the dispersion relation is obtained:

$$\frac{\sin^2(\omega\Delta t/2)}{c_0^2\Delta t^2} = \frac{F_{\Delta x}(\tilde{k}\cos\varphi)}{\varepsilon_{ry}} + \frac{F_{\Delta y}(\tilde{k}\sin\varphi)}{\varepsilon_{rx}} \tag{2}$$

where

$$F_{\Delta w}(u) = \left(\frac{27\sin(u\Delta w/2) - \sin(3u\Delta w/2)}{24\Delta w}\right)^2 \tag{3}$$

$\tilde{k}$ is the numerical wavenumber, φ is the angle of propagation in the 2-D lattice, $c_0 = (\mu\varepsilon)^{-1/2}$ is the speed of light and

$$\Delta t \leq \frac{6}{7c_0}\left(\frac{1}{\varepsilon_{ry}\Delta x^2} + \frac{1}{\varepsilon_{rx}\Delta y^2}\right)^{-1/2} \tag{4}$$

Using (2), $\tilde{k}$ is forced to be equal to the physical wavenumber k, for two distinct angles of propagation φ_1 and φ_2. Therefore, two equations with ε_{rx}, ε_{ry} being the unknown variables are derived and solved, yielding the following formulae:

$$\varepsilon_{rx} = \left[\frac{2}{\omega\Delta t'}\sin^{-1}\left(c_0\Delta t'\sqrt{\frac{F_{\Delta x}(k\cos\varphi_1) + CF_{\Delta y}(k\sin\varphi_1)}{C}}\right)\right]^2 \tag{5}$$

$$\varepsilon_{ry} = C\varepsilon_{rx} \tag{6}$$

where

$$C = -\frac{F_{\Delta x}(k\cos\varphi_1) - F_{\Delta x}(k\cos\varphi_2)}{F_{\Delta y}(k\sin\varphi_1) - F_{\Delta y}(k\sin\varphi_2)} \tag{7}$$

$$\Delta t' = \frac{Q}{c_0}\left(\frac{1}{C\Delta x^2} + \frac{1}{\Delta y^2}\right)^{-1/2}. \tag{8}$$

For $Q = 6/7$, the maximum allowable time step for numerical stability is reached, which is not known in advance. The objective is to make the mean value of the numerical phase velocity equal to the physical one. Hence, after ε_{rx}, ε_{ry} have been calculated, the deviation D of the numerical velocity's mean value from c_0 is computed and the final ε_{rx}, ε_{ry} are acquired from (5), (6) by merely considering $(c_0 - D)$ instead

of c_0. Choosing $\varphi_1 = 0$, $\varphi_2 = \pi/2$ always results in a periodic dispersion curve with an angular period of $\pi/2$, irrespective of the shape of the cells. Moreover, if the time step is determined beforehand, the following expression holds:

$$\varepsilon_{rx} = \frac{c_0^2 \Delta t^2}{\sin^2(\omega \Delta t/2)} \frac{F_{\Delta x}(k\cos\varphi_1) + C F_{\Delta y}(k \sin\varphi_1)}{C} \qquad (9)$$

while ε_{ry} is again obtained from (6). Of course, it should be then verified that the predetermined time step satisfies (4).

The extension of the aforementioned procedure to the 3-D case is straightforward. Specifically, we assume a medium that is both electrically and magnetically anisotropic. However, the relative permittivity and permeability tensors are chosen such that $\bar{\varepsilon}_r = \bar{\mu}_r = diag[\varepsilon_{rx}, \varepsilon_{ry}, \varepsilon_{rz}]$. In this way, $\mu_u / \varepsilon_u = \mu / \varepsilon$, $u = x, y, z$, i.e. the intrinsic impedance of the considered medium remains unaltered, despite the modification of its parameters. The final expressions for ε_{rx}, ε_{ry}, ε_{rz} will be given in the full paper.

In essence, the described method provides a corrected value for the phase velocity method and, thus, successfully minimizes phase inaccuracies. For example, Fig. 1 depicts the dispersion curves that correspond to the Yee algorithm, the (2,4) FDTD and the corrected (2,4) FDTD methods for $\Delta x = \lambda/6$, $\Delta y = \lambda/12$, considering the maximum time step for each case. Furthermore, this procedure reduces the anisotropy of the dispersion curves in non-cubic grids, while it remains uncomplicated, as it is founded on the simplest higher-order FDTD scheme. Finally, dispersion compensation is possible at a wide range of frequencies, thus making the optimization scheme suitable for wideband simulations as well.

NUMERICAL RESULTS

The efficiency of the proposed method is validated in various single-frequency and wideband problems, with 2-D and 3-D configurations. For instance, we consider the case of a 2-D parallel-plate waveguide, where propagation of the TM_1 mode is simulated. The 10×40 cm region of interest is discretized with a resolution of approximately 16 cells per wavelength. Initial values are prescribed to all field components, while boundary values are specified at the two ports for all time steps. It is stressed that fourth-order accuracy was retained in the entire domain, as higher-order, one-sided approximations of the spatial derivatives were used near the boundaries [3]. The errors produced by the Yee algorithm, the (2,4) FDTD and the corrected (2,4) FDTD methods are illustrated in Fig. 2, where the error at each time step is defined as

$$error = \sqrt{(i_{\max} j_{\max})^{-1} \sum_{i,j} \left(H_z^{num}\big|_{i+1/2, j+1/2} - H_z^{ex}\big|_{i+1/2, j+1/2} \right)^2} \qquad (10)$$

The time step is kept the same for all simulations. Compared to Yee's scheme, both higher-order approaches are more accurate. However, the corrected method outperforms the conventional one, proving its superiority at the specific test.

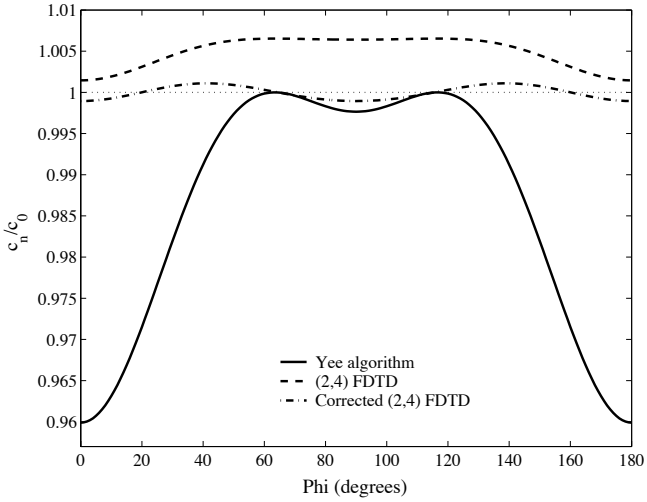

Fig. 1. Comparison of normalized numerical phase velocities

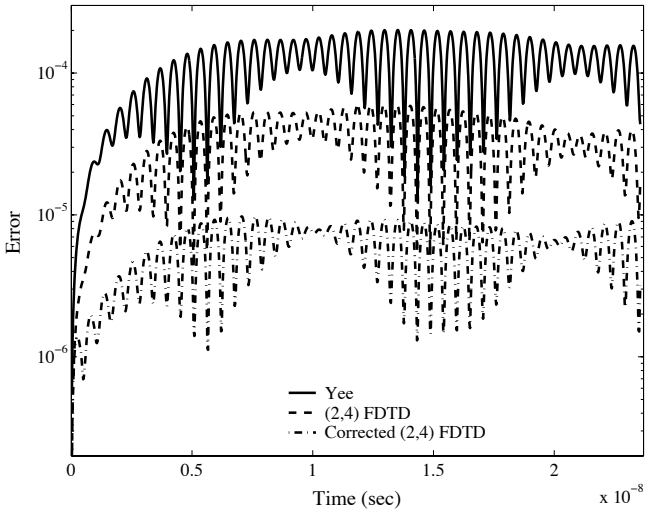

Fig. 2. Errors in the parallel-plate waveguide problem

REFERENCES

[1] M. F. Hadi, and M. Piket-May, "A modified FDTD (2, 4) scheme for modeling electrically large structures with high-phase accuracy," *IEEE Trans. Antennas Propagat.*, vol. 45, pp. 254-264, Feb. 1997.

[2] J. L. Young, D. Gaitonde, and J. S. Shang, "Toward the construction of a fourth-order difference scheme for transient EM wave simulation: staggered grid approach," *IEEE Trans. Antennas Propagat.*, vol. 45, pp. 1573-1580, Nov. 1997.

[3] A. Yefet, and P. G. Petropoulos, "A staggered fourth-order accurate explicit finite difference scheme for the time-domain Maxwell's equations," *J. Comp. Phys.*, vol. 168, pp. 286-315, 2001.

[4] J. B. Cole, "A high-accuracy realization of the Yee algorithm using non-standard finite differences," *IEEE Trans. Microwave Theory Tech.*, vol. 45, pp. 991-996, Jun. 1997.

[5] J. W. Nehrbass, J. O. Jevtić, and R. Lee, "Reducing the phase error for finite-difference methods without increasing the order," *IEEE Trans. Antennas Propagat.*,vol. 46, pp. 1194-1201, Aug. 1998.

[6] J. S. Juntunen, and T. D. Tsiboukis, "Reduction of numerical dispersion in FDTD method through artificial anisotropy," *IEEE Trans. Microwave Theory Tech.*, vol. 48, pp. 582-588, Apr. 2000.

[7] K. Suzuki, T. Kashiwa, and Y. Hosoya, "Reducing the numerical dispersion in the FDTD analysis by modifying anisotropically the speed of light," *Electron. Commun. Jpn*, pt. 2, vol. 85, pp. 389-396, May 2000.

An Unconditionally Stable Higher-Order ADI-FDTD Technique for the Dispersionless Analysis of Generalized 3-D EMC Structures

Nikolaos V. Kantartzis, Theodoros T. Zygiridis, and Theodoros D. Tsiboukis
Dept. of Electrical and Computer Engineering, Aristotle University of Thessaloniki, GR 54124 Thessaloniki, Greece

***Abstract*—An enhanced higher-order 3-D ADI-FDTD algorithm for the accurate and unconditionally stable modeling of complex curvilinear EMC problems, is introduced in this paper. The new technique launches a topologically-consistent family of non-standard concepts which eliminate the serious dispersion errors of the usual ADI-FDTD scheme as time-step increases, and cancel its strong dependence on cell shape or mesh resolution. Thus, temporal increments can greatly exceed the Courant limit with superior stability and convergence levels. To optimize computing, higher-order curvilinear PML absorbers are also developed. Theoretical analysis, along with the numerical verification of diverse structures reveal that the proposed method is highly precise, subdues the vector-parasitic mechanisms of the ADI approach and achieves significant computational savings.**

INTRODUCTION

The gradually increasing complexity of modern microwave devices has stipulated the needs for numerical schemes that combine top performance with realistic computational costs. A restrictive factor in the finite-difference time-domain (FDTD) analysis of such applications, where cells are much smaller than the shortest wavelength, is the Courant limit enforcing excessive numbers of temporal iterations to reach steady state. Lately, an efficient unconditionally stable alternating-direction implicit (ADI) formulation for the FDTD method has been developed [1, 2]. Its time-steps are not confined by cell attributes, while the profile of the modeled waveforms is highly resolved. However, various instructive studies [3-5] and algorithms [6-9] have shown that large dispersion errors are induced as the time interval is increased yielding thus, incorrect simulations.

In this paper, a 3-D ADI-FDTD technique, based on curvilinear tensorial forms, is presented for the mitigation of the preceding lattice reflection constraints and the consistent analysis of electromagnetic compatibility (EMC) applications. Through an advanced discretization policy, the novel algorithm introduces a parametric set of accurate higher-order non-standard schemes and conducts alternations in respect to mixed coordinates rather than to each direction. This perspective suppresses the inherent dispersion errors and allows time-steps to substantially surpass the Courant criterion. Also, the overall solution is further enhanced via higher-order perfectly matched layers (PMLs) which are derived in terms of a fully curvilinear procedure. The merits of the proposed methodology are numerically certified with several difficult arbitrarily-curved arrangements that would otherwise necessitate elongated simulations.

THE ADVANCED NON-STANDARD TOPOLOGICAL FORMULATION

The key feature of the higher-order (HO) strategy is the new class of non-standard operators which eliminate the structural defects of the common ADI-FDTD method. Their form is

$$\mathbf{P}^{M}_{\zeta,L}\left[f\big|^{t}_{u,v,w}\right]=\frac{g(u,v,w)}{c_s(kL\Delta\zeta)}\sum_{m=1}^{M}Q^{\zeta}_{m}\left\{\sum_{l=1}^{L}p^{\zeta}_{m,l}\mathbf{W}^{(m)}_{\zeta,l\Delta\zeta}\left[f\big|^{t}_{u,v,w}\right]\right\}, \quad (1)$$

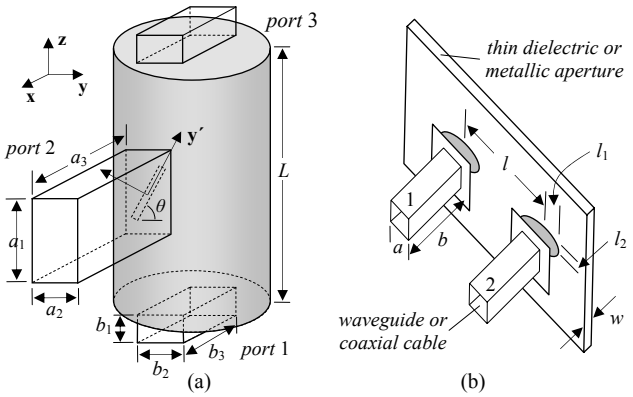

Fig. 1. (a) An inclined-slot sidewall coupled elliptical cavity, (b) an aperture with two elliptical slots fed by rectangular waveguides or coaxial cables.

where M is the order of accuracy and ζ a variable of the curvilinear coordinate system (u,v,w) defined by a set of g metrics. Coefficient L is very important, since it defines the suitable set of stencils, $l\Delta\zeta$, along each axis. For lattice consistency, operators $\mathbf{W}^{(m)}[.]$, cover all optimal node tessellations – independent of cell shape or mesh resolution – hence enabling the use of fairly coarse grids and multi-directional modeling of structural peculiarities. A typical choice of the prior parameters is $M = 4$ and $L = 3$, while an indicative u-directed $\mathbf{W}^{(m)}[.]$ is given by

$$\mathbf{W}^{(m)}_{u,l\Delta u}\left[f\big|^{t}_{u,v,w}\right]=\frac{9m^2}{8(2m-1)}\begin{pmatrix} f\big|^{t}_{l\Delta u/2,\Delta v,\Delta w}-m\,f\big|^{t}_{-l\Delta u/2,-\Delta v,-\Delta w} \\ +f\big|^{t}_{l\Delta u/2,-\Delta v,\Delta w}-m\,f\big|^{t}_{-l\Delta u/2,\Delta v,-\Delta w}\end{pmatrix}, \quad (2)$$

in which only the respective spatial increments towards the u,v,w are depicted. Function c_s, in (1), controls the convergence of the method, whereas the degrees of freedom p_m, Q_m augment its error-annihilating behavior via the fulfillment of

$$\sum_{l=1}^{L}p^{\zeta}_{m,l}=1 \quad \forall m, \qquad \sum_{m=1}^{M}Q^{\zeta}_{m}=1/2\,. \quad (3)$$

Therefore, space and time derivatives are approximated by very precise HO schemes and receive the following notation

$$\mathbf{D}_{\zeta}\left[f\big|^{t}_{u,v,w}\right]=\frac{q_{\mathrm{A}}}{4\Delta\zeta}\left\{\mathbf{P}^{M}_{\zeta,L}\left[f\big|^{t}_{u,v,w}\right]+\sum_{s=1}^{3}f\big|^{t}_{\zeta\pm s\Delta\zeta/2}\right\}, \quad (4)$$

$$\mathbf{T}\left[f\big|^{t}_{u,v,w}\right]=\left(f\big|^{t+\Delta t/2}_{u,v,w}-f\big|^{t-\Delta t/2}_{u,v,w}\right)/c_T(\Delta t)-q_{\mathrm{B}}\,\partial_{ttt}f\big|^{t}_{u,v,w}, \quad (5)$$

with q_{A}, q_{B} being certain tuning factors and c_T the non-standard function of $\mathbf{T}[.]$. The summation, in (4), combined with a self-adaptive compact regime, treats boundaries via the ± signs.

THE 3-D HO CURVILINEAR ADI-FDTD TECHNIQUE

The generalized HO classification hosts a dispersionless ADI-FDTD scheme which, unlike Yee's single advance from the n-th to $(n+1)$-th time-step, involves two sub-iterations: one from n to $n+1/2$ and the other from $n+1/2$ to $n+1$. Let us con-

sider Ampere's law expressed in its covariant form as $\varepsilon\partial_t e_u + g_{vw}\sigma e_u = g_{uw}\partial_v h_w - g_{uv}\partial_w h_v$ via the metrical coefficients g. In the first sub-iteration, partial derivative $\partial_v h_w$ is implicitly described by its unknown pivotal values at n+1/2, while $\partial_w h_v$ is explicitly substituted by its already computed values at n. Consequently,

$$\mathcal{A}^{+}\, e_u\big|_{pos}^{n+1/2} - \mathcal{A}^{-}\, e_u\big|_{pos}^{n} = g_{uw}\mathbf{D}_v\left[h_w\big|_{pos}^{n+1/2}\right] - g_{uv}\mathbf{D}_w\left[h_v\big|_{pos}^{n}\right], \quad (6)$$

with $pos = (i+1/2, j, k)$ and $\mathcal{A}^{\pm} = 2(4\varepsilon \pm g_{vw}\sigma)/\Delta t$ including additionally third-order time differentiations in g_{vw}. The same procedure for the magnetic h_w quantities (Faraday's law), results in

$$\mathcal{B}^{+}\, h_w\big|_{pos}^{n+1/2} - \mathcal{B}^{-}\, h_w\big|_{pos}^{n} = g_{wu}\mathbf{D}_v\left[e_u\big|_{pos}^{n+1/2}\right] - g_{wv}\mathbf{D}_u\left[e_v\big|_{pos}^{n}\right]. \quad (7)$$

Now, $pos = (i+1/2, j+1/2, j, k)$, $\mathcal{B}^{\pm} = 2(g_{vu}\sigma^{*} \pm 4\mu)/\Delta t$. Due to the concurrent definition of e_u, h_w in (6), we replace h_w via (7) and

$$\begin{aligned} a_1\, e_u\big|_{i+1/2,j,k}^{n+1/2} - a_2\, e_u\big|_{i+1/2,j+1,k}^{n+1/2} - a_3\, e_u\big|_{i+1/2,j-1,k}^{n+1/2} = \\ a_4\, e_u\big|_{i+1/2,j,k}^{n} + b_1\mathbf{D}_v\left[h_w\big|_{i+1/2,j,k}^{n}\right] - b_2\mathbf{D}_w\left[h_v\big|_{i+1/2,j,k}^{n}\right], \quad (8) \\ - b_3\left\{\mathbf{D}_u\left[e_v\big|_{i,j+1/2,k}^{n}\right] + \mathbf{D}_v\left[e_v\big|_{i,j-1/2,k}^{n}\right]\right\}, \end{aligned}$$

where a_m, b_m are suitable system metrics. As (8) have a tridiagonal form for every j, they can be recursively solved with a trivial overhead. On the other hand, the second sub-iteration reverses the time-update of $\partial_v h_w$ and $\partial_w h_v$ to give similar notions. Application to all Maxwell equations yields the full set of HO curvilinear formulae that evaluate fields along alternating directions. Expressing (8) in matrix notation, one can readily obtain

$$\left.\begin{aligned} \boldsymbol{\Xi}_1^{nst}\boldsymbol{\Psi}^{n+1/2} &= \boldsymbol{\Theta}_1^{nst}\boldsymbol{\Psi}^{n} \\ \boldsymbol{\Xi}_2^{nst}\boldsymbol{\Psi}^{n+1} &= \boldsymbol{\Theta}_2^{nst}\boldsymbol{\Psi}^{n+1/2} \end{aligned}\right\} \Rightarrow \boldsymbol{\Psi}^{n+1/2} = \left[\boldsymbol{\Xi}_2^{-1}\boldsymbol{\Theta}_2\boldsymbol{\Xi}_1^{-1}\boldsymbol{\Theta}_1\right]^{nst}\boldsymbol{\Psi}^{n}, \quad (9)$$

with $\boldsymbol{\Psi}^n = [\mathbf{E}^n, \mathbf{H}^n]$ and the sparse $\boldsymbol{\Xi}^{nst}$, $\boldsymbol{\Theta}^{nst}$ acquired by the non-standard time-marching concepts of (8). Theoretical analysis – provided in the full paper – indicates that all eigenvalues in (9) are always less than or equal to 1 and therefore the HO method is unconditionally stable. Its new dispersion relation becomes

$$\sin\left(\omega\Delta t\right) = \frac{26(\Delta t)^{(M-1)/4}}{4^{M+L}(\mu\varepsilon)^{1/2}}\mathcal{F}\left(S_u^2, S_v^2, S_w^2, \mu\varepsilon\right), \quad (10)$$

as a function of the existing ADI-FDTD relation, $\mathcal{F}$, with $S_\zeta = (\Delta t/\Delta\zeta)\sin(k_\zeta\Delta\zeta/2)$. Clearly, (10) exhibits a notable superiority.

Numerical Results

To verify the proposed algorithm, several 3-D scattering and EMC curvilinear problems, are analyzed with a resolution of $\lambda/6$ (instead of Yee's $\lambda/170$ one) and truncated by HO PMLs. Fig. 2 gives the numerically-calculated phase velocity for various CFLN = $\Delta t^{\mathrm{ADI}}/\Delta t^{\mathrm{FDTD}}$ values due to a dielectric sphere ($\varepsilon = 5.5\varepsilon_0$). As observed the HO ADI-FDTD method outperforms its 2nd-order counterpart. Next, we consider the hard-to-model cavity of Fig. 1a with a_1 = 23.44 mm, a_2 = 11.96 mm, a_3 = 32.87 mm, b_1 = 6.28 mm, b_2 = 10.26 mm, b_3 = 19.34 mm and θ = 45°. Results for the S_{21} parameter in Fig. 3a and the first five resonances in Table I (CFLN = 7.215) prove the high precision and savings of our technique (almost 85% grid and CPU time reduction). Finally, Fig. 3b shows the normalized phase velocity (large temporal increments) for the aperture of Fig. 1b. Note the great discrepancies of the regular ADI-FDTD approach.

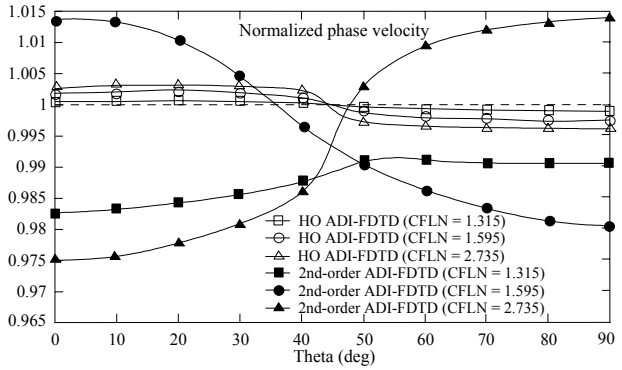

Fig. 2. Normalized phase velocity for HO and 2nd-order ADI-FDTD schemes.

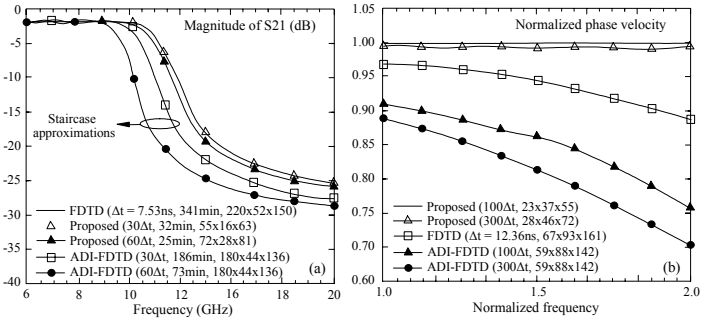

Fig. 3. (a) Magnitude of S_{21} parameter and (b) normalized phase velocity.

TABLE I. COMPARISON OF HO AND 2ND-ORDER FDTD METHODS

Reference modal analysis (GHz)	2nd-order ADI-FDTD		HO ADI-FDTD	
	Simulation 196×64×142	Relative error	Simulation 84×30×72	Relative error
5.2849	5.2098	1.42 %	5.2838	0.02 %
7.1563	7.0167	1.95 %	7.1522	0.06 %
9.3485	8.9914	3.82 %	9.3401	0.09 %
10.5621	9.8852	6.41 %	10.5493	0.12 %
13.9247	12.5921	9.57 %	13.9024	0.16 %

Conclusions

A practically dispersionless ADI-FDTD method, based on systematic HO non-standard forms, for 3-D curvilinear EMC problems has been presented in this paper. The technique decreases radically the overall burden, while demonstrating an overwhelming accuracy even for considerably large time-steps.

References

[1] T. Namiki, "A new FDTD algorithm based…direction implicit method," *IEEE Trans. Microwave Theory Tech.*, vol. 47, pp. 2003-2007, Oct. 1999.

[2] F. Zheng, Z. Chen, and J. Zhang, "A finite-difference...stability conditions," *IEEE Microwave Guided Wave Lett.*, vol. 9, pp. 441-43, Nov. 1999.

[3] S. Gedney, G. Liu, J. Roden, and A. Zhu, "Perfectly matched…method," *IEEE Trans. Antennas Propagat.*, vol. 49, pp. 1554-1559, Nov. 2001.

[4] S. Garcia, T.-W. Lee, and S. Hagness, "On the accuracy…ADI-FDTD method," *IEEE Antennas Wireless Propagat. Lett.*, vol. 1, pp. 31-34, 2002.

[5] A. Zhao, "Analysis of the numerical…direction implicit FDTD method," *IEEE Trans. Microwave Theory Tech.*, vol. 50, pp. 1156-1164, Apr. 2002.

[6] D. Gaitonde, J. Shang, and J. Young, "Practical aspects…wave propagation phenomena," *Int. J. Num. Methods Eng.*, vol. 45, pp. 1849-1869, 1999.

[7] S. Wang, F. Texeira, R. Lee, and J.-F. Lee, "Filtering schemes… algorithms" *in 2002 IEEE AP-S*, vol. 3, pp. 240-243, San Antonio, USA, 2002.

[8] T. Kashiwa, H. Kudo, Y. Sendo, T. Ohtani, and Y. Kanai, "The phase… FDTD method," *IEEE Trans. Magn.*, vol 38, pp. 661-664, Mar. 2002.

[9] P. Petropoulos, L. Zhao, and A. Cangellaris, "A reflectionless sponge layer …finite difference schemes," *J. Comp. Phys.*, vol. 139, pp. 184–208, 1998.

FDTD Analysis of Microstrip Patch Antennas and Arrays on High Dielectric-Constant Substrate Surrounded by a Soft-and-Hard Surface

R. L. Li, E. M. Tentzeris, J. Laskar, and J. Papapolymerou
School of Electrical and Computer Engineering
Georgia Institute of Technology
Atlanta, GA 30332-250
E-mail: rlli@ece.gatech.edu

Abstract—**The surface-wave diffraction at the edge of a finite size substrate with a high dielectric constant is the dominant mechanism affecting the radiation pattern of a microstrip patch antenna fabricated on this material. A soft-and-hard surface (SHS) can be used to block the surface waves from propagating outward along the dielectric substrate, thus reducing the unwanted diffraction. Microstrip antennas surrounded by the SHS are analyzed using the finite-difference time-domain (FDTD) technique that implements the SHS boundary conditions using a modified subcell model. A square patch antenna on the LTCC-GL660 multilayer substrate and a phased array of 2 × 2 patches are investigated as benchmarks and it is shown that the gain of the patch with SHS increases by more than 3 dB, while the front-to-back ratio is higher than 24 dB.**

I. Introduction

The explosive growth of wireless communication systems has led to an increasing demand for integrated compact antennas. Thus, fabricating microstrip antennas on a high dielectric-constant substrate (such as GaAs or LTCC) is becoming attractive for miniaturized wireless modules. However, direct use of high dielectric-constant substrates with microstrip antennas results in strong surface-wave modes. The diffraction from these surface waves at the edge of finite-size substrates contaminates the radiation pattern and reduces the radiation efficiency of the microstrip antennas [1]. This concern is particularly important in phased antenna arrays for beam steering.

For years, a number of techniques have been developed to improve the radiation patterns of microstrip antennas on high dielectric-constant substrates [2]. The most popular method is to construct a complete band gap (or perforated) structure surrounding the patch antenna to prevent energy from being trapped in the substrate. Unfortunately, to form a band gap in the substrate via periodic holes requires considerable area, which may make it impractical for some applications. Another approach is to lower the effective dielectric constant of substrate under the patch to allow for more effective radiation [3]. This approach results in an increase in the resonant frequency, losing the advantage of using high dielectric substrate for reduction of antenna size.

In this paper, a soft-and-hard surface (SHS) is employed to reduce the effect of surface waves on the radiation pattern of microstrip patch antennas. The concept of SHS was originated from acoustics and introduced in electromagnetic theory in [4]. As one of the basic electromagnetic boundaries, the SHS is a mathematical idealization of a surface that is both electrically and magnetically ideally conducting in one direction defined by a real unit vector. Such a surface can be realized by a combination of a perfect electric conductor (PEC) and a perfect magnetic conductor (PMC), a strip-loaded grounded dielectric slab, or a corrugated surface. The soft surface along which the power-density flux is zero can be used to design corrugated horn antennas with symmetrical radiation patterns and low cross polarization while the hard surface along which the density of power flow has a maximum could be applied to increase the aperture efficiency and the directivity.

The advantageous characteristics of the soft surface can be utilized to block the propagation of surface waves in a microstrip antenna, thus alleviating the diffraction at the edge of substrate. The microstrip patch antenna is surrounded by a substrate covered with an SHS that is formed as a soft surface in the outward direction. As a result, it would be difficult for surface waves to propagate from the microstrip patch to the substrate edge. The SHS-surrounded microstrip patch antenna is analyzed using the finite-difference time-domain (FDTD) method. Since the electric and magnetic fields in Yee's leapfrog scheme are not co-located in space or in time, the straight implementation of an SHS for the FDTD method requires the introduction of a modified cell (note that both electric and magnetic fields are enforced to be zero in one direction tangential to the SHS). A single patch and a phased array are investigated in this paper as a showcase of the benefits from the use of SHS.

II. Microstrip Patch Surrounded by SHS

Fig. 1 shows a microstrip patch antenna with arbitrary shape that has been fabricated on a finite substrate with a dielectric constant of ε_r and a thickness of h. The dielectric substrate is backed by a metal cavity and surrounded by an SHS ring that is supported by another metal cavity. The ideal SHS conditions can be characterized by the following symmetric boundary conditions for the electric and magnetic fields [5]

$$\hat{v} \cdot \vec{E} = 0 \,,\ \hat{v} \cdot \vec{H} = 0 \qquad (1)$$

where $\hat{v}$ is a unit vector tangential to the surface. In the direction parallel to $\hat{v}$, a hard surface, along which the density of power flow is maximized, may be realized, while in the direction transverse to $\hat{v}$, a soft surface where the power flow

is zero is present. In order to prevent the surface waves from propagating towards the edge of the substrate, it is desirable to have a soft-surface condition in the outward direction. Therefore we choose $\hat{v} = \hat{x}$ ($E_x = 0$, $H_x = 0$) and $\hat{v} = \hat{y}$ ($E_y = 0$, $H_y = 0$) along the left-and-right sides and the front-and-back sides, respectively (see Fig. 1).

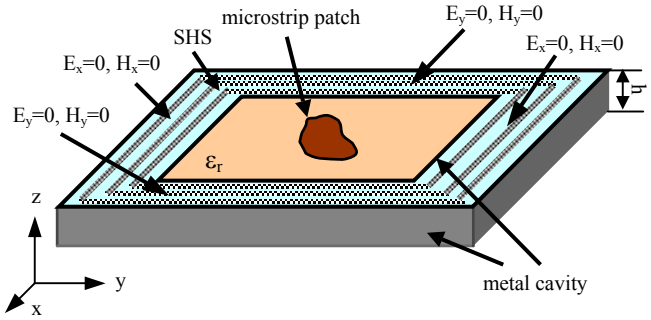

Fig. 1. Microstrip patch antenna surrounded by a soft-and-hard surface.

III. FDTD Modeling for SHS Surfaces

In the Yee algorithm for FDTD, $\vec{E}$ and $\vec{H}$ components are not co-located in space and time. Therefore it is impossible to directly enforce the boundary conditions both $\hat{v} \cdot \vec{E} = 0$ and $\hat{v} \cdot \vec{H} = 0$ simultaneously at same grid position. In this paper we introduce a modified subcell model to indirectly enforce the boundary condition for $\hat{v} \cdot \vec{H} = 0$.

Without loss of generality, we assume $\hat{v} = \hat{x}$, that is, both $E_x = 0$ and $H_x = 0$ on the SHS. The boundary condition $E_x = 0$ can be directly enforced in the FDTD grids while the condition $H_x = 0$ is taken into account through a modification of the updating equation for E_y . Consider a contour path C above the SHS, as shown in Fig. 2, where the SHS is placed in the middle of the FDTD cell. Applying Ampere's Law along the contour C and assuming that $E_y\big|_{i,j,k}$ equals to the average value over the contour surface, we can obtain the modified updating equation for $E_y\big|_{i,j,k}^{n+1/2}$:

$$E_y\Big|_{i,j,k}^{n+1/2} = E_y\Big|_{i,j,k}^{n-1/2} + H_x\Big|_{i,j,k+1/2}^{n} 2\Delta t/(\varepsilon_0 \Delta z) + \left(H_z\Big|_{i+1/2,j,k}^{n} - H_z\Big|_{i-1/2,j,k}^{n}\right)\Delta t/(\varepsilon_0 \Delta x) \quad (2)$$

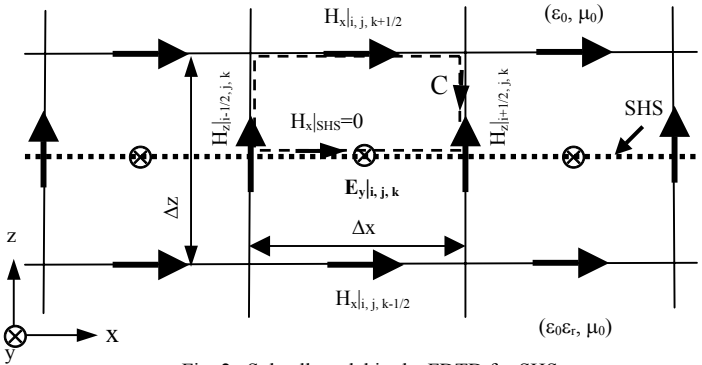

Fig. 2. Subcell model in the FDTD for SHS

Note that $H_x\big|_{i,j,k-1/2}$ is not used because it is located beneath the SHS, where all field values are completely isolated from outside by the PEC cavities and the SHS.

IV. Numerical Examples

A probe-fed square microstrip patch antenna and a 2 × 2 element phased array are investigated. The dielectric constant of the substrate is chosen to be 9.5, which corresponds to the relative permittivity of LTCC-GL660. The dimensions of the substrate and the patch are respectively 32 mm × 32 mm × 2 mm and 4 mm × 4 mm. The patch is surrounded by a square SHS ring (its inner side=16 mm and outer side =32 mm). The number of the FDTD computational cells is 100 × 100 × 50 with a uniform cell size of 0.4 mm × 0.4 mm × 0.2 mm. The radiation patterns for the microstirp patches with and without an SHS are compared in Fig. 3 at a resonant frequency of approximately 10 GHz. It can be seen that the radiation pattern of the patch with SHS is significantly improved. The gain at broadside is 9.2 dBi, about 3 dB higher than the maximum gain for the patch without SHS. It is also noticed that the level of the backside lobe for the SHS-surrounded patch is decreased by more than 14 dB. Results for the patch array will be presented in the full paper.

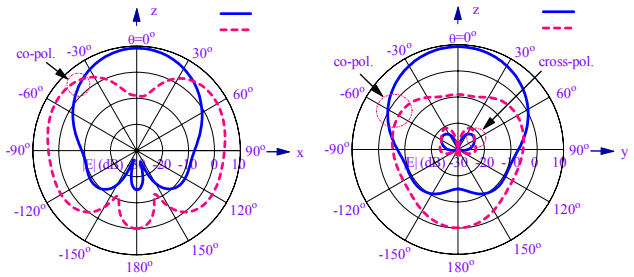

(a) E-plane (b) H-plane

Fig. 3. Radiation patterns for microstirp patches with and without an SHS.

V. Conclusion

A soft-and-hard surface (SHS) is used to prevent surface waves from diffraction at the edge of high dielectric-constant substrates. Microstrip patch antennas and arrays surrounded by the SHS are analyzed using a modified FDTD model that can effectively implement the SHS boundary conditions. The numerical results verify the validity of the enhanced FDTD scheme and show that the SHS can effectively block the surface-wave propagation on the substrate, therefore leading to a significant improvement of the radiation characteristics (increased gain and reduced backside radiation).

References

[1] D. H. Schaubert and K. S. Yngvesson, "Experimental study of a microstrip array on high permittivity substrate," *IEEE Trans. Antennas Propagat.*, vol. 34, no. 1, pp. 72-97, Jan. 1986.

[2] M. J. Vaughan, K. Y. Hur, and R. C. Compton, "Improvement of microstrip patch antenna radiation patterns," *IEEE Trans. Antennas Propagat.*, vol. 42, no. 6, pp. 882-885, Jun. 1994.

[3] J. Papapolymerou, R. F. Drayton, and L. P. B. Katehi, "Micromachined patch antennas," *IEEE Trans. Antennas Propagat.*, vol. 46, no. 2, pp. 275-283, Feb. 1998.

[4] P.-S. Kildal, "Artificially soft and hard surfaces in electromangetics,", *IEEE Trans. Antennas Propagat.*, vol. 38, no.10, pp. 1537-1544, Oct. 1990.

[5] I. V. Lindell, "Generalized soft-and-hard surface," *IEEE Trans. Antennas Propagat.*, vol. 50, no. 7, pp. 926-929, Jul. 2002.

Grid-Dispersion Error Reduction for Broadband FDTD Electromagnetic Simulations

Shumin Wang and Fernando L. Teixeira
ElectroScience Laboratory and Department of Electrical Engineering
The Ohio State University
1320 Kinnear Road, Columbus, OH 43212, U.S.A
E-mail: wangs@ee.eng.ohio-state.edu

***Abstract* — We introduce a generic procedure to reduce numeric (grid) dispersion error in finite-difference time-domain (FDTD) simulations. Dispersion error functionals are expanded in a Taylor series that, for a broadband signal, indicates larger dispersion errors for high frequency components. By a change of basis, modified FDTD update coefficients are obtained instead in order to minimize the dispersion error over some pre-assigned frequency band. Moreover, desirable properties such as a *local* dispersion error that decreases within a frequency band can be attained. In particular, Butterworth (maximally flat) or Chebyshev expansions are considered along with their application to the optimization of two high order FDTD schemes.**

I. INTRODUCTION

Higher-order finite-difference time-domain (FDTD) schemes are traditionally obtained by using a truncated Taylor (McLaurin) series about a particular grid location to derive a solution scheme with high-order accuracy in space [1]. A truncated Taylor expansion suffers residual errors, and for broadband problems this results in larger numerical (grid) dispersion error for high frequency components. Because the overall phase error is cumulative and proportional to the electrical size of the problem, this error is compounded by the fact that, at high frequencies, the problem size is electrically larger. The traditional way to combat this problem in FDTD is to include higher order terms in the approximation, which unfortunately produces increasingly larger spatial stencils. In this work, we discuss an alternative approach to minimize the dispersion error by employing expansions other than Taylor. Specifically, we illustrate its application to derive optimized FDTD schemes employing Chebyshev (CB) and Butterworth (BT) expansions around pre-assigned central frequencies (CB/BT) and ranges (CB).

II. FORMULATION

For a given FDTD scheme, dispersion error functionals can be introduced in order to quantify some aspect of the dispersion error to be analyzed [2,3]. For instance, an error functional can represent the dispersion error at a particular propagation angle [2]. Or it can alternatively represent the maximum dispersion error for all angles [3]. These error functional, denoted as δ, can in general be expanded in a Taylor series with respect to the parameter $q = h/\lambda$, where h denotes the (uniform) cell size and λ is the wavelength, as

$$\delta = [d_0, d_1, \ldots, d_n] \cdot V^T + \mathrm{O}(q^{n+1}) \tag{1}$$

where $[d_0\ ,\ d_1\ ,\ d_2\ ,\ldots\ d_n\ ]$ are unknown coefficients to be determined (related to the FDTD update coefficients), and $V = [1, q, q^2, \ldots, q^n]$. Traditional high-order FDTD schemes are (equivalently) usually obtained by enforcing the first m terms above to be zero. This determines the unknown coefficients, and the residual error becomes

$$\delta_{res} = \sum_{k=m}^{n} d_k' q^k + \mathrm{O}\left(q^{n+1}\right) \tag{2}$$

where d_k' are also determined. In Eq. (1), $[d_0\ ,\ d_1\ ,\ d_2\ ,\ldots\ d_n\ ]$ can be viewed as the projection of δ on the subspace $S^n = span\{1,\ q\ ,\ q^2\ \ldots\ q^n\}$. The key point here is to observe that alternative basis may be chosen to expand δ in S^n. In particular, we can choose a polynomial basis set such as (BT filter)

$$Q = \left\{1, (q - q_c), (q - q_c)^2, \cdots, (q - q_c)^n\right\} \tag{3}$$

or a first-kind Chebyshev polynomial basis set (CB filter)

$$Q = \left\{1, \frac{q - q_c}{\Delta q}, T_2\left(\frac{q - q_c}{\Delta q}\right), \ldots, T_n\left(\frac{q - q_c}{\Delta q}\right)\right\} \tag{4}$$

Here, q_c corresponds to a center frequency and Δq corresponds to a bandwidth of interest. The expansion on any of these new bases can be written as

$$\delta = [\tilde{d}_0, \tilde{d}_1, \ldots, \tilde{d}_n] \cdot Q^T + \mathrm{O}(q^{n+1}) \tag{5}$$

Enforcing the first m terms in Eq. (5) to be zero, we can solve for optimized coefficients. For a BT filter, the residual error is

$$\delta_{res} = \sum_{k=m}^{n} d_k' (q - q_c)^k + \mathrm{O}\left(q^{n+1}\right) \tag{6}$$

For a CB filter, the residual error is

$$\delta_{res} = \sum_{k=m}^{n} d_k' T_k\left(\frac{q - q_c}{\Delta q}\right) + \mathrm{O}\left(q^{n+1}\right) \tag{7}$$

From Eqs. (2), (6) and (7), the residual errors are split into two terms: the first characterized by the remaining *n-m-1* terms of the new basis and the second by the complement of the subspace S^n. For convergent error functionals, the second term can be made arbitrarily small by increasing *n*. So in practice, we can analyze the error behavior by choosing a sufficient large *n* for the finite sum above. Note that *m* is chosen independently of *n*.

The choice of expansion basis determines the behavior of the dispersion error functional in a frequency range. Using a BT expansion, a maximally flat behavior is obtained at a center frequency of choice (better group velocity properties). Using CB expansion, a smaller overall error is obtained in a bandwidth of interest (better phase velocity properties).

III. EXAMPLES

We apply the methodology above to two higher order FDTD schemes: (1) An angle-optimized FDTD (AO-FDTD), designed to exhibit zero dispersion error along a preassigned propagation direction [2], and (2) a dispersion-relation-preserving FDTD (DRP-FDTD) designed to produce a minimax dispersion error for all propagation angles [3]. The error functional for AO-FDTD is defined directly from its dispersion relation [2]. Forcing it to be zero implies finding a FDTD scheme with zero dispersion error for a certain angle withi a given frequency band. The error functional for DRP-FDTD is defined as the difference between the theoretical solution of its update coefficients and a series approximation that can be used in practical time-domain updates [3].

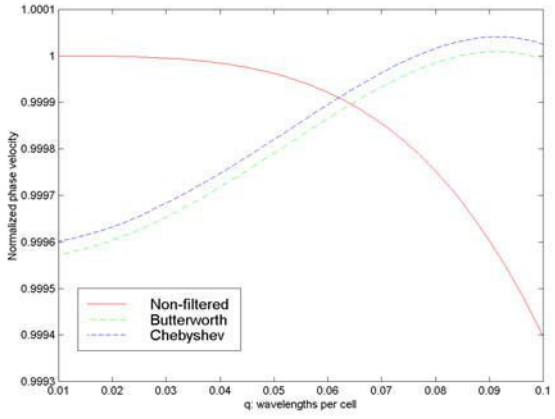

Fig. 1. Normalized phase velocity of BT, CB and non-filtered AO-FDTD schemes at $\theta = 90°$ and $\phi = 0°$. For the filtered schemes, the center frequency is such that $q_c = 0.09$

Fig. 1 shows the phase velocity, which is normalized to the exact phase velocity in free space, of non-filtered, BT- and CB- AO-FDTD schemes optimized at $\theta = 90°$ and $\phi = 0°$. For

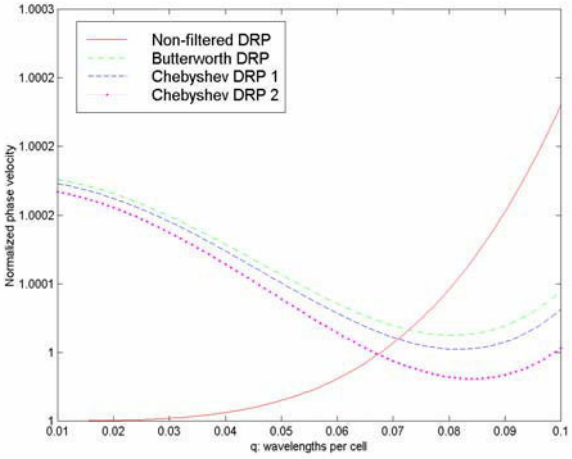

Fig. 2. Comparison of the maximum (for all angles) normalized phase velocity using different DRP (4,4) schemes.

filtered FDTD schemes, we choose a central frequency corresponding to $q_c = 0.09$. It is clear that the filtered schemes yield smaller dispersion errors throughout the frequency band considered. The BT filter is more accurate than the CB filter close to the center frequency but CB filter has smaller overall error. In the CB expansion, Δq provides an additional degree of freedom for optimization. This is illustrated in Fig. 2, where Δq=0.02 and Δq=0.035 are used for the schemes labeled as *Chebyshev-1* and *Chebyshev-2*, respectively. Both CB filters produce FDTD schemes with smaller overall errors and errors near the specified optimization center than the BT filter. Note in particular that the filtering schemes yield higher *local* dispersion errors at *lower* frequencies. Again, this is highly desirable since the *accumulated* dispersion error is proportional to the electric size of the FDTD domain, which is larger for high frequencies.

IV. CONCLUSIONS

In this paper, we have discussed a general approach to optimize FDTD schemes for broadband simulations. The approach utilizes Chebyshev or Butterworth expansions for error functionals related to the numerical dispersion error. In this manner, the behavior of the approximation error can be better controlled as a function of frequency and exhibit desirable characteristics such as, for instance, smaller local dispersion error in the high frequency end.

ACKNOWLEDGMENTS

The authors acknowledge R. Lee and J.-F. Lee for technical discussions.

REFERENCES

[1] A. Taflove (ed.) *Advances in Computational Electrodynamics: The Finite-Difference Time-Domain Method*, Boston: Artech, 1998.

[2] S. Wang and F. L. Teixeira "A three-dimensional angle-optimized FDTD algorithm*", IEEE Trans. Microwave Theory Tech.*, to be published, April 2003.

[3] S. Wang and F. L. Teixeira "Dispersion-relation-preserving FDTD algorithms for large-scale three-dimensional problems", *IEEE Trans. Antennas Propagat.*, to be published, August 2003.

FDTD Simulation of MWD Electromagnetic Tools in Large-Contrast Geophysical Formations

Yik-Kiong Hue and Fernando L. Teixeira
ElectroScience Laboratory and Department of Electrical Engineering
The Ohio State University
1320 Kinnear Road, Columbus, OH 43212, U.S.A.
hue.2@osu.edu

Abstract — **We describe numerical simulations of electromagnetic logging tools used in oil and gas exploration using a finite-difference time-domain (FDTD) scheme extended to cylindrical coordinates. We pay particular attention to the simulation in geophysical formations exhibiting large contrast on the conductivity values of adjacent beds. Phase and amplitude (CW) information are extracted from very early time domain data. A perfectly matched layer (PML) absorbing boundary condition extended to cylindrical coordinates and modified for conductive media (diffusion regime) is employed in the FDTD method to simulate the open domains of realistic oilfields. Results from the FDTD simulations of measurement-while-drilling (MWD) tools are compared against numerical mode matching (NMM) results, showing excellent agreement even for conductivity contrasts between adjacent beds as large as 10,000.**

I. INTRODUCTION

Measurement-while-drilling (MWD) constitute an important electromagnetic logging tool technology for the oil and gas exploration industry. Over the years, a variety of analytical and numerical methods have been developed to simulate logging tools in geophysical formations. Among all methods, those based on the direct discretization of the relevant partial differential equations, such as the finite-difference time-domain (FDTD) method, are perhaps the most flexible to handle the complex media and geometries present in realistic oilfield scenarios.

In this paper, we employ an extension of the FDTD scheme to 3-D cylindrical coordinates to study the response of MWD tools [1]. Frequency domain data is obtained from the time domain results using an efficient early-time phase/amplitude extraction algorithm [2]. Fig. 1 illustrates a typical MWD resistivity tool operating in a layered formation, consisting of one transmitter coil and two receiver coils wound around a steel mandrel. The transmitter emits continuous sinusoidal waves (CW) at 2MHz and from the voltage induced at the receiver coils, the conductivity of the surrounding formation can be estimated.

II. FORMULATION

Apart from its flexibility to handle complex geometric features of the tools, the use of FDTD allows for an easy incorporation of the conductive parameters of the geophysical formations. In addition, despite being computationally intensive, the FDTD has a low computational complexity, *O(N),* where *N* is the number of unknowns of the problem, and it is an explicit (matrix-free) method that requires less computer memory than competing methods such as the finite-element method. For cases in which the geometry of the problem is axisymmetric, the three-dimensional (3-D) cylindrical problem can be reduced to a series of 2-D problem in the ρ-z plane. However, a 3-D FDTD algorithm has been developed to model cases where the problem is not axisymmetric. The use of a cylindrical grid is important to eliminate the staircasing error when representing the (cylindrical) geometry of the tools.

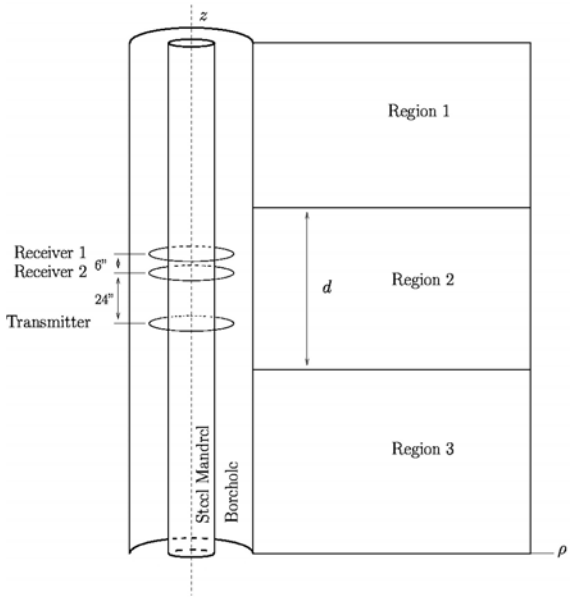

Fig. 1. Basic geometry of a MWD resistivity tool in a layered geophysical formation.

The cylindrical FDTD is augmented here by a cylindrical perfectly matched layer (PML) absorbing boundary condition (ABC). The PML ABC permits the use of a very compact cylindrical grid around the formation. The anisotropic medium (unsplit) version of the cylindrical PML is employed to yield a well-posed equations and avoid late time instabilities [1]. Both the real and imaginary parts of the complex stretching coefficients are modified to allow for the absorption of propagating spectrum and faster decay of evanescent spectrum, respectively.

The quantities of interest of the MWD tool are the phase difference and amplitude ratio between the signals at the receivers. The usual approach to obtain frequency domain data from time domain simulations is to resort to a fast Fourier

Transform (FFT). In this work, we adopt an alternative approach based on the so-called 2E2U algorithm [2], which requires only very early time data.

III. RESULTS

For validation purposes, we present here results from the simulation of symmetric formations, but the FDTD method is equally applicable to non-symmetric formations. The result depicted in Fig. 2 corresponds a case where the MWD tool penetrates a 3-layer (Fig. 1) formation with conductivities equal to 5, 5×10^{-4} and 1 [mho/m] in regions 1–3, respectively. The region 2 is a 60 [in] thick. As depicted in Fig. 1, the transmitter is 24 [in] apart from receiver 2 and 30 [in] from receiver 1. The radius of the antenna coil is 4.5 [in], wound around a 4 [in] radius steel mandrel, and residing within the 5 [in] radius borehole. The domain is discretized using a (Nρ,Nϕ,Nz) = (60,336,230) grid. The PML is set up using 10 cells both in ρ and z directions with cubic taper profile. The skin depth δ of the largest conductivity formation dictates the cell discretization size.

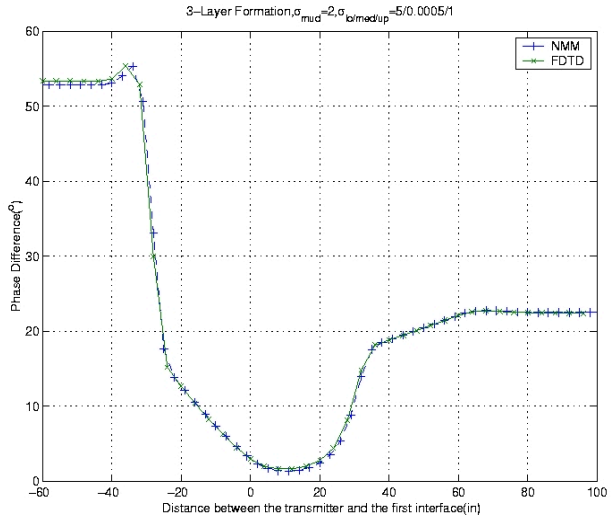

Fig. 2. Phase difference between the receivers along a large contrast 3-layer formation.

The cell discretization size is uniform in the z directions, Δz = 2.54 cm. The ρ directions cell is discretized non-uniform fashion from 0.635 [cm] close to the center to 2.64 [cm] at the outer regions. The source at the transmitter is a ramp sinusoidal function. The phase of the voltage at the receivers is extracted using 2E2U method using averaging of a sequence of two time steps apart by one tenth of wavelength, until convergence. At each location in the formation, the phase difference converges around 1.5 wavelengths. Fig. 2 illustrates the excellent agreement between FDTD and numerical mode matching (NMM) [3] results. Fig 3. shows the amplitude ratio between receivers in another 3-layer large-contrast formation. In this case, the conductivities in region 1, 2 and 3 are 1, 0.01 and 1 [mho/m] respectively. The domain discretized with (Nρ,Nϕ,Nz) = (50,235,180) grid. The z direction cell is uniform discretized with Δz = 3.81 [cm]. The ρ direction cell is discretized non-uniformly from 0.635 [cm] to 3.18 [cm]. Again, the result shows excellent agreement against the NMM result. All the simulations above were produced using a Cray SV1.

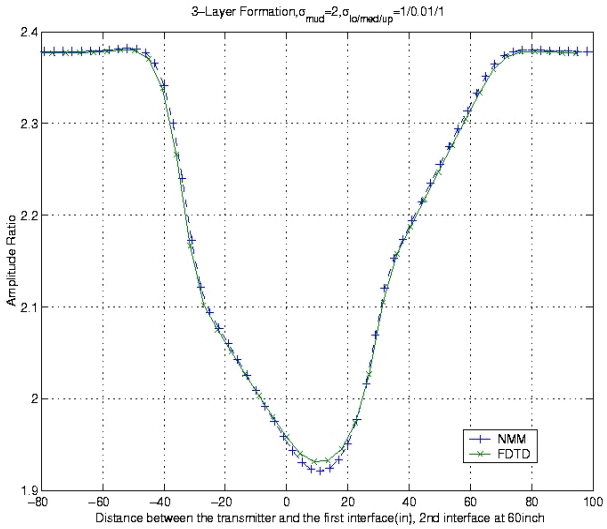

Fig 3. Amplitude ratio between the receivers along a large-contrast 3-layer formation

IV. CONCLUSIONS

The FDTD simulation of MWD logging tools in inhomogeneous conductive formations has been presented. Numerical results are validated against the NMM method. The present FDTD method has been shown to be instrumental in simulating the response of logging tools in formations with conductivity contrasts as large as 10^4.

V. ACKNOWLEDGMENTS

We thank Dr. L. San Martin from Halliburton Energy Services (Sensor Physics Group), Houston, Texas, for providing the NMM results for validation. Computational resources were provided by the Ohio Supercomputer Center.

REFERENCES

[1] F. L. Teixeira and W. C. Chew, "Finite-difference computation of transient electromagnetic waves for cylindrical geometries in complex media" *IEEE Trans. Geosci. Remote Sensing*, vol. 38, no. 4, pp. 1530-1543, 2000.

[2] C. M. Furse, "Faster than Fourier: Ultra-efficient time-to-frequency-domain conversions for FDTD simulations" *IEEE Trans. Antennas Propagat. Mag.*, vol. 42, no. 6, pp. 24-33, 2000.

[3] Q.-H Liu and W. C. Chew, "Numerical mode-matching method for the multiregion vertically stratified media (EM wave propagation)" *IEEE Trans. Antennas Propagat.* , vol. 38, no. 4 , pp. 498 –506, 1990.

FDTD-Macromodeling Technique For Simulation of Electromagnetic Interference at High-Speed Interconnects

Erping Li, En-Xiao Liu
Institute of High Performance Computing
National University of Singapore
1 Science Park Road
Singapore 117528, Fax: (65)67780522
*Email: eplee@ihpc.a-star.edu.sg

Le-Wei Li, *Senior Member, IEEE*
Dept. of Electrical and Computer Engineering
Faculty of Engineering
National University of Singapore
10 Kent Ridge Crescent
Singapore 119260

Abstract - This paper describes an efficient method for the transient simulation of high-speed interconnects system. FDTD method is employed to fully characterise the high-speed interconnects into a subnetwork. The resultant transient waveforms are then transformed as frequency-domain Y parameters by using FFT techniques. The macromodel of interconnect subnetwork is obtained by Vector Fitting [2] method. This macromodel is then synthesised into HSPICE circuit simulator to efficiently expedite the system transient simulation. A typical microstrip low-pass filter is analyzed to verify the efficiency and correctness of this method.

Keywords- Electromagnetic compatibility, FDTD-Macromodeling

INTRODUCTION

With the rapid advancements in modern VLSI technology, high-speed interconnect effects become a dominant factor in determining the system performance [1]. Macromodeling method is effective to enable a complex interconnects system to a lower order model and to achieve a balance between accuracy and efficiency of interconnect simulation.

One macromodeling approach is based on frequency-sampling data of interconnects generated from the full-wave electromagnetic modeling. Full-wave modeling becomes necessity when the discontinuity of interconnect structure as well as other electromagnetic effects need to be fully taken into account.

In this paper, the interconnect simulation employs the de-coupling FDTD and Fast Fourier transform (FFT) techniques, which are dedicated to extract the admittance (Y) parameters of interconnect subnetwork with fairly complex geometries. Interconnect macromodel can then be created by rational function approximation using robust Vector Fitting [2] method. Finally, the transient simulation of the circuit package containing interconnects can be fulfilled by the macromodel synthesis approach. Numerical examination is presented to validate this technique. Similar interconnect simulation technique has been presented in [3] but not with the Vector Fitting rational approximation method.

THREE DIMENSIONAL FDTD MACROMODELING

Three-dimensional Finite Difference Time-Domain algorithm is based on the discretization of Maxwell's equations usually from the differential form over FDTD unit cell in reference to [4]. We assume that the media are uniform, isotropic and lossless. Only the resultant difference form of Hz and Ez components are shown below,

$$H_z^{n+1/2}|_{(i,j,k)} = H_z^{n-1/2}|_{(i,j,k)} + \frac{\Delta t}{\mu \Delta y}(E_x^{\,n}|_{(i,j+1,k)} - E_x^{\,n}|_{(i,j,k)}) + \frac{\Delta t}{\mu \Delta x}(E_y^{\,n}|_{(i,j,k)} - E_y^{\,n}|_{(i+1,j,k)}) \quad (1)$$

$$E_z^{n+1}|_{(i,j,k)} = E_z^{n}|_{(i,j,k)} + \frac{\Delta t}{\varepsilon \Delta x}(H_y^{n+1/2}|_{(i,j,k)} - H_y^{\,n+1/2}|_{(i-1,j,k)}) + \frac{\Delta t}{\varepsilon \Delta y}(H_x^{n+1/2}|_{(i,j-1,k)} - H_x^{n+1/2}|_{(i,j,k)}) \quad (2)$$

The general form of Y parameter matrix is given as,

$$\{I(s)\} = [Y(s)]\{V(s)\} \qquad (3)$$

Where, vector I and V contain n components of the terminal currents and voltages respectively, i.e., $\{I\} = \{I_1, I_2, \cdots I_n\}$, $\{V\} = \{V_1, V_2, \cdots V_n\}$, which are obtained from Fast Fourier transform (FFT) of transient waveforms. The entry of the Y matrix, such as Y_{ij}, is defined as

$$Y_{ij} = \left.\frac{I_i}{V_j}\right|_{Vm=0,\ if\ m \neq j;\ m=1,2\cdots n} \qquad (4).$$

RATIONAL FUNCTION APPROXIMATION BY VECTOR FITTING METHOD

The frequency-domain representation of the interconnect subnetwork in (3) can not be directly inserted into the time-domain simulator for transient simulation. An efficient way to address this problem is approximating each of the elements in matrix Y(s) with its corresponding low order rational function, Where c^{ij} is the direct coupling constant, N the total number of poles, and $r_k^{\,ij}$ and p_k the pole-residue pair to be computed. Equation (5) can be efficiently solved by Vector Fitting method [2]. The main procedures of this method are described as follows,

$$Y_{ij}(s) = c^{ij} + \sum_{k=1}^{N} \frac{r_k^{\,ij}}{s - p_k} \qquad (5)$$

a) Introduce an unknown function $\lambda(s)$, and approximate it with a set of starting poles $\tilde{p}_k$, we get

$$\lambda(s) = 1 + \sum_{k=1}^{N} \frac{\tilde{r}_k}{s - \tilde{p}_k} \qquad (6)$$

b) Scale the original response function $Y_{ij}(s)$ with $\lambda(s)$, and take the rational function approximation, we obtain

$$W(s) = \lambda(s) Y_{ij}(s) = c' + \sum_{k=1}^{N} \frac{r_k'}{s - \tilde{p}_k} \qquad (7)$$

c) Substitute equation (6) into (7), and for a given frequency point s_l ($l = 1 \cdots m$, i.e., Y_{ij} has m sampled values), one can obtain

$$A_l X = b_l \tag{8}$$

Where

$$A_l = \left\{ (s_l - \tilde{p}_1)^{-1} \cdots (s_l - \tilde{p}_N)^{-1} \;\; 1 \;\; s_l \;\; -Y_{ij}(s_l)/(s_l - \tilde{p}_1) \cdots -Y_{ij}(s_l)/(s_l - \tilde{p}_N) \right\}$$

$$X = \{ r_1' \cdots r_N' \quad c' \quad \tilde{r}_1 \cdots \tilde{r}_N \}^T, \quad b_l = Y_{ij}(s_l)$$

d) Once the unknowns in (8) are computed, $Y_{ij}(s)$ can be expressed as $Y_{ij}(s) = W(s)/\lambda(s)$, which shows that the poles of $Y_{ij}(s)$ are coincident with the zeros of $\lambda(s)$. Substituting the values of the poles into equation (5) and solving the equation similar to (8), we can easily obtain the residues r_k^{ij} and constant c^{ij} of $Y_{ij}(s)$.

MACROMODEL SYNTHESIS

From the preceding section, the macromodel of interconnect subnetwork is created. And for a general n-port subnetwork characterized by $m1$ real poles and $m2$ complex conjugate pole pairs, the state-space representation by Jordan-canonical method [1] takes the following form,

$$\begin{cases} \{\dot{x}\} = [A]\{x\} + [B]u \\ i = [C]\{x\} + [D]u \end{cases} \tag{9}$$

Where $\{x\} = \{x_1 \quad x_2 \quad x_3\}^T$, $[A] = \begin{bmatrix} A_r & 0 & 0 \\ 0 & \mathrm{Re}(A_c) & \mathrm{Im}(A_c) \\ 0 & -\mathrm{Im}(A_c) & \mathrm{Re}(A_c) \end{bmatrix}$,

$[B] = [B_r \quad 2\mathrm{Re}(B_c) \quad 0]^T$, and $[C] = [C_r \quad \mathrm{Re}(C_c) \quad \mathrm{Im}(C_c)]^T$.

Matrix A, B and C are derived from pole-residue pairs. The subscripts (r and c) denote the real and complex conjugate pole-residue pairs respectively. Matrix i and u contain the port currents and voltages. The equivalent circuit from equation (9) can be inserted into HSPICE simulator to implement the transient simulation of circuit package.

SIMULATION EXAMPLE

A simple example circuit shown in Fig. 1. is used to verify the accuracy and efficiency of the interconnect-simulation approach presented in this paper.

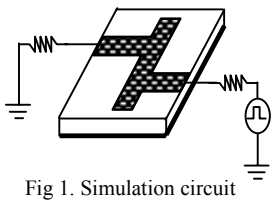

Fig 1. Simulation circuit

This example circuit is mainly composed of a typical microstrip low-pass filter, whose geometry is the same as that in [4]. The microstrip low-pass filter is simulated using de-coupling FDTD and FFT method to obtain its Y parameters. Some details in FDTD simulation are as follows: the unit cell size in millimeter is $\Delta x = 0.4233, \Delta y = 0.4064, \Delta z = 0.265$; the time step is $\Delta t = 0.441 ps$; total grid size is $80\Delta x \times 110\Delta y \times 160\Delta z$ and total simulation time steps are 8000. The dispersive ABC and Gussian pulse source are used in FDTD simulation.

Eighteen poles (2 real poles and 8 complex conjugate pole pairs) are extracted by vector Fitting method to match the Y parameters of this two-port low-pass filter up to 15 GHz. The good agreements between the Y parameters obtained by de-coupling FDTD & FFT techniques and Vector Fitting method [2] show that the rational approximation is accurate (Fig. 3.). The transient analysis by HSPICE is shown in Fig. 2.

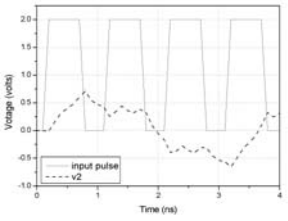

Fig 2 Transient simulation results: voltage at port 2 (dashed line)

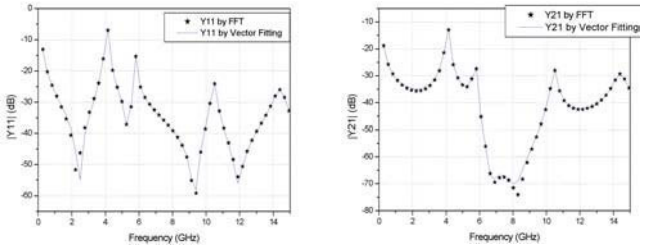

Fig. 3. Magnitude of Y11 and Y21: De-coupling FDTD & FFT vs. Vector Fitting Method

CONCLUSIONS

De-coupling full-wave FDTD and FFT method combined with rational function approximation is an efficient approach to address the hybrid electromagnetic (interconnect) and circuit problem, in which the electromagnetic field effects are fully considered and the strength of the HPSICE circuit simulator is also exploited. The Vector Fitting method used in this paper provides a considerably accurate way for macromodeling interconnect subnetwork. However, the deficiency of this rational function approximation approach is that it does not always assure a robust passive macromodel, which will need further study.

REFERENCES

[1] Achar R. and M. S. Nakhla, "Simulation of high-speed interconnects", Proceedings of the IEEE, Vol. 89, pp. 693-728, May 2001.

[2] Gustavsen B. and A. Semlyen, "Rational approximation of frequency domain responses by vector fitting", IEEE Trans. Power Delivery, Vol. 14 , pp. 1052-1061, July 1999.

[3] Watanabe T. and H. Asai, "Synthesis of time-domain models for interconnects having 3-D structure based on FDTD method", IEEE Trans. Circuits Syst., Vol. 47, pp.302-305, April 2000.

[4] Sheen D. M. et al., "Application of the three-dimensional finite-difference time-domain method to the analysis of planar microstrip circuits", IEEE Trans. Microwave Theory Tech., Vol. 38, pp. 849–857, July 1990

COMPUMAG Saratoga Springs, New York USA
July 13 - 17, 2003

Wave propagation schemes and space-fillers

Emmi Koljonen, Janne Keränen, Lauri Kettunen

Abstract— **The efficiency of Yee-like schemes depends on the properties of the cell complexes employed. We examine techniques to construct the mesh for explicit time domain schemes by replicating first a regular kind of polyhedron or cluster of tetrahedra, and then separately consider how to take the material interfaces into account.**

I. Introduction

In this paper we seek numerically efficient techniques for the wave propagation problem. We are especially interested in time domain schemes which enable to represent on the discrete level at least one of the constitutive laws with a diagonal matrix. The FIT and FDTD techniques are exmples of such approaches.

Our starting point is to find a tesselation of space consisting of a replication of one single polyhedron. We'll first ask whether other space-filling polyhedra than hexahedra can be exploited, and then examine separately how one should handle the material interfaces.

The advantage of a mesh constructed from a single polyhedron is the need to build the underlying matrices only for one replica. With smart indexing all the necessary equations can be constructed on fly, and this way one may avoid the explicit construction of the full system of linear equations. Thus, although one often looks down on regular meshes for their obvious downsides, regularity (or more precisely, the symmetry) also compensates a lot in efficiency, especially in complex problems.

II. Yee-like schemes and space-fillers

A sufficient condition for explicit Yee-like scheme is (i) a pair of dual cell complexes such that (ii) the primal edges and dual faces, and the dual edges and primal faces are orthogonal to each other.

It is important to notice that *any polyhedra* fulfilling these two basic conditions are admissible. In other words, not only tetrahedra and hexahedra (as in FIT) are possible, but other polyhedra may be considered as well. This motivates us to look at so called *space-fillers*, Fig. 1. A space-filler is a polyhedron which can be used to generate a tessellation of space. There are only five space-filling convex polyhedra with regular faces: the *triangular prism*, *hexagonal prism*, *cube*, *truncated octahedron*, and *gyrobifastigium* [1]. The *rhombic dodecahedron*, *elongated dodecahedron*, and *squashed dodecahedron* appearing in sphere packing are also space-fillers as is any non-self-intersecting quadrilateral prism.

Among these space-fillers at least the triangular prism, hexagonal prism, cube, truncated octahedron, and rhombic dodecahedron are eligible for Yee-like schemes: These polyhedra result in a mesh whose dual is properly "orthogonal" to the primal mesh. This condition is sufficient for solving the electric and magnetic fluxes on the faces and the emf's and mmf's along the edges. (Interpolation of the fields within the polyhedra needs to be considered separately.)

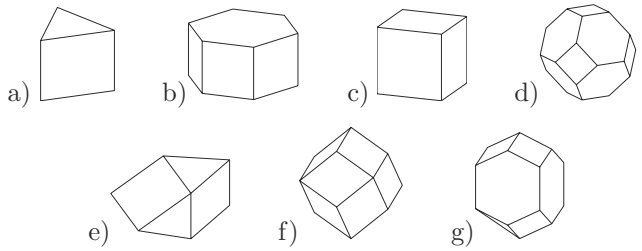

Fig. 1. Space-fillers: a) triangular prism, b) hexagonal prism, c) cube, d) truncated octahedron, e) gyrofastigium, f) rhombic dodecahedron and g) elongated dodecahedron

The space can be also filled with other less regular polyhedra. For instance, the Sommerville tetrahedron [2] can be copied to fill the whole space. More precisely, it is four symmetrical copies of the Sommerville tetrahedron that result in an octahedron filling space, as shown in Fig. 2. [3]

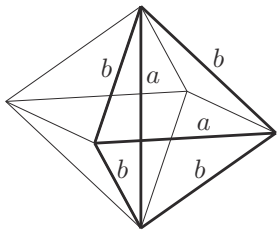

Fig. 2. A space-filling octahedron which is build from four copies of the Sommerville tetrahedron i.e. a tetrahedron with two edges of length a and four of length b, with relation $3a^2 = 4b^2$.

Another related approach to fill space is Üngör's [4] rather recent technique to create a tesselation of space based on a cluster of tetrahedra such that all dihedral angles of the tetrahedra become acute, Fig. 3. This implies, that one ends up with a tetrahedral mesh satisfying the Delaunay-Voronoi condition, which is also a sufficient condition for diagonal mass lumping and the construction of explicit Yee-like schemes [5].

III. Material interfaces

The use of space filling techniques based on replications of a single polyhedron lead to the obvious problem that material interfaces cannot be matched precisely. Before examining, how this problem can be circumvented, let's ask, how serious this problem is. Evidently, in some cases –e.g. the SAR-computations in the human head– one does not even have an exact geometrical representation of the domain.

This work is supported by the Academy of Finland, project 53972.
E. Koljonen, J. Keränen and L. Kettunen are with the Tampere University of Technology, Inst. of Electromagnetics, P.O.Box 692, FIN-33101 Tampere, Finland. E-mail: {emmi.koljonen,janne.keranen,lauri.kettunen}@tut.fi

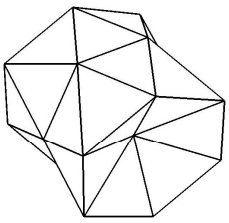

Fig. 3. A part of Üngör's mesh: 30 tetrahedra with all dihedral angles acute.

Second, although the mesh may appear visually as a rather poor approximation of the domain, the numerical error needs not to be significant compared to the use of a proper finite element mesh.

A simple example is employed to demonstrate this. Consider an air-filled cylindrical cavity resonator with perfectly conducting walls. In Fig. 4 three different meshes representing the cavity resonator are shown.

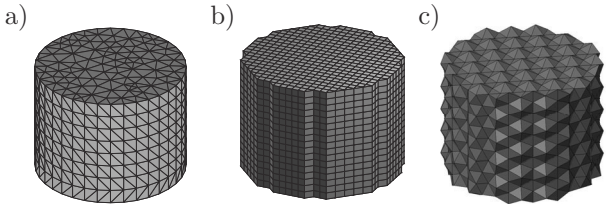

Fig. 4. Three meshes in a cylindrical cavity resonator (height 16.5 cm and diameter 22 cm). a) Tetrahedral finite element mesh. b) Hexahedral FIT-mesh. c) Üngör-type tetrahedral mesh.

The resonance frequencies of the cavity are compared with analytic solutions in Table I. The values were computed with three different meshes: typical FE-mesh, FDTD/FIT-kind of approximation, and Üngör's mesh, meshes a, b and c in Fig. 4. With Üngör's mesh, the cavity resonator problem was solved using standard finite elements (`FE`) and an explicit finite elements approach with diagonal mass lumping (`Diag`).

TABLE I
RESONANCE FREQUENCIES OF THE CYLINDRICAL CAVITY IN GHZ

		Mesh a)	Mesh b)	Mesh c)	
Mode	Analytic	FE	FIT	Diag	FE
TM_{010}	1.043	1.04	1.049	1.05	1.05
TE_{111}	1.210	1.21	1.207	1.23	1.23
TM_{011}	1.383	1.38	1.387	1.40	1.40
TE_{211}	1.606	1.61	1.593/1.603	1.59	1.59
TM_{110}	1.662	1.66	1.667	1.64/1.66	1.65/1.66
TM_{111}	1.894	1.88	1.889	1.88	1.89
TE_{011}	1.894	1.90	1.898	1.88	1.92
TE_{112}	1.985	1.98	1.974	-	-
TE_{311}	2.036	2.04	2.017	2.02	2.04
TM_{012}	2.095	2.09	2.089	2.12	2.14
TM_{210}	2.228	2.20	2.223	2.18	2.20
TE_{212}	2.249	2.25	2.223/2.233	2.23/2.25	2.25/2.27
				2.28/2.30	2.31/2.32

IV. Matching interfaces

However, it is sometimes necessary to model the geometry precisely. A possibility to overcome the difficulties related to material interfaces is to first generate a mesh by replicating a regular polyhedron (or an elementary cluster of tetrahedra), and then to remove at least all the elements which intersect the interfaces. Thereafter one may create tetrahedra refilling the space and matching with the interfaces. (Additional interface conditions may be needed to match the polyhedra to the tetrahedra.)

Removal of the polyhedra and replacing them with tetrahedra easily implies that the explicit nature of the time domain scheme is lost. To retain efficiency, the key issue is whether the matrices representing the constitutive law can be diagonalized. (As is, well known, the use of mass matrices guarantee stability, but does not lead to efficient computation.)

The diagonalization technique presented in [5] gives, however, some freedom in generating the tetrahedra. The numerical scheme is stable, if the entries

$$\mathbf{H}_{ee}(\epsilon) = -\int_{\Omega} \epsilon \nabla w_i^0 \cdot \nabla w_j^0 \, . \qquad (1)$$

of the diagonalized matrix are positive. This is a less restrictive condition than the acute dihedral angles, as in (1) acute angles compensate obtuse ones, and also permittivity has affect an effect as well. Even rather large angles can be compensated if the obtuse angles are on the side with the lower permittivity. Furthermore, some obtuse angles may still be acceptable and they do not necessarily degrade efficiency, if the non-diagonal block of the lumped mass matrix remains small [6].

V. Conclusions

The finite elements approach typically starts from the idea of representing the domain with a finite element mesh as accurately as possible. As the large experience with FIT and FDTD shows, this is not always necessary in wave propagation problems. The explicit time domain schemes allow to use any mesh consisting of replications of a single regular polyhedron or of clusters of rather regular tetrahedra. The material interfaces obviously do cause some problems, but on the other hand, efficiency can be maximized by exploiting regularity.

References

[1] E. W. Weisstein. Eric Weisstein's World of Mathematics. [Online]. Available: http://mathworld.wolfram.com/

[2] D. M. Y. Sommerville, "Division of space by congruent triangles and tetrahedra," *Proc. Edinburgh Math. Soc.*, no. 43, pp. 85–116, 1923.

[3] A. Bossavit, "The Sommerville mesh in Yee-like schemes," in *Scientific Computing in Electrical Engineering*, Eindhoven, The Netherlands, 2002.

[4] A. Üngör, "Tiling 3D Euclidean space with acute tetrahedra," in *Proc. of Canadian Conference on Computational Geometry, August 2001*, Waterloo, ON, 2001, pp. 169–172.

[5] A. Bossavit and L. Kettunen, "Yee-like schemes on a tetrahedral mesh with diagonal lumping," *Int. J. Numer. Modell.*, vol. 12, pp. 129–142, 1999.

[6] J. Keränen, J. Kangas, A. Ahola, and L. Kettunen, "Implicit Yee-like scheme on tetrahedral mesh," *IEEE Trans. Magn.*, vol. 38, no. 2, pp. 717–720, 2002.

COMPUMAG Saratoga Springs, New York USA
July 13 - 17, 2003

Transient Modal Analysis of Quasi-Implicit FDTD Schemes

Rolf Schuhmann and Thomas Weiland
Technische Universität Darmstadt, Computational Electromagnetics Laboratory (TEMF)
Schloßgartenstr. 8, 64289 Darmstadt, Germany
schuhmann/weiland @temf.tu-darmstadt.de

Abstract—**Time domain simulations for high-frequency applications are widely dominated by the leapfrog time-integration scheme, especially in combination with finite-difference methods (Finite Difference Time Domain, FDTD) or the Finite Integration Technique (FIT). As an explicit method, however, the leapfrog algorithm is restricted to a maximum stable time step, and recently some alternative, unconditionally stable techniques have been proposed to overcome this limitation. We analyze such schemes using a transient modal decomposition of the electric fields. It is shown that stability alone is not sufficient to guarantee correct results, but additionally important conservation properties have to be met.**

I. Introduction

Especially in high-frequency field simulations, where one often deal with lossless or at least low-loss structures and a large number of time steps, stability is one of the most important properties of time domain methods, and a required condition for their overall convergence. Here, very often Finite Difference methods (FDTD) and the time domain variant of the Finite Integration Technique (FIT, [1]) are used, and therein the so-called *leapfrog* (LF) time stepping algorithm. Based on central difference approximations for the time derivatives in Maxwell's equations, it is known to be conditionally stable — ruled by a maximum stable *Courant* time step width Δt_0 — and to conserve the electromagnetic energy in lossless structures.

Since the time step limitation in the LF scheme is coupled to the resolution of the spatial grid, it sometimes leads to strongly oversampled time signals and thus to a poor efficiency of the overall method. As a remedy, some alternative, 'quasi-implicit' approaches have been proposed, such as the Alternating Direction Implicit (ADI) variant of FDTD [2], or the family of unconditionally stable algorithms proposed in [3]. However, it has been shown by various authors [4], [5], [6], [7] that such schemes may have severe accuracy problems if the Courant limit of the related LF approach is considerably exceeded. In this paper this dissatisfying result is analyzed using an eigenmode decomposition of the transient fields.

II. Algebraic Formulation

We use here the notation of the FIT [1], where Maxwell's equations are transformed into a set of algebraic equations (linear case, without currents):

$$\mathbf{M}_\mu^{-1}\mathbf{C}\widehat{\mathbf{e}} = -\frac{d}{dt}\,\widehat{\mathbf{h}}, \qquad \mathbf{M}_\varepsilon^{-1}\mathbf{C}^T\widehat{\mathbf{h}} = \frac{d}{dt}\,\widehat{\mathbf{e}} \tag{1}$$

$$\mathbf{S}\widehat{\mathbf{b}} = \mathbf{0}, \qquad \widetilde{\mathbf{S}}\widehat{\mathbf{d}} = \mathbf{q}. \tag{2}$$

$\mathbf{C}$ and $\mathbf{S}$ are the topological 'curl'-, and 'source'-matrices, respectively, and the vectors $\widehat{\mathbf{e}}$ and $\widehat{\mathbf{h}}$ contain the electric and magnetic voltage-type degrees of freedom on a pair of staggered grids. The material matrices $\mathbf{M}_\varepsilon^{-1}$ and $\mathbf{M}_\mu^{-1}$ are diagonal and positive definite in the simplest case.

An important property of these equations — which can also be used to derive the FDTD-method — is the *exact* source-free property of curl-fields:

$$\mathbf{S}\,\mathbf{C} = \mathbf{0}, \qquad \widetilde{\mathbf{S}}\,\mathbf{C}^T = \mathbf{0}. \tag{3}$$

Finally, equations (1) can be combined to a large system of differential equations for a composite vector $\mathbf{x}$:

$$\frac{d}{dt}\mathbf{x} = \mathbf{A}\mathbf{x} \tag{4}$$

with

$$\mathbf{x} = \begin{pmatrix}\widehat{\mathbf{h}}\\ \widehat{\mathbf{e}}\end{pmatrix} \quad \text{and } \mathbf{A} = \begin{pmatrix}\mathbf{0} & -\mathbf{M}_\mu^{-1}\mathbf{C}\\ \mathbf{M}_\varepsilon^{-1}\widetilde{\mathbf{C}} & \mathbf{0}\end{pmatrix}. \tag{5}$$

The leapfrog scheme arises from the allocation of the fields on a staggered time axis and central difference approximations for the time derivatives. It can be summarized in the *update equations*

$$\mathbf{x}^{(n+1)} = \mathbf{G}_{LF}(\Delta t)\,\mathbf{x}^{(n)}, \qquad \mathbf{x}^{(n)} = \begin{pmatrix}\widehat{\mathbf{h}}^{(n)}\\ \widehat{\mathbf{e}}^{(n+1/2)}\end{pmatrix} \tag{6}$$

with the *iteration matrix*

$$\mathbf{G}_{LF}(\Delta t) = \begin{pmatrix}\mathbf{I} & -\Delta t\mathbf{M}_\mu^{-1}\mathbf{C}\\ \Delta t\mathbf{M}_\varepsilon^{-1}\widetilde{\mathbf{C}} & \mathbf{I}-\Delta t^2\mathbf{M}_\varepsilon^{-1}\widetilde{\mathbf{C}}\mathbf{M}_\mu^{-1}\mathbf{C}\end{pmatrix}. \tag{7}$$

The ADI-scheme is based on a splitting of the operator matrix $\mathbf{C} = \mathbf{C}_1 + \mathbf{C}_2$ in two parts, both of which are used in alternating order in the update equations [6]. This leads to an update scheme in two half-steps, which can be summarized by an iteration matrix $\mathbf{G}_{ADI}(\Delta t)$ (see [6] for the details).

For the eigenvalues of these iteration matrices one can find the relations

$$|\lambda_{G,LF}(\Delta t)| = 1 \quad \Leftrightarrow \quad \Delta t \le \Delta t_0 \tag{8a}$$

$$|\lambda_{G,ADI}(\Delta t)| = 1 \qquad \forall \Delta t > 0, \tag{8b}$$

which are a sufficient condition for the stability of the methods.

In most practical cases the dimension of the iteration matrices is too large to perform a further numerical analysis. For the small test example presented below, however, the matrices are of manageable size, and the results of (8) can be visualized as shown in Fig. 1.

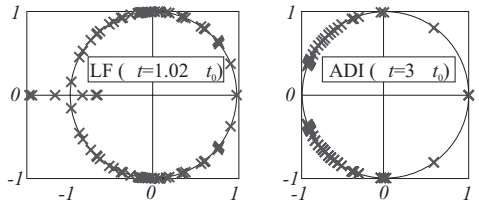

Fig. 1. Eigenvalues of the iteration matrices of LF (left) and ADI (right).

III. Transient Modal Expansion

In the following, the LF and ADI schemes are applied to a 2D (TE) model problem adapted from [7]. It describes the transient charging process of a simple plate capacitor, driven by a 750kHz current pulse (cf. Fig. 2).

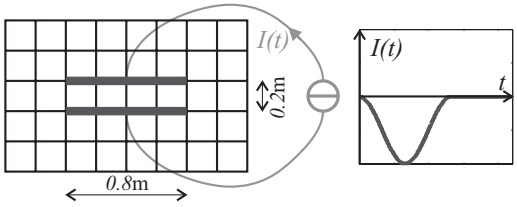

Fig. 2. Model problem: Charging process of a 2D plate capacitor.

Fig. 3 shows some eigenmodes of the related system matrix $\mathbf{A}$: A static mode (left) with $\nabla \times \vec{E} = 0$, $\lambda_A = 0$ and $\lambda_G = 1$, a second static mode ('plate mode') describing the desired stationary field solution, and a dynamic mode (right) with $\nabla \times \vec{E} \neq 0$, $\lambda_A \neq 0$, and $\lambda_G = e^{i\varphi}$.

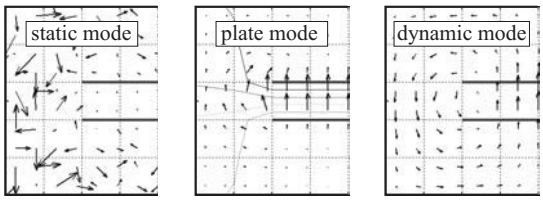

Fig. 3. Model problem (half structure): Electric fields of a static eigenmode, the plate mode, and a dynamic mode in the plate capacitor.

During the time stepping process the electric fields can now be decomposed into these (and all the other) eigenmodes. The results of this *transient modal expansion*, the expansion coefficients as a function of simulation time, are shown in Fig. 4.

For the Courant time step Δt_0 (upper figure) the ADI and LF curves for the plate mode and the dynamic modes are nearly indistinguishable. However, in the ADI simulation arises one more static mode with a magnitude of about 10% at steady state, which cannot be seen in the LF (reference) results, where all the static modes are below numerical noise. For an enlarged $\Delta t = 3\Delta t_0$ (lower figure, where no LF results are available any more) the amount of this 'parasitic' field reaches the order of magnitude of the desired field solution (plate mode).

In the final paper we will show that the reason for these parasitic solution is the loss of orthogonality between the eigenmodes in the ADI iteration matrix: Whereas the static modes remain unchanged compared to the system matrix $\mathbf{A}$ (which can be proven for the 2D TE-case), the dynamic modes are 'contaminated' by static fields from the kernel of the curl operator. As a consequence, the transient fields in the ADI process are not source-free, resulting in an energy transfer into parasitic (non-physical) fields.

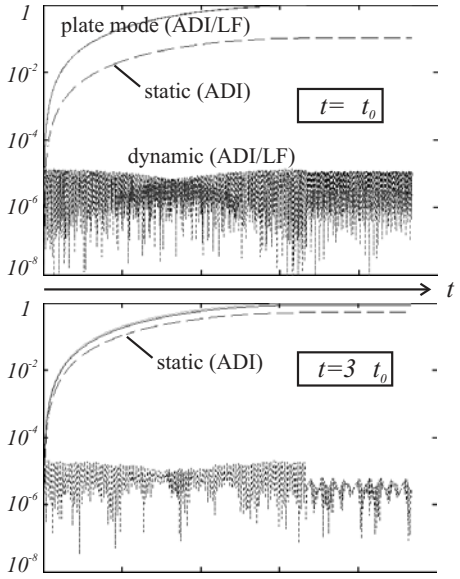

Fig. 4. Transient modal expansion coefficients (logarithmic) for different Δt.

Conclusion

A transient modal expansion of the electric field in time domain methods has been used to analyze different time stepping approaches. Using this powerful tool it can be shown that the ADI method, although being unconditionally stable, does not conserve the energy of the dynamic eigenmodes — even for moderate time steps.

References

[1] T. Weiland, "Time domain electromagnetic field computation with finite difference methods," *Int. Journal of Numerical Modelling*, vol. 9, pp. 295–319, 1996.

[2] T. Namiki, "3-D ADI–FDTD method — unconditionally stable time-domain algorithm for solving full vector Maxwell's equations," *IEEE Trans. on Microwave Theory and Techniques*, vol. 48, no. 10, pp. 1743–1748, 2000.

[3] J. Kole, M. Figge, and H. D. Raedt, "Unconditionally stable algorithms to solve the time-dependent Maxwell equations," *Physical Review E*, vol. 64, 066705, 2001.

[4] M. Darms, "Analyse des ADI Zeitintegrationsverfahrens für zeitlich veränderliche Feldprobleme," Student thesis, Technische Universität Darmstadt, 2001.

[5] S. Staker and M. Piket-May, "Algorithm study of ADI-FDTD," in *Digest of the 2001 USNC/URSI National Radio Science Meeting*, (Boston), p. 255, 2001.

[6] M. Darms, R. Schuhmann, and H. S. T. Weiland, "Dispersion and asymmetry effects of ADI–FDTD," *IEEE Microwave and Wireless Components Letters*, 2003. in press.

[7] S. Garcia, T. Lee, and S. Hagness, "On the accuracy of the ADI-FDTD method," *IEEE Antennas and Wireless Propagation Letters*, vol. 1, no. 1, pp. 31–34, 2002.

Path Loss Prediction Model for Indoor Wireless Communication using TLM Method

A. D. Rosa, H. Domínguez, A. Raizer
GEMCO/EEL/CTC/UFSC, C.P. 476
88040-900 - Florianópolis - SC - Brazil
e-mail: dalla@eel.ufsc.br, hugo@eel.ufsc.br, raizer@eel.ufsc.br

Abstract - A numeric model based on Transmission Line Matrix Method (TLM) is proposed to predict electromagnetic field's levels and calculate Path Loss for indoor wireless communication. For this purpose, an office room was modeled. Different constitutive room materials were considered. The excitation source was modeled by a quarter wave monopole antenna. The results show that the TLM numerical approach is well suited to be used as a tool for study of Path Loss prediction, being capable to provide accurate results.

INTRODUCTION

Nowadays the wireless indoor communication has suffered a great expansion. For that reason, during the last years, there has been increasing interest in the application of computational techniques to model indoor channel propagation. In this way, the aim of this work is to present the TLM (Transmission Line Matrix Method) as a tool to predict the electromagnetic waves propagation and to calculate de Path Loss in a typical urban indoor environment.

Although TLM has been used successfully for many years in solving RF and microwave problems, apparently, it has not been used in applications involving electromagnetic indoor propagation predictions.

CALCULATION MODEL AND METHOD

For simulations we used a 2D TLM algorithm. The mesh employed consists of "parallel" topology cells [1]. Our computational program positions the grid in a *x-y* plane, and calculates field components *Hx*, *Hy* and *Ez* (TM case).

The problem under study is show in Fig. 1. It consists in an office room (cross section) with a small omnidirectional quarter wave monopole inside, working as a transmitter of electromagnetic waves.

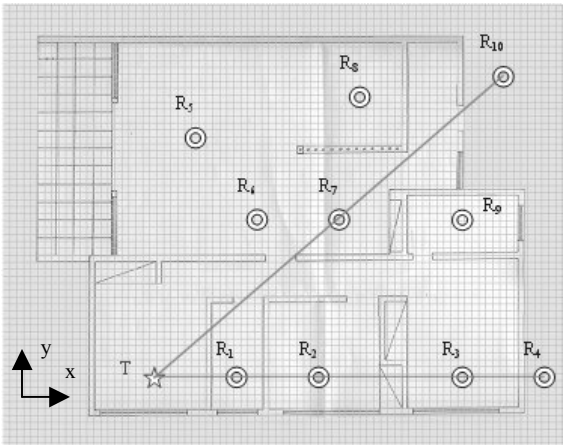

Fig. 1. Mesh over the Room. Antenna transmitter (T – Star) and points of measurement (Rn – Circles).

For the construction of the numeric model corresponding to the room geometry, it was chosen a mesh containing 1200 cells in x-axis direction and 945 cells in y-axis direction. We used square TLM cells with $\Delta l = 1{,}27$ cm. The cell size was chosen in order to have good description of physical features as well as to ensure adequate spatial sampling.

The constitutive electrical properties of room materials, taken from [4, 6] are listed in Table I.

TABLE I. ELECTRICAL PROPERTIES OF MATERIALS

Material	*Permittivity* ε_r	*permeability* μ_r	*Conductivity (S/m)*
AR	1.0	1.0	0.0
CONCRETE	5.0	1.0	0.0
GLASS	4.0	1.0	0.0
ALUMINUM	1.0	1.0	3.8E+07
WOOD	3.0	1.0	0.0

The transmitter was modeled by a λ/4 monopole antenna oriented in the z-axis direction. The carrier frequency was chosen to be 914 MHz and the antenna-radiated power was chose to be 1.0 watt. These are typical data of personal communication network (PCN) [2].

The antenna was excited with a gap voltage source (see fig. 2). The driven voltage source was then transferred into a sinusoidal time varying electric field polarized along the monopole axis with a uniform amplitude and phase over the gap.

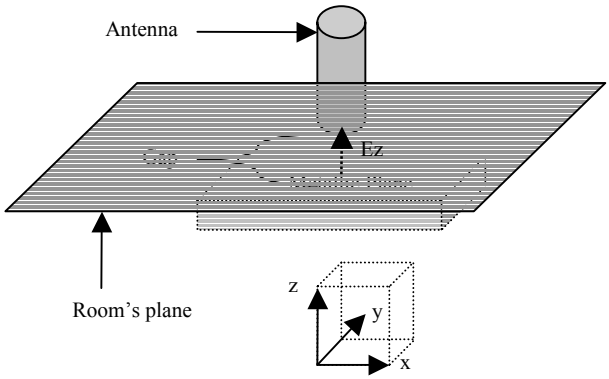

Fig. 2. Schematic representation of antenna and room's plane.

The mesh ends are open boundaries, and the TLM "matched" (absorbing) boundary condition described in [1] was used. The length of simulation time was dictated by the

time required for the transient solution to decay, and for the steady-state solution to appear.

Once the *rms* electric field values at the measurement points on the mesh are obtained by the TLM computation, the path loss at several points could be calculated by the electrical field ratio between the excitation (E_T) and measurement points (E_{Rn}), as show in Fig. 1 and (1).

$$\overline{L}_{TLM}(dB) = 20\log\left(\frac{E_T}{E_{R_n}}\right),\ n = 1,2,\ldots,10 \qquad (1)$$

Finally, to evaluate the TLM results, a comparison with the Statistical d^n Path Loss Prediction method [2] was done.

RESULTS

Figure 3 show the calculated *rms* electrical field levels inside the room. The electrical field strength at the excitation point was 475.06 V/m (attending the antennas characteristics data).

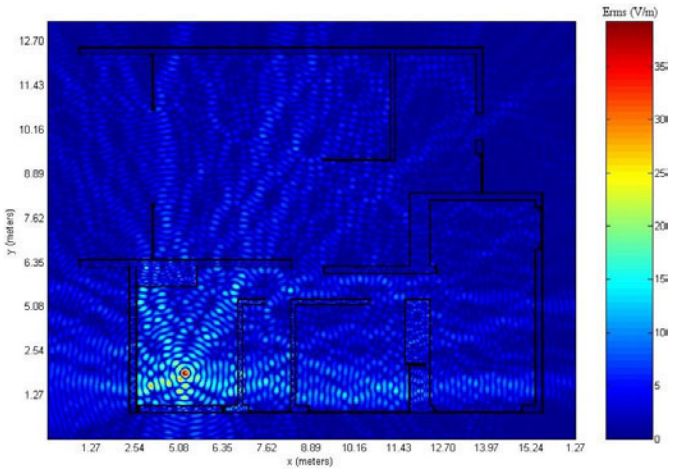

Fig.3. Electric Field distribution inside de room.

The results of TLM Path Loss Prediction using (1) are listed in table II. Also, the Statistical Path Loss Method results are showing for comparisons.

TABLE II – TLM RESULTS AND CALCULATIONS

Measurement Point	Transmitter Distance (m)	rms Electrical Field (V/m)	TLM Path Loss (dB)	Statistical Path Loss (dB)
R_1	2.60	5.25	39.13	42.34
R_2	4.02	3.54	42.65	48.51
R_3	9.08	2.03	47.38	59.35
R_4	10.48	1.32	51.12	62.98
R_5	6.56	1.91	47.91	50.38
R_6	5.60	3.26	43.27	49.01
R_7	6.43	2.82	45.97	52.60
R_8	9.88	0.99	53.62	57.61
R_9	13.00	0.67	57.03	58.70
R_{10}	9.57	0.86	54.86	60.80

A more detailed discussion and other important results will be presented in the extended paper.

REFERENCES

[1] C. Christopoulos, *The Transmission-Line Modeling Method- TLM*, New York: IEEE Press and Oxford University Press, 1995.

[2] S.Y. Seidel e T. S. Rappaport, "914 MHz path loss prediction models for indoor wireless communication in multifloored buildings," IEEE Trans. Antennas Propagation, vol. 40, pp. 207-217, Feb 1992.

[3] F. Aguado Agelet, A. Martinez, L. J. Alvarez Vázquez, "Optimization Methods for Optimal Transmitter Locations in a Mobile Wireless System", *Digest of the 9th Biennial IEEE Conference on Electromagnetic Field Computation – CEFC 2000*, pp. 441, Wisconsin USA, June 2000.

[4] J. D. Krauss, *Electromagnetics*, Fourth Edition, New York: McGraw – Hill, Inc. , 1992.

[5] D. Molkdar, "Review on radio propagation into and within buildings," *Inst. Elec. Eng. Proc.,* pt. H, vol. 138, no. 1. pp. 61-73, Feb. 1991.

[6] Y. Kotsuka and T. Tanaka, "Method of Improving EM Field Distribution in a Small Room with an RF Radiator", *IEEE Transactions on Electromagnetic Compatibility*, Vol. 41, No. 1, pp. 22 – 29, February 1999.

Prediction of Torque Characteristic on Barrier Type SRM Using Stochastic Response Surface Methodology Combined with Moving Least Square

Young-Kyoun Kim, Geun-Ho Lee, Jung-Pyo Hong, Senior Member, IEEE, and Jin Hur*
Dept. of Electrical Eng., Changwon National University, #Sarim, Changwon, Kyungnam, 641-773, Korea
* Precision Machinery Research Center, Korea Electronic Technology Institute, Puchon, Kyunggi, 420-130, Korea
e-mail: ensigma@hitel.net

***Abstract*—This paper describes a design of switched reluctance motor with rotor poles having inserted barriers. A shape of the rotor barrier leads to improvement of torque characteristics. As well, dimensional tolerances of the barrier directly affect electrical performances of the motor. Therefore, the torque characteristic prediction of the motor is accomplished by a combination technique employing Stochastic Response Surface Methodology and Moving Least Square Method.**

INTRODUCTION

Switched Reluctance Motor (SRM) has some advantages, such as, a high speed, efficient variable speed and a high reliability. Therefore, an application of switched reluctance motors is recently received attention in various industrial fields. However, a SRM is strongly nonlinear and suffer from high torque ripple. Also, the torque per volume of SRM strongly depends on the designed shape of salient poles. This paper proposed a barrier type SRM, which is designed by inserting separated barriers in the rotor. Separated barriers lead the reduction of a torque ripple and the improvement of torque performances. What is more describing in this paper, dimensional tolerances of electric machines can effect on electrical performances, and besides, the larger tolerance in manufacturing processes, the lower it is to cost of manufacturing electric machines [1]. A design of the barrier type SRM needs allowance for dimensional tolerances on especially barrier part of the SRM, beacuse of limitations on the manufacturing , measuring precision and so on.

Therefore, the design techniques are required to find the tolerance band of design variables in order to minimize the cost and satisfy required performance. The torque charectristic, according to tolerances of the dimensional barrier, of barrier type SRM is predicted by using Stochastic Response Surface Methodology (SRSM). SRSM can be illustrated as an extension of Response Surface Methodology (RSM), and it is then combined with Moving Least Square (MLS) to ehance the accuracy of stochastic response modeling in SRSM.

STRUCTURE OF BARRIER TYPE SWITCHED RELECTANCE MOTOR

Fig. 1 shows the proposed barrier type 8/6 SRM, which is designed to improve torque characteristics. With a proposed rotor inserted the flux barrier, the motor characteristics seriously vary according to the shape of flux barrier. Therefore, the geometric shape design of the barrier is required to find the design variables that consider manufacturing tolerance as well as improve the performance and exactly predict the torque characteristics. These tolerances can affect the machine performance, such as operating efficiency.

FRAMEWORK FOR TOLERANCE ANALYSIS

Stochastic Response Surface Methodology

In the SRSM, a relationship of the uncertainty between the outputs and inputs is addressed by the series expansion of standard normal variables in terms of Hermite polynomials. The output function can be approximated by an polynomial chaos expansion and the approximation is sampled to calculate a statistical distribution of outputs as described in [1].

Moving Least Square Method

Unknown coefficients of the Stochastic response modeling are estmated by MLS method. The main idea of the MLS method is that a whole approximation $U^h(x)$ of a sampling space can be accomplished by going through a moving proess and written as follows [2]:

$$U^h(x) = \sum_{j=1}^{N} \mathbf{P}(0)^{\mathrm{T}} \mathbf{M}(x)^{-1} \mathbf{P}(x - x_{\mathrm{I}}) \mathbf{W}(\bar{x} - x_{\mathrm{I}}) \mathbf{U}_{\mathrm{I}} \quad (1)$$

$$\mathbf{M}(\bar{x}) = \mathbf{P}\, \mathbf{W}(\bar{x})\, \mathbf{P}^{\mathrm{T}} \quad (2)$$

where **W** is weight function having form of a quartic spline, **P** and **U** are composed with a set of sample point regarding design variables and outputs, respectively.

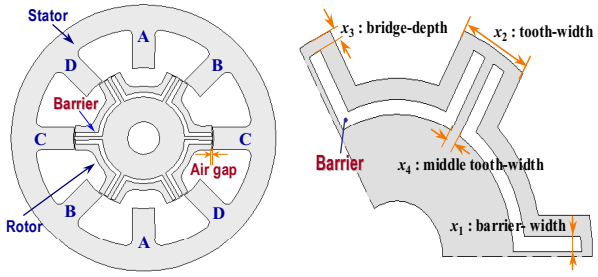

Fig. 1. Analysis model and design variables

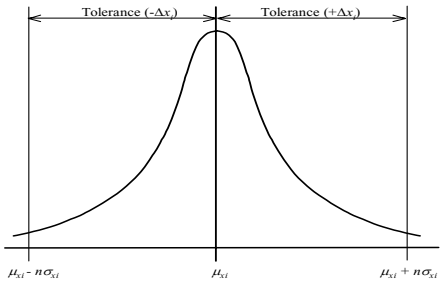

Fig. 2. Tolerance band of design variables

Introductory Statistics for tolerance Analysis

A variation band of design variables with assuming the distribution of a normal distribution is show in Fig. 2. In this symmetrical distribution, the tolerance band of design variables is easy to quantify in terms of the percentage of the area that will occur between one, two and more standard deviation from the mean μ as follows [1];

$$\Delta x = \pm n\sigma \quad (n = 1, 2, 3, \cdots) \tag{2}$$

Modeling variation of outputs according to tolerance of design variables is built by the SRSM. From a set of N samples, the basic moments of the distribution of an output y_i can be calculated as follows;

$$\mu_{y_i} = \mathrm{E}\{y_i\} = \frac{1}{N}\sum_{j=1}^{N} y_{i,j} \tag{3}$$

$$\sigma^2_{y_i} = \mathrm{E}\{(y_i - \mu_{y_i})^2\} = \frac{1}{N-1}\sum_{j=1}^{N} (y_{i,j} - \mu_{y_i})^2 \tag{4}$$

$$\sigma_{y_i} = \sqrt{\sigma^2_{y_i}} \tag{5}$$

where, μ_{yi} is a mean, σ^2_{yi} is a variance and σ_{yi} is a standard deviation, respectively.

RESULTS AND DISCUSSION

Fig. 3 shows the torque profile of one stroke of the proposed motor, the electromagnet field within the motor is computed by using the two-dimensional finite element method (2D-FEM). And then the manufacturing process is running at the design variable tolerance of 10 (%) based on the six-sigma level. The variation of the outputs is distributed as shown in both Fig. 4 and Fig. 5, which are concerned about both the average torque and the torque ripple, respectively. In order to reduce the scatter of outputs from their population, design variables need to be regulated at a tighter tolerance than 10 (%).

CONCLUSIONS

In this paper, the barrier sailent pole applied to the rotor of conventional SRM to a enhancement of the torque performance, and it is then accomplished by tolerance analysis to predicte torque variations according to the geometric shape of the barrier. Tolerance analysis is achieved by SRSM combined with MLS method. From the result, proposed approach will provide a great potential for improving robustness of production and reducing production cost. In full paper, more detailed descritions of tolerance analysis will be presented.

REFERENCES

[1] Young-Kyoun Kim et al, "Torque Characteristics Analysis Considering the Tolerance of Electric Machine by Stochastic Response Surface Method ", *Proceeding of IAS' 2002*, pp.752-758, October 2002.

[2] Simore. A. Viana et al "Moving Least Reproducing Kernel Method for Electromagnetic Field Computation", *IEEE Transactions on Magnetics,* vol. 35, No. 3, pp. 1372-1375, MAY 1999.

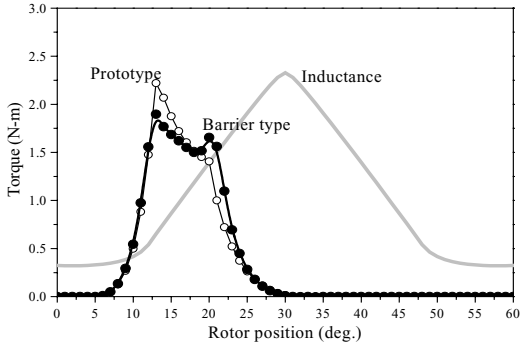

Fig. 3. Torque profile of one stroke

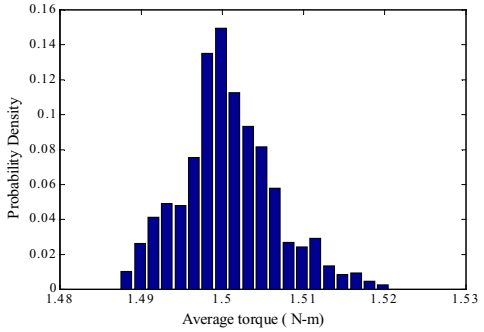

Fig. 4. Predicted probability distribution for the average torque.

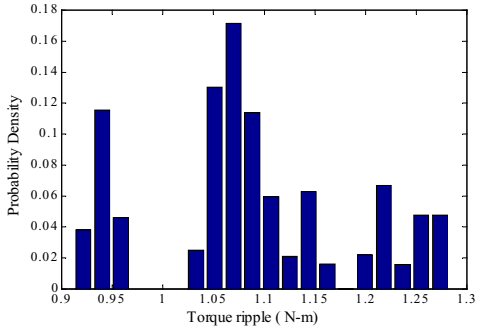

Fig. 5. Predicted probability distribution for the torque ripple.

Loss Analysis and Efficiency Evaluations of Synchronous Reluctance Motor Using Coupled FEM & Preisach Modelling

Jung Ho Lee
Dept. of Electrical Engineering
Hanbat National University
Daejeon, 305-719, KOREA
e-mail: limotor@hanbat.ac.kr

Min Myung Lee
Dept. of Electrical Engineering
Hanbat National University
Daejeon, 305-719, KOREA
e-mail: mmlee@hanbat.ac.kr

Eun Woong Lee
Dept. of Electrical Engineering
Chungnam National University
Daejeon 305-764, KOREA
e-mail: ewlee@cnu.ac.kr

***Abstract*— This paper deals with the loss analysis and efficiency evaluations in a synchronous reluctance motor (SynRM) using a coupled transient finite element method (FEM) and Preisach modeling, which is presented to analyze the characteristics under the effect of saturation and hysteresis loss. The focus of this paper is the efficiency evaluation relative to hysteresis loss, copper loss, etc. on the basis of speed, load condition in a SynRM. Computer simulation and experimental result for the efficiency using dynamometer show the propriety of the proposed method.**

I. Introduction

In high-speed applications, hysteresis loss can become the major cause of power dissipation. Therefore, whereas in other kinds of machines a rough estimation of hysteresis loss can be accepted, their importance in a SynRM justifies a greater effort in calculating them more precisely. The Preisach model is now generally accepted to be a powerful hysteresis model, and is therefore intensively studied [1]-[3].

Some papers which discussed the influence of hysteresis loss on a machine have been presented.

Reference [4], [5] have been investigated the steady state characteristics of inductances etc. using coupled FEM & Preisach modeling in a PMASynRM. Reference [6], [7] have been developed the transient analysis method coupled with vector control algorithm in a LIM and a SynRM respectively.

Reference [8], [9] have been discussed the hysteresis loss influence on the transient behavior of a SynRM and which have the coupled control algorithm & the analysis method.

Reference [10] have been proposed the control algorithm, which selects appropriate stator d, q-axis current component combination that the influence of iron core loss on the developed torque can be minimized in torque control, by the coupled finite element analysis and Preisach modeling in a SynRM.

In this paper, a coupled finite element analysis and Preisach modeling for a SynRM are presented and dynamic characteristic analyses are performed under the effect of saturation and hysteresis loss. The focus of this paper is the efficiency evaluation relative to hysteresis loss, copper loss, etc. on the basis of speed, load condition in a SynRM.

Also, TMS320C31 DSP installed experimental device and dynamometer are equipped and experiments are performed.

Computer simulation and experimental results for efficiency show the propriety of the proposed a coupled finite element analysis and Preisach modeling method.

II. Coupled Fem And Preisach's Modeling

Coupling governing equation and circuit equation, the system matrix is given as follows:

$$\begin{bmatrix} \begin{bmatrix} \upsilon_0[S] & -[N] \\ [0] & [R] \end{bmatrix} + \frac{1}{\Delta t}\begin{bmatrix} [0] & [0] \\ [LG]^T & [L_0] \end{bmatrix} \end{bmatrix} \begin{Bmatrix} \{A\} \\ \{I\} \end{Bmatrix}_t = \frac{1}{\Delta t}\begin{bmatrix} [0] & [0] \\ [LG]^T & [L_0] \end{bmatrix} \begin{Bmatrix} \{A\} \\ \{I\} \end{Bmatrix}_{t-\Delta t} + \begin{Bmatrix} \{M\} \\ \{V\} \end{Bmatrix}_t \quad (1)$$

Where, $\{E\}$: emf. vector in the winding, $\{V\}$: Supplying voltage vector, $\{I\}$: Phase current vector, $[L_0]$: Leakage inductance, $[LG]$: Coefficient matrix related to emf, $\{M\}$: Magnetization calculated by Preisach modeling

Fig. 1 shows the simulation scheme for the proposed analysis method. The torque acting on SynRM at each time is calculated by the line integral of the Maxwell stress tensor.

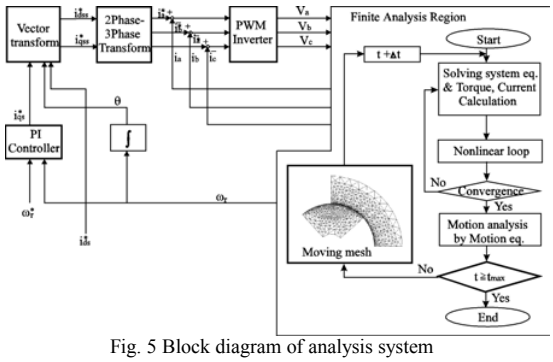

Fig. 5 Block diagram of analysis system

III. Result & Discussion

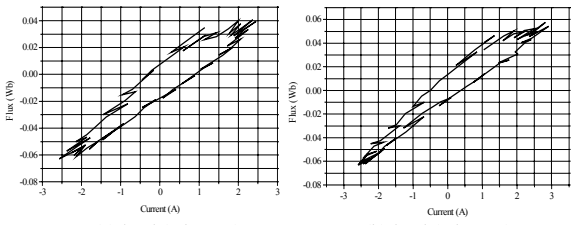

(a) load (6 kg-cm) (b) load (8 kg-cm)

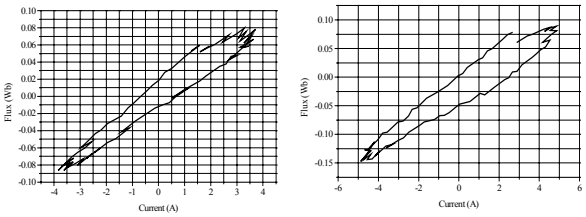

(c) load (10 kg-cm) (d) load (12 kg-cm)

Fig. 2 i-λ loci in each load condition at 2000 rpm

TABLE I
LOSS EVALUATION IN SIMULATION AT 2000 RPM

load (kg-cm)	ouput (W)	Hysteresis loss (W)	Copper Loss (W)	mechanical loss (W)	the rest loss (W)	phase current (A)
6	122	13.70	4.7	5	4.6	2.2
8	163	12.96	9.03	5	8.01	2.7
10	204	9.92	15.65	5	15.43	3.68
12	244	16.02	25.61	5	21.37	4.7

TABLE II
EFFICIENCY EVALUATION IN EXPERIMENTAL TEST AT 2000 RPM

Load (kg-cm)	input (W)	output (W)	Efficiency (%)	q-axis current (A)	phase current (A)	current angle (deg.)
6	150	122	80	2.35	2	39.2
8	198	163	82	2.8	2.77	47.9
10	250	204	83	3.3	3.65	55.2
12	312	244	78	3.9	4.7	61.5

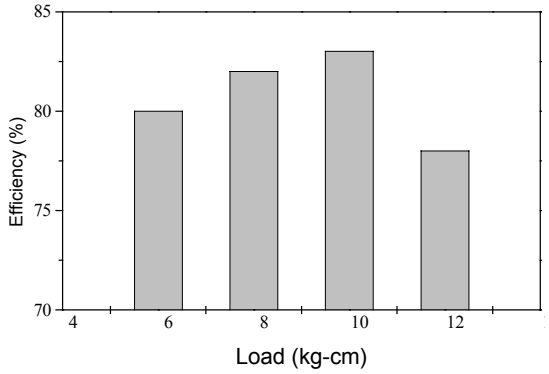

Fig. 3 Efficiency in each load condition

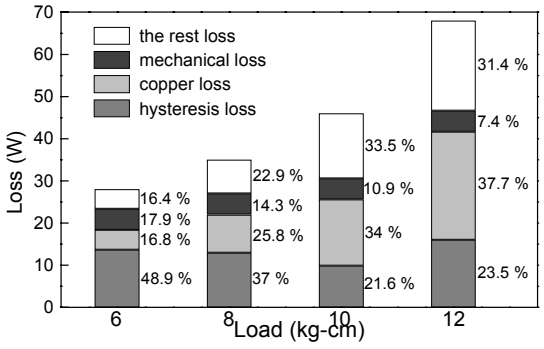

Fig. 4 loss analysis in each load condition

Fig.2 shows the i-λ loci per 1 cycle in each load condition at 2000 rpm.

The hysteresis loss can be calculated by the area of the i-λ loci times the frequency (66.7 Hz), and the copper loss can be calculated by the resistance times rms value square of phase current.

The mechanical loss is about 5 (W) in each load condition, which is experimental data.

The rest losses are the eddy current loss and the stray load loss, etc. These losses are denoted in TABLE I.

Output powers in simulation are the same with that developed in experimental test. Therefore, phase currents are similar to the experimental phase current as shown in TABLE II.

Fig.3 shows the efficiency of each load condition.

It is confirmed that the maximum efficiency current angle (55.2^o) is deviated from $\varphi = 45^o$, as shown in Fig. 3.

Fig. 4 shows the each loss ratio to the total loss in each load condition. Whereas in copper loss increasing current due to the increasing load should be enlarged, their rate in a hysteresis loss should be minimized in maximum efficiency condition precisely.

Through the more detailed analysis and experiment for the another speed (rpms), the variable comparisons for performance of the SynRM will be represented in next extended version

REFERENCES

[1] A. Ivanyi, Hysteresis Models in Electromagnetic Computation, AKADEMIAI KIADO, BUDAPEST

[2] I. D. Mayeroyz, "Mathematical Models of Hysteresis," *IEEE Trans. In Magnetics*, Vol. MAG-22, No.5, pp.603-608 Sept. 1986

[3] A. Visintin, Differential models of hysteresis, Applied Methematical Sciences, Springer, 1994.

[4] J. H. Lee, D. S. Hyun, "Hysteresis Characteristics Computation on PWM Fed Synchronous Reluctance Motor Using Coupled FEM & Preisach Modeling", *IEEE Transaction on Magnetics,* Vol. 36, No. 7, pp 1209-1212, July 2000.

[5] J. H. Lee, S. C. Ahn, D. S. Hyun, "Dynamic Characteristic Analysis of LIM Using Coupled FEM & Control algorithm", *IEEE Transaction on Magnetics,* Vol. 36, No. 7, pp 1876-1879, July 2000.

[6] J. H. Lee, J. C. Kim, D. S. Hyun, "Hysteresis Modelling of Synchronous Reluctance Motor Considering PWM input Voltage", *Journal of Physica B,* Vol. 275, pp 238-247, Jan. 2000.

[7] J. H. Lee, D. S. Hyun, "Hysteresis Analysis for Permanent Magnet Assisted Synchronous Reluctance Motor by Coupled FEM & Preisach Modelling", *IEEE Transaction on Magnetics,* Vol. 35, No. 5, pp. 1203-1206, May 1999.

[8] J. H. Lee, J. C. Kim, D. S. Hyun, "Effect of Magnet on Ld and Lq Inductance of Permanent Magnet Assisted Synchronous Reluctance Motor", *IEEE Transaction on Magnetics,* Vol. 35, No. 5, pp. 1199-1202, May 1999.

[9] J. C. Kim, J. H. Lee, I. S. Jung, D. S. Hyun, "Vector Control Scheme of Synchronous Reluctance Motor Considering Iron Core Loss", *IEEE Transaction on Magnetics,* Vol. 34, No. 5, pp. 2522-2525, Sep. 1998.

[10] J. H. Lee, J. C. Kim, D. S. Hyun, "Dynamic Characteristic Analysis of Synchronous Reluctance Motor Considering Saturation and Iron Loss by FEM", *IEEE Transaction on Magnetics,* Vol. 34, No. 5, pp. 2629-2632, Sep. 1998.

A Novel Stator Design of Synchronous Reluctance Motor by Loss & Efficiency Evaluations Related to Slot Numbers using Coupled Preisach Model & FEM

Jung Ho Lee
Dept. of Electrical Engineering
Hanbat National University
Daejeon, 305-719, KOREA
e-mail: limotor@hanbat.ac.kr

Min Myung Lee
Dept. of Electrical Engineering
Hanbat National University
Daejeon, 305-719, KOREA
e-mail: mmlee@hanbat.ac.kr

Eun Woong Lee
Dept. of Electrical Engineering
Chungnam National University
Daejeon 305-764, KOREA
e-mail: ewlee@cnu.ac.kr

***Abstract* - This paper deals with the stator design of a synchronous reluctance motor (SynRM) with concentrated winding by loss & efficiency evaluations related to slot numbers using coupled Preisach modeling & FEM.**

The focus of this paper is the stator design relative to torque density and efficiency on the basis of stator slot number and teeth width in a SynRM.

The coupled Finite Elements Analysis (FEA) & Preisach model have been used to evaluate the nonlinear solution.

Comparisons are given with characteristics of SynRM according to stator slot number, teeth width variation, respectively

I. Introduction

Synchronous reluctance motor (SynRM) has a simple structure, rugged characteristics and high efficiency because of negligible rotor loss. It doesn't have rotor winding and rotates at synchronous speed, so the controller is simpler than other types of AC machines. Many works have been carried out in the field of SynRM rotor design because they have many advantages [1]-[7].

If stator windings of a SynRM are not a conventional distributed one but the concentrated one, the decreasing of copper loss and decreasing of the production cost due to the simplification of winding in factory are obtained.

However it is difficult to expect a good performance from concentrated winding SynRM without considering the defects of torque ripple, lower inductance ratio and difference (efficiency, power factor), etc.

This paper deals with the stator design of a synchronous reluctance motor (SynRM) with concentrated winding by loss & efficiency evaluations related to slot numbers using coupled Preisach modeling & FEM.

The focus of this paper is the stator design relative to torque density and efficiency on the basis of stator slot number, teeth width, in order to improve performance and production cost problem of a SynRM.

The coupled Finite Elements Analysis (FEA) & Preisach model have been used to evaluate the nonlinear solution [8]-[10].

Comparisons are given with characteristics of normal distributed winding SynRM(24 slot) and those according to stator slot number, teeth width variation in concentrated winding SynRM(12, 6 slot), respectively. By means of these structures, anisotropy ratios up to 8 or more are obtained and the consequent torque performance approaches that of state of the art (distributed winding SynRM : 24 slot).

II. Analysis Model And Design

A. Governing Equation of SynRM

The governing equation can be written as

$$\upsilon_0(\nabla\times\nabla\times\vec{A}) = \vec{J}_0 + \vec{J}_m \qquad (1)$$

Where, J_m is Equivalent magnetizing current

B. System Matrix

The system matrix can be written as

$$[K^{(e)}]\{A^{(e)}\} + \{F^{(e)}\} + \{M^{(e)}\} = 0 \qquad (2)$$

where, $K_{ij}^{(e)} = \frac{\upsilon_0^{(e)}}{4\Delta^{(e)}}(c_{ie}c_{je} + d_{ie}d_{je})$, $F_i^{(e)} = -\Delta^{(e)}\frac{Ni}{3S}$

$$M_i^{(e)} = \upsilon_0^{(e)}(M_x^{(e)}d_{ie} + M_y^{(e)}c_{ie})$$

The overall model is described by following matrix.

$$[K]\{A\} + \{F\} + \{M\} = 0 \qquad (3)$$

Where, the magnetization {M} is calculated by preisach modeling.

The study concerns the SynRM with rotor flux barriers that present, respect to the axially laminated one, a simplicity in the mechanical construction, lower manufacturing cost, and the rotor skewing possibility.

Fig. 1 show the general shapes of distributed and concentrated winding SynRM. Starting from a standard motor of distributed winding SynRM, several optimized designs have been found according to design strategy of Fig.2.

Fig. 3 show the d-axis flux plots of distributed (24 slot) and concentrated (12, 6 slot) winding SynRM, respectively.

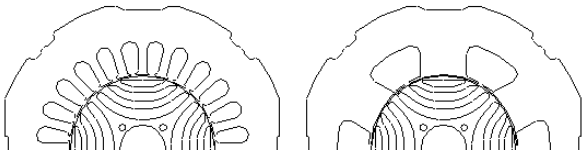

(a) distributed winding (b) concentrated winding

Fig. 1 general distributed and concentrated winding SynRM

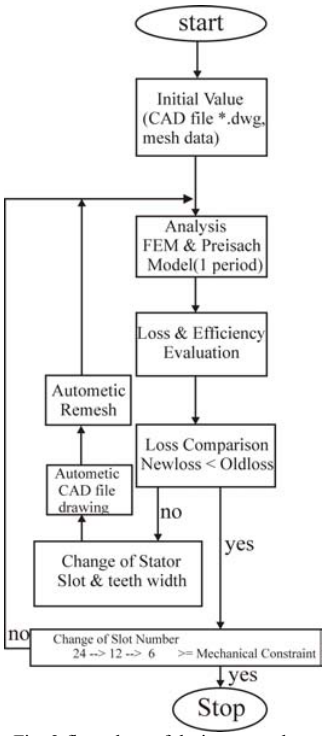

Fig. 2 flow chart of design procedure

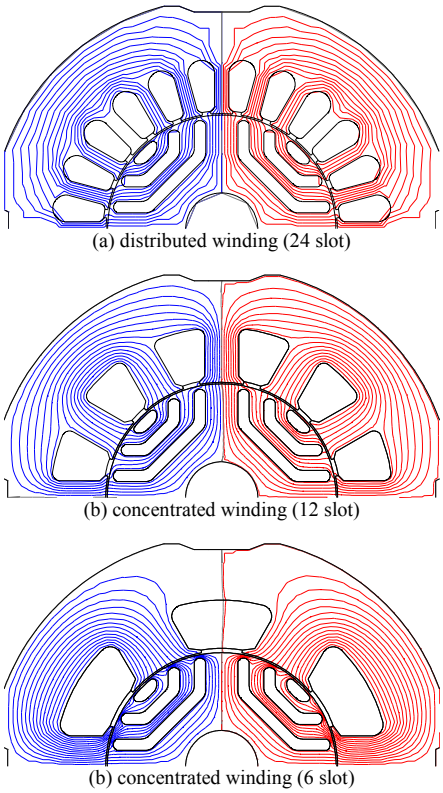

(a) distributed winding (24 slot)

(b) concentrated winding (12 slot)

(b) concentrated winding (6 slot)

Fig. 3 d-axis flux plots of distributed and concentrated winding SynRM

In this paper the slot number of a SynRM is considered those of 24 (distributed winding: 36 turn/slot), 12 and 6 (concentrated winding: 144 turn/ slot). The number of slot is a variable, which is related to torque ripple production together with the number of flux barrier.

And the number 24, 12, and 6 of stator slot is considered, because it is limited by mechanical and electrical constraint of 3 phase motor.

The shape coordinates of stator slot and teeth have been drawn as a condition from open to closed slot, symmetrically.

And then new CAD file is redrawn with regard to the change of slot and teeth width automatically as shown in fig.2.

Next the process of automatic mesh generation follows.

In mesh generation, mesh data doesn't change node number, element number, region, boundary condition, etc., but only x, y-coordinate data of stator slot and teeth at same slot number.

In this way the proposed Pre-processor procedure can be performed in a short period of time.

The comparison between present value and the past one for loss and efficiency evaluation are performed. And if past value is larger than the present one, number of slot will be changed. This procedure is going on until the moment mechanical constraint of machine is reached.

REFERENCES

[1] J. H. Lee, D. S. Hyun, "Hysteresis Characteristics Computation on PWM Fed Synchronous Reluctance Motor Using Coupled FEM & Preisach Modeling", *IEEE Transaction on Magnetics,* Vol. 36, No. 7, pp 1209-1212, July 2000.

[2] J. H. Lee, S. C. Ahn, D. S. Hyun, "Dynamic Characteristic Analysis of LIM Using Coupled FEM & Control algorithm", *IEEE Transaction on Magnetics,* Vol. 36, No. 7, pp 1876-1879, July 2000.

[3] J. H. Lee, J. C. Kim, D. S. Hyun, "Hysteresis Modelling of Synchronous Reluctance Motor Considering PWM input Voltage", *Journal of Physica B,* Vol. 275, pp 238-247, Jan. 2000.

[4] J. H. Lee, D. S. Hyun, "Hysteresis Analysis for Permanent Magnet Assisted Synchronous Reluctance Motor by Coupled FEM & Preisach Modelling", *IEEE Transaction on Magnetics,* Vol. 35, No. 5, pp. 1203-1206, May 1999.

[5] J. H. Lee, J. C. Kim, D. S. Hyun, "Effect of Magnet on Ld and Lq Inductance of Permanent Magnet Assisted Synchronous Reluctance Motor", *IEEE Transaction on Magnetics,* Vol. 35, No. 5, pp. 1199-1202, May 1999.

[6] J. C. Kim, J. H. Lee, I. S. Jung, D. S. Hyun, "Vector Control Scheme of Synchronous Reluctance Motor Considering Iron Core Loss", *IEEE Transaction on Magnetics,* Vol. 34, No. 5, pp. 2522-2525, Sep. 1998.

[7] J. H. Lee, J. C. Kim, D. S. Hyun, "Dynamic Characteristic Analysis of Synchronous Reluctance Motor Considering Saturation and Iron Loss by FEM", *IEEE Transaction on Magnetics,* Vol. 34, No. 5, pp. 2629-2632, Sep. 1998.

[8] A. Ivanyi, Hysteresis Models in Electromagnetic Computation, AKADEMIAI KIADO, BUDAPEST

[9] I. D. Mayeroyz, "Mathematical Models of Hysteresis," *IEEE Trans. In Magnetics*, Vol. MAG-22, No.5, pp.603-608 Sept. 1986

[10] A. Visintin, Differential models of hysteresis, Applied Methematical Sciences, Springer, 1994.

Static Characteristics of Linear BLDC Motor using Equivalent Magnetic Circuit and Finite Element Method

J.P. Hong*, J.K. Kim*, S.W. Joo*, S.C. Hahn*
*Dept. of Electrical Engineering, Dong-A University,
840, Hadan-2dong, Saha-gu, Busan 604-714, Korea
E-mail: schahn@daunet.donga.ac.kr
D.H. Kang**, D.H. Koo**
**Mechatronics Research Group
Korea Electrotechnology Research Institute (KERI)
PO Box 20, Changwon, Kyungnam 641 – 120, Korea

Abstract **- This paper presents the static characteristics of the linear BLDC motor. An equivalent magnetic circuit model is derived for the prototype motor. The air gap flux density is calculated using the derived model and compared results from Finite Element Analysis. The thrust force is measured for the prototype motor and is also compared with those from derived circuit model and F.E.M. These values agree well to show the validity of the equivalent circuit model. Using this equivalent circuit model, the thrust density variation according to the rate change of width of coil to pole pitch can be expected for the design purpose.**

INTRODUCTION

Linear BLDC motors are used widely for the purpose of precision speed and position control [1,2,3,4]. Moreover, the linear BLDC motor has less backrush and friction, so it can be used as a part of micro incremental motion control system with help of microprocessor and power electronics. Therefore, linear BLDC motor can broaden its usage in the area such as wafer stepper stage in the semiconductor industry. This paper deals with the static characteristics of linear BLDC motor for the future application in the semiconductor industry, where incremental precision control is needed. An equivalent magnetic circuit model [5] is derived to calculate the air gap flux density and thrust force. For the prototype linear BLDC motor, the static characteristic parameters such as the air gap flux density and thrust force are calculated and compared with those from measurements and F.E.A. These values agree well to show the validity of the equivalent magnetic circuit model.

ANALYSIS MODEL

The linear BLDC motor dealt in this paper consists of the stator and mover. The permanent magnets are mounted on each side of the stators for the magnetic flux to direct oppositely as shown in Fig. 1(a). The three phases windings on the mover are located to avoid overlapping each other. Fig. 1(b) shows the cross-sectional view, where τ, δ are length of pole pitch and air gap, h_m, w_m are height and width of magnet, and h_c, w_c are height and width of one-side section of the coil.

Fig. 2 represents a part of the equivalent magnetic circuit considered for analysis, where Θ_m is the magneto-motive force of magnet. Here, R_m and R_g are reluctance of magnet and air gap, respectively.

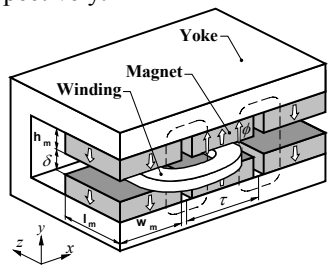

(a)

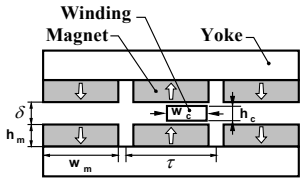

(b)

Fig. 1. Analysis model (a) 3-D model , (b) 2-D modeling for analysis

THEORETICAL CONSIDERATIONS

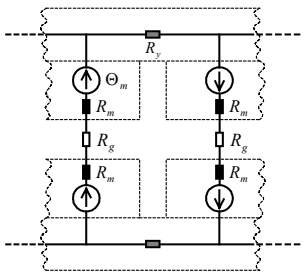

Fig. 2. An equivalent magnetic circuit along a loop

The air gap flux density B_g can be written as in Equation (1).

$$B_g = \frac{\phi_g}{A_m} = \frac{2 \cdot B_r h_m}{2h_m + \mu_m \delta} \tag{1}$$

The reluctance of yoke, R_y in Fig. 2 is neglected in the above equation. since it is assumed to be infinitely permeable. In Equation (1), μ_m is relative permeability of magnet and A_m is area of magnet (where $A_m = l_m \cdot w_m$).

The thrust force of the coil can be derived from Equation (1) and can be written as follows,

$$F_T = J \cdot A_w \cdot B_g \cdot l_{cond}$$
$$= J \cdot h_{coil} \cdot w_{coil} \cdot 2 \cdot \frac{B_r h_m}{2h_m + \mu_m \delta} \cdot l_{cond} \quad [N] \tag{2}$$

where J is current density of the coil, l_{cond} is length of the coil conductor along z-axis and A_w is cross-section area for one-side of the coil

Design and Result of Analysis

1. Prototype Model

The photograph of the prototype BLDC motor used in this paper is shown in Fig. 3 and Table I shows the model dimension. The 3-phase coils sit on the mover and the stator has Nd-Fe-B PM on each side. Pole pitch is 60 [mm] and air gap is 10 [mm].

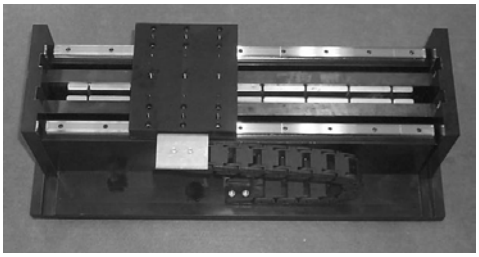

Fig 3. Prototype linear BLDC motor

TABLE I. MODEL DIMENSION

	SYMBOL	VALUE	
PM	B_r	1.2	[T]
	w_m	58	[mm]
	l_m	80	[mm]
	h_m	10	[mm]
	μ_m	1.05	
Coil	Turns	162	[turns]
	w_{coil}	10.7	[mm]
	h_{coil}	7.56	[mm]
Pole Pitch	τ	60	[mm]
Air gap	δ	10	[mm]
Conductor Length	l_{cond}	80	[mm]

2. Results

The calculated magnetic flux density in the air gap using Equation (1) is about 0.78 [T]. The air gap flux density obtained from Finite Element Analysis is shown in Fig. 4. Theses two results show good agreement in the air gap as seen in figure.

In Fig. 5, the measured thrust force of prototype motor is compared with those from equivalent magnetic circuit and F.E.M. In this case, the excitation current is 1 [A]. The thrust force obtained from magnetic circuit model agrees well with those from F.E.M. and measurement. Using Equation (2), the thrust density variation according to the rate change of width of coil to pole pitch can be expected for the design purpose.

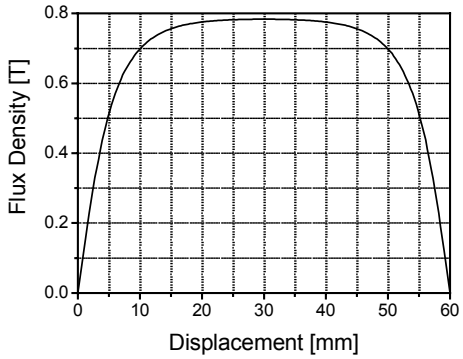

Fig. 4. Air gap flux density

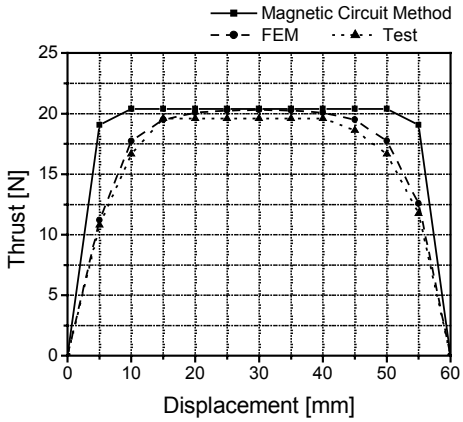

Fig. 5. Thrust force $(I_{coil} = 1\ A)$

Conclusion

This paper presents the static characteristics of the linear BLDC motor. An equivalent magnetic circuit model is derived for the prototype motor. The air gap flux density is calculated using the derived equivalent circuit model and compared with that from Finite Element Analysis. The thrust force is measured for the prototype motor and is also compared with those from derived circuit model and F.E.M. Using this equivalent circuit model, the thrust density variation according to the rate change of width of coil to pole pitch can be expected for the design purpose.

References

[1] R.Akmese and J.F.Eastham, "Design of Permanent Magnet Flat Linear Motors for Standstill Application",IEEE Trans. on Magnetics, vol. 28, No. 5, pp. 3042-3044,1992.

[2] J.S.Moghani, J.F.Eastham, R.Akmese, and R.J.Hill-Conttingham, "Three Dimensional Force Prediction in a Model Linear Brushless DC Motor",IEEE Trans. on Magnetics, vol. 30, No. 6, pp. 4752-4754, Nov.1994.

[3] S.X.Chen, T.S.Low, Y.A.Mah, and M.A.Jabber, "Super Convergence Theory And Its Application To Precision Force Calculation",IEEE Trans. on Magnetics, vol. 32, No. 5, pp. 4275-4277, Sep.1996.

[4] A.Basak, A.F.Flores, Filho,T.Nakata, and N.Takahashi, "Three Dimensional Computation of Force in a Novel Brushless DC Linear Motor",IEEE Trans. on Magnetics, vol. 33, No. 2, pp. 2030-2032, Mar.1997.

[5] J.F. Gieras and Z.J. Piech, Linear Synchronous motor, CRC Press, 2000

Design of Slotless Type PMLSM for High Power Density using Divided PM

Mi-Yong Kim, Yong-Chul Kim, Gyu-Tak Kim

Dept. of Electrical Engineering
Changwon National University
9 sarim-dong Changwon city, Kyungnam, 641-773, Korea
e-mail: miyongkim@mail.changwon.ac.kr, clman21@daum.net, gtkim@sarim.changwon.ac.kr

***Abstract* — Slotless type PMLSM (Permanent Magnet Linear Synchronous Motor) has a low power density due to having a large air-gap structurally. This paper presents an increase of power density of the slotless type PMLSM by inserted core between phase windings. The PMs(Permanent Magnets) are divided into two pieces to reduce detent forces and eliminate high order space harmonics affecting the ripples of a thrust. All analysis values are calculated using 2D FEM.**

INTRODUCTION

The slotless PMLSM is suitable for a precision machine demanded an accurate control capability due to a low normal force and a little existent detent force, but the motor has a low power density. On the other hand, a slotted PMLSM has a high power density, and it has bad control performance on account of having a high detent force[1,2].

Here, this paper proposes a inserted core type PMLSM to overcome demerits of the slotless type PMLSM and to improve its power density. But, a reluctance difference is produced in air-gap by inserting a core into a phase winding. And a constant force which is the best advantage of slotless type PMLSM does not obtained because a detent force exist by the slot-harmonics. The detent force makes ripple of force producing both vibration and noise of motors and deteriorating the control characteristics of speed control as well as of position control[3]. Therefore, this paper introduces concepts of a PWM in oder to eliminate the time harmonics, and a divided PM type of slotless LSM is proposed for removal of the 5th, 7th harmonics in the thrust.

ANALYSIS MODEL

A Slotless type PMLSM and The Proposed Model for High Power

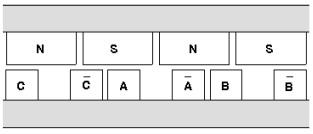

Fig.1. The analysis model of slotless type PMLSM

Fig. 1 shows the analysis model of a slotless type PMLSM. The armature stator is composed of an iron core with non-salient poles and concentrated windings. The slotless type has a low energy density than the core type because it has a large magnetic air-gap in structure.

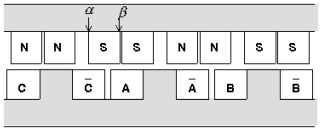

Fig.2. The proposed model.

In this paper, to supplement demerits of the large magnetic air-gap, the model with the inseted core among the phase windings is proposed as shown in Fig.2. And, it presentes the divided PM model to reduce thrust ripples. Here, to eliminate the 5th, 7th space harmonics component of the thrust affecting the thrust ripple, noise and mechanical vibraion, the arrangement angle of the PM is $\alpha=6/70\tau$ and $\beta=34/70\tau$ as shown in Fig. 2. In this part, τ is the pole pitch. Analysis models are calculated using 2D FEM.

ANALYSIS RESULT

Back-E.M.F and Inductance

The Back-E.M.F is computed by changing of a flux linkage in coils that is calculated by integrating y-component among the flux densities of PM.

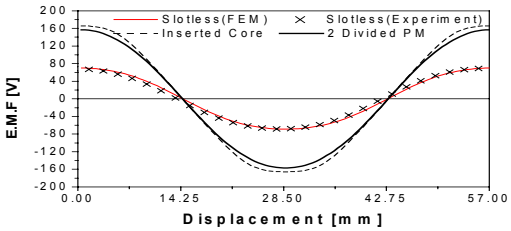

Fig.3. Back-E.M.F (v=2m/s)

Fig.3 shows the calculated results of back-E.M.F in each analysis model. As you see, the r.m.s value of back-E.M.F

increases highly about 238% from 49.03V in slotless type to 117.17V in inserted core type.

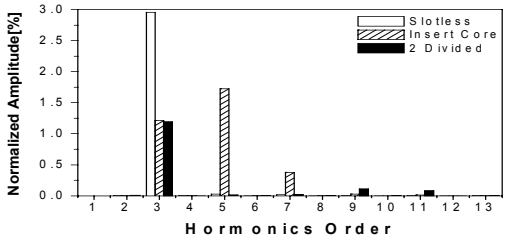

Fig.4. Higher harmonics component of back-E.M.F in each model.

Fig.4 shows the analysis results of harmonics component of back-E.M.F in each model. In inserted core model, the 5th and 7th harmonic component increase highly. But, these are eliminated in 2 divided PM model.

Inductance is calculated using the energy perturbation method. As results of analysis, the values of self and mutual inductance in slotless type are 30.86mH, 9.08mH. However, those values in inserted core type severally increase to 69.45mH and 39.93mH due to decreasing of magnetic air-gap as the core is inserted.

Detent force and Thrust

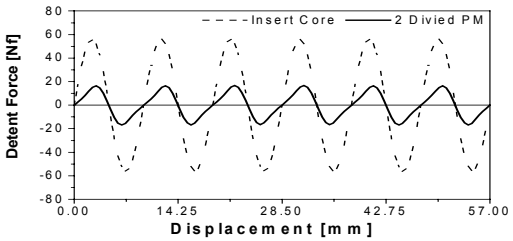

Fig.5. The calculation results of detent force

The detent force is generated by difference of the reluctance generated by a disproportion of the magnetic air-gap in the inserted core type. The detent force is calculated using the Maxwell stress tensor method. Fig.5 shows the results of analysis in each model. The detent force corresponding to 6th harmonics component of the thrust is a harmonic component which generates because of the teeth-slot structure. Peak value of the detent force is sharply decreased to 30% from 55N in inserted core type to 16.5N in divided PM type.

The force is calculated using the Maxwell stress tensor method, and Fig.6 present the thrust of each model. The thrust of the inserted core model increases more than twice over in comparison with it of the slotless model. The thrust of the inserted core type includes ripples somewhat owing to generating the detent force as inserting the core. The 5th, 6th and 7th components of harmonic generate in inserted core type, as shown in Fig.7. In case of the 2 divided PM type, the 6th harmonics component of thrust decrease and the 5th, 7th harmonics components are eliminated. And this type have not particular influence on the control characteristic of the motor since the rate of harmonic is less than 2% in comparison with fundamental component.

Fig. 8 shows the force in steady state operation when the electrical load angle is 90 degrees. The ripple of thrust generates as the core is inserted, but it reduces to 3% as the PM is divided. This means that the ripple of the thrust in the 2 divided PM type doesn't bad affect the running characteristic of motors.

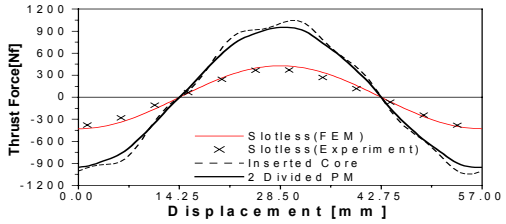

Fig.6. The calculation results of the thrust

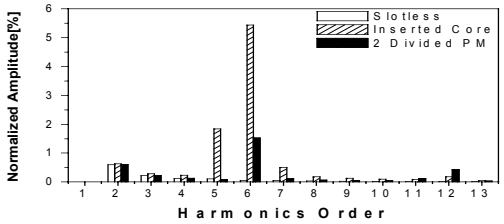

Fig.7. Higher harmonics component of thrust in each model

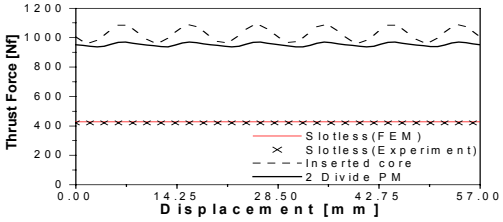

Fig.8. The steady state force when the electrical load angle is 90 °

CONCLUSION

In this paper, the inserted core type is proposed for high power density in the slotless PMLSM, and the 2 divided PM type is proposed to reduce the ripple of thrust. In the proposed model, the 6th harmonic component affecting the ripple of the thrust originates very small. Also, the thrust improves to 226.7% from 425.16Nf in the slotless type PMLSM to 964.36Nf in the 2 divided PM type.

REFERENCE

[1] G. H. Kang, J. P. Hong, G. T. Kim, "Improved Parameter Modeling of Interior Permanent Magnet Synchronous Motor Based on Finite Element Analysis" IEEE Trans. Mag, Vol. 36, No. 4, pp.1867-1870, 2000.

[2] K. C. Lim, J. K. Woo, G. H. Kang, J. P. Hong, G. T. Kim, " Detent Force Minimization Techniques in Permanent Magnet Linear Synchronous Motors", IEEE Trans. Mag, Vol. 38, No. 2, pp.1157-1160, 2002.

[3] K. C. Lim, J. P. Hong, G. T. Kim, "The Novel Technique Considering Slot Effect by Equivalent Magnetizing Current", IEEE Trans. Mag, Vol. 35, No. 5, pp.3691-3693, 1999

Minimization of Detent Force for PMLSM using the Moving Model Node Technique and the Neural Network

Dong-Yeup Lee, Ki-Chae Lim and Gyu-Tak Kim

Dept. of Electrical Engineering Changwon National University
9 sarim-dong Changwon city, Kyungnam, 641-773, Korea
e-mail: goldhand75@hotmail.com, heabin@netian.com, gtkim@sarim.changwon.ac.kr

Abstract — **This paper shows the Minimization of detent force for Permanent Magnet Linear Synchronous Motor(PMLSM) using the moving model node technique and the neural network. Design parameters are permanet magnet(PM) width, slot opening width, teeth width. Output parameters are thrust, detent force and inductance. Restricted conditions are selected for a thrust with 1250[Nf] overs, minimizations of detent force and inductance with 52.5[mH] below in order to make a power factor with 0.9 overs.**

INTRODUCTION

Recently, PMLSM with high energy density have been used in a wide variety of industrial applications such as robotics, power string and high-precision position control.

But, Detent force is arisen from magnet end and a tooth position in PMLSM. It is cause of thrust ripple, noise, vibration, and deterioration of a performance of position control[1]. Therefore, design techniques were demanded to reduce detent force in PMLSM. There are detent force minimization techniques such as varying the PM width, rearranging the PM position, and using semi-closed slot structure by using Finite Element Analysis(FEA).

In this paper, detent force and the thrust are calculated according to changes of PM width, slot opening and teeth width. And then, model is designed with parameters when the detent force becomes the minimum. Thrust must become 1250[Nf] overs and inductance does belows 52.5[mH] in order to make a power factor with 0.9 overs. Analysis methods are FEA in combination with Moving model node technique and neural network. The former cuts down modeling time and effort as compared with FEA. Moreover, the latter is used to reduce computational time of analysis according to changing design parameter.

ANALYSIS METHOD

Moving Model Node Technique

In this paper, the thrust and the detent force were calculated with FEA in combination with moving model node technique. The moving model node technique is used to create models with respect to the changes of the physical parameters of analysis model without additional pre-processing. Using this method, modeling time is greatly reduced and pre-processing is simplified[2]. Table.1 shows specifications of initial PMLSM. Fig.1 shows Flowchart of FEA with moving model node technique, and Fig.2 is Application of moving model node technique.

Table. I. Specifications of initial PMLSM

	Item	Symbol	Value (unit)
Stator (Primary)	Pole pitch	τ	69.0 (mm)
	Pole Number	p	*14*
	Slot pitch	τ_s	11.5 (mm)
	Slot width	w_s	6.5 (mm)
	Rated current	I	3.0 (A)
	Slot/pole/phase	Q	2
Mover (PM)	Height	H	10 (mm)
	Width	w_{PM}	55 (mm)
	Material		Nd-Fe-B
	Residual induction	B_r	1.12 (T)
	Mechanical airgap	g_m	5.0 (mm)

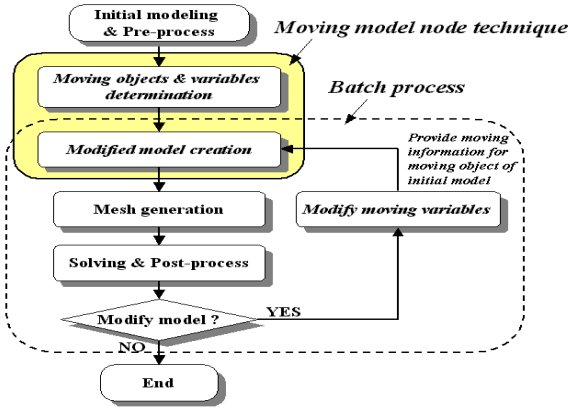

Fig. 1. Flowchart of FEA with moving model node technique

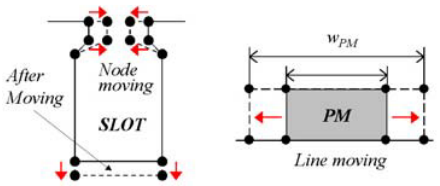

(a) Slot shape model (b) PM width model

Fig. 2 Application of moving model node technique

Neural Network

This paper is used back-propagation neural network model on multi-layer feed-forward neural network. Variables in input design include the width of PM, teeth and slot opening, while variables in output include thrust, detent force and inductance. The neural network has structure such as 3-50-50-50-3. Data sets of training neural network is 126[3].

Restricted conditions are selected for a thrust with 1250Nf overs, minimizations of detent force and inductance with 52.5mH below. PMLSM is used system which demanded frequent starting and stopping characteristic. Therefore, time constant should be reduced as little as possible. And, power factor is limited to 0.9 overs since characteristics of power factor is very important. Now that the steady speed of initial model is 2m/s, driving frequency is 14.747[Hz]. Inductance is 52.5[mH] when power factor is 0.9, because phase resistance of initial model is 9.825[Ω]. Thus, inductance is limited to become 52.5mH below.

Fig. 3 shows structure of neural nework.

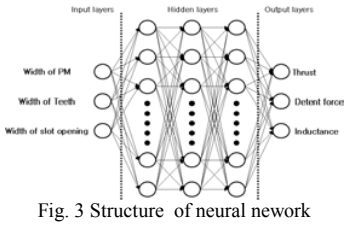

Fig. 3 Structure of neural nework

ANALYSIS RESULTS

Table 2. Some outputs of neural network

Teeth width [mm]	slot opening width [mm]	PM width [mm]	Thrust [N]	Detent force [N]	Inductance [mH]
4.5	2	61	1252.37	1.91	51.56
5	2	60	1248.52	2.21	52.12
5	2	61	1252.50	1.80	52.12
5	2	62	1255.60	4.04	52.43
5	3	61	1246.81	3.03	50.98
5.5	2	61	1252.82	2.07	55.26
6	2	61	1252.11	1.95	57.67

Table 2 shows some outputs of neural network. Parameters of optimum model are selected when the width of teeth is 5[mm] and the width of slot opening is 2[mm] and the width of permanent magnet is 61[mm],

Detent force and Thrust

The detent force and the thrust were calculated with Maxwell stress tensor. The analysis results for the initial model and the optimum model are shown in Fig. 4. For initial model, the maximum value of detent force is amounted to 57.4[Nf], while it of optimum model decreases considerably to 1.8[Nf].

Fig. 5 shows thrust for initial model and optimum model. The maximum value of the thrust is increase from 1252.5[Nf] to 1206.49 [Nf] compare with the initial model. Ripple of thrust get amaller because of reduction of detent force.

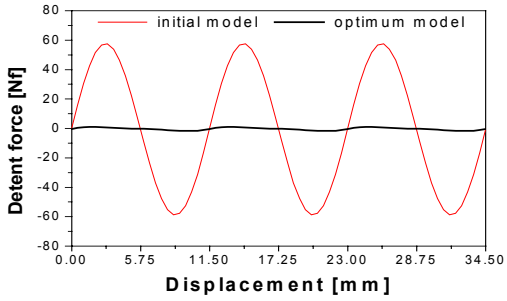

Fig. 4. Detent force

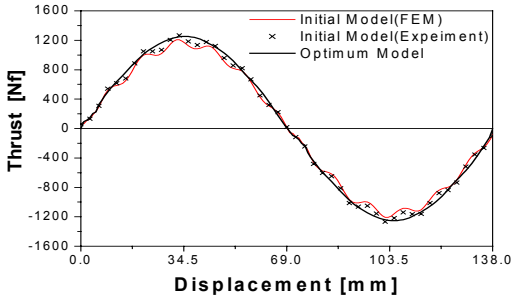

Fig. 5. Thrust

Inductance

In this paper, inductance was calculated using Energy Perturbation method. Inductacne increases in comparison with the initial model as shown in table 3.

Table 3. Comparison of Inductance

	initial model	optimum model
Values [mH]	48.73	52.12

CONCLUSION

In this paper, neural network is trained with design parameters like that permanet magnet width, slot opening width, teeth width. The thrust increases from 1252.5 [Nf] to 1206.49 [Nf] and detent force decreases considerably from 57.4[Nf] to 1.8[Nf]. Although, inductance in optimum model increases a little from 48.73[mH] to 52.12[mH], the power facter affecting to the driving charcterisitc of motors keep up 0.9 overs. Therefore, optimum model is expected to maintain a good performance.

REFERENCE

[1] C. Studer, A. Keyhani, T. Sebastian and S. K. Murthy, "Study of Cogginh Torque in Permanent Magnet Machines", IEEE IAS Annual Meeting, pp. 42-49, 1997.

[2] K. C. Lim, J. K. Woo, J. P. Hong and G. T. Kim, "Detent Force Minimization Techniques in Permanent Magnet Linear Synchronous Motors", Proceedings of COMPUMAG 2001, Vol. I, pp60-61, 2001.

[3] Simon Haykin, "Neural networks",WestWords.Inc.1999

The Optimum Design of Slotless Type PMLSM using Neural-Network and Space Harmonic Field Analysis

Jae-Yun Moon, Dong-yeup Lee, Gyu-Tak Kim
Dept. of Electrical Engineering
Changwon National University
9 sarim-dong Changwon city Kyungnam, 641-773, KOREA
e-mail: 1835616@hanmail.net, goldhand75@hotmail.com, gtkim@sarim.changwon.ac.kr

***Abstract*—This paper deals with the optimum design of slotless type Permanent Magnet Linear Synchronous Motor (PMLSM) via Neural-Network. The method using neural-network takes shorter time to analyze than existing method of analysis using space harmonic field method. In this article, conventional models were analyzed with space harmonic field method and resulting data were given to neural network for running. To identify the reliability of optimized data, it was compared with the results of space harmonic field method, and the results corresponded to those of space harmonic field method.**

INTRODUCTION

The slotless type PMLSM does not generate detent force which may have bad effects on control. Accordingly, this type is often applied to systems requiring high precision control such as X-Y gantry. Because of large magnetic air gap, however, this type has a disadvantage of lower thrust than slotted type. Due to these characteristics, slotless type PMLSM requires an optimum design to maximize thrust.

In order to calculate a distribution of an air gap magnetic field in the slotless type PMLSM, the space harmonic field method is more reasonable than the numerical analysis method such as a finite element method (FEM), because of their simple armature structure and non-saturation characteristics in a core.

Neural network was introduced to calculate the optimum value of design. It was led to learning by the results of space harmonic field analysis. The optimum values obtained from neural network were compared with the results of space harmonic field analysis. By using neural network, the calculation time to get the optimum parameter could be remarkably shortened. Parameter in input design include the width of coil, coil inner and permanent magnet, while parameter in output design is thrust.

ANALYSIS MODEL

Fig.1 shows a side view of a single-side of the moving magnet slotless type PMLSM. The dimensions and specifications are as shown in table 1.

The space harmonic field method is very fast than FE method in case of non-saturation characteristics and simple constructions. The results of this method are good agreement

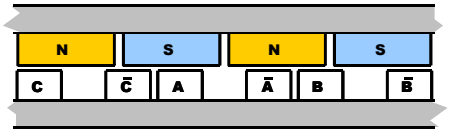

Fig. 1. Analysis Model

Table 1. Specifications of analysis model

Parameter	Values	Parameter	Values
Number of poles`	12	Turns / Phase	650 turns
Br	1.2 T	Height of coil	11 mm
Height of PM	12 mm	Width of coil	12 mm
Length of PM	73.5 mm	Distance of coil	12 mm
Width of PM	26 mm	Phase current(max)	2.66 A
Pole pitch	28.5 mm	Length of air-gap	2 mm

with FEM. Therefore the space harmonic method is widely used in the early design and characteristic analysis according to changing of design parameters. For an increase thrust, the conventional model is analyzed by the space harmonic method and the obtained data set to train Neural-Network. The input parameters of Neural-Network are coil width, PM width and coil inner width, and the output is thrust.

REDESIGN RESULT USING NEURAL-NETWORK

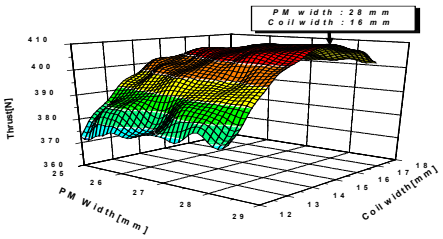

Fig. 2. Thrust distribution using Neural-Network

Fig. 2. shows thrust distribution by changing of the PM width and the coil width when a load angle is 60 degrees. The thrust increases as expanding the PM width, but parameter limited by constructional conditions. By using Neural-Network, the optimal thrust is 409.458[N] in case that the PM width, the coil width and the coil inner width are 28mm, 16mm and 5 mm, respectively.

Result Analysis

To confirm reliability of Neural-Network, result data compared with the space harmonic method result. Table 2. shows comparison between the Neural-Network result and the space harmonic method analysis. The result of Neural-Network is very good agreement with space harmonic method result.

Table.2. Thrust of the Neural-Network and the space harmonic field method

	Neural-Network	Space harmonic Method
Values	409.458 N	409.654 N

CHARACTERISTIC ANALYSIS

EMF and Inductance

Fig.3 shows the back-EMF waves of the conventional and the optimum model when a velocity of mover is 2m/s. Peak values of optimum model increase from 34.035[V] to 39.07[V] because PM width in optimum model larger than in conventional model. The ratio of increasing EMF is about 14.8 %.

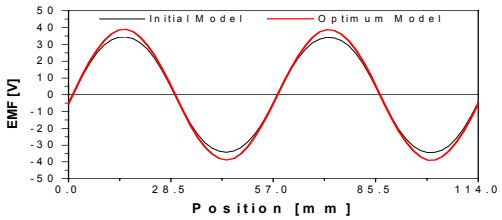

Fig. 3. back-EMF (v=2m/s)

In this study, inductance was calculated by linkage flux method. Experimental results of self and mutual in the conventional model are 29.38mH and 9.07mH, and calculation results of self and mutual inductance are 30.03 mH and 9.07 mH, respectively. The Optimum model's self and mutual inductance are 32.87mH and 7.67mH. As increasing the coil width, the self-inductance is increase but the mutual inductance is decrease.

Thrust and normal force

Fig. 4 and Fig. 5 show thrust and normal force according to load angle is 60 deg. The maximum value of thrust is increased from 428.671 N to 475.253 N, and the normal force of the optimal model is increased compare with the conventional model. However, normal force is little influence on operational characteristic of motor.

Fig. 6 shows driving trust of the conventional model and the optimum one when the load angle is 60 degrees. The thrust in the optimum model increases highly, but occur ripples of the thrust. But that is not affect to the performance in the motor because the peak-to-peak value of thrust ripple corresponding to 0.6% of the fundamental thrust in the optimum model is very small. This peak-to-peak value of ripple is 2.5N.

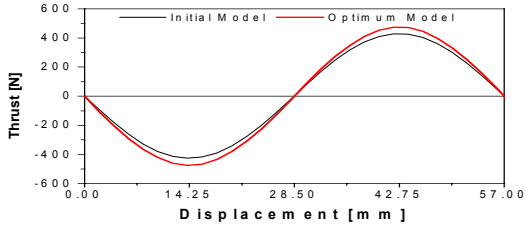

Fig. 4. Thrust

.

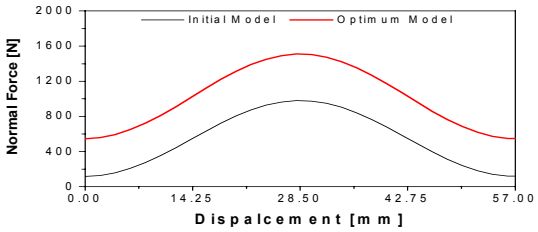

Fig. 5. Normal force

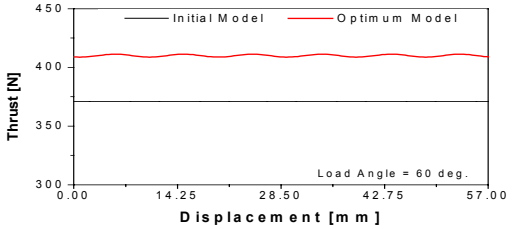

Fig. 6. Thrust in steady state driving

CONCLUSIONS

This paper presented optimum design PMLSM with neural network. Design parameter were selected width of PM, coil and coil inner. To confirm reliability of Neural-Network, result data compared with the space harmonic method result. The result of Neural-Network is very good agreement with space harmonic method result. A little ripple occurred along with increased thrust, but it was ignorable enough to have little effects on control. Introducing neural network into space harmonic field method could shorten the time to calculate.

REFERENCES

[1] K. C. Lim, J. K. Woo, J. P. Hong, G. T. Kim, 'Detent Force Minimization Techniques in Permanent Magnet Linear Synchronous Motor ' , IEEE Trans. Mag, Vol. 38, No. 2, pp. 1157-1160, 2002

[2] K. C. Lim, J. P. Hong, G. T. Kim, "The Novel Technique Considering Slot Effect by Equivalent Magnetizing Current" , IEEE Trans. Mag, Vol. 35, No. 5, pp. 3691-3693, 1999

A Self-training Numerical Method to Calculate the Magnetic Characteristics for Switched Reluctance Motor Drives

X. D. Xue, K. W. E. Cheng, and S. L. Ho
Department of Electrical Engineering, the Hong Kong Polytechnic University, Hung Hom, Kowloon, Hong
Emails: xdxue.ee@polyu.edu.hk; eeecheng@polyu.edu.hk; slho@polyu.edu.hk

***Abstract*—Based on the two-dimensional least squares algorithm, this paper presents a novel numerical method to compute the magnetic characteristics for switched reluctance motor drives. In this algorithm, the coefficients of the orthogonal polynomials, which are used to describe the magnetic characteristics, are determined by the two-dimensional least squares technique. Furthermore, these coefficients can be determined off line and trained on line. It is shown that the computed and experimental results agree well. The proposed algorithm is very helpful for torque prediction, simulation studies and sensorless control of switched reluctance motor drives.**

Introduction

Precise computation of the nonlinear magnetic characteristics at an arbitrary rotor position and current is crucial when performance predictions, simulations, computer-aided designs, torque control, as well as sensorless control of the switched reluctance motor (SRM) drives are carried out [1]-[3]. However, the previous methods [1]-[3] are obtained off line and hence could not describe accurately dynamics of SRM drives. The nonlinear magnetic characteristics in the SRM are functions of both rotor position and current. To implement accurate simulations and real-time controls, the designers have to develop novel techniques to calculate precisely the nonlinear magnetic characteristics of the SRM both on line and off line. Reference [4] presented a method based on artificial neutral networks (ANN), which can be suitable for off line and on line. In this study a novel method, which is based on orthogonal polynomials and which can be applicable to both off line and on line studies, is proposed to compute the motor's magnetic characteristics.

Computation Modeling

Modeling of Nonlinear Magnetic Characteristics

Assuming there are $n\times m$ flux linkage values ψ_{kj} with respect to the rotor position θ_k with the currents i_j being known (k=0, 1, … , n-1; j=0, 1, … , m-1), the modeling of the nonlinear magnetic characteristics in the SRM drives is given by

$$\psi(\theta,i)=\sum_{k=0}^{p-1}\sum_{j=0}^{q-1}a_{kj}(\theta-\bar{\theta})^k(i-\bar{i})^j \tag{1}$$

where ψ denotes the flux linkage, θ denotes the rotor position, i denotes the current, $p\le n$, $q\le m$, *and*

$$\bar{\theta}=\sum_{k=0}^{n-1}\theta_k/n,\bar{i}=\sum_{j=0}^{m-1}i_j/m \tag{2}$$

Determination of the Coefficients in the Model

For the rotor position θ, there are m polynomials as given in (3).

$$g_j(\theta)=\sum_{u=0}^{p-1}\lambda_{uj}\gamma_u(\theta),j=0,1,\cdots,m-1 \tag{3}$$

where the summation of $\gamma_u(\theta)$ (u=0,1,…, p-1) are the orthogonal polynomials and are determined by (u=1, 2, ⋯, p-1)

$$\begin{aligned}&\gamma_0(\theta)=1\\&\gamma_1(\theta)=\theta-\alpha_0\\&\gamma_{u+1}(\theta)=(\theta-\alpha_u)\gamma_u(\theta)-\beta_u\gamma_{u-1}(\theta)\end{aligned} \tag{4}$$

Assume

$$d_u=\sum_{k=0}^{n-1}\gamma_u^2(\theta_k),u=0,1,\cdots,p-1 \tag{5}$$

then one can obtain

$$\begin{aligned}&\alpha_u=\sum_{k=0}^{n-1}\theta_k\gamma_u^2(\theta_k)/d_u,u=0,1,\cdots,p-1\\&\beta_u=d_u/d_{u-1},u=1,2,\cdots,p-1\end{aligned} \tag{6}$$

From the least squares principle, one obtains

$$\lambda_{uj}=\sum_{k=0}^{n-1}\psi_{kj}\gamma_u(\theta_k)/d_u,j=0,1,\cdots,m-1 \tag{7}$$

The polynomials for an electrical current i are defined as

$$h_u(i)=\sum_{v=0}^{q-1}\mu_{uv}\eta_v(i),u=0,1,\cdots,p-1 \tag{8}$$

where the summation of $\eta_v(i)$ from v=0,1,…,q-1 are also orthogonal polynomials and are determined by v=1, 2, ⋯, q-1.

$$\begin{aligned}&\eta_0(i)=1\\&\eta_1(i)=i-\alpha_0'\\&\eta_{v+1}(i)=(i-\alpha_v')\eta_v(i)-\beta_v'\eta_{v-1}(i)\end{aligned} \tag{9}$$

Assume that

$$\delta_v=\sum_{j=0}^{m-1}\eta_v^2(i_j),v=0,1,\cdots,q-1 \tag{10}$$

then one can obtain

$$\begin{aligned}&\alpha_v'=\sum_{j=0}^{m-1}i_j\eta_v^2(i_j)/\delta_v,v=0,1,\cdots,q-1\\&\beta_v'=\delta_v/\delta_{v-1},v=1,2,\cdots,q-1\end{aligned} \tag{11}$$

From the least squares principle, one obtains

$$\mu_{uv} = \sum_{j=0}^{m-1} \lambda_{uj} \eta_v(i_j)/\delta_v, u = 0,1,\cdots,p-1 \quad (12)$$

From the above modeling and the 2-D least squares methods, the coefficients in (1) can be determined. The detailed derivations will be given in the full paper [5][6].

Training the Coefficients

Off line The coefficients can be computed off line if the $n \times m$ flux linkage values of the n rotor positions and m winding currents are obtained through either measurements on existing motor or numerical computations.

On line The coefficients is determined generally off line using the static magnetization data. Due to the static nature of the solution, these coefficients are unsatisfactory in the dynamic operating regime of the SRM drives. However, the above coefficients can be trained and corrected on line for the dynamic range if the voltage applied to phase winding, rotor position, and current are measured. The flux linkage is computed from the voltage and current waveforms using the trapezoidal method as given in (13).

$$\psi(l+1) = \psi(l) + \frac{1}{2} T_s [V(l+1) + V(l) - ri(l+1) - ri(l)] \quad (13)$$

where $\psi(l+1)$ and $\psi(l)$ are, respectively, the flux linkage values at the sampling instants $(l+1)$ and (l); $V(l+1)$ and $V(l)$ are, respectively, the voltage values applied to the phase winding at the sampling instants $(l+1)$ and (l); $i(l+1)$ and $i(l)$ are the phase current values at the sampling instants $(l+1)$ and (l), respectively; r is the resistance value of the phase winding and T_s is the sampling time.

It is seen that the proposed algorithm is similar to that of the artificial neural networks (ANN) in respect of the self-training features of the algorithms.

APPLICATIONS

13 rotor position data, 7 current data, and 13×7 linkage data are obtained through the experiment (i.e., m=13 and n=7). The maximum degree of the polynomials with respect to rotor position is equal to 7 and the maximum degree of the polynomial with respect to current is equal to 6 (i.e., p=8 and q=7). $\bar{\theta}$ and $\bar{i}$ in (1) are 15 degree and 6.0 A, respectively.

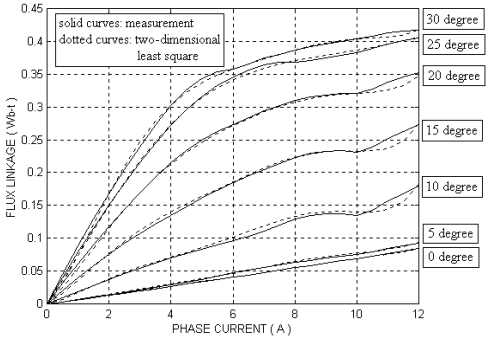

Fig.1 Comparisons between the experiment and the computation

Fig. 1 illustrates the comparisons of the phase flux linkage with phase current between the experiment and the proposed method. The comparisons of phase flux linkage with respect to the rotor position angle between the experimental and the proposed simulation results are given in Fig. 2.

It is clear from Fig. 1 and Fig. 2 that the experimental curves of flux linkage agree very well with the computed curves using the proposed method. The detailed analyses and results will be seen in the full paper.

CONCLUSIONS

This paper presents a novel numerical algorithm to compute precisely the nonlinear magnetic characteristics of SRM drives. The salient advantages of the proposed method are that the modeling can be trained both off line and on line, and that the nonlinear magnetic characteristics at arbitrary rotor position and current can be computed precisely. Experimental results are used to validate the effectiveness and accuracy of the proposed method. It can be seen that the proposed method is applicable to performance prediction, torque control, and sensorless control of the SRM drives, regardless of whether the machine is operating at static or dynamic state.

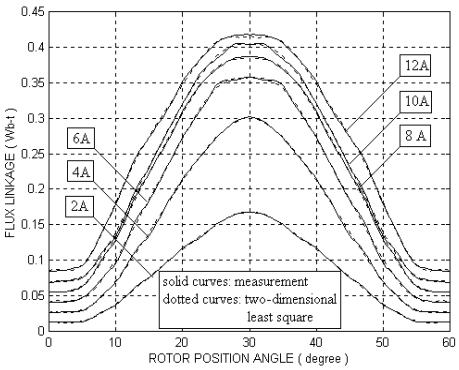

Fig. 2 Comparisons between the experimental and the computation

ACKNOWLEDGEMENT

The authors gratefully acknowledge the financial support of the RGC of Hong Kong (Project: PolyU5085/98E) and the Research Committee of the Hong Kong PolyU (Project: G-W081) for the study being reported in this paper.

REFERENCES

[1] D.A. Torrey and J.H. Lang, "Modelling a nonlinear variable-reluctance motor drive", *IEE PROCEEDINGS,* Vol. 137, Pt. B, No. 5, September 1990, pp314-326.

[2] V. Vujicic and S. N. Vukosavic, "A Simple Nonlinear Model of the Switched reluctance Motor", *IEEE TRANSACTIONS ON ENERGY CONVERSION,* Vol. 15, No. 4, December 2000, pp395-400.

[3] D.A. Torrey, X.-M. Niu, and E.J. Unkauf, "Analytical modelling of variable-reluctance machine magnetisation characteristics", *IEE Proc.-Electric Appl.,* Vol. 142, No.1, January 1995, pp14-22.

[4] E. Mese and D. A. Torrey, "An Approach for Sensorless Position Estimation for Switched Reluctance Motors Using Artifical Neural Networks", *IEEE Trans. Power Electronics*, 17(1), Jan 2002, pp66-75.

[5] Samuel S. M. Wong, *Computational Methods in Physics and Engineering*, World Scientific, 1997.

[6] Shiliang Xu, *The Frequently-used Algorithms and Programs Using C* , Tsinghua University Publisher, 1994.

Size Optimization of Steel-Cored PMLSM Aimed for Rapid and Smooth Driving on Short Reciprocating Trajectory by using Auto-Tuning Niching Genetic Algorithm

Sang-Yong Jung[1], Jae-Kwang Kim[1], Hyun-Kyo Jung[1], and Cheol-Gyun Lee[2]
[1]School of Electrical Engineering, Seoul National University, San 56-1, Shillim-dong, Kwanak-gu, Seoul, 151-742, KOREA
[2]Dong-Eui University, San 24, Gaya-dong, Pusanjin-gu, Pusan, 613-714, KOREA
e-mail : jsyjsy2@snu.ac.kr

Abstract — **Size optimization of Steel-Cored PMLSM(Permanent Magnet Linear Synchronous Motor) has been processed for realizing the rapid and smoth driving on short reciprocating trajectory by using Auto-Tuning Niching Genetic Algorithm. The varition of EMF and the detent force according to the size of teeth and magnets, and chamfering structure has been investigaed in detail. Furthermore, with the obtained design results, performance are compared with primitive one.**

INTRODUCTION

Steel-cored PMLSM generates more thrust force at given velocity than a conventional coreless one, which is mainly thanks to the existence of teeth. Such aspects make steel-cored PMLSM close to the high-power application such as machining tool, semiconductor devices, and etc. Higher power density in linear machines implies the meaning of rapid driving in an acceleration mode, which occurs frequently in a short travel length. On the contrary, the existence of teeth itself could be the main cause of much force ripple, which is usually referred as a detent force and should be minimized for the smooth driving. Accordingly, the optimized structure meeting the requirements of such running conditions as rapid and smooth driving should be developed with the help of optimization process[1]-[3].

In this paper, the size optimization of PMLSM under the fixed input power is done by using Auto-Tuning niching genetic algorithm which is embodied in clearing method, elitism and a deterministic method. In this method, the population size and niche radii of each elite individual are tuned up automatically[4]. Therefore without previous information about design target, optimal solution satisfying design aim of each application can be obtained. Only initial population size and the ratio of elite set size to population size are needed for optimal design process.

One of outstanding solutions in minimizing the detent force is applying the chamfering which means the additional cutting off the teeth edges. As the chamfering ratio is higher, i.e. if the teeth are cut wider and deeper, the detent force decreases dramatically whereas the EMF constant directly connected to the actuating force will decrease accordingly. In addition, the variation of height of teeth and magnets under the fixed intermediate space is giving an influence each other, whereby the magnetic and the electrical loading could be divided successfully through the optimization. Applied optimization has been processed according to the different ratio of the chamfering and the different height of magnets and teeth. The performance of optimized model will be compared with the primitive one, focusing on the decrease of detent force and maintaining the EMF constant.

Generally, input voltage limits the maximum velocity of mover, while input current manifests the feasible thrust force. The EMF constant(K_e [V/(m/sec)]) will be effective for expressing the influence of an input power in case of steel-cored PMLSM which corresponds to the conventional surface-mounted Permanent Magnet Machine. The variation of EMF constant proportional the detent force generation is remarkable, and it will be the significant criteria to the design of steel-cored PMLSM.

OPTIMAL DESIGN OF STEEL-CORED PMLSM

A. Design Variable, Objective and Constraints

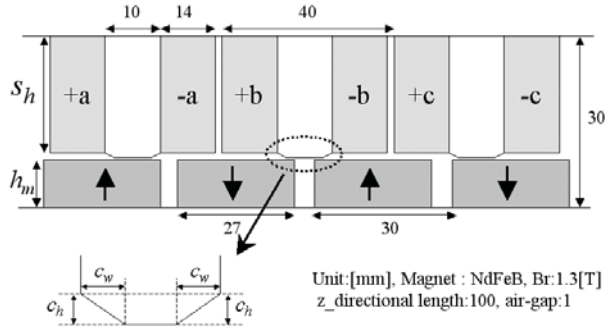

Fig. 1. Design variables in steel-cored PMLSM optimization

As shown in Fig. 1, the design variables for optimization are S_h, h_m, C_w, C_h, while the width of magnets, slots and teeth are fixed in a sense that the pole pitch and the combination of poles and coils(4 poles and 3 coils) are already determined by desired output power and manufacturing feasibility. Number of coil turns will be automatically adjusted along the given space of slots, and the yoke and back-iron are sufficiently thick escaping from the saturation effect. As mentioned, the objective of optimization will be the ratio of K_e to the detent force, which will be aimed for rapid acceleration and smooth driving. In addition, the fixed intermediate length between yoke and the bottom of

magnets, 30[mm], will be the constraint to the variation of the slot and magnets height, and the chamfering ratio is arbitrarily changed only under the manufacturing easiness.

B. Optimization Algotrithm

In the design of electromagnetic device, the object function calculation time takes most of computing time. So it is important to reduce the number of object function calls. To reduce the number of object function calls, the niching genetic algorithm combined with deterministic method (Pattern Search Method) was proposed. Using Auto-Tuning concept, the population size and niche radii of each elite individual are determined automatically.

The flow of auto-tuning niching genetic algorithm is as follows.

Step 1 : (Initializing)
N(initial population size) is determined.
N individuals are generated at random.
The number of generation is set, i.e., g = 1.

Step 2 : (Estimation of overlap)
If $d_{ij} < L_i$, the fitness of x_j is set to zero.
where, L_i : niche radius of elite individual(E_i)
d_{ij} : distance between E_i and x_j

Step 3 : *(Pattern Search Method)*
Survivors of step 2 are moved to peak by pattern search method.

Step 4 : *(Determination of elite set and niche radii)*
Peaks searched on step 3 become elite individual.
Duplicate peaks are excluded.
The longest distance from survivors of step 2 to an elite individual becomes the niche radius of the elite individual.

Step 5 : *(Selection of next generation)*
Population size of next generation is twice elite set size.
(elite set + high fitness individuals among the rest)

Step 6 : *(Reproduction)*
They are crossed and mutated to produce population.

Step 7 : *(Determination of termination)*
If $g < G_n$, g is set to next value and go to step 2.
If $g \geq G_n$, stop.
where, g : the number of generation
G_n : termination condition

C. Design Results

TABLE I. RESULTS OF OPTIMAL DESIGN

	Specification	Dimension
Magnets	Height	9 (8) [mm]
Teeth	Height	16 (17) [mm]
Chamfering	Height	3 (1) [mm]
	Bottom width	3 (1) [mm]
	Bottom height	3 (1) [mm]

(data in a parenthesis are on the primitive one)

Inherently, optimal algorithm produces the many seletable design candidates which are agreeable to the design objective. Proposed optimal design specification in Table I has been selected from the admissible design results based on the manufacturing feasibility of cost and easiness.

PERFORMANCE COMPARISON WITH OTIMIZED PMLSM AND PRIMITIVE ONE

TABLE II. COMPARISON RESULTS OF PERFORMANCE

	K_e [V/(m/sec)]	Detent Force[N]	K_e /Detent Force
Primitive PMLSM	36	231	0.156
Optimized PMLSM	34.69	71.28	0.487

(Rated current for continuous driving : 23.4[Arms])

Optimized PMLSM shows notably better performance than the primitive one, which holds twice as much. In considering the rated current for continuous driving(without concerning about temperature rise), thrust force decreased from 1786[N] to 1721[N], while detent force decreases approximately 70%. In addition, more magnetic loading(8->9) is distinguished to the electrical loading(17->16), where even the number of turns also decreases(200->186 with 1.0[mm] diameter of coil). Consequently, another design results can be generated if the width of magnets and teeth are taken into account, and the consideration of saturation, which is so significant in short-time rating on the restricted track, will give the best answer to the desired aims and its ultimate running characteristics.

CONCLUSION

In this paper, size optimization of steel-cored PMLSM using auto-tuning niching genetic algorithm has been performed, which produces optimal design variables manifesting the raped and smooth driving on required trajectory. Moreover, performance comparison of EMF constant and the decrease of detent force shows the effectiveness of optimally designed PMLSM to the primitive one

REFERENCES

[1] Sang-Yong Jung, Hyun-Kyo Jung, Jang-Sung Chun, "Performance Evaluation of Slotless Permanent Magnet Linear Synchronous Motor Energized by Partially Excited Primary Current." *IEEE Trans. On Magnetics*, Vol. 28, No. 2., pp.3757-3761, 2001.

[2] Sang-Yong Jung, Hyun-Kyo Jung, "Running characteristics of permanent magnet linear synchronous motor energize by partially exicted primary current," *International Journal of Applied Electromagnetics and Mechanics*, vol. 13, July, 2002

[3]Woo-Seok Kim, Sang-Yong Jung, Ho-Yong Choi, Hyun-Kyo Jung, Ji Hoon Kim, Song-Yop Hahn, "Development of a superconducting linear synchronous motor," *IEEE Transactions on Applied Superconductivity*, Vol. 12 Issue: 1 , pp.842-845, Mar. 2002

[4] Jae-Kwang Kim, Dong-Hyeok Cho, H.K. Jung, Cheol-Gyun Lee, "Niching Genetic Algorithm adopting Restricted Competition Selection Combined with Pattern Search Method," *IEEE Trans. On Magnetics*, V. 38, P.1, pp. 1001-1004, March, 2002.

New Rotor Shape Design for Minimum Torque Ripple of SRM using FEM

* H. S. Kim, *J. W. Lee, *B. I. Kwon, **B. T. Kim.
*Graduate school of Hanyang University, Ansan 425-791
**LG Electronics Inc, Seoul 152-050
E-mail: bikwon@hanyang.ac.kr

Abstract – **A major problem of Switched Reluctance Motor (SRM) is torque ripple, which causes undesirable acoustic noise and vibration. It is caused by the geometric characteristic, that is, saliency of the stator and rotor. In this paper, the geometry for low torque ripple is researched and a motor having notched tooth is presented.**

INTRODUCTION

Recently, SRM is studied for high speed application because of its simple structure and development of power electronics. But a major demerit of SRM is large torque ripple, which produces acoustic noises and vibrations. Those are mainly produced by non-linear property of the inductance according to the current and rotor position [1].
To reduce the torque ripple of SRM, the optimization of control method and design of motor shape must be performed simultaneously. Studies for the former are performed, but that for the latter is relatively not much [2]-[4].

General cause of toque ripple in geometry is fringing flux produced just before overlap of the teeth of stator and rotor. High current rise is caused in long period, and torque variation is produced consequently. In this paper, the new shape of rotor tooth is proposed, which reduces fringing flux and torque ripple.

ANALYSIS MODEL

Fig. 1 shows the analysis model and Table 1 presents the detail specification.

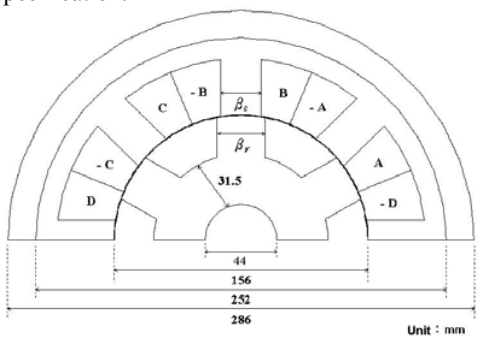

Fig. 1 analysis model

TABLE I. SPECIFICATION OF MODEL

Rated Power	13.5 [kW]
Rated Voltage	80 [V]
Air gap	0.5 [mm]
Rated Speed	1800 [rpm]
Number of turn	10 [turn]
Number of Pole (Stator / Rotor)	8 / 6

Torque waveform at 1800[rpm] is shown in Fig. 2. The torque ripple in region A and B produces the noise and vibrations. The average torque of the motor is 86.4[Nm] and the ratio of torque ripple, 9.5[%], can be calculated by eq (1).

$$\text{Torque ripple} = \frac{\sqrt{\sum_{n=1}^{N} T_n^2}}{T_0} \times 100 \quad [\%] \qquad (1)$$

T_0 : average torque, n : harmonic order

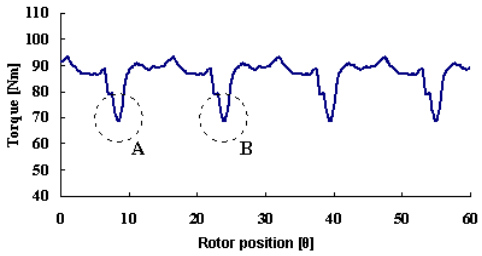

Fig. 2 Torque waveform of analysis model

The inductance profile of an ideal SRM is given in Fig. 3, in the figure, the inductance in the region prior to overlap teeth is constant, and the current is increased linearly and torque is not produced. But the actual inductance of the analysis model is not constant in the region prior to overlap teeth in Fig. 4.

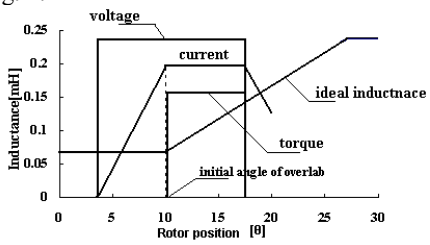

Fig. 3 Characteristic of ideal SRM

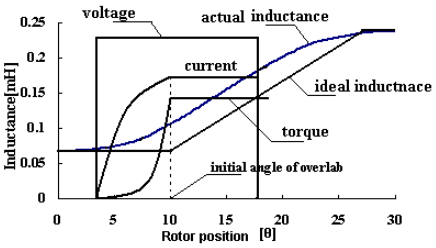

Fig. 4 Characteristic of analysis model

The variation of the inductance in this region makes torque, which is the reason of torque ripple, and current non-linear. While the torque ripple is produced, the maximum torque in the overlap region is reduced. The variation of inductance is mainly caused by the fringing flux in Fig. 5.

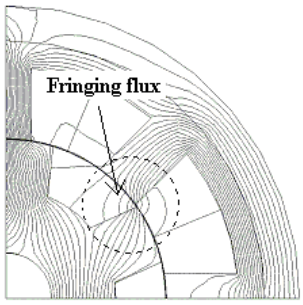

Fig. 5 Flux lines of analysis model

DESIGN OF ROTOR POLE

In this paper, to reduce the fringing flux prior to the overlap angle, the notched tooth of rotor in the forward rotating direction is proposed. And its flux lines and inductance are calculated by F.E.A and shown in Fig. 6. It is shown that the fringing flux is reduced in the proposed model in Fig. 6(a) and the inductance is similar to the ideal in Fig. 6(b). In order to find the optimum shape of the proposed model, some simulations are performed using F.E.A according to the position of the edge of the notch. In Fig. 7, the position of the edge of the notch varies from 1 [mm] to 6[mm] horizontally and from A to G vertically.

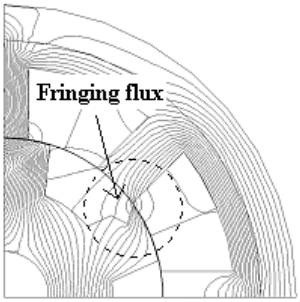

(a) Propose model's flux line

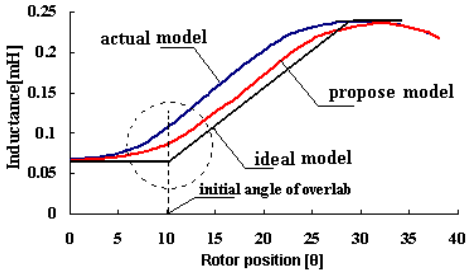

(b) Comparison of inductance waveform

Fig. 6 Flux line and inductance profile of the propose model

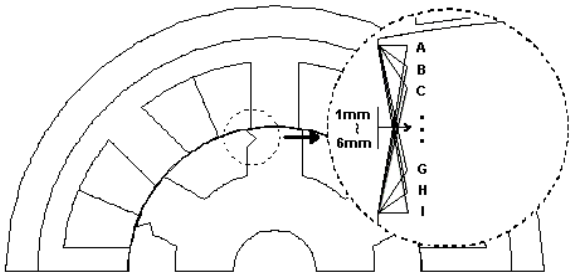

Fig 7. Design of rotor pole

ANALYSIS RESULT

Fig. 8 shows the analysis results of torque ripple according to shape of notch. The torque ripple is reduced about 4.1 [%] in the model of 2[mm]-depth and C-shape. Fig. 9 shows the torque waveforms in the initial model and the proposed model. It can be known that the torque ripple is improved in proposed model in the figure.

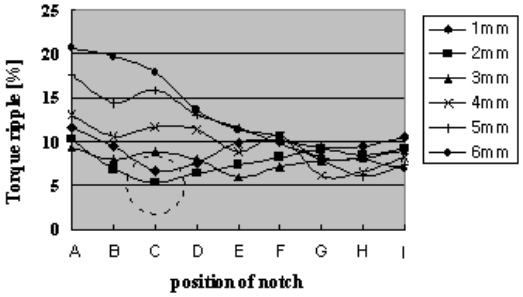

Fig. 8 Torque ripples according to the shape of notch

Fig. 9 Comparison of torque waveform

REFERENCES

[1] TJE Miller, "Switched Reluctance Motors and Their Control", Magna physics publishing and clarendon press, 1993

[2] Iqbal Husain, M.Ehsani, "Torque Ripple Minimization in Switched Reluctance Motor Drives by PWM Current Control",IEEE Trans. on PE, Vol.11, No.1, pp.91-98, 1996.

[3] Chang-sub Kim, Seok-gyu Oh, Jin-woo Ahn, "Reduction characteristics of vibration and acoustic noise of SRM using Hybrid Excitation Method", KIEE Trans, Vol. 50B, No. 9, pp 438-444, 2001. 9.

[4] Funda Sahin, H. Bulent Ertan, Kemal Leblebicioglu, "Optimum Geometry for Torque Ripple Minimization of Switched Reluctance Motors." IEEE Trans. on EC, Vol. 15, No. 1, March 2000

3D approaches to determine the end winding inductances of a PMLSM

[1]A. Tounzi, [1]T. Henneron, [1]Y. Le Menach, [2]R. Askour, [3]E. Dumetz, [1]F. Piriou

L2EP, USTL
Bat. P2
59655 Villeneuve d'ascq, France
mounaim.tounzi@univ-lille1.fr

ENSAM - MEKNES
Université Moulay Ismaïl
Meknes – Maroc

L2EP, ENSAM CER LILLE
8, Bd Louis XIV
59046 LILLE Cedex, France
eric.dumetz @lille.ensam.fr

Abstract – **The present paper deals with the determination of the end winding inductance of a permanent magnet linear synchronous motor. The methods to determine the inductances in 3D are given for both classical complementary formulations. In first step, an elementary cell of the structure is modeled and the results are analyzed and discussed. In the second step the complete structure is studied in 2D and 3D with only scalar potential formulation. For this last step, the numerical results are compared with experimental ones.**

INTRODUCTION

Nowadays, the numerical approach, based on the 3D Finite Element Method (3D-FEM), is more and more used to study electromagnetic structures as, for example, linear motors [1-2]. However, even if the calculation capacities are growing very fast, the study of electromechanical devices, when only little symmetry exists, remains heavy using a full 3D package. Indeed, this increases the number of unknowns and consequently the computation time. Moreover, some other constraints have to be introduced when the motion is taken into account. Hence, it is still interesting to use 2D-FEM while taking into account 3D effects. These ones, which must be principally taken into account, in the electrical machine studies, are the eventual skew of the teeth or the magnets, and the end winding effects. Previous studies showed that the skew effects could be considered, with accuracy, by the 2D-slide approach [3].

In the case of end winding effects, one can determine, using 2D and 3D magnetostatic calculations, the end winding inductance (EWI). Then, this last is generally not affected by the non linearity of the material, it can be introduced into 2D model, in series with the armature resistance [4].

In this paper, we determine the end winding inductances of a PMLSM. First, we introduce 3D approaches, which allow us to model the structure in magnetostatic case. The methods used to calculate the inductances and the EWI are also introduced [5]. Then, we apply the different approaches to determine the end winding inductance of an elementary cell and the one of the whole structure. The different results obtained are discussed. At last, we introduce it into 2D-model and we show that the results are in good agreement with the experimental ones.

NUMERICAL MODELS

Formulations in term of potentials

In the case of an electromagnetic system, the magnetostatic Maxwell's equations are written, on a domain "V" of boundary Γ, under the form:

$$\mathbf{curl h} = \mathbf{j}_s \text{ with } \mathbf{h}\times\mathbf{n}=0 \text{ on } \Gamma_h \quad (1)$$

$$\mathrm{div}\mathbf{b} = 0 \text{ with } \mathbf{b}.\mathbf{n}=0 \text{ on } \Gamma_b \quad (2)$$

such as $\Gamma_h \cup \Gamma_b = \Gamma$ and $\Gamma_h \cap \Gamma_b = 0$. In these expressions, **h** represents the magnetic field, **b** the magnetic flux density and $\mathbf{j}_s$ the current density. In our development, the studied domain "V" is considered simply connected. Vector fields **b** and **h** are linked by the constitutive relationship $\mathbf{b}=\mu\mathbf{h}$. To solve these equations, we can use a formulation in term of scalar potential φ (called φ-formulation) with a source field $\mathbf{h}_s$ or the formulation in term of magnetic vector potential **a** (called **a**-formulation).

In the case of the φ-formulation, as the current density is expressed from the curl of magnetic field, the latter can be written:

$$\mathbf{h} = \mathbf{h}_s - \mathbf{grad}\varphi \text{ with } \mathbf{h}_s\times\mathbf{n}=0 \text{ on } \Gamma_h \quad (3)$$

The magnetic scalar potential φ is then the unknown and the source field $\mathbf{h}_s$ is defined by:

$$\mathbf{curl}\,\mathbf{h}_s = \mathbf{j}_s \quad (4)$$

The formulation in term of vector potential is obtained from equation (2) so that:

$$\mathbf{curl}\,\mathbf{a} = \mathbf{b} \quad (5)$$

To impose the uniqueness of **a**, it is necessary to add a gauge condition.

Flux linkage expressions

We assume that the domain V has one inductor and we denote "i" the current. We also note that the current density distribution is assumed to be uniform in each cross section. Consequently, $\mathbf{j}_s$ in the inductor can be written as:

$$\mathbf{j}_S = \mathbf{N}i \quad (6)$$

where **N** is the vector of turn density. Its magnitude is given by the ratio of the number of turns to the winding section and its direction by its spatial orientation. As the current density, vector **N** is with divergence free. The flux linkage in a winding can be obtained by integrating, on the whole domain, the projection of magnetic vector potential on the vector turns density. Thus, we can write [4]:

$$\Phi = \int_V \mathbf{a}.\mathbf{N}\,dv \quad (7)$$

To determine the flux linkage in the case of φ-formulation a

vector **K** is introduced under the form: c**urlK**=**N**. Then, from equation (7) by permuting **N** with its expression in function of **K** and using Green formula, we can write:

$$\Phi_w = \int_V \mathbf{K}.\mathbf{curla}\,dv \qquad (8)$$

From equations (8) and (5) and considering the constitutive relationship and the expression of magnetic field (3) we can write the flux in function of **K** and φ under the form:

$$\Phi_w = \int_V \mu\mathbf{K}.(\mathbf{K}i - \mathrm{grad}\varphi)dv \qquad (9)$$

Equations (7) and (9) permit to calculate the flux in the winding using both classical formulations.

To compute flux Φ_s flowing through a surface S defined by its contour ∂S we introduce the exploration coil. In the case of **a**-formulation the classical formula can be used:

$$\Phi_s^a = \int_{\partial S} \mathbf{a}.d\mathbf{l} \qquad (10)$$

In the case of φ-formulation we introduce vector $\mathbf{K}_{\partial S}$ [5]. This one corresponds to the source field vector created by a coil flowing by 1 A formed by the turn defined from contour ∂S. In these conditions, the flux through a surface S is given by:

$$\Phi_s^{\varphi} = \int_V \mathbf{b}_{\varphi}.\mathbf{K}_{\partial S}dv \qquad (11)$$

From equations (10) and (11), the end winding inductances can be determined considering the flux trough an exploration coil. Another possibility is the calculation in 2D and 3D.

NUMERICAL COMPUTATION

The machine studied is a permanent magnet linear synchronous motor (PMLSM) of 6.6kN, 45A, and 1.67m/s. The double layer armature windings, of 8 pole pair number, are disposed in 51 slots. To compute the EWI, we only consider the armature winding shown in figure 1.a. The complete structure will be modeled in 2D.

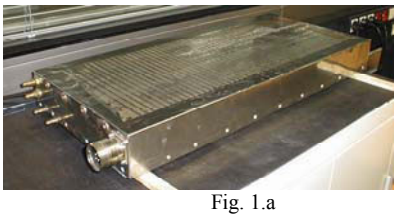

Fig. 1.a

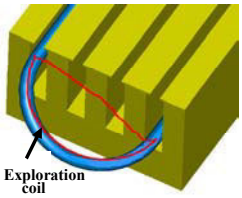

Fig. 1.b

Fig. 1. Structure studied (fig. 1.a) and definition of exploration coil (fig. 1.b).

Using complementary solutions we study, in a first step, an elementary cell shown figure 1.b. We can see, in this figure, the definition of the exploration coil. For this cell the flux in the winding, for a current of 1A, has been calculated in 2D and 3D using both complementary formulations. To complete the study, the flux in the exploration coil has also been determined. The results are presented in Table I. The estimated flux corresponds to the difference between 2D and 3D calculation. So the estimated end winding inductance must be compared with the results of exploration coil.

TABLE I. FLUXES (10^{-6} Wb)

Formulation	2D	3D	Estimated	Exploration – coil
A	1.849	1.954	0.105	0.094
Ω	2.068	2.188	0.12	0.106

As expected from complementary solutions, φ-formulation gives values slightly higher than the ones calculated by **a**-formulation. However, for both formulations, the fluxes calculated by the exploration coil are in good agreement with the estimated end winding ones.

Now, we consider the whole armature winding. The mesh, which corresponds to the half part, is constituted of 220,000 nodes and 690,000 elements. To limit the computation time the structure has been only studied with φ-formulation. As in the case of the cell the flux has been calculated in 2D, 3D and with the exploration coil which defines EWI. The results obtained are shown in Table II.

TABLE II. FLUXES (10^{-3} Wb)

2D	3D	Estimated	Exploration-coil
7.28	7.68	0.4	0.39

It may be noted that exploration coil flux is deduced easily from the one calculated in an unique exploration coil, placed in the end pole of the considered winding and multiplied by the pole number. Moreover, computations show that the end winding mutual inductances are negligible.

To validate the model (2D+EWI), we have compared the results obtained by calculations in 2D and 2D+EWI to measures. Hence, a sinusoidal voltage supplies two-phase windings in series. Knowing the phase resistance, it is easy to obtain the cyclic inductance of the structure. The results are given in Table III. From this Table we can see that the result taken into account EWI is more accurate.

TABLE III. COMPARISON OF THE CYCLIC INDUCTANCES

Method	Experiment	2D	2D+EWI
L-M (mH)	8.51	7.64	8.12

CONCLUSION

In this paper, we have studied the calculation of the end winding inductance of a PMLSM. In 3D two approaches have been introduced, the classical computation of inductance winding and the use of the exploration coil. In both cases, for an elementary cell the inductances have been determined using both complementary formulations. In the last step, the results obtained from 2D and 2D+EWI have been compared to the experiment.

REFERENCES

[1] B. Kwon, K. Woo, D. Jin Kim, S. Chan Park, "Finite element analysis for dynamic characteristics of an inverter-fed PMLSM by a new moving mesh technique", *IEEE Trans. Mag.*, vol 36, n°.4, pp 1574-1577, 2000.

[2] T.Yamaguchi, Y. Kawase, M. Yoshida, Y. Saito, Y. Ohdachi, "3D Finite element analysis of a linear induction motor" *IEEE Trans. Mag.,* vol 37, n°5, pp 3668-3671, 2001.

[3] P. Dziwniel, B. Boualem, F. Piriou, J.P. Ducreux, P. Thomas, "Comparison Between two Approaches to model Induction Machines with Skewed Slots", *IEEE Trans. Mag.*, vol. 36, pp 1453-1457, 2000.

[4] Y. Sofiane, A. Tounzi, F. Piriou and M. Liese, "Study of Head Winding Effects in a Switched Reluctance Machine", *IEEE Trans Mag.,* vol 32, n° 2, pp 1453-1457, 2002.

[5] Th. Henneron et al, "Evaluation of 3D FEM to study and design a SMC Electrical Machine" Submitted to Compumag 2003.

Field and Circuit Approaches for Diffusion Phenomena in Magnetic Cores

O. Bottauscio, A. Manzin
Istituto Elettrotecnico Nazionale *Galileo Ferraris*
Strada delle Cacce 91, I-10135 Torino, Italy
e-mail: botta@ien.it, manzin@ien.it
A. Canova, M. Chiampi, G. Gruosso, M. Repetto
Politecnico di Torino, Dipartimento di Ingegneria Elettrica Industriale
Corso Duca Abruzzi 24, I-10129 Torino, Italy
e-mail: canova@polel1.polito.it, chiampi@polel1.polito.it), gruosso@polel1.polito.it, repetto@polel1.polito.it

***Abstract*— This paper presents two approaches for nonlinear dynamic modeling of voltage-driven magnetic circuits. The field approach is based on a FEM method; in 2D laminated cores an in-plane magnetic analysis is coupled with a 1D eddy current solution across lamination thickness. The circuit approach subdivides the magnetic core in flux tubes according to geometrical symmetries and solves the coupled electric and magnetic circuits. The two analysis methods are applied to the study of magnetic cores and comparisons between them and with experimental data are performed and discussed.**

INTRODUCTION

The simulation of magnetic cores under dynamic supply is important in different areas of applied research. The diffuse presence of ferromagnetic cores in electronic systems and their complex behavior under distorted flux waveforms is the reason for this need. Usually eddy currents present inside the cores are strongly reduced by means of lamination; nevertheless there are applications where eddy current effects cannot be neglected, as for example in high frequency supply or in axially-symmetric bulk structures. In all these cases a study that take into account induced eddy currents and their interaction with nonlinearities of the material is compulsory.

Several analysis approaches can be devised to this aim starting from a thorough three-dimensional model of the structure to simplified ones [1], [2], [3]. While the first study would be for sure accurate, its complexity and computational cost is unacceptable, thus some simplifying considerations can be taken into account. In this paper two approaches with different degrees of accuracy are presented: a two dimensional finite element model of the core and a circuit based one. Both approaches have been adapted to the particular structure taking into account symmetries and engineering considerations.

FIELD APPROACH

The field approach is based on a 2D voltage-driven electromagnetic field formulation in terms of a magnetic vector potential $\boldsymbol{A}$. Introducing FEM, linear shape functions are employed; for axial-symmetric problems, shape function are weighted by r^{-1} in all the regions far from the symmetry axis. The discretized problem uses as unknowns the nodal values of the magnetic vector potential and the branch currents of the supply circuits. The magnetic nonlinearity is exploited by the Fixed Point (FP) iterative technique. In laminated cores, the skin effect in the lamination depth is accounted for by coupling the 2D solution in the (xy)-plane with the 1D nonlinear diffusion problems defined in the sheet thickness (z-axis) [5].

CIRCUIT APPROACH

The analysis of eddy currents induced inside a ferromagnetic core can be approached by means of a magnetic equivalent circuit (MEC) if some electric and magnetic flux tubes can be defined. Taking into account the usual hypotheses of magnetic circuits study and geometrical shapes typical of the industrial applications, these flux tubes can be defined in easy way. Once the geometry of the flux tubes is known, electrical (resistance) and magnetic (reluctance) lumped parameters can be computed and a network built. The main conceptual difficulty of this process is the definition of an efficient interface between the electric and the magnetic domains. Different schemes for this aim have been proposed in the literature [2], [3], here a coupling based on a magneto electric differential gyrator has been adopted. The scheme of the coupled circuits is represented in Fig. 1. In Fig. 2 an axially-symmetric core subdivided in three magnetic flux tubes and two electrical ones is reported together with its lumped parameters representation.

For complex structures, more than one block with eddy currents can be used and all blocks can be linked by topological relations and solved by means of some network solution algorithm.

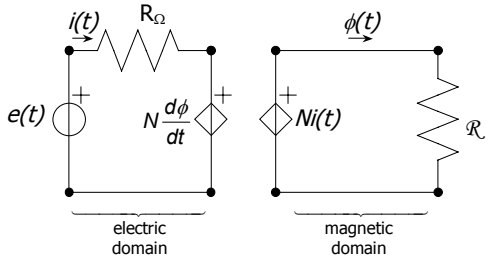

Fig. 1 Coupled electric and magnetic circuit: R_Ω ohmic resistance of the electric circuit, N number of turns, $\mathcal{R}$ reluctance of the magnetic circuit.

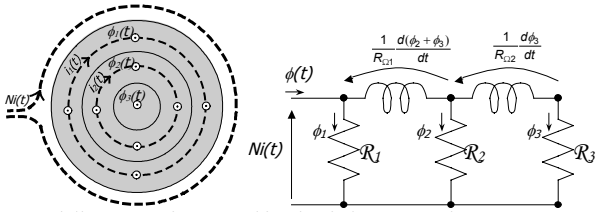

Fig. 2 Axially-symmetric core and its circuital representation

APPLICATIONS

Two test cases have been studied by means of the two approaches: an axially symmetric magnet and a laminated ferromagnetic core (Fig. 3). In the first case experimental data are available.

The axially symmetric device is composed by a cylinder (internal core) surrounded by a winding, by a hollow cylinder, and by two disks representing the closures of the magnetic path. The upper disk (moving core) is supposed to remain in the closed position with a 0.45 mm air-gap. Several supply conditions are tried in order to change the saturation level of the core and its dynamical behavior. In Fig. 4 the comparison of the two approaches with experimental data are reported under sinusoidal supply. The FEM case has a mesh made of 7940 elements, while circuit approach uses 9 blocks to model the magnetic circuit taking into account also leakage flux. Eddy current blocks are subdivided in 6 flux tubes. As it can be seen the agreement between supply currents is more than satisfactory.

The 2D device is a C-shape electromagnet constituted by a laminated core (lamination thickness equal to 0.5 mm), with a 0.4 mm air-gap. Each lamination is discretized along the thickness in 10 flux tubes. Sinusoidal voltage supply with frequency value of 5 kHz is applied. In absence of eddy current, the mean value of magnetic flux density will be ~1.2 T, while, due to flux skin effect, the magnetic flux density reaches a peak value of ~1.6 T, that results in a distortion in the current waveform. The two methods are found to be in satisfactory agreement.

A deep comparison between the proposed approaches will be discussed in the full paper.

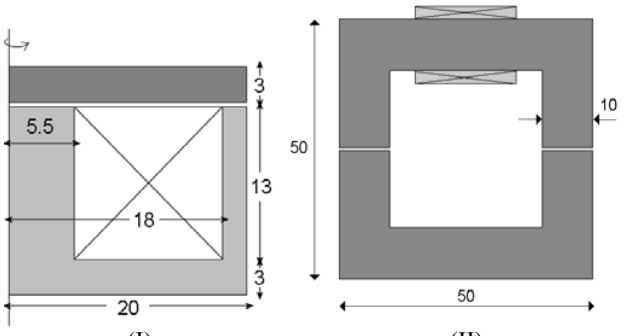

Fig. 3 Devices under study (dimensions in millimeters): (I) axisymmetric device, (II) C-shape device

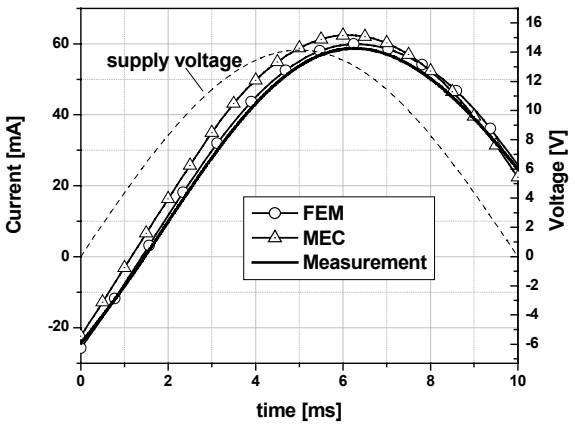

Fig. 4 Computed and experimental supply current under sinusoidal supply for test device I: field approach (FEM), circuit approach (MEC)

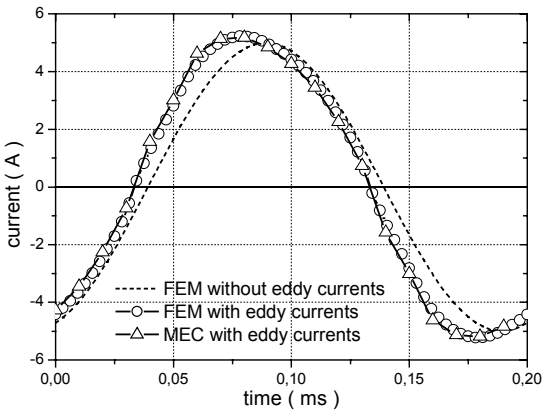

Fig. 5 Computed supply current under sinusoidal supply for test device II: field approach (FEM), circuit approach (MEC)

REFERENCES

[1] K. Hollaus.,O. Biro,"A FEM formulation to treat 3D eddy currents in laminations", *IEEE Trans. Mag*., Volume: 36 Issue: 4 Part: 1 , July 2000, 1289 -1292

[2] D.C. Hamill, "Lumped equivalent circuits of magnetic components: the gyrator-capacitor approach", *IEEE Trans. on Power Electronics*, vol. 8, pp. 97-103, April 1993

[3] A.D. Brown, J.N. Ross; K.G. Nichols,"Time-domain simulation of mixed nonlinear magnetic and electronic systems", *IEEE Trans. Mag.*, Vol. 37, 2001, pp 522 -53

[4] Grandi, G.; Massarini, A.; Reggiani, U.; Sancineto, G, "Laminated iron-core inductor model for time-domain analysis" Power Electronics and Drive Systems 2001. Proceedings. 4th IEEE International Conference on , Volume: 2 , 2001 pp: 680 –686.

[5] O. Bottauscio, M. Chiampi, "Analysis of Laminated Cores through a Directly Coupled 2D-1D Electromagnetic Field Formulation", to appear on *IEEE Trans. Mag*.

Regularization on Ill-posed Source Terms in FEM Computation Using Two Magnetic Vector Potentials

Akihisa Kameari
Science Solutions International Laboratory, Inc.
2-21-7, Naka-cho, Meguro-ku, Tokyo, 153-0065, Japan
kamearia@ssil.com

***Abstract* - In the formulation with two magnetic vector potentials, the inaccuracy of the Biot-Savart integration for the source term causes the divergence of the conjugate gradient method. The ill-posed equations are regularized by subtracting a rotational field from the numerically integrated field. The convergence is drastically improved. Even when the current continuity is not satisfied strictly we can get reasonable results.**

***Index Terms* - finite element methods, edge elements, two potential method, reduced magnetic vector potential, ICCG convergence .**

I. INTRODUCTION

In electromagnetic analyses using the Finite Element Method, matching the discretization of complex-shaped source coils with the rest of the mesh is a time-consuming and difficult task. One method to avoid this burden is using two potentials (total and reduced potentials) in different regions and connecting the regions based on field continuity[1]. In this case, the coils can be defined independently from the FEM mesh. When the total and reduced magnetic vector potentials are used with edge elements, the accuracy of the Biot-Savart integration becomes essential for ensuring the well-posedness of the equations. One often encounters the divergence of the conjugate gradient method (ICCG) due to the ill-posedness of the equations in this formulation. Obviously, one can improve the convergence by increasing the accuracy of the Biot-Savart integration, but the computation for the integration becomes time-consuming and impractical in the engineering sense.

In this paper, a regularization method for the ill-posedness of the equations in the two potential method is proposed.

II. TWO POTENTIAL METHOD

In the two potential method, the total magnetic vector potential $\mathbf{A}_t$ and the reduced magnetic vector potential $\mathbf{A}_r$ are used for: regions (Ω_t) which include conductive and/or magnetic materials, and for the air region (Ω_r) surrounding the total potential regions, respectively. For the magnetic vector potentials, the edge element functional space is used.

In the total potential region, usual A formulation is adopted and the following equation is solved.

$$\nabla\times\frac{1}{\mu}\nabla\times\mathbf{A}_t+\sigma\dot{\mathbf{A}}_t=0 \tag{1}$$

Current sources embedded in the discretized mesh can also be included in this region, but for simplicity they are not considered in the formulation presented here. We can adopt here the A-ϕ formulation, that is equivalent to the A formulation when using edge elements and which is known to improve the convergence of the ICCG method.

In the reduced potential region, the equation

$$\nabla\times\frac{1}{\mu_0}\nabla\times\mathbf{A}_r=0 \quad , \tag{2}$$

is solved. At the interface (Γ_{tr}) of the two regions, the following continuity conditions are applied.

$$\mathbf{A}_t\times\mathbf{n}=(\mathbf{A}_r+\mathbf{A}_s)\times\mathbf{n} \tag{3}$$

$$\mathbf{H}_t\times\mathbf{n}=(\mathbf{H}_r+\mathbf{H}_s)\times\mathbf{n}. \tag{4}$$

Here, $\mathbf{n}$ is the normal unit vector on the interface. $\mathbf{H}_t$, $\mathbf{H}_r$ and $\mathbf{H}_s$ are the magnetic intensities of the total, reduced and source field. $\mathbf{H}_t=1/\mu\nabla\times\mathbf{A}_t$, $\mathbf{H}_r=1/\mu_0\nabla\times\mathbf{A}_r$ and $\mathbf{H}_s$ is given by Biot-Savart integration of the source currents located outside of the total potential regions.

The Galerkin's weak form is derived from these equations as:

$$\int_{\Omega_t}\left(\nabla\times\mathbf{N}\cdot\frac{1}{\mu}\nabla\times\mathbf{A}_t+\mathbf{N}\cdot\sigma\dot{\mathbf{A}}\right)dV+\int_{\Omega_t}\left(\nabla\times\mathbf{N}\cdot\frac{1}{\mu_0}\nabla\times\mathbf{A}_r\right)dV = \int_{\Gamma_{tr}}\mathbf{N}\times\mathbf{H}_s\cdot\mathbf{n}dS. \tag{5}$$

Here, $\mathbf{N}$ is the weighting function represented by the edge shape functions and includes the gradient of the scalar functions. The condition (3) is enforced strongly. Equation (5) must be satisfied when $\mathbf{N}$ is replaced by the gradient $\nabla\omega$ of any scalar function in the allowable functional space. Of course, the L.H.S. of the equation becomes zero, and the R.H.S. becomes,

$$\int_{\Gamma_{tr}}\nabla\omega\times\mathbf{H}_s\cdot\mathbf{n}dS=\int_{\Gamma_{tr}}\omega\nabla\times\mathbf{H}_s\cdot\mathbf{n}dS+\oint\omega\mathbf{H}_s dC \tag{6}$$

In the R.H.S. of (6), the line integration appears when the interface is open and becomes zero according to boundary conditions and the surface integration becomes zero when the source current does not flow through the interface. Thus,

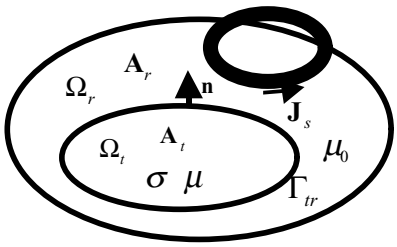

Fig. 1. Analysis regions for two potential method

ideally this substitution would make the R.H.S. of (5) to be zero, so that (5) is a non-definite equation as usual in the formulation using edge elements. But, when the integration of the R.H.S. of (5) is not strictly accurate, the equation becomes an ill-posed equation. In solving using the ICCG method, it converges to some extent according to the accuracy of the integration and finally diverges.

III. Regularization of Ill-poseness

In general, the source field can be calculated by the Biot-Savart integration as,

$$\mathbf{H}_s = \int \frac{\mathbf{J}_s \times \mathbf{r}}{r^3} dV \,. \tag{7}$$

In case of simple coil geometry, analytical expressions can be used. However, for arbitrary coil shapes it is difficult and time-consuming to perform accurate integrations Rather, it would be preferable to be allowed to the accuracy of the integration.

The R.H.S. of (5) can be regularized as follows. The source field $\mathbf{H}_s$ on the interface is modified as,

$$\tilde{\mathbf{H}}_s = \mathbf{H}_s - \nabla\varphi \times \mathbf{n} \,. \tag{8}$$

The following equation is imposed:

$$\int_{\Gamma_{tr}} \nabla\omega \times \tilde{\mathbf{H}}_s \cdot \mathbf{n} dS = \int_{\Gamma_{tr}} \nabla\omega \times \mathbf{H}_s \cdot \mathbf{n} dS - \int_{\Gamma_{tr}} \nabla\omega \times \mathbf{n} \cdot \nabla\varphi \times \mathbf{n} dS = 0 \tag{9}$$

and solved for φ, and $\mathbf{H}_s$ in (5) is replaced with $\tilde{\mathbf{H}}_s$. The regularization potential φ is in the functional space of the nodal scalar functions on the interface. Equation (9) is a positive-definite symmetric equation and easily solved. This procedure corresponds to subtracting the rotational field component $\nabla\varphi \times \mathbf{n} = \nabla \times (\varphi \mathbf{n})$ from the calculated field.

IV. Example

One example of the regularization is shown. We consider the model shown in Fig.2, where an iron core is magnetized by a coil. The coil is simulated by 4 rectangular parallelepipeds, overlapping on each other at sides. The current continuity is not satisfied strictly.

In Fig. 3, the convergence processes are shown for the cases with and without the regularization. Without the regularization, the ICCG method diverges after reaching an error of 3.5×10^{-3}. With the regularization, it converges to 1.3×10^{-14}, which probably is the numerical limit in the double precision. In Fig. 4, the distribution of the regularization potential φ is shown. In this example, the magnetic fields resulted with and without the regularization are almost identical, and the difference is in the order of the minimum error in the ICCG iteration without the regularization.

V. Discussion

As shown in the example, using the regularization method we can get a convergent solution even when the source current continuity is not satisfied. We should note, though, that the solution obtained by regularization might still reflect the error caused by the inaccuracy of the source current condition. The author is expecting that the regularization is valuable in non-linear or transient analyses involving small perturbations. More test computations and validation of the method will be presented in the extended paper.

References

[1]A. Kameari, "Solution of asymmetric conductor with a hole by FEM using edge-elements", *COMPEL, The International Journal for Computation and Mathematics in Electrical and Electronic Engineering*, Vol. 9, Supplement A, 1990, pp. 230-232.

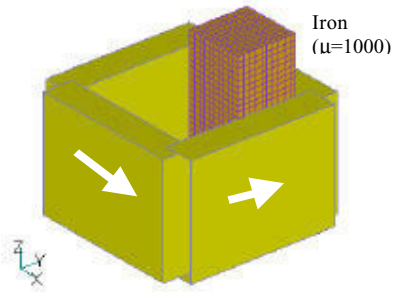

Fig. 2. Model for test calculation. The iron core is shown for 1/8 region.

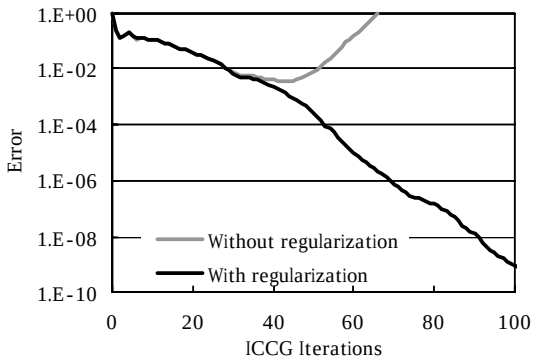

Fig. 3. Convergence of ICCG iterations with and without the regularization.

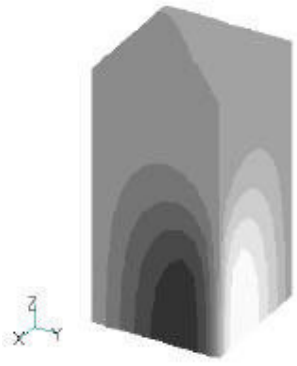

Fig. 4. Distribution of regularization potential

COMPUMAG Saratoga Springs, New York USA
July 13 - 17, 2003

3D Eddy Current Analysis with the *Cell Method* for NDE Problems

Francesco Trevisan

***Abstract*—An algebraic formulation has been developed for 3D eddy current problems, according to the *Cell Method* philosophy. This formulation is presented in the frequency domain and it is based on the circulation of the magnetic vector potential along primal edges and on the electric scalar potential in primal nodes of the conductors. It has been applied and validated respect to the solution of NDE TEAM problem 15. The flaw has been modeled as a zero-thickness defect and the superposition of effects and compensation theorem have been applied to compute the impedance variation respect to the flawless configuration.**

***Index Terms*— Eddy currents, NDE, Cell Method.**

INTRODUCTION

In Electromagnetic Nondestructive Evaluation (NDE) problems the development of analysis models for computing the field perturbation at the measurement probe locations, due to the presence of a specified flaw, is a crucial issue. In recent years, several sophisticated computational models have been proposed and applied for the solution of the direct problem, based on different approaches like Finite Elements or Integral models [1-2]. In this paper the solution of the direct eddy current problem has been tackled on the basis of an alternative approach based on the *Cell Method*. Starting from the general ideas of the Tonti's Finite Formulation [3] for electromagnetic fields, an algebraic formulation for 3D eddy current analysis has been developed, based on the circulation of the magnetic vector potential a and on the electric scalar potential V in the conducting region. The proposed numerical formulation is presented for linear conducting media in the frequency domain and the flaw is modeled as a *zero thickness* defect. As test problem, the TEAM problem 15 has been considered to validate the formulation and the obtained results, in terms of impedance variations, have been compared [4].

According to the Cell Method, a tessellation of the 3D space is considered based on oriented geometrical elements like *points*, *edges*, *faces*, *cells* of a pair of cell complexes $K=\{\mathbf{p}_h, \mathbf{l}_i, \mathbf{s}_j, \mathbf{v}_k\}$ and $\tilde{K}=\{\tilde{\mathbf{v}}_h, \tilde{\mathbf{s}}_i, \tilde{\mathbf{l}}_j, \tilde{\mathbf{p}}_k\}$ one dual of the other, endowed with *inner* and *outer* orientation respectively; the bold face indicates that the geometrical elements are oriented while the tilde denotes the outer orientation. The cells $\mathbf{v}_k$ are tetrahedral while the dual complex $\tilde{K}$ is built from K according to the *barycentric* subdivision. This means, in particular, that a dual point $\tilde{\mathbf{p}}_k$ is the barycentre of $\mathbf{v}_k$ and that a dual line $\tilde{\mathbf{l}}_j$ is a broken line between the barycentres of two contiguous tetrahedra sharing a primal face $\mathbf{s}_j$ and passing through the barycentre of that face. Analogously, also on the time axis, two mono-dimensional cell complexes $\{\mathbf{t}_n, \mathbf{T}_n\}$ and $\{\tilde{\mathbf{T}}_n, \tilde{\mathbf{t}}_n\}$ can be introduced one dual of the other, made of primal instants, primal intervals with inner orientation and of dual intervals, dual instants with outer orientation respectively.

THE CELL METHOD FOR EDDY CURRENTS

A. Classification of physical variables

According to the Finite Formulation, the physical variables can be distinguished in *configuration* and *source* variables and satisfy to the following fundamental property: configuration variables are referred to space elements endowed with inner orientation and so to the primal cell complex K, while the source variables are referred to space elements endowed with outer orientation and so to the dual cell complex $\tilde{K}$. Therefore, the association of physical variables to the right cell complex is *univocally* specified by the above principle. For the case of eddy current problems, the physical variables vectors of interest and their association to the space elements of a cell complex are reported in the following [5]:

- $\mathbf{V}$ is the vector of electric potentials associated to primal points $\mathbf{p}_h$;
- $\mathbf{U}$ is the vector of electric voltages associated to primal edges $\mathbf{l}_i$;
- $\mathbf{\Phi}$ is the vector of fluxes relative to primal faces $\mathbf{s}_j$;
- $\mathbf{a}$ is the vector of circulations of the magnetic vector potential and is relative to primal edges $\mathbf{l}_i$;
- $\mathbf{I}$ is the vector of electric currents across dual faces $\tilde{\mathbf{s}}_i$;
- $\mathbf{F}$ is the vector of magnetic voltages relative to dual edges $\tilde{\mathbf{l}}_j$.

As concerns the time association, it is convenient here to regard the time axis as a continuum by taking the limit to zero of the primal, dual intervals $\mathbf{T}_n$, $\tilde{\mathbf{T}}_n$ in the time tessellation. Therefore all the introduced global variables become functions of a time instant t. Usually in NDE problems the external impressed currents are sinusoidal with fixed frequency and all the media are linear; therefore the formulation of the eddy current problem can be cast directly in

Manuscript received November 1, 2002. F. Trevisan is with the Dep. Ingegneria Elettrica, Gestionale e Meccanica, Università di Udine, Via delle Scienze 208, 33100 Udine, Italy, e-mail: trevisan@uniud.it.

the harmonic regime, considering the complex transformation of the above vectors.

B. *Physical laws and constitutive equations*

The physical laws for eddy current problems, in algebraic form are: the *Gauss magnetic* law $\mathbf{D\Phi = 0}$, with $\mathbf{D}$ the incidence matrix between $[\mathbf{v}_k : \mathbf{s}_j]$, that is identically satisfied when the flux is expressed as $\mathbf{\Phi = C\,a}$ with $\mathbf{C}$ the incidence matrix between $[\mathbf{s}_j : \mathbf{l}_i]$; the *Faraday-Neumann* law $\mathbf{U} = -j\omega\mathbf{a} - \mathbf{GV}$ with $\mathbf{G}$ the incidence matrix between $[\mathbf{l}_i : \mathbf{p}_h]$, the *Ampère* law $\widetilde{\mathbf{C}}\,\mathbf{F} = \mathbf{I}$ with $\widetilde{\mathbf{C}} = \mathbf{C}^T$ and the *continuity* law $\widetilde{\mathbf{D}}\,\mathbf{I} = \mathbf{0}$ with $\widetilde{\mathbf{D}} = -\mathbf{G}^T$. These topological equations are valid independently of the media and of the size of the cell complexes. The magnetic $\mathbf{F} = \mathbf{M\Phi}$ and Ohm $\mathbf{I} = \mathbf{NU}$ constitutive equations can be easily derived under the hypothesis of uniformity of the fields and homogeneity of the media within each tetrahedron.

C. *The algebraic equations*

Combining the physical laws with the constitutive equations, different sets of equations can be written according to the region considered: air, coil with impressed current or conductor respectively. Precisely, in the air or in the coil we derive:

$$\widetilde{\mathbf{C}}\mathbf{M}\mathbf{C}\,\mathbf{a} = \mathbf{I} \tag{1}$$

with $\widetilde{\mathbf{C}}\mathbf{M}\mathbf{C}$ symmetric, while in the conducting region we have:

$$[\widetilde{\mathbf{C}}\mathbf{M}\mathbf{C} + j\omega\mathbf{N}]\,\mathbf{a} + \mathbf{NGV} = \mathbf{0} \tag{2}$$

$$j\omega\widetilde{\mathbf{D}}\,\mathbf{N}\mathbf{a} + \widetilde{\mathbf{D}}\,\mathbf{N}\mathbf{G}\mathbf{V} = \mathbf{0} \tag{3}$$

To get the unique solution in terms of $\mathbf{a}$, $\mathbf{V}$ a primal tree elimination process must be performed together with the elimination of a primal node in the conducting region; this process is similar to the tree-cotree decomposition described in [1, 6]. Null boundary conditions have been imposed on the external edges of the model.

SOLUTION OF THE DIRECT PROBLEM

The developed numerical formulation has been applied to the solution of TEAM problem 15. To reduce the computational effort, the flaw has been modeled as a zero thickness flaw represented with a surface S_f union of a number of dual faces $\tilde{\mathbf{s}}_i$; therefore S_f is not a plane surface. The current I_{fi} relative to each dual face $\tilde{\mathbf{s}}_i \in S_f$ have been forced to zero. To this aim, (1) is written for the flaw dual faces with $I_{fi} = 0$, while (2) gives no contribution on the flaw; (3) is modified in order to account for $I_{fi} = 0$. Of course the proposed numerical formulation can be also applied to the case of volumetric cracks. Then the *superposition of effects* and the *compensation* theorems have been applied to compute the impedance variation $\Delta\mathbf{Z} = \mathbf{Z} - \mathbf{Z}_0$ between the flawless plate impedance $\mathbf{Z}_0$ and the defected plate impedance $\mathbf{Z}$.

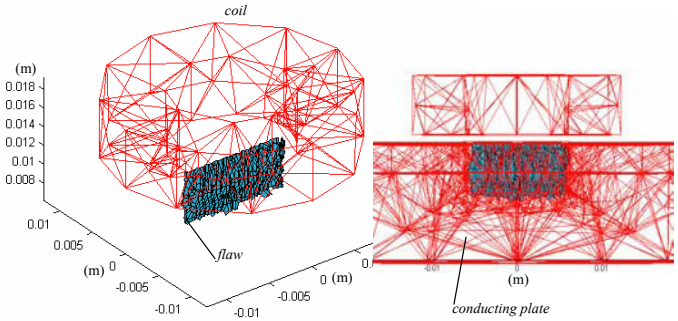

Fig. 1. On the left an isometric view of the coil primal mesh and of the 130 dual faces modeling the flaw. On the right a side view of the coil and plate primal mesh, together with the surface of the flaw.

NUMERICAL IMPLEMENTATION AND RESULTS

The numerical implementation of the 3D eddy currents code has been developed in MATLAB, with the advantage of good libraries and the drawback of limits in memory use and run time, while the standard preprocessor of ANSYS has been used to create the primal mesh.

The test experiment No 1 at 900 Hz has been considered in TEAM problem 15, where the flaw is a rectangular slot ($12.6 \times 5 \times 0.28\ \ mm^3$) in a thick conducting plate. In Fig. 1 the surface S_f modeling the defect is shown together with the primal mesh of the model. The number of tetrahedra of the primal mesh is 3030, and the number of primal edges is 3671, while 130 are the dual faces of S_f.

As an example the variation of impedance computed with the Cell Method when the coil is placed symmetrically above the defect (first position in the reference problem) is $\mathrm{Re}(\Delta\mathbf{Z}^{cell}) = 0.86\,\Omega$, $\mathrm{Im}(\Delta\mathbf{Z}^{cell}) = 1.95\,\Omega$ while the corresponding measured variations are $\mathrm{Re}(\Delta\mathbf{Z}^{meas}) = (0.2 \pm 0.1)\,\Omega$, $\mathrm{Im}(\Delta\mathbf{Z}^{meas}) = (2.2 \pm 0.2)\,\Omega$.

REFERENCES

[1] R.Albanese, G.Rubinacci, "Finite Element Method for the Solution of 3D Eddy Current Problems", Advances in Imaging and Electron Physics, vol.102, pp.1–86, April 1998.

[2] R.Albanese, G.Rubinacci, F. Villone, "An Integral Computational Model for Crack Simulation and Detection via Eddy Currents", Journal of Computational Physics 152, pp. 736-755, 1999.

[3] Tonti E., Finite Formulation of the Electromagnetic Field, Progress in Electromagnetic Research, PIER 32, 2001, pp. 1-42.

[4] S. K. Burke, "A Benchmark Problem for Computation of ΔZ in Eddy-Current Nondestructive Evaluation (NDE)," J. Nondestructive Evaluation, Vol. 7, Nos. 1/2, 1988, pp. 35-41.

[5] F. Bellina, P. Bettini, E. Tonti, F. Trevisan, Finite Formulation for the Solution of a 2D Eddy Current Problem, IEEE Trans. Mag. Vol. 38, March 2002, pp. 561-564.

[6] O. Biro, K. Preis, K. Richter, "On the use of the magnetic vector potential in the nodal and edge finite element analysis of 3D magnetostatic problems", IEEE Trans. on Mag, Vol. 32, pp. 651-654, 1996.

A Dynamic Core Loss Model for Soft Ferromagnetic and Power Ferrite Materials in Transient Finite Element Analysis

D. Lin, P. Zhou, W. N. Fu, Z. Badics and Z. J. Cendes

Ansoft Corporation, 4 Station Square, Pittsburgh, PA 15219, USA
dlin@ansoft.com ping@ansoft.com wfu@ansoft.com badics@ansoft.com zol@ansoft.com

***Abstract*—A dynamic core loss model is proposed to estimate core loss in both soft ferromagnetic and power ferrite materials with non-sinusoidal flux waveforms. The computation is based on standard core loss coefficients that are either directly provided by manufacturers, or can be extracted from the loss curve associated with sinusoidal excitation. The model is used to calculate the core loss in both 2D and 3D transient finite element analysis, and the results are compared with measured data.**

INTRODUCTION

It is still a challenging task to accurately predict the magnetization losses under various waveforms of flux density in the design of magnetic power devices such as inductors, transformers and electrical machines. Many approaches have been developed for loss computation in the frequency domain. They can be separated into two primary groups: the loss separation approach and the empirical approach.

The loss separation approach is widely used with magnetic laminations. It breaks the total core loss P_v into static hysteresis loss P_h, classical eddy current loss P_c, and anomaly loss or excess loss P_e [1]

$$\begin{aligned} P_v &= P_h + P_c + P_e \\ &= k_h f B_m^{\beta} + k_c (f B_m)^2 + k_e (f B_m)^{1.5}. \end{aligned} \quad (1)$$

From the coefficients k_h, k_c, k_e and the parameter β, the total core loss per unit volume P_v can be calculated in terms of different peak induction B_m and frequency f in the frequency domain. When this approach is applied in the time domain, computing the eddy current loss and the excess loss is straightforward, however, computing the hysteresis loss is still difficult.

A well-known empirical approach often used with ferrite materials was proposed by Steinmetz more than a century ago

$$P_v = C_m f^{\alpha} B_m^{\beta}, \quad (2)$$

where C_m, α and β are empirical parameters obtained from experimental measurement under sinusoidal excitation [2].

Many time-domain hysteresis models have been developed for instantaneous loss calculation during the last decades. These are mainly based on the Jiles-Atherton model [3, 4] or the Preisach model [5]. Although these models describe hysteresis phenomena quite well, their practical use is limited by the high number of empirical parameters required, or by the tremendous experimental effort required [6].

In this paper, an alternative dynamic hysteresis model is developed for soft magnetic and power ferrite materials. This model accurately predicts instantaneous hysteresis loss and includes the effects of minor loops. The required parameters in this model are the same as those required in the loss separation approach (1) and in the Steinmetz equation (2). These parameters are directly provided by manufacturers or can be easily extracted from standard loss curves.

FORMULATIONS

The magnetic field H in a static hysteresis loop can be decomposed into two components: a reversible component H_{rev} and an irreversible component H_{irr}. As a result, hysteresis loss can be computed by

$$\begin{aligned} P_h &= \frac{1}{T}\int_0^T (H_{rev} + H_{irr})\frac{dB}{dt}dt \\ &= \frac{1}{T}\int_0^T H_{irr}\frac{dB}{dt}dt. \end{aligned} \quad (3)$$

The reversible component can be directly obtained from the normal B-H curve without considering a hysteresis loop. It follows that H_{rev} is related to the reactive power in the material and H_{irr} is associated with the hysteresis loss. Consequently, the instantaneous hysteresis loss is

$$p_h(t) = H_{irr}\frac{dB}{dt}. \quad (4)$$

Equation (4) indicates that the key to computing $p_h(t)$ is the procedure used to obtain H_{irr}. If an equivalent elliptical loop can be provided which gives the same hysteresis loss as the original hysteresis loop, H_{irr} can be approximately evaluated.

Experiment observations indicate that under sinusoidal excitation the H_{irr}-B loop is an ellipse when the magnetic field is not saturated. When the field is saturated, we need to use an equivalent ellipse with the same area as that of the original hysteresis loop, as is shown in Figure 1.

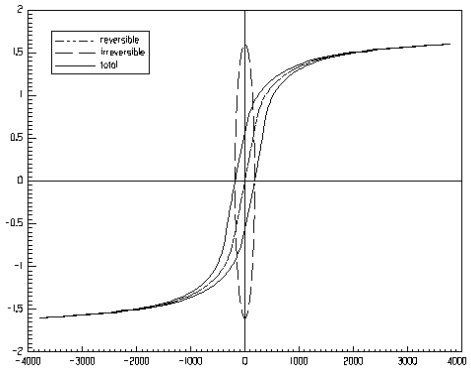

Figure 1 Reconstruction of the hysteresis loop

The ellipse in Figure 1 is described as

$$\begin{cases} B = B_m \sin(\theta) \\ H_{irr} = H_m \cos(\theta) \end{cases}. \quad (5)$$

In the above equation, B_m is obtained from a historical record of the flux density and H_m is determined using the principle that the core loss calculated from the time domain has to be the same as that from the frequency domain under the same sinusoidal excitation. Let the time-average loss derived from (3) and (5) be the same as that obtained from

$$P_h = k_h f B_m^{\beta}. \quad (6)$$

Then one obtains

$$H_m = k_h B_m^{\beta-1} / \pi. \quad (7)$$

Once H_m becomes available, H_{irr} can be determined by tracing the ellipse defined by (5). Finally, the total instantaneous core loss can be calculated as

$$p_v(t) = H_{irr} \frac{dB}{dt} + k_{ct} \left(\frac{dB}{dt} \right)^2 + k_{et} \left| \frac{dB}{dt} \right|^{1.5}. \quad (8)$$

In (8), $k_{ct} = k_c / 19.73921$, and $k_{et} = k_e / 8.763363$, where the constants are obtained by numerical integration.

Two rules are impressed in this model to obtain B_m from the history record. One is the wiping-out rule: all ellipses inside the current ellipse are wiped out. The other rule is that the current ellipse is stored in the history list if a smaller ellipse (minor loop) is created.

Similarly, the core loss formulation in the time domain for the Steinmetz equation (2) is derived as

$$p_v(t) = |K| \cdot \left| \frac{dB}{dt} \right|^{\alpha}. \quad (9)$$

In (9), K is determined in the same way as H_{irr} in (5). Thus

$$H_m = C_m B_m^{\beta-1} / I_{\alpha}, \quad (10)$$

and

$$I_{\alpha} = (2\pi)^{\alpha} \frac{2}{\pi} \int_0^{\frac{\pi}{2}} \cos^{\alpha+1} \theta d\theta. \quad (11)$$

Note that K is the irreversible component of the magnetic field H if α in (9) is 1.

APPLICATIONS

The proposed model has been used to compute the core loss in 2D and 3D transient finite element analysis (FEA) for both soft ferromagnetic and power ferrite materials. For 3D core loss computation, (8) is extended to

$$p_h(t) = \left\{ \left| H_x \frac{dB_x}{dt} \right|^{\frac{2}{\beta}} + \left| H_y \frac{dB_y}{dt} \right|^{\frac{2}{\beta}} + \left| H_z \frac{dB_z}{dt} \right|^{\frac{2}{\beta}} \right\}^{\frac{\beta}{2}}, \quad (12)$$

$$p_c(t) = k_{ct} \left\{ \left(\frac{dB_x}{dt} \right)^2 + \left(\frac{dB_y}{dt} \right)^2 + \left(\frac{dB_z}{dt} \right)^2 \right\}, \quad (13)$$

$$p_e(t) = k_{et} \left\{ \left(\frac{dB_x}{dt} \right)^2 + \left(\frac{dB_y}{dt} \right)^2 + \left(\frac{dB_z}{dt} \right)^2 \right\}^{0.75}. \quad (14)$$

Based on each component p_{vx}, p_{vy} and p_{vz}, (9) becomes

$$p_v(t) = \left\{ (p_{vx})^{2/\beta} + (p_{vy})^{2/\beta} + (p_{vz})^{2/\beta} \right\}^{\beta/2}. \quad (15)$$

Equations (12) to (15) can also be used for 2D core loss computation if B_z is set to zero.

Two application examples are provided in this paper. One application is calculating the core loss in a 250kVA three-phase amorphous metal power transformer with five legs based on 3D transient finite element analysis. The computed instantaneous core loss is shown in Figure 2. The computed time-average core loss is compared with the measured result in Table I.

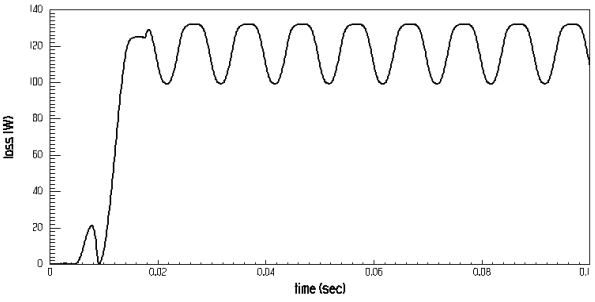

Figure 2 Computed instantaneous core loss

TABLE I. COMPUTED AND MEASURED CORE LOSS

	Computed	Measured
Core Loss	119 watts	126 watts

The other application is to evaluate the core loss in a 6/4 pole switched reluctance motor using 2D transient finite element analysis. Details will be provided in the full paper.

CONCLUSIONS

A dynamic core loss model is proposed to predict instantaneous core losses in unison with both 2D and 3D transient FE analysis. This model is practical for industrial applications because it provides reasonable accuracy and all necessary parameters are either provided directly by manufacturers, or can be extracted from manufacturer-provided loss curves.

REFERENCES

[1] G. Bertotti, "General properties of power losses in soft ferromagnetic materials," *IEEE Transactions on Magnetics,* vol. 24, no. 1, pp. 621-630, 1988.

[2] C. P. Steinmetz, "On the law of hysteresis," *AIEE Transactions*, vol. 9, pp. 3-64, 1892, Reprinted under the title "A Steinmetz contribution to the ac power revolution," introduction by J. E. Brittain, in *Proc. IEEE*, vol. 72, pp. 196-221, Feb. 1984.

[3] D. C. Jiles and D. L. Atherton, "Theory of ferromagnetic hysteresis," *J. Magn. Magn. Mater.,* vol. 61, pp. 48-60, 1986.

[4] A. Brockmeyer and L. Schulting, "Modeling of dynamic losses in magnetic material," in *Proc. EPE'93*, vol. 3, Brighton, U.K., 1993, pp. 112-117.

[5] Mayergoyz I. D., *Mathematical Models of Hysteresis,* Springer, New York, 1991.

[6] J. Reinert, A. Brockmeyer, and R. W. De Doncker, "Calculation of losses in ferro- and ferromagnetic materials based on the modified Steinmetz equation," *IEEE Transactions on Industry Applications,* vol. 37, no. 4, pp. 2087-2092, 2001

[7] Y. Saito, M. Namiki, S.Hayano, and N. Tsuya, "Experimental Verification of Chua Type Magnetization Model," *IEEE Transactions on Magnetics,* vol. 25, no. 4, pp. 2968-2970, 1989.

COMPUMAG Saratoga Springs, New York USA
July 13 - 17, 2003

Reducing the Computation Time of Non-Linear Problems by an Adaptive Linear System Tolerance

H. Vande Sande, W. Deprez., J. Decoster, F. Henrotte and K. Hameyer
Katholieke Universiteit Leuven, Dept. ESAT, Div. ELECTA, Kasteelpark Arenberg 10
B-3001 Heverlee-Leuven, Belgium
Email: hans.vandesande@esat.kuleuven.ac.be

Abstract— **Within the finite element framework, non-linear magnetic problems are often solved by an iterative line search strategy. The efforts to achieve convergence concentrate on the selection of an adequate relaxation factor. The line search is performed along a direction obtained by solving a linear system of equations. However, it is not required to compute this intermediate solution with a high accuracy, to ensure convergence. This paper shows how the accuracy of the solver can be modified at each non-linear iteration, in order to minimize the overall computation time.**

I. Introduction

NON-LINEAR problems are common in computational magnetics. When formulated in the finite element framework, they give rise to non-linear systems of equations, of which the solution is often obtained by an iterative line search procedure. Each individual cycle essentially consists of two phases: the solution of a linear system of equations in order to determine the Newton direction and the line search along that direction for a better approximation of the solution of the non-linear problem. For reducing computation time, one usually considers the second phase [1], [2], [3]. However, it is not necessary to compute the exact solution of the linear system to obtain convergence. It is rather recommended to modify the accuracy of the iterative linear solver at each non-linear step. This paper discusses how this can be done at best.

II. Test Problem

The approach to minimize the computational efforts by an adaptive system tolerance is applied to the simulation of the short-circuit operation of a 400 kW four-pole induction motor. The geometry and the computed flux lines are shown in Fig. 1. The triangular finite element mesh contains 1419 nodes and 2772 elements. The magnetic vector potential is discretized by first order nodal elements. The non-linear time-harmonic problem is solved by the Picard-method (successive substitution). The ILU-preconditioned COCG-algorithm is applied to solve the associated complex symmetric system of equations [4]. At each non-linear iteration, the relaxation parameter is determined by the cubic line search method [3]. For the analysis, the mathematical software library PETSc (Portable Extensible Toolkit for Scientific Computing) has been used [5].

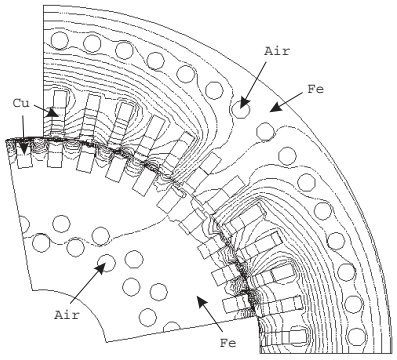

Fig. 1. The magnetic flux lines in a 400 kW induction motor under short-circuit operation.

III. Fixed Linear System Tolerance

The solution $\mathbf{d}_k$ of the linear system at the k^{th} non-linear iteration is a direction for the line search algorithm. For achieving convergence, it is only required that this direction is *descent*. This means that a relaxation parameter $\alpha_k \in [0, 1]$ can be determined such that $\|\mathbf{r}(\mathbf{A}_k + \alpha_k \mathbf{d}_k)\| < \|\mathbf{r}(\mathbf{A}_k)\|$, with $\mathbf{A}_k$ the k^{th} non-linear approximation and $\mathbf{r}$ theresidual. The exact solution $\mathbf{d}_k^*$ of the linear system is a quasi-Newton-direction here, as the Picard approach is used. Reducing the accuracy of the linear system solver causes a deviation of the computed direction $\mathbf{d}_k$ towards the steepest descent direction [3]. As long as this deviation remains small, the non-linear convergence rate is hardly affected.

Fig. 2 shows the overall computation time as a function of the linear system solver relative tolerance ϵ, at two different saturation levels. The lower curve corresponds to the case with the smallest current and requires no relaxation, whereas the upper curve requires a significant relaxation. Irrespective of the observed oscillations, it is obvious that an optimal tolerance exists. Moreover, it has a rather high value (≈ 0.3).

IV. Adaptive Linear System Tolerance

The norm of the residual, for two different values of ϵ is plotted in Fig. 3, as a function of the iteration number. Between $+$ and $\circ$ the system matrix is updated. Hence, the circles indicate the non-linear residuals $\mathbf{r}_k$ of the iteration

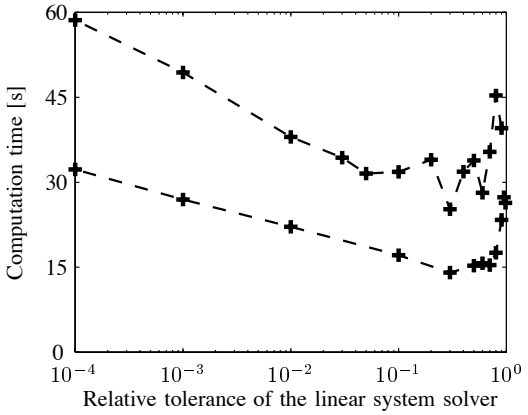

Fig. 2. The computation time as a function of the relative tolerance of the linear system solver, at two different saturation levels.

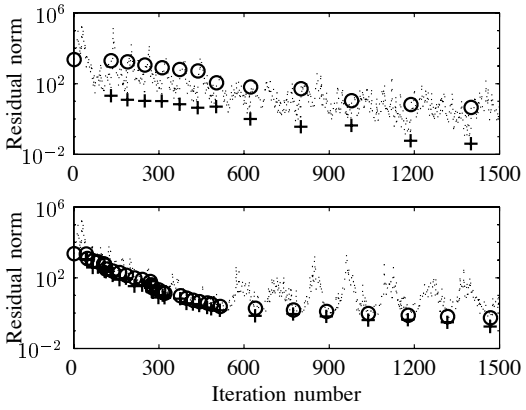

Fig. 3. The norm of the linear residual while iterating with a fixed linear system solver relative tolerance of 0.01 (top) and 0.5 (down) .

process, whereas the crosses indicate the last residual $\mathbf{r}_k^{\mathrm{lin},N}$ obtained when solving the system. The upper part of the figure, which counts for a tolerance $\epsilon = 0.01$, illustrates that the effort for solving the linear system is high, when compared to the decrease it yields for the non-linear residual. As a consequence, the ratio

$$\rho_k = \frac{\log(\|\mathbf{r}_k\|) - \log(\|\mathbf{r}_{k+1}\|)}{\log(\|\mathbf{r}_k\|) - \log(\|\mathbf{r}_k^{\mathrm{lin},N}\|)} \qquad (1)$$

is low. The lower part of the figure, obtained with $\epsilon = 0.5$, yields a much higher value of this ratio. As the latter converges faster, it is suggested to increase ϵ if ρ_k is low. However, if ρ_k is too high, the linear system solver is terminated at a moment that the non-linear residual could be further decreased. Therefore, high values of ρ_k suggest a reduction of ϵ.

Next to these observations, the lower part of Fig. 3 reveals that initially many short non-linear steps are performed. This increases the ratio of the time for building the linear system of equations to the time for solving it. Besides the fact that increasing ϵ gradually transforms the quasi-Newton method in a steepest descent method having slower convergence rates, it explains why the computation time increases at even higher values of ϵ in Fig. 2. As a consequence, it is recommended to decrease ϵ in an appropriate way if this situation occurs.

V. Results

The computations have been repeated taking the previous considerations into account. If $\rho_k > 0.6$, ϵ is divided by a factor between 1.0 and 2.0 . If $\rho_k < 0.6$, ϵ is multiplied by a factor such that ϵ cannot exceed 0.9 . The multiplication factors depend on the value of $\rho_k - 0.6$, which will be more thoroughly discussed in the full paper. Short non-linear steps are penalized by dividing ϵ by a factor between 1.0 and 2.0 . When initiating the computations with the same relative tolerances as in Fig. 2, the averages of the computation time become 17.0 s and 32.4 s, with a standard deviation of 0.8 s and 3.0 s respectively. Compared to these, the minimal computation times in Fig. 2 are 14.1 s and 25.2 s, but their average value is much higher. This obviously shows the improvement that can be obtained by modifying the relative tolerance of the linear system solver at each non-linear iteration.

VI. Conclusions

The computation time of a non-linear line search strategy is decreased by modifying the linear system solver relative tolerance at each new non-linear step. It is discussed which considerations should be taken into account. By the simulation of the short-ciruit test of an induction motor, it is illustrated that this technique yields computation times, which only slightly depend on the initial linear system solver tolerance.

Acknowledgments

The authors are grateful to the Belgian "Fonds voor Wetenschappelijk Onderzoek Vlaanderen" (project G.0427.98) and the Belgian Ministry of Scientific Research (IUAP No. P5/34).

References

[1] K. Fujiwara, T. Nakata, and N. Okamoto, "Method for determining relaxation factor for modified Newton-Raphson method," *IEEE Transactions on Magnetics*, vol. 29, no. 2, pp. 1962–1965, Mar. 1993.

[2] J. O'Dwyer and T. O'Donnell, "Choosing the relaxation parameter for the solution of nonlinear magnetic field problems by the Newton-Raphson method," *IEEE Transactions on Magnetics*, vol. 31, no. 3, pp. 1484–1487, May 1995.

[3] J. Nocedal and S.J. Wright, *Numerical Optimization*, Springer Series in Operations Research. Springer, New York, USA, 1st edition, 1999.

[4] H.A. Van der Vorst and J.B.M. Melissen, "A Petrov-Galerkin type method for solving $Ax = b$, where A is symmetric complex," *IEEE Transactions on Magnetics*, vol. 26, no. 2, pp. 706–708, Mar. 1990.

[5] S. Balay, W.D. Gropp, L. Curfman McInnes, and B.F. Smith, "PETSc users manual," Tech. Rep. ANL-95/11 - Revision 2.1.2, Mathematics and Computer Science Division, Argonne National Laboratory, 2002, See http://www.mcs.anl.gov/petsc.

Influence of Nonlinear Hysteretic Inductance on the behaviour of Electric Circuit

P.I.Koltermann - UFMS, V.M.Pereira, J.M.Ortega
Departamento de Engenharia Elétrica/DEL/CCET/UFMS/C.P. 549
79070-900 – Campo Grande – MS – Brazil
e-mail: koltermann@del.ufms.br
L.A.Righi
Departamento de Eletromecânica e Sistemas de Potência – DESP/CT/UFSM
97195-900 – Santa Maria – RS - Brazil
e-mail: righi@ct.ufsm.br

***Abstract*—This work presents an improved method for non-linear inductance calculation using the differential hysteretic reluctivity of a magnetic material. The analysis of a circuit with resistance, capacitance and inductance including non linearitiy´s and hysteresis is complex. Calculation of the non-linear inductance is important for the analysis of the low-frequency phenomena caused by switching off non-linear circuits under special circumstances. The simulation results with anhysteretic and differential hysteretic inductance calculation provides strong numerical evidence numerical for the suitability of methodology. Numerical convergence is faster than classical procedures.**

INTRODUCTION

The study of practical magnetic systems with hysteresis phenomenon is of great importance in Electric Engineering. They are employed in magnetic circuits as inductors and transformers. These magnetic circuits are strongly non-linear and can lead to serious damaged in a operation of electric systems. Ferroresonance is an oscillation which occurs in electric circuits containing a ferromagnetic-core inductor and a linear capacitor excited by a sinusoidal voltage source. Howewer, to predict ferroresonance behavior in a circuit, it is important for the magnetization characteristic of the inductor be accurately modeled since this is the only nonlinearity in the system [1].

The aim of this work is to describe a methodology for non-linear indutance calculation using the differential hysteretic reluctivity of a magnetic circuit and provide useful qualitative insights into the effect of magnetic hysteresis on the electric circuit´s behavior [2],[3].

HYSTERESIS MODEL

There are many hysteresis models and most of them are successful on situations from which they are derived using the field **H** as input variable, as for instance the well known Jiles-Atherton model [4].

We propose in this work, a method presenting as independent variable, the magnetic induction **B**. We define the static hysteresis in terms of a first-order differential equation which can readly be incorporated into the overall differential equation that describes the circuit. The differential equation of static hysteresis is given by [5]:

$$\int_{\Delta B} H_H dB = \int_{\Delta B} H_{HS} L(\lambda_H) dB - I_D \gamma_H \int_{\Delta B} \frac{dH_H}{dB} dB \quad (1)$$

where $L(\lambda_H)$ is the Langevin function of λ_H and,

$$\lambda_H = \frac{H_H + I_D H_{HS}}{a_H} \quad (2)$$

where "I_D" is a directional variable and ΔB is the flux density variation. In (1) and (2), "a_H", "H_{HS}" and "γ_H" are model parameters. An iterative procedure can be used to obtain H_H from (1). Newton's method is employed in this work.

One can express the relationship between the magnetic field **H** and magnetic induction **B** by means of a differential reluctivity tensor $\|\nu_d\|$. Using Euler's scheme to represent the derivatives, we can express [5]:

$$\|\nu_d\| = \frac{\Delta \mathbf{H}}{\Delta \mathbf{B}} \quad (3)$$

where $\Delta \mathbf{H} = \mathbf{H}(t) - \mathbf{H}(t - \Delta t)$, $\Delta \mathbf{B} = \mathbf{B}(t) - \mathbf{B}(t - \Delta t)$, and Δt is the time step.

Equation (3) can now be written in terms of two successive time steps as:

$$\mathbf{H}(t) = \|\nu_d\| \Delta \mathbf{B} + \mathbf{H}(t - \Delta t) \quad (4)$$

The inductance depends on the differential reluctivity, which is the slope of the hysteresis curve. Normaly as the current drives the flux into saturation the inductance drops to its lowest value. The variation in inductance can be minimized by limiting the current swings since the smaller BH loops are more linear. It is known that the relationship between inductance, flux and number of turns is expressed by means of the following expression:

$$L = \frac{\psi}{i} = \frac{N^2 S}{\upsilon \ell_{Fe}} \quad (5)$$

where ν is the reluctivity. It has been considered here two cases: classical anhysteretic reluctivity and differential hysteretic reluctivity.

CIRCUIT APPLICATION

Fig. 1 shows the circuit diagram. The capacitor C and resistor R are linear. For the simulation V_s= 62.5 V, C=148.6μF and R= 1.5 ohms. For the magnetic circuit we have S_{FE}=0.000105 m^2, N=700 and ℓ_{FE} = 0,94 m.

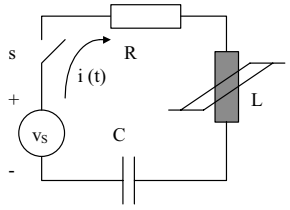

Fig. 1 - Circuit RLC – Nonlinear inductance

It is now possible to write the governing equations in the time domain for the circuit. Kirchoff´s voltage law gives

$$\begin{aligned} &Ri(t) + L\frac{di(t)}{dt} + \frac{1}{C}\int i(t)dt = V_s(t) \\ &C\frac{dV_s(t)}{dt} = i(t) \end{aligned} \tag{6}$$

where $V_s(t)$ denotes the sinusoidal supplied voltage.

Equation (6) is calculated by differentiating the first term, as below,

$$L\frac{d^2i(t)}{dt^2} + R\frac{di(t)}{dt} + \frac{1}{C}i(t) = \frac{dV_s(t)}{dt} \tag{7}$$

The system in Fig. 1 is governed by a second order differential equation. There are two variable states: the flux-linkage Ψ in the inductor and the voltage V of the capacitor.

We can introducing the differential inductance L_Δ that allows us to write the current as,

$$i_k = i_{k-1} + \frac{1}{L_\Delta}(\psi_k - \psi_{k-1}) \tag{8}$$

This calculation represents the fundamental step of numerical integration in (9) by Euler procedure considering the hysteresis.

$$\begin{cases} \dfrac{dV_C}{dt} = \dfrac{1}{C}i_{k-1} + \dfrac{1}{CL_\Delta}(\psi_k - \psi_{k-1}) \\ \dfrac{d\Psi}{dt} = -V_C - Ri_{k-1} - \dfrac{R}{L_\Delta}(\psi_k - \psi_{k-1}) \end{cases} \tag{9}$$

If X is the state vector, X(1) =ψ, X(2)=V_C, the equation is written dX/dt=F(X,t). This is a nonlinear differential equation where time appears explicitly, but through a periodic function.

OBTAINED RESULTS

With the objective of evaluating the studied model under the practical view, a simulation test has been realized. The utilized circuit has the following parameters of the hysteresis model [5]: M_s=1.12 x10^6 A/m, a=110.16 A/m e α=0.0001433, H_{HS}=270 A/m, γ_H=0.15252.

For the resolution of the differential circuit equation the Euler procedure has been used. The results obtained to nonlinear inductance calculation are presented as follows, considering the anhysteretic and hysteretic modeling.

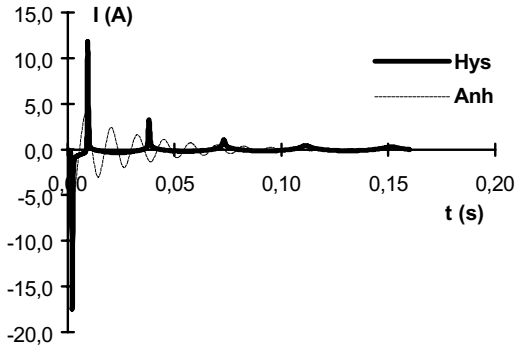

Fig. 2 - Current versus time

The magnetizing current is cleared and the frequency of oscillation is determined by the primary inductance at each moment and the capacitance. The remaining energy in the coil oscillates between the inductance and capacitance and is dissipated in a short time. One hypothesis is that reduced core loss levels are contributing to the apparent increase in ferroresonance susceptibility of recent transformers.

CONCLUSIONS

The numerical calculation of a non-linear hysteretic inductance shows good convergence and we consider that the adopted methodology is efficient. More details will be provided in the full paper.

REFERENCES

[1] H. Lamba, M. Grinfeld, S. Mckee, et al, "Subharmonic Ferroresonance in an LCR Circuit with Hysteresis", *IEEE Transactions on Magnetics,,* vol. 33, No.4, pp. 2495-2500, July 1997.

[2] F. Delincé, A. Nicolet, F. Henrote, et al, "Influence of Hysteresis on the Behaviour of Coupled Finite Element – Electric Circuit Models", *IEEE Transactions on Magnetics,,* vol. 30, No.5, pp. 3383-3386, September 1994.

[3] J. H.B. Deane "Modeling the Dynamics of Nonlinear Inductor Circuits", *IEEE Transactions on Magnetics,,* vol. 30, No.5, pp. 2795-2801, September 1994.

[4] D. Jiles, *Introduction to Magnetism and Magnetic Materials*, Chapman & Hall, 1991, London.

[5] P. I. Koltermann, L. A. Righi, J. P. A. Bastos, et al, "A modified Jiles method for hysteresis computation including minor loops", *Physica B N.H Elsevier Science,* pp. 233-237, 275(2000), The Netherlands.

[6] L. A. Righi, P.I.Koltermann, N.Sadowski, et al, "Non-Linear Magnetic Field Analysis by FEM using Langevin Function", *IEEE Transactions on Magnetics,* vol. 36, No.4, pp.1263-1266, July 2000.

COMPUMAG Saratoga Springs, New York USA
July 13 - 17, 2003

TEQSAS - Transient Electro-Quasi-Statics Adaptive Simulation - Schemes

Markus Clemens, Herbert De Gersem, Wigand Koch, Markus Wilke, and Thomas Weiland

Technische Universität Darmstadt, Dept. Electrical Engineering and Information Technology,

Computational Electromagnetics Laboratory (TEMF), Schloßgartenstr. 8, D-64289 Darmstadt, Germany

email: clemens/degersem/wilke/weiland@temf.tu-darmstadt.de. wigand.koch@cst.de

Abstract— **A transient electro-quasi-static solver based on the Finite Integration Technique (FIT) is presented which is capable of simulating high-voltage devices where both dielectric and nonlinear conductive effects are considered in the insulation materials. Metallic conductors are modeled by floating potential constraints which require specialized solution techniques. The applied error-controlled adaptive linear–implicit time-integration scheme avoids an inner nonlinear iteration loop. The efficiency of the algorithms is illustrated by numerical tests.**

I. Introduction

Recently, a transient electro-quasi-static formulation and related numerical schemes for the time domain analysis of high voltage devices such as thermistors, capacitors or condenser bushings were published in [1], [2]. In the electro-quasi-static regime, the diffusion time is much smaller than the characteristic time of the considered problem. While effects related to the variation of the magnetic flux densities can be neglected ($\frac{\partial}{\partial t}\vec{B} \equiv 0$), the irrotational parts of the displacement currents have to be taken into account. Introducing such electro-quasi-static assumptions into Maxwell's equations allows the representation of the electric field strength by a scalar potential ϕ such that $\vec{E} = -\operatorname{grad}\phi$ and

$$\operatorname{div}\left(\frac{d}{dt}(\epsilon \operatorname{grad}\phi(t))\right) + \operatorname{div}\left(\kappa \operatorname{grad}\phi(t)\right) = 0. \qquad (1)$$

The presence of materials as pressboard or insulator oils with low electrical conductivity values $\sigma(\vec{r}) = \sigma(\vec{r}, \vec{E})$ depending on the electric field intensity and externally applied transient voltages render the formulation (1) a nonlinear initial boundary value problem.

II. Transient Electro-Quasi-static Fields with FIT

The spatial discretization of (1) with the Finite Integration Technique (FIT) [3] leads to the governing system of stiff ordinary differential equations (ODEs)

$$\widetilde{\mathbf{S}}\mathbf{M}_{\varepsilon}\widetilde{\mathbf{S}}^T \frac{d}{dt}\mathbf{\Phi}(t) + \widetilde{\mathbf{S}}\mathbf{M}_{\kappa}(\mathbf{\Phi})\widetilde{\mathbf{S}}^T\mathbf{\Phi}(t) = 0. \qquad (2)$$

where $\widetilde{\mathbf{S}}$ and $\widetilde{\mathbf{S}}^T$ are the discrete divergence and gradient matrices and where $\mathbf{M}_{\varepsilon}$ and $\mathbf{M}_{\kappa} = \mathbf{M}_{\kappa}(\mathbf{\Phi})$ are material matrices combining the permittivities and field dependent electrical conductivities with the the metric information of the grid [2]. The stiffness of this ODE system necessitates the use of implicit time integration schemes to follow the nonlinear transient evolution of the discretized high voltage problems.

M. Wilke is supported by the Deutsche Forschungsgemeinschaft (DFG) under grants WE1239/13-1 and WE1239/17.

III. Numerical Approach

A. Adaptive Time Stepping

In [1] and [2] only standard implicit $\theta-$time integration methods with a Richardson-extrapolation time step selection scheme and standard nonlinear iterations were used for the transient simulation of electro-quasi-static fields. Here, motivated by previous experience for magneto-quasi-static simulations [4], we propose the use of linear-implicit Rosenbrock-Wanner time integration schemes [5] for the electro-quasi-static system (2).

These one-step methods of implicit Runge-Kutta-type are s-stage schemes, which allow to combine an error-controlled time integration of (2) and nonlinear updates in a single iteration loop:

$$\left[\frac{1}{\gamma\Delta t}\widetilde{\mathbf{S}}\mathbf{M}_{\varepsilon}\widetilde{\mathbf{S}}^T + \widetilde{\mathbf{S}}\mathbf{M}_{\frac{\partial J}{\partial E}}\left(\Phi^n\right)\widetilde{\mathbf{S}}^T\right]\hat{\mathbf{\Phi}}_{ni} = -\widetilde{\mathbf{S}}\mathbf{M}_{\kappa}(\hat{\mathbf{\Phi}}_i)\widetilde{\mathbf{S}}^T\hat{\mathbf{\Phi}}_i - \widetilde{\mathbf{S}}\mathbf{M}_{\varepsilon}\widetilde{\mathbf{S}}^T \cdot \sum_{j=1}^{i-1}\frac{c_{ij}}{\Delta t}\hat{\mathbf{\Phi}}_{nj}, \qquad (3)$$

for $i = 1 \ldots s$ with $t^i = t^n + \alpha_i\Delta t$, $\hat{\mathbf{\Phi}}_i = \Phi^n + \sum_{j=1}^{i-1} a_{ij}\hat{\mathbf{\Phi}}_{nj}$ and the new time solution $\Phi^{n+1} = \Phi^n + \sum_{i=1}^{s} m_i\hat{\mathbf{\Phi}}_{ni}$. The coefficients a_{ij}, c_{ij}, α_i ,γ_i, γ and m_i determine the specific Rosenbrock method. A second coefficient set $\hat{m}_i$ yields an embedded lower order solution, which compared to the higher order solution, yields an error criterion. Only the accuracy threshold , i.e., the relative error tolerance $rtol$, specified to control the combined time-integration and the nonlinear iteration process has to be specified and only linear algebraic systems of equations have to be solved in (3).

B. Floating Potentials

If metallic bodies have to be considered in the computational domain, they can be interpreted as macro elements with one unknown potential value, i.e., a floating potential, [6]. In order to keep the band structure of the system matrix in (2) unperturbed, the floating potentials are inserted as additional constraints $\mathbf{\Phi}_i - \mathbf{\Phi}_j = 0$ for all nodes i and j in a floating potential body in a saddle-point formulation [7] The constraints are collected in a matrix $\mathbf{B}$ with $\mathbf{B}\mathbf{\Phi} = \mathbf{0}$ and added to the time discretized system (2) introducing a set of Lagrange multipliers λ [2] to yield

$$\begin{bmatrix} \mathbf{K} & \mathbf{B}^T \\ \mathbf{B} & \mathbf{0} \end{bmatrix}\begin{bmatrix} \mathbf{\Phi} \\ \lambda \end{bmatrix} = \begin{bmatrix} \mathbf{f} \\ \mathbf{0} \end{bmatrix}. \qquad (4)$$

The symmetric, indefinite, linear system (4) can be solved by the Minimal Residual method using a Jacobi-block-preconditioner based on $\mathrm{diag}(\tilde{\mathbf{K}}, \tilde{\mathbf{A}})$, where $\tilde{\mathbf{K}}$ denotes a preconditioner for $\mathbf{K}$, preferably multigrid, and $\tilde{\mathbf{A}}$ an approximation to the Schur complement $\mathbf{A} = \mathbf{B}\mathbf{K}^{-1}\mathbf{B}^T$ [8]. A fair choice for $\tilde{\mathbf{A}}$ is $\tilde{\mathbf{A}} = \mathbf{B}\mathbf{D}^{-1}\mathbf{B}^T$, where $\mathbf{D}$ is the main diagonal of $\mathbf{K}$. A better $\tilde{\mathbf{A}}$ can be constructed based on the underlying differential problem. The Lagrange multiplier vector λ represents the charges at the equi-potential surfaces. The system

$$\mathbf{A}\lambda = \mathbf{B}\mathbf{K}^{-1}\mathbf{f} \tag{5}$$

expresses the relation between these charges and and the applied volume charges and boundary potentials, as represented by $\mathbf{f}$. As a consequence, (5) can be interpreted as a system $\mathbf{C}\mathbf{q} = \mathbf{V}$ with $\mathbf{C}$ a capacitance matrix, $\mathbf{q}$ a vector of unknown charges at the equipotential surfaces and $\mathbf{V}$ a vector of applied voltages. An alternative formulation for (4) is obtained by using the orthogonal projection operator $\mathbf{P} = \mathbf{I} - \mathbf{B}^T\left(\mathbf{B}\mathbf{B}^T\right)^{-1}\mathbf{B}$ and solving the symmetric, positive-definite system $\mathbf{P}^T\mathbf{K}\mathbf{P}\mathbf{u} = \mathbf{P}^T\mathbf{f}$ by the Conjugate Gradient (CG) method. The preconditioned system is $\mathbf{P}\tilde{\mathbf{K}}^{-1}\mathbf{P}^T\mathbf{K}\mathbf{P}\mathbf{u} = \mathbf{P}\tilde{\mathbf{K}}^{-1}\mathbf{P}^T\mathbf{f}$ and requires two applications of the projector in each CG step.

IV. Numerical Results

For a verification of the proposed schemes a simple test configuration is studied: A plate capacitor with a layered dielectricum of 10 cm depth (Fig. 1). The layers parallel to the plates consists of two lossy dielectric materials with different permittivities and conductivities dependent on the surrounding potential distribution according to $\kappa_i\left(|\vec{E}|\right) = \kappa_{0i}\left(\frac{|\vec{E}|}{E_0}\right)^2 + \bar{\kappa}_i$.

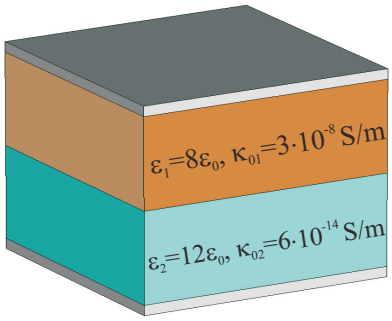

Fig. 1. Plate capacitor with layered dielectricum with nonlinear conductivity

Since the model represents an infinitely extended configuration parallel to the plates by adopting appropriate boundary conditions, an analytical calculation yields the occuring potentials as well as the nonlinear conductivity distribution. Fig. 2 compares the corresponding values near the top plate. The diagrams also show the sampling of the applied excitation consisting of a DC voltage of 200kV superposed by a sinusoidal oscillation with a frequency of 50Hz and an amplitude of 50kV. The relative tolerance for the nonlinear time-stepping process was set to 10^{-3} and resulted in a sequence of 12 accepted and 12 rejected steps in the transient simulation, following a calculation of a nonlinear stationary current flow problem for the start time.

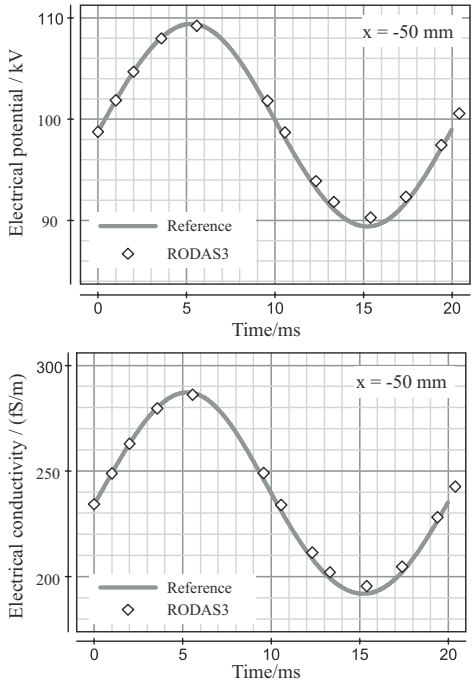

Fig. 2. Comparison of analytical and numerical calculations with the adaptive linear-implicit scheme RODAS3 [5] for a potential and a conductivity values

V. Conclusion

Transient electro-quasi-static adaptive simulation (TEQSAS) schemes were introduced, using error-controlled time step selective linear-implicit time integration methods for a nonlinear electro-quasi-static field formulation based on the FIT. Floating potentials that can be included by a Lagrange multiplier formulation result in indefinite algebraic systems of equations, for which a positive definite alternative and several preconditioning strategies are presented. First numerical results with the adaptive scheme (3) are achieved for a simple problem. More realistic problems will be presented in the upcoming full paper.

References

[1] K. Preis, O. Bíró, P. Supancic, and I. Ticar, "Fem simulation of thermistors including dielectric effects," in *Proc. CEFC 2002, Perugia, Italy, 16.-19. June*, E. Cardelli, Ed., 2002.

[2] M. Clemens, H. De Gersem, W. Koch, M. Wilke, and T. Weiland, "Transient simulation of nonlinear electro-quasistatic problems using the finite integration technique," in *Proc. IGTE 2002, Graz*, 2002.

[3] T. Weiland, "Time domain electromagnetic field computation with finite difference methods," *Int. J. Num. Mod.:ENDF*, vol. 9, pp. 259–319, 1996.

[4] M. Clemens, M. Wilke, and T. Weiland, "Linear-implicit time integration schemes for error-controlled transient nonlinear magnetic field simulations," in *Proc. CEFC 2002, Perugia*, 2002, p. 332, Submitted to IEEE Trans. Magn.

[5] J. Lang, *Adaptive Multilevel Solution of Nonlinear Parabolic PDE Systems: Theory, Algorithm and Application*, Springer-Verlag, Berlin, Heidelberg, New York, 2001.

[6] P. Dular, W. Legros, and A. Nicolet, "Coupling of local and global quantities in various finite element formulations and its application to electrostatics, magnetostatics and magnetodynamics," *IEEE Trans. Magn.*, vol. 34, no. 5, pp. 3078–3081, September 1998.

[7] F. Brezzi and M. Fortin, *Mixed and Hybrid Finite Element Methods*, Springer-Verlag, Berlin, 1991.

[8] B. Fischer, A. Ramage, D.J. Silvester, and A.J. Wathen, "Minimum residual methods for augmented systems," *BIT*, vol. 38, no. 3, pp. 527–543, 1998.

2D Electric Field Computation in HV Insulation Using Non Linear Semi Conducting Material by Coupling BE and FETD Methods.

T. Toledo, F. Buret, J. A. De Vasconcelos, L. Krähenbühl
CEGELY - UMR CNRS 5005 - Ecole Centrale de Lyon - 36, av. Guy de Collongue - Ecully - 69131 - France
Depto. Eng. Elétrica - Universidade Federal de Minas Gerais (UFMG) - Belo Horizonte - Minas Gerais - Brasil

***Abstract* - Semi-conducting material with non linear behavior are used in HV insulating system to make uniform the electric field in order to lower the dielectric constraints. The optimization of this kind of structure needs an accurate evaluation of the electric field. BEM is known to be very well adapted to electric field computation especially in open boundary configuration that is mainly encountered in outdoor insulation. On the other hand this method is restricted to linear problems and the presence of a material with a non-linear behavior implies the implementation of another type of discretisation like the FEM. This paper presents a coupling between BEM and FEM that will permit to simulate, thanks to a time step method, the evolution of the electric field in an insulation structure built with classical dielectric materials and other material with a non-linear conductivity.**

INTRODUCTION

The interest of non-linear material is well known in HV insulation technology [1]. Indeed this kind of material permits to make uniform the electric field in bushing type structure that are encountered each time there is a transition from an internal to outdoor insulation.

The efficiency of non-linear materials is mainly linked to the degree of non-linearity that can concern the permittivity and the electrical conductivity. The non-linear conductivity should be implemented only with time varying voltage. Presently it is for the electrical conductivity that the technology permits to elaborate materials with the largest scale of variation. HV apparatus are concerned by a frequency domain ranging from 50 Hz to a few hundreds of kHz. Hence, the conductivity has to be in the domain from 10^{-6} to 10^{-14} Sm^{-1} for electric field value about a few kV/mm; that let them considered as non-linear semi conducting material (NLSC).

This kind of material can be implemented in thin layer (less than 1 mm) as a coating. They are available as paint or ribbon. An example of utilization is the anti corona layer which is deposed on the stator bars at the coil head in rotating machine. These configurations can be computed by modeling the layer as a surface with adapted property (surface conductivity). This description fits quite well with BEM [2].

In other situation like in solid cable extremity, the semiconducting (SC) zone is a volume with non-negligible dimension in each direction. The required conductivity is obtained by introducing the appropriate quantity of ZnO grains (Zinc oxyde) added directely in the polymere. For these configurations the NLSC region must be discretized using FEM to take into account the permittivity and the non-linear conductivity. The other regions are treated by BEM.

At each time step (Region NL, Fig. 1), the convergence of the non-linearity is obtained by a direct iteration scheme that found the values of the conductivity at each node of the FE mesh.

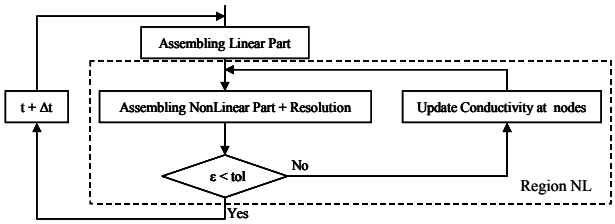

Fig. 1. Global algorithm of the method

BOUNDARY ELEMENT FORMULATION

For each time step, in the dielectric region it is necessary to solve an electrostatic problem governed by Laplace's equation. The boundary element method applied to an electrostatic problem came from the second Green identity in the space:

$$\iiint_{\Omega}\left(V\nabla^2 G - G\nabla^2 V\right)d\Omega = \oiint_{\Gamma}\left(V\nabla G - G\nabla V\right)\cdot d\boldsymbol{\Gamma}\,. \qquad (1)$$

Where G is the Green function to 3D electrostatic case :

$$G(\mathbf{r},\mathbf{r}') = \frac{1}{4\pi\,|\,\mathbf{r}-\mathbf{r}'|}\,. \qquad (2)$$

From Eq. (1), we can express the potential in every node of the boundary Γ by superposition of the potential and its normal derivative of each node of the boundary.

Considering Fig. 2, the Laplace's equation gets the following integral form where c is equivalent to the solid angle at the observation point:

$$cV(\mathbf{r}) = \oint_{\Gamma}\left\{\frac{\partial G_{2d}(\mathbf{r},\mathbf{r}')}{\partial n}V(\mathbf{r}') - G_{2d}(\mathbf{r},\mathbf{r}')\frac{\partial V(\mathbf{r}')}{\partial n}\right\}d\Gamma\,, \quad (3)$$

where **r**, **r`** and **n** are, respectively, the vector position of the observation point, of the integration point and the unit normal vector of the boundary (Γ) enclosing the region (Ω).

The system of equations enables us to find the potential V and its normal derivative $\partial V/\partial n$ unknowns on the borders of the dielectric region.

FINITE ELEMENT METHOD

The conducting region is characterized by a conductivity σ and a relative permittivity ε. If we write the total electric

current density **J** as the sum of the conduction and displacement current densities, we obtain the following relation:

$$\mathbf{J} = -\sigma\nabla V - \varepsilon_0\varepsilon\frac{\partial}{\partial t}\nabla V \qquad (4)$$

Taking the divergence of both sides of Eq. (4) and considering the continuity equation ($\nabla\cdot\mathbf{J} = 0$), the following conduction equation can be derived:

$$\nabla\sigma.\nabla V + \sigma\nabla^2 V + \varepsilon_0\varepsilon\frac{\partial}{\partial t}\nabla^2 V = 0 \qquad (5)$$

Because of the non-linearity, we cannot study the phenomenon in harmonic regime. So, we approximate the time derivative by an Euler difference scheme [3]:

$$\left.\frac{\partial V}{\partial t}\right|_i = \frac{V^i - V^{i-1}}{\Delta t} \qquad (6)$$

Finally, the equation governing the conductivity is:

$$\Delta t\nabla\sigma.\nabla V^i + \Delta t\sigma\nabla^2 V^i + \varepsilon_0\varepsilon\nabla^2 V^i - \varepsilon_0\varepsilon\nabla^2 V^{i-1} = 0 \qquad (7)$$

Weighting Eq. (7) by functions W, integrating over the conducting area, and integrating by parts, we obtain:

$$-\iint_\Omega (\Delta t\sigma + \varepsilon_0\varepsilon)\nabla W.\nabla V^i d\Omega + \int_\Gamma (\Delta t\sigma + \varepsilon_0\varepsilon) W\frac{\partial V^i}{\partial n}d\Gamma$$
$$= -\iint_\Omega \varepsilon_0\varepsilon\nabla W.\nabla V^{i-1}d\Omega + \int_\Gamma \varepsilon_0\varepsilon W\frac{\partial V^{i-1}}{\partial n}d\Gamma \qquad (8)$$

This equation after discretization gives a system of equations that must be coupled with the equation system originated by the boundary element method.

COUPLING

To permit the coupling of both equation systems originated by FEM and BEM [4], we must impose at the dielectric–conductor interface the boundary condition:

$$\varepsilon_1\frac{\partial V_1}{\partial n} - \varepsilon_2\frac{\partial V_2}{\partial n} = \frac{\Theta}{\varepsilon_0} \qquad (9)$$

The Eq. (9) introduces a new unknown in each node of the interface dielectric-conductor, the electric charge density (Θ). To complete the system of equations, the continuity equation (Eq. (10)) for the linear current density can be used to have the same number of equations and unknowns.

$$\sigma\frac{\partial V}{\partial n} - \frac{\partial\Theta}{\partial t} = 0 \qquad (10)$$

VALIDATION

We validate the code, with a cylinder capacitor, infinite along z, with a non-linear conducting (Fig. 3, gray region).

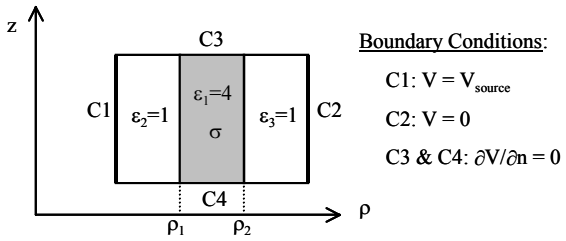

Fig. 3. Cylindrical Capacitor.

The non-linear conductivity is governed by Eq. (11), where σ_o is the conductivity amplitude for E = 0:

$$\sigma(E) = \sigma_0\exp(\alpha E). \qquad (11)$$

Two kinds of voltage sources, a sinusoidal source (s_1) $V_0 sin(100\pi t)$ and a lighting impulse source (s_2) $V_0\left(\exp(-2.10^4 t) - \exp(-1.10^6 t)\right)$, were used. The parameter values to (11) used are $\sigma_0 = 1.10^{-9}$ and $\alpha = 1.10^{-4}$.

To validate the code, the problem was analyzed as a one-dimensional and as a two-dimensional model. The results are presented in Table I, obtained by using the proposed hybrid technique and a one dimensional FEM, for two points ρ_1 and ρ_2 as showed in Fig. 3.

TABLE I
COMPARISON BETWEEN THE TWO METHODS

V_0		S1			S2		
		FEM1D	BEMFEM	Error	FEM1D	BEMFEM	Error
1000 V	$V(\rho_1)$	506	517	2 %	676	708	4 %
	$V(\rho_2)$	248	244	1.6%	107	111	3.7%
3000 V	$V(\rho_1)$	1170	1178	0.6%	1670	1777	6 %
	$V(\rho_2)$	877	865	1.3%	504	558	10 %

The accuracy of the results is acceptable for the power frequency but became worse for the lightning impulse constraint, which has much higher frequency components. This problem may be due to a too simple time scheme used that can be improved by introducing a relaxation coefficient (implicit method).

In the full paper, a complete analysis of these results will be given and the problem of an HV cable extremity of NLSC material will be presented.

Acknowledgement **- This work was carried out at the UFMG, Brazil. We wish to thank the Franco/Brazilian convention CAPES/COFECUB to support this research.**

REFERENCE

[1] M. Msuda, A. Ogata, M. Nitta and T. Tani, "A study of volume resistivity for high voltage power cable semiconducting layer", *Proc. 5th Int. Conf. on Properties and applications of Dielectric Materials*, May 25-30, 1997, Seoul, Korea.

[2] Z. Yeo, F. Buret, L. Kräenbühl and Ph. Auriol, "A non linear model for surface conduction", *IEEE Trans. on Magnetics*, vol. 34, n°5, September 1988, pp 2617-2620.

[3] J. C. Heinrich, D. W. Pepper, *Intermediate Finite Element Method*, Taylor & Francis, 1999, pp. 260.

[4] J. Fetzer, S. Kurz, and G. Lehner, "The coupling of boundary elements and finite elements for nondestructive testing application," *IEEE Transaction on Magnetics*, Vol. 33, No. 1, Janury 1997.

Magnetic Field Analysis of Ferrite Core Considering Frequency Dependence of Complex Permeability

Masato Enokizono and Takuji Kawashima
Department of Electrical and Electric Engineering, Factory of Engineering, Oita University
700 Dannoharu, Oita, 870-1192, Japan
e-mail: kawashima@mag.eee.oita-u.ac.jp

Abstract — **This paper presents magnetic flux distribution and iron loss distribution in a ferrite core under pulse excitation by using the finite element method. It is difficult to consider the magnetic characteristics in numerical analysis under the pulse excitation. The magnetic characteristics under the pulse excitation is examined by using the magnetic characteristics of each frequency component after Fourier expansion.**

INTRODUCTION

RECENTRY, the switching power supplies are widely being used as the stabilized DC power supplies for applied electronic devices. Mn-Zn ferrite cores have been widely used to the transformers of the switching power supplies. The high efficiency of the switching power supplies has been performed by the higher frequency of the switching.

Mn-Zn ferrite can keep the high permeability up to the limited frequency range, though, the permeability decreases immediately after this range because of the resonance and magnetic domain resonance which are known as Snoek's limit [1]. Therefore, the permeability of the ferrite materials has non-linearity depending on the frequency.

Conventionally, the numerical analysis for the magnetic materials whose permeability has frequency dependence hasn't been examined yet. Moreover, the eddy currents are usually neglected because of the high-resistivity of ferrite cores. However, the resistivity of Mn-Zn ferrite cores is rather small in higher frequency range, so, the eddy currents should not be neglected. The ferrite materials of the transformers of the switching supplies are excited under the pulse waveform, then the numerical analysis of them is difficult. In this paper, Fourier expansion was applied to the pulse wave of the excitation to carry out the numerical analysis at each frequency component. The permeability depending on the frequency derived from the measured data was used for the numerical analysis to each frequency component to take account into the frequency dependence of the complex permeability. After the numerical analysis of each frequency, the results are supervised to examine the magnetic characteristics under the pulse excitation. The Chua-Type-Model was applied for the numerical procedure to consider the complex permeability [2].

FORMULATION

Governing Equation

We used the complex approximation to introduce the complex permeability into the finite element method. The governing equation in the linear two-dimension can be written as (1) from Maxwell's equations with the assumption that all physical quantities vary sinusoidally,

$$\dot{\mu}(\omega)\left(\frac{\partial^2}{\partial x^2}\dot{A}+\frac{\partial^2}{\partial y^2}\dot{A}\right)=-\dot{J}_0+\sigma\frac{d\dot{A}}{dt}, \tag{1}$$

where $\dot{A}$ is the magnetic vector potential in z direction, $\dot{J}_0$ the exciting current density, $\dot{\mu}$ the complex permeability, ω the supply angular frequency, and σ the conductivity. All physical quantities are assumed as the complex number in this paper. The magnetic vector potential and exciting current can be presented as (2) after Fourier expansion.

$$\begin{cases}\dot{J}_0=\sum_{n=1}^{\infty}\dot{J}_{0n}\cos\{(2n-1)\omega t+\varphi_{Jn}\}\\ \dot{A}=\sum_{n=1}^{\infty}\dot{A}_n\cos\{(2n-1)\omega t+\varphi_{An}\}\end{cases}, \tag{2}$$

where $\varphi_{Jn},\varphi_{An}$ are the phase difference of the exciting current and magnetic vector potential between real part and imaginary part, respectively. Also, Electric devices are usually supplied by constant terminal voltage, so we adopted the terminal voltage method for the numerical analysis.

Complex permeability

The phase difference occurs when the magnetic materials are excited by the high alternating field. Then, we used the Chua-Type-Model as the magnetization characteristic model of the magnetic material to consider the phase difference. The relation between the magnetic flux density *B* and magnetic field strength *H* is expressed by the following equation by the Chua-Type Model,

$$H=\frac{1}{\mu}B+\frac{1}{s}\left(\frac{dB}{dt}-\mu_r\frac{dH}{dt}\right), \tag{3}$$

where s is the hysterics coefficient, μ the permeability, and

μ_r the reversible permeability. By substituting $j\omega$ for $\partial/\partial t$, Eq (3) is written as ,

$$\mu(\omega)=\frac{B}{H}$$
$$=\mu\left(\frac{s^2+\omega^2\mu\mu_r}{s^2+(\omega\mu)^2}\right)-j\mu\left(\frac{\omega(\mu-\mu_r)s}{s^2+(\omega\mu)^2}\right)=\mu_R(\omega)-j\mu_I(\omega) \quad (4)$$

where μ_R is the real part of complex permeability and μ_I the imaginary part. Complex permeability calculated from Eq(4) is used for our numerical analysis.

RESULTS AND DISCUSSIONS

Fig. 1 shows the complex permeability curve of the ferrite core by calculating the Chua-Type Model. The calculated and the measurement curves are obtained by Eq. (4) by using the values, μ is 8.564e-4, μ_d 1.0091e-5 and s 5.3809e4. These parameter values were derived from the measurement. Figs.2 (a) and (b) show the hysterics loops between the magnetic flux density B and the magnetic field strength H under the sinusoidal alternating excitation at 1MHz. Figs. 2 (c) and (d) show the waveforms of them under the same excitation. Fig .2 (a) and (c) show the measured results and (b) and (d) show the calculated ones. By comparing the measured with the calculated, it can be said that the numerical results agree with the measured ones very well. Fig.3 show the iron loss distribution under the pulse excitation considering up to 15th harmonic components. To consider frequency dependence of the complex permeability, we used the each complex permeability value at each frequency component.

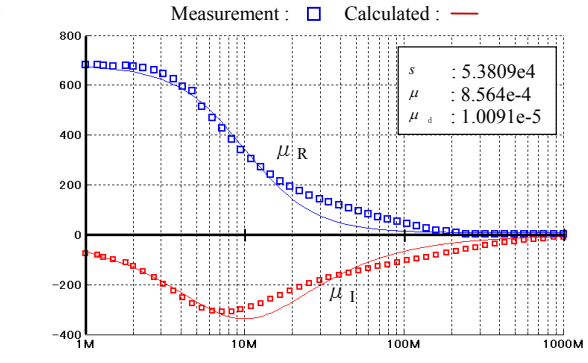

Fig. 1. Complex permeability by using Chua-Type-Model

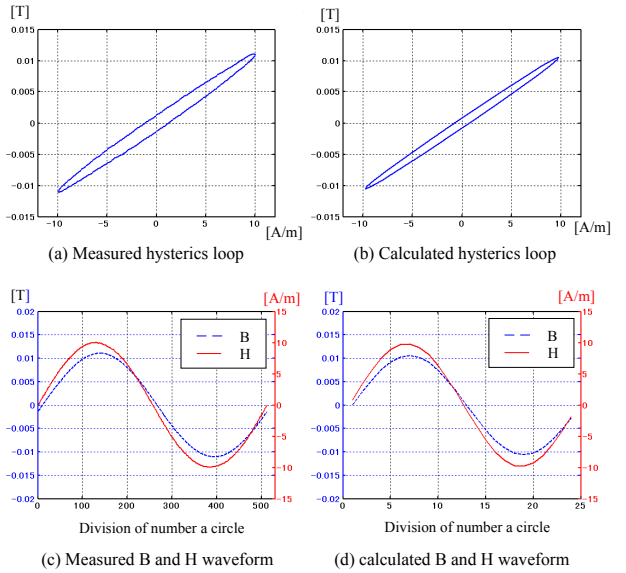

Fig. 2. Hysterics loop in the ferrite core and waveforms of magnetic flux density B and magnetic field strength H under sinusoidal alternating excitation at 1MHz

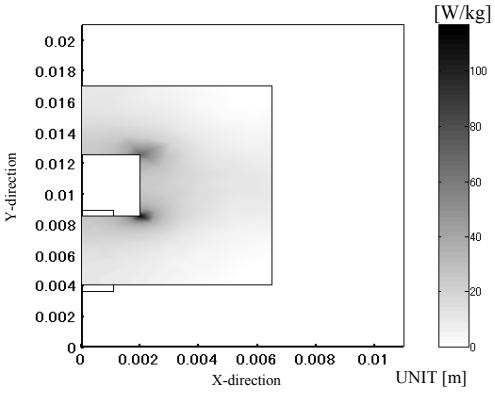

Fig. 3. Iron loss distribution under the pulse excitation considering 15th harmonic components (Switching frequency 1MHz)

CONCLUSION

We can conclude our paper as follow,

(1) The iron loss distribution was shown under the pulse excitation by considering the frequency dependence of the complex permeability.

However, the comparison between the measured data and the calculated data is required under the pulse excitation to verify our proposal method.

REFERENCE

[1] S.GOTHO, N.SOGA and T.KAWANO, "A New Interpretation of the Frequency Dependence of the Initial Permeability on MnZn ferrites" Journal of Magnetics Society of Japan Vol.22, Supplement, No.S1,1998

[2] Nobuyuki KOBAYASHI, Seiji HAYANO and Yoshifuru SAITO, "An analysis of the electromagnetic field distributions for a ferrite toroidal core"

Time Domain Analysis of Quasi-static Electric Fields in Media with Frequency Dependent Permittivity

K. Preis, O. Bíró
IGTE
Graz University of Technology
Kopernikusgasse 24, A-8010 Graz, Austria
email: preis@igte.tu-graz.ac.at
biro@igte.tu-graz.ac.at,

P. Supancic
Institute of Structural and Functional Ceramics, University of Leoben,
Materials Center, Peter-Turner Straße 5,
A-8700 Leoben, Austria
email: phs@unileoben.ac.at

I. Tičar
Faculty of Electrical Engineering and Computer Science
University of Maribor
Smetanova ul. 17, 2000 Maribor, Slovenia
email: ticar@uni-mb.si

***Abstract*— A time domain method is presented to treat transient quasi-static electric problems if the permittivity depends on frequency. The inverse Fourier transform of the complex permittivity spectrum is used in a time stepping procedure. The method is numerically realized using finite element techniques. An example illustrates the effect of the frequency dependence of permittivity on the time domain solution.**

INTRODUCTION

In many problems involving applications ranging from microwave substrates to high voltage isolators, capacitive and conductive effects have to be simultaneously taken into account, whereas inductive phenomena can be neglected [1]. This means that the quasi-static electric field intensity is curl free and can hence be described by an electric scalar potential, but both the conduction and displacement current density have to be considered. In case of steady state time harmonic problems, the use of the complex notation allows the constant permittivity and conductivity of linear materials to be described by a complex permittivity or, equivalently, by a complex conductivity. In problems with general time variation or ones involving nonlinear material properties, a transient treatment is necessary [2].

It is however known that the permittivity of certain materials strongly depends on frequency [3]. This fact can be easily taken into account in single frequency time harmonic problems, but it is not straightforward to consider it in the time domain. The aim of this paper is to present a method applicable to transient problems which is, however, capable of treating the frequency dependence of permittivity.

QUASI-STATIC ELECTRIC FIELD

If the influence of magnetic effects on the electric field can be neglected, but both conduction and dielectric effects occur, the relevant Maxwell's equations describing the resulting quasi-static electric field are

$$curl\mathbf{E} = 0\,, \tag{1}$$

$$div(\mathbf{J} + \frac{\partial \mathbf{D}}{\partial t}) = 0 \tag{2}$$

where $\mathbf{E}$ is the electric field intensity, $\mathbf{J}$ is the conduction current density, $\mathbf{D}$ is the electric displacement and t denotes time. Due to (1), the electric scalar potential can be introduced as

$$\mathbf{E} = -gradV \tag{3}$$

and, using the constitutive relationships

$$\mathbf{J} = \sigma\mathbf{E}\,, \tag{4}$$

$$\mathbf{D} = \varepsilon\mathbf{E} \tag{5}$$

where σ is the conductivity and ε is the permittivity, the differential equation

$$-div\left(\sigma gradV\right) - div\frac{\partial}{\partial t}\left(\varepsilon gradV\right) = 0 \tag{6}$$

is obtained for the scalar potential.

FREQUENCY DEPENDENT PERMITTIVITY

In the frequency domain, (6) has the form

$$-div\left[\left(\sigma + j\omega\hat{\varepsilon}(j\omega)\right) grad\hat{V}(j\omega)\right] = 0 \tag{7}$$

where ω is the angular frequency, $\hat{V}(j\omega)$ is the Fourier transform of the scalar potential, $\hat{\varepsilon}(j\omega)$ is the frequency dependent permittivity describing the relationship between the Fourier transforms of the displacement, $\hat{\mathbf{D}}(j\omega)$, and of the electric field intensity, $\hat{\mathbf{E}}(j\omega)$, as

$$\hat{\mathbf{D}}(j\omega) = \hat{\varepsilon}(j\omega)\hat{\mathbf{E}}(j\omega)\,. \tag{8}$$

The complex function $\hat{\varepsilon}(j\omega)$ can be assumed to be known from measurements. Now, using the convolution theorem [4], (8) can be transformed into the time domain to yield

$$\mathbf{D}(t) = \varepsilon(t) * \mathbf{E}(t) = \int_0^t \varepsilon(\tau)\mathbf{E}(t-\tau)d\tau \tag{9}$$

where $\varepsilon(t)$ is a fictitious time function obtained as the inverse Fourier transform of $\hat{\varepsilon}(j\omega)$:

$$\varepsilon(t) = \mathfrak{F}^{-1}\left(\hat{\varepsilon}(j\omega)\right) = \frac{1}{2\pi}\int_{-\infty}^{\infty}\hat{\varepsilon}(j\omega)e^{j\omega t}dt\,. \tag{10}$$

This can be easily computed using fast Fourier techniques. In (9) it has been assumed that both $\varepsilon(t)$ and $\mathbf{E}(t)$ are casual functions, i.e. they are zero for $t < 0$.

TIME STEPPING PROCEDURE

Using (9), the differential equation (7) can be written in the time domain as

$$-div\left(\sigma\, grad V\right) - div\left(\frac{\partial\varepsilon}{\partial t} * grad V\right) = 0\,. \tag{11}$$

For the sake of simplicity, let us assume that a backward Euler procedure with a constant time step Δt is used to account for the time variation. Approximating the time derivative by a difference quotient and the convolution integral using the rectangle rule, one obtains

$$\left(\frac{\partial\varepsilon}{\partial t} * grad V\right)^{(n)} \approx \sum_{k=0}^{n-1}\left[\varepsilon^{(k+1)} - \varepsilon^{(k)}\right] grad V^{(n-k)} \tag{12}$$

where the superscript (k) refers to values at $t_k = k\Delta t$.

Setting (12) in (11) and applying finite element Galerkin techniques, the following recursive scheme is obtained for the potential at the n-th time step:

$$\left(\boldsymbol{K}_\sigma + \boldsymbol{K}_\varepsilon^{(1)} - \boldsymbol{K}_\varepsilon^{(0)}\right)\mathbf{V}^{(n)} = -\sum_{k=1}^{n-1}\left(\boldsymbol{K}_\varepsilon^{(k+1)} - \boldsymbol{K}_\varepsilon^{(k)}\right)\mathbf{V}^{(n-k)} \tag{13}$$

where the vector **V** is formed by the nodal values of the scalar potential, $\boldsymbol{K}_\sigma$, and $\boldsymbol{K}_\varepsilon$ are the stiffness matrices corresponding to the current field and the electric field, respectively.

NUMERICAL EXAMPLE

A cylindrical piece of $BaTiO_3$ ceramic with both its radius and height 10 mm is situated between circular electrodes whose radius is 8 mm [2]. A voltage step of 2 V is switched on the series connection of this element and of a resistor of 0.6 MΩ. The conductivity of the ceramic is $2.9\text{x}10^{-7}$ S/m and its frequency dependent permittivity is given as

$$\hat{\varepsilon}(j\omega) = \varepsilon_0\varepsilon_\infty + \frac{\varepsilon_0\Delta\varepsilon}{1+\left(j\omega\tau\right)^\alpha} \tag{14}$$

where $\varepsilon_\infty = 9.9\text{x}10^3$, $\Delta\varepsilon = 1.0\text{x}10^5$, $\tau = 3.83$ s and $\alpha = 0.38$. The temperature is taken to be constant (200 °C) and the dependence of the conductivity and permittivity on the electric field intensity has not been taken into account.

The inverse Fourier transform of (14) turns out to be casual. The method of the paper has been incorporated into a 2D finite element code. The resulting time function of the voltage between the electrodes is shown in Fig. 1 with and without frequency dependence of the permittivity.

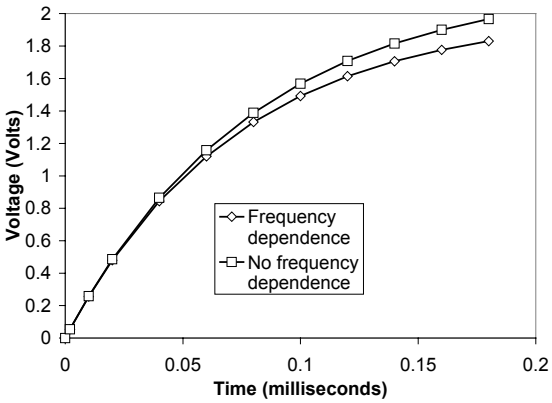

Fig. 1. Time function of the voltage between the electrodes. The permittivity in the frequency independent case is ε_∞.

REFERENCES

[1] P. Alotto, C. Bianchi, P. Girdinio, M. Nervi, and A. Pitto, "Static and sinusoidal analysis of "current flow" problems in imperfect dielectric," 12th COMPUMAG Sapporo, Japan, October 25-28, 1999, vol. 2, pp. 454-455.

[2] K. Preis, O.Bíró, P. Supancic and I. Ticar, "FEM simulation of thermistors including dielectric effects," 10th IEEE CEFC 2002, Perugia, Italy, June 16-19, 2002, pp. 279.

[3] J. R. Macdonald, ed., *Impedance Spectroscopy - Emphasizing Solid Materials and Systems*, John Wiley & Sons, 1987.

[4] A. Papoulis, *The Fourier Integral and its Applications*, New York, San Fransisco, London, Toronto: McGraw-Hill Book Co., Inc. 1962.

3D Finite Element Modelling of micro-inductors

M. Bensetti*, Y. Le Bihan*, C.Marchand*, E. Dufour Gergam**, J.-P. Gilles**, C.-M. Tassetti***, G. Lissorgues***
* LGEP, CNRS UMR 8507 - SUPELEC - 91192 Gif sur Yvette cedex - France
** IEF, CNRS UMR 8622 - Bât. 220, Centre d'Orsay, 91405 Orsay cedex France
*** Groupe ESIEE, SIGTEL – Cité Descartes – BP 99- 93162 Noisy Le Grand - France
E-mail: bensetti@lgep.supelec.fr

Abstract — **The aim of this proposal is to give an overview of the conception including modelling and technological realisation of micro-inductors dedicated for different applications : Non destructive testing (NDT), Radio frequency (RF) , Nuclear magnetic resonance (NMR), ... In this paper a circle micro-inductor is considered with 1 turn at 3 GHz frequency. The modelling is realised by using a magneto-dynamic 3D finite element formulation. This paper reports the modelling and measurement results.**

INTRODUCTION

This work presents the first step before developing various micro-inductors dedicated for different applications (NDT, RF, NMR...). The finite element method (FEM) is one of the most used numerical method for solution of electromagnetic problems. In this paper, the resistance and the inductance of a circle micro-inductor with 1 turn are evaluated. The proposed methodology can be generalised to any inductor. The studied structure have a total wire length on a scale much shorter than the wavelength of the signal so that any propagation effect can be neglected [1]. The numerical and measurement results are presented and compared.

TECHNOLOGICAL REALISATION

For fabrication of the samples we use UV copper micromoulding (poor LIGA). This process is of great interest as it allows a fast and low cost realization of metallic microstructures that may present complex shapes with good mechanical, electric or magnetic performances.
The two major steps are the creation of a photoresist mould by U.V. photolithography and metal electrodeposition through this mould thanks to a metallic seed-layer previously coated on the glass substrate (1500 Å evaporated Cu/Cr). The moulds are elaborated using the AZ 4562 thick positive photoresist because of its large scale of thicknesses (ranging from 6µm to 40 µm), its high transparency in the U.V. wavelength range used and its good behavior in electrodeposition solutions. The resist is classically spin-coated and then pre-baked on a ramped hotplate (from ambient temperature to 90 °C with a 30 % ramp). After exposure, the samples are revealed in an alkaline bath (AZ 400 K, with 1:4 proportion to desionised water) and carefully rinsed. The moulds are thus ready to be filled by copper electrodeposition. Copper is electroplated using a three-electrodes system with a copper anode, the wafer as cathode and a saturated calomel reference electrode. All deposits are made at room temperature, with magnetic stirring and dc current density of 50 mA/cm². The electrical resistivity is close to the bulk value. After the electrodeposition step, the seed-layer is etched of electrical isolation.

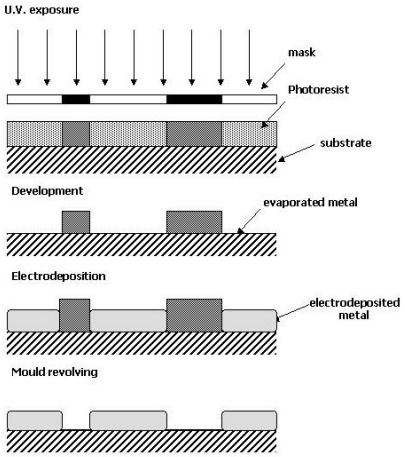

Fig.4 Main steps for micro-moulding process

MODELLING

The vector potential method is applied considering dynamic fields and neglecting displacement currents, the electromagnetic phenomena can be modelled in the harmonic domain by Maxwell equations [2]:

$$\nabla \times \mathbf{H} = \mathbf{J} \quad (1)$$

$$\nabla . \mathbf{B} = 0 \quad (2)$$

$$\nabla \times \mathbf{E} = -j\omega \mathbf{B} \quad (3)$$

The constitutive relations must be added to these relations:

$\mathbf{B} = \mu \mathbf{H}$ and $\mathbf{J} = \sigma \mathbf{E}$ where **B, H, E, J**, σ and μ are respectively the magnetic flux density, the magnetic field, the electric field, the current density, the electric conductivity and the magnetic permeability. The solution can be obtained by introducing the magnetic vector potential **A** which allow the flux density **B** to be expressed by:

$$\mathbf{B} = \nabla \times \mathbf{A} \qquad (4)$$

To calculate L and R, the RMS values of the magnetic energy and power losses are considered. The inductance is calculated by using the magnetic energy (W), this energy is given by the following expression:

$$W = \frac{1}{2}\iiint_V \mathbf{HB}\, dv = \frac{1}{2}\iiint_V \frac{1}{\mu}\|\mathbf{B}\|^2 dv \qquad (5)$$

where V is the considered domain of integration.

The expression connecting the energy to the inductance is given by this expression :

$$W = \frac{1}{2}LI^2 \qquad (6)$$

The resistance is calculated from the dissipated power in metallic copper conductors by the Joule effect. The electrical resistivity is denoted by ρ . The equation for the power losses (p) is :

$$p = \int_0^v \rho \|J\|^2 dv = RI^2 \qquad (7)$$

.

RESULTS

The geometry of the circle micro-inductor is shown in Fig. 1, the inner and the outer radius are respectively r_1 = 220 µm and r_2 = 230 µm. The thickness and the width are 10 µm. The resistivity of the metallic copper conductor is 1.7 µΩ.cm.

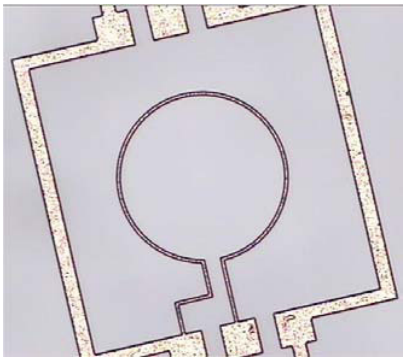

Fig. 1. Photography of the micro-inductor

To apply the FEM to the considered problem, the studied domain is decomposed into three regions (Fig.2).

The first region (R_1) constitutes the micro-inductor, the second region (R_2)constitute the air. Finally, the third region (R_3) is constituted by infinite elements [3].

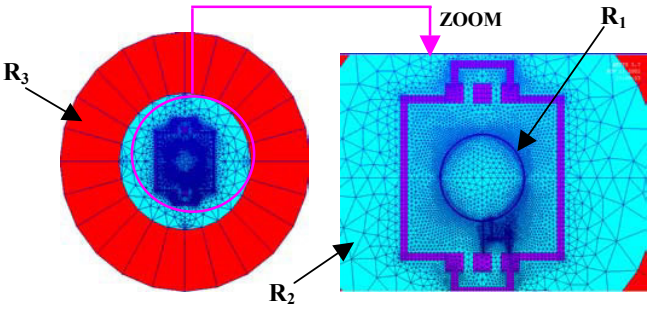

Fig. 2. FEM for the solution domain

Fig. 3 shows the distribution of the flux density field:

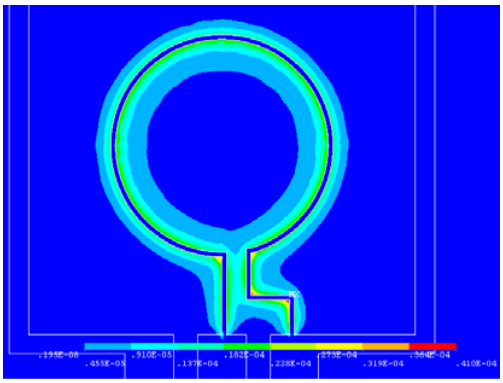

Fig.3. Distribution of the flux density

To calculate L, we consider the energy localised in R_1 and R_2. For 3 GHz frequency, The inductance numerical value is 1.2 nH and the measurement value is 1.4nH. The resistance value (R) is dependent of the frequency, the obtained numerical value is 1.12 Ω .

CONCLUSIONS

In this work, the aptitude of the FEM to modelling micro-inductors is demonstrated.. It constitutes the first step for the conception aid of micro-inductors dedicated to specific applications (NDT, RF, NMR,…). In the final paper, the electrical equivalent circuit will be presented and the behaviour in function frequency will be analysed.

REFERENCES

[1] C. M. Tassetti, G. Lissorgues, A. Ospina, A-L Coutrot, E. Dufour-Gergam and J-P. Gilles, "Micro-inductors for RF MEMS applications", MME 2002, Micro Mechanic's Europe, pp 311-314, October 6-8- 2002, Sinaia- Romania.

[2] N. Ida and J. P. A. Bastos, "Electro-magnetics and calculation of fields", 2 nd edition- 1997 Springer- verlag New-york, Inc.

[3] M. N. O. Sadiku, "Numerical techniques in electromagnetics", CRC Press,1992.

Modeling of 3D Stranded Inductors with the Magnetic Vector Potential Formulation and Spatially Dependent Turn Voltages of Reduced Support

P. Dular, J. Gyselinck
University of Liège - Dept. of Electrical Engineering and Computer Science
Institut Montefiore - Sart Tilman Bât. B28 - B-4000 Liège - Belgium
e-mail: Patrick.Dular@ulg.ac.be

***Abstract*— A method is developed to efficiently take 3D stranded inductors into account with the magnetic vector potential magnetodynamic formulation. The definition of the turn voltages as a continuous spatially dependent quantity of reduced support enables to simplify the turn circuit relations, relating currents and turn voltages. The continuous extension of these relations for all the wire turns then reduces the bandwidth in the system matrix in comparison with the usual method. The voltage of each turn is moreover directly known and, hence, does not require a tedious post-processing.**

I. Introduction

Magnetic vector potential 3D finite element formulations are well known, either with nodal [1] or edge finite elements [2], [3]. Circuit relations for inductors, relating currents to voltages, are often needed for electric circuit coupling to enable any kind of excitation.

The circuit relation of a stranded inductor relates its current to its total voltage and contains information about the magnetic flux linked to the turns. It generally leads to a wide bandwidth in the algebraic system matrix since it involves the distribution of the magnetic vector potential in the whole inductor region, which can slow down the convergence of an iterative solver, especially in a 3D model.

Moreover, the a posteriori calculation of the voltage associated with each turn of a 3D coil necessitates the integration of a local relation along the path following this turn; this integration is trivial in a 2D model. The knowledge of the turn voltages can be of interest to check the voltage constraints in high voltage apparatus; the voltage between two points would be given by the sum of the voltages of all the intermediate turns.

A method is developed here to reduce the support of integration involved in 3D stranded inductor circuit relations, herewith reducing the bandwidth of the circuit relations and facilitating the calculation of the turn voltages. This method is based on the developments done in [3] and [4] for taking massive and foil winding inductors respectively into account. It uses a coupling between edge and nodal finite elements, for the magnetic vector potential and the electric scalar potential respectively. The voltages associated with massive and foil winding inductors have been expressed through global sets of nodal functions giving particular forms to the electric scalar potential and reducing its support. Such a support reduction will be applied for stranded inductors.

The accuracy and the efficiency of the method will be pointed out through the study of a test problem.

The work has been carried out in the frame of the Interuniversity Attraction Poles IAP P5/34, funded by the Belgian federal government. P. Dular is a Research Associate with the Belgian National Fund for Scientific Research (F.N.R.S.).

II. Magnetodynamic a-v-Formulation and Massive Conductor Circuit Relations

A bounded domain Ω of the two- or three-dimensional Euclidean space is considered, in which the magnetodynamic problem is defined. The eddy current conducting part of Ω is denoted Ω_c and the non-conducting one Ω_c^C, with $\Omega=\Omega_c\cup\Omega_c^C$. Massive inductors belong to Ω_c.

The general expression of the electric field $\mathbf{e}$ via a magnetic vector potential $\mathbf{a}$ involves the gradient of an electric scalar potential v in Ω_c, i.e.

$$\mathbf{e}=-\partial_t\mathbf{a}-\operatorname{grad} v \ \text{ in } \Omega_c\,, \quad \text{with} \quad \mathbf{b}=\operatorname{curl}\mathbf{a} \ \text{ in } \Omega\,, \quad (1\text{-}2)$$

so that the Faraday equation is satisfied. With these two potentials, the **a**-v magnetodynamic formulation is obtained from the weak form of the Ampere equation, i.e. [2], [3]

$$(\mu^{-1}\operatorname{curl}\mathbf{a},\operatorname{curl}\mathbf{a}')_\Omega+(\sigma\partial_t\mathbf{a},\mathbf{a}')_{\Omega_c}+(\sigma\operatorname{grad} v,\mathbf{a}')_{\Omega_c}=0\,, \quad \forall\mathbf{a}'\in F_a(\Omega)\,, \quad (3)$$

where μ is the magnetic permeability, σ is the electric conductivity, $F_a(\Omega)$ is the function space defined on Ω and containing the basis functions for **a** as well as for the test function **a'**; $(\cdot\,,\cdot)_\Omega$ denotes a volume integral in Ω of the product of its vector field arguments.

The total current I_i flowing in a massive conductor i is shown in [3] to be weakly expressed by the circuit relation

$$I_i=(\sigma\partial_t\mathbf{a},\operatorname{grad} v_{s,i})_{\Omega_c}+V_i\,(\sigma\operatorname{grad} v_{s,i},\operatorname{grad} v_{s,i})_{\Omega_c}\,, \quad (4)$$

where $v_{s,i}$ is a global basis function for the voltage V_i. At the discrete level, this function is reduced to the sum of the nodal basis functions of all the nodes located in a cross-section with a support limited to a transition layer (composed of the elements located on one side of the cross-section and having nodes on this section). Circuit relation (4) appears to be the natural extension in 3D of its usual form in 2D.

III. Stranded Conductor Circuit Relations

As is commonly done, a turn voltage continuum will be built with the aim to make superfluous the explicit definition of all the wires. However, this continuum will explicitly appear in the final formulation and its support will be reduced, which distinguishes the proposed method from the classical one.

Three principal local perpendicular directions are defined in the winding, i.e. $\mathbf{e}_\alpha$, $\mathbf{e}_\beta$ and $\mathbf{e}_\gamma$, being respectively two arbitrary directions perpendicular to the wires and one direction

parallel to them (Fig. 1). Coordinates α, β and γ are associated with these directions. The winding has N_s turns and its total surface area is S_s.

Expression (4) applied to a given turn of the winding, located at mean position (α, β) in a cross-section of the inductor, gives the associated circuit relation, which is then divided by the surface area S_s/N_s of this turn (a fill factor can be considered without difficulties), i.e.

$$\frac{N_s}{S_s} I_i = (\sigma \partial_t \mathbf{a}, \mathrm{grad} v_{s,i})_{\Omega_\gamma} + V_i (\sigma \mathrm{grad} v_{s,i}, \mathrm{grad} v_{s,i})_{\Omega_\gamma} , \quad (5)$$

where Ω_γ denotes the line described by γ for the fixed position (α, β), i.e. the mean path of the turn. The assumption made is that **a** does not vary in the wire cross-section. Voltage V_i depends on the considered turn, i.e. $V_i = V_i(\alpha, \beta)$, while function grad $v_{s,i}$ is independent of (α, β) (Fig. 1).

In order to weakly satisfy (5) for all the turns, $V_i(\alpha, \beta)$ is extended to a continuum for all the turns (α and β are given a continuous nature) and a projection equation is expressed, i.e.

$$-\frac{N_s}{S_s} I_i \int_{\Omega_{\alpha\beta}} V'(\alpha,\beta)\, d\Omega_{\alpha\beta} + (\sigma \partial_t \mathbf{a}, V'(\alpha,\beta) \mathrm{grad} v_{s,i})_{\Omega_{\alpha\beta\gamma}} + (\sigma\, V_i(\alpha,\beta)\, \mathrm{grad} v_{s,i}, V'(\alpha,\beta) \mathrm{grad} v_{s,i})_{\Omega_{\alpha\beta\gamma}} = 0 , \quad \forall\, V'(\alpha,\beta) \in \mathrm{IR} , \quad (6)$$

where $\Omega_{\alpha\beta\gamma}$ is the whole volume of the stranded inductor. The test function for the turns circuit relation thus appears to be $V'(\alpha, \beta)$ grad $v_{s,i}$, while it is grad $v_{s,i}$ for a single massive conductor. The total voltage of the winding can be determined by integrating $V_i(\alpha, \beta)$ in the cross-section.

At the discrete level, an approximate form of $V_i(\alpha, \beta)$, being also used for $V'(\alpha, \beta)$, has to be defined. Polynomial or 2D finite element variations are examples of possible approximations. These approximations can be independent of the mesh used for the vector potential. They can also be based on the trace of the 3D mesh in the cross-section. Various approximate form will be detailed and discussed in the extended paper. Note that a constant approximation would amount to considering a massive inductor.

As a result, thanks to the limited support of function $v_{s,i}$ (Fig. 1), the number of unknowns involved in (6) can be significantly reduced. In return, it is however necessary to define an anisotropic tensor value for the conductivity σ, with a zero value in directions $\mathbf{e}_\alpha$ and $\mathbf{e}_\beta$. The actual distribution of the current density is then considered through the tensorial conductivity.

IV. Application

The developed tools have been applied to a 3D stranded inductor. Turn voltages obtained with the proposed method, with polynomial and 2D finite element variations, have been compared to those obtained with the classical method using an integration in the whole inductor region for defining the circuit relation (e.g. Fig. 2). Other interesting validation results will concern the computation of the turn resistances, the effect of the tensorial conductivity and the resulting correct distribution of the current density. The efficiency of the method will also be studied in the extended paper.

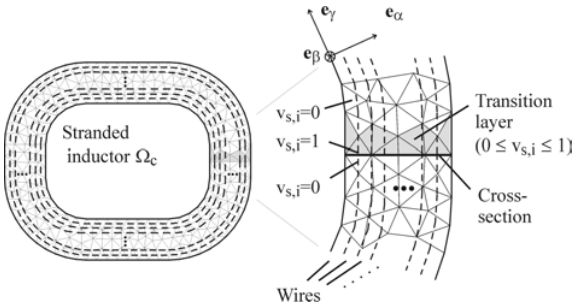

Fig. 1. Stranded conductor and its continuous representation (can be seen as a section of a 3D structure showing a layer of turns).

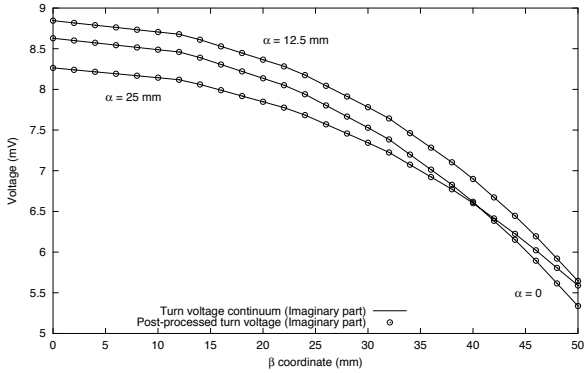

Fig. 2. Turn voltage continuum in a 3D stranded inductor compared to the post-processed turn voltage with the classical method (imaginary part); the results are shown along three particular lines in the cross-section of the inductor.

V. Conclusions

An alternative method has been developed to efficiently take stranded inductors into account in the frame of the magnetic vector potential 3D magnetodynamic formulation. In order to avoid the explicit definition of multiple wire turns and to reduce the bandwidth of their circuit relation, the turn voltages are explicitly considered in the formulation as a continuous spatially dependent quantity of which the support is limited to a cross-section of the inductor and its neighborhood. The turn voltages are then also directly a part of the solution and, hence, does not require a tedious post-processing.

References

[1] P.J. Leonard, D. Rodger, "Voltage forced coils for 3D finite element method electromagnetic model", *IEEE Trans. Magn.*, Vol. 24, No. 5, pp. 2579-2581, Sept. 1988.

[2] C. Golovanov, Y. Maréchal, G. Meunier, "3D edge element based formulation coupled to electric circuits", *IEEE Trans. Magn.*, Vol. 34, No. 5, pp. 3162-3165, Sept. 1998.

[3] P. Dular, F. Henrotte, W. Legros, "A general and natural method to define circuit relations associated with magnetic vector potential formulations", *IEEE Trans. Magn.*, Vol. 35, No. 3, pp. 1630-1633, May 1999.

[4] P. Dular, C. Geuzaine, "Spatially dependent global quantities associated with 2-D and 3-D magnetic vector potential formulations for foil winding modeling", *IEEE Trans. Magn.*, Vol. 38, No. 2, pp. 633-636, March 2002.

COMPUMAG Saratoga Springs, New York USA
July 13 - 17, 2003

The Hybrid Scalar and Vector Potential Formulation for Magnetic Field Computations by means of the FE Method

J. Gyselinck*, L. Vandevelde**, C. Geuzaine*, and P. Dular*

* Department of Electrical Engineering, Institut Montefiore, University of Liège
Sart Tilman Campus, Building B28, B-4000 Liège, Belgium, johan.gyselinck@ulg.ac.be

** Electrical Energy Laboratory (EELAB), Ghent University, Sint-Pietersnieuwstraat 41, B-9000 Ghent, Belgium

***Abstract* – In this paper the authors propose an original approach for coupling the scalar and vector potential formulation in 2D and 3D magnetic field computations by means of the FE method. The hybrid formulated is elaborated for the 2D case, showing that the simplicity of the vector potential formulation can be partly retained. The method is applied to a simple test case. The 3D extension is briefly discussed as well.**

Introduction

For 2D magnetostatic and magnetodynamic field computations by means of the FE method, the magnetic vector potential formulation, in which the potential $\underline{a}$ can be reduced to a scalar quantity, is almost invariably adopted. Unlike its scalar potential counterpart, its elaboration and implementation are very simple as no source fields and/or cuts have to be introduced [1]. However, the scalar potential formulation may offer a considerable advantage when a hysteresis model is to be considered in some parts of the FE model, as most hysteresis models take the magnetic field vector $\underline{h} = -\mathrm{grad}\,\phi$ as input [1].

In the 3D case, the vector potential cannot be reduced to a scalar field, and various formulations, based on various magnetic and electrical potentials, have been proposed. Hybrid scalar and vector potential formulations, e.g. [2], are rarely used.

In this paper an original approach to the 2D hybrid $a-\phi$ formulation is elaborated and validated by means of a simple test case. The extension to 3D formulations is straightforward, as will be discussed.

2D Formulations

We consider a bounded domain Ω in the xy-plane of the 3D Euclidean space. (The unit vectors along x, y and z axis are denoted $\underline{x}$, $\underline{y}$ and $\underline{z}$.) The z-component of both the magnetic field vector $\underline{h}$ and the induction vector $\underline{b}$ vanishes. The latter are related through the permeability μ and reluctivity $\nu = \mu^{-1}$. In the subdomains Ω_s and Ω_c, the current density $\underline{j} = j(x,y,t)\,\underline{z}$, along the z-axis, is imposed and induced respectively. In domain Ω_c, Ohm's law $\underline{j} = \sigma\underline{e}$ applies, with $\underline{e}$ the electric field and σ the conductivity.

Vector potential formulation

The induction $\underline{b} = \mathrm{curl}\,\underline{a} = \underline{z} \times \mathrm{grad}\,a$ and the electric field $\underline{e} = -\partial_t \underline{a}$ derived from any continuous one-component potential $\underline{a} = a(x,y,t)\,\underline{z}$ satisfy the magnetic Gauss law $\mathrm{div}\,\underline{b} = 0$ and Faraday's law $\mathrm{curl}\,\underline{e} = -\partial_t \underline{b}$. After partial integration, on account of $\mathrm{curl}\,\underline{a} \cdot \mathrm{curl}\,\underline{a}' = \mathrm{grad}\,a \cdot \mathrm{grad}\,a'$, the weak formulation of Ampère's law $\mathrm{curl}\,\underline{h} = \underline{j}$ can be written as

$$(\nu \mathrm{grad}\,a, \mathrm{grad}\,a')_\Omega + (\sigma\partial_t a, a')_{\Omega_c} + \langle h_t, a'\rangle_{\partial\Omega} = (j, a')_{\Omega_s}, \quad \forall a' \in F_a(\Omega)\,, \qquad (1)$$

where $F_a(\Omega)$ is the function space defined on Ω containing the basis functions for a as well as for the test functions a'; $(\cdot,\cdot)_\Omega$ and $\langle\cdot,\cdot\rangle_{\partial\Omega}$ denote the surface integral in Ω and the line integral on the boundary of Ω of the (scalar) product of their (vector) field arguments. The integral on $\partial\Omega$ comprises the tangential magnetic field $h_t = \underline{h}\cdot\underline{t}$ with $\underline{t} = \underline{z} \times \underline{n}$, where $\underline{n}$ is the outward pointing normal on $\partial\Omega$.

The electrical circuit coupling of the current carrying regions in Ω can be easily elaborated [1]. Consider e.g. n_s stranded conductors, i.e. domains Ω_{sk}, $k = 1, \ldots, n_s$, in which the current density is determined by given normalised functions $j_k(x,y)$ and the strand currents $I_k(t)$: $j(x,y,t) = j_k(x,y)I_k(t)$. The corresponding flux linkage and the electromotive force are $\Phi_k(t) = (l_z a(x,y,t), j_k(x,y))_{\Omega_{sk}}$ and $E_k(t) = \frac{d\Phi_k}{dt}$ respectively, where l_z is the axial length. Massive conductors can be treated in an equally straightforward manner.

Scalar potential formulation

A single-valued scalar potential $\phi(x,y,t)$ can be considered in a subdomain Ω_ϕ if the latter is current-free ($\underline{j} = 0$) and if the circulation of $\underline{h}$ along any contour C in Ω_ϕ is zero ($\oint_C \underline{h}\cdot d\underline{l} = 0$). The derived magnetic field $\underline{h} = -\mathrm{grad}\,\phi$ satisfies Ampère's law $\mathrm{curl}\,\underline{h} = 0$. The weak formulation of $\mathrm{div}\,\underline{b} = 0$ in Ω_ϕ reads

$$(\mu \mathrm{grad}\,\phi, \mathrm{grad}\,\phi')_{\Omega_\phi} + \langle b_n, \phi'\rangle_{\partial\Omega_\phi} = 0\,, \quad \forall \phi' \in F_\phi(\Omega_\phi)\,, \qquad (2)$$

with $b_n = \underline{b}\cdot\underline{n}$, where $\underline{n}$ is the outward pointing normal on $\partial\Omega_\phi$.

When the scalar potential ϕ is multi-valued, which generally is the case in a multiply connected domain [3], some cuts allowing discontinuities of ϕ have to be introduced in Ω_ϕ, which is thus made simply connected and in which a single-valued scalar potential can be defined. A minimum number of cuts, equal to the number of holes in Ω_ϕ, is usually introduced in order to avoid linear dependence. The discontinuities $\Delta\phi$ accross the cuts are equated to the driving magnetomotive forces, thus strongly imposing Ampère's law in the complete domain Ω_ϕ.

Hybrid formulation

The domain Ω is split up into two complementary domains, Ω_a and Ω_ϕ, in which the vector and the scalar potential formulation respectively are adopted. Ω_s and Ω_c are subdomains of Ω_a.

In the present approach, the domain Ω_ϕ is further split up into an arbitrary but sufficiently large number of simply connected subdomains Ω_{ϕ_i}, $i = 1, \ldots, n_\phi$, in each of which a single-valued scalar potential ϕ_i, with $\underline{h} = -\mathrm{grad}\,\phi_i$, is defined. The circulation of $\underline{h}$ along a closed contour C situated in several Ω_{ϕ_i} is weakly imposed via the coupling of the scalar potentials ϕ_i with the vector potential a. Hereto, a is defined in Ω_a and on all the boundaries $\partial\Omega_{\phi_i}$, including the two-layer surface of each cut. Cuts are therefore only defined in Ω_ϕ and do not necessarily meet the inductor regions, unlike in the $\underline{h}-\phi$ formulation [4].

A practical case with $n_\phi = 2$ is shown in Fig. 1. It concerns e.g. the cross-section of a single-phase transformer, the magnetic core of which is split up in Ω_{ϕ_1} and Ω_{ϕ_2}. (Note that in this case, the number of cuts could have been limited to one.) On the two dashed lines in

The work has been carried out in the frame of the Interuniversity Attraction Poles IAP P5/34, funded by the Belgian federal government. P. Dular and C. Geuzaine are Research Associate and Postdoctoral Researcher respectively with the Belgian National Fund for Scientific Research (F.N.R.S.). L. Vandevelde is a Postdoctoral Fellow with the Fund for Scientific Research - Flanders (Belgium)(F.W.O.-Vlaanderen).

Fig. 1, which connect the inner to the outer part of Ω_a, all three potentials a, ϕ_1 and ϕ_2 are defined. In order to ensure their uniqueness, they have to be fixed in exactly one point in their domain of definition (when disregarding possible Dirichlet boundary conditions).

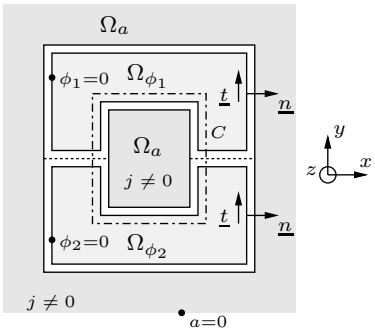

Fig. 1: Definition of the domains Ω_a and $\Omega_\phi = \Omega_{\phi_1} \cup \Omega_{\phi_2}$

On account of $-h_t = -\underline{t} \cdot \underline{h} = \underline{t} \cdot \operatorname{grad} \phi_i$ and $b_n = \underline{n} \cdot \operatorname{curl} \underline{a} = \underline{t} \cdot \operatorname{grad} a$, the weak forms (1) and (4) become for Ω_a and Ω_{ϕ_i} $(i = 1, \ldots, n_\phi)$ respectively:

$$(\nu \operatorname{grad} a, \operatorname{grad} a')_{\Omega_a} + (\sigma \partial_t a, a')_{\Omega_c} + \sum_{i=1}^{n_\phi} \langle \underline{t} \cdot \operatorname{grad} \phi_i, a' \rangle_{\partial \Omega_{\phi_i}} + \langle h_t, a' \rangle_{\partial \Omega_a \setminus \cup_{i=1}^{n_\phi} \partial \Omega_{\phi_i}} = (\underline{j}, \underline{a}')_{\Omega_s}, \ \forall a' \in F_a(\Omega), \quad (3)$$

$$(\mu \operatorname{grad} \phi_i, \operatorname{grad} \phi_i')_{\Omega_{\phi_i}} + \langle \underline{t} \cdot \operatorname{grad} a, \phi_i' \rangle_{\partial \Omega_{\phi_i}} = 0, \quad \forall \phi_i' \in F_{\phi_i}(\Omega_{\phi_i}), \quad (4)$$

with $\underline{t} = \underline{z} \times \underline{n}$ and $\underline{n}$ the outward pointing normal on $\partial \Omega_{\phi_i}$.

Note that the contribution of the cut regions to the first term of (3) tends to zero as the thickness of these regions tends to zero as well.

An advantage of the proposed hybrid formulation is that the electrical circuit coupling of the a formulation can remain as it is. Indeed, as the circuit coupling concerns current carrying domains in Ω_a only and as the vector potential a is continuous throughout Ω_a (having a single reference point $a = 0$), the additional terms and equations are not affected by the coupling with the scalar potentials ϕ_i.

Consequently, no basis function have to be defined and associated with each cut for considering the currents and voltages of the inductors [4]. Furthermore, no source fields have to be calculated for the stranded inductors [5].

In 3D computations, one can benefit from the hybrid approach by limiting the magnetic vector potential domain Ω_a to the inductors. The cuts will then meet the inductor boundaries and will therefore have the same form as those defined in the $\underline{h} - \phi$ formulation. Their number does not have to be limited.

2D Application Example

The plain a formulation and the proposed hybrid formulation have been applied to a simple 2D test case, which is analogous to the situation shown in Fig. 1. A constant magnetomotive force of 1 A is enforced with a coil, one side of which is situated in the hole of the magnetic core. Magnetostatic calculations with several meshes and first order interpolation of a, ϕ_1 and ϕ_2 have been carried out. Some isolines of a, ϕ_1 and ϕ_2 are depicted in Fig. 2. The normalised flux linkage calculated with the a and the $a - \phi$ formulation is depicted in Fig. 3 as a function of the total number of degrees of freedom. The two curves clearly converge to each other.

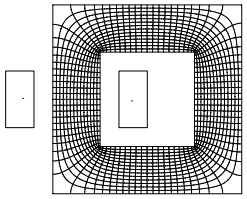

Fig. 2: Isolines of a obtained with the a formulation, and isolines of ϕ_1 and ϕ_2 obtained with the $a - \phi$ formulation

As can be seen in Fig. 4, the circulation of $\underline{h}$ along a contour C encircling the coil (see Fig. 1) is not exactly the driving 1 A. The deviation depends on the position of the contour and is in average zero. The amplitude of the error decreases as the FE mesh is refined.

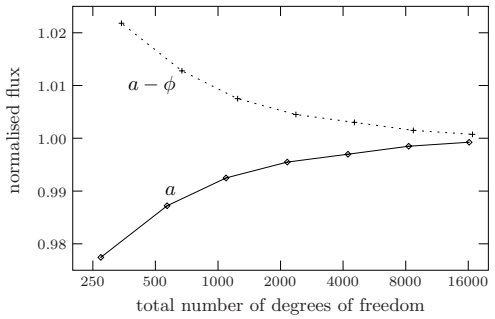

Fig. 3: Normalised flux calculated with the a and the $a - \phi$ formulation, as a function of the total number of degrees of freedom

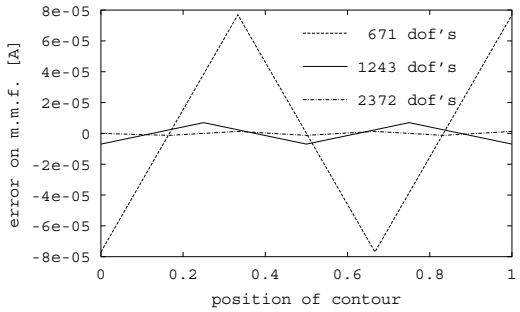

Fig. 4: Circulation of $\underline{h}$ along the contour C minus 1 A as a function of the position of the contour (between the inner and the outer boundary of the magnetic core) obtained with the $a - \phi$ formulation and three different meshes

In the extended paper, the 3D case will also be elaborated in more detail and a 3D application will be considered.

References

[1] J. Gyselinck et al., "Calculation of no load losses in an induction motor using an inverse vector Preisach model and an eddy current loss model," *IEEE Trans. on Magn.*, Vol. 36, No. 4, pp. 856–860, July 2000.

[2] R. Wang et al., "A combined vector potential - scalar potential method for FE computation of 3D magnetic fields in electrical devices with iron cores," *IEEE Trans. on Magn.*, Vol. 27, No. 5, pp. 3971–3977, Sept. 1991.

[3] A. Bossavit, "Magnetostatic problems in multiply connected regions: some properties of the curl operator," *IEE Proceedings*, Vol. 135, Pt. A, No. 3, pp. 179–187, 1988.

[4] P. Dular et al., "A natural method for coupling magnetodynamic h-formulations and circuit equations," *IEEE Trans. on Magn.*, Vol. 35, No. 3, pp. 1626–1629, May 1999.

[5] P. Dular et al., "A generalized source magnetic field calculation method for inductors of any shape," *IEEE Trans. on Magn.*, Vol. 33, No. 2, pp. 1398–1401, March 1997.

COMPUMAG Saratoga Springs, New York USA
July 13 - 17, 2003

Parallel and Distributed Processing for *h-p* Adaptive Finite Element Analysis: A Comparison of Simulated and Empirical Studies

Steve McFee, Qingying Wu, Mark Dorica and Dennis Giannacopoulos

Computational Analysis and Design Laboratory
Electrical & Computer Engineering, McGill University
3480 University Street, Montreal, H3A 2A7, Canada
email: steve.mcfee@mcgill.ca

Abstract – **Parallel processing has been widely promoted as a feasible, and even promising, solution to the very high computational demands of practical *h-p* adaptive finite element analysis for electromagnetic device design and system performance simulation. A combination of emulated and empirical studies designed to explore the validity of these claims are presented and compared. Practical parallel processing efficacy results, computed using a pair of interconnected Sun E450 and v880 platforms (4 processors each), are reported.**

INTRODUCTION

Concurrent, combined and integrated *h*- and *p*-refinement adaptive finite element analysis (AFEA) for electromagnetics has become increasingly important over this past decade, and now represents a reasonably mature and well-established area of computational engineering research. Current views on this subject widely acknowledge the broad potential of intelligent *h-p* adaption, as well as, the computational complexities and bottlenecks associated with guiding the evolution of practical and effective *h-p* discretizations. Recent work has proposed that parallel computing should be well suited to managing, or even circumventing, the computational difficulties associated with implementing and controlling the key adaptive feedback processes [1][2]. While the primary techniques and strategies of AFEA for engineering electromagnetics are well-defined [3], definitive and categorical contributions on *h-p* adaption for 3-D applications remain rather limited [4], and practicable contributions on 3-D *h-p* AFEA for workstation-level parallel and distributed computing environments are not available [5]. Serial computing work on 3-D *h-p* AFEA has mainly focused on resolving the difficulties related to: implementing flexible high-order *h-p* edge-elements [6][7]; building effective initial *h-p* meshes [8][9]; developing effective and efficient mesh discretization refinement strategies [10][11]; and, improving local AFEA error estimators [3][4][12]. While, parallel and distributed computing contributions for general AFEA have focused on the difficulties inherent to: discretization domain decomposition [13][14]; computational task load balancing [15][16][17]; database structures and management [18][19]; data communications management [20][21]; software design, prototyping and development environments [19][22][23]; and solver design [24]. While it seems clear that all the essential ingredients are available [4], a recipe for combining them into a practicable *h-p* AFEA system for effective 3-D engineering electromagnetics in any realistic type of parallel or distributed computing environment remains absent [5]. It should also be noted that the bulk of all research contributions on 3-D *h-p* AFEA is founded almost exclusively on hexahedral elements, and it is limited to fully-conforming or 1-irregular (at most) formulations [5][18][22]. Unlike in computational mechanics applications, tetrahedral elements are commonly preferred for electromagnetics AFEA, and "irregular-cut" formulations are now known to provide the greatest modeling and refinement flexibility for tetrahedral *h-p* discretizations [25][26].

The purpose of this contribution is to summarize the main state-of-the-art research directions which are currently under investigation for parallel and distributed processing methods designed for *h-p* AFEA of electromagnetics problems; outline their theoretical foundations; and then investigate the validity of their results empirically, using direct controlled testing and actual runtime experimentation with a practical, workstation-level, parallel and distributed computing environment.

TEST ENVIRONMENT AND PROCEDURES

The AFEA parallel processing test environment consists of two primary elements: a highly adaptable parallel computing emulator, designed to simulate, monitor and assess processor to processor communications scheduling overhead and costs; and, a highly configurable parallel and distributed processing system, based on a side-by-side integrated pair of 4-processor workstations, which are directly connected together through a dedicated gigabit optical communications link. The emulator software was developed specifically for this hardware system, and it is designed to be able to simulate and trace the runtime operation of the core parallel platform, together with a locally connected set of satellite serial workstations, for all possible configurations. Through this combination of test bench tools, it is possible to both: accurately assess the actual start-to-end runtime performances of *h-p* AFEA parallel implementations, on a range of practical platform configurations; and, to trace, investigate and evaluate the details of the runtime operations overhead, communication costs and system bottlenecks. This combination of empirical and simulated runtime information is proposed to facilitate the accurate and reliable assessment of the impact of parallel processing on practical *h-p* AFEA.

The hardware implementations are based on the Sun E450 (Enterprise 450) and Sun v880 parallel processing computers, locally networked together with a cluster of five serial work-stations, through a 100-Mbit switch. These parallel machines

support four independent, fully accessorized, processors each (480-700MHz; 1-2Gb Ram; 30-48Gb disk). The full study is intended to examine a broad representative range of practical parallel and distributed processing configurations for AFEA.

ILLUSTRATIVE RESULTS

One of the most significant performance characteristics for most parallel processing systems is communications overhead and transmission cost. For AFEA implementations on certain platforms (e.g. AVX Series 2), transaction initialization costs alone can outweigh the potential computational advantages of evaluating elemental error estimators in parallel – even if data transmission costs are negligible. The results in Table I show the potential ramifications of this performance characteristic for a range of AFEA error estimator implementations. In this study, an 8-processor configuration (1 control + 7 compute nodes), with fixed cost communications, is considered. Even for this idealized environment, it is noteworthy that the best numbers of compute processors (and resulting speedup), for a given level of communications overhead, is not obvious. For more practical parallel AFEA environments, which integrate added computational requirements (e.g. mesh refinement and discretization convergence analysis), performance prediction is more difficult. A variety of less obvious and more in depth cases will be reported at the conference and in the long paper.

Table I. Normalized Cost of Full Mesh Error Estimation Computation [1]

Number of Compute Processors [3]	One-way Control-Compute Communications Cost [2]					
	3%	6%	9%	12%	15%	18%
2	0.59	0.68	0.77	0.86	0.95	1.04
3	0.45	0.57	**0.69**	**0.81**	**0.93**	1.08
4	0.40	**0.55**	0.72	0.96	1.20	1.44
5	0.38	0.60	0.90	1.20	1.50	1.80
6	**0.38**	0.72	1.08	1.44	1.80	2.16
7	0.42	0.84	1.26	1.68	2.10	2.52

[1] Cost expressed relative to error estimation computational cost for full mesh, via single-processor (serial processing), which has been normalized to 1.00.

[2] Cost columns denoted by percentage of total serial processing cost for full mesh; initialization + transmission for one-way communication represented.

[3] Only compute processor nodes counted; control processor is not included.

REFERENCES

[1] S. McFee and D. Giannacopoulos, "The implications of parallel processing on *h-p* adaptive finite element analysis for electromagnetics", *IEEE Trans. Magn.*, V. 34, pp. 3284-3287, 1998.

[2] J.T. Oden and A. Patra, "Parallel adaptive strategy for *hp* finite element computations", *Comp. Meth. Appl. Mech. Engrg*., V. 121, pp. 449-470, 1995.

[3] P. Fernandes and P. Girdinio, "Adaptive finite element analysis of 2-D static and steady-state electromagnetic problems", *Int. J. Numer. Meth. Engng.*, V. 45, pp. 215-243, 1999.

[4] J. Mackerle, "Error estimates and adaptive finite element methods: a bibliography (1990-2000)", *Engrg. Comput.*, V. 18, pp. 802-914, 2001.

[5] W. Rachowicz and L. Demkowicz, "An hp-adaptive finite element method for electromagnetics Part II: A 3D implementation", *Int. J. Numer. Meth. Engng*., V. 53, pp. 147-180, 2002.

[6] L. Demkowicz, Hp-adaptive finite element method for Maxwell's equations", *Annu. Rev. Progr. Appl. Comput. Electro*., V. 1, pp. 19-27, 2000.

[7] L. Vardapetyan and L. Demkowicz, "hp-adaptive finite elements in electromagnetics", *Comp. Meth. Appl. Mech. Engrg*., V. 169, pp. 331-344, 1999.

[8] A. Patra and A. Gupta, "A systematic strategy for simultaneous adaptive hp finite element mesh modification using nonlinear programming", *Comp. Meth. Appl. Mech. Engrg*., V. 190, pp.3797-3818, 2001.

[9] A.A. Novotny et al., "A fast hp adaptive finite element mesh design", *Comp. Meth. Appl. Mech. Engrg*., V. 190, pp. 133-148, 2000.

[10] S. Taylor and J.K. Sykulski, "Anisotropic adaptive mesh refinement for EM finite element analysis in 2 dimensions", *IEEE Trans. Magn*., V. 35, pp. 1322-1325, 1999.

[11] S.H. Lo and C.K. Lee, "Selective regional refinement procedure for adaptive finite element analysis", *Computers and Structures*, V. 68, pp. 325-341, 1998.

[12] C. Carstensen and S.A. Funken, "Coupling of Nonconforming finite elements and boundary elements II: A posteriori estimates and adaptive mesh refinement", *Computing*, V. 62, pp. 243-259, 1999.

[13] R.E. Bank and P.K. Jimack, "A new parallel domain decomposition method for the adaptive finite element solution of elliptic partial differential equations", *Concur. Comp.: Prac. Exp*., V.13, pp.327-350, 2001.

[14] A. Kaveh and A. Davaran, "Spectral bisection of adaptive finite element meshes for parallel processing", *Computers and Structures*, V. 70, pp. 315-323, 1999.

[15] S. Kopyssov and A. Novikov, "Parallel adaptive mesh refinement with load balancing for finite element method", *Lecture Notes in Computer Science*, V. LNCS 2127, pp. 266-276, 2001.

[16] C. Liao and Y. Chung, "Tree-based parallel load-balancing methods for solution-adaptive finite element graghs on distributed memory multicomputers", *IEEE Trans. Par. Dist. Sys*., V. 10, pp. 360-370, 1999.

[17] G. Heber et al., "Using multithreading for the automatic load balancing of adaptive finite element meshes", *Proc. IRREGULAR'98 (Solving Irregularly Structured Problems in Parallel*, pp. 132-143, 1998.

[18] A. Laszloffy et al., "Simple data management, scheduling and solution strategies for managing the irregularities in parallel adaptive hp finite element simulations", *Parallel Comp*., V. 26, pp. 1765-1788, 2000.

[19] A.K. Patra et al., "Efficient parallel adaptive finite element methods using self-scheduling data and computations", *Lecture Notes in Computer Science*, V. 1745, pp. 359-363, 1999.

[20] V. Annamalai et al., "Adaptive finite element analysis on a parallel and distributed environment", *Parallel Comp.*, V. 25, pp. 1413-1434, 1999.

[21] M. Papadrakakis and D.C. Harbis, "Computationally efficient methods for parallel adaptive finite element analysis", *Adv. Computat. Mech. High-Perform. Comp*., V. 2, pp. 79-86, 1998.

[22] R. Niekamp and E. Stein, "An object-oriented approach for parallel two- and three-dimensional adaptive finite element computations", *Computers and Structures*, V. 80, pp. 317-328, 2002.

[23] J.D. Teresco et al., "A hierarchichal partition model for adaptive finite element computation", *Comp. Meth. Appl. Mech. Engrg*., V. 184, pp. 269-285, 2000.

[24] J.A. Scott, "A parallel frontal solver for finite element applications", *Int. J. Numer. Meth. Engng*., V. 50, pp. 1131-1144, 2001.

[25] S. McFee and D. Ma, "Irregular tetrahedra for finite element analysis in electromagnetics", *IEEE Trans. Magn.*, V. 37, pp. 3550-3553, 2001.

[26] S. McFee and D. Ma, "Irregular vector triangles and tetrahedra for finite element analysis in electromagnetics", *IEEE Trans. Magn.*, V. 38, pp. 353-356, March 2002.

An O($N^{3/2}$) Integral Equation Method for Solving PEC Scattering Problems

Seung Mo Seo and Jin-Fa Lee
ElectroScience Lab., Dept. of Electrical Engineering
The Ohio State University
jinlee@ee.eng.ohio-state.edu

Abstract– A novel 2-level dual rank SVD algorithm is described in this paper to significantly reduce the memory consumption and CPU time for EFIE formulation for solving PEC scattering problems. It is shown, with the number of groups chosen to be proportional to $N^{1/2}$, where N is the number of unknowns, the memory and CPU time for the resulting algorithm are both $O(N^{3/2})$. Also, presented in this paper is a "mesh-neighboring" preconditioner. This "mesh-neighboring" preconditioner when used in conjunction with GMRES is proven to be both efficient and effective for solving the compressed matrix equations.

I. Introduction

The solution of large-scale electromagnetic (EM) scattering problems by the method of moments (MoM) is burdened by the creation and storage of a dense system impedance matrix. For a general MoM problem using N basis functions, the computational complexity is $O(N^2)$ for filling the $N \times N$ matrix, storing it, and solving the matrix equation via an iterative algorithm such as GMRES. This paper presents a new algorithm, a 2-level dual rank singular value decomposition (SVD), for efficiently compress the MoM matrix to reduce the memory requirement, matrix fill time, and the time of the iterative solution. The unique feature of the proposed approach is that the compression is achieved without assembling the entire matrix.

II. EFIE Formulation for Scattering Problems

Application of the Galerkin method to the electric field integral equation results in

$$k_o^2 \int_D \vec{J}(\vec{r}) \bullet \int_D \frac{e^{-jkR}}{R} \vec{J}'(\vec{r}')ds'ds - \int_D \nabla \bullet \vec{J} \int_D \frac{e^{-jkR}}{R} \nabla' \bullet \vec{J}ds'ds = -\frac{jk_o}{Z_c} \int_D \vec{J} \bullet \vec{E}^{inc} ds \quad (1)$$

where D is the problem domain or the scatterer, $k_0 = \frac{\omega}{c}$ is the free space wavenumber, $R = |\vec{r} - \vec{r}'|$ the distance between observation and source points, and $Z_c \approx 377\Omega$ is the characteristic wave impedance in free space. In the current work, we have employed surface div-conformal vector basis functions for $\vec{J}$, namely the RWG basis functions [1].

III. 2-level dual rank SVD algorithm

The dual rank SVD algorithm is based on the rank deficiency feature of the integral equation for well-separated groups of basis functions [3]. The algorithm factorizes the local matrix $Z^{ij}_{m\times n}$ due to the groups i and j into $Q^{ij}_{m\times r}$ and $R^{ij}_{r\times n}$ matrices without a priori knowledge of $Z^{ij}_{m\times n}$, where m and n are the number of receiving and transmitting basis functions, respectively, and r is the rank of interaction:

$$Z^{ij}_{m\times n} = \begin{bmatrix} z_1 & z_2 & z_n \end{bmatrix} = \begin{bmatrix} \nu_1 \\ \nu_2 \\ \\ \nu_m \end{bmatrix} \approx Q^{ij}_{m\times r} \times R^{ij}_{r\times n} \quad (2)$$

Here, z_p is the column vector due to the p^{th} transmitter and ν_q is the row vector due to the q^{th} receiver. Note that the SVD matrix, $[Z]^{SVD}_{m\times n} = Q_{m\times r} \times R_{r\times n}$, is still a dense matrix. However, instead of forming $[Z]^{SVD}_{m\times n}$ explicitly, any matrix vector multiplication operation is performed first by multiplying R followed by the multiplication of the Q matrix. In this fashion, the operational count is proportional to $r(n+m)$ rather than brute force nm operations. Significant saving in memory as well as computational time will be achieved when the rank r is sufficiently smaller than n and m.

IV. Mesh-neighboring preconditioner

In this section, we consider the efficient solution of dense linear system $[\mathbf{Z}]^{SVD}\mathbf{x} = \mathbf{b}$ by preconditioned iterative methods, particularly GMRES method. An insightful discussion of three types of preconditioners, the operator splitting preconditioner (OSP), the least squares approximate inverse preconditioner (LSAI), and the diagonal block approximate inverse preconditioner (DBAI), for dense matrices arising from the application of BIEs is provided in Ref. [4]. The "mesh-neighboring" preconditioner proposed in the current work is based upon

a two-step process. In the first step, we extract from the full impedance matrix, $[\mathbf{Z}]^{SVD}$, a sparse version, $[\mathbf{Z}^s]$, which includes the near range interactions as well as a heuristic bias toward geometrical singularities. Once the sparse matrix, $[\mathbf{Z}^s]$, is obtained, the final preconditioner, $[\mathbf{M}]$, will be formed through an incomplete factorization with a heuristic dropping strategy.

V. NUMERICAL RESULTS

To demonstrate the efficiency and validate the current 2-level SVD approach, we have conducted studies on two numerical examples. One is an open cone PEC scatterer, shown as inset in Figure 1, whose height and diameter of the bottom are 20 cm. The second example is the Northrop VFY218 airplane as discussed in [6]. In both examples, we employed a constant, as constant as we possibly can, mesh density of 5 elements per wavelength. To study the memory and CPU time complexities of the novel 2-level dual rank SVD algorithm, we increase the operating frequencies and subsequently enlarge the problem sizes. The memory consumption and CPU time of the SVD process are shown in Figure 1, and they both exhibit $O(N^{3/2})$ complexity. Moreover, the approximation in the SVD process, using a tolerance of 10^{-2}, does not affect the solution quality, as evidenced in Figure 2. The results computed by the SVD and those obtained from full EFIE matrix are in very good agreement. Finally, in Table 1, we summarize the computational details of the application of the proposed SVD algorithm to the VFY218 airplane example. Note that, it only took 5 hours and 30 minutes to assemble the SVD matrix for 101,352 unknowns, and it further took (on average) 45 minutes for every incident angle on a Pentium 4, 1.2 GHz, PC with 2GB RAM.

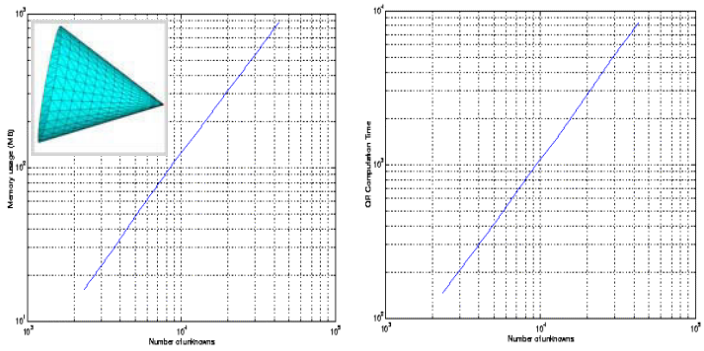

Figure 1: Memory and CPU complexities for the IE-SVD for an open cone, height 20 cm and diameter 20cm on the bottom, scattering example.

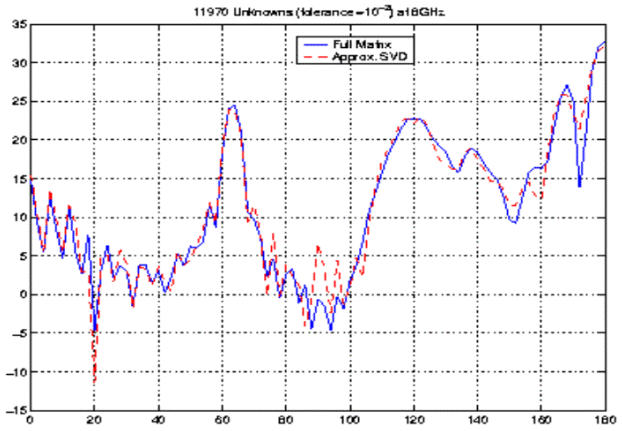

Figure 2: Monostatic RCS results from dual rank SVD algorithm compared to the full MOM results for the cone example with 11,970 unknowns.

Number of Unknowns	Frequnecy (MHz)	Memory (MB)	CPU for SVD Algorithm	Average GMRES Iterations
8,538	100	48.23	6m:38s	56
32,976	300	382.1	1h:2m:25s	37
101,352	600	1975.2	5h:30m:53s	45

Table 1: Computational details of the 2-level SVD algorithm for the Northrop VFY218 airplane.

REFERENCES

[1] S. M. Rao, D. R. Wilton, and A. W. Glisson, "Electromagnetic scattering by surfaces of arbitrary shape," *IEEE Trans. Antennas Propagat.*, vol. AP-30, pp. 409-418, May 1982.

[2] A. F. Peterson, S. L. Ray, and R. Mittra, Computational Methods for Electromagnetics. Piscataway, NJ: IEEE Press, 1998.

[3] S. Kapur, D. E. Long, "IES^3: A Fast Integral Equation Solver for Efficient 3-Dimensional Extraction," ICCAD 1997,pp.448-455.

[4] Ke Chen, "An analysis of sparse approximate inverse preconditioners for boundary integral equations," SIAM J. Matrix Anal. Appl., 22, pp. 1058-1078, 2001.

[5] S. Vavasis, "Preconditioning for boundary integral equations," SIAM J. Matrix Anal. Appl., 13, pp. 905-925, 1992.

[6] W. C. Chew, J.-M. Jin, C.-C. Lu, E. Michielssen, and J. M. Song, "Fast solution methods in electromagnetics, "*IEEE Trans. Antennas Propagat.*, vol. 45, pp. 533-543, Mar. 1997.

COMPUMAG Saratoga Springs, New York USA
July 13 - 17, 2003

Detection of State Variables for Coupled Circuit-Field Problems

Saku Suuriniemi, Jari Kangas, Lauri Kettunen
Tampere University of Technology, Institute of Electromagnetics
P.O. Box 692, FIN-33101 Tampere, Finland
Email: {saku.suuriniemi, jari.kangas, lauri.kettunen}@tut.fi

Abstract— **We study systematical detection of the state variables for a general coupled circuit-field problem that may consist of several disjoint domains for field problems and electric networks. The objective is to cast the problem into a framework whose structures are readily programmable. To couple the field and circuit sides in terms of computable concepts, we employ *homology* theory, which leads to linear algebraic problems.**

Keywords— **Coupled problems, homology, exact homology sequence**

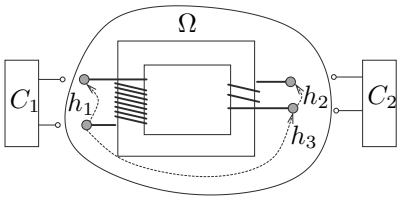

Fig. 1. Transformer as a model problem.

I. Introduction

Our interest is in finding a technique which tackles a general coupled circuit-field problem and naturally translates to software. The properties of topologically non-trivial regions are systematically treated with tools of so-called homology. Their use in the current context has been previously discussed e.g. in [1], [2], [3], [4], [5], together with their intimate connection with analysis of fields.

The approach produces information about the non-trivial topology inside the field-domains, how networks are connected to a certain field domain and how the field-domains and distinct networks are interconnected to form the coupled problem. In order to detect the appropriate state variables for the coupled problem, we need to organize the data into a useful entity. This is accomplished with the *exact homology sequence* [6].

Example 1: Figure 1 shows a simplified model problem, two galvanically isolated circuits connected to a transformer. The integral of $\mathbf{E}$ over the curve h_1 equals to the voltage at the terminals of C_1 and the integral over h_2 to the voltage at the terminals of C_2. They are needed as state variables, but what about the voltage over h_3?

Intuitively, the voltage over h_3 doesn't count, because the circuits are galvanically isolated. However, we aim at automatic computation of coupled circuit-field problem without user intervention, and computers have no intuition. The computer is to solve the potential difference between every two nodes of the circuit problem, including the voltage over h_3. However, the voltage over h_3 is clearly not determined by the circuit. *What is the role of h_3 in automatic computation? What to do with it and how to recognize it automatically?*

II. Problem description

The model problem belongs to the problem class we address with algebraic—programmable—analysis; coupled problem consisting of circuit part C and field problem domain Ω, both possibly in several disjoint components. We assume that both are tessellated into cell complexes (FEM mesh and circuit graph), and call also the complexes C and Ω. Terminals of the circuit are connected to the field problem with connectors $\Gamma = C \cap \Omega$. Components of Ω may be multiterminals, such as the transformer in figure 1. We define Γ^0 such that $\partial\Omega = \Gamma \cup \Gamma^0$ and $\Gamma \cap \Gamma^0$ is one-dimensional.There are n components of circuit and β_0 components of Ω, each component Ω_i with k_i connectors, and they are all connected into one coupled problem.

III. Separation into field and circuit problems

The field part of the problem has to satisfy the following requirements in order to be an appropriate model of a circuit component: i) Magnetic isolation, i.e. no magnetic flux, across $\partial\Omega$, ii) no current flow through Γ^0, and iii) connectors Γ are equipotential surfaces [4]. Inside Ω, the quasistatic Maxwell's equations hold.

The circuit analysis rests on Kirchhoff's voltage and current laws. The voltage law imposes zero electric circulation over the loops of the circuit[1]. Some of these loops may pass through Ω_i, and we need to express the corresponding voltages. The voltage between any two of the k_i connectors in Ω_i can be expressed with a combination of $k_i - 1$ curves[2], if the combinations of the curves have no boundary outside Γ, and they couple any two connectors. These curves are formally a set of generators of the group of *1-cycles*, which are *non-bounding relative to* Γ (i.e. the first relative homology group modulo Γ), $H_1(\Omega, \Gamma)$. It is an example of *relative group*, inherent to the analysis of circuit-field coupled problems [1], [2].

The Kirchhoff current law in Ω is a statement concerning the currents through surfaces of $H_2(\Omega, \Gamma^0)$ [1], [2]. Its close relation to $H_1(\Omega, \Gamma)$ establishes a power equivalence which leads to the concepts of impedance and Thevenin

[1]It suffices to pose this condition on all linearly independent loops.
[2]The concept of potential only makes sense on the boundary $\partial\Omega$, and the curves actually reside on Γ^0 [3].

equivalence. [3], [5]

Example 2: In the model problem of figure 1, we need the voltages $\int_{h_1} \mathbf{E}$ and $\int_{h_2} \mathbf{E}$ to pose the Kirchhoff's voltage law for all loops. The curve h_3 is not needed in expression of any loop, hence its voltage is not determined by any loop of the circuit. The automated computation of the model problem requires at least i) computation of h_1, h_2, and h_3, ii) computation of loops, iii) detection of curve h_3, with indeterminate voltage, iv) solution: computation of voltages over of h_1, h_2 with the voltage over h_3 fixed.

Another example motivates exhaustive analysis:

Example 3: Generally, the computation of h_1, h_2, h_3 differs from computing $H_1(\Omega, \Gamma)$, because the *non-bounding cycles* of $H_p(\Omega)$ add to $H_p(\Omega, \Gamma)$: The group $H_p(\Omega)$ contains cycles, which have zero boundaries—no boundary outside Γ!

IV. Tools for analysis of entire problem

Our problem involves several complexes, Ω_i, Ω, C, and Γ, which contribute to groups needed in circuit analysis, i.e. the loops of the whole problem in $H_1(\Omega \cup C)$, and their segments in $H_1(\Omega, \Gamma)$ and $H_1(\Omega_i, \Gamma)$.

Let A be a complex and B its subcomplex. The following results [6] for relative groups hold for A and B:

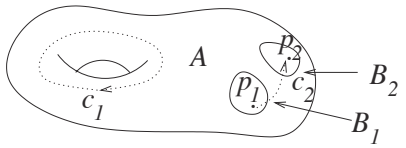

Fig. 2. Example of a complex and its subcomplex.

1. Each element $c \in H_p(B)$ either qualifies as an element $c \in H_p(A)$ or is generated by a boundary $c = \partial_{p+1}\tilde{r}$ of an element $r \in H_{p+1}(A, B)$.

Example 4: In figure 2, a point p_1 at B_1 is a generator of $H_0(B)$. This also generates $H_0(A)$ (if p_1 is chosen, no other point will do anymore). An arbitrary point p_2 at B_2 is $p_2 = p_1 + \partial c_2$ for any curve c_2 from p_1 to p_2. This c_2 is a generator of $H_1(A, B)$.

2. The generators of $H_p(A)$, which are not homologous to an element of $H_p(B)$ constitute elements of $H_p(A, B)$.

Example 5: If there was a circular, annular, or toroidal component of B encircling the hole in A of figure 2, $c_1 \in H_1(A)$ would be homologous to some element of $H_1(B)$. This is not the case. Hence, it is a generator of $H_1(A, B)$: c_1 has no boundary outside B.

3. The elements of $H_p(A, B)$ which do not qualify as elements of $H_p(A)$, have boundaries which generate $H_{p-1}(B)$.

Example 6: $H_p(A, B)$ is generated by $\{c_1, c_2\}$. $c_1 \in H_1(\Omega)$ holds, and example 4 shows why ∂c_2 generates $H_0(B)$.

This triple of results is the *exact homology sequence* [6], and we utilize it to systematically study coupled problems.

We now relate the homological properties of the field problem and the coupled problem: The nonbounding curves which generate $H_p(\Omega, \Gamma)$, generate $H_p(\Omega, C)$ as well, because any modifications to the curves inside C are as irrelevant as the modifications in Γ. The groups are, in a sense, identical. This reasoning extends to $H_p(\Omega \cup C, C)$ as well, and the *isomorphisms* $H_p(\Omega, \Gamma) \cong H_p(\Omega \cup C, C)$ and $H_p(\Omega_i, \Gamma) \cong H_p(\Omega \cup C, (\Omega - \Omega_i) \cup C)$ establish the other cornerstone of our method.

V. Analysis of the model problem

The computation of the field problem-side groups, $H_p(\Gamma), H_p(\Omega), H_p(\Omega, \Gamma), H_p(\Omega_i)$, and $H_p(\Omega_i, \Gamma)$ require homological computation. Only graph theoretic methods are needed at the circuit side, as they yield special cases of homological constructions.

The model problem has no holes through the *field part*, i.e. $H_1(\Omega) = 0$. There is one component in Ω (i.e. $\beta_0 = 1$), with $\dim(H_0(\Gamma))$ =4 connectors, and $\Omega_1 = \Omega$ holds. Then $H_1(\Omega, \Gamma)$ has $\sum_{i=1}^{\beta_0} k_i - 1 = 3$ generators, some of which may be parts of circuit loops.

The *circuit part* C has $\dim(H_1(C)) = z$ loops, and $\dim(H_0(C)) = n = 2$ components. For the whole problem, $\dim(H_0(\Omega \cup C)) = 1$ holds. From the isomorphism $H_1(\Omega, \Gamma) \cong H_1(\Omega \cup C, C)$ we know that $\dim(H_1(\Omega \cup C, C))$ equals to 3. There are $(\sum_{i=1}^{\beta_0} k_i - 1) - n + 1 + z = z + 2$ independent circuit loops which generate $H_1(\Omega \cup C)$, and 2 of these pass through Ω.

Two loops of $H_1(\Omega \cup C)$ pass through Ω_1, and we can project these loops onto the elements of $H_1(\Omega_1, \Gamma)$. Whenever a loop contains an element of $H_1(\Omega_1, \Gamma)$, the voltage over that element can be deduced with KVL from a loop completed in $(\Omega - \Omega_1) \cup C$. Because $\dim(H_1(\Omega_1, \Gamma)) = 3$, but two loops pass through Ω_1, one generator of $H_1(\Omega_1, \Gamma)$, h_3, corresponds to an indeterminate voltage[3]. The assigned voltage over this generator adds a link between the two components of $(\Omega - \Omega_1) \cup C$, lowering $\dim(H_0((\Omega - \Omega_1) \cup C))$ to one. In the general case, voltages are assigned until $\dim(H_0((\Omega - \Omega_i) \cup C)) = 1$ holds for every i.

The analysis illustrates the use of exact homology sequence for coupled problems. The technique enables us to detect the appropriate state variables and express the effect of the assigned voltages in precise terms.

References

[1] Pierre E. Conner, "The Neumann's problem for differential forms on Riemannian manifolds," *Memoirs of the AMS*, vol. 20, 1956.

[2] Peter Robert Kotiuga, *Hodge decompositions and computational electromagnetics*, Ph.D. thesis, McGill University, Montréal, 1984.

[3] Alain Bossavit, "Most general 'non-local' boundary conditions for the Maxwell equations in a bounded region," in *Proceedings of ISEF'99 -9th Int. Symp. Elec.magn. fields. in Elec. Eng.*, Pavia, Italy, 1999.

[4] Lauri Kettunen, "Fields and circuits in computational electromagnetism," *IEEE Transactions on Magnetics*, vol. 37, no. 5, September 2001.

[5] Timo Tarhasaari and Lauri Kettunen, "Topological approach to computational electromagnetism," in *Geometric Methods for Computational Electromagnetics*, Fernando L. Teixeira, Ed., Cambridge, Mass., 2001, number 32 in PIER, EMW Publishing.

[6] James R. Munkres, *Elements of algebraic topology*, Perseus Books, Cambridge, Mass., 1984.

[3]More generally, the detection is a matter of linear algebra: Even if e.g. h_1 was not directly produced by the homological computation, one could express it with a linear combination of the generators.

A Neural Network Approach for the Differentiation of Numerical Solutions of 3D Electromagnetic Problems

G. Capizzi, S. Coco, C. Giuffrida and A. Laudani
DIEES, University of Catania
Viale A. Doria 6
Catania, I-95125, Catania
alaudani@dees.unict.it

Abstract – **A novel neural network (NN) approach is presented to compute accurately derivatives of numerical solutions to 3D electromagnetic problems. The adopted NN is a Multi Layer Perceptron, whose training is performed off-line by employing a class of suitably selected polynomial functions. The desired degree of accuracy can be chosen by the user by selecting the appropriate order of the training polynomials. The on-line utilization of the trained NN allows us to obtain accurate results with a negligible computational cost Comparative examples of differentiation performed both on analytical functions and FE solutions are given in order to illustrate the computational advantages.**

Introduction

The differentiation of numerical solutions to 3D electromagnetic problem is often used in post-processing for the evaluation of typical local and global quantities, such as forces, energy, charges and others. Several techniques have been developed to evaluate accurate estimates of derivatives even in case of rough numerical solutions, but some limitations make these methods either not easily utilizable, because of stringent hypotheses on which they are based, or not easily implementable and computationally expensive [1][2][3].

In this paper a new procedure based on a neural approach is illustrated to compute accurate estimates of derivatives of numerical solutions to 3D Electromagnetic problems at an arbitrary point P, exploiting the knowledge of the values of the solution at a few points, in the neighbourhood of point P.

An important feature of this approach is that the training of the neural network is performed off-line by employing a class of suitably selected polynomial functions, in such a way that the desired degree of accuracy of the neural model is established during the training phase, by choosing the appropriate degree of the training polynomials. The on-line utilization of the trained ND allows us to obtain accurate results with a negligible computational cost. A further advantage of this neural model is its easy implementation in existing post-processing modules.

The MLP NN differentiator

The neural differentiator is based on a Multi Layer Perceptron (MLP) neural network and foresees as inputs the values of the function at some selected points belonging to the neighbourhood of an arbitrary point P and as output its derivatives at P.

The positioning of the input points around P has been chosen on the basis of simplicity and uniformity of coverage by using a minimum number of input points. Satisfactory results have been achieved by using the point disposition shown in fig. 1.

After several experiments on some tentative MLP networks employing various different topologies, the network architecture was established; it foresees 3 hidden layers suitably interconnected.

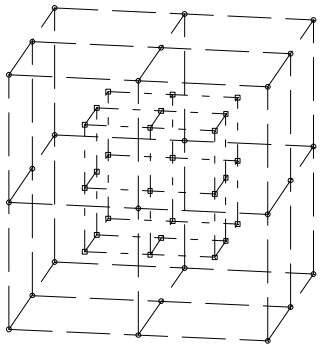

Fig. 1. Disposition of the Neural Network Differentiator input points.

The neural network has been trained off-line by providing to it a set of suitably chosen polynomial functions P(x, y, z) in 3D space in such a way that the neural network learns the relationship between the polynomial function on the input points and its derivatives in P.

An advantage of this off-line training is its modularity with respect to the polynomial functions degree and flexibility in pattern generation, allowing us to reduce effectively the number of training functions required to reach a target precision. The details of MLP NN structure and its training phase will be described in the full paper.

The precision reachable by this neural differentiator depends on the order of the polynomials used in the training phase, as will be shown in the next section.

Results

The trained neural differentiator (in which the weights are already established during the training) is used as a traditional post-processing operator acting on data from either a numerical solution or a known analytical function.

The accuracy of MLP neural differentiator (ND) has been tested first by comparing its results against the analytical derivatives of the following function

$$f(x,y,z)=\frac{1}{x^2+y^2+z^2}$$

In order to assess the achievable level of accuracy of the neural differentiator various MLP ND evaluations employing a different number of input points have been performed. In particular the values of the first derivatives of the above function with respect to spatial coordinates at about a thousand points randomly assigned have been analytically computed and then compared with those evaluated by using three different MLP NDs with an increasing number of input points.

Table I reports the derivatives relative error and its mean value in correspondence of test points for the three MLP NDs trained with polynomials up to 4th degree employing a different number of input points (34, 40, 52). As expected, the degree of accuracy increases by adopting an higher number of input points.

Table II reports the maximum and average errors in derivatives computation for four MLP NDs having each a fixed number of input points (52), but trained by using 1st, 2nd, 3rd and 4th order polynomial functions respectively. The results show that the level of accuracy is closely linked to the degree of the polynomials used during training.

TABLE I – AVERAGE AND MAXIMUM ERROR IN DERIVATIVES COMPUTATION FOR MLP ND TRAINED WITH POLYNOMIALS UP TO 4TH DEGREE EMPLOYING DIFFERENT INPUT POINTS

	Average error	Maximum error
34 points	$1.57 \cdot 10^{-1}$	$3.23 \cdot 10^{-1}$
40 points	$5.40 \cdot 10^{-5}$	$1.05 \cdot 10^{-4}$
52 points	$2.10 \cdot 10^{-5}$	$7.18 \cdot 10^{-5}$

TABLE II – AVERAGE AND MAXIMUM ERROR IN DERIVATIVES COMPUTATION FOR MLP ND EMPLOYING 52 POINTS TRAINED RESPECTIVELY WITH 1ST, 2ND, 3RD AND 4TH DEGREE POLYNOMIAL FUNCTIONS

	Average error	Maximum error
Up to 1st degree	$0.73 \cdot 10^{-2}$	$1.80 \cdot 10^{-2}$
Up to 2nd degree	$3.40 \cdot 10^{-3}$	$0.68 \cdot 10^{-3}$
Up to 3rd degree	$2.69 \cdot 10^{-4}$	$5.17 \cdot 10^{-4}$
Up to 4th degree	$2.10 \cdot 10^{-5}$	$7.18 \cdot 10^{-5}$

Hereafter the application of the trained differentiator to rough FE solutions for the computation of local electromagnetic quantities is presented. This example regards the evaluation of the electric field inside the collector region of a travelling wave tube (TWT), a vacuum electron device used as RF amplifier. In the collector region, recovering the spent beam energy, a steady state electromagnetic analysis is performed involving the 3D FE solution of a Poisson equation for the scalar electric potential having as source term the space charge density of the spent electron beam. The analysed collector, consisting of only one asymmetric stage, has been discretized by using a mesh of 5880 tetrahedral finite elements. The electron trajectories shown in figure 3 have been computed by COCA, a tool appositely developed by the authors for the 3D electromagnetic simulation of TWT collectors [4]. These trajectories define the space-charge source term of the Poisson equation. Two finite element solutions were computed: the first one related to a discretization employing 1st order tetrahedra and the other employing 2nd order tetrahedra.

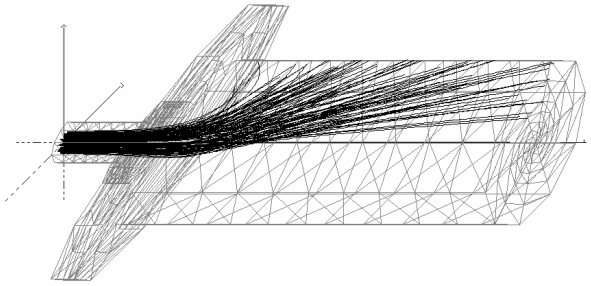

Fig. 2. The analysed TWT collector region, including 3D space charge source term.

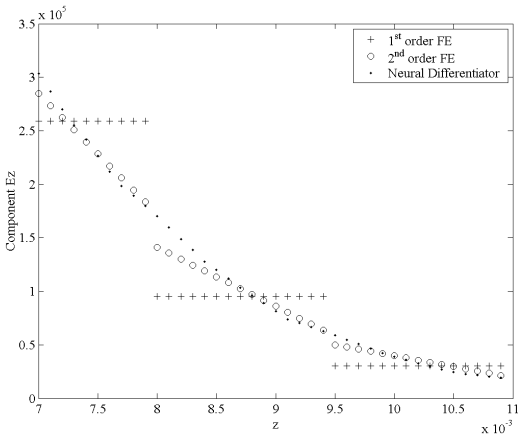

Fig. 3. Z-axis longitudinal electric field values computed by means of FE solution direct differentiation and MLP Neural Differentiator post-processing approach.

Figure 3 shows the results of the computation of the interesting local quantity, the on-axis longitudinal (z-directed) electric field E_z, performed by following two different approaches, the first by using straightforward differentiation of the 1st order and 2nd order FE solutions and the other by applying a MLP Neural Differentiator to the rough 1st order FE solution. These latter results refer to evaluations performed by using 52 input points disposed as shown in fig. 1. Even in such a non-trivial problem, exhibiting 3D space charge distribution and complicated geometry, the increase of accuracy due to utilization of MLP ND is remarkable.

REFERENCES

[1] D. Omeragic and P. P. Silvester, "Progress in Differentiation of Approximate Data", IEEE Antennas and Propagation Magazine, Vol. 38, No. 1, Feb. 1996.

[2] S. Coco and C. Ragusa, "Accurate Computation of Local and Global Electrostatic Quantities from FE Solutions", IEEE Trans. on Magnetics, Vol. 36, N. 4, July 2000.

[3] S. Coco and A. Laudani, "Numerical Differentiation of Laplacian 3D FE Solutions by using Regular Polyhedra Quadrature of Poisson Integrals", IEEE Trans. on Magnetics, Vol. 37, N. 5, Sept. 2001.

[4] S. Coco, F. Emma, A. Laudani, S. Pulvirenti, and M. Sergi, "COCA: A novel 3D FE simulator for the design of TWT's multistage collectors", IEEE Trans. Electron Devices, vol. 48, pp. 24-31, Jan. 2001.

On the Convergence of Transient Eddy-Current Problems

B. Weiß, O. Bíró
IGTE
University of Technology, Graz
Kopernikusgasse 24 - 8010 Graz - Austria
email:weiss@igte.tu-graz.ac.at - biro@igte.tu-graz.ac.at

***Abstract*— In the computation of eddy current fields with edge elements it is known that the numerical stability can be rather inferior for the A^*-formulation, in comparison to that of the A, v-formulation. In this paper, the differences of the two formulations with regard to the convergence of an iterative solver will be pointed out. The results is a suggestion about the preconditioner for the conjugate gradient method.**

INTRODUCTION

In the numerical analysis of three-dimensional eddy current problems, the finite element method (FEM) with edge elements is very common. Various formulations for the vector and the scalar potential have been reviewed in [1]. In the transient case, time stepping is used for the time discretization. In every time step a large system of equations has to be solved.

Two common formulations for the eddy current problem are the A^*-formulation and the A, v-formulation. The advantage of the A, v-formulation in FEM applications using iterative solvers like a preconditioned conjugate gradient method (PCG) is its good numerical stability. For the A^*-formulation, the numerical stability can be rather inferior.

In high-frequency problems, some small negative eigenvalues arise which deteriorate the convergence rate [2]. In case of quasi-static fields, it has been shown, that the good convergence of the A, v-formulation is due to the preconditioning of the system matrix [3].

In this paper, we consider the case of transient eddy current fields. The different behavior of the PCG-method for the two formulations is analyzed. A closer look is given to the kernel of the curl-operator. As a preconditioner, the symmetric Gauss-Seidel iteration is used (SGSCG).

FEM FORMULATIONS

The A^*-formulation

One possibility to describe the eddy current field is by means of a modified vector potential $\boldsymbol{A}^*$ where $\boldsymbol{B} = \operatorname{curl}\boldsymbol{A}^*$ and $\boldsymbol{E} = -\frac{\partial}{\partial t}\boldsymbol{A}^*$. This formulation leads to the differential equation in the region Ω

$$\operatorname{curl}(\nu \operatorname{curl}\boldsymbol{A}^*) + \sigma \frac{\partial}{\partial t}\boldsymbol{A}^* = 0 \qquad \text{in } \Omega\,. \tag{1}$$

Approximating the modified vector potential by edge basis functions and applying Galerkin techniques to (1) results in the following equation:

$$\left(\operatorname{curl}\boldsymbol{N}_i, \nu \operatorname{curl}\boldsymbol{A}_h^*\right) + \left(\boldsymbol{N}_i, \sigma \frac{\partial}{\partial t}\boldsymbol{A}_h^*\right) = \left(\operatorname{curl}\boldsymbol{N}_i, \boldsymbol{T}_0\right) \tag{2}$$

for $i = 1, 2, \ldots, n_e$ with $\boldsymbol{A}_h^*$ being the edge element discretization of $\boldsymbol{A}^*$ and $(\boldsymbol{a}, \boldsymbol{b}) = \int_\Omega \boldsymbol{a} \cdot \boldsymbol{b} d\Omega$.

The A, v-formulation

In case of the A, v-formulation, an additional modified electric scalar potential v is introduced as $\boldsymbol{E} = -\frac{\partial}{\partial t}\boldsymbol{A} - \operatorname{grad}\frac{\partial}{\partial t}v$. The differential equations for this formulation are:

$$\operatorname{curl}(\nu \operatorname{curl}\boldsymbol{A}) + \sigma \frac{\partial}{\partial t}\boldsymbol{A} + \sigma \operatorname{grad}\frac{\partial}{\partial t}v = \boldsymbol{0} \qquad \text{in } \Omega\,, \tag{3}$$

$$-\operatorname{div}\left(\sigma \frac{\partial}{\partial t}\boldsymbol{A} + \sigma \operatorname{grad}\frac{\partial}{\partial t}v\right) = 0 \qquad \text{in } \Omega\,. \tag{4}$$

Using edge basis functions for the vector potential and nodal basis functions for the scalar potential, the Galerkin equations can be written as

$$\left(\operatorname{curl}\boldsymbol{N}_i, \nu \operatorname{curl}\boldsymbol{A}_h\right) + \left(\boldsymbol{N}_i \cdot \sigma \frac{\partial}{\partial t}\boldsymbol{A}_h\right) + \left(\boldsymbol{N}_i \cdot \sigma \operatorname{grad}\frac{\partial}{\partial t}v_h\right) = \left(\operatorname{curl}\boldsymbol{N}_i, \boldsymbol{T}_0\right), \qquad i = 1, 2, \ldots, n_e \tag{5}$$

$$\left(\operatorname{grad}N_i \cdot \sigma \frac{\partial}{\partial t}\boldsymbol{A}_h\right) + \left(\operatorname{grad}N_i \cdot \sigma \operatorname{grad}\frac{\partial}{\partial t}v_h\right) = 0, \qquad i = 1, 2, \ldots, n_n \tag{6}$$

where v_h is the approximation of the scalar potential.

Time discretization

The time discretization with the backward-Euler scheme leads to a system of equations

$$A\boldsymbol{x}^{(n)} + \frac{1}{\Delta t} B\boldsymbol{x}^{(n)} = \frac{1}{\Delta t} B\boldsymbol{x}^{(n-1)} + \boldsymbol{b}^{(n)}, \tag{7}$$

where Δt is the length of a time step, $\boldsymbol{x}^{(n)}$ is the vector of unknowns at the time instant $t = n\Delta t$ and $\boldsymbol{b}^{(n)}$ is the right hand side vector.

KONVERGENCE OF THE PCG

A factor $\phi = \frac{h^2 \sigma \mu}{\Delta t}$ can be defined to describe the ratio of the norms of the matrices A and B, where h is a mesh size parameter. In Fig. 1 the dependency of the number of iterations on ϕ is shown.

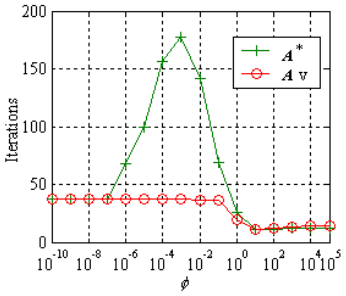

Fig. 1. Number of iterations vs. ϕ.

The distribution of the eigenvalues is similar for both formulations except the zero eigenvalues, which only appear in the A, v-formulation. In Fig. 2, the eigenvalues of the system matrix for different ϕ are shown. Since the eigenvalues of the system matrices arising in the A^*- and the A, v-formulations are similar, the good convergence of the latter one is the consequence of preconditioning [3].

In each iteration step of the PCG algorithm, the error of an initial value is reduced. Expanding the new error in terms of the eigenvectors of the system matrix, the reduction of the components of the error, corresponding to the eigenvectors can be shown (Fig. 3).

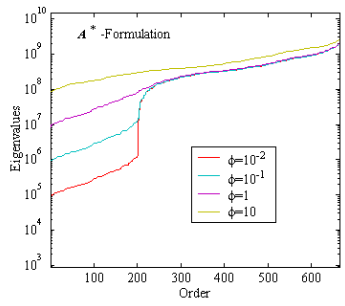

Fig. 2. Eigenvalues for different ϕ. The upper curve belongs to $\phi = 10$, the lowest one to $\phi = 10^{-2}$

The reduction of the eigenvectors, belonging to the first 200 low eigenvalues is very poor. For the A^*-formulation, these eigenvectors describe the kernel of the curl-operator. They are responsible for the slow convergence.

For the A, v-formulation, the first 200 eigenvectors describe the kernel of the system matrix arising from (5) and (6). These functions can be written as $\sigma A + \sigma \mathrm{grad} v = 0$ [4]. It is clear that $A \in \ker(\mathrm{curl})$. These functions don't have any influence on the convergence since they are not in the range of the system matrix.

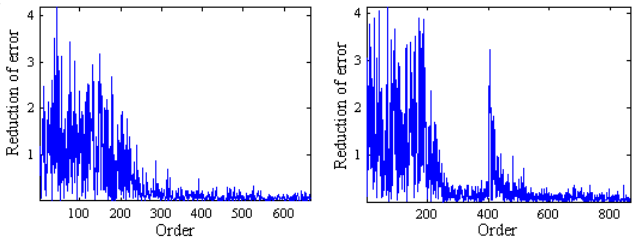

Fig. 3. Ratio of the error components between two consecutive iteration steps versus order of the components. Left: A^*-formulation, right: A, v-formulation.

The next 200 eigenvectors describe the divergence-free current density $J = -\sigma \frac{A}{\Delta t} - \sigma \mathrm{grad} \frac{v}{\Delta t}$. It can be seen, that the divergence-free condition in (6) combines the scalar potential with the vector potential in a weak form. But this is done only for vector functions which can be described as a gradient of a scalar function. This means that these vector functions are part of the kernel of the curl-operator.

Moreover, (6) has the same weak form as the scalar Laplace equation, which works very fine with iterative solvers.

To sum it up it can be said that in one iteration step, (6) successfully reduces the error of the kernel of the curl-operator, while (5) solves $(\mathrm{curl} N_i, \nu \mathrm{curl} A_h) + \left(N_i \cdot \sigma \frac{A_h}{\Delta t} \right) = (\mathrm{curl} N_i, T_0)$ for $N_h, A_h \notin \ker(\mathrm{curl})$. Both parts, $A \notin \ker(\mathrm{curl})$ and $A \in \ker(\mathrm{curl})$ are taken into consideration, resulting in an overall good convergence of the A, v-formulation.

Due to these facts, a preconditioner for the A^*-formulation should also take the kernel of the curl-operator into consideration.

REFERENCES

[1] O. Bíró, "Edge element formulations of eddy current problems," *Computer methods in applied mechanics and engineering*, no. 169, pp. 391-405, Elsevier, 1999.

[2] R. Dyczij-Edlinger, O. Bíró, "A Joint Vector and Scalar Potential Formulatiom for Driven High Frequency Problems Using Hybrid Edge and Nodal Finite Elements," *IEEE Trans. Microwave Theory Tech.*, vol. 44, no. 1, pp.15-23, January 1996.

[3] H. Igarashi, T. Honma, "On Convergence of ICCG Applied to Finite-Element Equation for Quasi-Static Fields" *IEEE Trans. Magn.*, vol. 38, no. 2, pp. 565-568, March 2002.

[4] B. Weiß, O. Bíró, "Multigrid for transient 3d eddy current analysis" *Proceedings of the 10th International IGTE Symposium*, September 2002.

Using Filters to Design Absorbing Boundary Conditions for High-Order CEM

Michael D. White† and Miguel R. Visbal‡
Air Force Research Laboratory, AFRL/VAAC, Building 146B,
2210 Eighth Street, Wright-Patterson AFB,
OH 45433-7521, USA
Michael.White@wpafb.af.mil

Abstract **– Sharp low-pass filters used to stabilize high-order numerical algorithms have been adapted to provide a simple yet robust absorbing boundary with negligible impact on the interior solution. By taking advantage of energy transfer to high frequencies caused by rapidly stretched meshes, the artificially reflected waves are annihilated while preserving the content in the region of interest.**

INTRODUCTION AND THEORY

Accurate simulation of wave propagation in different materials and environments is of great import to both civilian and military interests. Due to large spatial scales relative to typical wavelengths of propagation, it is increasingly desirable to design methods that have low dispersion error and little or no dissipation. One approach to this is through the use of high-order compact-difference schemes [1]. These schemes are typically 4th-order accurate or higher and exhibit spectral-like resolution [2]. The schemes lack of dissipation leads them to have a tendency toward spurious high-frequency oscillations and instability. This stability problem has typically been addressed by applying sharp, high-order, low-pass filters designed to destroy the high-frequency spurious waves.

Vichnevetsky studied the behavior of a smooth solution as it passes through a sudden grid coarsening [3]. His analysis indicated that although total energy is preserved at the interface of the two grids, a significant portion of the energy is reflected. This reflected energy was composed primarily of modulated odd-even modes. This artificial reflection propagates with a negative group velocity and, if left unchecked, has the potential to contaminate the entire solution.

Visbal and Gaitonde used this idea to construct a simple absorbing boundary condition for acoustic and other fluid dynamics problems [4]. By employing a rapid rate of stretching, a significant amount of energy can be reflected back into the interior of the domain. Provided this energy is deposited in the high-frequency modes, the baseline low-pass filters already being used to stabilize the solution will quickly dissipate it. Since the buffer zone is rapidly stretched, the filter acts to quickly dissipate the transmitted wave as well. Thus the proposed boundary condition eliminates the need for more sophisticated (and likely less robust) formulations.

†M. D. White is a visiting scientist, Ohio Aerospace Institute (OAI/ICOMP).
‡M.R. Visbal is a Technical Area Leader of AFRL/VAAC.

IMPLEMENTATION AND RESULTS

Filter Construction

If a typical component of the solution at point i is given by ϕ_i, then the filtered value $\hat{\phi}_i$ satisfies:

$$\alpha_f \hat{\phi}_{i-1} + \hat{\phi}_i + \alpha_f \hat{\phi}_{i+1} = \sum_{n=0}^{N} \frac{a_n}{2}\left(\phi_{i+n} + \phi_{i-n}\right) \tag{1}$$

where α_f is a free parameter subject to the constraint that its absolute magnitude be less than ½. Equation (1) is solved by the use of a standard tri-diagonal solver. The coefficients for the right hand side may be calculated using the values given in Table I. While general boundaries may require the use of high-order biased stencils, in the absorbing boundary region one may simply step down the filter to second order as the edge of the domain is approached.

Examples

The one-dimensional pulse is a good example to demonstrate the effect of the grid stretching and filters. The pulse is defined as a simple Gaussian.

$$\left.\begin{aligned} E_z(x,t=0) &= e^{-50x^2} \\ H_y(x,t=0) &= e^{-50x^2} \end{aligned}\right\} \tag{2}$$

TABLE I. COEFFICIENTS FOR INTERIOR FILTERS

Coef.	Scheme F2	F4	F6	F8
a_0	$\frac{1+2\alpha_f}{2}$	$\frac{5+6\alpha_f}{8}$	$\frac{11+10\alpha_f}{16}$	$\frac{93+70\alpha_f}{128}$
a_1	$\frac{1+2\alpha_f}{2}$	$\frac{1+2\alpha_f}{2}$	$\frac{15+34\alpha_f}{32}$	$\frac{7+18\alpha_f}{16}$
a_2	0	$\frac{-1+2\alpha_f}{8}$	$\frac{-3+6\alpha_f}{16}$	$\frac{-7+14\alpha_f}{32}$
a_3	0	0	$\frac{1-2\alpha_f}{32}$	$\frac{1-2\alpha_f}{16}$
a_4	0	0	0	$\frac{-1+2\alpha_f}{128}$

The scheme in this case utilized a 4th-order explicit centered scheme in space and a standard 4th-order Runge-Kutta in time. The time-step was set equal to the smallest spatial step. At x=2, the grid was stretched geometrically with a factor of 1.3. A sixth order filter was used and the outer boundary condition at the end of the absorbing region (buffer zone) was a simple, 1st-order characteristic.

Fig. 1 demonstrates quite clearly that without the filter, the abrupt jump in the metrics will lead to a spurious high-frequency reflected wave. With the filter however (Fig. 2), the wave maintains its shape until entering the buffer zone where it is quickly damped.

A more complicated case is shown for a pulse reflecting off a perfectly magnetic conducting cylinder. This case used 6th-order compact-differencing with 8th-order filters. Fig. 3 shows that the pulse retains its qualities in the region of interest while the solution is damped in the absorbing region.

CONCLUSIONS

By using mesh stretching and sharp filters, a simple absorbing zone can be created without polluting the content in the region of interest. The boundary condition is effective even when the outgoing waves are not normal to the boundary itself. Thus, through energy transfer into high-frequency odd-even modes and the annihilation of those modes through the use of a filter, a simple yet highly effective absorbing boundary region may be implemented.

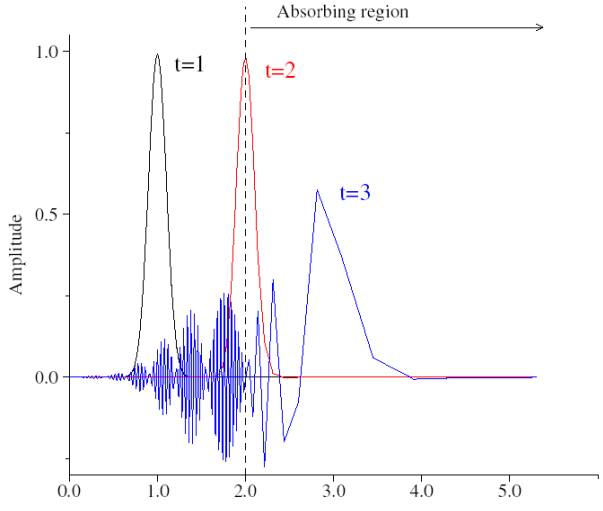

Fig. 1. Propagation of Gaussian Pulse from constant spacing onto a geometrically stretched mesh without the use of a filter.

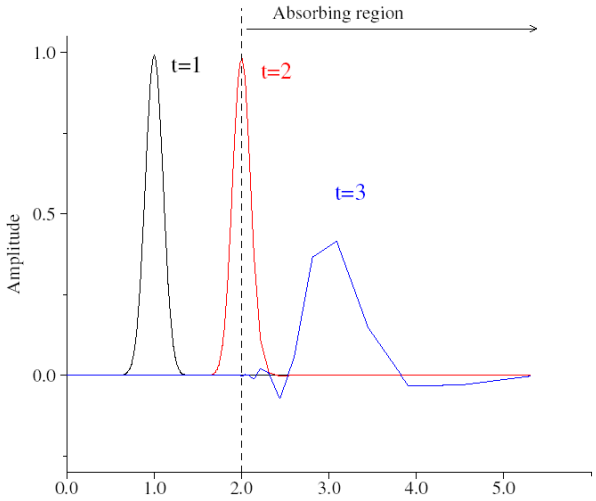

Fig. 2. Propagation of Gaussian Pulse from constant spacing onto a geometrically stretched mesh using an implicit filter.

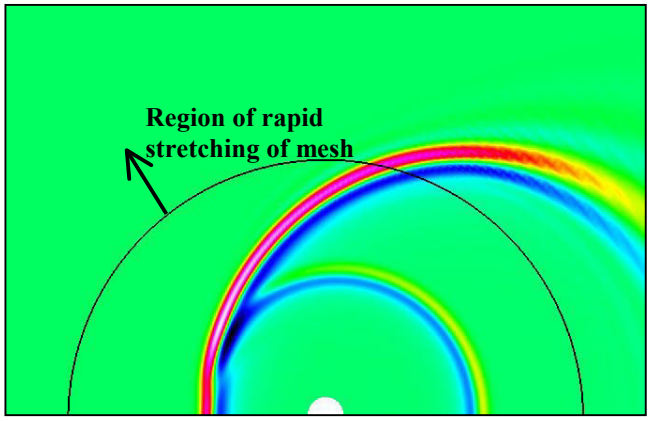

Fig. 3. EM Pulse scattering by a circular cylinder.

REFERENCES

[1] J. S. Shang, "High Order Compact-Difference Schemes for Time-Dependent Maxwell Equations," *J. of Comp. Phys.*, vol. 153, pp. 312-333, 1999.

[2] S. K. Lele, "Compact finite difference schemes with spectral-like resolution," *Journal of Comp. Phys.*, vol. 103, pp. 16-42, 1992.

[3] R. Vichnevetsky, "Propagation through numerical mesh refinement for hyperbolic equations," *Math. and Comp. in Simulation*, vol. 23, pp. 344-353, 1981.

[4] M. R. Visbal and D. V. Gaitonde, "Very high-order spatially implicit schemes for computational acoustics on curvilinear meshes," *J. of Comp. Acoustics*, vol. 9, No. 4, pp. 1259-1286, 2001

Author Index

Author Index

Author Index

Author Index

The 14th COMPUMAG Conference on the Computation of Electromagnetic Fields will be held in Saratoga Springs, NY USA, from July 13 to 18, 2003.

Previous COMPUMAG Conferences were held at
Oxford, UK · 1976
Grenoble, France · 1978
Chicago, USA · 1981
Genoa, Italy · 1983
Fort Collins, USA · 1985
Graz, Austria · 1987
Tokyo, Japan · 1989
Sorrento, Italy · 1991
Miami, USA · 1993
Berlin, Germany · 1995
Rio de Janeiro, Brazil · 1997
Sapporo, Japan · 1999
Evian, France · 2001

www.compumag2003.com

For more information, please e-mail the Secretariat for Compumag 2003 at secretariat@compumag2003.com

Chairman
Dr. Sheppard Salon,
Rensselaer Polytechnic Institute

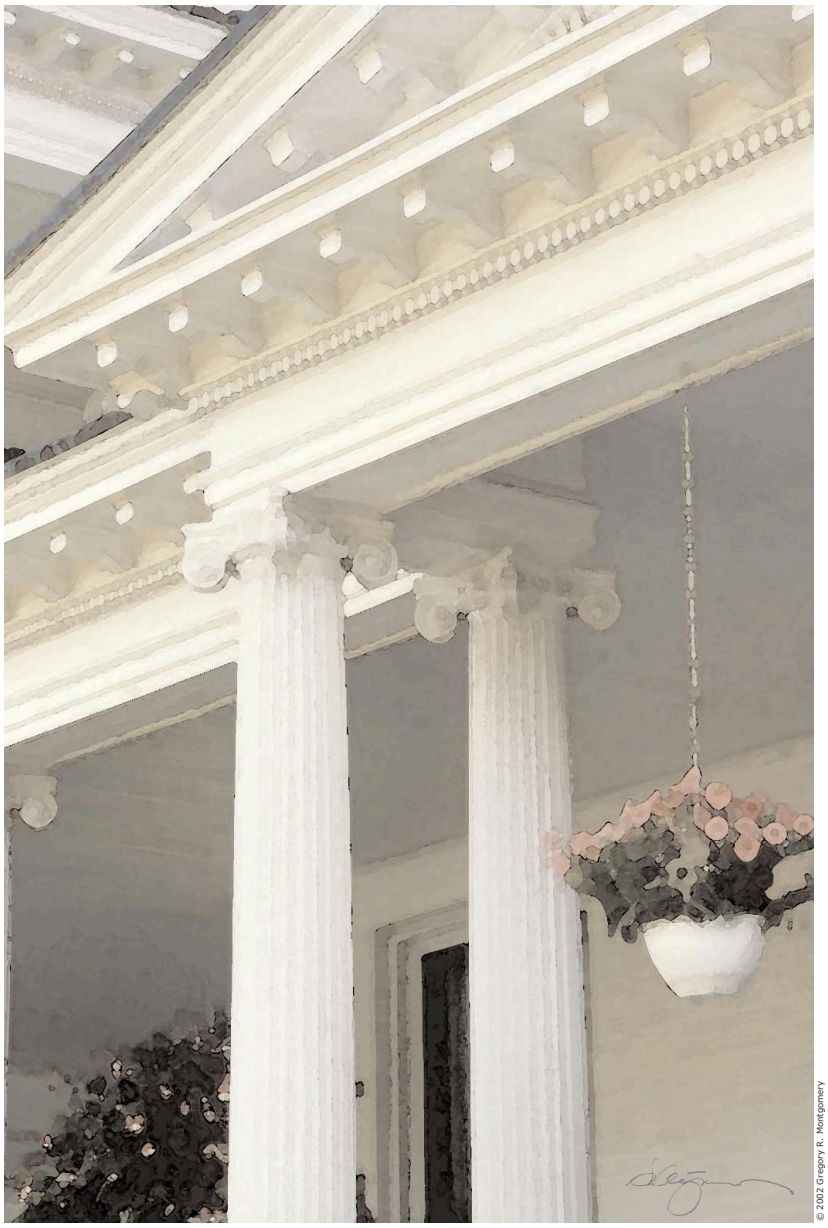

COMPUMAG 2003

Conference on the Computation of Magnetic Fields

Saratoga Springs, NY, USA

July 13–18, 2003